

Science

Science
Advances

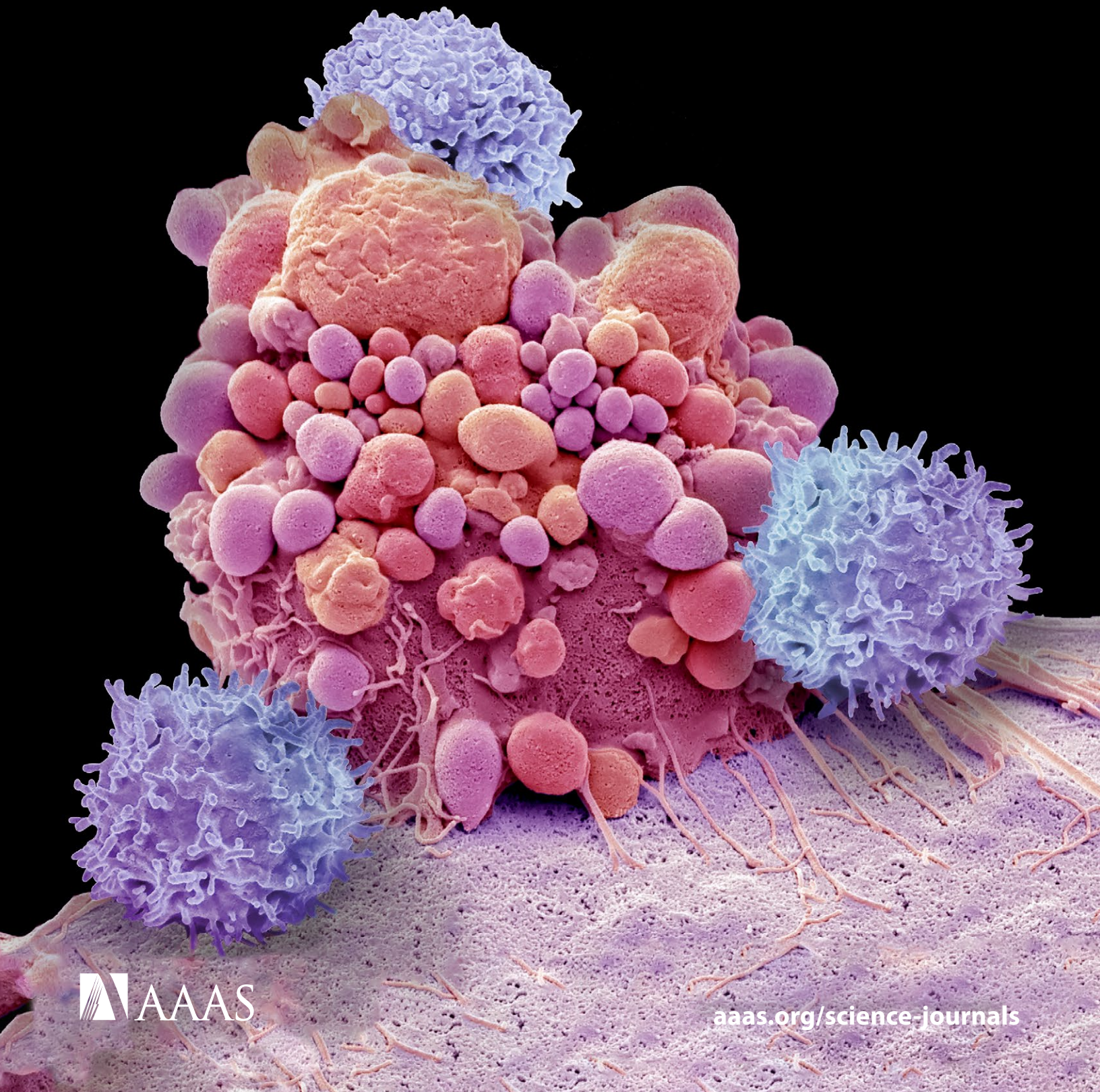
Science
Immunology

Science
Signaling

Science
Translational
Medicine

[SPECIAL EDITION]

CANCER



AAAS

aaas.org/science-journals



GemPharmatech
www.gempharmatech.com

GemPharmatech Co., Ltd. (GPT), currently operating both in China and United States, is a leading international company focusing on mouse model development, production and services. We are dedicated to support the biomedical research and pharmaceutical R&D. GPT provides one-stop solutions related to mouse model.

5,000+
Annual Capacity of Mouse Model Generation

10,000+
In-house Animal Models

140,000+
Total Cages in SPF Facility

AAALAC-Accredited Facility

Knock-Out All Project (KOAP) Mice Resources:

aiming to generate cKO/KO mouse strains for over 20,000 protein-coding genes in three years

ACE2, ALKBH1, C3AR1, CGAS, DNM1L, FNDC5, GPNMB, GPX4, IFNAR1, METTL3, NAT10, NSUN2, OPA1, SENP1, TET3, TLR2, TMEM173, VDR, etc.

Search your ideal models via signal pathways:
<http://pathway.gempharmatech.com:8082/pathway>

Immuno-Deficiency Mice and Derivatives:

severe immuno-deficiency mice displaying excellent engraftment of human tissue

NCG, NCG-B2M-KO, NCG-hIL15, NCG-X (No irradiation required), HuPBMC-NCG, HuHSC-NCG, etc.

Humanized I/O Mice Resources:

single, double, and triple knock-in models covering almost all published human immune checkpoint targets

Bispecific Antibody Evaluation: BALB/c-hCD3e

Humanized Immune Checkpoint: PD1, PDL1, CTLA4, 4-1BB, TIGIT, TIM3, LAG3, SIGLEC9, SIGLEC15, OX40, CD47/SIRPa, CD73, VISTA, CSF1R, etc.

GemPharmatech

*Support disease studies with
right animal models*

Web: www.gempharmatech.com

Tel: +86 (025) 5864-1508 China +1 (857) 600-6638 USA

E-mail: globalservice@gempharmatech.com

The background features several glowing, circular motifs resembling viruses or cells. These motifs have a red outer ring with small spikes and a blue/orange interior with a grid pattern. They are surrounded by numerous thin, glowing orange lines radiating outwards, creating a sense of motion and energy.

immunoSEQ®

The Power to Propel Your Research

Illuminate the properties and dynamics of the immune repertoire with the quantitative power of the immunoSEQ assay. In our lab or yours, our proven solution elucidates the breadth and depth of T- and B-cell receptors to help you interpret the vast immune system with clarity. Adaptive Biotechnologies champions your research so you can accelerate your path to discovery.

Set your research in motion at AdaptiveBiotech.com

WE WRITE THE FUTURE OF DIGITAL PCR



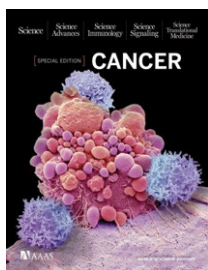
Introducing the fastest track to discovery

Bio-Rad has set the standard for digital PCR since 2011. This year, we raise the standard — fully automated multiplexed digital PCR. The new QX ONE Droplet Digital PCR (ddPCR) System integrates partitioning, amplification, and four-color detection into a single high-throughput experience that delivers superior precision, sensitivity, and absolute quantification.

Take an interactive first look at bio-rad.com/info/QXONE

BIO-RAD

SPECIAL EDITION: Cancer



Select research published in *Science*, *Science Advances*, *Science Immunology*, *Science Signaling*, and *Science Translational Medicine*

Recent developments in the fast-moving area of cancer research give us reason to hope for the future. This collection of research papers from five members of the *Science* family of journals highlights advances in improving immunotherapies, enhancing drug delivery, identifying new therapeutic targets, understanding the tumor microenvironment, and improving patient responses.

Image: Science Source/STEVE GSCHMEISSNER

All *Science* family journals are Green Open Access with the exception of *Science Advances* which is Gold Open Access.

© 2020 by The American Association for the Advancement of Science.
All Rights Reserved.



Editor-in-Chief
H. Holden Thorp, Ph.D.
Science family of journals
AAAS, Washington, DC

Science | AAAS

Science is a leading outlet for scientific news, commentary, and cutting-edge research. The journal publishes original peer-reviewed research across the sciences, with articles that consistently rank among the most cited in the world.

Editors

Lisa D. Chong, Ph.D.
Valda J. Vinson, Ph.D.
Jake S. Yeston, Ph.D.

Cancer Editors

Priscilla N. Kelly, Ph.D.
Paula A. Kiberstis, Ph.D.

Science Advances | AAAS OPEN ACCESS

Science Advances is the digital, open access expansion of *Science* magazine. The journal publishes significant, innovative original research that advances the frontiers of science across a broad range of disciplines, from bioscience and medicine to neuroscience, physics, ecology, and material sciences.

Editor

Ali Shilatifard, Ph.D.

Deputy Editors

Lynden Archer, Ph.D.
Julia Chan, Ph.D.
Aaron Clauset, Ph.D.
Juan de Pablo, Ph.D.
Dale Dorset, Ph.D.
Karen Gleason, Ph.D.
Douglas Green, Ph.D.
Kip Hodges, Ph.D.
Jeremy Jackson, Ph.D.
Mietek Jaroniec, Ph.D.
Alexandra Joyner, Ph.D.
Jonathan Katz, Ph.D.

OPEN ACCESS

Science Immunology | AAAS

Science Immunology publishes original, peer-reviewed, science-based research articles that report critical advances in all areas of immunological research, including important new tools and techniques.

Editor

Ifor Williams, M.D., Ph.D.

Editorial Team

Anand Balasubramani, Ph.D.

Science Signaling | AAAS

Science Signaling publishes peer-reviewed, original research investigating cell signaling that underlies physiology and disease, on the molecular, cellular, intercellular and organismal levels.

Chief Scientific Advisor and Academic Editor

Michael B. Yaffe, M.D., Ph.D.
Massachusetts Institute of Technology

Deputy Editor

Wei Wong, Ph.D.

Editorial Team

Leslie K. Ferrarelli, Ph.D.
Annalisa M. VanHook, Ph.D.

Editor

John F. Foley, Ph.D.

Science Translational Medicine | AAAS

Science Translational Medicine is an interdisciplinary journal that publishes translational research with impact for human health that fills the knowledge gaps between preclinical studies and clinical applications.

Chief Scientific Advisors

Elazer R. Edelman, M.D., Ph.D.
Massachusetts Institute of Technology
Garret FitzGerald, M.D.
University of Pennsylvania

Editorial Team

Catherine A. Charneski, Ph.D.
Caitlin A. Czajka, Ph.D.
Mattia Maroso, Ph.D.
Melissa Norton, M.D.
Yevgeniya Nusinovich, M.D., Ph.D.
Lindsey Pujanandez, Ph.D.

Editor

Orla M. Smith, Ph.D.

Learn more and submit your research today: aaas.org/science-journals

IN THIS BOOKLET

Science

8

REPORT

Enhanced CAR-T cell activity against solid tumors by vaccine boosting through the chimeric receptor
Leyuan Ma *et al.* (Darrell J. Irvine)

15

RESEARCH ARTICLE

Adaptive mutability of colorectal cancers in response to targeted therapies

Mariangela Russo *et al.* (Alberto Bardelli)



Science Advances

23

RESEARCH ARTICLE

Highly efficient and tumor-selective nanoparticles for dual-targeted immunogene therapy against cancer

Kuan-Wei Huang *et al.* (Yunching Chen)

36

RESEARCH ARTICLE

Tracking extracellular vesicle phenotypic changes enables treatment monitoring in melanoma

Jing Wang *et al.* (Matt Trau)

Science Immunology

50

RESEARCH ARTICLE

Targeted deletion of PD-1 in myeloid cells induces antitumor immunity

Laura Strauss *et al.* (Vassiliki A. Boussiotis)

64

RESEARCH ARTICLE

Gasdermin E-mediated target cell pyroptosis by CAR T cells triggers cytokine release syndrome

Yuying Liu *et al.* (Bo Huang)

Science Signaling

77

RESEARCH ARTICLE

A systems mechanism for KRAS mutant allele-specific responses to targeted therapy

Thomas McFall *et al.* (Edward C. Stites)

91

RESEARCH ARTICLE

Adipocytes sensitize melanoma cells to environmental TGF- β cues by repressing the expression of miR-211

Tamar Golan *et al.* (Carmit Levy)

Science Translational Medicine

106

RESEARCH ARTICLE

Off-target toxicity is a common mechanism of action of cancer drugs undergoing clinical trials

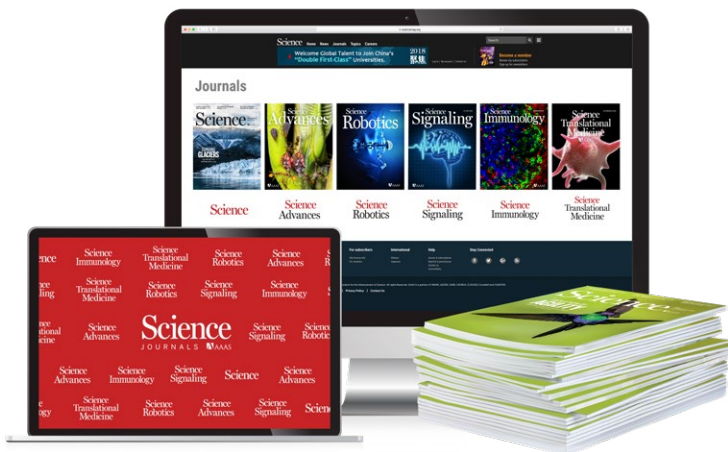
Ann Lin *et al.* (Jason M. Sheltzer)

124

RESEARCH ARTICLE

An innate-like V δ 1 γ δ T cell compartment in the human breast is associated with remission in triple-negative breast cancer

Yin Wu *et al.* (Adrian Hayday)



Publisher/Science family of journals: Bill Moran
AD/Business Development: Justin Sawyers
Marketing Manager: Shawana Arnold
Layout/Design: Kim Huynh

Sponsorship Opportunities:

Tracy Holmes, *Science*

tholmes@science-int.co.uk | (44) 1223 326525 ext 5525

1200 New York Ave NW, Washington DC 20005

Learn more and submit your research today: aaas.org/science-journals



CORNING

WE GET YOU

Every day. Every step of the way.

As a laboratory scientist, you never stop thinking about where your research is headed, or if there's a better way to get there. At Corning, we get it. That's why we offer you a comprehensive portfolio of vessels, advanced surfaces, and cell culture media, and work with you one-on-one to help you make the most of Corning products – from start-up to scale-up.

Our products deliver consistency, reliability, and reproducibility so you can achieve your research goals faster, at every stage of the journey. Learn more at www.corning.com/cellculture

VESSELS | SURFACES | MEDIA



IMMUNOTHERAPY

Copyright © 2019 The Authors, some rights reserved*

Enhanced CAR-T cell activity against solid tumors by vaccine boosting through the chimeric receptor

Leyuan Ma^{1,2}, Tanmay Dichwalkar¹, Jason Y. H. Chang¹, Benjamin Cossette¹, Daniel Garafolo¹, Angela Q. Zhang¹, Michael Fichter¹, Chensu Wang¹, Simon Liang¹, Murillo Silva¹, Sudha Kumari¹, Naveen K. Mehta^{1,3}, Wuhbet Abraham¹, Nikki Thai¹, Na Li¹, K. Dane Wittrup^{1,3,4}, Darrell J. Irvine^{1,2,3,5,6*}

Chimeric antigen receptor-T cell (CAR-T) therapy has been effective in the treatment of hematologic malignancies, but it has shown limited efficacy against solid tumors. Here we demonstrate an approach to enhancing CAR-T function in solid tumors by directly vaccine-boosting donor cells through their chimeric receptor *in vivo*. We designed amphiphile CAR-T ligands (amph-ligands) that, upon injection, trafficked to lymph nodes and decorated the surfaces of antigen-presenting cells, thereby priming CAR-Ts in the native lymph node microenvironment. Amph-ligand boosting triggered massive CAR-T expansion, increased donor cell polyfunctionality, and enhanced antitumor efficacy in multiple immunocompetent mouse tumor models. We demonstrate two approaches to generalizing this strategy to any chimeric antigen receptor, enabling this simple non-human leukocyte antigen-restricted approach to enhanced CAR-T functionality to be applied to existing CAR-T designs.

Chimeric antigen receptor-T cell (CAR-T) immunotherapy targeting the CD19 antigen has produced some marked clinical responses in patients with leukemia and lymphoma, including a high proportion of durable complete remissions (1, 2). However, poor functional persistence of CAR-Ts in some patients results in disease progression (3). Despite the success of CAR-T therapy in hematological cancers, it has to date been much less effective for solid tumors, and strategies to enhance efficacy in this setting remain an important goal (4, 5). Therapeutic vaccination is one well-established approach to enhance endogenous T cell responses against cancer (6). Several groups have demonstrated the concept of preparing CAR-Ts from virus-specific endogenous lymphocytes or introducing a CAR together with a second antigen receptor specific for a target peptide and then vaccinating recipients against the viral or secondary antigen to boost CAR-T therapy (7–9). However, these approaches suffer from being human leukocyte antigen (HLA) restricted, and the use of endogenous T cell receptors (TCRs) may be superseded by recent advances where CARs genetically targeted to

the native TCR locus (thereby deleting the native TCR) have significantly enhanced activity (10).

We recently developed a strategy to target vaccines to lymph nodes by linking peptide antigens to albumin-binding phospholipid polymers (11). Small peptides are normally rapidly dispersed into the blood after parenteral injection, but binding of amphiphile peptides to endogenous albumin, which constitutively traffics from blood to lymph, retargets these molecules to lymph nodes (LNs). In addition to exhibiting efficient lymph trafficking, these lipid-tailed molecules can also insert into cell membranes (12). We therefore hypothesized that by attaching a small molecule, peptide, or protein ligand for a CAR to the same polymer-lipid tail, CAR ligands could be delivered by albumin to LNs and subsequently partition into membranes of resident antigen-presenting cells (APCs), thereby codisplaying the amphiphile ligand (amph-ligand) from the APC surface together with native cytokine-receptor costimulation (Fig. 1A). Here we show how the dual properties of amph-ligands, lymph node targeting and membrane insertion, combine to create a booster vaccine for CAR-Ts. This amph-ligand strategy safely expands CAR-Ts *in vivo*, while increasing their functionality and enhancing antitumor activity in multiple models of solid tumors.

To test the ability of amph-ligands to functionally decorate APCs *in vivo*, we first employed a recently described “retargetable” CAR recognizing the small molecule fluorescein isothiocyanate (FITC), which is directed against tumors by coadministration of a FITC-conjugated antitumor antibody (13). The anti-FITC scFv 4m5.3 peptide (14) was fused to the CD8α transmembrane do-

main followed by CD28 and CD3ζ intracellular domains; the cognate amph-ligand for this murine CAR is FITC-poly(ethylene glycol) (PEG)-1,2-distearyl-sn-glycero-3-phosphoethanolamine (amph-FITC; Fig. 1B). When incubated with model APCs *in vitro*, amph-FITC was absorbed into the plasma membrane in a dose-dependent manner, and despite ongoing endocytosis, many molecules remained accessible to surface staining with an anti-FITC antibody (Fig. 1, C and D). Amph-FITC-coated cells stimulated FITC-CAR-Ts in a dose-dependent manner and were killed by FITC-CAR-Ts (Fig. 1, E and F).

On the basis of these findings, we next tested whether amph-FITC molecules could decorate APCs in LNs to prime FITC-CAR-Ts *in vivo*. Subcutaneous (s.c.) immunization of mice with free FITC did not result in accumulation in the draining LNs, whereas 10 nmol of amph-FITC was detectable for 21 days (fig. S1A). Amph-FITC primarily accumulated in draining LNs, with low to negligible levels detectable in the liver, spleen, and other organs (fig. S1B). Confocal imaging of LNs showed that amph-FITC initially accumulated in interfollicular regions but partitioned onto CD11c⁺ dendritic cells (DCs) in T cell areas over time (Fig. 2, A and B, and fig. S1C). Surface-displayed FITC could be detected on sorted FITC⁺ CD11c⁺ cells stained with an antibody against FITC (Fig. 2C and fig. S1D). In contrast to the efficient amph-FITC insertion into the membranes of many LN cell types *in vitro*, surface-accessible FITC was present primarily on macrophages and CD11c⁺ CD11b⁺ DCs *in vivo* (Fig. 2D and fig. S2, A and C). DCs line collagen conduits that carry lymph fluid into the LN, and we hypothesize that the anatomic structure of LNs in part dictates preferential access of these cells to amph-vax molecules entering LNs (15). This is supported by the observation that amph-FITC coinjected with a low-molecular-weight dextran [which is known to be transported through the LN conduit system (16)] showed substantial colocalization in fiber-like structures extending from the sinuses (fig. S2D). Immunization using amph-FITC together with the STING agonist adjuvant cyclic-di-GMP increased the duration of amph-FITC display on multiple APCs and, as expected, led to up-regulation of costimulatory molecules on amph-FITC⁺ DCs (Fig. 2E and fig. S2E). Notably, however, surface-accessible FITC decayed quickly and persisted on only a small fraction of cells.

To test the ability of amph-ligand immunization to expand CAR-Ts *in vivo*, we transferred CD45.1⁺ FITC-CAR-Ts into lymphocyte (lympho)-depleted congenic CD45.2⁺ recipient mice and subsequently vaccinated twice with amph-FITC and adjuvant. The CAR-Ts expanded substantially after amph-FITC vaccination, and expansion was increased by coadministering adjuvant (Fig. 2F). For example, transfer of 5×10^4 FITC-CAR-T followed by amph-FITC vaccination with adjuvant expanded these cells to a peak of ~70% of the total CD8⁺ T cell compartment, yielding a CAR-T population nearly double the size achieved by administering a 200-fold-greater

*David H. Koch Institute for Integrative Cancer Research, Massachusetts Institute of Technology, Cambridge, MA 02139, USA. ²Howard Hughes Medical Institute, Chevy Chase, MD 20815, USA. ³Department of Biological Engineering, Massachusetts Institute of Technology, Cambridge, MA 02139, USA. ⁴Department of Chemical Engineering, Massachusetts Institute of Technology, Cambridge, MA 02139, USA. ⁵Department of Materials Science and Engineering, Massachusetts Institute of Technology, Cambridge, MA 02139, USA. ⁶Ragon Institute of Massachusetts General Hospital, Massachusetts Institute of Technology, Cambridge, MA 02139, USA.

*Corresponding author. Email: djirvine@mit.edu

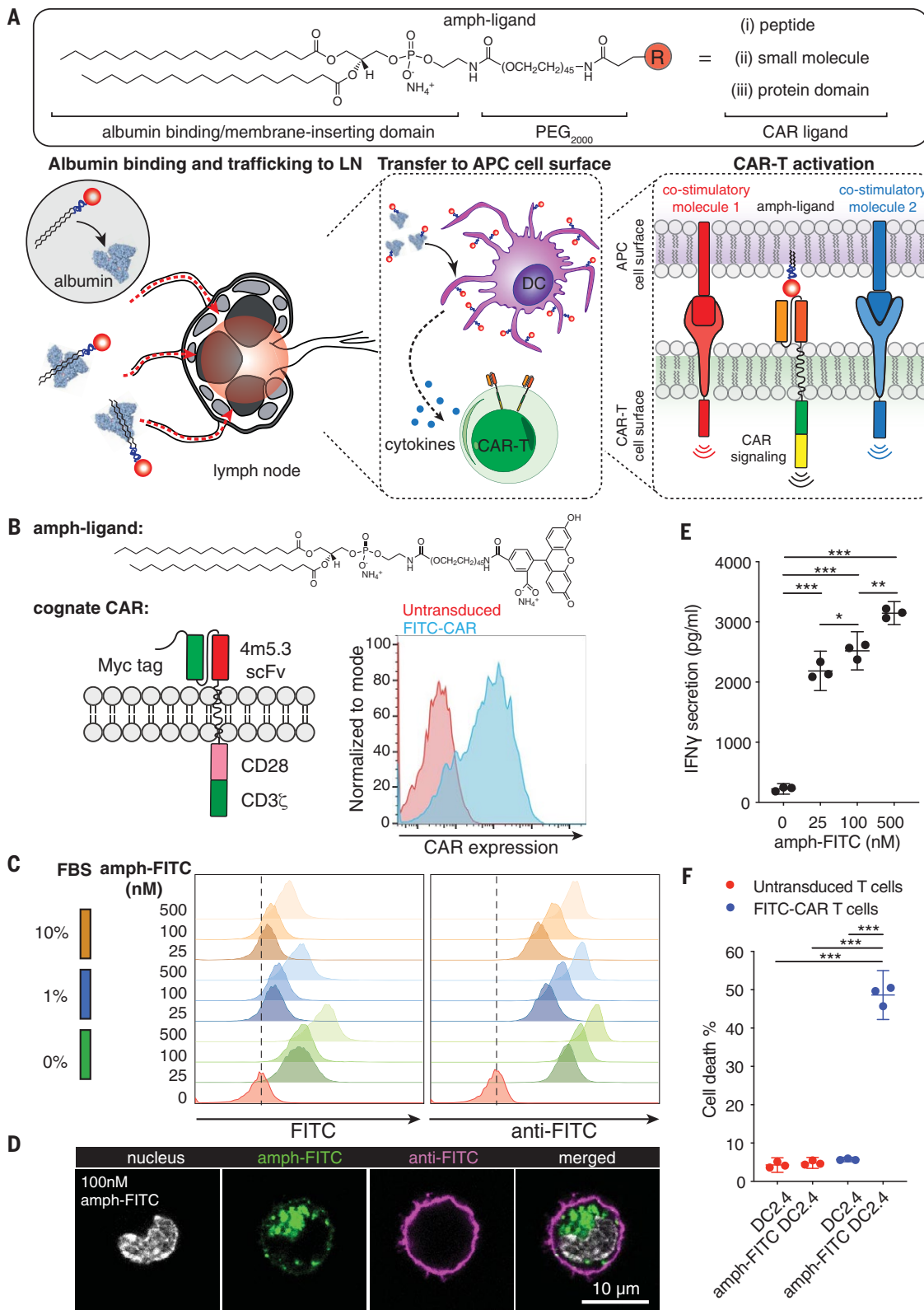


Fig. 1. Design of an amph-ligand vaccine to boost CAR-Ts. (A) Schematic of the general chemical structure of amph-ligands (top) and the steps in amph-ligand vaccine boosting in vivo (bottom). Upon injection, amph-ligands associate with albumin at the injection site and are subsequently trafficked to the draining LNs. The amphiphiles then transfer to the membrane of lymph node–resident cells, including APCs. CAR-Ts that encounter decorated APCs in the LNs are stimulated by the surface-displayed amph-ligand as well as costimulatory receptors and cytokines produced by the APCs. (B) Structures of amph-FITC and cognate FITC-CAR and a representative flow cytometry analysis of T cell surface expression for FITC-CAR. (C and D) Flow cytometry analysis at 24 hours (C) and confocal imaging after 30 min (D) of amph-FITC insertion into DC2.4 cell membranes, by direct FITC fluorescence or staining with an anti-FITC antibody. (E and F) IFN-γ secretion (in picograms per milliliter) (E) and killing (the percentage of target cell death) (F) of amph-FITC-coated DC2.4 cells after 6 hours coculture with FITC-CAR or control untransduced T cells at a 10:1 effector:target (E:T) ratio. Shown in (E) and (F) are representative experiments with technical triplicates. *P* values were determined by unpaired Student's *t* test. Error bars represent 95% confidence intervals (CI). ****P* < 0.0001; ***P* < 0.01; **P* < 0.05.

number of CAR-Ts without vaccination (Fig. 2F). By 3 weeks after boost, the persisting CAR-Ts were a mixture of effector/effector memory and central memory cells (Fig. 2G). Amph-vax boosting also expanded CAR-Ts in lympho-replete mice;

in this setting, two immunizations could expand 10^6 transferred cells from undetectable levels to ~20% of the total CD8 compartment (Fig. 2H). To determine whether professional APCs played an important role in CAR-T priming by amph-

ligand immunization, we depleted different cell types in LNs. CAR-T expansion in response to amph-FITC immunization was not impaired in *Batf3*^{-/-} mice lacking cross-presenting DCs, but depletion of total DCs in CD11c-diphtheria

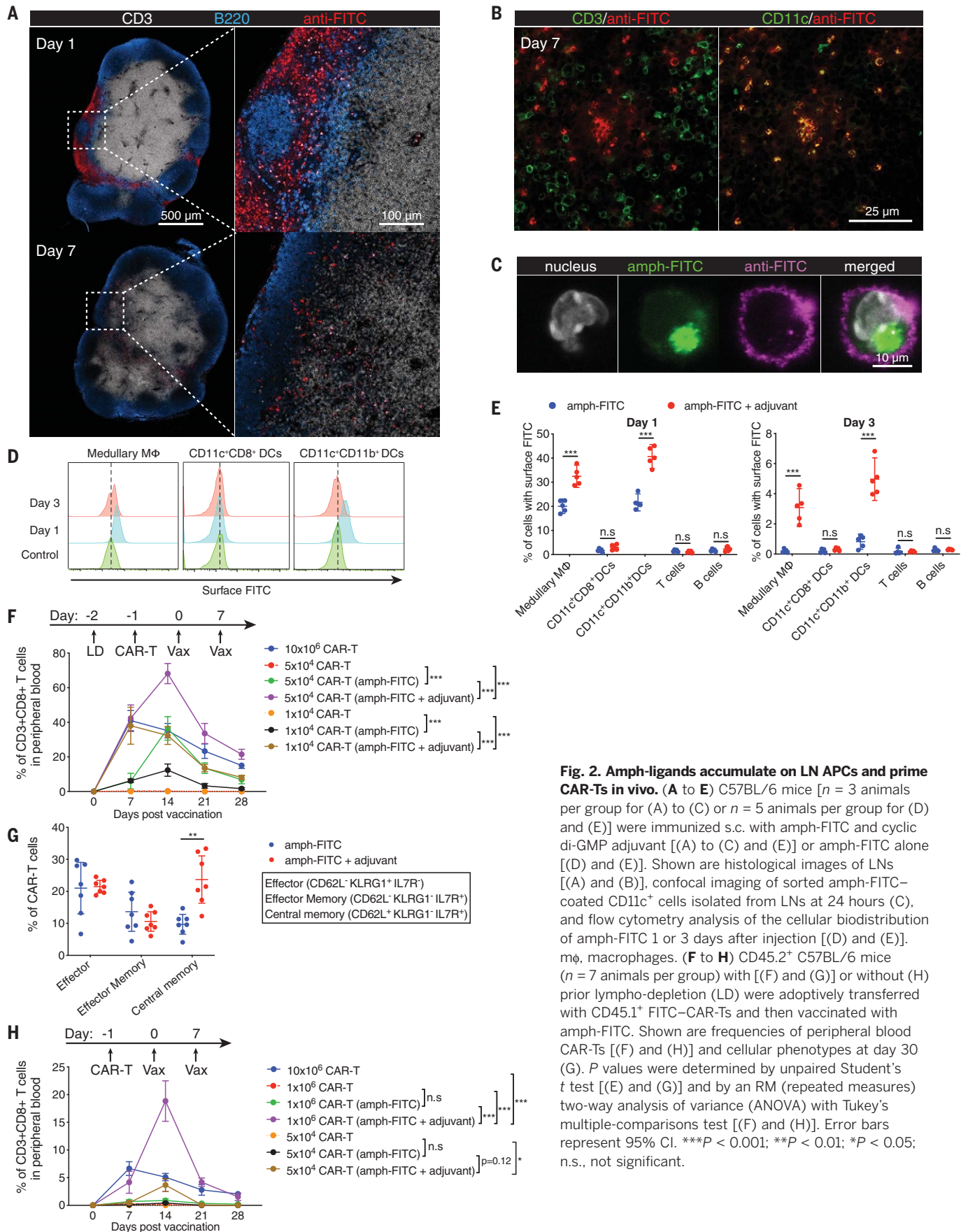


Fig. 2. Amph-ligands accumulate on LN APCs and prime CAR-Ts in vivo. (A to E) C57BL/6 mice [$n = 3$ animals per group for (A) to (C) or $n = 5$ animals per group for (D) and (E)] were immunized s.c. with amph-FITC and cyclic di-GMP adjuvant [(A) to (C) and (E)] or amph-FITC alone [(D) and (E)]. Shown are histological images of LNs [(A) and (B)], confocal imaging of sorted amph-FITC-coated CD11c⁺ cells isolated from LNs at 24 hours (C), and flow cytometry analysis of the cellular biodistribution of amph-FITC 1 or 3 days after injection [(D) and (E)]. mφ, macrophages. (F to H) CD45.2⁺ C57BL/6 mice ($n = 7$ animals per group) with [(F) and (G)] or without (H) prior lympho-depletion (LD) were adoptively transferred with CD45.1⁺ FITC-CAR-Ts and then vaccinated with amph-FITC. Shown are frequencies of peripheral blood CAR-Ts [(F) and (H)] and cellular phenotypes at day 30 (G). P values were determined by unpaired Student's t test [(E) and (G)] and by an RM (repeated measures) two-way analysis of variance (ANOVA) with Tukey's multiple-comparisons test [(F) and (H)]. Error bars represent 95% CI. *** P < 0.001; ** P < 0.01; * P < 0.05; n.s., not significant.

toxin receptor (DTR) mice or macrophages using chlodronate liposomes led to significant reductions in CAR-T cell numbers (fig. S3, A to C). In addition, the cytokine functionality of responding CAR-Ts was reduced in all three settings (fig. S3, A to C). *In vivo* blockade of a collection of co-stimulatory molecules expressed by APCs also markedly suppressed both FITC-CAR-T expansion and cytokine functionality in response to amph-FITC immunization (fig. S3D).

A key concern with amph-ligand delivery is the potential for toxicity from CAR-T-mediated killing of decorated cells in LNs or other tissues. Consistent with the low fraction of any cell type with detectable surface FITC ligand, no significant changes in viable LN cell populations were detectable 1 day, 3 days, or 14 days after amph-FITC immunization (fig. S4, A to C). No changes in systemic liver enzymes, liver histopathology or CAR-T infiltration, or serum cytokine levels were observed after amph-FITC boosting (fig. S4, D to I). We further evaluated the functional integrity of vaccinated LNs by administering an amph-FITC boost in the presence or absence of transferred FITC-CAR-Ts and then immunizing animals with ovalbumin at the same site 5, 7, or 14 days later (fig. S4J). We observed decreased expansion and functionality of endogenous SIINFEKL-specific T cells when animals were immunized 5 days—but not 7 or 14 days—after amph-FITC boost, suggesting that the combination of CAR-T transfer and amph-FITC vaccination has a short-term effect on priming of endogenous T cell responses [which recovers rapidly (fig. S4K)]. Owing to the lack of T cell help, repeated amph-FITC immunization with adjuvant elicited no antibody response against the amph-ligand itself (fig. S5).

We next evaluated if amph-ligands could be used to prime a bona fide tumor antigen-specific CAR. The EGFRvIII-specific 139scFv CAR recognizes a short linear epitope derived from EGFRvIII (17). We prepared murine T cells expressing this CAR and synthesized an amph-vax molecule composed of PEG-DSPE linked to the peptide ligand with or without an N-terminal FITC label (amph-pepvIII; Fig. 3A). Similar to amph-FITC, amph-pepvIII inserted in cell membranes in vitro and the amph-pepvIII-coated cells stimulated EGFRvIII-CAR-Ts (fig. S6, A and B). Immunization of mice with amph-pepvIII triggered EGFRvIII-CAR-T proliferation in vivo (Fig. 3B). To test the therapeutic impact of vaccine boosting, we transduced murine CT-2A glioma cells with EGFRvIII; these cells were efficiently killed by EGFRvIII-CAR-Ts in vitro (fig. S6, C and D). Transfer of EGFRvIII-CAR-T into lympho-depleted CT-2A-mEGFRvIII tumor-bearing mice that were then immunized with amph-pepvIII expanded the CAR-Ts substantially in the periphery (Fig. 3C). Vaccination induced significant increases in the proportion of cells with an effector phenotype (fig. S6E) and 5- to 10-fold increases in CAR-T cell polyfunctionality (Fig. 3D). Amph-vax boosting greatly increased CAR-T infiltration into tumors, and these tumor-infiltrating lymphocytes expressed higher levels of granzyme B and Ki67 than un-

boosted CAR-Ts (Fig. 3E). In therapeutic studies, animals receiving both CAR-T and repeated amph-vax boosting had significantly delayed tumor growth and prolonged survival (Fig. 3, F and G). Treatment with 1×10^6 CAR-Ts alone led to no long-term survivors, while this same CAR-T dose boosted by amph-vaccination eliminated tumors in a majority of animals (Fig. 3, F and G). Administration of amph-pepvIII with adjuvant in the absence of CAR-Ts had no therapeutic impact (fig. S6F). EGFRvIII-CAR-Ts from vaccinated animals persisted over time, and surviving animals rejected tumor rechallenge at day 75 (fig. S6, G and H). Notably, animals that rejected primary tumors after CAR-T plus amph-vax boosting therapy also rejected rechallenge with parental CT-2A tumor cells lacking the ligand and for the CAR-Ts, suggesting induction of an endogenous T cell response against other tumor antigens (fig. S6I). Motivated by this finding, we evaluated the reactivity of splenocytes from CT-2A-mEGFRvIII tumor-bearing mice that received CAR-Ts with or without two amph-pepvIII boosts. Enzyme-linked immunosorbent spot (ELISPOT) analysis of interferon- γ (IFN- γ) production by splenocytes cultured with parental CT-2A cells revealed a strong endogenous T cell response against parental tumors (Fig. 3H). Similar to amph-FITC-vaccinated mice, no antibody response was elicited against pepvIII after three rounds of weekly vaccination (fig. S6J). We also evaluated the therapeutic efficacy of CAR-T plus amph vaccination in tumor-bearing mice without lympho-depletion preconditioning. Tumor progression in animals receiving CAR-T alone was indistinguishable from that in animals receiving control untransduced T cells, whereas CAR-T transfer combined with amph-pepvIII immunization delayed tumor growth and prolonged animal survival (Fig. 3, I and J). In both the lympho-depleted and non-lympho-depleted settings, amph-vax boosting was accompanied by small transient alterations in animal body weight and minimal alterations in serum cytokine levels (fig. S6, K and L). To assess the utility of amph-vax boosting with a more potent “third-generation” CAR design, we generated an EGFRvIII-targeting CAR containing both CD28 and 41BB co-stimulatory domains. This CAR was well-expressed and functional in vitro (fig. S7, A and C). We then treated large ($\sim 50\text{-mm}^2$) established CT-2A-mEGFRvIII tumors with EGFRvIII-28BBzCAR-T cells, with or without amph-pepvIII boosting. In this high tumor burden setting, the CAR-Ts alone had a modest impact on tumor progression, and amph-ligand boosting greatly improved tumor control and enhanced overall survival (fig. S7, D and E).

Although use of a peptide ligand for CAR-Ts was effective, some CARs recognize three-dimensional structural epitopes (18). As an alternative strategy to amph-ligand boost with any CAR regardless of the nature of its binding domain or specificity, we devised a tandem scFv-based bispecific CAR based on recently reported designs (19). The anti-FITC scFv was fused to the N-terminal extracellular domain of a tumor-targeting CAR

(TA99) that recognized the melanoma-associated antigen TRP1 (Fig. 4, A and B). FITC/TRP1-CAR-Ts were activated both by amph-FITC-coated target cells and by TRP1-expressing B16F10 cells (fig. S8A), and killed TRP1 $^+$ target cells at levels equivalent to those cells expressing monospecific TRP1-CAR (Fig. 4C). *In vivo*, amph-FITC vaccination stimulated FITC/TRP1-bispecific CAR-T proliferation (fig. S8B). Similar to observations in the EGFRvIII system, amph-vax boosting of FITC/TRP1-CAR-T in B16F10 tumor-bearing animals led to pronounced CAR-T expansion in the periphery and increased tumor infiltration (fig. S8, C and D), with minimal serum cytokine elevation and transient fluctuations in body weight after each vaccination (fig. S8, E and F). Whereas adoptive therapy with FITC/TRP1-CAR-T alone had almost no effect on B16F10 tumor progression, repeated boosting after transfer with amph-FITC led to pronounced slowing in tumor growth and extended survival (Fig. 4, D and E). One resistance mechanism to CAR-T therapy is loss of surface antigen (20), but we did not observe apparent Trp1 loss upon tumor outgrowth in this model (fig. S8, G and H). To assess potential autoimmune toxicity induced by amph-vax boosting, we examined thymus and skin tissues (which naturally express Trp1) from treated animals, but we found no changes in histopathology or CAR-T infiltration into the thymus with amph-vax boosting (fig. S8, I to K). We also assessed whether CAR-T therapy with vaccine boosting would be more effective if mixed CD4/CD8 CAR-Ts were used. In vitro, both CD4 $^+$ and CD8 $^+$ CAR-Ts were activated by culture with amph-ligand-coated target cells (fig. S8L), and similar therapeutic efficacy was observed when B16F10 tumors were treated with CD8 as with mixed CD4/CD8 FITC/Trp1-CAR-Ts boosted by amph-FITC vaccination (fig. S8, M and N).

To assess the broad applicability of this bispecific CAR platform irrespective of animal strain or haplotype and to evaluate treatment of metastatic disease, we prepared 4T1 tumor cells transduced to express mEGFRvIII and luciferase, modeling EGFRvIII $^+$ breast cancer (21) on the BALB/c background. A cognate FITC/EGFRvIII-bispecific CAR was generated, which was well-expressed in BALB/c T cells and was functional in vitro and in vivo (fig. S9, A and D). 4T1-mEGFRvIII tumor cells were injected intravenously (i.v.) into BALB/c mice to induce lung metastases and then treated with FITC/EGFRvIII-CAR-T with or without amph-FITC boosting. Tumor progression as assessed by bioluminescence imaging was significantly impacted only when CAR-Ts were supplemented with amph-ligand boosting (fig. S9E), leading to prolonged survival and clearance of tumors in two of five animals (fig. S9F). In the CAR-T plus amph-vax-treated animals that relapsed, EGFRvIII surface levels were markedly reduced, suggesting selection of low-antigen-expressing or null tumor cells during therapy (fig. S9G). Finally, to verify that this bispecific CAR approach could also be used to boost human CAR-T, we constructed a FITC/hCD19-bispecific human

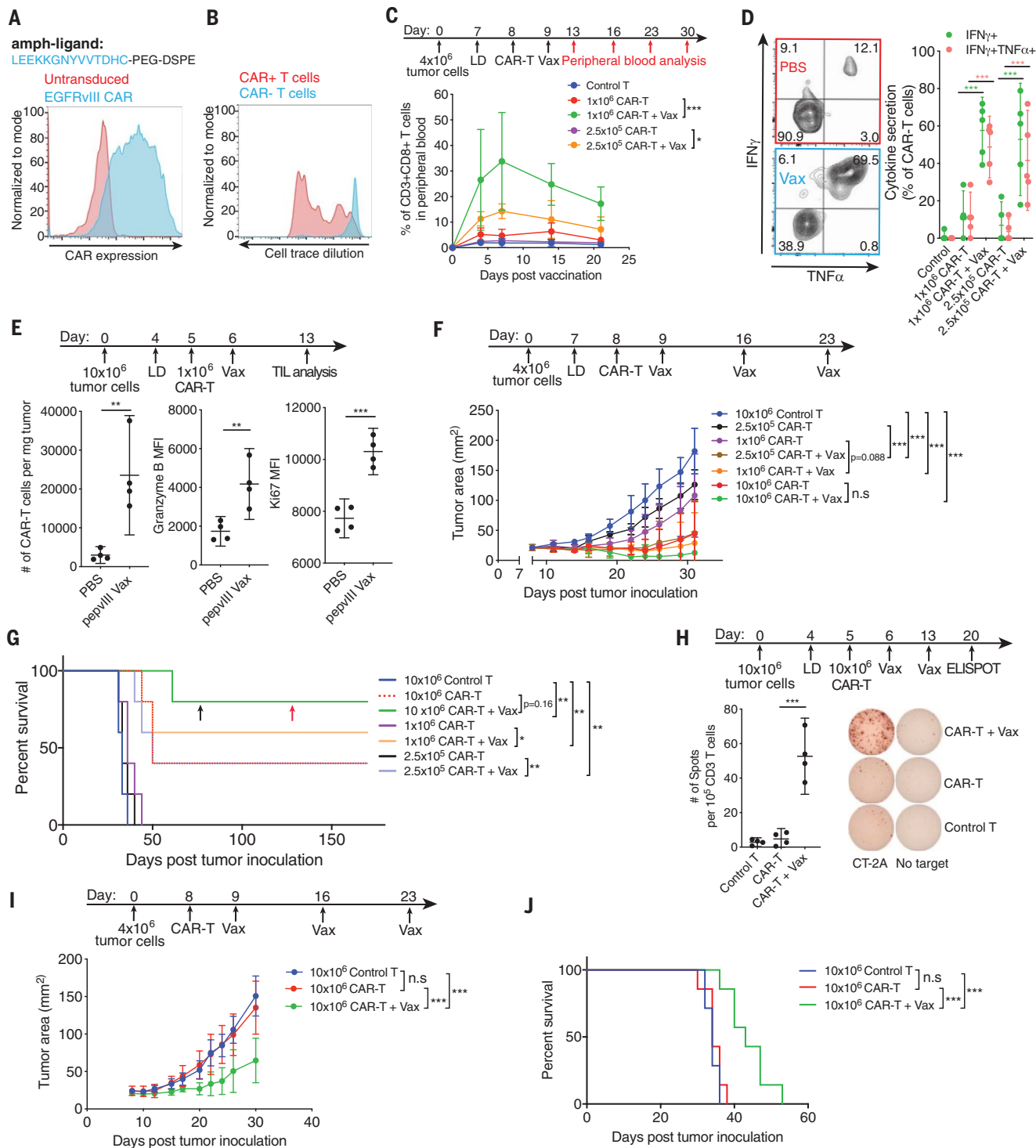


Fig. 3. Amph-peptide ligands boost CAR-Ts in vivo for enhanced solid tumor immunotherapy in mice. (A) Structure of amph-pepvIII and surface expression of EGFRvIII CAR. (B) Representative histogram showing EGFRvIII-CAR-T proliferation in LNs 48 hours after amph-pepvIII vaccination ($n = 3$ animals per group). (C and D) Expansion (C) and cytokine polyfunctionality at day 7 (D) of circulating EGFRvIII-CAR-Ts following a single amph-pepvIII immunization ($n = 5$ animals per group). (E) Enumeration, granzyme B levels, and Ki67 levels of tumor-infiltrating EGFRvIII-CAR-Ts ($n = 4$ animals per group) with or without amph-pepvIII boost. (F to J) Tumor growth [(F) and (I)], ELISPOT of enriched CD3⁺ splenocytes cultured with irradiated parental CT-2A tumor cells (H), and

survival [(G) and (J)] of mEGFRvIII-CT-2A tumor-bearing mice treated with EGFRvIII-CAR-T with or without amph-pepvIII vaccination for animals that were lympho-depleted [(F) and (G)] ($n = 5$ animals per group; (H) $n = 4$ animals per group), or lympho-replete [(I) and (J)] ($n = 7$ animals per group) prior to adoptive transfer. The black arrow indicates time of CT-2A-EGFRvIII tumor rechallenge. The red arrow indicates time of parental CT-2A tumor rechallenge. P values were determined by unpaired Student's t test [(D), (E), and (H)], by an RM two-way ANOVA with Tukey's multiple-comparisons test [(C), (F), and (I)], or by log-rank test [(G) and (J)]. Error bars represent 95% CI. *** $P < 0.001$; ** $P < 0.01$; * $P < 0.05$; n.s., not significant.

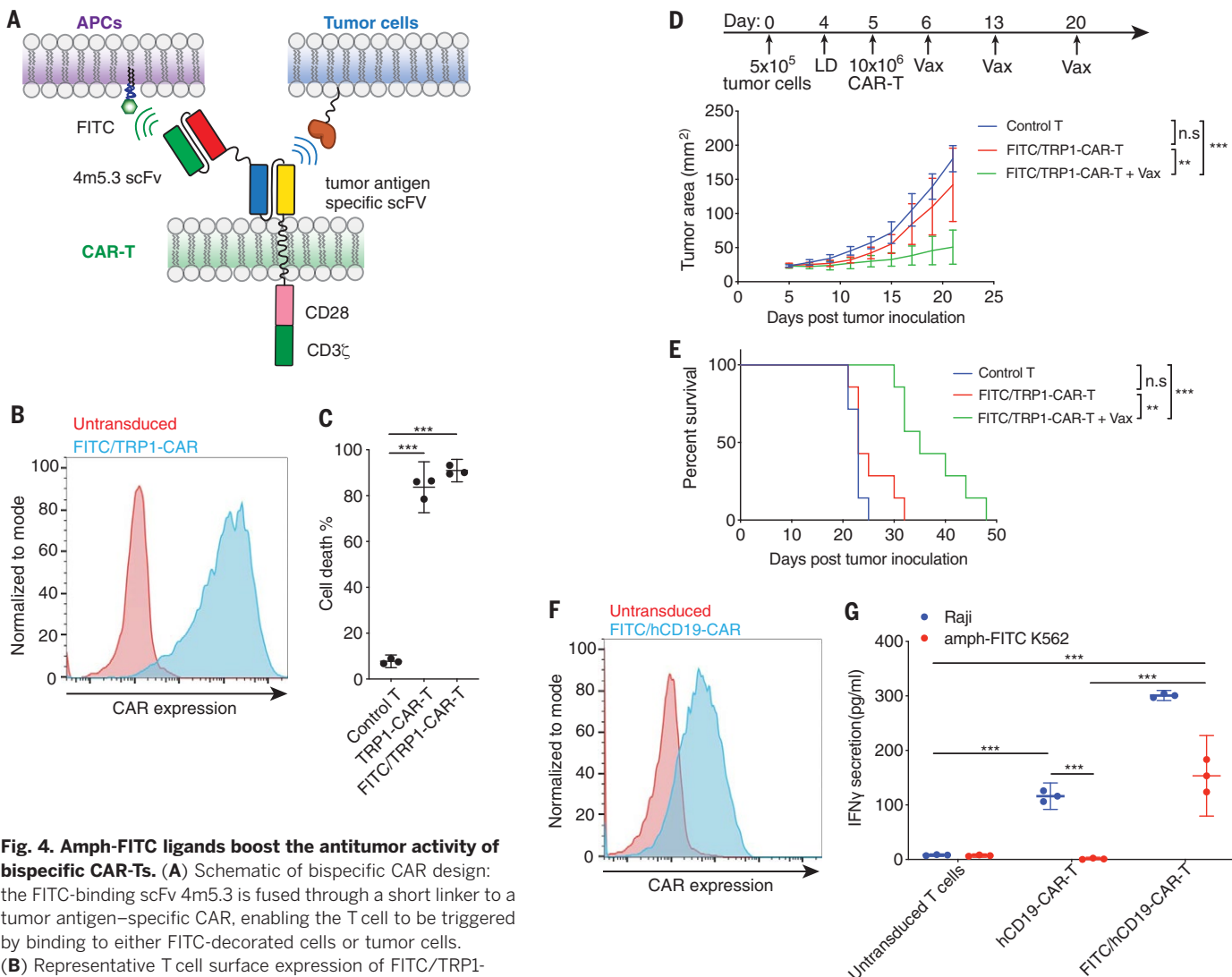


Fig. 4. Amph-FITC ligands boost the antitumor activity of bispecific CAR-Ts. (A) Schematic of bispecific CAR design:

the FITC-binding scFv 4m5.3 is fused through a short linker to a tumor antigen-specific CAR, enabling the T cell to be triggered by binding to either FITC-decorated cells or tumor cells. (B) Representative T cell surface expression of FITC/TRP1-CAR. (C) Killing of TRP1-expressing B16F10 cells in vitro after 6-hour coculture with FITC/TRP1-CAR-T, monospecific TRP1-CAR-T, or control untransduced T cells at an E:T of 10:1. (D and E) Tumor growth (D) and survival (E) of B16F10 tumor-bearing mice ($n = 7$ animals per group) treated with 10×10^6 CAR-Ts alone or CAR-Ts plus amph-FITC vaccination. P values were determined by an RM two-way ANOVA with Tukey's multiple-comparisons test (D) or by log-rank test (E). (F) Surface

expression of FITC/hCD19-bispecific CAR on human T cells. (G) FITC/TRP1-bispecific CAR-Ts responding to either hCD19⁺ Raji cells or amph-FITC-coated K562 cells as monitored by IFN- γ secretion. Shown in (C) and (G) are representative experiments with technical triplicates. P values were determined by an unpaired Student's t test [(C) and (G)]. Error bars represent 95% CI. *** $P < 0.0001$; ** $P < 0.01$; * $P < 0.05$; n.s., not significant.

CAR using the established FMC63 antibody against CD19 (22) and expressed this CAR in human T cells (Fig. 4F). Human FITC/hCD19-CAR-Ts were stimulated by both CD19⁺ Raji cells as well as amph-FITC-coated target cells (Fig. 4G). Altogether, we present here a new vaccine approach to boosting CAR-T numbers and functionality *in vivo* with low toxicity, enabling enhanced efficacy in syngeneic solid tumor models. Although not directly evaluated here, this approach might be further enhanced by nascent strategies to improve CAR function, such as insertion of the CAR into the *TRAC* locus (10). The bispecific vaccinable CAR design with amph-FITC vaccine offers a simple and universal solution to boosting CAR-Ts with any antigen specificity.

REFERENCES AND NOTES

1. A. D. Fesnak, C. H. June, B. L. Levine, *Nat. Rev. Cancer* **16**, 566–581 (2016).
2. D. N. Khalil, E. L. Smith, R. J. Brentjens, J. D. Wolchok, *Nat. Rev. Clin. Oncol.* **13**, 273–290 (2016).
3. S. Gudan et al., *JCI Insight* **3**, e96976 (2018).
4. K. Newick, S. O'Brien, E. Moon, S. M. Albeda, *Annu. Rev. Med.* **68**, 139–152 (2017).
5. C. H. June, R. S. O'Connor, O. U. Kawalekar, S. Ghassemi, M. C. Milone, *Science* **359**, 1361–1365 (2018).
6. S. H. van der Burg, R. Arens, F. Ossendorp, T. van Hall, C. J. Melief, *Nat. Rev. Cancer* **16**, 219–233 (2016).
7. M. Tanaka et al., *Clin. Cancer Res.* **23**, 3499–3509 (2017).
8. X. Wang et al., *Clin. Cancer Res.* **21**, 2993–3002 (2015).
9. C. Y. Slaney et al., *Clin. Cancer Res.* **23**, 2478–2490 (2017).
10. J. Eyquem et al., *Nature* **543**, 113–117 (2017).
11. H. Liu et al., *Nature* **507**, 519–522 (2014).
12. H. Liu, B. Kwong, D. J. Irvine, *Angew. Chem. Int. Ed. Engl.* **50**, 7052–7055 (2011).
13. J. S. Ma et al., *Proc. Natl. Acad. Sci. U.S.A.* **113**, E450–E458 (2016).
14. E. T. Boder, K. S. Midelfort, K. D. Wittrup, *Proc. Natl. Acad. Sci. U.S.A.* **97**, 10701–10705 (2000).
15. M. Sixt et al., *Immunity* **22**, 19–29 (2005).
16. J. E. Gretz, C. C. Norbury, A. O. Anderson, A. E. Proudfoot, S. Shaw, *J. Exp. Med.* **192**, 1425–1440 (2000).
17. J. H. Sampson et al., *Clin. Cancer Res.* **20**, 972–984 (2014).
18. S. N. De Oliveira et al., *J. Transl. Med.* **11**, 23 (2013).
19. E. Zah, M. Y. Lin, A. Silva-Benedict, M. C. Jensen, Y. Y. Chen, *Cancer Immunol. Res.* **4**, 498–508 (2016).
20. E. Sotillo et al., *Cancer Discov.* **5**, 1282–1295 (2015).
21. C. A. Del Vecchio et al., *Cancer Res.* **72**, 2657–2671 (2012).
22. J. N. Kochenderfer et al., *Blood* **116**, 4099–4102 (2010).

ACKNOWLEDGMENTS

We thank the Koch Institute Swanson Biotechnology Center for technical support, specifically, the whole-animal imaging core facility, histology core facility, and flow cytometry core facility. We thank T. Seyfried for providing the CT-2A cell line. **Funding:** This work was supported by the NIH (award EB022433), the Marble Center for Nanomedicine, and Johnson & Johnson. D.J.I. is an investigator of the Howard Hughes Medical Institute. The project

was also supported by award no. T32GM007753 from the National Institute of General Medical Sciences. M.F. was supported by Deutsche Forschungsgemeinschaft grant FI 2249/1-1. The content is solely the responsibility of the authors and does not necessarily represent the official views of the National Institute of General Medical Sciences or the National Institutes of Health. **Author contributions:** L.M., D.J.I., and K.D.W. designed the studies. L.M. and D.J.I. analyzed and interpreted the data and wrote the manuscript. L.M., T.D., D.G., A.Q.Z., J.Y.H.C., S.K., B.C.,

C.W., S.L., M.S., M.F., N.K.M., W.A., N.T., and N.L. performed experiments. **Competing interests:** D.J.I. and L.M. are inventors on international patent application PCT/US2018/051764 submitted by Massachusetts Institute of Technology, which covers the use of amphiphile-vaccine technology as a vaccine for CAR-Ts. D.J.I. is a consultant for Elicin Therapeutics that has licensed IP related to this technology. **Data and materials availability:** Materials are available under a material transfer agreement (contact person D.J.I.).

SUPPLEMENTARY MATERIALS

science.sciencemag.org/content/365/6449/162/suppl/DC1
Materials and Methods
Figs. S1 to S9
References (23–28)

28 October 2018; accepted 10 June 2019
10.1126/science.aav8692

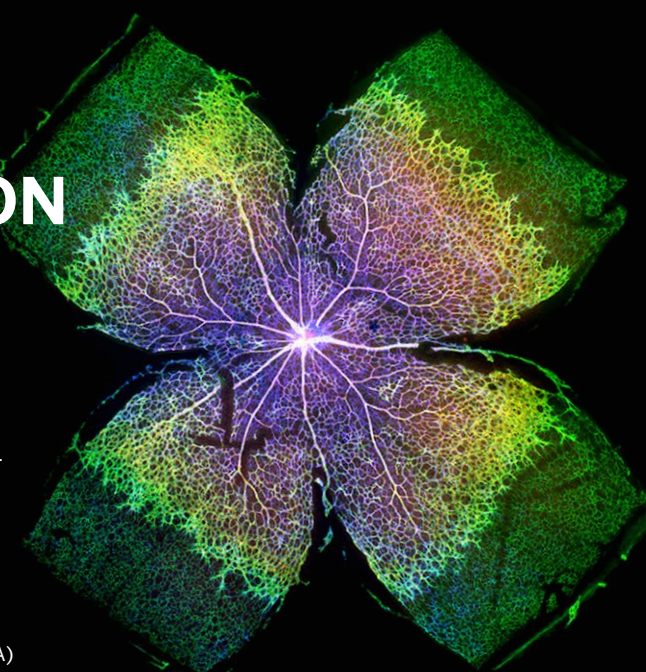
THIS IS NOT SCIENCE FICTION

This is captivating, impactful Science

Contact us today to discuss pricing options for adding any of these journals to your collection of *Science* resources.

Institutional Licensing

ScienceMag.org/request | scienceonline@aaas.org
1-866-265-4152 (USA) | +1-202-326-6730 (outside USA)



Science
AAAS

Science
Advances

Science
Immunology

Science
Robotics

Science
Signaling

Science
Translational
Medicine

Copyright © 2019 The Authors, some rights reserved; exclusive licensee American Association for the Advancement of Science. No claim to original U.S. Government Works.

CANCER

Adaptive mutability of colorectal cancers in response to targeted therapies

Mariangela Russo^{1,2*}, Giovanni Crisafulli^{1,2}, Alberto Sogari^{1,2}, Nicole M. Reilly³, Sabrina Arena^{1,2}, Simona Lamba¹, Alice Bartolini¹, Vito Amodio^{1,2}, Alessandro Magri^{1,2}, Luca Novara¹, Ivana Sarotto¹, Zachary D. Nagel⁴, Cortt G. Piett⁴, Alessio Amatu^{5,6}, Andrea Sartore-Bianchi^{5,6}, Salvatore Siena^{5,6}, Andrea Bertotti^{1,2}, Livio Trusolino^{1,2}, Mattia Corigliano^{7,8}, Marco Gherardi^{7,8}, Marco Cosentino Lagomarsino^{7,8}, Federica Di Nicolantonio^{1,2}, Alberto Bardelli^{1,2*}

The emergence of drug resistance limits the efficacy of targeted therapies in human tumors. The prevalent view is that resistance is a fait accompli: when treatment is initiated, cancers already contain drug-resistant mutant cells. Bacteria exposed to antibiotics transiently increase their mutation rates (adaptive mutability), thus improving the likelihood of survival. We investigated whether human colorectal cancer (CRC) cells likewise exploit adaptive mutability to evade therapeutic pressure. We found that epidermal growth factor receptor (EGFR)/BRAF inhibition down-regulates mismatch repair (MMR) and homologous recombination DNA-repair genes and concomitantly up-regulates error-prone polymerases in drug-tolerant (persister) cells. MMR proteins were also down-regulated in patient-derived xenografts and tumor specimens during therapy. EGFR/BRAF inhibition induced DNA damage, increased mutability, and triggered microsatellite instability. Thus, like unicellular organisms, tumor cells evade therapeutic pressures by enhancing mutability.

More than 75 years ago, Luria and Delbrück demonstrated that bacterial resistance to phage viruses was due to random mutations that spontaneously occurred in the absence of selection (1). Resistance to targeted therapies in human tumors is also widely thought to be due to mutations that exist before treatment (2). The conventional view is that relapses occur because drug-resistant mutant subclones are present in any detectable metastatic lesion before the initiation of therapy. According to this view, resistance is a fait accompli, and the time to recurrence is merely the interval required for preexisting drug-resistant (mutant) cells to repopulate the lesion (3).

Here, we explore the hypothesis that resistance to targeted therapies can also be fostered by a transient increase in genomic instability during treatment, leading to de novo mutagenesis. A similar process has been shown to increase the emergence of microbial strains

resistant to antibiotics (4, 5). In a stable microenvironment, the mutation rate of microorganisms is usually low, which precludes the accumulation of deleterious mutations. However, several mechanisms of stress-induced genetic instability and increased mutability, known as stress-induced mutagenesis (SIM), have been described in bacteria and yeast (6–12).

Bacterial persister cells can survive lethal stress conditions imposed by antibiotics through a reduction in growth rate. A subsequent reduction in the efficiency of DNA mismatch repair (MMR) (4, 9, 13) and a shift to error-prone DNA polymerases increases the rate at which adaptive mutations occur in the surviving population (4, 9, 14, 15). Selection then allows the growth of mutant subpopulations capable of replicating under stressful conditions. Once the stressed population has adapted to the new conditions, the hypermutator status is counterselected to avoid the accumulation of deleterious mutations and to prevent the continuous increase of mutational load (9, 16–20). Together, these processes boost genetic diversity, foster adaptability to new microenvironments, and contribute to the development of resistance (9, 12, 18, 19).

In the setting of cancer, the emergence of a drug-tolerant persister population is often observed when oncogene-dependent tumor cells are challenged with targeted agents (21). Persister cancer cells survive exposure to targeted therapies through poorly understood mechanisms (21) and represent a reservoir

from which genetically divergent, drug-resistant derivatives eventually emerge (22, 23). Recent work showed that drug-resistant mutant cancer cells can originate not only from rare, preexisting mutant clones, but also from drug-tolerant subpopulations (24). The probability that the latter resistance mechanism occurs would be greatly increased if the genetic diversity of tumor cells were enhanced during treatment. Accordingly, we hypothesized that during the persister state, tumor cells, like unicellular organisms, alter DNA-repair and DNA-replication mechanisms to enhance adaptive mutability.

Targeted therapy-induced down-regulation of MMR and HR proficiency of CRC cells

To test our hypothesis, we studied the response of microsatellite-stable (MSS) human colorectal cancer (CRC) cell lines to the anti-EGFR (epidermal growth factor receptor) antibody cetuximab, which is approved, together with panitumumab, for the treatment of patients with metastatic CRC whose tumors lack *RAS* and *BRAF* mutations (25), or with the BRAF inhibitor dabrafenib (DAB) as combinatorial treatment, which has shown promising activity in patients with CRC harboring *BRAF* mutations (26). We selected human CRC cell lines that are *RAS* and *BRAF* wild-type and sensitive to EGFR blockade (DiFi cells, fig. S1A) or that carry the oncogenic *BRAF* p.V600E mutation and are sensitive to concomitant EGFR and BRAF inhibition (WiDr cells, fig. S1A). Treatment with targeted agents led to G₁ cell-cycle arrest (fig. S1B). However, a small number of drug-tolerant persister cells survived several weeks after treatment initiation (fig. S1, C and D). Indeed, when drug pressure was removed, these cells rapidly resumed growth and again showed sensitivity to targeted therapy, thus demonstrating that persisters are only transiently and reversibly resistant to the treatment (fig. S1, E and F). By contrast, prolonged treatment led to the generation of permanently resistant cells, which did not reacquire sensitivity after the removal of drug pressure (fig. S1, E and F).

We next assessed whether CRC cells modulate the expression of DNA-repair genes upon drug treatment. Transcriptional profiles revealed decreased expression of the MMR genes *MLH1*, *MSH2*, and *MSH6*, as well as of homologous recombination (HR) effectors such as *BRCA2* and *RAD51* (Fig. 1A and fig. S1, G and H). Expression of *EXO1*, a gene coding for an exonuclease that participates in mismatch and double-strand break (DSB) repair, was also affected (Fig. 1A and fig. S1, G and H). A time-dependent down-regulation of MMR and HR proteins was also observed (Fig. 1B and fig. S2, A and B). Comparable results were obtained in another cetuximab-sensitive human CRC cell line, NCIH508 (fig. S3, A to C), and in

¹Candiolo Cancer Institute, FPO-IRCCS, Candiolo (TO) 10060, Italy. ²Department of Oncology, University of Torino, Candiolo (TO) 10060, Italy. ³Fondazione Piemontese per la Ricerca sul Cancro ONLUS, Candiolo (TO) 10060, Italy.

⁴Department of Environmental Health, JBL Center for Radiation Sciences, Harvard T.H. Chan School of Public Health, Boston, MA 02115, USA. ⁵Niguarda Cancer Center, Grande Ospedale Metropolitano Niguarda, 20162 Milan, Italy. ⁶Department of Oncology and Hemato-Oncology, Università degli Studi di Milano, 20133 Milan, Italy. ⁷IFOM-FIRC Institute of Molecular Oncology, 20139 Milan, Italy. ⁸Department of Physics, Università degli Studi di Milano, and I.N.F.N., 20133 Milan, Italy.

*Corresponding author. Email: alberto.bardelli@unito.it (A.B.); mariangela.russo@unito.it (M.R.)

BRAF-mutant HT29 cells that were derived from the same patient from whom the WiDr cell line originated (fig. S3, D and E). Furthermore, we confirmed that down-regulation or loss of DNA-repair components is maintained in persister cells (fig. S4, A to D). Therapy-induced modulation of DNA-repair gene expression was transient and expression levels returned to normal upon removal of treatment (fig. S5A). Cancer cells that had previously developed permanent resistance to targeted agents did not modulate the expression of DNA-repair genes in response to drugs (fig. S5, B and C).

To ascertain whether targeted therapies affect DNA-repair competence in CRC cells, we used fluorescence-based multiplex host-cell reactivation (FM-HCR) assays (27). CRC cells were transfected with a G:G mismatch-containing plasmid to determine the impact of drug treatment on MMR capacity. An MMR-deficient (MMRd) human CRC cell line (LIM1215) was used as a positive control for MMR loss. We found that in CRC cells treated with targeted agents, MMR proficiency (MMRp) was significantly reduced (Fig. 1C and fig. S6A).

We next evaluated cellular HR capability by using the two-step, plasmid-based pDRGFP/pCBASce-I assay (28). Upon stable expression of the pDRGFP plasmid, we measured the generation of a green fluorescent signal upon DSBs induced by Sce-I expression. This assay showed that both DiFi and WiDr cells had a marked reduction in HR proficiency upon treatment with targeted therapies (Fig. 1D and fig. S6B).

MMR proteins are down-regulated in samples of CRC residual disease after targeted treatment

To determine whether the cell-based findings extend to patient-derived tumor samples, we exploited our CRC biobank of molecularly and therapeutically annotated patient-derived xenograft (PDX) models (29, 30). We selected six MSS PDX models with wild-type *KRAS*, *NRAS*, and *BRAF* in which EGFR inhibition by cetuximab led to tumor regression to a variable extent, paralleling the clinical scenario (Fig. 2A). Immunohistochemistry analysis unveiled areas with down-regulation of MLH1 and/or MSH2 in all neoplastic samples obtained when tumors were at the point of maximum response to cetuximab but still contained residual persisters (Fig. 2, B and C, and fig. S7, A to D), as compared with placebo-treated controls.

We next investigated whether down-regulation of DNA-repair proteins also occurs in clinical specimens from two CRC patients who achieved an objective partial response upon treatment with FOLFOX (folinic acid, 5-fluorouracil, and oxaliplatin) plus panitumumab. In both instances, tumor specimens were longitudinally

collected at diagnosis and at maximal therapeutic response, when a limited number of tumor cells persist despite treatment. MLH1 and MSH2 were down-regulated in tumor samples obtained at response compared with pretreatment specimens, confirming the clinical relevance of our findings (Fig. 2D).

Induction of DNA damage and error-prone DNA polymerases in CRC cells treated with targeted therapies

In addition to reduced DNA-repair ability, we found that targeted therapies triggered a switch from high-fidelity to low-fidelity DNA polymerases. DNA polymerases usually

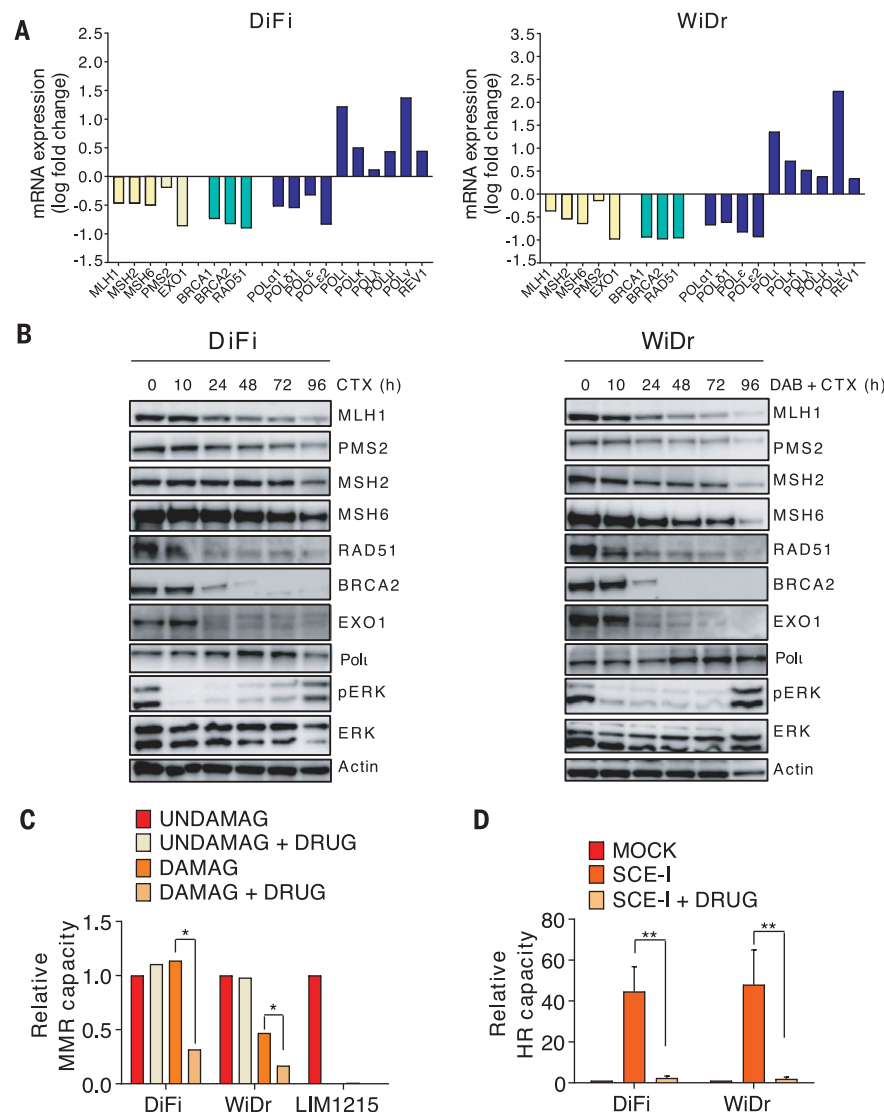


Fig. 1. CRC cells modulate DNA-repair effectors in response to targeted agents. (A) CRC cells were treated with cetuximab alone (DiFi) or in combination with the BRAF inhibitor DAB (WiDr) for 96 hours and RNA-seq analysis was performed. MMR (yellow), HR (green), and DNA polymerase (blue) genes are reported. Results represent means of two independent experiments. (B) CRC cells were treated and analyzed at the indicated time points by Western blot. CTX, cetuximab; pERK, phosphorylated extracellular signal-regulated kinase. (C) CRC cells were transfected with G:C undamaged (UNDAMAG) plasmid or with G:G mismatch-damaged (DAMAG) plasmid. Where indicated (DRUG), cells were treated with targeted therapies for 50–60 hours and analyzed by flow cytometry. A mock transfection was used as a control. Quantification of MMR capacity of each cell line relative to control is reported in the bar graph. LIM1215, MMR-deficient CRC cells, were used as a positive control for MMR loss. Results represent means of two independent experiments. * $p < 0.05$ (Student's *t* test). (D) pDRGFP-stably expressing CRC cells were transfected with the pCBASce-I plasmid and then either left in the absence of drug or treated with targeted therapies for 50–60 hours and analyzed by flow cytometry. A mock transfection was used as a control. Quantification of HR capacity of each cell line relative to mock is reported in the bar graph. Results represent means \pm SD ($n = 3$). ** $p < 0.01$ (Student's *t* test).

involved in accurate DNA replication, such as POL δ and POL ϵ , were down-regulated, whereas DNA polymerases characterized by poor accuracy, low processivity, and absence of proofreading capacity (i.e., error-prone polymerases) were induced (Fig. 1A and fig.

S4A). These included PolI, PolK, and Rev1 (which belong to the Y family of polymerases, orthologous to the bacterial stress-induced polymerases Pol IV and Pol V), as well as Pol λ and Pol μ (31) (Fig. 1, A and B, and figs. S1, G and H; S2B; S3, B to C and E; and S4,

A and D). Error-prone polymerases replace canonical high-fidelity polymerases that stall when encountering a DNA lesion and facilitate DNA replication across DNA damage sites in a manner that introduces errors into the genome (15, 16, 20); this may lead to base

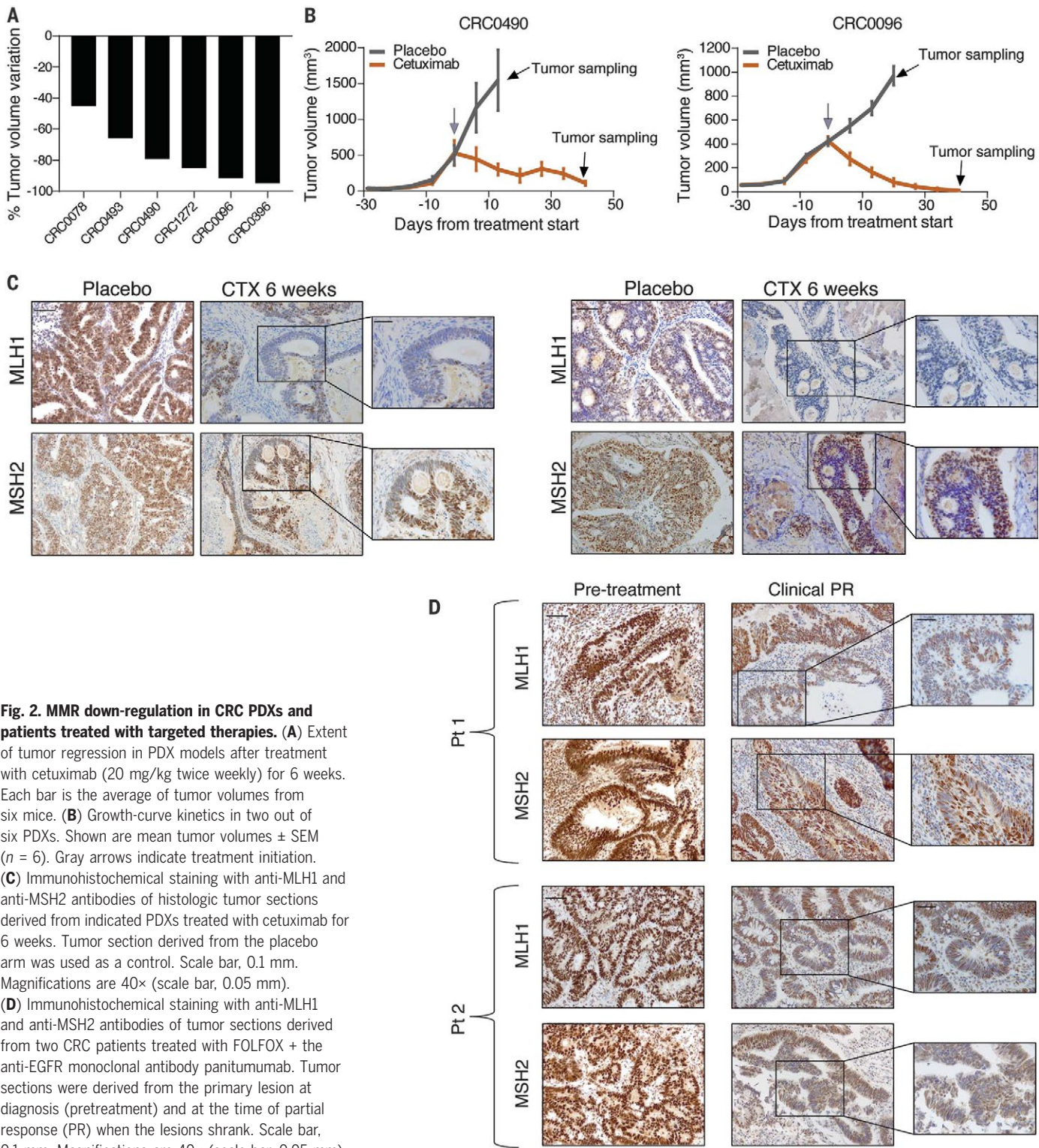


Fig. 2. MMR down-regulation in CRC PDXs and patients treated with targeted therapies. (A) Extent of tumor regression in PDX models after treatment with cetuximab (20 mg/kg twice weekly) for 6 weeks. Each bar is the average of tumor volumes from six mice. (B) Growth-curve kinetics in two out of six PDXs. Shown are mean tumor volumes \pm SEM ($n = 6$). Gray arrows indicate treatment initiation. (C) Immunohistochemical staining with anti-MLH1 and anti-MSH2 antibodies of histologic tumor sections derived from indicated PDXs treated with cetuximab for 6 weeks. Tumor section derived from the placebo arm was used as a control. Scale bar, 0.1 mm. Magnifications are 40 \times (scale bar, 0.05 mm). (D) Immunohistochemical staining with anti-MLH1 and anti-MSH2 antibodies of tumor sections derived from two CRC patients treated with FOLFOX + the anti-EGFR monoclonal antibody panitumumab. Tumor sections were derived from the primary lesion at diagnosis (pretreatment) and at the time of partial response (PR) when the lesions shrank. Scale bar, 0.1 mm. Magnifications are 40 \times (scale bar, 0.05 mm).

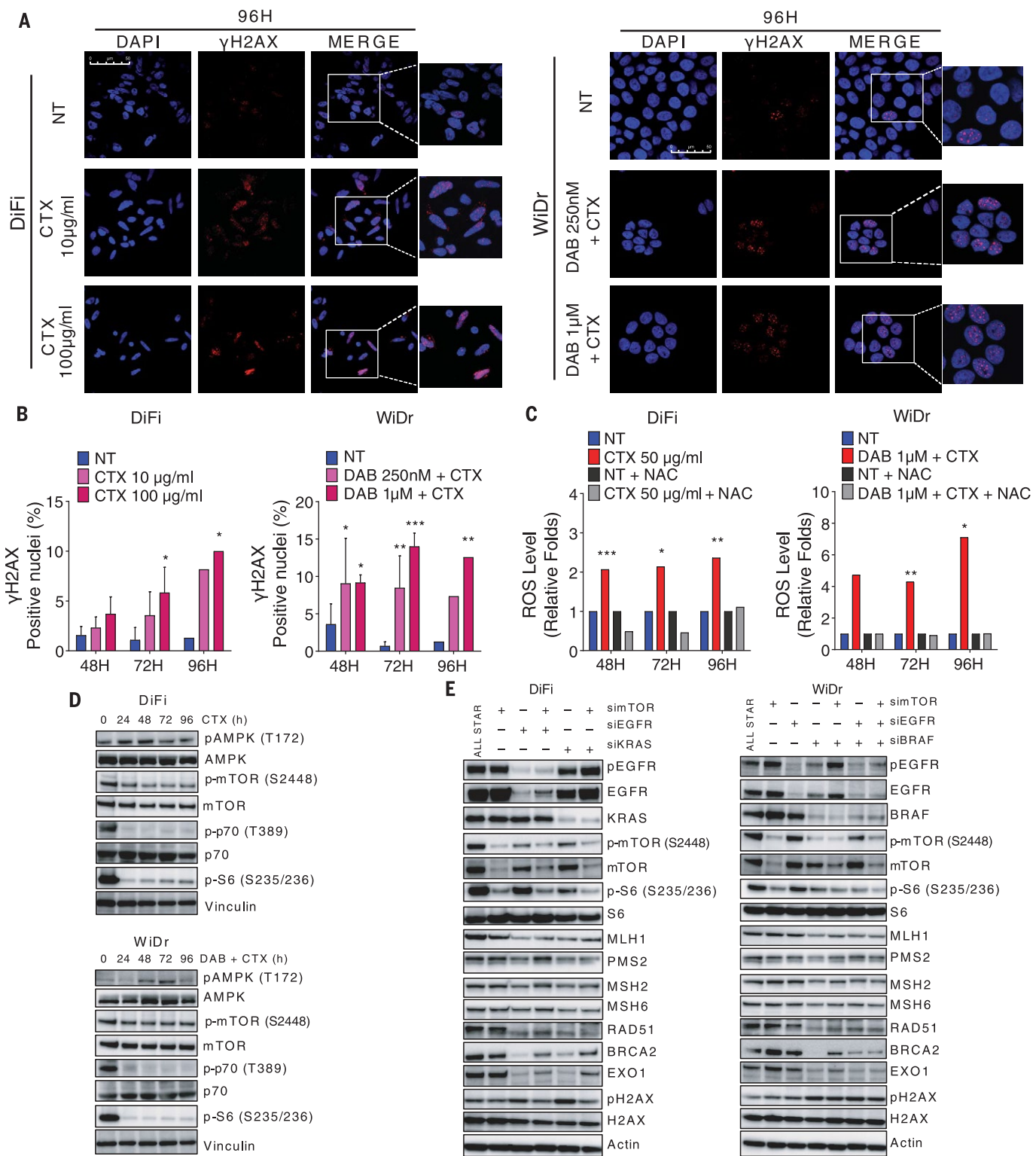


Fig. 3. Targeted therapies trigger a stress response, increase ROS levels, and induce DNA damage in CRC cells. (A) CRC cells were treated as reported and fixed and stained with anti- γ H2AX antibody at the indicated time points. Vehicle-treated cells (NT) were used as controls. Nuclei are stained with DAPI (blue) and anti- γ H2AX antibody (red). Scale bar, 50 μ m. Representative images for each condition are shown. (B) Quantification of nuclear γ H2AX foci in DiFi (left panel) and WiDr (right panel) cells. Results represent means \pm SD ($n = 3$ for 48 and 72 hours; $n = 2$ for 96 hours). * $p < 0.05$; ** $p < 0.01$; *** $p < 0.001$ (two-way ANOVA).

(C) CRC cells were treated as indicated and ROS levels were measured. NAC was used as a control to rescue ROS production. Results represent means of two independent experiments. * $p < 0.05$; ** $p < 0.01$; *** $p < 0.001$ (Student's *t* test). **(D)** CRC cells were treated with targeted therapies and analyzed by Western blot at the indicated time points. pAMPK, phosphorylated adenosine monophosphate kinase. **(E)** Wild-type DiFi (left panel) and *BRAF*-mutated WiDr (right panel) cells were transfected with the indicated siRNA or combination of siRNAs for 72 hours and analyzed by Western blot. ALL STAR, nontargeting siRNA.

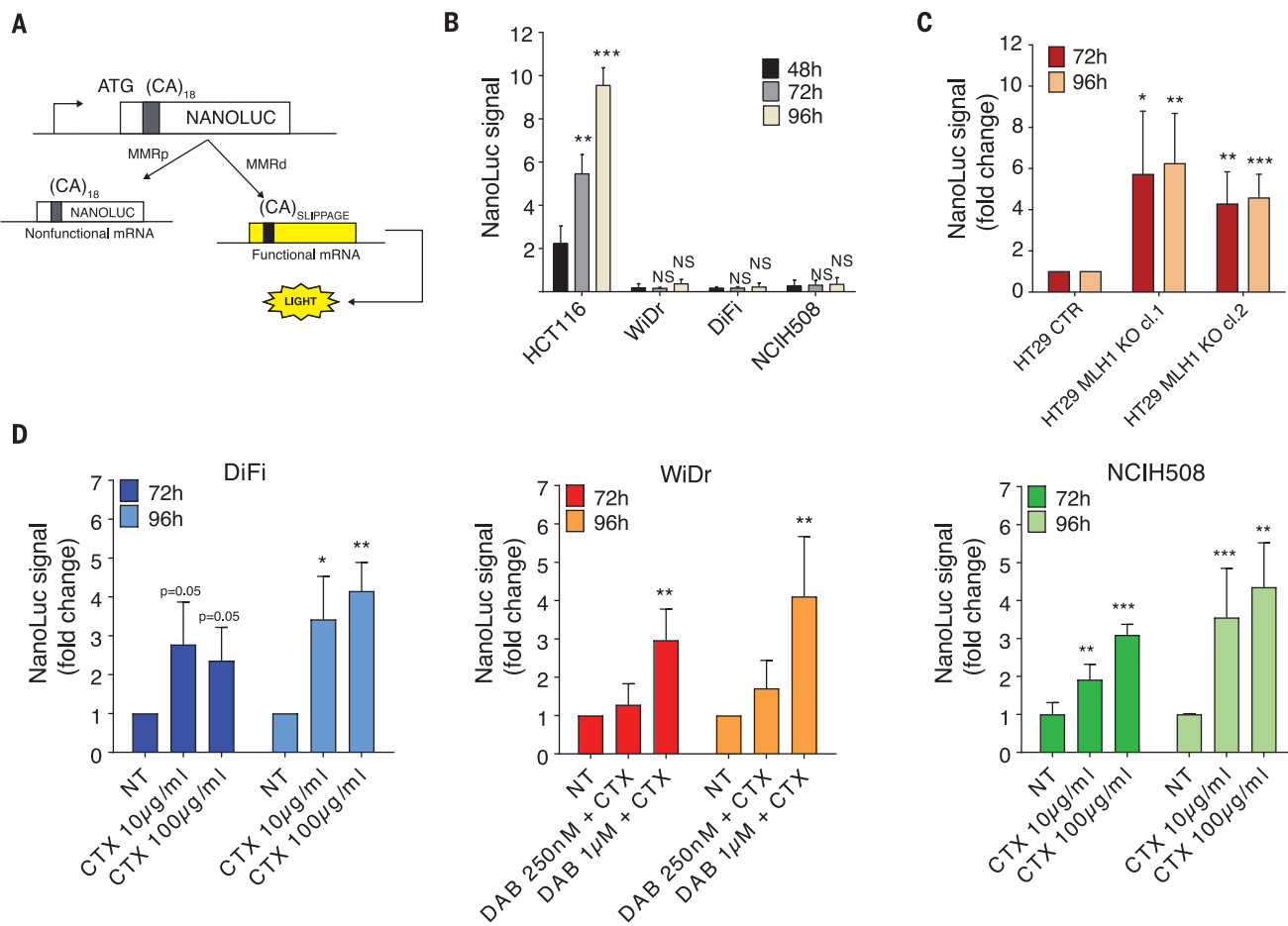


Fig. 4. Treatment with targeted therapies promotes mutagenesis in CRC cells. (A) Schematic representation of the CA-NanoLuc reporter assay. (B) MMRd HCT116 and MMRp DiFi, WiDr, and NCIH508 CRC cells were transduced with the NanoLuc lentivirus. At the indicated time points, NanoLuc signal was evaluated and normalized to cell viability. Results represent means \pm SD ($n = 3$). ** $p < 0.01$; *** $p < 0.001$ (Student's t test). NS, not a statistically significant difference. (C) NanoLuc signal in HT29 MLH1-KO clones (cl. 1 and cl. 2). NanoLuc signal was evaluated after 72 and 96 hours of growth in standard

conditions and normalized to cell viability. NanoLuc signal from MLH1 KO clones was then compared with signal detected in MLH1 wild-type cells (CTR). Results represent means \pm SD ($n = 4$). * $p < 0.05$; ** $p < 0.01$; *** $p < 0.001$ (Student's t test). (D) DiFi, WiDr, and NCIH508 CRC cells were treated as indicated. NanoLuc signal was normalized to cell viability. NanoLuc signal from treated cells was then compared with signal detected in untreated (NT) cells. Results represent means \pm SD ($n = 3$). * $p < 0.05$; ** $p < 0.01$; *** $p < 0.001$ (Student's t test).

mispairings, incorporation of aberrant DNA primer ends, and increased mutagenesis rate (32, 33).

We therefore investigated whether treatment with targeted therapies leads to genomic damage in cancer cells and if error-prone-mediated repair of DNA damage is favored when CRC cells encounter the hostile environment imposed by targeted therapies. Indeed, quantification of phosphorylation of H2AX at Ser¹³⁹ (γ H2AX), a common marker of DNA damage (34), revealed a dose- and time-dependent increase in the number of foci-positive nuclei upon drug treatment (Fig. 3, A and B, and fig. S8, A and B), whereas no further increase was observed in permanently resistant cells upon drug treatment (fig. S8, C and D). In addition, we observed a dose- and time-dependent increase in the number of

53BP1-positive nuclei upon EGFR and BRAF blockade (fig. S9, A and B). In direct opposition to BRCA1, 53BP1 promotes nonhomologous end joining-mediated DSB repair while preventing HR through restriction of end resection (35). These data suggest that targeted therapies trigger a switch from high-fidelity to error-prone-mediated repair of DNA damage, thereby potentially increasing the occurrence of mutations conferring drug resistance.

We next explored the possible causes of the DNA damage observed upon the administration of targeted therapies. Although several chemotherapeutic agents directly generate DNA damage, drugs interfering with oncogenic signaling (such as EGFR or BRAF inhibitors) are not directly genotoxic. However, it has been shown that certain targeted therapies, such as ABL and BRAF inhibitors, increase the levels

of reactive oxygen species (ROS) in cancer cells (36, 37), potentially contributing to DNA damage during treatment. ROS levels significantly increased when CRC cells were exposed to EGFR and BRAF inhibitors (Fig. 3C). By contrast, ROS levels were not increased in permanently drug-resistant (adapted) cells upon drug treatment (fig. S9C).

The drug-induced increase in ROS levels was abrogated when targeted therapies were administered in the presence of the antioxidant N-acetyl-L-cysteine (NAC) (Fig. 3C). NAC administration partially reduced the number of γ H2AX foci-positive nuclei upon EGFR and BRAF blockade (fig. S10, A and B). However, cotreatment with NAC did not prevent or rescue down-regulation of DNA-repair genes (fig. S10C). The addition of NAC delayed onset of relapse to targeted therapies when administered

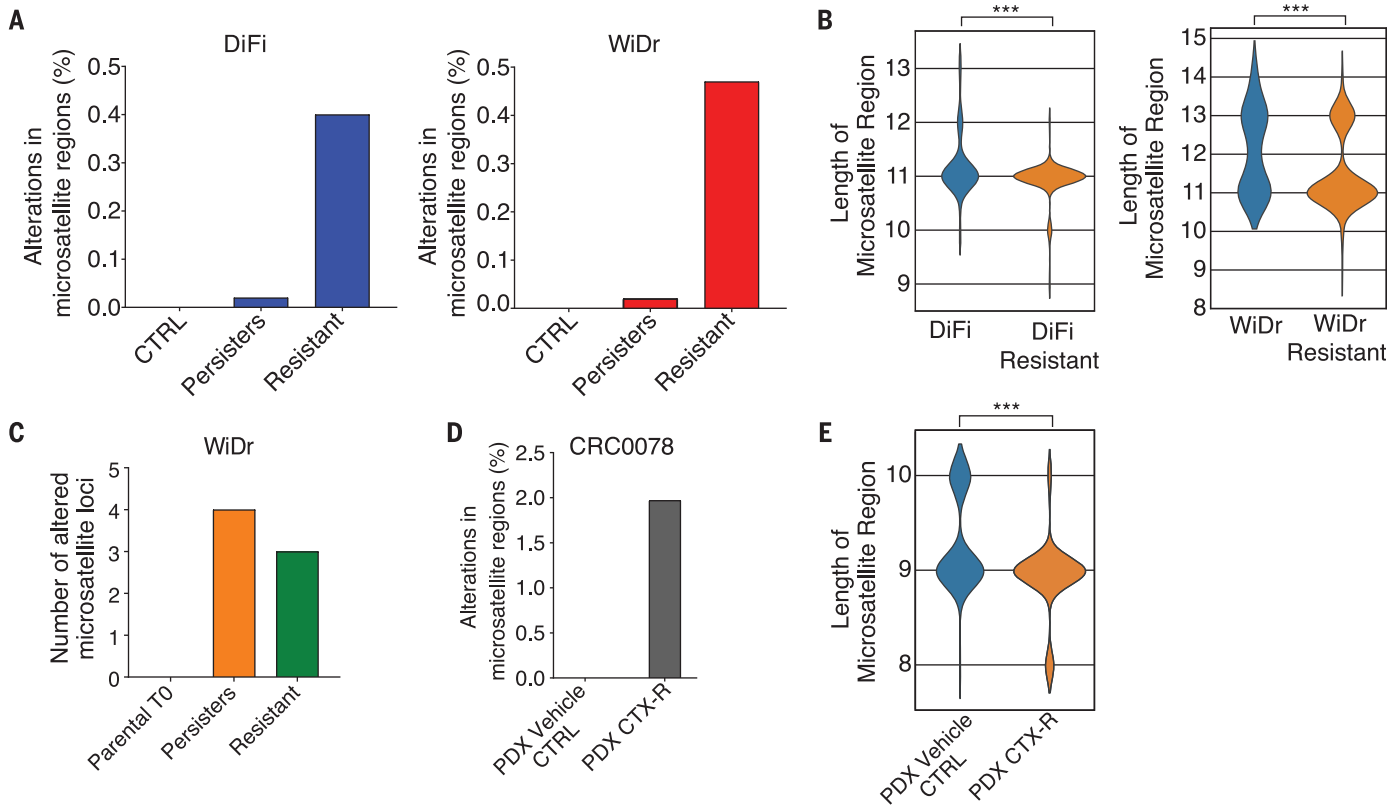


Fig. 5. Adaptive mutability leads to genetic instability in CRC cells in response to therapy-induced stress. (A) Percentage of unstable microsatellite regions in DiFi and WiDr persister and resistant cells compared with their parental counterpart (CTRL). (B) Length distribution of one representative microsatellite region for drug-resistant DiFi and WiDr cell lines. *** $p < 0.001$ (χ^2 test). (C) Number of unstable microsatellite sites detected by NGS-based high-depth capture panel in

WiDr cells (parental) treated with cetuximab + DAB for 14 days (persisters) and at resistance. (D) DNA was collected from one vehicle-treated and one cetuximab-resistant PDX. Percentage of unstable microsatellite regions of the tumor collected from the cetuximab-resistant mouse (PDX CTX-R) compared with the vehicle-treated (CTRL) mouse is reported. (E) Length distribution of one representative microsatellite region. *** $p < 0.001$ (χ^2 test).

together with mitogen-activated protein kinase (MAPK) pathway inhibitors (fig. S10, D and E) (38, 39).

Interfering with oncogenic dependencies initiates a stress response in CRCs

To elucidate the mechanistic basis of therapy-induced mutagenesis in cancer cells, we tested whether the adaptive mutability that we observed in response to targeted therapies was simply a secondary response to G₁ cell-cycle arrest or DNA damage or if it represented an active stress response. We found that thymidine-mediated cell-cycle stress (fig. S11, A to C) or direct DNA damage with the alkylating agent oxaliplatin (fig. S11, D to F) instead promoted the up-regulation of the MMR- and HR-repair systems (fig. S11, C and F), and G₁ cell-cycle arrest by nutrient starvation did not lead to modulation of DNA-repair gene expression (fig. S11, G to I). In bacterial cells, both the DNA damage-activated SOS response and the general stress response appear to be required to induce adaptive mutagenesis (74). We therefore examined the modulation of the kinase

mammalian target of rapamycin (mTOR), which is a master regulator of mammalian cellular stress response (40). Indeed, the mTOR effectors pS6K-p70K were down-regulated with kinetics comparable to that of MMR and HR regulation upon EGFR and BRAF pharmacological blockade (Fig. 3D). However, silencing of mTOR did not affect the expression of DNA-repair proteins or γ H2AX (Fig. 3E). It is therefore plausible that down-regulation of mTOR contributes to stress-induced mutagenesis of cancer cells but is not sufficient to activate this phenotype.

The exquisite sensitivity of DiFi and WiDr cells to EGFR and BRAF blockade reflects cell-specific oncogenic alterations. The EGFR locus is amplified in DiFi cells (2); the WiDr cells carry the BRAF p.V600E oncogenic mutation, but they also become dependent on feedback activation of EGFR when treated with BRAF inhibitors (41). We therefore investigated whether interfering with the oncogenic dependency of cancer cells could directly initiate the drug-induced stress phenotype. Indeed, small interfering RNA (siRNA)-mediated knockdown

of EGFR or KRAS in DiFi cells and of BRAF (\pm EGFR) in WiDr cells led to reduced expression of DNA-repair proteins, triggered DNA damage and mTOR down-regulation (Fig. 3E), and increased ROS levels (fig. S12). These results exclude the possibility that drug-induced down-regulation of DNA-repair pathways could be due to a nonspecific (off-target) effect of the anti-EGFR antibody cetuximab or the BRAF inhibitor dabrafenib.

Targeted therapies induce adaptive mutability in CRC cells

Next, we tested whether the stress response induced by targeted therapies translated into increased mutagenesis in CRC cells. We used a reporter assay in which a dinucleotide CA-repeat microsatellite drives the NanoLuc enzyme coding sequence out of frame (Fig. 4A). Random mutations that introduce frameshifts in this region, in the absence of a functional MMR, would restore the NanoLuc open reading frame, leading to bioluminescence. Analogous approaches have previously been used to measure MMR defects in cancer cells (42–44).

To validate the assay, we first introduced the CA-NanoLuc vector into a MMRd human CRC cell line (HCT116) and three MMRp human CRC cell lines (DiFi, WiDr, and NCIH508). The NanoLuc signal was significantly higher in MMRd cells after 48 hours of standard growth conditions (Fig. 4B). This difference was further increased when HCT116 cells were kept in culture for several days, whereas the signal in the MMRp lines remained low (Fig. 4B), indicating that the CA-NanoLuc assay effectively detects MMR deficiency in cancer cells.

We next used the CA-NanoLuc system to measure the impact of ectopic inactivation of MMR in CRC cells. To this end, we used CRISPR-CAS9 to inactivate the *MLH1* gene in the HT29 human CRC cell line. After the isolation of two independent *MLH1* knockout (KO) clones (fig. S13, A and B), they were transduced with the CA-NanoLuc vector. *MLH1* KO clones exhibited higher levels of NanoLuc signal as expected, confirming that the assay can detect inactivation of DNA MMR (Fig. 4C). Next, drug-dependent (transient) MMR down-regulation was evaluated. EGFR and BRAF inhibition led to time-dependent increases of bioluminescence (Fig. 4D), paralleling the down-regulation of DNA-repair effectors and the up-regulation of low-fidelity polymerases. We further found that permanently resistant derivatives no longer exhibited adaptive mutability in response to targeted therapies (fig. S14).

Genomic alterations in CRC cells upon treatment with targeted therapies

To determine whether molecular evidence of adaptive mutability was present in the genome of CRC cells treated with EGFR and BRAF inhibitors, we analyzed whole-exome sequencing (WES) data from DiFi and WiDr parental, persister, and drug-resistant derivative cells. The overall mutational burden (i.e., the number of mutations per megabase) of persisters and the drug-resistant cell population was only marginally affected (fig. S15, A and B). As a control, we assessed whether MMR permanent inactivation induced by *MLH1* KO affected the mutational burden of HT29 CRC cells and found that it was only marginally affected (fig. S16A).

Given these results, we changed our approach. Because treatment with targeted therapies led to a transient MMR-deficient phenotype, we reasoned that MMR status could be more easily detected by examining microsatellite regions, where DNA replication slippage errors occur frequently and are ineffectively repaired in the absence of MMR. Indeed, WES analysis unveiled alterations in microsatellite regions of HT29 in which the *MLH1* gene was genetically knocked out (fig. S16, B and C). We also detected increased genetic instability in the microsatellite regions of CRC cells made resistant

to targeted agents (Fig. 5, A and B), as shown by a shift in the length of microsatellite regions, highlighting the impact of targeted therapies on the DNA-repair process and mutagenicity. To detect the occurrence of microsatellite alterations in nonclonal cell populations, we utilized a high-depth capture panel that detects hotspot somatic variants and shifts in the length of microsatellite regions. Indeed, such high-sensitivity analysis unveiled a significant shift in the length of microsatellite regions in both persister and drug-resistant cells (Fig. 5C and fig. S17).

We next assessed the impact of targeted therapies on the genomic landscape of PDXs by studying a PDX model (CRC0078) (Fig. 2A and fig. S7D) that was continuously treated with cetuximab until it developed resistance (fig. S18). WES analysis of the cetuximab-resistant tumor tissue revealed alterations in microsatellite genomic regions that were not present in the PDX tumor collected from the corresponding untreated mouse (Fig. 5, D and E). Overall, these results indicate that CRC cells and a CRC PDX model exposed to targeted therapies experience loss of replication fidelity in regions of nucleotide repeats.

Discussion

The development of resistance has emerged as a major limitation of targeted therapies directed against oncoproteins such as EGFR, BRAF, and ABL (25).

In this study, we tested the hypothesis that cancer cells treated with targeted therapies activate stress-induced mutagenic mechanisms. We found that persister (drug-tolerant) cancer cells that survive EGFR and/or BRAF inhibition exhibit DNA damage, down-regulate mismatch and HR repair proteins, switch from high-fidelity to error-prone-mediated repair of DNA damage, and transiently increase their mutagenic ability.

Stress-induced mutagenesis is a characteristic trait of unicellular organisms to transiently accelerate genetic diversity in a fraction of the population when encountering a hostile environment. (16). Indeed, we found that therapy-induced modulation of DNA repair in cancer cells is also transitory and reverts back once a mutational landscape able to restore the ability to grow in the presence of the drug is achieved. We postulate that in cells of multicellular organisms, stress-induced mutagenesis is not operational. However, in cancer cells that have lost tissue-imposed homeostasis—and in many ways operate like unicellular organisms—this ancestral program is still available and is unleashed by oncoprotein-targeted drugs. A similar process has also been observed in cancer cells undergoing hypoxia-driven stress (7, 45, 46).

The analysis of mutational signatures has emerged as a valuable tool with which to docu-

ment the mutational processes operative in cells (47). In future studies, it will be interesting to establish whether specific mutational signatures emerge under targeted therapies. Resolving such processes, which we postulate occur transiently in small cell subpopulations, is likely to require extensive genomic comparisons of multiple clones and independent data points.

These results may have clinical implications. The knowledge that cancer cells under therapeutic stress down-regulate key effectors of the DNA-repair machinery, such as MMR and HR, exposes a vulnerability that could be clinically exploited. For example, it will be important to assess whether down-regulation of HR proteins confers sensitivity to poly-ADP-ribose polymerases (PARP) inhibitors as observed in HR-deficient cancers (48–50). Moreover, pharmacological or genetic interference could be deployed to curb the cellular mechanisms that initiate drug-driven adaptive mutagenesis with the goal of reducing the generation of new variants during treatment. This strategy could potentially increase and prolong the clinical efficacy of targeted therapies.

REFERENCES AND NOTES

1. S. E. Luria, M. Delbrück, *Genetics* **28**, 491–511 (1943).
2. S. Misale et al., *Nature* **486**, 532–536 (2012).
3. L. A. Diaz Jr. et al., *Nature* **486**, 537–540 (2012).
4. A. Gutierrez et al., *Nat. Commun.* **4**, 1610 (2013).
5. H. Long et al., *Proc. Natl. Acad. Sci. U.S.A.* **113**, E2498–E2505 (2016).
6. I. Bjedov et al., *Science* **300**, 1404–1409 (2003).
7. D. M. Fitzgerald, P. J. Hastings, S. M. Rosenberg, *Annu. Rev. Cancer Biol.* **1**, 119–140 (2017).
8. P. L. Foster, *Crit. Rev. Biochem. Mol. Biol.* **42**, 373–397 (2007).
9. R. S. Galhardo, P. J. Hastings, S. M. Rosenberg, *Crit. Rev. Biochem. Mol. Biol.* **42**, 399–435 (2007).
10. E. Shor, C. A. Fox, J. R. Broach, *PLOS Genet.* **9**, e1003680 (2013).
11. E. Heidenreich, *Crit. Rev. Biochem. Mol. Biol.* **42**, 285–311 (2007).
12. D. M. Fitzgerald, S. M. Rosenberg, *PLOS Genet.* **15**, e1007995 (2019).
13. G. P. Rodriguez et al., *Proc. Natl. Acad. Sci. U.S.A.* **109**, 6153–6158 (2012).
14. R. G. Ponder, N. C. Fonville, S. M. Rosenberg, *Mol. Cell* **19**, 791–804 (2005).
15. G. J. McKenzie, S. M. Rosenberg, *Curr. Opin. Microbiol.* **4**, 586–594 (2001).
16. P. L. Foster, *BioEssays* **22**, 1067–1074 (2000).
17. F. Taddei et al., *Nature* **387**, 700–702 (1997).
18. J. Torkelson et al., *EMBO J.* **16**, 3303–3311 (1997).
19. W. A. Rosche, P. L. Foster, *Proc. Natl. Acad. Sci. U.S.A.* **96**, 6862–6867 (1999).
20. G. J. McKenzie, R. S. Harris, P. L. Lee, S. M. Rosenberg, *Proc. Natl. Acad. Sci. U.S.A.* **97**, 6646–6651 (2000).
21. S. V. Sharma et al., *Cell* **141**, 69–80 (2010).
22. G. R. Oxnard, *Nat. Med.* **22**, 232–234 (2016).
23. M. Ramirez et al., *Nat. Commun.* **7**, 10690 (2016).
24. A. N. Hata et al., *Nat. Med.* **22**, 262–269 (2016).
25. S. Misale, F. Di Nicolantonio, A. Sartore-Bianchi, S. Siena, A. Bardelli, *Cancer Discov.* **4**, 1269–1280 (2014).
26. S. Kopetz et al., *N. Engl. J. Med.* **381**, 1632–1643 (2019).
27. Z. D. Nagel et al., *Proc. Natl. Acad. Sci. U.S.A.* **111**, E1823–E1832 (2014).
28. A. J. Pierce, R. D. Johnson, L. H. Thompson, M. Jaslin, *Genes Dev.* **13**, 2633–2638 (1999).
29. A. Bertotti et al., *Nature* **526**, 263–267 (2015).
30. C. Isella et al., *Nat. Commun.* **8**, 15107 (2017).
31. A. J. Rattray, J. N. Strathern, *Annu. Rev. Genet.* **37**, 31–66 (2003).

32. V. M. Krutikov, *Mol. Biol. (Mosk.)* **40**, 3–11 (2006).
33. M. F. Goodman, *Annu. Rev. Biochem.* **71**, 17–50 (2002).
34. L. J. Mah, A. El-Osta, T. C. Karagiannis, *Leukemia* **24**, 679–686 (2010).
35. S. Panier, S. J. Boulton, *Nat. Rev. Mol. Cell Biol.* **15**, 7–18 (2014).
36. G. Cesì, G. Walbrecq, A. Zimmer, S. Kreis, C. Haan, *Mol. Cancer* **16**, 102 (2017).
37. M. Koptyra et al., *Blood* **108**, 319–327 (2006).
38. M. L. Sagristá, A. E. García, M. A. De Madariaga, M. Mora, *Free Radic. Res.* **36**, 329–340 (2002).
39. E. D. Chan, D. W. Riches, C. W. White, *Am. J. Respir. Cell Mol. Biol.* **24**, 627–632 (2001).
40. R. A. Saxton, D. M. Sabatini, *Cell* **168**, 960–976 (2017).
41. A. Prahallad et al., *Nature* **483**, 100–103 (2012).
42. J. Shen et al., *Nat. Med.* **24**, 556–562 (2018).
43. N. Chatterjee, Y. Lin, B. A. Santillan, P. Yotnda, J. H. Wilson, *Proc. Natl. Acad. Sci. U.S.A.* **112**, 3764–3769 (2015).
44. R. Parsons et al., *Cell* **75**, 1227–1236 (1993).
45. V. T. Mihaylova et al., *Mol. Cell. Biol.* **23**, 3265–3273 (2003).
46. R. S. Bindra, P. M. Glazer, *Cancer Lett.* **252**, 93–103 (2007).
47. M. Petljak et al., *Cell* **176**, 1282–1294.e20 (2019).
48. L. Li, H. Wang, E. S. Yang, C. L. Arteaga, F. Xia, *Cancer Res.* **68**, 9141–9146 (2008).
49. S. Nowsheen et al., *PLOS ONE* **6**, e24148 (2011).
50. J. Mateo et al., *Ann. Oncol.* **30**, 1437–1447 (2019).

ACKNOWLEDGMENTS

We thank members of Molecular Oncology Laboratory at Candiolo Cancer Institute for critically reading the manuscript, A. Cassingena and F. Sassi for their help with experiments, and G. McKenzie for the NanoLuc plasmid design. **Funding:** This research was supported by Fondazione AIRC under the 5 per Mille 2018 ID 21091 Program (P.I. A. Bardelli), G.L. S. Siena, G.L. A. Bertotti, G.L. L. Trusolino, G.L. F. Di Nicolantonio); AIRC 2010 Special Program Molecular Clinical Oncology 5 per Mille, Project No. 9970 Extension Program (A. Bardelli); AIRC IG no. 16788 (A. Bardelli); AIRC IG 2018-ID 21923 project (P.I. A. Bardelli); H2020 grant agreement no. 635342-2 MoTriColor (A. Bardelli); Ministero Salute, Ricerca Corrente 2019 RC2019 (A. Bardelli); H2020 grant agreement no. 754923 COLOSSUS (L.T.). A. Bardelli has also received research funding from PhoreMost and NeoPhore. **Author contributions:** M.R. and A. Bardelli conceived the study. M.R., A.S., N.M.R., S.A., S.L., V.A., A.M. M.C., M.G., and M.C.L. conducted the experiments and analyzed data. G.C. performed NGS and bioinformatics analysis. A. Bartolini performed NGS panel-based experiments. L.N. performed RNAseq bioinformatics analysis. Z.D.N. and C.G.P. provided plasmids harboring DNA damage. A. Bertotti and L.T. analyzed and provided PDX material. I.S. performed and analyzed IHC data; A.A., A.S.-B., and S.S. provided patient samples. F.D.N. analyzed data. M.R. and A. Bardelli wrote the manuscript. A. Bardelli supervised the study. **Competing interests:** L.T. is a paid consultant for Eli Lilly, AstraZeneca, and Merck KGaA. Z.D.N. is an inventor on a patent (U.S. 9,938,587) covering methods and kits for determining

DNA-repair capacity. A. Bardelli is a member of the scientific advisory board of NeoPhore and a shareholder of NeoPhore and PhoreMost. The other authors declare no competing interests.

Data and materials availability: The FM-HCR reporter plasmids are available from Z.D.N. under a material transfer agreement. The pDRGFp and the pCBASce-I plasmids are available from AddGene under a material transfer agreement. The NanoLuc-expressing plasmid is available from PhoreMost, Ltd. (Cambridge, UK) under a material transfer agreement. The HT29 empty and MLH1 KO cells are available from A. Bardelli (UNITO) under a material transfer agreement. RNA-sequencing and DNA-sequencing data have been deposited in ENA (from EBI; no. PRJEB28674).

SUPPLEMENTARY MATERIALS

science.sciencemag.org/content/366/6472/1473/suppl/DC1
Materials and Methods
Figs. S1 to S18
Tables S1 and S2
References (51–61)

[View/request a protocol for this paper from Bio-protocol.](#)

21 September 2018; resubmitted 24 July 2019
Accepted 26 October 2019
Published online 7 November 2019
10.1126/science.aav4474

SOMETIMES THE GRASS REALLY IS GREENER SOMEPLACE NEW.



[Find a new job at ScienceCareers.org/cancer](https://www.ScienceCareers.org/cancer)

There's scientific proof that when you're happy with what you do, you're better at what you do. Access career opportunities, see who's hiring and take advantage of our proprietary career-search tools. Get tailored job alerts, post your resume and manage your applications all in one place. Start here: [sciencecareers.org](https://www.ScienceCareers.org)

Science Careers

FROM THE JOURNAL SCIENCE AAAS

CANCER

Highly efficient and tumor-selective nanoparticles for dual-targeted immunogene therapy against cancer

Kuan-Wei Huang^{1*}, Fu-Fei Hsu^{2*}, Jiantai Timothy Qiu^{3,4,5*}, Guann-Jen Chern¹, Yi-An Lee¹, Chih-Chun Chang¹, Yu-Ting Huang⁶, Yun-Chieh Sung¹, Cheng-Chin Chiang¹, Rui-Lin Huang¹, Chu-Chi Lin⁵, Trinh Kieu Dinh¹, Hsi-Chien Huang¹, Yu-Chuan Shih¹, Donia Alson⁵, Chun-Yen Lin^{3,7}, Yung-Chang Lin⁸, Po-Chiao Chang⁷, Shu-Yi Lin^{6†}, Yunching Chen^{1†}

While immunotherapy holds great promise for combating cancer, the limited efficacy due to an immunosuppressive tumor microenvironment and systemic toxicity hinder the broader application of cancer immunotherapy. Here, we report a combinatorial immunotherapy approach that uses a highly efficient and tumor-selective gene carrier to improve anticancer efficacy and circumvent the systemic toxicity. In this study, we engineered tumor-targeted lipid-dendrimer-calcium-phosphate (TT-LDCP) nanoparticles (NPs) with thymine-functionalized dendrimers that exhibit not only enhanced gene delivery capacity but also immune adjuvant properties by activating the stimulator of interferon genes (STING)-cGAS pathway. TT-LDCP NPs delivered siRNA against immune checkpoint ligand PD-L1 and immunostimulatory IL-2-encoding plasmid DNA to hepatocellular carcinoma (HCC), increased tumoral infiltration and activation of CD8⁺ T cells, augmented the efficacy of cancer vaccine immunotherapy, and suppressed HCC progression. Our work presents nanotechnology-enabled dual delivery of siRNA and plasmid DNA that selectively targets and reprograms the immunosuppressive tumor microenvironment to improve cancer immunotherapy.

INTRODUCTION

Immunotherapy is rapidly emerging as a promising therapeutic strategy against cancer. In contrast to conventional anticancer agents that are often directly cytotoxic toward cancer cells, immunotherapy activates immune cells to recognize and eradicate tumor cells. Recently developed cancer immunotherapies include vaccines, chimeric antigen receptor T cell therapy, immune checkpoint blockade, and cytokine therapy (1). For example, in the clinic, interleukin-2 (IL-2), a key cytokine that drives the proliferation and activation of T cells, is used as an effective immunotherapy against cancer (2). Nivolumab—the first anti-PD-1 (programmed cell death 1) antibody—has shown substantial clinical activity in various cancer types. Vaccines composed of genetically modified tumor cells secreting various cytokines [i.e., granulocyte-macrophage colony-stimulating factor (GM-CSF) and IL-2] reportedly stimulate potent, specific, and long-lasting antitumor effects (3). However, immunotherapy-based stimulation of the immune system often induces adverse autoreactive immune responses and related side effects (4). Confoundingly, an immunosuppressive tumor microenvironment (TME) limits the efficacy of immunotherapy. The structurally and functionally aberrant tumor vasculature leads to a highly heterogeneous and hypoxic TME that facilitates the release of immunosuppressive cytokines from both

tumor and stromal cells, promotes the infiltration of immunosuppressive bone marrow-derived cells, and limits the tumor infiltration of T cells, leading to suppression of the antitumor immune response (4, 5). Thus, the application of immunotherapy to treat cancer remains challenging, and there is an urgent need to explore new strategies that are safe and effective (6).

Hepatocellular carcinoma (HCC), an aggressive primary liver cancer, develops from chronically damaged tissue (7). HCC is associated with a hypoxic and inflammatory TME that promotes tumor progression and causes resistance to therapy (8). Immunosuppression mechanisms, such as deficiency of immunostimulatory cytokines and induction of immunosuppressive cytokines and immunoregulatory cells caused by tumor hypoxia, are involved in the development of immunotherapy resistance and limit its therapeutic outcome (8). Although recently developed immune checkpoint inhibitors provided clinical benefit to patients with advanced HCC, targeting a single pathway may not be sufficient to achieve potent immunotherapeutic effects (9, 10). Thus, the development of combination strategies targeting multiple immune regulatory pathways may effectively shift the TME in HCC toward a proimmune state and achieve potent antitumor immunity with substantial therapeutic benefit (10, 11).

Here, we propose applying dual-targeted immunogene therapy using small interfering RNA (siRNA) against immunosuppressive factors and plasmid DNA (pDNA) encoding immunostimulating cytokines to modulate the TME and activate immune effector cells. Despite the potential of immunogene therapy in cancer treatment, the barriers against therapeutic siRNA/pDNA reaching their target cells and exerting efficient gene silencing/gene expression effects limit their potential. The short half-life in blood circulation, lack of tumor-specific cellular uptake, inefficient intracellular release of siRNA/pDNA, and poor nuclear entry of pDNA limit their efficacy *in vivo* (12). To overcome these challenges, nanoscale formulations were designed and used to encapsulate the therapeutic genetic cargoes with enhanced stability, controlled cargo release properties, and increased transfection activity (13, 14). In this study, we designed

Copyright © 2020
The Authors, some
rights reserved;
exclusive licensee
American Association
for the Advancement
of Science. No claim to
original U.S. Government
Works. Distributed
under a Creative
Commons Attribution
NonCommercial
License 4.0 (CC BY-NC).

¹Institute of Biomedical Engineering and Frontier Research Center on Fundamental and Applied Sciences of Matters, National Tsing Hua University, Hsinchu 30013, Taiwan. ²Institute of Biomedical Sciences, Academia Sinica, Taipei, Taiwan. ³College of Medicine, Chang Gung University, Taoyuan, Taiwan. ⁴Department of Obstetrics and Gynecology, Chang Gung Memorial Hospital, Taoyuan, Taiwan. ⁵Department of Biomedical Sciences, School of Medicine, Chang Gung University, Taoyuan, Taiwan. ⁶Institute of Biomedical Engineering and Nanomedicine, National Health Research Institutes, Miaoli County 35053, Taiwan. ⁷Division of Hepatology, Department of Gastroenterology and Hepatology, Linkou Medical Center; Chang Gung Memorial Hospital, Taoyuan, Taiwan. ⁸Division of Medical Oncology/Hematology, Chang Gung Memorial Hospital, Taoyuan, Taiwan.

*These authors contributed equally to this work.

†Corresponding author. Email: yunching@mx.nthu.edu.tw (Y.C.); shuyi@nhri.org.tw (S.-Y.L.)

nanoparticles (NPs) that contain an HCC-targeting peptide and a unique dendrimer–calcium phosphate (CaP) core that harbors nucleic acids for gene delivery. Figure 1 illustrates our design of a tumor-targeted NP that carries siRNA against the immune checkpoint PD-L1 and pDNA encoding the immunostimulating cytokine IL-2 to promote antitumor immunity and increase the efficacy of whole-cell cancer vaccines. This nanoscale immunogene therapy exhibits multi-functional characteristics, including (i) a tumor-targeting peptide (SP94) that enhances the tumor accumulation of NPs and increases the efficiency of intracellular delivery of the therapeutic pDNA/siRNA to HCC cells (15, 16); (ii) a pH stimuli-responsive CaP core to achieve endosomal escape, along with enhanced release of the nucleic acid; (iii) thymine-capped polyamidoamine (PAMAM) dendrimers loaded in the CaP core to further enhance the endosomal escape and nuclear entry of pDNA, leading to promising gene transfection activity; and (iv) thymine-capped PAMAM dendrimers that can activate the stimulator of interferon genes (STING)–cyclic GMP-AMP synthase (cGAS) pathway and serve as immunotherapy adjuvants to promote cellular immunity. Efficient tumor-targeted delivery of therapeutic gene cocktails that achieve tumor-specific expression of immunostimulating cytokines and down-regulation of immune checkpoints holds promise for effective and safe immunotherapy regimens.

RESULTS

Preparation and characterization of tumor-targeted lipid/dendrimer/CaP NPs loaded with siRNA and pDNA

To overcome the challenges of current gene delivery carriers, we designed complex NPs with a core-shell structure composed of a dendrimer-CaP core loaded with nucleic acids that are coated with a synthetic lipid bilayer shell. The preparation and proposed structure of the siRNA/pDNA-loaded, HCC-targeted lipid-dendrimer-CaP (LDCP) NPs are shown in Fig. 1. While excessive nucleic acid condensation can impede the release of siRNA/pDNA, insufficient interaction of dendrimers with nucleic acid may limit the transfection efficiency. We found that unmodified, 10 and 50% thymine-modified PAMAM more readily condensed siRNA/pDNA than 90% thymine-modified PAMAM (Fig. 2A). Alternatively, both 50 and 90% thymine-modified PAMAM showed efficient dissociation of siRNA/pDNA in the presence of anionic materials, such as heparin (Fig. 2B). Of the tested thymine coverages, only the 50% thymine-modified PAMAM promoted both siRNA/pDNA condensation and efficient release of siRNA/pDNA, which is predictive of increased transfection activity. This finding is consistent with previous studies suggesting enhanced gene transfection mediated by the 50% thymine-capped PAMAM dendrimer/pDNA complex (17). Thus, 50% thymine-capped PAMAM dendrimers were used to form the dendrimer/siRNA/pDNA complex at a weight ratio of approximately 2:1:1. Assembly of the dendrimer/siRNA/pDNA complex in 1,2-dioleoyl-sn-glycero-3-phosphate (DOPA)-coated CaP cores was performed in a water-in-oil microemulsion containing Igepal-520 as a surfactant (18). To increase the in vivo stability and cellular uptake of NPs, outer leaflet lipids {1,2-dioleoyl-3-trimethylammonium-propane (DOTAP), cholesterol, and 1,2-distearoyl-sn-glycero-3-phosphoethanolamine-N-[methoxy(polyethylene glycol)-2000] (DSPE-PEG2000)} were added to the DOPA-coated dendrimer/siRNA/pDNA/CaP cores. To achieve tumor-specific uptake of siRNA/pDNA, we further modified the surface of the NPs with the HCC-targeting peptide SP94.

To assess the impact of 50% thymine-capped PAMAM dendrimers on NP characteristics, transmission electron microscopy (TEM) was performed. Dendrimer incorporation did not significantly affect NP sphere formation as NPs with or without added dendrimers formed well-dispersed spheres (Fig. 2C). The average diameters of lipid-CaP (LCP) NPs without added dendrimers and LDCP NPs with 50% thymine-capped PAMAM dendrimers were 87.1 ± 3.6 and 110.5 ± 8.7 nm, respectively (Fig. 2D). NPs with or without added dendrimers showed a similar negative zeta potential of approximately -7 mV and a polydispersity index of 0.2 to 0.3 (Fig. 2D). While the percentage of pDNA encapsulated in NPs (greater than 95%) was not affected by dendrimers, the percentages of encapsulated siRNA increased from 64% in LCP NPs to 87% in LDCP NPs (Fig. 2D). To evaluate whether siRNA/pDNA would be efficiently released in acidic endosomes/lysosomes after entering cancer cells, TEM images were captured under acidic pH conditions. Structural alteration of the NPs due to decomposition of the CaP cores was observed (Fig. 2C). As expected, the release of genetic cargoes (FAM-labeled siRNA) from LDCP NPs under physiological conditions (pH 7.4) was much slower than that observed under acidic conditions (pH 5.5) (fig. S1), indicating pH-dependent decomposition of the CaP cores in NPs, which signifies the endosomal/lysosomal release of siRNA/pDNA from LDCP NPs.

TT-LDCP NPs efficiently deliver siRNA and pDNA into HCC cells with potent transfection efficiency in vitro and in vivo

We next examined how the thymine-capped PAMAM dendrimer and HCC-targeted SP94 peptide affected uptake of NPs in vitro and in vivo. We examined the cellular uptake of siRNA/pDNA loaded in LDCP NPs in two HCC cell lines: human Hep3B and murine HCA-1. The cellular uptake of fluorescently labeled siRNA/pDNA in both cell lines was higher when the siRNA/pDNA was loaded in tumor-targeted LDCP (TT-LDCP) NPs than when it was loaded in non-targeted LDCP NPs or in TT-LCP (TT-LCP) NPs without dendrimers (Fig. 3, A and B). In addition, enhanced nuclear uptake of pDNA was observed for pDNA delivered by TT-LDCP NPs containing 50% thymine-capped PAMAM, compared with pDNA delivered by TT-LCP NPs or by TT-LDCP NPs containing unmodified PAMAM (Fig. 3, A and B, and figs. S2 and S3).

We further evaluated the biodistribution of TT-LDCP NPs in murine orthotopic HCC (HCA-1) models after intravenous administration of NPs. FAM-labeled siRNA was used to track the biodistribution of TT-LDCP NPs (fig. S4). Increased uptakes of TT-LDCP NPs in tumor, liver, spleen, and lung were observed compared with free siRNA 2 hours after intravenous administration. More significantly, most TT-LDCP NPs were accumulating to a larger extent in tumors and liver as compared with other organs (fig. S4). We then studied the uptake of fluorescently labeled siRNA/pDNA in murine orthotopic HCC (HCA-1) models after intravenous administration of LDCP NPs. Higher siRNA/pDNA delivery was observed in HCC tumor tissue of mice that received TT-LDCP NPs compared with mice that received nontargeted NPs (Fig. 3C and fig. S5). Delivery was mostly cytosolic with a heterogeneous distribution within the HCC tumor tissues (Fig. 3C).

Next, we studied how the thymine-capped PAMAM dendrimer and HCC-targeted SP94 peptide affected the transfection efficiency of pDNA encoding firefly luciferase (luc pDNA) in human (Hep3B, JHH-7) and murine (HCA-1) HCC cells. At higher concentrations of pDNA, all cell lines exhibited significantly increased luciferase expression when luc pDNA was delivered by TT-LDCP NPs compared

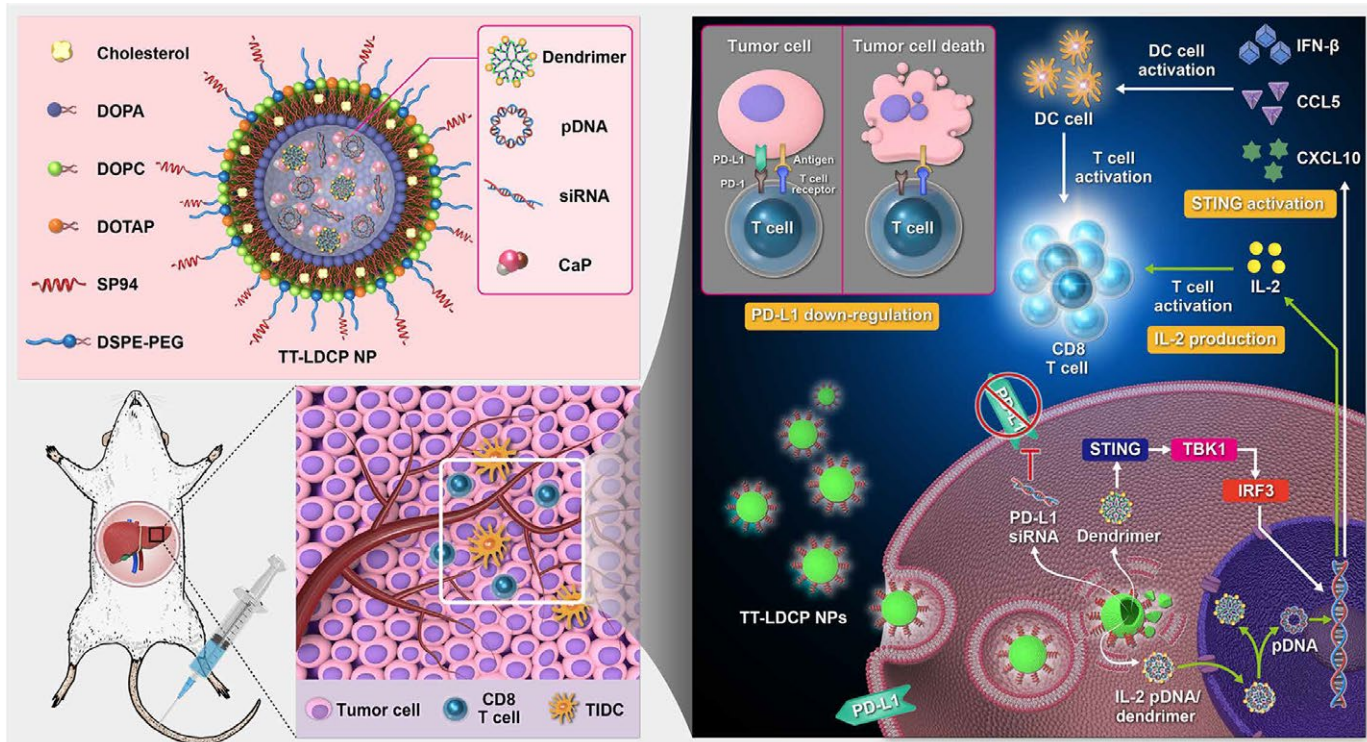


Fig. 1. Schematic representation of the mechanism of immunogene therapy by TT-LDCP NPs containing siRNA against the immune checkpoint PD-L1 and pDNA encoding the immunostimulating cytokine IL-2. Active tumor targeting was achieved through the addition of the HCC-targeted SP94 peptide to the surface of the NPs. The thymine-capped PAMAM dendrimer/CaP complexes achieved highly efficient gene transfection efficacy by enhancing nuclear delivery of the pDNA. Furthermore, thymine-capped PAMAM dendrimers stimulate the STING pathway and serve as an adjuvant to promote the maturation of intratumoral DCs. Efficient tumor-targeted codelivery of PD-L1 siRNA and IL-2 pDNA achieves tumor-specific expression of IL-2 and down-regulation of PD-L1, increases infiltration and activation of CD8⁺ T cells in HCC, and induces a strong tumor-suppressive effect in HCC in synergy with a vaccine. CaP, calcium phosphate; TIDC, tumor-infiltrating dendritic cell; TT-LDCP NPs, tumor-targeted lipid-dendrimer-calcium-phosphate NPs; IFN- γ , interferon- γ .

to delivery by LDCP NPs or TT-LCP NPs (Fig. 3D and fig. S6). In addition, enhanced transfection efficacy was observed when luc pDNA was delivered by TT-LDCP NPs containing 50% thymine-capped PAMAM, compared to delivery by NPs containing unmodified, 10 or 90% modified PAMAM. Our results indicate that 50% thymine coverage is optimal for dendrimer-mediated delivery of pDNA through the nuclear barrier to achieve effective gene transfection (fig. S7).

We further evaluated the transfection efficiency of pDNA in orthotopic HCC (HCA-1) models by measuring luciferase expression in different organs 48 hours after systemic administration of luc pDNA in different formulations. Luciferase expression in liver tumors was significantly higher in mice that received TT-LDCP NPs, compared to that in mice that received LDCP NPs, TT-LCP NPs, or free pDNA. No significant difference in luciferase expression was observed in the liver, heart, spleen, kidney, and lung (Fig. 3E). Our results using TT-LDCP NPs demonstrate ligand (HCC-targeted SP94 peptide)- and dendrimer-dependent cellular uptake and transfection efficiency in HCC in vitro and in vivo.

Codelivery of PD-L1 siRNA and IL-2 pDNA by TT-LDCP NPs silences PD-L1 expression and increases IL-2 production in HCC cells in vitro and in vivo

To enhance antitumor immunity, siRNA against the immune checkpoint ligand PD-L1 and pDNA encoding the immunostimulatory cytokine IL-2 were loaded into TT-LDCP NPs, and their effect on target gene expression was examined in HCA-1 HCC cells. Compared

with delivery by nontargeted NPs, IL-2 pDNA delivered by TT-LDCP NPs significantly increased IL-2 secretion from HCA-1 cells (Fig. 4A). In addition, PD-L1 siRNA loaded in TT-LDCP NPs efficiently silenced PD-L1 expression in HCA-1 cells, whereas PD-L1 siRNA formulated in nontargeted LDCP NPs did not affect PD-L1 expression (Fig. 4B). Neither the control siRNA nor the control pDNA (pEGFP pDNA) delivered by TT-LDCP NPs altered IL-2 or PD-L1 expression in HCA-1 cells (Fig. 4, A and B).

We next evaluated the effects of PD-L1 siRNA and IL-2 pDNA codelivered by TT-LDCP NPs on the expression of PD-L1 and IL-2 in an orthotopic HCC (HCA-1) model (Fig. 4, C and D). Systemic co-administration of PD-L1 siRNA and IL-2 pDNA in TT-LDCP NPs significantly decreased PD-L1 and increased IL-2 expression in liver tumors (Fig. 4, C and D). PD-L1 siRNA and IL-2 pDNA codelivered by LDCP NPs or TT-LCP NPs showed minimal impact on the expression of PD-L1 or IL-2 in HCA-1 tumors (Fig. 4, C and D). Our results indicate that delivery of PD-L1 siRNA and IL-2 pDNA by TT-LDCP NPs is efficient and can decrease the expression of the immune checkpoint ligand PD-L1 and increase the production of the immunostimulatory cytokine IL-2 in HCC.

Codelivery of PD-L1 siRNA and IL-2 pDNA by TT-LDCP NPs significantly increases tumoral infiltration of CD8⁺ T cells, suppresses primary HCC growth, and inhibits distal metastasis

We next assessed whether TT-LDCP NPs that codeliver PD-L1 siRNA/IL-2 pDNA could effectively shape antitumoral effector immunity

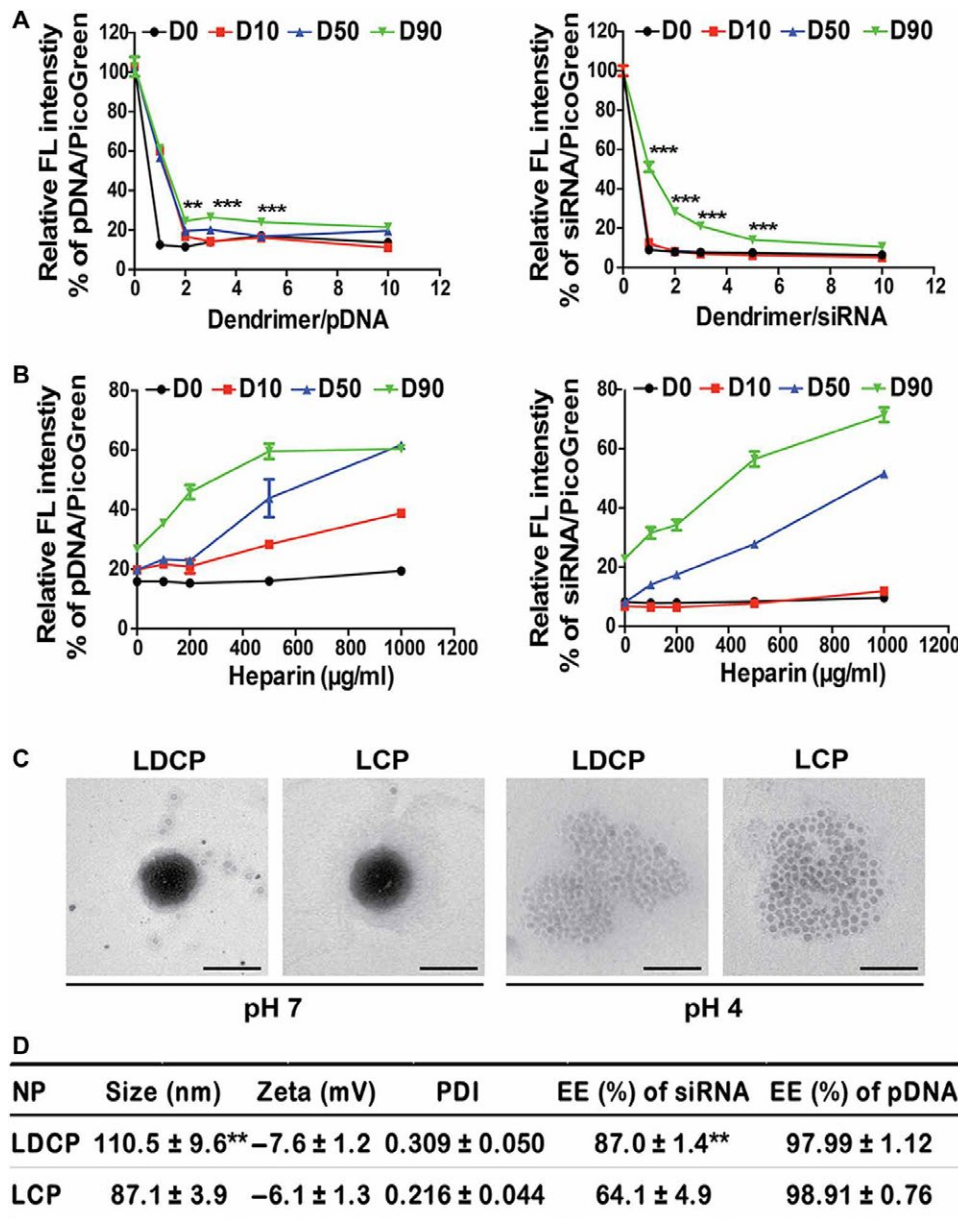


Fig. 2. Characterization of LDCP NPs. (A and B) Assay of interaction between dendrimer and pDNA or siRNA. For the condensation assays (A), dendrimer was mixed with PicoGreen-labeled pDNA (or siRNA) at various dendrimer:pDNA (or siRNA) weight ratios (1:1, 2:1, 3:1, 5:1, and 10:1) (pDNA, $n = 4$; siRNA, $n = 5$). ** $P < 0.01$ and *** $P < 0.001$ compared with the D50 group. For the dissociation assays (B), the dendrimer was mixed with pDNA (or siRNA) at a weight ratio of 2:1. Heparin was added to PicoGreen-labeled dendrimer-pDNA (or siRNA) complexes in a range of concentrations (0, 100, 200, 500, and 1000 $\mu\text{g/ml}$) to mimic the environment in the cytoplasm, to reduce the interaction between dendrimers and pDNA (or siRNA), and force dendrimer release of pDNA or siRNA ($n = 5$). Relative fluorescence intensity was quantified compared with PicoGreen-labeled pDNA or siRNA without adding dendrimer. D0, dendrimer without thymine group; D10, dendrimer modified with 10% thymine group; D50, dendrimer modified with 50% thymine group; and D90, dendrimer modified with 90% thymine group. The data are the means \pm SEM. (C) Representative TEM images of LDCP and LCP NPs. Scale bars, 100 nm. (D) Sizes, zeta potentials, and encapsulation efficacies of LDCP and LCP NPs. PDI, polydispersity index; EE, encapsulation efficiency; FL, fluorescence. Data are means \pm SD ($n = 4$ to 6). ** $P < 0.01$ compared with the LCP group.

in HCC. Treatment of mice bearing orthotopic HCC tumors with PD-L1 siRNA and IL-2 pDNA in TT-LDCP NPs significantly facilitated tumoral infiltration of CD8⁺ T cells, compared with that seen upon treatment with PD-L1 siRNA or IL-2 pDNA alone in TT-LDCP NPs (Fig. 4E). No effect on CD8⁺ T cell numbers was observed in the absence of dendrimers (Fig. 4E), and none of the combinations tested affected the number of tumor-infiltrating CD4⁺ T cells (Fig. 4F).

Accordingly, we evaluated whether the increase in tumor-infiltrating T cells in HCC cells upon codelivery of PD-L1 siRNA and IL-2 pDNA led to suppression of tumor growth. Compared with treatment with PD-L1 siRNA or IL-2 pDNA alone in TT-LDCP NPs, cotreatment with PD-L1 siRNA and IL-2 pDNA in TT-LDCP NPs significantly suppressed tumor growth in the HCC orthotopic model (Fig. 4G). Codelivery of PD-L1 siRNA and IL-2 pDNA in nontargeted NPs or in TT-LCP NPs without dendrimers showed only a moderate

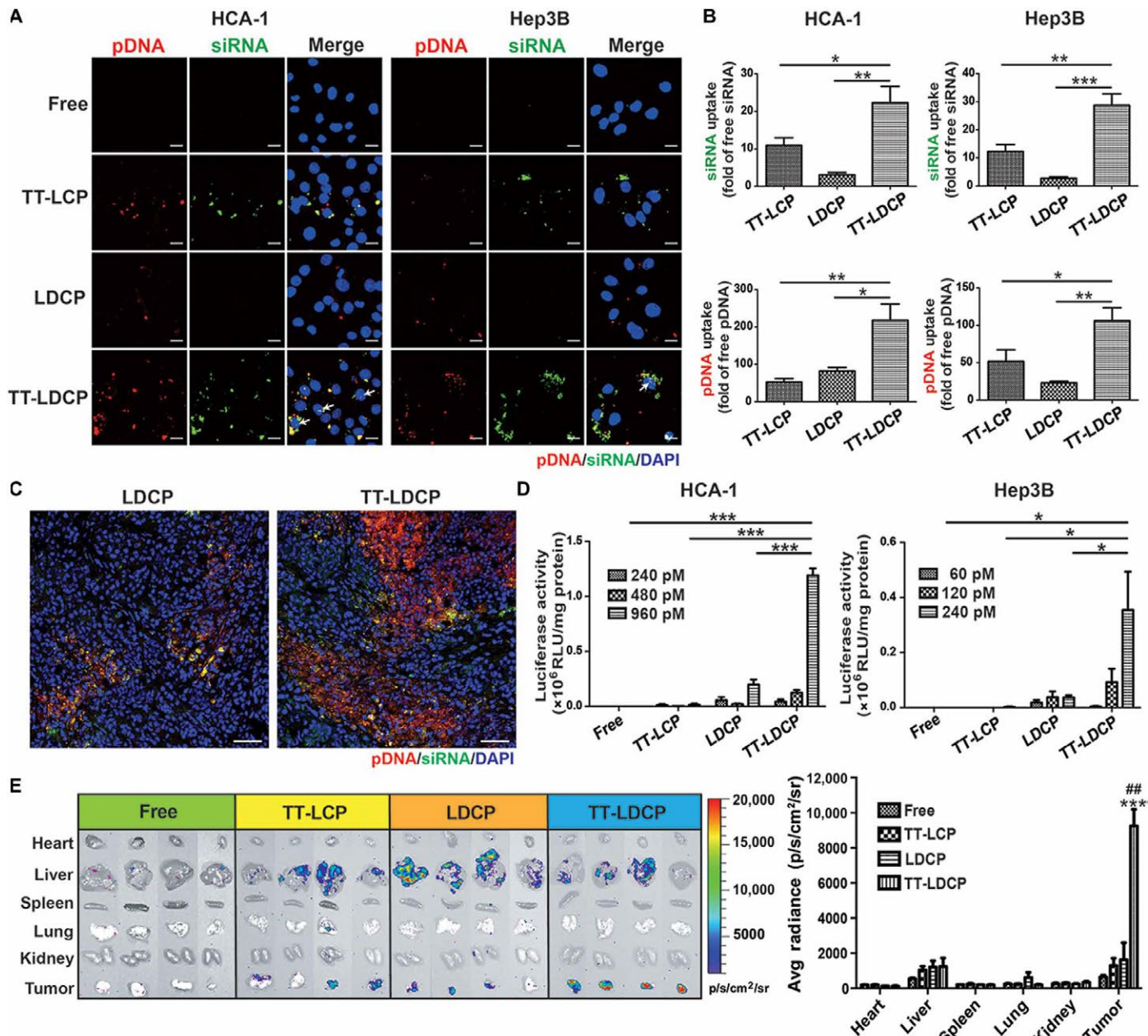


Fig. 3. Tumoral uptake and transfection efficiency of TT-LDCP NPs containing pDNA and siRNA in vitro and in vivo. (A) HCA-1 and Hep3B cells were treated with Cy5-labeled pDNA (red, 0.2 μ g/ml) and FAM-labeled siRNA (green, 0.2 μ g/ml) in TT-LCP, LDCP, or TT-LDCP NPs for 12 hours and observed with confocal microscopy. The arrowhead represents Cy5-labeled pDNA in the nucleus. The nuclei are blue [4',6-diamidino-2-phenylindole (DAPI)]. Scale bars, 20 μ m. (B) Uptake of fluorescently labeled pDNA, and siRNA was imaged and quantified with a Zeiss LSM 780 confocal microscope (TT-LCP, LDCP, $n = 5$; TT-LDCP, $n = 4$). Data are means \pm SEM. * $P < 0.05$, ** $P < 0.01$, and *** $P < 0.001$. (C) Tumoral uptake of siRNA (green) and pDNA (red) was detected 4 hours after intravenous administration of siRNA/pDNA loaded in LDCP or TT-LDCP at a dose of 1.2 mg/kg. Scale bar, 50 μ m. (D) Transfection efficiency as a measure of luciferase expression was evaluated by treating HCC cells (HCA-1 and Hep3B) with luc pDNA loaded in different formulations for 48 hours. Data are means \pm SEM. * $P < 0.05$ and *** $P < 0.001$ ($n = 6$). (E) Representative images of luciferase expression in dissected organs of mice with orthotopic HCA-1 tumors 48 hours after receiving an intravenous injection of luc pDNA (0.6 mg/kg) in different formulations. Images were taken with an In Vivo Imaging System (IVIS-200, XENGEN, USA) after intraperitoneal administration of D-luciferin (60 mg/kg, Promega). Bioluminescence quantification in major organs (free pDNA/siRNA, LDCP, $n = 3$; TT-LCP, TT-LDCP, $n = 4$), expressed as average radiance \pm SEM. ## $P < 0.01$ compared with LDCP; *** $P < 0.001$ compared with TT-LCP.

inhibitory effect on tumor growth (Fig. 4G). Because mice bearing orthotopic HCA-1 tumors develop metastases in the lungs 4 weeks after HCC implantation (19), we also evaluated the effect of PD-L1 siRNA and IL-2 pDNA codelivery on metastasis. We observed that codelivery of PD-L1 siRNA and IL-2 pDNA in TT-LDCP NPs not

only inhibited primary HCC growth but also suppressed distal lung metastasis (Fig. 4, H and I). The combination of PD-L1 siRNA and IL-2 pDNA in TT-LDCP NPs was well tolerated by mice, as demonstrated by unchanged hepatic enzyme levels [aspartate aminotransferase (AST), alanine aminotransferase (ALT), alkaline

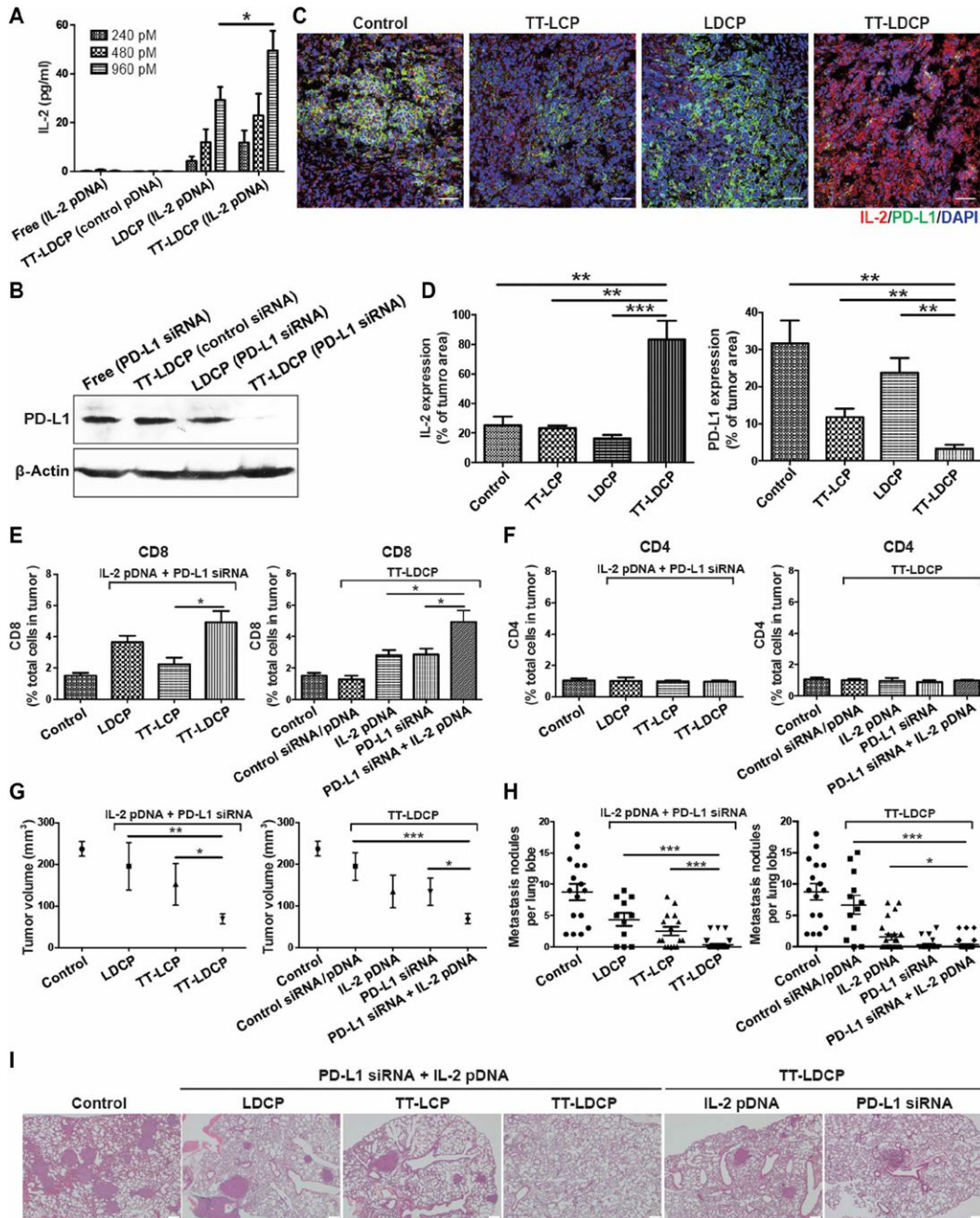


Fig. 4. Delivery of IL-2 pDNA and PD-L1 siRNA in TT-LDCP NPs modulated TME and suppressed tumor progression in a murine orthotopic HCC model. HCA-1 cells were treated with TT-LDCP NPs containing IL-2 pDNA or PD-L1 siRNA, followed by enzyme-linked immunosorbent assay (ELISA)-based estimation of IL-2 secretion (A) and Western blotting for PD-L1 expression (B). (A) Samples from supernatants were collected 48 hours after treatment and tested for the presence of IL-2 by ELISA. Data are means \pm SEM ($n = 6$), * $P < 0.05$. (B) PD-L1 inhibition of HCA-1 cells was investigated by Western blotting. HCA-1 cells were incubated with PD-L1 siRNA (4 $\mu\text{g}/\text{ml}$) loaded in different formulations for 48 hours. (C and D) On the 14th day after HCC tumor implantation, tumor-bearing mice were treated with TT-LDCP NPs containing IL-2 pDNA and PD-L1 siRNA with two consecutive intravenous administrations (1.2 mg/kg per dose), and euthanized 24 hours after the last treatment for immunostaining of tumors. The expression of IL-2 and PD-L1 in murine orthotopic HCC tumors was imaged and quantified with a Zeiss LSM 780 confocal microscope. Scale bars, 50 μm . Data are means \pm SEM (control, TT-LCP, TT-LDCP, $n = 5$; LDCP, $n = 7$); ** $P < 0.01$ and *** $P < 0.001$. (E and F) Orthotopic HCA-1 tumor-bearing mice were intravenously injected with different formulations containing IL-2 pDNA and PD-L1 siRNA (1.2 mg/kg per dose, 3 doses per week) starting on the 10th day after tumor implantation. The mice were euthanized 2 weeks after the first treatment for further analysis. Recruitment of CD8⁺ (E) and CD4⁺ (F) T cells in tumors subjected to different treatments was measured by flow cytometry (control, $n = 18$; TT-LCP, $n = 7$; LDCP, $n = 4$; TT-LDCP, $n = 10$; TT-LDCP/IL-2 pDNA, $n = 10$; TT-LDCP/PD-L1 siRNA, $n = 12$). Data are means \pm SEM. (G) Size of tumors in orthotopic tumor-bearing mice was significantly reduced upon treatment with IL-2 pDNA and PD-L1 siRNA loaded in TT-LDCP NPs (control, $n = 12$; TT-LCP, $n = 5$; LDCP, $n = 5$; TT-LDCP, $n = 12$; TT-LDCP/IL-2 pDNA, $n = 8$; TT-LDCP/PD-L1 siRNA, $n = 7$). Data are means \pm SEM. (H) The number of lung metastatic nodules was significantly reduced in mice treated with IL-2 pDNA and PD-L1 siRNA in TT-LDCP NPs. (I) Hematoxylin and eosin staining images showing distant metastasis tumor nodules in the lung. Scale bars, 200 μm . Data are means \pm SEM. * $P < 0.05$, ** $P < 0.01$, and *** $P < 0.001$.

phosphatase (ALP), and gamma-glutamyl transferase (γ -GT)] when compared with untreated mice (fig. S8). Evaluation of systemic toxicities by hematoxylin and eosin staining showed no histopathological changes in the major organs after treatment of PD-L1 siRNA and IL-2 pDNA in TT-LDCP NPs (fig. S8).

PD-L1 siRNA and IL-2 pDNA codelivered by TT-LDCP NPs reprogram the TME and sensitize HCC to a cancer vaccine

The immunosuppressive TME is a major cause for failure of cancer vaccine immunotherapy (20). Therefore, we next examined whether codelivery of PD-L1 siRNA and IL-2 pDNA could modulate the immunosuppressive TME to restore the efficacy of a tumor vaccine in HCC. To establish an immunostimulating whole-cell hepatoma vaccine, HCA-1 cells were transfected with the codon-optimized GM-CSF (cGM-CSF) as an adjuvant to promoting dendritic cell (DC) recruitment and maturation and augment vaccine efficacy by facilitating the development of both humoral and cellular immunity (3, 21). Mice implanted with HCA-1 HCC tumors were vaccinated with the GM-CSF-secreting HCA-1 cells in combination with our TT-LDCP-based immunogene therapy (Fig. 5A). Vaccination alone only moderately increased the T cell infiltration in tumors compared with untreated mice (Fig. 5B). Treatment with PD-L1 siRNA and IL-2 pDNA in TT-LDCP NPs significantly enhanced the intratumoral infiltration of CD8⁺ T cells in mice vaccinated with cGM-CSF-transduced HCA-1 cells: The number of tumor-infiltrating CD8⁺ T cells in the combined immunogene therapy and vaccine group was threefold higher than that of the control group and twofold higher than that of the vaccine group (Fig. 5B). Although the combination of TT-LDCP-based immunogene therapy and HCC vaccination only slightly increased the number of tumor-infiltrating T cells compared with that of TT-LDCP-based immunogene therapy alone (Fig. 5B), the combination significantly increased the activation of tumor-infiltrating CD8 T cells, as indicated by granzyme B (Fig. 5, C and D) and interferon- γ (IFN- γ) expression (Fig. 5E), compared with that of TT-LDCP-based immunogene therapy or vaccine treatment alone (Fig. 5, C to E).

We further assessed whether a combination of TT-LDCP NPs containing PD-L1 siRNA/IL-2 pDNA and vaccine treatment could effectively suppress HCC progression. Vaccination alone led to moderate tumor growth inhibition, suggesting that the immunosuppressive TME limited the anticancer efficacy of the HCC vaccine (Fig. 5F). The combined administration of the HCC vaccine together with PD-L1 siRNA and IL-2 pDNA loaded in TT-LDCP NPs significantly suppressed cancer progression and increased the overall survival of mice, compared with mice that received immunogene therapy or vaccination alone (Fig. 5, F and G).

Our findings demonstrating a role for CD8⁺ T cells in immunogene-mediated tumor growth suppression prompted us to assess the role of splenic CD8⁺ T cells in response to combined immunogene and HCC vaccine therapy. To further verify the tumor-specific T cell response induced by the combination of immunogene therapy and HCC vaccination, lymphocytes were collected from the spleens of HCA-1 tumor-bearing mice after treatment with PD-L1 siRNA and IL-2 pDNA in TT-LDCP NPs and/or HCC vaccine. The splenic lymphocytes were cocultured with mitomycin C-treated HCA-1 cells, followed by estimation of IFN- γ secretion. Splenic lymphocytes from mice treated with a combination of TT-LDCP-based immunogene therapy and HCC vaccination secreted higher levels of IFN- γ than those from mice treated with TT-LDCP-based immunogene

therapy or vaccine treatment alone, indicating increased activity (Fig. 5H). In addition, the splenic lymphocytes were cocultured with HCA-1 cells for 48 hours, followed by the staining with 7-AAD (7-aminoactinomycin D) to assess the cell-mediated cytotoxicity. Splenic lymphocytes from mice treated with a combination of TT-LDCP-based immunogene therapy and HCC vaccination showed enhanced cell death in HCA-1 cells compared with the controls (fig. S9). Moreover, splenic CD8⁺ T cells isolated from HCA-1 tumor-bearing mice after immunogene and/or HCC vaccine treatments were adoptively transferred into mice that had received intrahepatic inoculations of HCA-1 HCC cells (Fig. 5I). Splenic CD8⁺ T cells from mice treated with the combination of immunogene therapy and HCC vaccination significantly suppressed tumor growth after being adoptively transferred into HCA-1 tumor-bearing mice (Fig. 5I). These results verified that PD-L1 siRNA and IL-2 pDNA in TT-LDCP together with the HCC vaccine efficiently activate tumor-specific immune responses to suppress cancer progression.

To examine whether immunogene therapy is able to regulate antigen-specific immune response, we investigated the effect of immunogene therapy in hemagglutinin (HA)-expressing BNL HCC models. The murine HCC BNL-HA cells were generated by stable transfection of BNL-HCC cells with the HA gene and orthotopically implanted in the livers of 6- to 8-week-old male BALB/c mice. Consistently, treatment with PD-L1 siRNA and IL-2 pDNA in TT-LDCP NPs significantly increased activation of CD8⁺ T cells and suppressed HCC progression in the orthotopic BNL-HA HCC model (fig. S10). To obtain direct evidence that immunogene therapy led to the accumulation of antigen-specific cytotoxic T cells in tumors, an HA tetramer assay was performed in mice treated with immunogene therapy. The proportion of HA peptide-specific CTLs among intratumor CD8⁺ T cells was increased after treatment of immunogene therapy compared with the control group (fig. S10).

Thymine-capped PAMAM dendrimers in TT-LDCP NPs stimulate the STING pathway and promote the maturation of tumor-infiltrating DCs

Although production of IL-2 and down-regulation of immune checkpoint molecules such as PD-L1 may help recruit and activate cytotoxic T cells, the antitumor immune response in the TME may still be limited due to tumor-induced functional deficiency of tumor-associated antigen-presenting cells (APCs), such as intratumoral DCs (22). Cationic macromolecules (i.e., chitosan) or nanoformulations (i.e., NPs containing DNA) can promote the maturation of DCs and stimulate innate immunity through activation of the STING pathway (23). We, therefore, examined the possible adjuvant mechanisms underlying enhanced tumor immunity seen with TT-LDCP NPs. We examined whether thymine-capped dendrimers loaded in TT-NPs could activate the STING pathway in HCC cells and indirectly trigger the maturation of intratumoral DCs. TT-LDCP NPs loaded with control siRNA and pDNA (pEGFP pDNA) significantly induced STING-dependent TBK1 and IRF3 activation (Fig. 6A) and increased the expression of STING-triggered proinflammatory cytokines, CCL5, CXCL10, and IFN- β , in HCA-1 cells (Fig. 6B). Naked dendrimer/siRNA/pDNA complex (Fig. 6A, left, lane 3) or siRNA/pDNA loaded in TT-LCP without dendrimers (Fig. 6A, right, lane 2) only moderately stimulated the STING-TBK1-IRF3 pathway. Dendrimer or siRNA/pDNA alone did not significantly activate the STING pathway. Our results indicate that the incorporation of

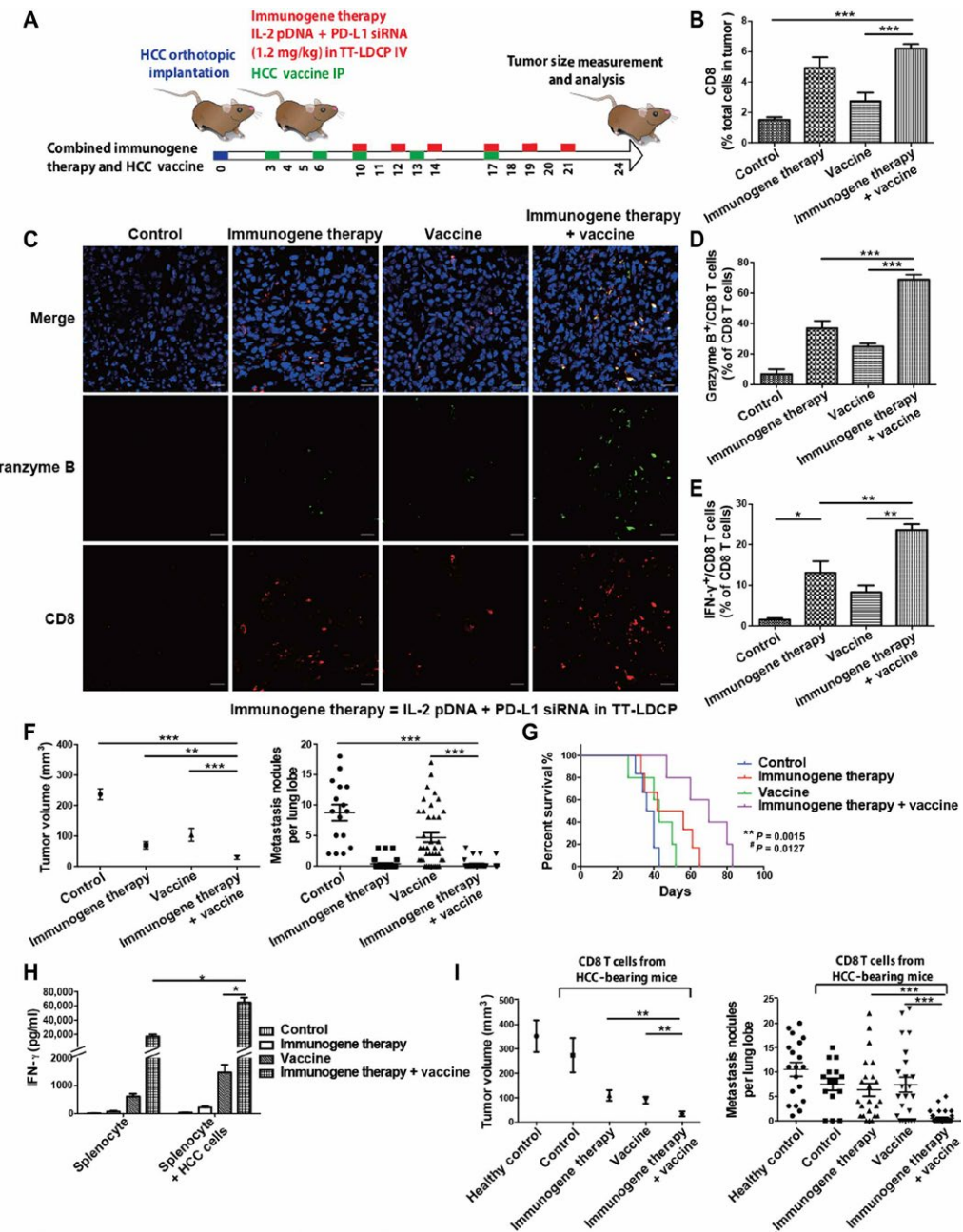


Fig. 5. IL-2 pDNA and PD-L1 siRNA in TT-LDCP NPs enhanced cytotoxic T cell activation and suppressed tumor progression in combination with a whole-cancer cell vaccine in a murine orthotopic HCA-1 HCC model. **(A)** Three days after the implantation of HCA-1 cells, mice were injected intraperitoneally five times (at 2- to 3-day intervals) with the HCC vaccine. For the combination groups, mice treated with the HCC vaccine received intravenous immunogene therapy (1.2 mg siRNA and pDNA/kg per dose) on days 10, 12, 14, 17, 19, and 21. Immunogene therapy: IL-2 pDNA and PD-L1 siRNA in TT-LDCP; vaccine: 5×10^6 mitomycin C-treated cGM-CSF-overexpressing HCA-1 cells. **(B)** Combination of immunogene therapy and the vaccine increased the number of CD8⁺ T cells in tumors, as measured by flow cytometry (control, $n = 18$; immunogene therapy, $n = 10$; vaccine, $n = 6$; combination group, $n = 6$). Data are means \pm SEM. **(C and D)** The percentage of granzyme B-positive CD8⁺ T cells in HCA-1 tumors was imaged and quantified 24 days after implantation for the treatment with immunogene therapy or the HCC vaccine. DAPI, blue; granzyme B, green; CD8⁺ T cells, red (control, $n = 8$; immunogene therapy, $n = 6$; vaccine, $n = 6$; combination group, $n = 7$). **(E)** IFN- γ intracellular staining in tumor-infiltrating CD8⁺ T cells measured by flow cytometry ($n = 5$). **(F and G)** The combination of immunogene therapy and vaccine treatment significantly reduced tumor sizes (control, $n = 12$; immunogene therapy, $n = 12$; vaccine, $n = 12$; combination group, $n = 24$) and distal lung metastatic nodules (F) and increased the overall survival (G) ($n = 5$, ** $P < 0.01$ compared with control; # $P < 0.05$ compared with vaccine treatment) in an orthotopic HCC model. **(H)** IFN- γ production by splenocytes from HCA-1 tumor-bearing mice that were subjected to different treatments. Splenocytes from HCA-1 tumor-bearing mice were incubated with or without mitomycin C-treated HCA-1 cells for 48 hours at 37°C. Samples from supernatants were collected and analyzed for IFN- γ secretion by ELISA ($n = 6$). Data are means \pm SEM. **(I)** Mice with established orthotopic HCA-1 tumors received adoptive transfer of CD8⁺ T cells from HCA-1 tumor-bearing mice treated with different treatments. The adoptive transfer of tumor-specific effector T cells from mice that received the combined immunogene therapy and vaccine treatment resulted in a significant reduction in the size of primary tumors and the number of distal lung metastatic nodules ($n = 6$). Data are means \pm SEM. * $P < 0.05$, ** $P < 0.01$, and *** $P < 0.001$.

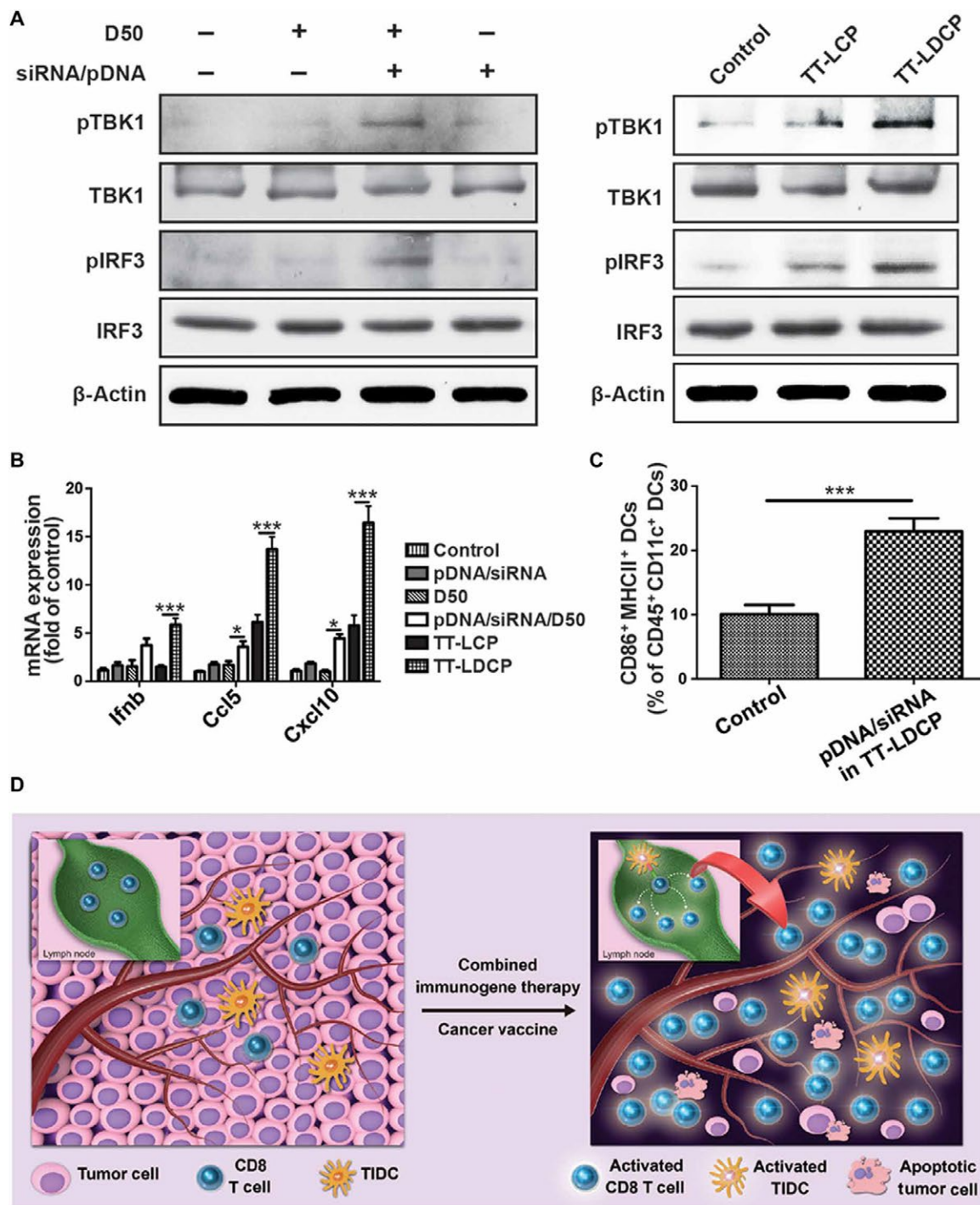


Fig. 6. STING activation and DC maturation after treatment with TT-LDCP NPs containing siRNA/pDNA. (A) Protein extracts from HCA-1 cells treated with different formulations including dendrimers alone, pEGFP pDNA/control siRNA, dendrimers/pEGFP pDNA/control siRNA complex, or pEGFP pDNA/control siRNA loaded in TT-LCP or TT-LDCP for 6 hours were resolved by SDS-polyacrylamide gel electrophoresis, and phosphorylation of the indicated proteins was detected by Western blot. (B) Quantitative polymerase chain reaction analysis of *Ifnb*, *Ccl5*, and *Cxcl10* mRNA expression by HCA-1 cells stimulated for 6 hours with different formulations ($n = 4$ to 7). Data are means \pm SEM. * $P < 0.05$ and *** $P < 0.001$. (C) Thymine-capped PAMAM dendrimers/pEGFP pDNA/control siRNA loaded in TT-LDCP NPs induced intratumoral DC maturation. Orthotopic HCA-1 tumor-bearing mice were intravenously injected with different formulations containing pEGFP pDNA/control siRNA (1.2 mg/kg per dose, three doses per week) on the 10th day after tumor implantation. The mice were euthanized 2 weeks after the first treatment for flow cytometry analysis. The number of MHCII $^+$ CD86 $^+$ mature intratumoral DCs increased after treatment with pDNA/siRNA in TT-LDCP NPs. D50, dendrimer modified with 50% thymine group. $n = 10$. Data are means \pm SEM. *** $P < 0.001$. (D) Efficient tumor-targeted codelivery of PD-L1 siRNA and IL-2 pDNA by TT-LDCP NPs achieves tumor-specific expression of IL-2 and down-regulation of PD-L1, activates TIDCs and increases infiltration and activation of CD8 $^+$ T cells in HCC, and induces a strong tumor-suppressive effect in HCC in synergy with a vaccine.

dendrimers in the gene delivery system is critical to the stimulation of STING-mediated innate immunity in cancer cells.

We next evaluated whether TT-LDCP-mediated STING activation in HCC cells could promote the maturation of tumor-infiltrating DCs *in vivo*. Treatment of mice bearing orthotopic HCC implants with TT-LDCP NPs carrying control siRNA and pEGFP pDNA resulted in substantial up-regulation of the DC maturation markers, CD86 and major histocompatibility complex II (MHCII), on CD45⁺ tumor-infiltrating DCs (Fig. 6C). Thus, thymine-capped PAMAM dendrimers incorporated into TT-LDCP NPs perform dual functions, working not only as gene carriers for the codelivery of siRNA and pDNA into malignant HCC but also as adjuvants that stimulate the STING pathway and activate tumor-infiltrating DCs.

In conclusion, efficient infiltration and activation of effector immune cells in the immunosuppressive TME are key to the success of immunotherapy. We designed a nanodelivery system, TT-LDCP NP, that enables high stability, efficient endosomal release, and selective tumor delivery of therapeutic genetic cargoes. We incorporated 50% thymine-capped PAMAM dendrimer to stimulate innate immunity and facilitate the cellular and nuclear delivery of genetic cargoes, achieving potent gene transfection efficacy. Using this gene delivery system, we codelivered PD-L1 siRNA and IL-2 pDNA into HCC cells, resulting in enhanced tumoral CD8⁺ T cell infiltration and activation, leading to suppression of HCC progression (Fig. 6D). The immunogene therapy acted synergistically with a cancer vaccine to achieve tumor-specific immune responses, leading to improved overall survival in an orthotopic HCC model (Fig. 6D). This highly efficient tumor-targeted siRNA/pDNA dual delivery system simultaneously inhibited an immune checkpoint and provided an immunostimulating cytokine. This system has the potential to be translated into a safe and promising immunotherapy approach for clinical cancer treatment.

DISCUSSION

The 50% thymine-capped PAMAM dendrimer loaded in LDCP NPs provides distinct advantages for immunogene therapy. First, this dendrimer condenses the genetic cargoes (siRNA and pDNA) and increases the stability of the nanoscale nucleic acid–dendrimer–CaP cores. Thymines and primary amines on the thymine-capped dendrimer may synergistically interact with and protect siRNA/pDNA via electrostatic interaction and hydrogen bonding (17). Second, the dendrimer triggers efficient endosomal escape and intracellular release of genetic cargoes (24), increases pDNA uptake in the nucleus, and induces strong transfection activity.

In addition to serving as an efficient gene carrier, the thymine-capped PAMAM dendrimer incorporated in NPs promoted STING-dependent signaling in HCC cells and activated intratumoral DCs, which play a crucial role in mediating antitumor immunity in the immunosuppressive TME. CD103⁺ DCs, a specific subset of intratumoral DCs, produce cytokines to stimulate T cells, cross-present cell-associated antigens to CD8⁺ T cells, and activate immune responses to overcome immune-evasion mechanisms in the TME (25). Thus, the development of strategies to increase the sufficient and active presence of intratumoral DCs is required to activate T cell-mediated immune responses that may increase the efficacy of immunotherapy (26). We showed that treatment with tumor-targeted LDCP NPs containing dendrimers and siRNA/pDNA up-regulated the expression levels of the costimulatory molecules CD86 and

MHCII in tumor-infiltrating DCs, indicating enhanced DC maturation and activation. Therefore, the thymine-capped PAMAM dendrimer can serve as both a gene delivery carrier and an adjuvant that can stimulate the STING pathway and activate tumor-associated APCs to shape antitumoral effector immunity and enhance the therapeutic response for immunogene therapy.

Several immunotherapy strategies are used or are being developed as effective cancer treatments, including (i) vaccines and adoptive T cell therapy directed to tumor-associated neoantigens to prime T cell responses, (ii) low-dose radiotherapy or chemotherapy to induce immunogenic cell death as an *in situ* vaccination approach, (iii) inhibition of checkpoints promoting T cell anergy or exhaustion, and (iv) immunostimulating agents to activate immune cells in the TME (27). However, the development of resistance mechanisms that prevent immune cell infiltration or activation in the TME limits the therapeutic outcomes of such immunotherapies (4, 28). Thus, approaches combining immunotherapies have been developed to simultaneously induce mechanisms that can interact synergistically to achieve enhanced anticancer immunity. In the clinic, the combined use of antibodies blocking the CTLA-4 (cytotoxic T lymphocyte antigen 4) and PD-1 checkpoints is a promising approach for the treatment of advanced melanoma (29). In addition to checkpoint blockades, there is preclinical evidence that anti-CD137 immunostimulatory monoclonal antibodies increase anticancer efficacy of adoptive T cell therapy (30). While an immunotherapy cocktail may increase anticancer efficacy, it may augment immune-related adverse toxicity (31). In this study, TT-LDCP NP, a highly efficient and tumor-selective gene carrier, not only delivers combined genetic cargoes to simultaneously block immune checkpoints and provide costimulating molecules but also maximizes the bioavailability of therapeutic cargoes in tumors to reduce side effects.

In this study, we showed that delivery of PD-L1 siRNA into HCC cells not only augmented anticancer immunity, as indicated by increased tumor-infiltrating CD8⁺ T cells, but also significantly suppressed distal metastasis. In addition to the immunosuppressive effect of PD-L1 via engagement of its receptor PD-1 on T cells, recent studies have reported that cancer cell–intrinsic PD-L1 reprograms metabolic activities and promotes metastasis-related phenotypes (32). Down-regulating PD-L1 reverses epithelial-to-mesenchymal transition in cancer cells and inhibits their invasion and migration activity, suggesting that PD-L1 may serve as a potential target for suppressing metastasis (33). In addition to PD-L1, several other immunosuppressive molecules, such as indoleamine 2,3-dioxygenase (IDO), and cytokines [i.e., transforming growth factor-β (TGF-β), IL-10, and prostaglandin E2] produced by cancer cells or stromal cells also play important roles in modulating immune cell phenotypes in the TME, inhibiting T cell activation and promoting immune tolerance, resulting in suppression of anticancer immunity (34–36). We envision that in the future, the TT-LDCP NPs developed in this study can serve as efficient tools to deliver siRNA cocktails against multiple key immunosuppressive factors and reprogram immune cells residing in the TME, leading to reduced tumor progression.

IL-2 has long been recognized as a key cytokine that drives T cell proliferation and enhances effector T cell activity, and IL-2 was the first effective immunotherapy for human cancer (2). However, repetitive systemic administration of IL-2, which is required to obtain sufficient exposure at tumor tissues and achieve tumor suppression, causes adverse events in patients (37). In addition, recent studies have shown that treatment with low-dose IL-2 induces immune tolerance

and promotes the development of regulatory T cells that may impair antitumor immunity and limit therapeutic efficacy (37). Our findings, on the other hand, showed that TT-LDCP NP-mediated delivery of IL-2 pDNA to tumor cells resulted in high levels of secreted IL-2 in the TME and enhanced tumor immunity by increasing the proliferation of tumor-specific cytotoxic T cells and facilitating infiltration of activated T cells into tumors when combined with PD-L1 siRNA. Furthermore, tumor-targeted delivery of IL-2 pDNA with NPs may further decrease the systemic side effects observed with systemic administration of IL-2 for treatment.

Although TT-LDCP NPs can selectively and efficiently deliver siRNA/pDNA into tumors, their transient transfection efficacy may limit clinical application. To prolong pDNA/siRNA expression and the antitumor response, cutting-edge technologies, such as the Sleeping Beauty transposon and CRISPR-based genome editing systems, can be exploited. If the death of tumor cells results in reduced expression of IL-2 that limits immune stimulation, stromal cells can be targeted instead of cancer cells. For example, targeted delivery of pDNA into tumor-associated fibroblasts causes the stromal cells to sustainably produce immunostimulating cytokines, modulate the immunosuppressive TME, and achieve long-term antitumor immunity (38). More studies are needed to overcome limitations and achieve successful clinical translation of cancer gene therapy.

In summary, nanotechnology-enabled delivery of siRNA against immunosuppressive factors and pDNA encoding immunostimulating cytokines is safe, highly efficient, selectively targeted to the TME, synergistic in action with a cancer vaccine, and suitable as a next-generation cancer immunotherapy strategy. This system has the potential for new immunotherapy cocktails to be used in the clinic.

MATERIALS AND METHODS

Study design

This was a preclinical study to assess the efficacy and safety of a PD-L1 siRNA and IL-2 pDNA delivered by a tumor-targeted nanocarrier to silence PD-L1 expression and increase IL-2 production in HCC cells. We hypothesized that down-regulation of PD-L1 and production of IL-2 in HCC would stimulate antitumor immunity and suppress HCC progression, as well as improve anticancer efficacy when combined with cancer vaccine treatment. This hypothesis was tested through an established orthotopic murine HCC model. The numbers of mice used for the in vivo experiments are specified in the figure legends.

Cells and materials

The murine HCC cell line HCA-1 and the human HCC cell lines Hep3B and JHH-7 were provided by D. Duda, MGH Boston. Hep3B cells were maintained in minimum essential medium (MEM)-alpha medium, JHH-7 cells were maintained in Dulbecco's Modified Eagle Medium (DMEM)/F12 medium, and HCA-1 cells were maintained in DMEM medium (Sigma-Aldrich, St. Louis, MO). All media were supplemented with 10% fetal bovine serum and were purchased from Invitrogen (Carlsbad, CA). The SP94 peptide (NH₂-CGGSFSIIHTPILPL-COOH) was synthesized and purified (95% purity) by Kelowna International Scientific Inc. (Taipei, Taiwan). Dimethyl sulfoxide and cholesterol were purchased from Sigma-Aldrich (St. Louis, MO). Ethanol (EtOH) was obtained from Alfa Aesar (Ward Hill, MA). DOPA, 1,2-dioleoyl-sn-glycero-3-phosphocholine (DOPC), DOTAP, DSPE-PEG2000, and DSPE-PEG2000-maleimide were purchased from Avanti Polar Lipids

(Alabaster, AL). Luciferin was purchased from Promega Corp. (Madison, WI). Plasmids encoding firefly Luc driven by the cytomegalovirus (CMV) promoter were gifts from C.-W. J. Chang, National Tsing Hua University, Taiwan. pCMV-Luc plasmid was cloned by inserting luciferase DNA (from pGL3, Promega) into the pcDNA3 plasmid. pEGFP-C3 plasmids were purchased from Addgene. Control siRNA with the sequence 5'-AAUUCUCCGAACGUGUCAC-GUTT-3', PD-L1_01 siRNA with the sequence 5'-GAUAUUG-CUGGCAUUUAUU-3', and PD-L1_02 siRNA with the sequence 5'-GAGGUAAUCUGGACAAACAUU-3' were purchased from Dharmacon (Lafayette, CO, USA).

The synthesis of thymine-capped PAMAM dendrimers

The thymine was converted to (bromobutyl)thymine according to a previous report (39). Upon mixing (bromobutyl)thymine (47.8 mg) with G₄NH₂ (Sigma-Aldrich, 1 ml, 5.7 μmol, 10 weight % methanol solution) in deionized water (4 ml), dendrimers capped with thymine molecules of 50% coverage were successfully synthesized by microwaving the relevant mixture at 300 W and 120°C for 30 min (CEM, Discover LabMate System). For each synthesis, the resulting crude mixture was extracted by dichloromethane to remove excess (bromobutyl)thymine, and the compound was freeze dried from the aqueous solution.

Preparation of LDCP NPs loaded with siRNA and pDNA

LDCP NPs were prepared using a modified protocol (16, 40). Two separate microemulsions (3 ml each) were prepared. To prepare the calcium-loaded microemulsion, pDNA (6.5 μg) and siRNA (6.5 μg), dendrimer (26 μg), and 40 μl of 500 mM CaCl₂ (pH 7) were added to the oil phase of cyclohexane and Igepal-520 (7:3, v/v). To prepare the phosphate buffer-loaded microemulsion, Na₂HPO₄ solution (74 μl, 100 mM, pH 9) and DOPA (74 μl, 35 mM) were added into the oil phase of cyclohexane and Igepal-520 (7:3, v/v). Two separate microemulsions were stirred for 10 min at room temperature. The emulsions were then mixed for 20 min to form the condensed cores of CaP/pDNA/siRNA/dendrimer. Later, 6 ml of 100% EtOH was added to disrupt the emulsion, and the mixture was centrifuged at 10,000g for 20 min. After removing the supernatant solution, the CaP/pDNA/siRNA/dendrimer cores were collected and washed twice with 100% EtOH to remove residual organic solvents. The CaP/pDNA/siRNA/dendrimer cores were suspended in chloroform, vortexe, and sonicated. A mixture of free lipids (DOPC:DOTAP:DSPE-PEG2000:DSPE-PEG2000-MAL:cholesterol = 1:1:1:8:0.2:4 molar ratio) was added into the CaP/pDNA/siRNA/dendrimer cores (2.5:1 ratio of total free lipids to DOPA) and then dried under N₂. After evaporating the chloroform, 160 μl of water was added to form LDCP NPs. For peptide conjugation, peptide was reduced using immobilized TCEP disulfide-reducing gel (Thermo Fisher Scientific) according to the manufacturer's recommendations. SP94 peptides were added into LDCP NPs where they reacted with DSPE-PEG2000-maleimide on the surface of the NPs. Four hours later, the unreacted maleimide groups were quenched by adding L-cysteine.

Characterization of NPs

The LDCP or LCP NPs were formulated as described above and were resuspended in deionized water. The morphology of the NPs was characterized by TEM (H-7500, Hitachi High-Tech, Tokyo, Japan). The NPs were dropped on dried Formvar-coated 100-mesh copper grids at room temperature. All grids were further dried for 2 days

before imaging. The particle size and surface charge were examined using a Zetasizer system (Zetasizer nano zs, Malvern Instruments Ltd., Worcestershire, UK) at room temperature.

Animals and orthotopic HCC models

C3H/HeNcrNarl male mice were purchased from the National Laboratory Animal Center (Taipei, Taiwan). Murine HCC HCA-1 cells were orthotopically implanted in the livers of 6- to 8-week-old male C3H mice as previously described (19). Briefly, 1.0×10^6 HCC cells [suspended in 20 μ l in a 1:1 solution of Matrigel in phosphate-buffered saline (PBS)] were injected in the subcapsular region using a 28-gauge needle. All animals received humane care in compliance with the *Guide for the Care and Use of Laboratory Animals* published by the National Academy of Sciences, and all study procedures and protocols were approved by the Animal Research Committee of the National Tsing Hua University (Hsinchu, Taiwan).

To evaluate the anticancer effect of immunogene therapy, PD-L1 siRNA and IL-2 pDNA loaded in different formulations (1.2 mg/kg per dose, three doses per week) were intravenously administered to mice with orthotopic HCC beginning 10 days after the implantation. The tumor volume was evaluated 2 weeks after the first treatment. The tumor tissue was collected for further analysis. Tumor size was measured using a caliper and estimated using the formula: tumor volume = length \times width 2 /2.

Quantitative reverse transcription polymerase chain reaction

To evaluate gene expression by quantitative reverse transcription polymerase chain reaction (PCR), the cells were seeded in 12-well plates and allowed to grow for 12 hours. Later, the cells were exposed to different formulations. The cells were washed in PBS and lysed by TRIzol reagent (Thermo Fisher, USA) at 6 hours after treatment. Then, 1 μ g of total RNA was reverse transcribed into cDNA using the High-Capacity cDNA Reverse Transcription Kit (Applied Biosystems, USA) on a Piko Thermal Cycler (Thermo Fisher Scientific, USA) according to the manufacturer's instructions. Quantitative PCR was performed using TaqMan Universal PCR Master Mix (Applied Biosystems, USA) on a 7500 Real-Time PCR System (Applied Biosystems, USA). The gene expression levels were evaluated using Ct in all tested samples and normalized to β -actin as a reference gene. The primer sequences are listed in table S1.

SUPPLEMENTARY MATERIALS

Supplementary material for this article is available at <http://advances.sciencemag.org/cgi/content/full/6/3/eaax5032/DC1>

Supplementary Materials and Methods

Table S1. List of genes examined by real-time PCR and the primer sequences used.

Fig. S1. The kinetic profile for the release of genetic cargoes from LDPC NPs.

Fig. S2. Cellular uptake of TT-LDPC NPs containing pDNA and siRNA in vitro.

Fig. S3. Intracellular uptake of FITC-labeled dendrimers delivered by TT-LDPC NPs.

Fig. S4. Tissue distribution of TT-LDPC NPs in orthotopic HCC models.

Fig. S5. Tumoral uptake of Cy5-labeled pDNA and FAM-labeled siRNA delivered by TT-LDPC NPs.

Fig. S6. Transfection efficiency of TT-LDPC NPs containing pDNA in human HCC JHH-7 cells.

Fig. S7. Transfection efficiency of TT-LDPC NPs containing pDNA in vitro.

Fig. S8. In vivo administration of PD-L1 siRNA and IL-2 pDNA in TT-LDPC NPs did not show systemic toxicity.

Fig. S9. Comparison of cytotoxicity mediated by splenic lymphocytes as assessed by flow cytometry.

Fig. S10. IL-2 pDNA and PD-L1 siRNA in TT-LDPC NPs suppressed tumor progression, enhanced cytotoxic T cell activation, and increased HA-specific CD8 $^{+}$ T cells in a murine orthotopic BNL-HA HCC model.

[View/request a protocol for this paper from Bio-protocol.](#)

REFERENCES AND NOTES

- A. Hoos, Development of immuno-oncology drugs - from CTLA4 to PD1 to the next generations. *Nat. Rev. Drug Discov.* **15**, 235–247 (2016).
- S. A. Rosenberg, IL-2: The first effective immunotherapy for human cancer. *J. Immunol.* **192**, 5451–5458 (2014).
- C. C. Lin, C. C. Tsai, J. M. Lee, C. H. Fang, K. S. Chang, K. K. Wong, C. T. Lin, J. T. Qiu, The efficacy of a novel vaccine approach using tumor cells that ectopically express a codon-optimized murine GM-CSF in a murine tumor model. *Vaccine* **34**, 134–141 (2016).
- L. Galluzzi, T. A. Chan, G. Kroemer, J. D. Wolchok, A. López-Soto, The hallmarks of successful anticancer immunotherapy. *Sci. Transl. Med.* **10**, eaat7807 (2018).
- Y. Huang, S. Goel, D. G. Duda, F. Fukumura, R. K. Jain, Vascular normalization as an emerging strategy to enhance cancer immunotherapy. *Cancer Res.* **73**, 2943–2948 (2013).
- R. S. Riley, C. H. June, R. Langer, M. J. Mitchell, Delivery technologies for cancer immunotherapy. *Nat. Rev. Drug Discov.* **18**, 175–196 (2019).
- G. Ramakrishna, A. Rastogi, N. Trehanipati, B. Sen, R. Khosla, S. K. Sarin, From cirrhosis to hepatocellular carcinoma: New molecular insights on inflammation and cellular senescence. *Liver Cancer* **2**, 367–383 (2013).
- Y. Chen, R. R. Ramjiawan, T. Reiberger, M. R. Ng, T. Hato, Y. Huang, H. Ochiai, S. Kitahara, E. C. Unan, T. P. Reddy, C. Fan, P. Huang, N. Bardeesy, A. X. Zhu, R. K. Jain, D. G. Duda, CXCR4 inhibition in tumor microenvironment facilitates anti-programmed death receptor-1 immunotherapy in sorafenib-treated hepatocellular carcinoma in mice. *Hepatology* **61**, 1591–1602 (2015).
- M. J. Flynn, A. A. Sayed, R. Sharma, A. Siddique, D. J. Pinato, Challenges and opportunities in the clinical development of immune checkpoint inhibitors for hepatocellular carcinoma. *Hepatology* **69**, 2258–2270 (2018).
- L. Wen, B. Xin, P. Wu, C. H. Lin, C. Peng, G. Wang, J. Lee, L. F. Lu, G. S. Feng, An Efficient Combination Immunotherapy for Primary Liver Cancer by Harmonized Activation of Innate and Adaptive Immunity in Mice. *Hepatology* **69**, 2518–2532 (2019).
- S. Koyama, E. A. Akbay, Y. Y. Li, G. S. Herter-Sprie, K. A. Buczkowski, W. G. Richards, L. Gandhi, A. J. Redig, S. J. Rodig, H. Asahina, R. E. Jones, M. M. Kulkarni, M. Kuraguchi, S. Palakurthi, P. E. Fecchi, B. E. Johnson, P. A. Janne, J. A. Engelman, S. P. Gangadharan, D. B. Costa, G. J. Freeman, R. Bueno, F. S. Hodis, G. Dranoff, K. K. Wong, P. S. Hammerman, Adaptive resistance to therapeutic PD-1 blockade is associated with upregulation of alternative immune checkpoints. *Nat. Commun.* **7**, 10501 (2016).
- H. Yin, R. L. Kanasty, A. A. Eltoukhy, A. J. Vegas, J. R. Dorkin, D. G. Anderson, Non-viral vectors for gene-based therapy. *Nat. Rev. Genet.* **15**, 541–555 (2014).
- J. Shi, P. W. Kantoff, R. Wooster, O. C. Farokhzad, Cancer nanomedicine: Progress, challenges and opportunities. *Nat. Rev. Cancer* **17**, 20–37 (2017).
- E. Blanco, H. Shen, M. Ferrari, Principles of nanoparticle design for overcoming biological barriers to drug delivery. *Nat. Biotechnol.* **33**, 941–951 (2015).
- A. Lo, C. T. Lin, H. C. Wu, Hepatocellular carcinoma cell-specific peptide ligand for targeted drug delivery. *Mol. Cancer Ther.* **7**, 579–589 (2008).
- C. H. Liu, G. J. Chern, F. F. Hsu, K. W. Huang, Y. C. Sung, H. C. Huang, J. T. Qiu, S. K. Wang, C. C. Lin, C. H. Wu, H. C. Wu, J. Y. Liu, Y. Chen, A multifunctional nanocarrier for efficient TRAIL-based gene therapy against hepatocellular carcinoma with desmoplasia in mice. *Hepatology* **67**, 899–913 (2018).
- J. Y. Yan, C. Y. Liu, Z. W. Wu, C. T. Chien, W. C. Chiu, S. Y. Lin, Designed nucleus penetrating thymine-capped dendrimers: A potential vehicle for intramuscular gene transfection. *J. Mater. Chem. B* **3**, 9060–9066 (2015).
- J. Li, Y. Yang, L. Huang, Calcium phosphate nanoparticles with an asymmetric lipid bilayer coating for siRNA delivery to the tumor. *J. Control. Release* **158**, 108–114 (2012).
- T. Reiberger, Y. Chen, R. R. Ramjiawan, T. Hato, C. Fan, R. Samuel, S. Robarge, P. Huang, G. Y. Lauwers, A. X. Zhu, N. Bardeesy, R. K. Jain, D. G. Duda, An orthotopic mouse model of hepatocellular carcinoma with underlying liver cirrhosis. *Nat. Protoc.* **10**, 1264–1274 (2015).
- A. Terbuch, J. Lopez, Next generation cancer vaccines-make it personal. *Vaccines* **6**, E52 (2018).
- T. W. Yu, H. Y. Chueh, C. C. Tsai, C. T. Lin, J. T. Qiu, Novel GM-CSF-based vaccines: One small step in GM-CSF gene optimization, one giant leap for human vaccines. *Hum. Vaccin. Immunother.* **12**, 3020–3028 (2016).
- D. Laoui, J. Keirsse, Y. Morias, E. van Overmeire, X. Geeraerts, Y. Elkrim, M. Kiss, E. Bolli, Q. Lahmar, D. Sichien, J. Serneels, C. L. Scott, L. Boon, P. de Baetselier, M. Mazzzone, M. Guilliams, J. A. van Ginderachter, The tumour microenvironment harbours ontogenetically distinct dendritic cell populations with opposing effects on tumour immunity. *Nat. Commun.* **7**, 13720 (2016).
- E. C. Carroll, L. Jin, A. Mori, N. Muñoz-Wolf, E. Oleszycka, H. B. T. Moran, S. Mansouri, C. P. McEntee, E. Lambe, E. M. Agger, P. Andersen, C. Cunningham, P. Hertzog, K. A. Fitzgerald, A. G. Bowie, E. C. Lavelle, The vaccine adjuvant chitosan promotes cellular immunity via DNA sensor cGAS-STING-dependent induction of Type I interferons. *Immunity* **44**, 597–608 (2016).

24. L. Palmerston Mendes, J. Pan, V. P. Torchilin, Dendrimers as nanocarriers for nucleic acid and drug delivery in cancer therapy. *Molecules* **22**, E1401 (2017).
25. H. Salmon, J. Idoyaga, A. Rahman, M. Leboeuf, R. Remark, S. Jordan, M. Casanova-Acebes, M. Khudynazarova, J. Agudo, N. Tung, S. Chakarov, C. Rivera, B. Hogstad, M. Bosenberg, D. Hashimoto, S. Gnijatic, N. Bhardwaj, A. K. Palucka, B. D. Brown, J. Brody, F. Ginhoux, M. Merad, Expansion and activation of CD103(+) dendritic cell progenitors at the tumor site enhances tumor responses to therapeutic PD-L1 and BRAF inhibition. *Immunity* **44**, 924–938 (2016).
26. A. Gardner, B. Ruffell, Dendritic cells and cancer immunity. *Trends Immunol.* **37**, 855–865 (2016).
27. I. Melero, D. M. Berman, M. A. Aznar, A. J. Korman, J. L. P. Gracia, J. Haanen, Evolving synergistic combinations of targeted immunotherapies to combat cancer. *Nat. Rev. Cancer* **15**, 457–472 (2015).
28. N. P. Restifo, M. J. Smyth, A. Snyder, Acquired resistance to immunotherapy and future challenges. *Nat. Rev. Cancer* **16**, 121–126 (2016).
29. C. Hao, J. Tian, H. Liu, F. Li, H. Niu, B. Zhu, Efficacy and safety of anti-PD-1 and anti-PD-1 combined with anti-CTLA-4 immunotherapy to advanced melanoma: A systematic review and meta-analysis of randomized controlled trials. *Medicine* **96**, e7325 (2017).
30. B. Weigelin, E. Bolaños, A. Teijeira, I. Martínez-Forero, S. Labiano, A. Azpilikueta, A. Morales-Kastresana, J. I. Quetglas, E. Wagena, A. R. Sánchez-Paulete, L. Chen, P. Friedl, I. Melero, Focusing and sustaining the antitumor CTL effector killer response by agonist anti-CD137 mAb. *Proc. Natl. Acad. Sci. U.S.A.* **112**, 7551–7556 (2015).
31. R. R. Caspi, Immunotherapy of autoimmunity and cancer: The penalty for success. *Nat. Rev. Immunol.* **8**, 970–976 (2008).
32. S. Wang, J. Li, J. Xie, F. Liu, Y. Duan, Y. Wu, S. Huang, X. He, Z. Wang, X. Wu, Programmed death ligand 1 promotes lymph node metastasis and glucose metabolism in cervical cancer by activating integrin β4/SNAI1/SIRT3 signaling pathway. *Oncogene* **37**, 4164–4180 (2018).
33. P. Dong, Y. Xiong, J. Yue, S. J. B. Hanley, H. Watari, Tumor-intrinsic PD-L1 signaling in cancer initiation, development and treatment: Beyond immune evasion. *Front. Oncol.* **8**, 386 (2018).
34. D. H. Munn, A. L. Mellor, IDO in the tumor microenvironment: Inflammation, counter-regulation, and tolerance. *Trends Immunol.* **37**, 193–207 (2016).
35. L. Yang, Y. Pang, H. L. Moses, TGF-beta and immune cells: An important regulatory axis in the tumor microenvironment and progression. *Trends Immunol.* **31**, 220–227 (2010).
36. D. Wang, R. N. DuBois, The role of prostaglandin E₂ in tumor-associated immunosuppression. *Trends Mol. Med.* **22**, 1–3 (2016).
37. H. Choudhry, N. Helmi, W. H. Abdulaal, M. Zeyadi, M. A. Zamzami, W. Wu, M. M. Mahmoud, M. K. Warsi, M. Rasool, M. S. Jamal, Prospects of IL-2 in Cancer Immunotherapy. *Biomed. Res. Int.* **2018**, 9056173 (2018).
38. L. Miao, Q. Liu, C. M. Lin, C. Luo, Y. Wang, L. Liu, W. Yin, S. Hu, W. Y. Kim, L. Huang, Targeting tumor-associated fibroblasts for therapeutic delivery in desmoplastic tumors. *Cancer Res.* **77**, 719–731 (2017).
39. J. S. Nowick, J. Chen, G. Noronha, Molecular recognition in micelles: The roles of hydrogen bonding and hydrophobicity in adenine-thymine base-pairing in SDS micelles. *J. Am. Chem. Soc.* **115**, 7636–7644 (1993).
40. T. J. Goodwin, Y. Zhou, S. N. Musetti, R. Liu, L. Huang, Local and transient gene expression primes the liver to resist cancer metastasis. *Sci. Transl. Med.* **8**, 364ra153 (2016).

Acknowledgments: We are grateful to H.-Y. Tang for assisting with the flow cytometry. We thank C.-W. J. Chang for providing plasmids encoding firefly Luc driven by the CMV promoter.

Funding: This study was supported by the Ministry of Science and Technology (MOST 105-2628-E-007-007-MY3, 108-2321-B-009-004, and 108-2221-E-007-104-MY5), the Chang Gung Memorial Hospital-National Tsing Hua University Joint Research Grant (104N2744E1, 108Q2508E1, and CORPG3I0071), the National Health Research Institutes (NHRI-EX108-10609BC), and the “Frontier Research Center on Fundamental and Applied Sciences of Matters” from the Featured Areas Research Center Program within the framework of the Higher Education Sprout Project by the Ministry of Education (MOE 107QR00115 and 108QR00115) and by the Ministry of Science and Technology (MOST 107-3017-F-007-002 and MOST 108-3017-F-007-003). **Author contributions:** K.-W.H. prepared Figs. 1 to 6 and edited the manuscript text. F.-F.H. constructed and purified IL-2 plasmid and performed experiments. J.T.Q., C.-C.L., and D.A. developed whole-cell HCC vaccine. G.-J.C. prepared Figs. 2 and 3 and figs. S2, S3, and S5 to S7. Y.-A.L. prepared Figs. 5 and 6 and figs. S8 to S10. C.-C.Cha. prepared figs. S1 and S8 to S10. Y.-T.H. synthesized dendrimers. Y.-C.Su. prepared Figs. 4 and 5. C.-C.Chi. prepared fig. S4. R.-L.H. prepared Fig. 6. T.K.D. prepared Fig. 6. H.-C.H. and Y.-C.Sh. performed and assisted in the experiments. C.-Y.L., Y.-C.L., and P.-C.C. developed the BNL-HA HCC model. S.-Y.L. synthesized dendrimers, supervised the study, and edited the manuscript text. Y.C. performed experiments, supervised the study, and edited the manuscript text. **Competing interests:** The authors declare that they have no competing interests. **Data and materials availability:** All data needed to evaluate the conclusions in the paper are present in the paper and/or the Supplementary Materials. Additional data related to this paper may be requested from the authors.

Submitted 28 March 2019

Accepted 15 November 2019

Published 15 January 2020

10.1126/sciadv.aax5032

Citation: K.-W. Huang, F.-F. Hsu, J. T. Qiu, G.-J. Chern, Y.-A. Lee, C.-C. Chang, Y.-T. Huang, Y.-C. Sung, C.-C. Chiang, R.-L. Huang, C.-C. Lin, T. K. Dinh, H.-C. Huang, Y.-C. Shih, D. Alson, C.-Y. Lin, Y.-C. Lin, P.-C. Chang, S.-Y. Lin, Y. Chen, Highly efficient and tumor-selective nanoparticles for dual-targeted immunogene therapy against cancer. *Sci. Adv.* **6**, eaax5032 (2020).

CANCER

Tracking extracellular vesicle phenotypic changes enables treatment monitoring in melanoma

Jing Wang^{1*}, Alain Wuethrich^{1*}, Abu Ali Ibn Sina¹, Rebecca E. Lane¹, Lynlee L. Lin^{1,2}, Yuling Wang^{3†}, Jonathan Cebon^{4,5}, Andreas Behren^{4,5}, Matt Trau^{1,6†}

Monitoring targeted therapy in real time for cancer patients could provide vital information about the development of drug resistance and improve therapeutic outcomes. Extracellular vesicles (EVs) have recently emerged as a promising cancer biomarker, and EV phenotyping shows high potential for monitoring treatment responses. Here, we demonstrate the feasibility of monitoring patient treatment responses based on the plasma EV phenotypic evolution using a multiplex EV phenotype analyzer chip (EPAC). EPAC incorporates the nanomixing-enhanced microchip and the multiplex surface-enhanced Raman scattering (SERS) nanotag system for direct EV phenotyping without EV enrichment. In a preclinical model, we observe the EV phenotypic heterogeneity and different phenotypic responses to the treatment. Furthermore, we successfully detect cancer-specific EV phenotypes from melanoma patient plasma. We longitudinally monitor the EV phenotypic evolution of eight melanoma patients receiving targeted therapy and find specific EV profiles involved in the development of drug resistance, reflecting the potential of EV phenotyping for monitoring treatment responses.

INTRODUCTION

Targeted therapies can slow down the progress of many cancers by disrupting molecular activities of targeted cellular pathways and mutated genes, which, in turn, blocks the outgrowth of tumor cells (1). Although targeted therapies are effective, most patients develop a drug nonresponsiveness within months, which eventually results in tumor relapse (1). A promising way to improve therapeutic outcomes could be the use of informative biomarkers and technologies to track therapy responses in real time and predict the early development of drug resistance with the aim of treatment adjustment (2). In this context, extracellular vesicles (EVs) have emerged as informative biomarkers with high potential to become an important tool for cancer diagnosis and therapy monitoring (3, 4). EVs are membrane-encapsulated nanoscopic bodies that are secreted from cells (3). EVs carry functional molecular cargoes that include transmembrane/cytoplasmic proteins, DNAs/RNAs, and lipids, which serve as biomarkers for tumor staging and predicting responses to therapy (5). For instance, by characterizing EV phenotypes (defined by the relative levels of transmembrane proteins), recent studies have successfully obtained proteomic information to forecast the metastatic stages in glioma (6) and melanoma (7). In addition, tracking of treatment responses via EV phenotypes has been demonstrated in glioblastoma (8, 9), breast carcinoma (10, 11), pancreatic cancer (12), and colorectal cancer (13). In the case of colorectal cancer, the EV phenotype served as an indication for successful surgical removal of the tumor by a decreased level of a double-positive CD147/CD9 EV subpopulation (13).

While there is growing evidence suggesting that EV phenotypes reflect biological functions including metastasis and therapy resistance (5), the clinical translation of EVs is limited by the EV heterogeneity. The EV heterogeneity makes it extremely difficult to isolate and detect specific EV subpopulations (e.g., tumor-derived EVs) among other nontarget EVs present in circulation. For example, different EV subpopulations can have similar morphological and physical properties (e.g., size), which can result in co-isolation of bulk EV populations and render the interrogation of target EV subpopulations intractable (5). In addition, multiplex phenotyping of EVs in a small volume for treatment monitoring is also impractical to be achieved with conventional methods such as immunoblotting and enzyme-linked immunosorbent assay (ELISA). Recently, there are a few new technologies that have been developed for the multiplex EV phenotype analysis; however, most of them are not a real multiplex assay, as these methods do not measure multiple biomarkers simultaneously (8, 14, 15). These methods have not been used to perform longitudinal studies to better understand EV phenotypic evolution in response to treatment. Here, we develop an EV phenotype analyzer chip (EPAC) for EV phenotype analysis to enable the monitoring of therapy responses over time. EPAC uses a nanomixing strategy to minimize the nonspecific adsorption, which is particularly beneficial when capturing EVs directly from complex biological samples. This is followed by a multiplex phenotype readout using surface-enhanced Raman spectroscopy (SERS). We achieve multiplex biomarker detection by simultaneously labeling the target EVs with unique SERS nanotags [i.e., gold nanoparticles (AuNPs) with dedicated reporters and tumor-specific antibodies].

Using EPAC, we monitor the EV phenotypic changes in four patient-derived melanoma cell lines treated with the BRAF inhibitor that targets mutant BRAF V600, which is found in approximately 40% of melanoma patients (16). We focus on the detection of four selected biomarkers in EVs including melanoma chondroitin sulfate proteoglycan (MCSP), melanoma cell adhesion molecule (MCAM), low-affinity nerve growth factor receptor (LNGFR), and receptor tyrosine protein kinase (ErbB3). These biomarkers have been demonstrated to often change with treatment and melanoma progression

¹Centre for Personalized Nanomedicine, Australian Institute for Bioengineering and Nanotechnology (AIBN), The University of Queensland, Brisbane, QLD 4072, Australia. ²Dermatology Research Centre, University of Queensland Diamantina Institute, The University of Queensland, Brisbane, QLD 4102, Australia. ³Department of Molecular Sciences, ARC Centre of Excellence for Nanoscale BioPhotonics, Faculty of Science and Engineering, Macquarie University, Sydney, NSW 2109, Australia.

⁴Olivia Newton-John Cancer Research Institute, School of Cancer Medicine, La Trobe University, Heidelberg, VIC 3084, Australia. ⁵Department of Medicine, University of Melbourne, Heidelberg, VIC 3084, Australia. ⁶School of Chemistry and Molecular Biosciences, The University of Queensland, Brisbane, QLD 4072, Australia.

*These authors contributed equally to this work.

†Corresponding author. Email: yuling.wang@mq.edu.au (Y.W.); m.trau@uq.edu.au (M.T.)

Copyright © 2020
The Authors, some
rights reserved;
exclusive licensee
American Association
for the Advancement
of Science. No claim to
original U.S. Government
Works. Distributed
under a Creative
Commons Attribution
NonCommercial
License 4.0 (CC BY-NC).

(17). We monitor and observe EV heterogeneity and phenotype variations based on changes in the expression levels of these four biomarkers during the treatment. EPAC further enables the differentiation of 11 melanoma patients and 12 healthy individuals based on plasma EV phenotypes, as well as the monitoring of phenotypic changes in EVs from 8 melanoma patients receiving targeted therapies.

RESULTS AND DISCUSSION

Working scheme

The schematic workflow of EPAC for monitoring the EV phenotypic evolution during treatment is shown in Fig. 1. As indicated in Fig. 1A, we selected melanoma cell-derived EVs as a model whose parental cell lines harbor the BRAF V600E mutation to evaluate

responses to the BRAF inhibitor treatment. The BRAF V600E mutation leads to constitutive activation of the cellular mitogen-activated protein kinase (MAPK) signaling pathway (Fig. 1A), thereby driving cell cycle progression and tumor growth (18). Treating BRAF V600 mutant melanoma patients or cell lines with BRAF inhibitors specifically disrupts this pathway to shrink or slow tumor growth (18). As the molecular information packaged within EVs originates directly from their parental tumor cells, we speculated that profiling melanoma EV phenotypes might provide a snapshot of the host cell state, making it feasible to be implemented as a treatment monitoring biomarker.

To analyze the phenotypes of melanoma EVs directly from complex biological samples (i.e., cell culture medium and diluted patient plasma) without the need for purification and enrichment

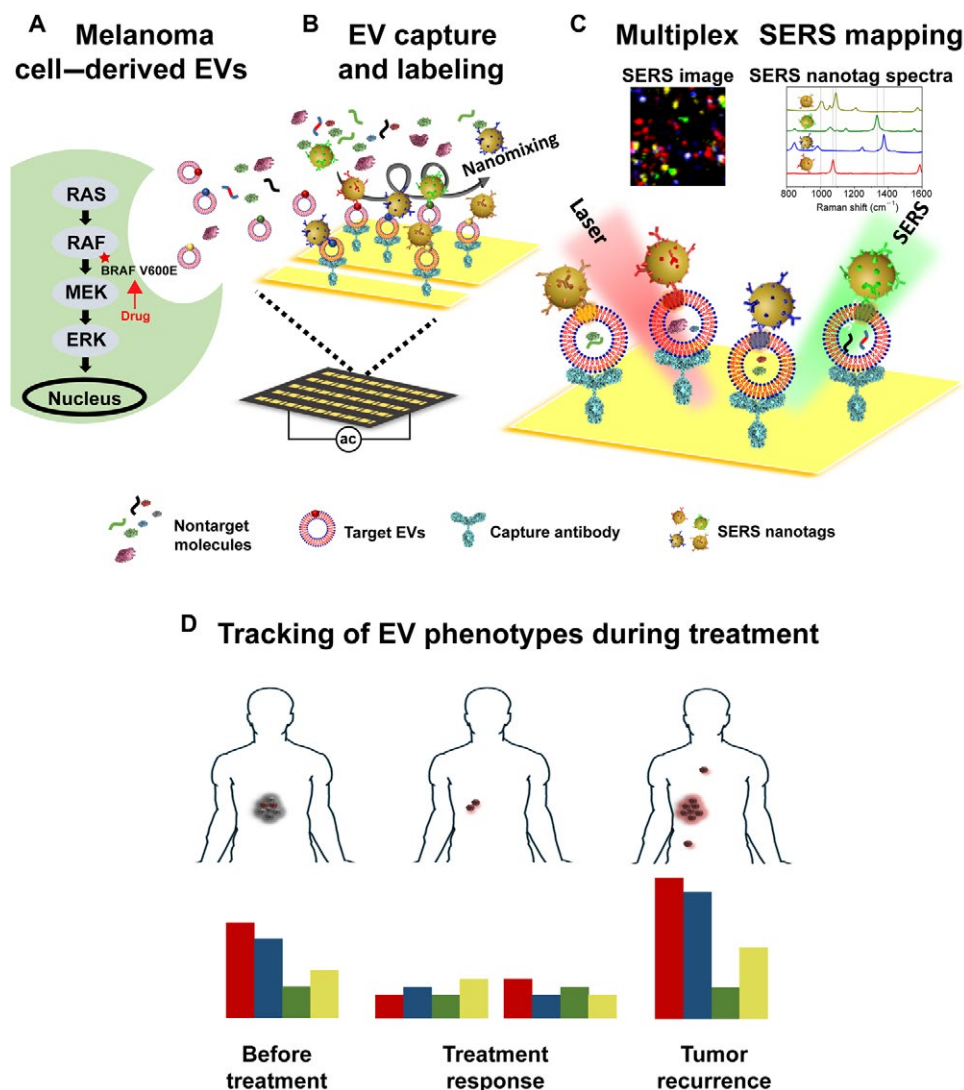


Fig. 1. Schematic for EV phenotyping by EPAC. (A) A melanoma cell with a BRAF V600E mutation secretes EVs into circulation or cell culture medium. (B) The sample is directly injected into EPAC, where the applied nanomixing fluid flow increases EV collisions with the capture antibody and SERS nanotags and shears off nontarget molecules (e.g., protein aggregates and apoptotic bodies) and free SERS nanotags. (C) The characterization of EV phenotypes is performed by SERS mapping. The false-color SERS spectral images are established on the basis of the characteristic peak intensities of SERS nanotags (MCSP-MBA, red; MCAM-TFMBA, blue; ErbB3-DTNB, green; LNG-FR-MPY, yellow). (D) EV phenotypes defined by the relative expression levels of four biomarkers are extracted from the average signal spectra of false-color SERS spectral images. EV phenotypes are unique to each EV subpopulation. By analyzing EV samples before, during, and after BRAF inhibitor treatment, the phenotypic evolution can be tracked to provide information on treatment responses and early signs of drug resistance.

steps, we performed the immunoaffinity-based isolation and labeling via the EPAC (Fig. 1B). To characterize the EVs using EPAC, we used a nanomixing strategy developed in our laboratory (see Materials and Methods) (19, 20). The EPAC not only improved the EV capture efficiency as indicated previously (20) but also addressed the critical problems present in current EV SERS phenotyping technologies, such as nonspecific adsorption and long incubation time because of slow binding kinetics of SERS nanotags to target EVs. The nanomixing force thereby enabled a streamlined plasma EV phenotype analysis within 40 min, which was faster than conventional methods [e.g., >3 hours given by >1 hour for EV isolation (21) and >2 hours for ELISAs (22)]. The stepwise functionalization of EPAC is shown in fig. S1.

To profile EV phenotypes in a small sample volume, EPAC relies on a multiplex SERS nanotag system (Fig. 1C). Each type of SERS nanotags targeted a single biomarker: 4-mercaptopbenzoic acid (MBA) for MCSP, 2,3,5,6-tetrafluoro-MBA (TFMBA) for MCAM, 5,5'-dithiobis (2-nitrobenzoic acid) (DTNB) for ErbB3, and 4-mercaptopypyridine (MPY) for LNGFR. The signal readout was achieved by SERS mapping. The false-color SERS spectral image was generated on the basis of the characteristic peaks of Raman reporters (1075 cm^{-1} for MBA, 1375 cm^{-1} for TFMBA, 1335 cm^{-1} for DTNB, and 1000 cm^{-1} for MPY). The signal intensities in the mapped area were proportional to the numbers of EVs and their expressing biomarker levels.

The EPAC was then applied for the characterization of EV phenotypes before, during, and after treatment (Fig. 1D). The EV phenotypes were obtained from false-color SERS spectral images by calculating the relative intensities of Raman reporter peaks. We hypothesized that the overall EV phenotypic changes could reflect changes in cancer cell populations during treatment and could thus be useful for monitoring of patient treatment responses.

EPAC characterization

To demonstrate the capture capability of EPAC, we characterized SK-MEL-28 cell-derived EVs before and after being captured by EPAC. Nanoparticle tracking analysis (NTA) was used to determine the size distribution of particles (including EVs) present in the conditioned culture medium of SK-MEL-28, showing a mean particle diameter of 148.9 nm and a modal diameter of 102.3 nm (fig. S2A). Atomic force microscopy (AFM) measurements were then applied to *in situ* characterize SK-MEL-28 cell-derived EVs captured by EPAC (fig. S2, B and C). To capture CD63-positive EVs from the conditioned culture medium, we functionalized EPAC with anti-CD63 antibodies (fig. S2B). We further tested the capture of EVs from simulated patient plasma (i.e., pooled plasma from healthy donors spiked with the same concentration of SK-MEL-28 cell-derived EVs) using the anti-MCSP antibody functionalized EPAC (fig. S2C). The anti-MCSP antibody functionalized EPAC was designed for clinical sample detection, as melanoma-derived EVs are found at low concentrations (less than 1% of total plasma EVs) (23), and MCSP is highly expressed in melanoma cells (24). The anti-MCSP functionalized EPAC exposed to normal plasma (fig. S2D) and the anti-MCSP functionalized EPAC (fig. S2E) were used as controls to provide an indication of background signals. Compared to the controls (fig. S2, D and E), both two-dimensional (2D) and 3D AFM images indicated that anti-CD63 and anti-MCSP antibody functionalized EPAC captured particles (i.e., EVs) from the conditioned culture medium and the simulated patient plasma, respectively (fig. S2, B and C). The diameters of two representative particles in each group ranged from

155 to 277 nm, which was in line with the diameter distribution of EVs measured by NTA data (fig. S2A) and thus suggested the successful capture of EVs by EPAC.

To further evaluate the performance of anti-CD63 and anti-MCSP functionalized EPACs in sensing melanoma-specific EVs, we applied these two types of EPACs to detect MCSP-positive EVs present in the conditioned culture medium of SK-MEL-28 cells. To avoid the binding of anti-MCSP capture and detection antibodies toward the same epitope binding site of MCSP, we used antibodies from two different monoclonal clones. We observed a stronger MCSP SERS signal from the anti-MCSP functionalized EPAC than the anti-CD63 functionalized EPAC (Fig. 3D and fig. S7C), possibly due to a higher level of MCSP expression than CD63 in MCSP-positive EVs derived from SK-MEL-28 cells and/or a stronger binding affinity of the MCSP antibody than the anti-CD63 antibody. Hence, we applied the anti-MCSP functionalized EPAC for detection of melanoma-specific EVs derived from patient plasma.

To explore the sensitivity of EPAC in detecting MCSP-positive EVs, we captured different numbers of EVs released from SK-MEL-28 cells in conditioned culture medium and simulated patient plasma samples by the anti-CD63 (Fig. 2A) and anti-MCSP (Fig. 2B) functionalized EPACs, respectively, followed by the labeling of MCSP-MBA SERS nanotags. As shown in Fig. 2, there were statistically significant differences between each of these dilutions [one-way analysis of variance (ANOVA), $P < 0.05$]. According to the signal-to-noise ratio > 3 (the noise signal was measured from medium/plasma only), the anti-CD63 functionalized EPAC was able to detect 10^8 EVs/ml from the conditioned culture medium (Fig. 2A), while the anti-MCSP functionalized EPAC could detect as low as 10^5 EVs/ml in the simulated patient plasma (Fig. 2B). The detection sensitivity of the anti-MCSP functionalized EPAC meets the clinical requirement, given that the average melanoma EV concentration in plasma is $\sim 10^6$ EVs/ml (23, 25). Both resulting sensitivities are also comparable to or better than other EV detection technologies such as the miniaturized EV capture device developed by Kvizera and co-workers (14), although direct comparisons are difficult due to differences in capture/detection antibodies and sample sources.

To demonstrate the detection specificity of EPAC, we measured EVs derived from two cell lines (melanoma SK-MEL-28 and breast cancer MCF7) with known differences in biomarker expression levels (17), together with control experiments (i) EV-free cell culture medium, (ii) without the CD63 capture antibody, and (iii) with non-target CD45 detection antibodies on SERS nanotags. According to previous reports (26–31), SK-MEL-28 cells show high expressions of MCSP and MCAM and low expressions of ErbB3 and LNGFR; MCF7 cells have low expressions of all four biomarkers. We also performed flow cytometry to validate these four biomarker expressions in SK-MEL-28 and MCF7 cell lines before performing their EV characterization (Fig. 3A). As shown in Fig. 3 (B to D), SK-MEL-28 cell-derived EVs provided a unique signal profile compared to MCF7 cell-derived EVs—with the SERS intensity order of MCSP > MCAM > LNGFR > ErbB3—according to the representative false-color SERS spectral images, average SERS spectra obtained from corresponding SERS imaging datasets, and average SERS intensities at 1075 , 1375 , 1335 , and 1000 cm^{-1} from three replicates. Only negligible nonspecific signals were observed from the MCF7 cell-derived EVs and other control experiments. The unique phenotypes of SK-MEL-28 cell-derived EVs and the negligible backgrounds from controls indicated that EPAC was capable of performing multiplex

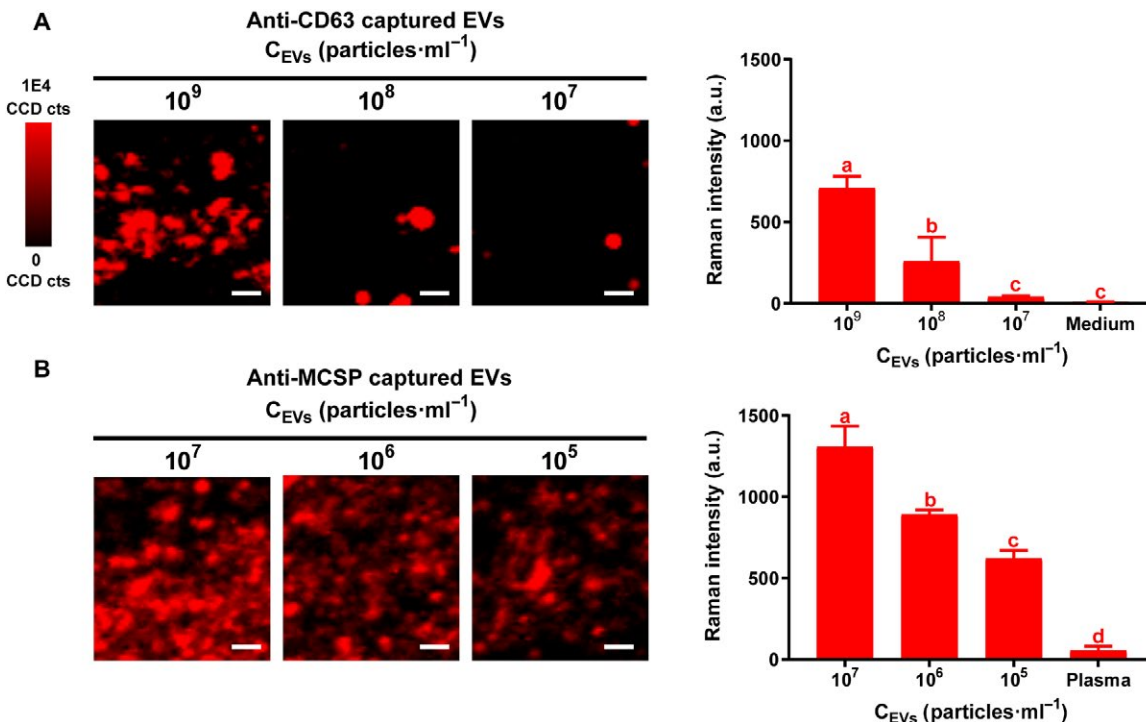


Fig. 2. EPAC sensitivity. The EPAC sensitivity was studied by analyzing designated concentrations of SK-MEL-28 cell-derived EVs from (A) the conditioned culture medium using an anti-CD63 functionalized EPAC and (B) the simulated patient plasma using an anti-MCSP functionalized EPAC, followed by labeling with MCSP-MBA SERS nanotags. The left side shows the representative false-color SERS spectral images, and the right side is the concentration-dependent average SERS intensity at 1075 cm^{-1} . Data are represented as means \pm standard deviation, where error bars represent standard deviation of three separate experiments. Means not sharing a common letter are significantly different ($P < 0.05$). Scale bars, $10\text{ }\mu\text{m}$. a.u., arbitrary units.

EV phenotype characterization and accurately recognizing different EV subpopulations. We believe that our method would be valuable for the study of EV biogenesis, tumor heterogeneity, tumor staging, and phenotypic changes concomitantly during treatment.

To further validate EPAC results, we then measured the expressions of MCSP, MCAM, ErbB3, and LNGFR biomarkers in EVs derived from SK-MEL-28 and MCF7 cell lines using Western blot (fig. S3). As indicated in fig. S3, SK-MEL-28 cell-derived EVs showed MCSP, MCAM, and LNGFR signals and negligible ErbB3 signals; MCF7 cell-derived EVs indicated negative signals for all four biomarkers. These Western blot results were in line with EPAC results and confirmed the presence of MCSP, MCAM, and LNGFR in SK-MEL-28 cell-derived EVs and the low abundance of all four biomarkers in MCF7 cell-derived EVs (Fig. 3B).

Monitoring the EV phenotypic evolution during treatment in preclinical models

Detecting the emergence of drug resistance and identifying potential resistance mechanisms are clinically important for personalized therapy management. To understand the effect of drug treatment on the expression of tumor-specific biomarkers in EVs, we strategically selected generic EV biomarkers as the capture antibody instead of melanoma-associated MCSP. We then investigated the capture efficiency of using three tetraspanin EV biomarkers (i.e., CD63, CD9, and CD81) for detecting MCSP-positive EVs derived from SK-MEL-28. The captured EVs were recognized using MCSP-MBA SERS nanotags. The false-color SERS spectral images derived from anti-CD63/CD9/CD81 functionalized EPACs (fig. S4A) were estab-

lished on the basis of the characteristic peak of MBA at 1075 cm^{-1} . We then selected CD63 as the biomarker for EV capture because the anti-CD63 functionalized EPAC provided the highest signal density in SERS mapping data (fig. S4A), corresponding average SERS spectral signals from the SERS mapping data (fig. S4B), and average SERS intensities at 1075 cm^{-1} from triplicate measurements (fig. S4C). This result might be due to (i) a higher level of CD63 expression than those of CD9/CD81 in SK-MEL-28 cell-derived EVs and (ii) a stronger binding affinity of the anti-CD63 antibody than anti-CD9/CD81 antibodies. These possibilities, however, are extremely difficult to validate by antibody-based methods, given the different binding affinities for each antibody.

To investigate whether and how the phenotypes of CD63-positive EVs change during treatment, we characterized EVs from four patient-derived melanoma cell lines harboring either a BRAF mutation (LM-MEL-33, LM-MEL-64, and SK-MEL-28) or an NRAS mutation in a BRAF wild type setting as a control (LM-MEL-35) (32). We first characterized the EV phenotype before drug treatment (Fig. 4, day 0). MCSP that is expressed in more than 85% of primary and metastatic melanoma lesions (33) was highly expressed in EVs from all four melanoma cell lines. MCAM, cell adhesion-associated surface protein potentially implicated in metastatic spread (27), showed higher expression in LM-MEL-33 cell-derived EVs than in the other studied EVs. Together, EPAC provided a unique phenotypic snapshot that reflected cell type-specific fingerprints (e.g., overexpressed proteins).

To monitor treatment responses of melanoma cell lines, we characterized their EV phenotypic evolution (Fig. 4) and performed

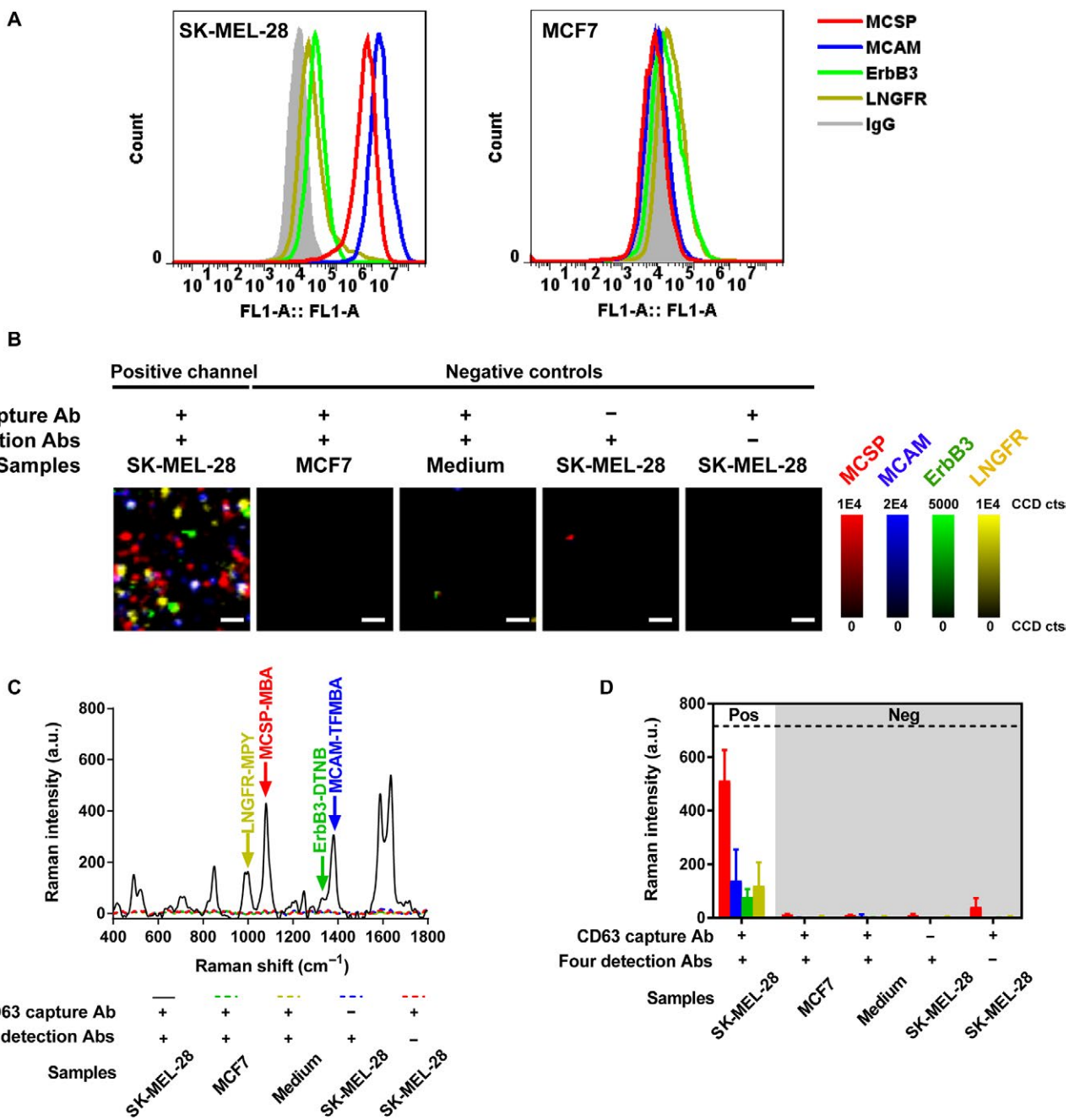


Fig. 3. Anti-CD63 functionalized EPAC specificity. The specificity was studied using EV samples released from SK-MEL-28 and MCF7 cell lines, as well as control experiments including (++) EV-free cell culture medium, (−+) without the CD63 capture antibody, and (+−) with nontarget CD45 detection antibodies on SERS nanotags. (A) The expressions of MCSP, MCAM, ErbB3, and LNGFR in SK-MEL-28 and MCF7 cells were detected by flow cytometry. (B) Representative false-color SERS spectral images, (C) average SERS spectra obtained from corresponding SERS mapping datasets, and (D) average SERS intensities at 1075 cm^{-1} (red, MCSP), 1375 cm^{-1} (blue, MCAM), 1335 cm^{-1} (green, ErbB3), and 1000 cm^{-1} (yellow, LNGFR). Data in (D) are represented as means \pm standard deviation, where error bars represent standard deviation of three separate experiments. Scale bars, $10 \mu\text{m}$.

one-way ANOVA to statistically evaluate the changes of each biomarker (fig. S5) during 30 days of drug treatment and 9 days after treatment. LM-MEL-64 cells without drug treatment were used as a control, which showed no obvious EV phenotypic changes across four selected biomarkers over the same period ($P > 0.05$), suggesting negligible effects from cell passaging artifacts (fig. S5). With the initiation of drug treatment, BRAF inhibitors affect BRAF mutant cells'

proliferation, differentiation, and survival by disrupting the MAPK signaling pathway (18). We observed significant down-regulation of ErbB3 in LM-MEL-33- and LM-MEL-64 cell-derived EVs on day 3 ($P < 0.05$; fig. S5, B and D). After chronic drug exposure for 9 days, LM-MEL-64 cell-derived EVs showed an increase of the MCAM/MCSP expression ratio from 31.3 to 110.5% (Fig. 4D), and SK-MEL-28 cell-derived EVs from 20.7 to 82.6% (Fig. 4C). LM-MEL-28 cell-derived

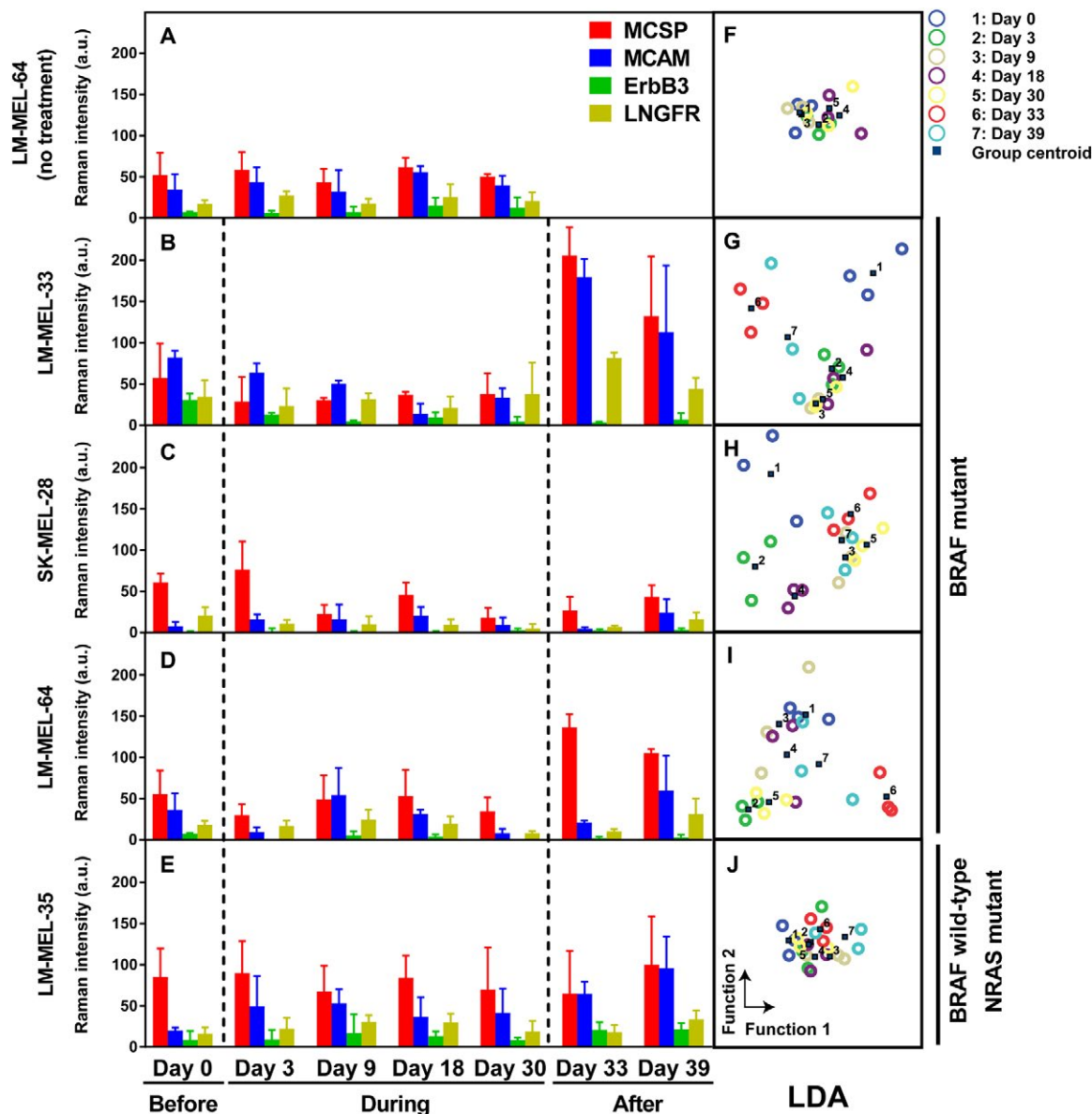


Fig. 4. The anti-CD63 functionalized EPAC for monitoring phenotypic changes of EVs from melanoma patient-derived cell lines in response to BRAF inhibitor treatment. EVs released from (A) LM-MEL-64 cells without treatment were used as a control and followed for 30 days. EVs derived from (B) LM-MEL-33, (C) SK-MEL-28, (D) LM-MEL-64, and (E) LM-MEL-35 cell lines were collected before (day 0), during (days 3 to 30), and after treatment (days 33 and 39). (A to E) Average biomarker signals are represented by red (MCSP), blue (MCAM), green (ErbB3), and yellow (LNGFR). LM-MEL-35 cell line is BRAF wild type but NRAS mutant, and the other three cell lines are BRAF mutant. Data in (A) to (E) are represented as means \pm standard deviation, where error bars represent standard deviation of three separate experiments. (F to J) Clustering of EV populations before, during, and after treatment via LDA of SERS signals.

EVs showed a significant decrease of the MCSP level on day 9 compared to day 3 ($P < 0.05$; fig. S5C). With the continuous drug treatment for 30 days, only the ErbB3 level in EVs derived from LM-MEL-33 and LM-MEL-64 cell lines showed significant down-regulation compared to EVs from their parental cell lines ($P < 0.05$; fig. S5, B and D). When the drug was removed (days 33 and 39), a strong up-regulation of MCSP and/or MCAM levels appeared in EVs derived from these two BRAF V600E mutant melanoma cell lines ($P < 0.05$; fig. S5, B and D), potentially suggesting the release from MAPK block.

Our control cell line used here, LM-MEL-35, is BRAF wild type but NRAS mutant, and is therefore susceptible to the paradoxical MAPK pathway activation by BRAF inhibition (34). Levels of MCSP, LNGFR, and ErbB3 did not change significantly during and after treatment ($P > 0.05$; fig. S5E). However, the MCAM level gradually increased and was significantly higher on day 39 compared with day 0 ($P < 0.05$; fig. S5E). If this observed increase is caused by enhanced MAPK signaling itself, direct cross-talk to the phosphoinositide 3-kinase (PI3K) pathway or just a correlation remains to be further explored. However, this seems to be in line with MCAM up-regulation

in the treatment-susceptible cell lines after BRAF inhibition removal and proliferation rebounce (35, 36).

To comprehensively evaluate the effect of drug treatment on EV phenotypes based on the chosen biomarkers, we performed linear discriminant analysis (LDA) on the SERS data of Fig. 4 (A to E). The LDA result showed an obvious shift of BRAF V600E mutant cell-derived EV populations during and after treatment (Fig. 4, G to I), compared to the closely grouped EVs from LM-MEL-64 cells without treatment (Fig. 4F). In contrast, the drug-insensitive LM-MEL-35 cell-derived EV populations before, during, and after treatment still partially overlapped with each other (Fig. 4J), indicating minor phenotypic changes due to treatment. These LDA results further suggested the effect of BRAF inhibitor treatment on the phenotypes of EVs derived from BRAF mutant cell lines.

Drug-sensitive cells under treatment may degrade and release cell debris into their environment (37). These cell debris including cellular breakdown products (membranes and nucleosomes) might be detected by EPAC and thus might cause false-positive signals. Therefore, to explore the potential interferences of cell debris in characterizing EV phenotypes during drug treatment, we selected the time point of drug-treated SK-MEL-28 cells with the lowest cell viability (i.e., day 5, ~65% viability; fig. S6A), where the concentration of cell debris was expected to be the highest. The purity of EVs analyzed by EPAC was determined by an “exclusion marker”—endoplasmic reticulum protein calnexin—which is cell specific and is expected to be absent in EVs (21). We then analyzed the conditioned culture medium of drug-treated SK-MEL-28 cells by the anti-CD63 functionalized EPAC. The drug-treated SK-MEL-28 cell lysate was used as a positive control to mimic the cellular breakdown products during the treatment, although it is unknown whether treatment effects on cells could be recapitulated by the chemical cell lysis. The false-color SERS spectral images based on the signals of calnexin-TFMBA SERS nanotags at 1375 cm⁻¹ (fig. S6B) showed the high abundance of calnexin in the cell lysate and the absence of calnexin in EVs isolated from the conditioned culture medium, indicating that EPAC results were unaffected by cellular debris and apoptotic bodies. The corresponding average SERS spectra (fig. S6C) and characteristic peak intensity measurements (fig. S6D) showed 82-fold stronger signals for calnexin in the cell lysate compared to the EVs captured from the conditioned culture medium, further suggesting that EPAC efficiently minimized the interferences from cellular debris and apoptotic bodies. These findings were further validated using Western blotting of the cell lysate and purified EVs (fig. S6E). These results provided additional evidence for demonstrating the accurate characterization of the obtained EV phenotypic evolution during the treatment.

Collectively, our results showed that our technology is capable of tracking and characterizing the phenotypic evolution of cancer cell-derived EVs during treatment with BRAF inhibitors. Here, we used four biomarkers chosen mainly due to their well-described expression in melanoma and their potential involvement in tumorigenesis. In addition, it is unknown whether CD63 or these four biomarkers are affected by oncogenic drivers or therapy in melanoma (cells and EVs), thereby affecting the assay interpretation. We envision that using biomarkers that are carefully validated in large and well-annotated patient cohorts in future will allow the successful identification of emerging drug resistance. This will hopefully aid in the prompt modification of therapeutic strategies before treatment failure.

Patient plasma EV phenotypes

The plasma EVs from 11 melanoma patients and 12 healthy individuals were detected by the anti-MCSP functionalized EPAC (Fig. 5A). Specifically, to mimic intra- and interpatient heterogeneity, we tested 15 random melanoma patient plasma samples from 11 melanoma patients (P1, P4, P7, and P9 samples are from the same patient but different time points, as are P5 and P10). Before the patient sample analysis, the specificity of the anti-MCSP functionalized EPAC was demonstrated in EVs derived from high MCSP-expressing SK-MEL-28 and low MCSP-expressing MCF7 cell lines (fig. S7). The captured EVs were subsequently detected by labeling with four-plexed SERS nanotags. We observed a strong MCSP signal for SK-MEL-28 cell-derived EVs and only a low signal for EVs from MCF7 and other control studies (i.e., EV-free cell culture medium, without the capture antibody, or nontarget CD45 detection antibodies on SERS nanotags), demonstrating the specificity of the anti-MCSP functionalized EPAC. We found that anti-MCSP captured SK-MEL-28 cell-derived EVs had different phenotypes (fig. S7C) in comparison to the anti-CD63 captured ones (Fig. 3D), likely due to the distinct EV subpopulations secreted from the SK-MEL-28 cell line. This EV heterogeneity might further reflect potential genetic or epigenetic heterogeneity in the SK-MEL-28 cell population or a differential sorting mechanism in a clonal population.

We then analyzed plasma EVs from melanoma patients and healthy controls. It is noticed that our melanoma patients’ and healthy donors’ samples are from different sources. However, as shown in Fig. 5A, melanoma patient samples (P1 to P15) could be differentiated from both sources of healthy controls (H1 to H5 and H6 to H12) based on the high melanoma-associated MCSP level. The representative false-color SERS spectral images (Fig. 5B) and corresponding average SERS spectra (Fig. 5C) from patient plasma samples (P1 and P8), and normal controls (H1), were given as an example, further suggesting that the unique plasma EV phenotypes of individual patients provided by the anti-MCSP functionalized EPAC enabled the successful differentiation of melanoma patients and healthy controls. Furthermore, these data suggested that EPAC could potentially shed light on the EV heterogeneity, which could help to elucidate the precise role of EV subpopulations in individual patients’ pathophysiological processes, ultimately advancing the development of EVs as personalized therapeutics and diagnostics (38).

We validated anti-MCSP functionalized EPAC results by conventional ELISAs. Given the limited amounts of patient samples available, we strategically performed ELISA for validating the expression of MCSP and ErbB3 in EVs from melanoma patient (P1 to P10) and normal plasma (H1 to H5) samples. We found that no MCSP signals were detected, which was likely due to the insufficient ELISA sensitivity (i.e., the limit of detection = 1.23 ng/ml). For ErbB3, the ELISA results were in agreement with EPAC findings in P8, P9, and P10 plasma samples, as indicated in fig. S8. There was a result deviation between ELISA and EPAC for ErbB3 levels in P4, H3, and H5 plasma samples, which might have been caused by differences in the immunoassay formats. The conventional ErbB3 ELISA captured and labeled EVs with anti-ErbB3 antibodies, while EPAC used anti-MCSP antibodies for EV capture and anti-ErbB3 antibodies for detection. Different immunoassay formats thus might bias the assay toward a specific subset of EVs, which could explain the result differences.

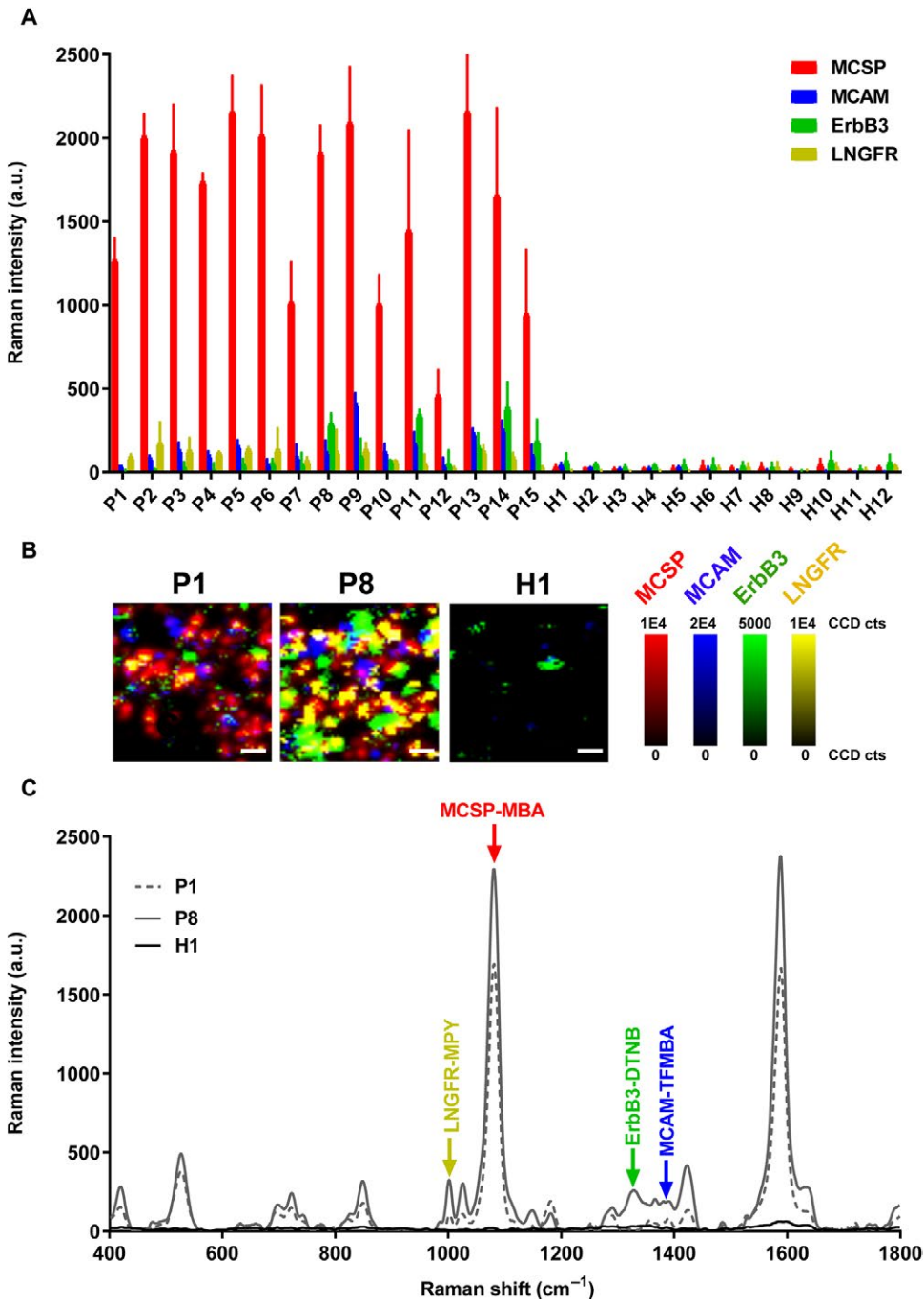


Fig. 5. The anti-MCSP functionalized EPAC for phenotyping of plasma EVs from melanoma patients. (A) EV phenotypes of 15 melanoma samples (P1 to P15) and 12 healthy controls (H1 to H12). P1, P4, P7, and P9 are from the same patient but different time points, as are P5 and P10. (B) Representative false-color SERS spectral images and (C) corresponding average SERS spectra from patient and normal samples (P1, P8, and H1). For (A) and (B), the biomarker signals are represented by red (MCSP), blue (MCAM), green (ErbB3), and yellow (LNGFR). Data in (A) are represented as means \pm standard deviation, where error bars represent standard deviation of three separate experiments. Scale bars, 10 μ m.

Monitoring the phenotypic evolution of patients' plasma EVs in response to treatment

To explore the potential applications of plasma EV phenotypes for monitoring treatment responses, we performed serial measurements of eight melanoma patients before, during, and after targeted therapies (patients 16 to 23; Fig. 6 and fig. S9) using the anti-MCSP

functionalized EPAC. The patients were followed for 143 to 840 days and received intermittent to continuous BRAF inhibitor monotherapy (e.g., dabrafenib) and/or combined therapy with BRAF and MAPK/ERK kinase (MEK) inhibitors (e.g., dabrafenib and trametinib). Disease staging into progressive disease, partial response, and stable disease was made according to the radiological imaging. The SERS measurement

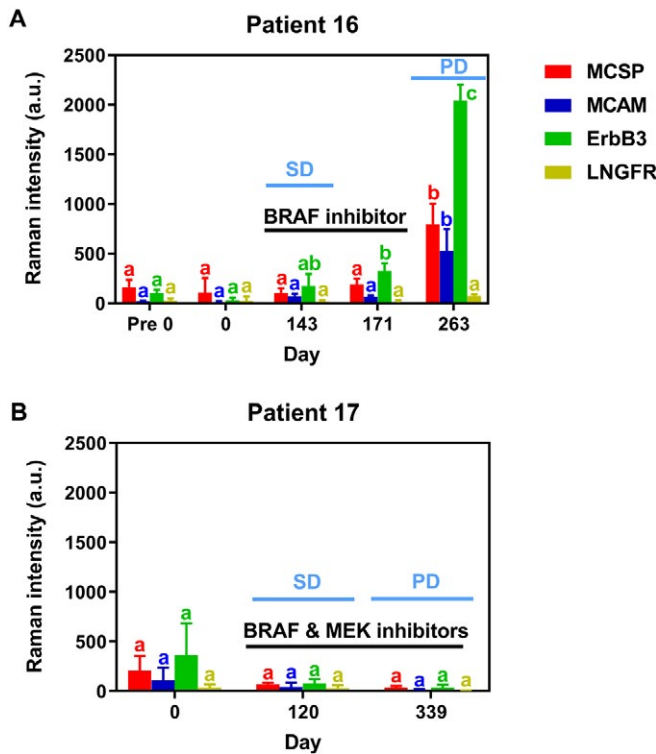


Fig. 6. The anti-MCSP functionalized EPAC for monitoring EV phenotypic evolution of patients 16 and 17 during targeted therapies. (A) Patient 16 was treated with the BRAF inhibitor monotherapy (dabrafenib). The radiological imaging test indicated that this patient showed stable disease (SD) on day 143 and developed progressive disease (PD) after cessation of treatment (day 263). (B) Patient 17 received the combination treatment of BRAF and MEK inhibitors (dabrafenib and trametinib). This patient showed stable disease on day 120 and progressive disease at the third visit (day 339). Data are represented as means \pm standard deviation, where error bars represent standard deviation of three separate experiments. Means not sharing a common letter are significantly different ($P < 0.05$).

data of these patients were compared with healthy controls' using one-way ANOVA and summarized in table S1. Our method also enabled the monitoring of patients' EV phenotypic evolution and allowed unique insights into the plasticity of melanoma EVs during treatment. For instance, patient 16 showed the elevated ErbB3 expression on day 171 compared to day 0 ($P < 0.05$). We also observed the significant up-regulation of MCSP, MCAM, and ErbB3 on day 263, which was consistent to the phenomenon that we observed in EVs derived from BRAF inhibitor-treated BRAF mutant melanoma cells after release from drug treatment and rebound in cellular proliferation (Fig. 4 and fig. S5). Nevertheless, any correlation between EV phenotype and clinical data is mere speculation at this stage.

Patient 17 received combination treatment with BRAF and MEK inhibitors (Fig. 6B). Before treatment, this patient showed significantly higher expressions of MCSP, MCAM, and ErbB3 compared to the mean values of healthy controls (table S1). During treatment, this patient showed low expressions of all four target biomarkers, whose radiological imaging indicated stable disease on day 120 and progressive disease on day 339. This demonstrates that, while the described technology has exciting potential and allows sensitive multiplex biomarker-based EV tracking, the choice of biomarkers

(and the number of biomarkers to be monitored) will be critical for clinical translation.

In conclusion, monitoring patient responses is important to guide treatment management and improve the clinical outcome. Here, we proposed to monitor patient treatment responses based on plasma EV phenotypes using EPAC. EPAC integrates a nanomixing-enhanced EV microchip and a multiplex SERS signal readout system to enable a comprehensive investigation of low-abundance tumor-specific EVs present in complex biological fluids, without the need for EV purification and enrichment steps. The reliability of EPAC was evaluated carefully and demonstrated to precisely profile the EV phenotypic evolution during treatment. By tracking the EV phenotypic changes, we were able to infer the treatment response and obtain tumor cell-specific information. The successful identification of melanoma patient plasma EV phenotypes with high sensitivity further demonstrated the potential of EPAC for routine EV analysis in the clinic. We also observed changes in plasma EV phenotypes during treatment in eight melanoma patients receiving molecular-targeted therapies. The biomarker combination chosen here was used to demonstrate the potential of the technology but not specifically designed or validated to allow the identification of specific treatment responses to BRAF inhibition. As we only used four biomarkers of known value in tracking melanoma (17), it seems feasible that—with biomarker panels specifically targeted for cancer types and treatments and given the streamlined features of EPAC—our method has great potential to guide personalized cancer medicine.

MATERIALS AND METHODS

Clinical sample acquisition

This study was conducted according to the National Health and Medical Research Council (NHMRC) Australian Code for the responsible conduct of Research and the National Statement on Ethical Conduct in Human Research. Patients and healthy donors (H6 to H12) have provided their written informed consent for the research study protocol, which were approved by the Human Research Ethics Committee of the Austin Hospital (Melbourne) and Princess Alexandra Hospital (Brisbane), respectively. Ethics approvals were obtained from The University of Queensland Institutional Human Research Ethics Committee (approval nos. 2011001315 and 2016000876). Healthy donors' blood samples (H1 to H5) were obtained from Red Cross blood. All blood samples were processed using the same standard protocol in accordance with approved guidelines. The demographic data for all patients and healthy donors have been summarized in table S2.

Cell culture

Three melanoma cell lines—LM-MEL-33, LM-MEL-35, and LM-MEL-64—were established at the Ludwig Institute for Cancer Research in Melbourne from patient tumor samples. SK-MEL-28 and MCF7 were obtained from the American Type Culture Collection. All cell lines were authenticated by short-tandem repeat profiling (CellBank Australia) and cultured for <6 months after authentication. Cells were maintained in RF10 medium, which is made up of RPMI 1640 medium (Gibco), 10% fetal bovine serum (Gibco), 2 mM GlutaMAX (Gibco), and 1% penicillin-streptomycin (Gibco), and kept in a humidified incubator in 5% CO₂ at 37°C. All cell lines were routinely tested for mycoplasma.

Preparation of conditioned culture medium

In the sensitivity and specificity assays, SK-MEL-28 and MCF7 cell lines were maintained in serum-free medium for 48 hours to generate conditioned culture medium. In the study of investigating drug effects on EV phenotypes, SK-MEL-28, LM-MEL-33, LM-MEL-35, and LM-MEL-64 cell lines were maintained in Medium 254 (Gibco) with Human Melanocyte Growth Supplement, and with/without 1 μ M PLX4720 (Selleckchem), whose conditioned culture media were collected every 3 days. To remove detached cells and cellular debris, conditioned culture media were centrifuged at 800g for 10 min. The cell-free supernatant was then stored at -80°C for the following experiments.

Proliferation assays

Cellular viability was assessed using the CellTiter 96 AQueous One Solution Cell Proliferation Assay (Promega Corporation, Madison, WI) according to the manufacturer's protocol.

Flow cytometry

The collected cells were first labeled with either mouse anti-human MCSP (R&D Systems, MAB2585), MCAM (R&D Systems, MAB932), ErbB3 (R&D Systems, MAB3481), LNGFR (R&D Systems, MAB367) monoclonal antibodies, or isotype-matched control [normal mouse immunoglobulin G (IgG), sc-2025, Santa Cruz Biotechnology], followed by Alexa Fluor 488-labeled goat anti-mouse IgG (H+L) secondary antibodies. The flow cytometry measurements were performed with BD Accuri C6, and the data were analyzed with FlowJo (TreeStar, Ashland, OR).

EV preparation for Western blot analysis

EVs were isolated by the combination of ultrafiltration (Amicon Ultra-15 Centrifugal Filter Device, Merck) and Total Exosome Isolation Kit (Life Technologies Australia Pty Ltd.), according to manufacturers' instructions. Briefly, conditioned culture media were centrifuged at 2000g for 30 min to further remove cells and debris. The 12 ml of resulting conditioned culture media was then transferred to an Ultra-15 50-kDa device and concentrated to 120 μl using an Allegra X-22R centrifuge at 4000g for 20 min at 4°C . The concentrate was transferred to a new tube and mixed with 60 μl of Total Exosome Isolation reagent by vortexing. The concentrate/reagent mixture was incubated overnight at 4°C and subsequently centrifuged at 10,000g for 1 hour at 4°C . The supernatants were discarded, and EVs were contained in the pellet at the bottom of the tube.

Western blot analysis

The collected EVs were lysed in Pierce immunoprecipitation lysis buffer containing 1 \times protein inhibitor (Roche) and 1 mM phenylmethylsulfonyl fluoride (Thermo Fisher Scientific), and the protein concentration was quantified using the bicinchoninic acid assay (BCA assay; Thermo Fisher Scientific). Protein lysates were resolved by SDS-polyacrylamide gel electrophoresis and transferred onto polyvinylidene difluoride (PVDF) membranes (Invitrogen). The PVDF membrane was blocked with 5% nonfat dry milk in tris-buffered saline buffer for 1 hour at room temperature (RT) and then immunoblotted with 500-fold diluted primary antibodies overnight at 4°C . The primary antibodies used in this study included mouse anti-human MCSP (R&D Systems, MAB2585), MCAM (R&D Systems, MAB932), ErbB3 (R&D Systems, MAB3482), LNGFR (R&D

Systems, MAB367; or Santa Cruz Biotechnology, sc-271708), calnexin (Abcam, ab112995), and CD63 (Novus, NBP2-42225). Proteins were analyzed under denaturing and reducing/nonreducing conditions according to the manufacturer's instructions. After incubation, the PVDF membrane was washed with phosphate-buffered saline (PBS) containing 0.1% Tween 20 and then incubated with IRDye 800CW-conjugated goat anti-mouse (LI-COR, 926-32210, 10,000-fold dilution) for 1 hour at RT. After washing, protein bands were detected using the Odyssey LI-COR CLx Imaging System.

Size exclusion purification

Five hundred microliters of processed plasma (centrifuged at 10,000g for 10 min) was overlaid on size exclusion columns filled with Sepharose 4B resins (Sigma Aldrich, Australia) and followed by elution with PBS. The fractions were then collected to determine the particle and protein concentrations via the Micro BCA assay. High particle/low protein fractions were pooled and concentrated in an Amicon Ultra-2 50-kDa centrifugal filter device for the ELISA assay.

Enzyme-linked immunosorbent assay

The expressions of MCSP and ErbB3 on the surface of EVs were measured using commercial ELISA kits: MCSP (Sigma-Aldrich, RAB1594) and ErbB3 (Sigma-Aldrich, RAB0174). The assays were conducted according to the manufacturer's instructions. Briefly, 100 μl of standards, controls, and unknown samples was introduced to selected wells and incubated at 4°C overnight. Afterward, the reaction wells were washed four times with wash buffer. One hundred microliters of biotinylated detection antibody was then added to all wells and incubated for 1 hour at RT with gentle shaking. The wells were subsequently washed four times with wash buffer. The horseradish peroxidase-streptavidin reagent was added to all wells and incubated for 45 min at RT. The reaction wells were then washed four times with wash buffer, followed by 30-min incubation with 100 μl of 3,3',5,5'-tetramethylbenzidine reagent at RT in the dark with gentle shaking. Last, all wells were supplemented with 50 μl of stop solution and analyzed for absorbance at 450 nm.

Nanoparticle tracking analysis

The concentrations and particle size distributions of EVs present in conditioned culture medium were analyzed using NanoSight N300 (Malvern Panalytical, UK), based on their properties of both light scattering and Brownian motion. For each sample, three videos of 60-s duration were recorded, with a short delay between recordings. The recorded video was analyzed with NTA software, which tracked many particles individually and, using the Stokes-Einstein equation, calculated their hydrodynamic diameters. Camera sensitivity and detection threshold were set to 12 and 5, respectively. The concentration of each detection sample was between 2×10^8 and 6×10^8 particles/ml, which was prepared by 10-fold dilution of the stock conditioned culture medium with PBS that has passed through a 0.22- μm filter. Samples were administered and recorded under controlled flow, using the NanoSight syringe pump and script control system.

SERS nanotag synthesis

SERS nanotags were prepared by functionalizing AuNPs with antibodies and Raman reporters and stabilizing with bovine serum albumin (BSA; Life Technologies Australia Pty Ltd.) coatings. Briefly, 60-nm AuNPs were synthesized by citrate reduction of HAuCl₄

(39). Ten microliters of 1 mM Raman reporters in ethanol (either MBA, TFMBA, DTNB, or MPY) and subsequently 2 μ l of 1 mM dithiobis(succinimidyl propionate) (Thermo Fisher Scientific) in dimethyl sulfoxide were added into 1 ml of AuNP solutions and incubated for 5 hours at RT to form a complete self-assembled monolayer. For the functionalization of MPY Raman reporters, 20 μ l of 0.1 M NaOH was first added to adjust AuNP solutions to pH = 8. After incubation, the mixture was centrifuged at 7600 rpm for 10 min to remove the residual reactants. The mixture was then resuspended in 200 μ l of 0.1 mM PBS and incubated with 2 μ g of primary antibodies against either MCSP (R&D Systems, MAB2585), MCAM (R&D Systems, MAB932), ErbB3 (R&D Systems, MAB3481), LNGFR (R&D Systems, MAB367), calnexin (Abcam, ab112995), or CD45 (BioLegend, 368502) for 30 min at RT. The mixture was then centrifuged at 600g at 4°C for 10 min to remove free antibodies and resuspended in 200 μ l of 0.1% (w/v) BSA for 0.5 hour at RT to block nonspecific binding sites and stabilize SERS nanotags. The SERS nanotags were stored at 4°C and were stable for months.

Microchip fabrication

The device was fabricated using standard photolithography and soft lithography according to the procedure reported previously (20). Briefly, the device was assembled from a glass chip with patterned asymmetric gold electrode structures and a polydimethylsiloxane (PDMS) slab consisting of the microfluidic channel structures. The PDMS slab consisted of five parallel channels, each 3.5 cm long, 400 μ m wide, and 500 μ m high. The chip accommodated five channels, and each channel was made up of an array of 40 pairs of asymmetric gold electrodes (fig. S1, A and B). The distance between two adjacent electrode pairs was 150 μ m. An electrode pair consisted of a small (100 μ m width) and large (400 μ m width) electrodes that were spaced by a distance of 50 μ m (fig. S1C). The nanoscopic fluid flow was generated by applying an alternating potential difference across each asymmetric electrode pair. The potential difference changed the charge distribution in the electrical double layer that gave rise to a lateral fluid movement in nanometer distance to the electrode surface. This lateral fluid movement increased the diffusion of molecules and SERS nanotags, leading to frequent antigen–antibody collisions while simultaneously shearing off weakly bound nonspecific molecules.

The electrode structures were designed in L-Edit (Tanner Research, USA) and written to a 12.7 cm chrome mask (Shenzhen Qingyi Precision Mask Making, Singapore) using a direct laser writer (Heidelberg μ PG 101, Germany). Borofloat wafers (Bonda Technology Pte Ltd., Singapore) were rinsed with isopropanol and acetone and dried for 25 min at 150°C. Subsequently, negative photoresist AZ nLOF 2020 (MicroChemicals GmbH, Germany) was spin-coated on the wafer for 30 s at 3000 rpm before a soft bake for 2 min at 110°C. Next, the coated wafer was exposed at a constant dose of 340 mJ/cm with an EVG 620 mask aligner (EV Group, Austria), followed by a postback of 1 min at 110°C. The exposed wafer was then developed for 45 s in AZ 726 MIF (MicroChemicals GmbH, Germany), dried, and subjected to deposition of 10 nm of Ti and 200 nm of Au with a Temescal FC-2000 electron beam evaporator (Ferrotec, USA). After overnight liftoff in Remover PG (MicroChemicals GmbH, Germany), the excess material was washed off and the electrode pattern was revealed (fig. S1B).

PDMS microfluidic channels were prepared by casting an activated silicon elastomer solution (Sylgard 184, Dow, USA) onto the

master mold containing microfluidic channels. After curing for 20 min at 80°C, the PDMS was carefully detached from the master. The sample inlet and outlet reservoirs were then punched at the ends of microfluidic channels. The PDMS microfluidic structures were aligned with the array of asymmetric electrodes on the glass chip and thermally bonded overnight at 65°C.

Microchip functionalization

The device was functionalized in a three-step procedure using biotin-avidin chemistry (fig. S1D). Initially, the device channels were washed with PBS buffer. Next, the channels were sequentially incubated with solutions of biotinylated BSA (200 μ g/ml) for 2 hours, streptavidin (100 μ g/ml) for 1 hour, biotinylated anti-human CD63 antibody (10 μ g/ml) (BioLegend, 353018) or biotinylated anti-human MCSP antibody (10 μ g/ml) (MACS Miltenyi Biotec, 130-099-049) for 2 hours, and 1% (w/v) BSA for 0.5 hour at RT. After each incubation step, the channels were washed with PBS buffer to remove excess reagents.

EV capture and labeling

One hundred microliters of samples (i.e., conditioned culture medium or 10-fold diluted plasma) and 30 μ l of diluted SERS nanotags were subsequently run in each microfluidic channel for 40 min under the field condition of 100 mV and 1 kHz. Under these previously optimized conditions (20), the stimulated nanoscopic fluid flow was the most efficient for EV capture and labeling due to the increased collision frequency of EVs with capture antibodies and SERS nanotags, and the minimum nonspecific binding.

SERS measurements

SERS mapping was performed using a WITec Alpha300 R microspectrometer configured with a 632-nm laser and a highly sensitive electron multiplying charge-coupled device (EMCCD). The laser power of 4 mW and the system frequency were calibrated by the peak of a silicon wafer at \sim 520 cm^{-1} . SERS mapping was performed at an area of 60 μ m \times 60 μ m (60 pixels \times 60 pixels) with 1- μ m spatial resolution using a 20 \times microscope objective. The SERS spectrum from each pixel was generated with 50-ms integration time. The sample was measured in triplicate; for each replicate, three different positions (left, middle, and right) across the entire channel were scanned. The selected region was scanned to simultaneously detect all four biomarkers, and average SERS spectra were calculated from these spectral images.

Atomic force microscopy

EVs captured on the electrode surface were *in situ* characterized using a Cypher AFM system (Asylum Research, USA) on air tapping mode with cantilevers (HA_NC, ETALON, TipsNano, Russia) with a resonant frequency of 140 kHz (dispersion \pm 10%), a force constant of 3.5 N/m (dispersion \pm 20%), and a $<$ 10-nm curvature radius sharp silicon tip.

Statistical analyses

Data were presented as means \pm standard deviation. One-way ANOVA followed by either Tukey's or Dunnett's multiple comparisons test was performed to identify significant variations at 95% confidence interval, using GraphPad Prism 7.0 (GraphPad Software Inc., USA).

To statistically investigate the EV phenotypic changes in response to treatment, SERS intensities at peaks of 1075, 1375, 1335,

and 1000 cm^{-1} —representing the expression of each biomarker—were used as LDA input variables. LDA then generated discriminant functions that consisted of different linear combinations of input variables. The resulting discriminant functions were uncorrelated with each other, and each function maximized the difference between groups on that function. The first two discriminant functions that explained most input variables were selected for EV phenotypic clustering. Discriminant scores generated from these two discriminant functions were plotted to describe the differences between each data point. LDA was performed with SPSS 19.0 software package (SPSS Inc., USA).

SUPPLEMENTARY MATERIALS

Supplementary material for this article is available at <http://advances.sciencemag.org/cgi/content/full/6/9/eaax3223/DC1>

Fig. S1. EPAC design and functionalization.

Fig. S2. EPAC-captured EV characterization.

Fig. S3. Western blot analysis of isolated EVs from SK-MEL-28 and MCF7 cells.

Fig. S4. Performance evaluation of the anti-CD63, anti-CD9, or anti-CD81 functionalized EPAC for detection of MCSP-positive EVs from SK-MEL-28 cells.

Fig. S5. Monitoring the changes of individual biomarker levels in EVs from drug-treated melanoma cell lines, using the anti-CD63 functionalized EPAC.

Fig. S6. Effect of cell debris on the anti-CD63 functionalized EPAC performance.

Fig. S7. Anti-MCSP functionalized EPAC specificity.

Fig. S8. The ErBB3 expression in EVs derived from melanoma patient (P1 to P10) and normal plasma (H1 to H5) samples, measured with a commercial ELISA kit.

Fig. S9. The anti-MCSP functionalized EPAC for tracking EV phenotypic changes of patients 18 to 23 during targeted therapies.

Table S1. The anti-MCSP functionalized EPAC for measurements of plasma EVs from 12 healthy donors (H1 to H12) and 8 melanoma patients (P16 to P23).

Table S2. Demographic data for melanoma patients and healthy donors.

[View/request a protocol for this paper from Bio-protocol.](#)

REFERENCES AND NOTES

- E. V. Abel, K. J. Basile, C. H. Kugel III, A. K. Witkiewicz, K. Le, R. K. Amaravadi, G. C. Karakousis, X. Xu, W. Xu, L. M. Schuchter, J. B. Lee, A. Ertel, P. Fortina, A. E. Aplin, Melanoma adapts to RAF/MEK inhibitors by FOXD3-dependent upregulation of *ERBB3*. *J. Clin. Invest.* **123**, 2155–2168 (2013).
- A. Toss, Z. Mu, S. Fernandez, M. Cristofanilli, CTC enumeration and characterization: Moving toward personalized medicine. *Ann. Transl. Med.* **2**, 108 (2014).
- G. Raposo, W. Stoorvogel, Extracellular vesicles: Exosomes, microvesicles, and friends. *J. Cell Biol.* **200**, 373–383 (2013).
- R. E. Lane, D. Korbie, M. M. Hill, M. Trau, Extracellular vesicles as circulating cancer biomarkers: Opportunities and challenges. *Clin. Transl. Med.* **7**, 14 (2018).
- S. Fais, L. O'Driscoll, F. E. Borras, E. Buzas, G. Camussi, F. Cappello, J. Carvalho, A. Cordeiro da Silva, H. D. Portillo, S. E. Andaloussi, T. F. Trček, R. Furlan, A. Hendrix, I. Gursel, V. Kralj-Ilgic, B. Kaeffer, M. Kosanovic, M. E. Lekka, G. Lipps, M. Logozzi, A. Marcilla, M. Sammar, A. Llorente, I. Nazarenko, C. Oliveira, G. Pocsfalvi, L. Rajendran, G. Raposo, E. Rohde, P. Siljander, G. van Niel, M. H. Vasconcelos, M. Yáñez-Mó, M. L. Yliperttula, N. Zarovni, A. B. Zavec, B. Giebel, Evidence-based clinical use of nanoscale extracellular vesicles in nanomedicine. *ACS Nano* **10**, 3886–3899 (2016).
- K. Al-Nedawi, B. Meehan, J. Micallef, V. Lhotak, L. May, A. Guha, J. Rak, Intercellular transfer of the oncogenic receptor EGFRVIII by microvesicles derived from tumour cells. *Nat. Cell Biol.* **10**, 619–624 (2008).
- H. Peinado, M. Alečković, S. Lavotshkin, I. Matei, B. Costa-Silva, G. Moreno-Bueno, M. Hergueta-Redondo, C. Williams, G. García-Santos, C. M. Ghajar, A. Nitadori-Hoshino, C. Hoffman, K. Badal, B. A. Garcia, M. K. Callahan, J. Yuan, V. R. Martins, J. Skog, R. N. Kaplan, M. S. Brady, J. D. Wolchok, P. B. Chapman, Y. Kang, J. Bromberg, D. Lyden, Melanoma exosomes educate bone marrow progenitor cells toward a pro-metastatic phenotype through MET. *Nat. Med.* **18**, 883–891 (2012).
- H. Shao, J. Chung, L. Balaj, A. Charest, D. Bigner, B. S. Carter, F. H. Hochberg, X. O. Breakefield, R. Weissleder, H. Lee, Protein typing of circulating microvesicles allows real-time monitoring of glioblastoma therapy. *Nat. Med.* **18**, 1835–1840 (2012).
- H. Shao, J. Chung, K. Lee, L. Balaj, C. Min, B. S. Carter, F. H. Hochberg, X. O. Breakefield, H. Lee, R. Weissleder, Chip-based analysis of exosomal mRNA mediating drug resistance in glioblastoma. *Nat. Commun.* **6**, 6999 (2015).
- Y. Chen, L. Wang, Y. Zhu, Z. Chen, X. Qi, L. Jin, J. Jin, D. Hua, X. Ma, Breast cancer resistance protein (BCRP)-containing circulating microvesicles contribute to chemoresistance in breast cancer. *Oncol. Lett.* **10**, 3742–3748 (2015).
- X. Ma, Z. Chen, D. Hua, D. He, L. Wang, P. Zhang, J. Wang, Y. Cai, C. Gao, X. Zhang, F. Zhang, T. Wang, T. Hong, L. Jin, X. Qi, S. Chen, X. Gu, D. Yang, Q. Pan, Y. Zhu, Y. Chen, D. Chen, L. Jiang, X. Han, Y. Zhang, J. Jin, X. Yao, Essential role for TrpC5-containing extracellular vesicles in breast cancer with chemotherapeutic resistance. *Proc. Natl. Acad. Sci. U.S.A.* **111**, 6389–6394 (2014).
- K. Liang, F. Liu, J. Fan, D. Sun, C. Liu, C. J. Lyon, D. W. Bernard, Y. Li, K. Yokoi, M. H. Katz, E. J. Koay, Z. Zhao, Y. Hu, Nanoplasmonic quantification of tumour-derived extracellular vesicles in plasma microsamples for diagnosis and treatment monitoring. *Nat. Biomed. Eng.* **1**, 0021 (2017).
- Y. Yoshioka, N. Kosaka, Y. Konishi, H. Ohta, H. Okamoto, H. Sonoda, R. Nonaka, H. Yamamoto, H. Ishii, M. Mori, K. Furuta, T. Nakajima, H. Hayashi, H. Sugisaki, H. Higashimoto, T. Kato, F. Takeshita, T. Ochiya, Ultra-sensitive liquid biopsy of circulating extracellular vesicles using ExoScreen. *Nat. Commun.* **5**, 3591 (2014).
- E. A. Kwizera, R. O'Connor, V. Vinduska, M. Williams, E. R. Butch, S. E. Snyder, X. Chen, X. Huang, Molecular detection and analysis of exosomes using surface-enhanced Raman scattering gold nanorods and a miniaturized device. *Theranostics* **8**, 2722–2738 (2018).
- H. Im, H. Shao, Y. I. Park, V. M. Peterson, C. M. Castro, R. Weissleder, H. Lee, Label-free detection and molecular profiling of exosomes with a nano-plasmonic sensor. *Nat. Biotechnol.* **32**, 490–495 (2014).
- H. Davies, G. R. Bignell, C. Cox, P. Stephens, S. Edkins, S. Clegg, J. Teague, H. Woffendin, M. J. Garnett, W. Bottomley, N. Davis, E. Dicks, R. Ewing, Y. Floyd, K. Gray, S. Hall, R. Hawes, J. Hughes, V. Kosmidou, A. Menzies, C. Mould, A. Parker, C. Stevens, S. Watt, S. Hooper, R. Wilson, H. Jayati lake, B. A. Gusterson, C. Cooper, J. Shipley, D. Hargrave, K. Pritchard-Jones, N. Maitland, G. Chenevix-Trench, G. J. Riggins, D. D. Bigner, G. Palmieri, A. Cossu, A. Flanagan, A. Nicholson, J. W. C. Ho, S. Y. Leung, S. T. Yuen, B. L. Weber, H. F. Seigler, T. L. Darrow, H. Paterson, R. Marais, C. J. Marshall, R. Wooster, M. R. Stratton, P. A. Futreal, Mutations of the *BRAF* gene in human cancer. *Nature* **417**, 949–954 (2002).
- S. C.-H. Tsao, J. Wang, Y. Wang, A. Behren, J. Cebon, M. Trau, Characterising the phenotypic evolution of circulating tumour cells during treatment. *Nat. Commun.* **9**, 1482 (2018).
- E. R. Cantwell-Dorris, J. J. O'Leary, O. M. Sheils, BRAF^{V600E}: Implications for carcinogenesis and molecular therapy. *Mol. Cancer Ther.* **10**, 385–394 (2011).
- Y. Wang, R. Vaidyanathan, M. J. A. Shiddiky, M. Trau, Enabling rapid and specific surface-enhanced Raman scattering immunoassay using nanoscaled surface shear forces. *ACS Nano* **9**, 6354–6362 (2015).
- R. Vaidyanathan, M. Naghibosadat, S. Rauf, D. Korbie, L. G. Carrascosa, M. J. A. Shiddiky, M. Trau, Detecting exosomes specifically: A multiplexed device based on alternating current electrohydrodynamic induced nanoshearing. *Anal. Chem.* **86**, 11125–11132 (2014).
- R. J. Lobb, M. Becker, S. W. Wen, C. S. F. Wong, A. P. Wiegmans, A. Leimgruber, A. Möller, Optimized exosome isolation protocol for cell culture supernatant and human plasma. *J. Extracell. Vesicles* **4**, 27031 (2015).
- F. A. W. Coumans, E. L. Gool, R. Nieuwland, Bulk immunoassays for analysis of extracellular vesicles. *Platelets* **28**, 242–248 (2017).
- N. Koliha, U. Heider, T. Ozimkowski, M. Wiemann, A. Bosio, S. Wild, Melanoma affects the composition of blood cell-derived extracellular vesicles. *Front. Immunol.* **7**, 282 (2016).
- P. Sharma, S. Ludwig, L. Muller, C. S. Hong, J. M. Kirkwood, S. Ferrone, T. L. Whiteside, Immunoaffinity-based isolation of melanoma cell-derived exosomes from plasma of patients with melanoma. *J. Extracell. Vesicles* **7**, 1435138 (2018).
- J. de Vrij, S. L. N. Maas, M. van Nispen, M. Sena-Esteves, R. W. A. Limpens, A. J. Koster, S. Leenstra, M. L. Lamfers, M. L. D. Broekman, Quantification of nanosized extracellular membrane vesicles with scanning ion occlusion sensing. *Nanomedicine* **8**, 1443–1458 (2013).
- E. S. Gray, A. L. Reid, S. Bowyer, L. Calapre, K. Siew, R. Pearce, L. Cowell, M. H. Frank, M. Millward, M. Ziman, Circulating melanoma cell subpopulations: Their heterogeneity and differential responses to treatment. *J. Invest. Dermatol.* **135**, 2040–2048 (2015).
- Q. Zeng, W. Li, D. Lu, Z. Wu, H. Duan, Y. Luo, J. Feng, D. Yang, L. Fu, X. Yan, CD146, an epithelial-mesenchymal transition inducer, is associated with triple-negative breast cancer. *Proc. Natl. Acad. Sci. U.S.A.* **109**, 1127–1132 (2012).
- X. Wang, T. Osada, Y. Wang, L. Yu, K. Sakakura, A. Katayama, J. B. Mc Carthy, A. Brufsky, M. Chivukula, T. Khouri, D. S. Hsu, W. T. Barry, H. K. Lyerly, T. M. Clay, S. Ferrone, CSPG4 protein as a new target for the antibody-based immunotherapy of triple-negative breast cancer. *J. Natl. Cancer Inst.* **102**, 1496–1512 (2010).
- Z. Aguilar, R. W. Akita, R. S. Finn, B. L. Ramos, M. D. Pegram, F. F. Kabbinavar, R. J. Pietras, P. Pisacane, M. X. Sliwkowski, D. J. Slamon, Biologic effects of heregulin/neu differentiation factor on normal and malignant human breast and ovarian epithelial cells. *Oncogene* **18**, 6050–6062 (1999).

30. T. N. Alver, T. J. Lavelle, A. S. Longva, G. F. Øy, E. Hovig, S. L. Bøe, MITF depletion elevates expression levels of ERBB3 receptor and its cognate ligand NRG1-beta in melanoma. *Oncotarget* **7**, 55128–55140 (2016).
31. J. Kim, R. Villadsen, T. Sørlie, L. Fogh, S. Z. Grønlund, A. J. Fridriksdottir, I. Kuhn, F. Rank, V. T. Wielenga, H. Solvang, P. A. W. Edwards, A.-L. Borresen-Dale, L. Rønnow-Jessen, M. J. Bissell, O. W. Petersen, Tumor initiating but differentiated luminal-like breast cancer cells are highly invasive in the absence of basal-like activity. *Proc. Natl. Acad. Sci. U.S.A.* **109**, 6124–6129 (2012).
32. A. Behren, M. Anaka, P.-H. Lo, L. J. Vella, I. D. Davis, J. Catimel, T. Cardwell, C. Gedye, C. Hudson, R. Stan, J. Cebon, The Ludwig institute for cancer research Melbourne melanoma cell line panel. *Pigment Cell Melanoma Res.* **26**, 597–600 (2013).
33. V. De Giorgi, P. Pinzani, F. Salvianti, M. Grazzini, C. Orlando, M. Santucci, T. Lotti, M. Pazzaglia, D. Massi, Circulating tumor cells in cutaneous melanoma. *J. Invest. Dermatol.* **131**, 1776–1777 (2011).
34. G. T. Gibney, J. L. Messina, I. V. Fedorenko, V. K. Sondak, K. S. M. Smalley, Paradoxical oncogenesis—The long-term effects of BRAF inhibition in melanoma. *Nat. Rev. Clin. Oncol.* **10**, 390–399 (2013).
35. L. Tentori, P. M. Lacal, G. Graziani, Challenging resistance mechanisms to therapies for metastatic melanoma. *Trends Pharmacol. Sci.* **34**, 656–666 (2013).
36. D. B. Johnson, J. A. Sosman, Update on the targeted therapy of melanoma. *Curr. Treat. Options Oncol.* **14**, 280–292 (2013).
37. M. L. Sulciner, C. N. Serhan, M. M. Gilligan, D. K. Mudge, J. Chang, A. Gartung, K. A. Lehner, D. R. Bielenberg, B. Schmidt, J. Dalli, E. R. Greene, Y. Gus-Brautbar, J. Piwowarski, T. Mammoto, D. Zurakowski, M. Perretti, V. P. Sukhatme, A. Kaipainen, M. W. Kieran, S. Huang, D. Panigrahy, Resolvinins suppress tumor growth and enhance cancer therapy. *J. Exp. Med.* **215**, 115–140 (2017).
38. E. Willims, C. Cabañas, I. Mäger, M. J. A. Wood, P. Vader, Extracellular vesicle heterogeneity: Subpopulations, isolation techniques, and diverse functions in cancer progression. *Front. Immunol.* **9**, 738 (2018).
39. G. Frens, Controlled nucleation for the regulation of the particle size in monodisperse gold suspensions. *Nature* **241**, 20–22 (1973).

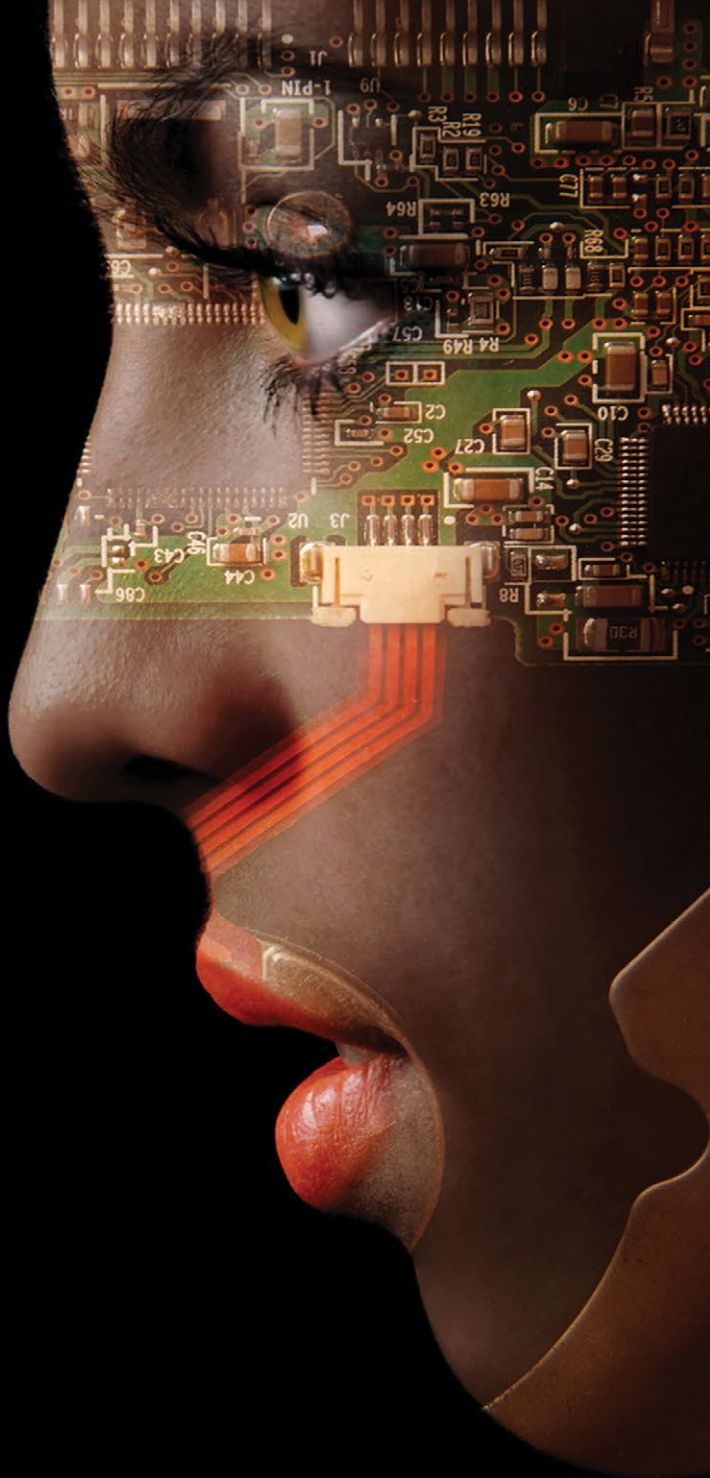
Acknowledgments: We thank the Australian National Fabrication Facility of Queensland node (ANFF-Q) for providing instruments for SERS mapping and device fabrication. We also thank the suggestions from R. Lobb and F. Antaw. **Funding:** We acknowledge funding from the National Breast Cancer Foundation of Australia (CG-12-07) and the Australian Research Council (DP160102836) to M.T. and Y.W. A.W. is supported by the Swiss National Science Foundation (P2SKP2_168309) and the UQ Development Fellowships (UQFEL1831057). L.L.L. is supported by the NHMRC Peter Doherty Biomedical Fellowship (APP1111216). A.B. is supported by a fellowship (MCRF17019) from the Department of Health and Human Services acting through the Victorian Cancer Agency (VCA). J.W. and R.E.L. acknowledge support from the Australian Government Research Training Program Scholarships. **Author contributions:** J.W., A.W., and Y.W. designed the research. J.W. and A.W. performed the experiment, analyzed the data, and prepared the manuscript. All authors contributed to the manuscript revision. **Competing interests:** The authors declare that they have no competing interests. **Data and materials availability:** All data needed to evaluate the conclusions in the paper are present in the paper and/or the Supplementary Materials. Additional data related to this paper may be requested from authors.

Submitted 13 March 2019
Accepted 10 December 2019
Published 26 February 2020
10.1126/sciadv.aax3223

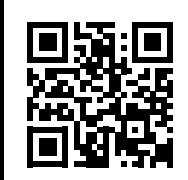
Citation: J. Wang, A. Wuethrich, A. A. I. Sina, R. E. Lane, L. L. Lin, Y. Wang, J. Cebon, A. Behren, M. Trau, Tracking extracellular vesicle phenotypic changes enables treatment monitoring in melanoma. *Sci. Adv.* **6**, eaax3223 (2020).

DOESN'T
YOUR
RESEARCH
DESERVE
THE BEST
READERS?

Submit your research:
cts.ScienceMag.org



Science
Robotics
AAAS



TUMOR IMMUNOLOGY

Targeted deletion of PD-1 in myeloid cells induces antitumor immunity

Laura Strauss^{1,2,3}, Mohamed A. A. Mahmoud^{1,2,3*}, Jessica D. Weaver^{1,2,3}, Natalia M. Tijaro-Ovalle^{1,2,3}, Anthos Christofides^{1,2,3}, Qi Wang^{1,2,3}, Rinku Pal^{1,2,3}, Min Yuan³, John Asara³, Nikolaos Patsoukis^{1,2,3}, Vassiliki A. Boussiotis^{1,2,3†}

PD-1, a T cell checkpoint receptor and target of cancer immunotherapy, is also expressed on myeloid cells. The role of myeloid-specific versus T cell–specific PD-1 ablation on antitumor immunity has remained unclear because most studies have used either PD-1–blocking antibodies or complete PD-1 KO mice. We generated a conditional allele, which allowed myeloid-specific ($\text{PD-1}^{\text{f/fLysMcre}}$) or T cell–specific ($\text{PD-1}^{\text{f/fCD4cre}}$) targeting of *Pdcd1* gene. Compared with T cell–specific PD-1 ablation, myeloid cell–specific PD-1 ablation more effectively decreased tumor growth. We found that granulocyte/macrophage progenitors (GMPs), which accumulate during cancer-driven emergency myelopoiesis and give rise to myeloid-derived suppressor cells (MDSCs), express PD-1. In tumor-bearing $\text{PD-1}^{\text{f/fLysMcre}}$ but not $\text{PD-1}^{\text{f/fCD4cre}}$ mice, accumulation of GMP and MDSC was prevented, whereas systemic output of effector myeloid cells was increased. Myeloid cell–specific PD-1 ablation induced an increase of T effector memory cells with improved functionality and mediated antitumor protection despite preserved PD-1 expression in T cells. In PD-1-deficient myeloid progenitors, growth factors driving emergency myelopoiesis induced increased metabolic intermediates of glycolysis, pentose phosphate pathway, and TCA cycle but, most prominently, elevated cholesterol. Because cholesterol is required for differentiation of inflammatory macrophages and DC and promotes antigen-presenting function, our findings indicate that metabolic reprogramming of emergency myelopoiesis and differentiation of effector myeloid cells might be a key mechanism of antitumor immunity mediated by PD-1 blockade.

INTRODUCTION

Programmed cell death protein 1 (PD-1) is a major inhibitor of T cell responses expressed on activated T cells. It is also expressed on natural killer cells, B cells, regulatory T cells, T follicular helper cells, and myeloid cells (1). The current model supports that a key mechanism dampening antitumor immune responses is the up-regulation of PD-1 ligands in cancer cells and antigen-presenting cells (APCs) of the tumor microenvironment (TME), which mediate ligation of PD-1 on tumor-infiltrating CD8⁺ T cells, leading to the development of T incapable of generating antitumor responses (2). Therapeutic targeting of the PD-1 pathway with antibodies blocking the PD-1 receptor or its ligands induces expansion of oligoclonal CD8⁺ tumor-infiltrating lymphocytes that recognize tumor neo-antigens (3). Thus, in the context of cancer, PD-1 is considered a major inhibitor of T effector cells, whereas on APC and cancer cells, emphasis has been placed on the expression of PD-1 ligands. PD-1 ligand-1 expression in the TME is often a prerequisite for patient enrollment to clinical trials involving blockade of the PD-1 pathway. However, responses do not always correlate with PD-L1 expression, and it remains incompletely understood how the components of the PD-1:PD-L1/2 pathway suppress antitumor immunity.

Recent studies indicated that PD-1 can be induced by Toll-like receptor (TLR) signaling in macrophages (MΦ) and negatively correlates with M1 polarization (4). PD-1 expression in macrophages plays a pathologic role by suppressing the innate inflammatory

response to sepsis (5) and inhibiting *Mycobacterium tuberculosis* phagocytosis in active tuberculosis (6). Our knowledge about the function of PD-1 on myeloid cells in the context of cancer is very limited. However, similar to its role in infections, PD-1 expression inversely correlates with M1 polarization and phagocytic potency of tumor-associated MΦ (TAM) against tumor (7, 8). The mechanisms of PD-1 expression in myeloid cells and the role of PD-1-expressing myeloid cells in tumor immunity remain unknown.

The rapid increase in myeloid cell output in response to immunologic stress is known as emergency myelopoiesis. Terminally differentiated myeloid cells are essential innate immune cells and are required for the activation of adaptive immunity. Strong activation signals mediated by pathogen-associated molecular pattern or danger-associated molecular pattern molecules lead to a transient expansion and subsequent differentiation of myeloid progenitors to mature monocytes and granulocytes to protect the host. In contrast, during emergency myelopoiesis mediated by continuous low-level stimulation mediated by cancer-derived factors and cytokines, bone marrow common myeloid progenitors (CMPs) but, predominantly, granulocyte/macrophage progenitors (GMPs) undergo modest expansion with hindered differentiation, and a fraction of myeloid cells with immunosuppressive and tumor-promoting properties, named myeloid-derived suppressor cells (MDSCs), accumulates. MDSCs suppress CD8⁺ T cell responses by various mechanisms (9). In the mouse, MDSCs consist of two major subsets, CD11b^{hi}Ly6G[−] (hereafter named CD11b^{hi}Ly6C⁺) monocytic (M-MDSC) and CD11b^{hi}Ly6C^{lo}Ly6G⁺ (hereafter named CD11b^{hi}Ly6G⁺) polymorphonuclear (PMN-MDSC) (10). These cells have similar morphology and phenotype to normal monocytes and neutrophils but distinct genomic and biochemical profiles (9). In humans, in addition to M-MDSC and PMN-MDSC, a small subset of early-stage MDSC has been identified (10).

¹Division of Hematology-Oncology, Beth Israel Deaconess Medical Center, Harvard Medical School, Boston, MA 02115, USA. ²Department of Medicine, Beth Israel Deaconess Medical Center, Harvard Medical School, Boston, MA 02115, USA. ³Cancer Center, Beth Israel Deaconess Medical Center, Harvard Medical School, Boston, MA 02215, USA.

*Present address: Heidelberg University, German Cancer Research Center (DKFZ), Heidelberg, Germany.

†Corresponding author. Email: vboussio@bidmc.harvard.edu

Copyright © 2020
The Authors, some
rights reserved;
exclusive licensee
American Association
for the Advancement
of Science. No claim
to original U.S.
Government Works

Although PMN-MDSCs represent the major subset of circulating MDSC, they are less immunosuppressive than M-MDSC when assessed on a per cell basis (11–13). Current views support the two-signal requirement for MDSC function. The first signal controls MDSC generation, whereas the second signal controls MDSC activation, which depends on cues provided by the TME and promotes MDSC differentiation to TAM (14). Proinflammatory cytokines and endoplasmic reticulum stress response in the TME contribute to pathologic myeloid cell activation that manifests as weak phagocytic activity, increased production of reactive oxygen species and nitric oxide (NO) and expression of arginase-1 (ARG1), and convert myeloid cells to MDSC (9). MDSCs are associated with poor outcomes in many cancer types in patients and negatively correlate with response to chemotherapy, immunotherapy, and cancer vaccines (15–19).

In the present study, we examined how PD-1 regulates the response of myeloid progenitors to cancer-driven emergency myelopoiesis and its implications on antitumor immunity. We determined that myeloid progenitors, which expand during cancer-driven emergency myelopoiesis, express PD-1 and PD-L1. PD-L1 was constitutively expressed on CMPs and GMPs, whereas PD-1 expression displayed a notable increase on GMPs that arose during tumor-driven emergency myelopoiesis. PD-1 was also expressed on tumor-infiltrating myeloid cells—including M-MDSCs and PMN-MDSCs, CD11b⁺F4/80⁺ MΦ, and CD11c⁺major histocompatibility complex class II-positive (MHCII⁺) dendritic cells (DCs) in tumor-bearing mice—and on MDSCs in patients with refractory lymphoma. Ablation of PD-1 signaling in PD-1 knockout (KO) mice prevented GMP accumulation and MDSC generation and resulted in increase of Ly6C^{hi} effector monocytes, MΦ and DC. We generated mice with conditional targeting of the *Pdcd1* gene (PD-1^{f/f}) and selectively eliminated PD-1 in myeloid cells or T cells. Compared with T cell-specific ablation of PD-1, myeloid-specific PD-1 ablation more effectively decreased tumor growth in various tumor models. At a cellular level, only myeloid-specific PD-1 ablation skewed the myeloid cell fate commitment from MDSC to effector Ly6C^{hi} monocytes MΦ and DC and induced T effector memory (T_{EM}) cells with improved functionality. Our findings reveal a previously unidentified role of the PD-1 pathway and suggest that skewing of myeloid cell fate during emergency myelopoiesis and differentiation to effector APCs, thereby reprogramming T cell responses, might be a key mechanism by which PD-1 blockade mediates antitumor function.

RESULTS

PD-1 is expressed in myeloid cells during cancer-mediated emergency myelopoiesis

For our studies, we selected the murine B16-F10 melanoma tumor model because it has been informative in dissecting mechanisms of resistance to checkpoint immunotherapy (20). First, we examined whether B16-F10 induces tumor-driven emergency myelopoiesis similarly to the MC17-51 fibrosarcoma, a mouse tumor model well established to induce cancer-driven emergency myelopoiesis (21). We assessed the expansion of myeloid progenitors in the bone marrow and the increase of CD11b⁺CD45⁺ myeloid cells in the spleen and tumor (figs. S1 and S2). Both tumor types induced increase of myeloid progenitors in the bone marrow and systemic increase of CD45⁺CD11b⁺ myeloid cells (fig. S3), providing evidence that B16-F10 melanoma is an appropriate tumor model to study tumor-driven emergency myelopoiesis and its consequences in tumor immunity. In the spleen of non-tumor-bearing mice, few myeloid cells

constitutively expressed very low levels of PD-L1, whereas PD-1 was very low to undetectable (Fig. 1, A and B). In B16-F10 tumor-bearing mice, expression of PD-1 and PD-L1 was up-regulated on myeloid cells of the spleen (Fig. 1, C to F). PD-1 and PD-L1 were also expressed on myeloid cells at the tumor site (Fig. 1, G to I). All subsets of myeloid cells expanding in tumor-bearing mice including M-MDSCs, PMN-MDSCs, CD11b⁺F4/80⁺ MΦs, and CD11c⁺MHCII⁺ DCs expressed PD-1 (Fig. 1, D and G). Kinetics studies of PD-1 expression on myeloid cells in the spleen of tumor-bearing mice showed a gradual increase over time (Fig. 1, J to M).

Because myeloid cells that give rise to MDSC and TAM are generated from myeloid progenitors in the bone marrow during tumor-driven emergency myelopoiesis, we examined PD-1 and PD-L1 expression in these myeloid progenitors. In non-tumor-bearing mice, PD-1 was detected at very low levels on GMPs (Fig. 2A), whereas PD-L1 was constitutively expressed in CMPs but mostly on GMPs (Fig. 2B). In tumor-bearing mice, PD-L1 was up-regulated in CMPs and GMPs, and its expression levels remained elevated during all assessed time points (Fig. 2, F to J). PD-1 expression was induced on CMPs but more prominently on GMPs (Fig. 2, C to I). Kinetics studies showed that PD-1 expression on GMPs peaked early after tumor inoculation (Fig. 2, C, E, and I), at a time point when tumor growth was not yet measurable. Thus, induction of PD-1 expression in myeloid progenitors is an early event during tumor development.

To determine whether PD-1 expression on GMPs was mediated by growth factors regulating emergency myelopoiesis, we cultured bone marrow cells from non-tumor-bearing mice with granulocyte colony-stimulating factor (G-CSF), granulocyte-macrophage colony growth factor (GM-CSF), and the TLR4 ligand lipopolysaccharide. PD-1 that was constitutively expressed at low levels in GMPs was up-regulated by culture with each of these factors (fig. S4A), consistent with our findings that PD-1 expression was rapidly induced on GMPs of tumor-bearing mice *in vivo* (Fig. 2, C, E, and I). Quantitative polymerase chain reaction (qPCR) in purified Lin^{neg} bone marrow cells showed that PD-1 mRNA was constitutively expressed in myeloid progenitors and was up-regulated by culture with G-CSF or GM-CSF (fig. S4B). Together, these *in vivo* and *in vitro* studies provide evidence that PD-1 expression on myeloid progenitors is regulated by a direct cell-intrinsic effect of factors driving cancer-mediated emergency myelopoiesis.

To examine whether PD-1 was expressed in MDSCs in humans, we used samples from healthy donors and patients with malignant non-Hodgkin's lymphoma (NHL) (figs. S5 and S6). A high level of PD-1-expressing M-MDSCs was detected in the peripheral blood of three patients with treatment-refractory NHL but not in two patients who responded to treatment or five healthy donors (fig. S6). These results show that PD-1 expression is detected in human MDSCs and serve as a paradigm, suggesting that PD-1 expression in MDSCs of patients with cancer might be a clinically relevant event.

PD-1 ablation alters emergency myelopoiesis and the profile of myeloid cell output

To examine whether PD-1 might have an active role in tumor-induced stress myelopoiesis, we used PD-1-deficient (PD-1^{-/-}) mice. PD-1 deletion, which resulted in decreased tumor growth (Fig. 3, A and B), substantially altered tumor-induced stress myelopoiesis (Fig. 3, C to E). Although accumulation of CMPs was comparable, accumulation of GMPs was significantly diminished in PD-1^{-/-} mice (Fig. 3, C and D), indicating that GMPs might be a key target on which PD-1 mediated

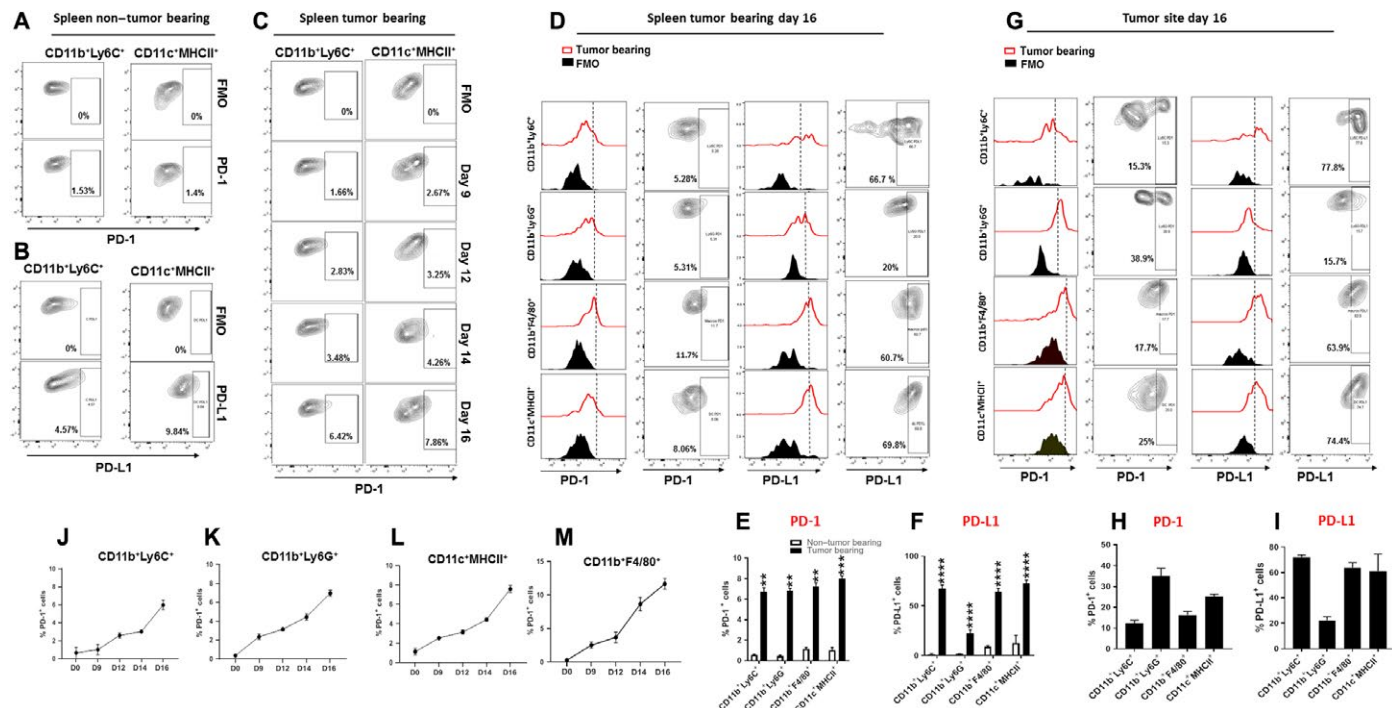


Fig. 1. PD-1 and PD-L1 are expressed on myeloid cells that expand in tumor-bearing mice. (A and B) Expression of PD-1 and PD-L1 on CD11b⁺Ly6C⁺ monocytes and CD11c⁺MHCII⁺ DC in the spleen of non-tumor-bearing C57BL/6 mice. FMO, fluorescence minus one. (C) C57BL/6 mice were inoculated with B16-F10 mouse melanoma, and at the indicated time points, expression of PD-1 was examined by flow cytometry in the spleen after gating on the indicated myeloid populations; contour plots depicting the percentage of positive cells are shown. On day 16 after tumor inoculation, expression of PD-1 and PD-L1 was assessed in the spleen (D) and the tumor site (G) after gating on the indicated myeloid populations. (E and F) Fluorescence-activated cell sorting (FACS) histograms and contour plots depicting the percentage of positive cells and bar graphs (E, F, H, and I) of mean \pm SEM positive cells. Results are representative of 12 independent experiments with six mice per group. (J to M) Kinetics of PD-1 up-regulation on CD11b⁺Ly6C⁺, CD11b⁺Ly6G⁺, CD11b⁺F4/80⁺, and CD11c⁺MHCII⁺ of the spleen after tumor inoculation. ** P < 0.01, *** P < 0.005, **** P < 0.0001.

its effects on myeloid progenitors (Fig. 3E). Kinetics studies showed sustained GMP expansion in wild-type (WT) tumor-bearing mice. In contrast, in PD-1^{-/-} tumor-bearing mice, GMPs displayed a rapid expansion and subsequent decline (fig. S7). In parallel, in PD-1^{-/-} mice, there was an increase of differentiated CD11b⁺Ly6C^{hi} monocytic cells not only in the tumor (Fig. 3H) but also in the spleen and the small intestine, which also displayed an increase in CD11c⁺MHCII⁺ DCs (Fig. 3, F and G). Moreover, at these sites, there was a significant increase of the CD11b⁺Ly6C⁺/CD11b⁺Ly6G⁺ ratio (Fig. 3, I to K), indicating a shift of myelopoiesis output toward monocytic lineage dominance. These Ly6C^{hi} monocytes, CD11b⁺F4/80⁺ MΦs, and CD11c⁺MHCII⁺ DCs in PD-1^{-/-} tumor-bearing mice expressed interferon (IFN) regulatory factor 8 (IRF8), and all myeloid subsets had elevated expression of the retinoic acid receptor-related orphan receptor γ (RORC or ROR γ) (Fig. 3, L to N, and fig. S8). Similar results were observed in two additional tumor models, the MC38 colon adenocarcinoma and the MC17-51 fibrosarcoma model (fig. S9), both of which induced cancer-driven emergency myelopoiesis (fig. S3).

IRF8 regulates myeloid cell fate to monocyte/macrophage and DC differentiation versus granulocyte differentiation (22, 23), explaining the increase of CD11b⁺Ly6C⁺/CD11b⁺Ly6G⁺ ratio that we observed in tumor-bearing PD-1 KO mice. IRF8 is designated as one of the “terminal selectors” that control the induction and maintenance of the terminally differentiated state of these myeloid cells (22, 23). Moreover, IRF8 shifts the fate of myeloid cells away from immature MDSC, which are characterized by a restriction in IRF8 expression

(24, 25). Retinoid-related orphan nuclear receptors not only are required for myelopoiesis and are mediators of the inflammatory response of effector Ly6C^{hi} monocytes and macrophages (21, 26) but also can be expressed by MDSC (21). For these reasons, we examined the functional properties of CD11b⁺Ly6C⁺ cells in PD-1^{-/-} tumor-bearing mice. A key mechanism by which CD11b⁺Ly6C⁺ M-MDSCs mediate suppression of T cell responses involves the production of NO (27). We assessed the immunosuppressive function and found diminished NO production and diminished suppressor capacity of CD11b⁺Ly6C⁺ myeloid cells isolated from tumor-bearing PD-1^{-/-} mice compared with their counterparts isolated from tumor-bearing WT control mice (Fig. 3, O and P). Thus, PD-1 ablation switches the fate and function of myeloid cells away from immunosuppressive MDSC and promotes the generation of differentiated monocytes, MΦ, and DC. The expansion of CD11b⁺Ly6C^{hi} monocytes, the increase of the CD11b⁺Ly6C⁺/CD11b⁺Ly6G⁺ ratio, and the up-regulation of RORC in myeloid cells of the spleen of PD-1^{-/-} mice were already observed on day 9 after tumor inoculation, when tumors were not yet measurable, and on day 12, when tumors in WT and PD-1^{-/-} mice had comparable size (fig. S10). These results indicate that the effects of PD-1 ablation on the myeloid compartment of PD-1^{-/-} tumor-bearing mice preceded the differences in tumor growth.

To determine the potential therapeutic relevance of these findings, we examined whether changes in the myeloid compartment might be detected during treatment with PD-1-blocking antibody. Compared

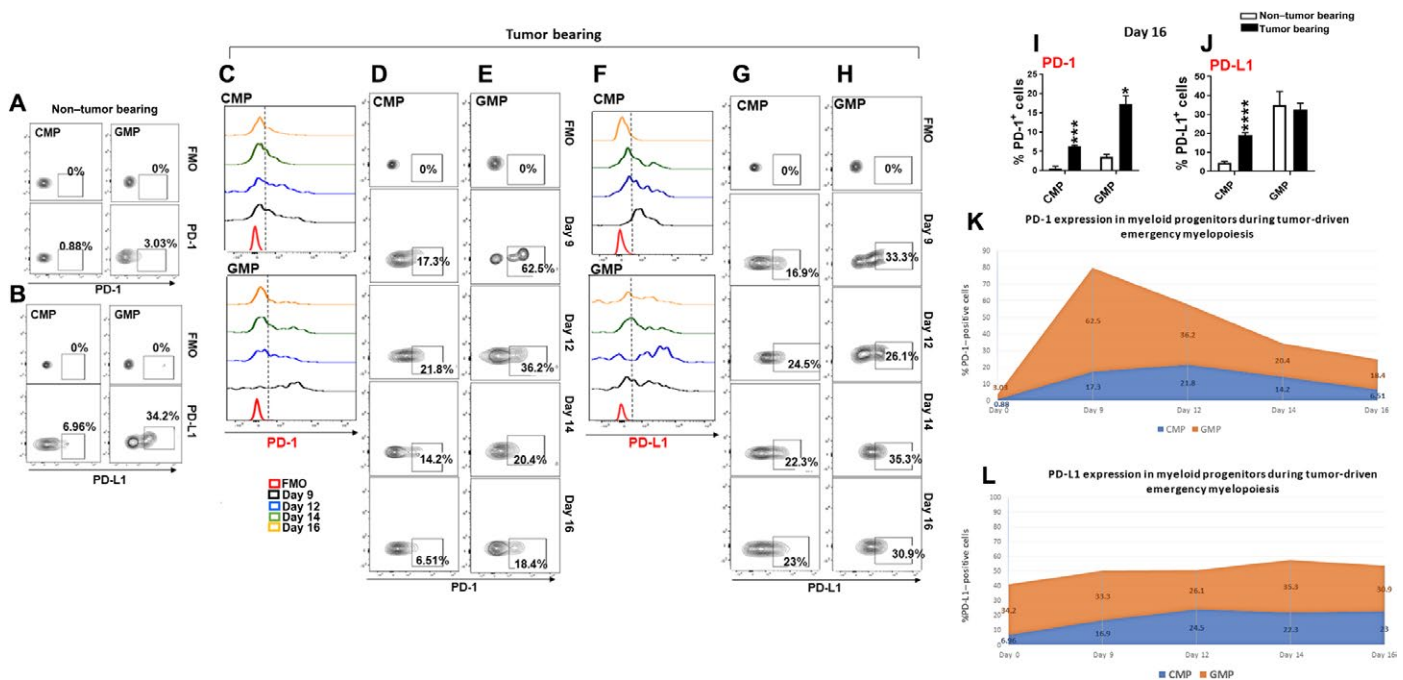


Fig. 2. PD-1 and PD-L1 are expressed on CMP and GMP myeloid progenitors during cancer-driven emergency myelopoiesis. (A and B) Expression of PD-1 and PD-L1 on CMPs and GMPs of non-tumor-bearing mice. (C to J) C57BL/6 mice were inoculated with B16-F10 mouse melanoma, and expression of PD-1 and PD-L1 on CMPs and GMPs was examined on days 9, 12, 14, and 16 after implantation. FACS histograms (C and F) and contour plots (D, E, G, and H) indicating the percentage of positive cells and bar graphs of mean \pm SEM positive cells (I and J) are shown. Results are representative of four independent experiments with six mice per group. (K and L) Kinetics of PD-1 (K) and PD-L1 (L) expression on CMPs (blue) and GMPs (orange) during tumor-driven emergency myelopoiesis. Results are representative of four separate experiments with six mice per group. * $P < 0.05$, ** $P < 0.005$, *** $P < 0.001$.

with the control treatment group, mice receiving anti-PD-1 antibody (fig. S11A) had diminished accumulation of GMP in the bone marrow (fig. S11B) and increased expansion of Ly6C⁺ monocytes and DC in the tumor site (fig. S11D), with effector features characterized by the expression of RORC, IRF8, and IFN- γ (fig. S11, E to G and I). In contrast, cells expressing interleukin-4 receptor α (IL-4Ra), a marker of MDSC (10, 28), were significantly decreased (fig. S11H). Thus, treatment with anti-PD-1-blocking antibody promotes the differentiation of myeloid cells with effector features while suppressing expansion of MDSC in tumor-bearing mice.

Myeloid-specific PD-1 ablation is the key driver of antitumor immunity

To determine whether these changes on myeloid cell fate in PD-1^{-/-} mice were mediated by myeloid cell-intrinsic effects of PD-1 ablation or by the effects of PD-1^{neg} T cells on myeloid cells, we generated mice with conditional targeting of *Pdcd1* gene (PD-1^{f/f}) (fig. S12A) and crossed them with mice expressing cre recombinase under the control of the lysozyme (LysM) promoter to induce selective ablation of the *Pdcd1* gene in myeloid cells (PD-1^{f/fLysMcre}) or with mice expressing cre recombinase under the control of the CD4 promoter to induce selective ablation of the *Pdcd1* gene in T cells (PD-1^{f/fCD4cre}) (fig. S12, B and C). In PD-1^{f/fLysMcre} mice, tumor growth was significantly diminished (Fig. 4, A and B), indicating that despite the preserved PD-1 expression in T cells, myeloid-specific PD-1 ablation in PD-1^{f/fLysMcre} mice was sufficient to inhibit tumor growth. Tumor-driven emergency myelopoiesis was selectively affected in PD-1^{f/fLysMcre} mice. Although myeloid-specific PD-1 ablation resulted in expansion

of CMPs, accumulation of GMPs was prevented (Fig. 4C). In contrast, no change on cancer-driven emergency myelopoiesis was detected in PD-1^{f/fCD4cre} mice, which had comparable expansion of CMP and GMP to PD-1^{f/f} control mice (Fig. 5A).

Myeloid-specific PD-1 ablation in PD-1^{f/fLysMcre} mice not only shifted the differentiation of CD11b⁺Ly6C⁺ and CD11b⁺Ly6G⁺ myeloid subsets and increased the CD11b⁺Ly6C⁺/CD11b⁺Ly6G⁺ ratio in the spleen and tumor site as in PD-1^{-/-} mice (Fig. 4, D to F) but also resulted in a notably different immunological profile of CD11b⁺Ly6C⁺ monocytic myeloid cells, consistent with effector myeloid function as indicated by the expression of effector myeloid cell markers including CD80, CD86, CD16/32 (Fc receptor II/III), and CD88 (C5aR) (Fig. 4G). Consistent with the improved function of myeloid cells, PD-1^{f/fLysMcre} mice also had higher levels of IFN- γ -expressing CD11b⁺Ly6C^{hi} monocytes and CD11b⁺F4/80⁺ MΦs (Fig. 4G and fig. S13, A and B) and increase of IRF8⁺ and RORC⁺ CD11b⁺Ly6C^{hi} monocytes (fig. S13, C and D). In contrast, cells expressing IL-4Ra, CD206, and ARG1—which are markers of MDSC, immunosuppressive neutrophils, and tolerogenic DCs (29–33)—were diminished (Fig. 4, H and I). Thus, myeloid-intrinsic PD-1 ablation skews the fate of myeloid cells away from immunosuppressive MDSCs; promotes the differentiation of functional effector monocytes, MΦs, and DCs; and has a decisive role in systemic antitumor immunity despite PD-1 expression in T cells.

We studied antitumor responses in mice with T cell-specific PD-1 ablation and found that PD-1^{f/fCD4cre} mice had diminished antitumor protection (Fig. 5, B and C). Consistent with the causative role of myeloid cell-specific PD-1 targeting in the differentiation and function

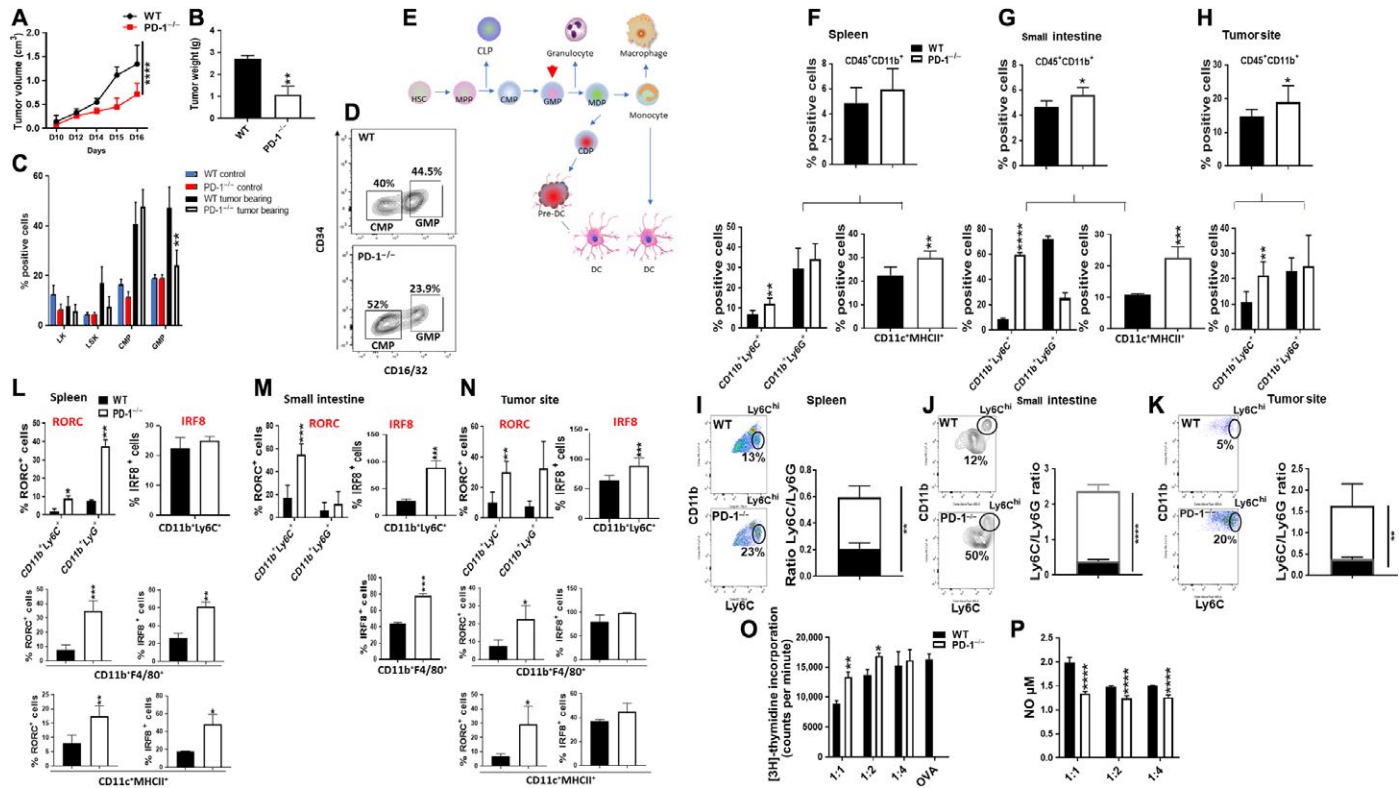


Fig. 3. PD-1 ablation alters emergency myelopoiesis and the profile of myeloid cell output. (A and B) WT and PD-1^{-/-} mice were inoculated with B16-F10 melanoma, and tumor size was monitored daily (A). Mice were euthanized on day 16, and tumor weight was measured (B). Data shown are means \pm SEM of six mice per group and are representative of six independent experiments. (C) Mean percentages \pm SEM of LSK (Lin^{neg} , $\text{Sca}1^{\text{pos}}$, $\text{CD127}^{\text{neg}}$, c-kit $^{\text{pos}}$) and LK (Lin^{neg} , $\text{Sca}1^{\text{neg}}$, $\text{CD127}^{\text{neg}}$, c-kit $^{\text{pos}}$) hematopoietic precursors, CMP, and GMP in the bone marrow of non-tumor-bearing and tumor-bearing WT and PD-1^{-/-} mice. GMPs in PD-1^{-/-} mice were significantly lower compared with GMPs in WT mice (**P < 0.01). (D) Representative contour plots of FACS analysis for CMP and GMP in the bone marrow of tumor-bearing WT and PD-1^{-/-} mice. (E) Schematic presentation of myeloid lineage differentiation. The arrowhead indicates GMP, the key target population of PD-1 during emergency myelopoiesis. HSC, hematopoietic stem cells; MPP, multi-potent progenitor; MDP, monocyte/macrophages and DC precursors; CDP, common dendritic cell progenitors; CLP, common lymphoid progenitors. (F to H) Mean percentages of CD45⁺CD11b⁺, CD11b⁺Ly6C⁺, CD11b⁺Ly6G⁺, and CD11c⁺MHCII⁺ in the spleen (F), small intestine (G), and B16-F10 site (H) of tumor-bearing WT and PD-1^{-/-} mice. (I to K) Representative plots of FACS analysis for CD11b⁺Ly6Ch and CD11b⁺Ly6C⁺/CD11b⁺Ly6G⁺ ratio in the spleen (I), small intestine (J), and B16-F10 site (K). (L to N) Mean percentages \pm SEM of RORC and IRF8 expressing CD11b⁺Ly6C⁺, CD11b⁺Ly6G⁺, CD11b⁺F4/80⁺, and CD11c⁺MHCII⁺ myeloid cells within the CD45⁺CD11b⁺ gate in the spleen (L), small intestine (M), and B16-F10 site (N). Data from one representative experiment of three independent experiments with six mice per group are shown. (O and P) Diminished suppressive activity (O) and NO production (P) of CD11b⁺Ly6C⁺ cells isolated from PD-1^{-/-} tumor-bearing mice. CD11b⁺Ly6C⁺ cells were isolated from tumor-bearing WT and PD-1^{-/-} mice and cultured at various ratios with OTI splenocytes stimulated with OVA_{257–264}. Data show means \pm SEM of one representative of two experiments (*P < 0.05, **P < 0.01, ***P < 0.001, and ****P < 0.0001).

of myeloid cells, T cell-specific PD-1 ablation did not induce expansion of CD11b⁺CD45⁺ leukocytes, CD11b⁺F4/80⁺ MΦs, and CD11c⁺MHCII⁺ DCs and increase of CD11b⁺Ly6C⁺/CD11b⁺Ly6G⁺ ratio (Fig. 5, D and E) or immunological features of functional effector myeloid cells (Fig. 5F) in PD-1^{f/f}CD4^{cre} tumor-bearing mice, compared with control tumor-bearing mice. Moreover, despite PD-1 ablation, tumor-bearing PD-1^{f/f}CD4^{cre} mice did not have quantitative differences in tumor-infiltrating T_{EM} cells compared with control tumor-bearing mice (Fig. 5G) or features of enhanced effector function as determined by assessment of cytokine-producing cells (Fig. 5, H to M).

Similar outcomes to those observed with B16-F10 tumor in the differentiation of myeloid cells toward myeloid effectors versus MDSC were obtained when PD-1^{f/f}LysM^{cre} and PD-1^{f/f}CD4^{cre} mice were inoculated with MC38 colon adenocarcinoma cells (Fig. 6, B to I). Moreover, PD-1^{f/f}LysM^{cre} but not PD-1^{f/f}CD4^{cre} mice inoculated with MC38 had functional differences in tumor-infiltrating T_{EM} and T central memory (T_{CM}) cells compared with control tumor-bearing

mice (Fig. 6, J to L). In the context of this highly immunogenic tumor, PD-1 ablation in myeloid cells resulted in complete tumor eradication, whereas mice with PD-1 ablation in T cells showed progressive tumor growth (Fig. 6A). Together, these results suggest that by preventing the differentiation of effector myeloid cells and promoting generation of MDSC, myeloid-specific PD-1 expression has a decisive role on T cell function. Thus, although PD-1 is an inhibitor of T cell responses (2, 34, 35), ablation of PD-1 signaling in myeloid cells is an indispensable requirement for induction of systemic antitumor immunity *in vivo*.

To further investigate the direct effects of PD-1 on myeloid cell fate in the absence of T cells, we used recombination activating gene 2 (RAG2) KO mice (lacking mature T cells and B cells). Treatment of RAG2 KO tumor-bearing mice with anti-PD-1-blocking antibody resulted in decreased accumulation of GMPs during tumor-driven emergency myelopoiesis (fig. S14A), myeloid cell expansion in the spleen and tumor site (fig. S14, B and C), and enhanced generation of effector myeloid cells (fig. S14, D to G), providing evidence that blockade of PD-1-mediated signals skews myeloid lineage fate to

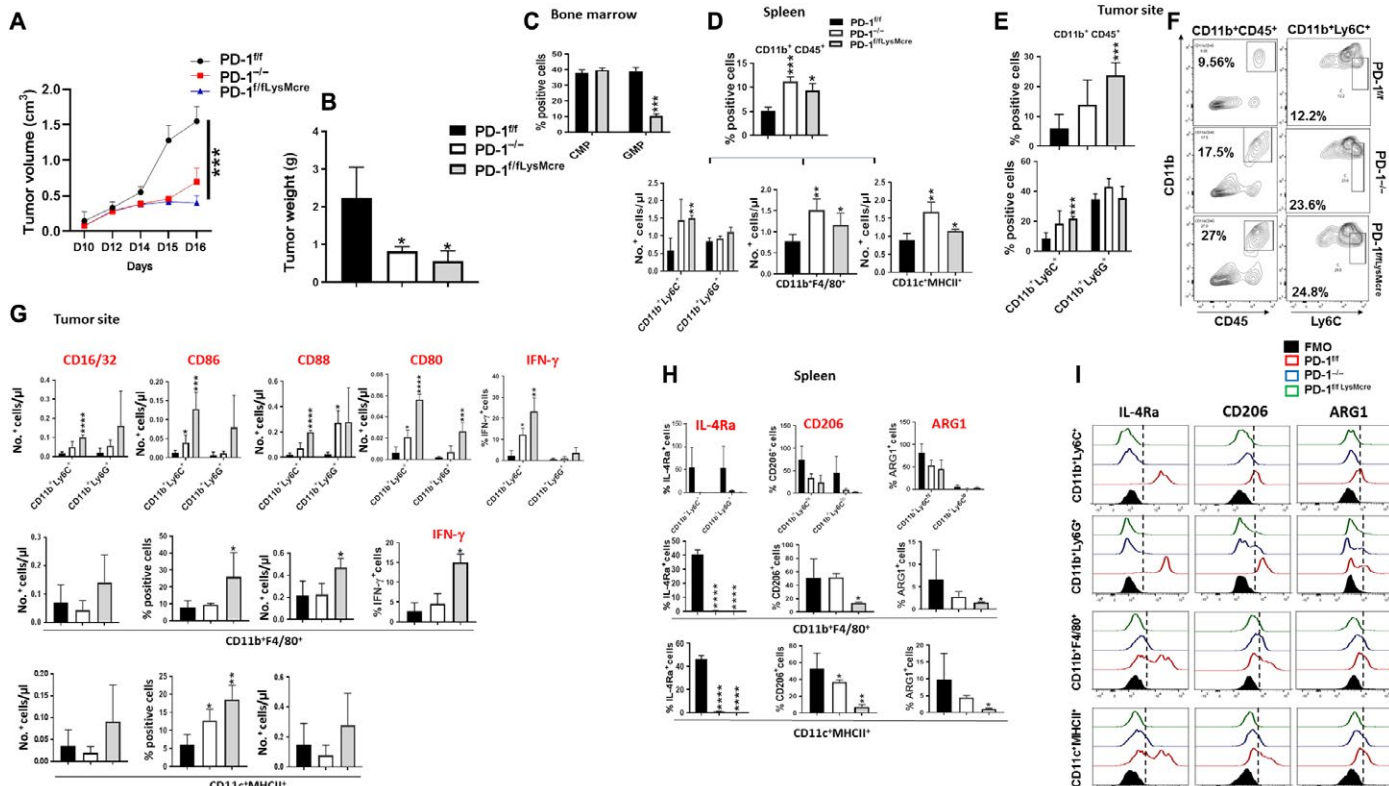


Fig. 4. Myeloid-specific PD-1 ablation is the driver of altered tumor-driven emergency myelopoiesis, inflammatory myeloid cell differentiation, and antitumor immunity. (A and B) PD-1^{f/f}, PD-1^{f/fLysMcre}, and PD-1^{-/-} mice were inoculated with B16-F10 melanoma, and tumor size was monitored daily (A). After mice were euthanized, tumor weight was measured (B). (C) Mean percentages \pm SEM of CMP and GMP in the bone marrow of tumor-bearing PD-1^{f/f} and PD-1^{f/fLysMcre} mice. (D) Mean percentages \pm SEM of CD11b⁺CD45⁺ cells and CD11b⁺Ly6C⁺, CD11b⁺Ly6G⁺, CD11b⁺F4/80⁺, and CD11c⁺MHCII⁺ myeloid subsets in the spleen of tumor-bearing mice. (E) Mean percentages \pm SEM of CD11b⁺CD45⁺, CD11b⁺Ly6C⁺, and CD11b⁺Ly6G⁺ cells and (F) representative contour plots of FACS analysis for CD11b⁺CD45⁺ and CD11b⁺Ly6C⁺ cells at the tumor site in PD-1^{f/f}, PD-1^{f/fLysMcre}, and PD-1^{-/-} mice. (G) Mean percentages \pm SEM of CD16/CD32⁺, CD86⁺, CD88⁺, and CD80⁺ cells and IFN- γ -expressing myeloid cell subsets within the CD45⁺CD11b⁺ gate in B16-F10 tumors from PD-1^{f/f}, PD-1^{f/fLysMcre}, and PD-1^{-/-} mice. (H) Mean percentages \pm SEM and (I) FACS histograms of IL-4Ra, CD206, and ARG1 expression in CD11b⁺Ly6C⁺, CD11b⁺Ly6G⁺, CD11b⁺F4/80⁺, and CD11c⁺MHCII⁺ myeloid cells within the CD11b⁺CD45⁺ gate in the spleen of tumor-bearing PD-1^{f/f}, PD-1^{f/fLysMcre}, and PD-1^{-/-} mice. Data are from one representative of three independent experiments with six mice per group are shown in all the panels (*P < 0.05, **P < 0.01, ***P < 0.005, and ****P < 0.001).

myeloid effector cells in a myeloid cell–intrinsic and T cell–independent manner. In RAG2 KO mice treated with anti–PD-1 antibody, despite the absence of T cells, a decrease of tumor growth was also observed (fig. S14, H and I), suggesting that ablation of PD-1 signaling promotes myeloid-specific mechanisms that induce tumor suppression, one of which might involve increased phagocytosis (8).

PD-1 ablation alters the signaling responses of myeloid cells to factors of emergency myelopoiesis

To understand mechanisms that might be responsible for the significant differences of myeloid cell fate commitment induced by myeloid-specific PD-1 targeting, we examined whether PD-1-deficient bone marrow myeloid progenitors might have distinct signaling responses to the key hematopoietic growth factors that mediate cancer-driven emergency myelopoiesis, which also induced PD-1 expression in GMP during *in vitro* culture. To avoid any potential impact of bone marrow-residing PD-1^{-/-} T cells or mature myeloid cells on the signaling responses of myeloid progenitors, we used Lin^{neg} bone marrow from PD-1^{f/fLysMcre} mice because LysMcre is expressed in CMPs and GMPs (36), allowing us to take advantage of the selective deletion of PD-1 in these myeloid progenitors. PD-1-deficient GMPs (fig. S15)

had enhanced activation of extracellular signal-regulated kinase 1/2 (Erk1/2), mammalian target of rapamycin complex 1 (mTORC1), and signal transducer and activator of transcription 1 (STAT1) in response to G-CSF, a main mediator of emergency myelopoiesis (37, 38). These results are notable because each of these signaling targets has a decisive role in the differentiation and maturation of myeloid cells while preventing the generation of immature immunosuppressive MDSC (39–42). These findings indicate that PD-1 might affect the differentiation of myeloid cells by regulating the fine tuning of signaling responses of myeloid progenitors to hematopoietic growth factors that induce myeloid cell differentiation and lineage fate determination during emergency myelopoiesis.

PD-1 ablation alters the metabolic program of myeloid progenitors and activates cholesterol synthesis

Metabolism has a decisive role in the fate of hematopoietic and myeloid precursors. Stemness and pluripotency are regulated by maintenance of glycolysis (43). Switch from glycolysis to mitochondrial metabolism and activation of oxidative phosphorylation and trichloroacetic acid (TCA) cycle are associated with differentiation (44). This is initiated by glycolysis-mediated mitochondrial biogenesis

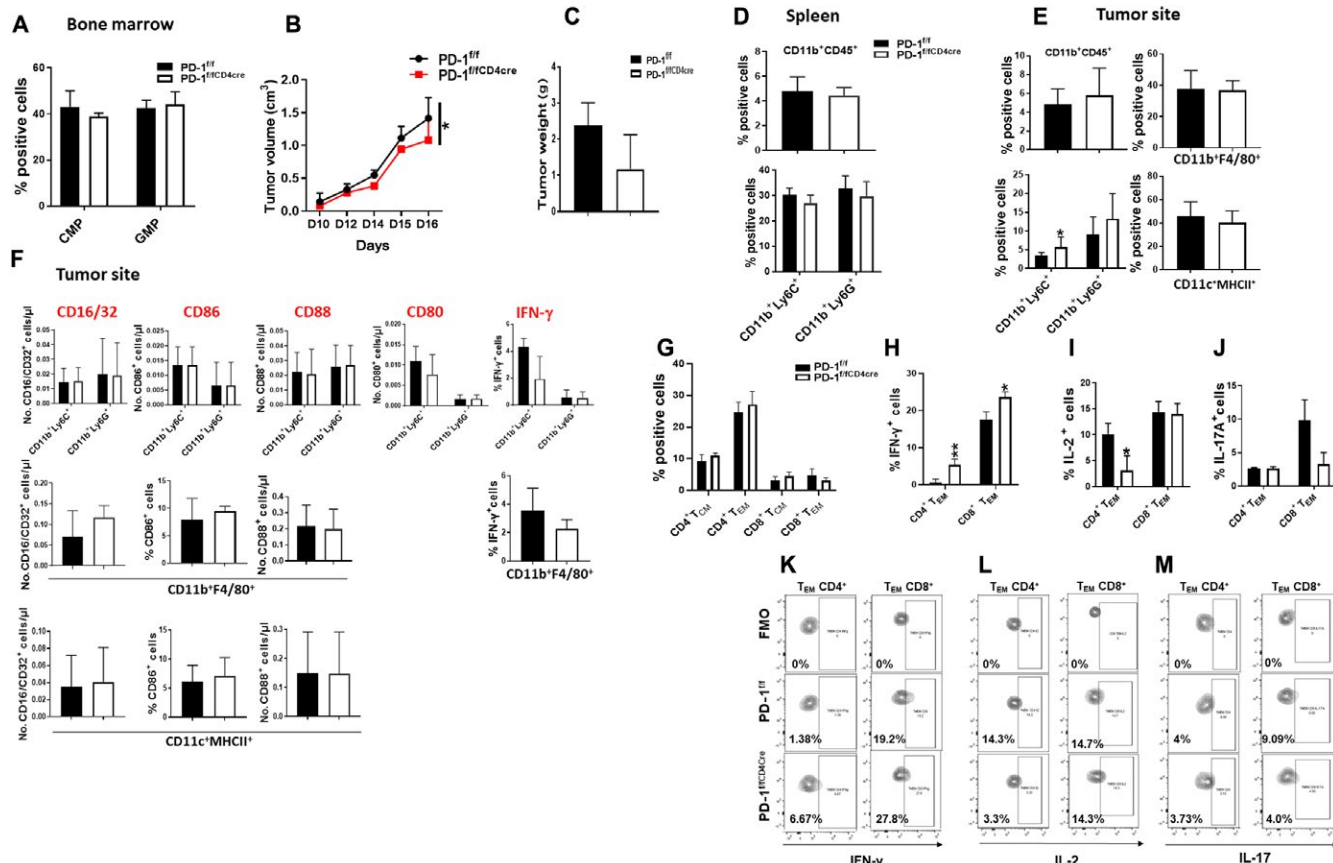


Fig. 5. T cell–specific PD-1 ablation has no impact on tumor-driven emergency myelopoiesis and the profile of myeloid cell output and provides minimal protection against tumor growth. PD-1^{f/f} and PD-1^{f/f}CD4cre mice were inoculated with B16-F10 melanoma. (A) On day 16, mice were euthanized, and bone marrow CMPs and GMPs were examined by flow cytometry. Mean percentages ± SEM of CMP or GMP are shown. (B) and (C) Tumor size was assessed every other day from inoculation (B). On the day of euthanasia, tumor weight was measured (C). (D) Mean percentages ± SEM of CD11b⁺CD45⁺ cells and CD11b⁺Ly6C⁺ and CD11b⁺Ly6G⁺ populations within the CD11⁺CD45⁺ gate in the spleen. (E) Mean percentages ± SEM of CD11b⁺CD45⁺ cells and CD11b⁺Ly6C⁺, CD11b⁺Ly6G⁺, CD11b⁺F4/80⁺, and CD11c⁺MHCII⁺ cells within the CD11b⁺CD45⁺ gate in the tumor site. (F) Mean percentages ± SEM of CD16/CD32⁺, CD86⁺, CD88⁺, CD80⁺, and IFN-γ expression in the indicated myeloid subsets (CD11b⁺Ly6C⁻, CD11b⁺Ly6G⁺, CD11b⁺F4/80⁺, and CD11c⁺MHCII⁺) within the CD11b⁺CD45⁺ gate in the tumor site. (G to J) Mean percentages ± SEM of CD4⁺ and CD8⁺ T_{CM} and T_{EM} (G), as well as IFN-γ, IL-2, and IL-17 (H to J) expression in CD4⁺ and CD8⁺ T_{EM} and T_{CM} at the tumor site, and respective contour plots (K to M). Results are from one representative of two independent experiments with six mice per group are shown (*P < 0.05 and **P < 0.01).

and epigenetic regulation of gene expression (43). The structural remodeling of the mitochondrial architecture during differentiation is characterized by increased replication of mitochondrial DNA to support production of TCA cycle enzymes and electron transport chain subunits, linking mitochondrial metabolism to differentiation (45).

We examined whether PD-1 ablation, which promoted the differentiation of myeloid cells in response to tumor-mediated emergency myelopoiesis, might affect the metabolic properties of myeloid precursors. Lin^{neg} bone marrow myeloid precursors were cultured with the cytokines G-CSF/GM-CSF/IL-6 that drive tumor-mediated emergency myelopoiesis in cocktail (Fig. 7, A and B) or individually (Fig. 7, C and D). Hematopoietic stem cell differentiation was documented by decrease of Lin^{neg}, which was more prominent in the cultures of PD-1-deficient bone marrow cells, and coincided with increase of CD45⁺CD11b⁺ cells (Fig. 7, A and B). Ly6C⁺ monocytic cells dominated in the PD-1^{f/f}LysMcre cultures, whereas Ly6G⁺ granulocytes were decreasing compared with PD-1^{f/f} control cultures (Fig. 7, C and D), providing evidence for a cell-intrinsic mechanism of PD-1-deficient myeloid precursors for monocytic lineage com-

mitment. Glucose uptake, but more prominently, mitochondrial biogenesis, was elevated in PD-1-deficient CMP and GMP (Fig. 7, E and F). Bioenergetics studies showed that PD-1-deficient cells developed robust mitochondrial activity (Fig. 7G) and increase of oxygen consumption rate (OCR)/extracellular acidification rate (ECAR) ratio during culture (Fig. 7H), indicating that mitochondrial metabolism progressively dominated over glycolysis. This bioenergetic profile is consistent with metabolism-driven enhanced differentiation of hematopoietic and myeloid precursors (45, 46).

We performed unbiased global metabolite analysis to determine whether PD-1-deficient myeloid precursors developed a distinct metabolic program. Compared with control, PD-1-deficient cells had elevated metabolic intermediates of glycolysis and pentose phosphate pathway (PPP), acetyl-coenzyme A (coA), and the TCA cycle metabolites citrate and α-ketoglutarate, but the most prominent difference was the elevated cholesterol (Fig. 7I, figs. S16 and S17, and table S1). Abundant cytosolic acetyl-coA can be used for fatty acid and cholesterol biosynthesis (fig. S17) (43). Moreover, mTORC1 activates de novo cholesterol synthesis via sterol regulatory element-binding

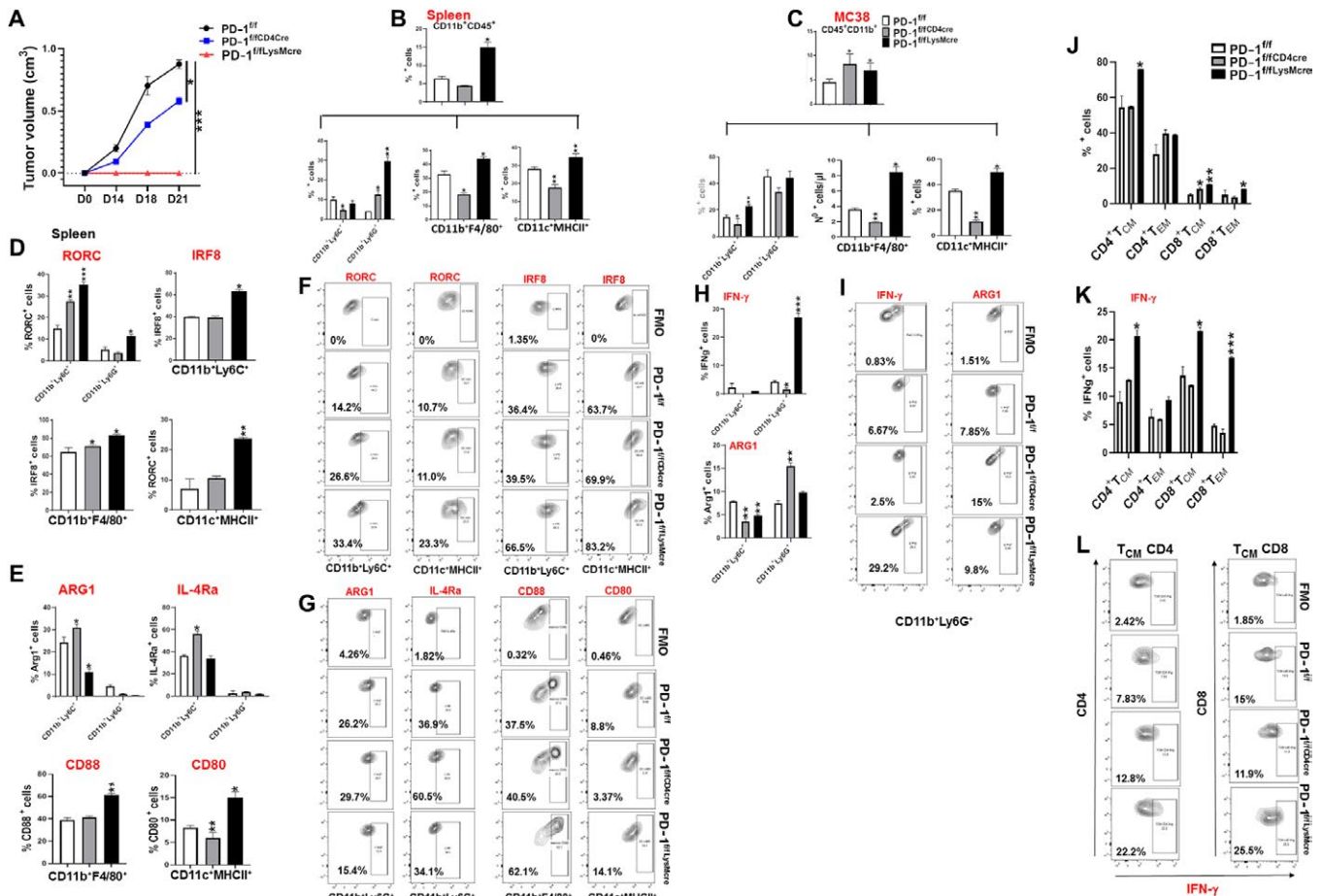


Fig. 6. T cell–specific PD-1 ablation provides diminished protection against tumor growth compared with myeloid-specific PD-1 ablation. (A) PD-1^{f/f}, PD-1^{f/f}CD4Cre, and PD-1^{f/f}LysMcre mice were inoculated with MC38 colon adenocarcinoma, and tumor size was monitored daily. Mice were euthanized on day 21, and mean percentages \pm SEM of CD45⁺CD11b⁺ cells and CD11b⁺Ly6C⁺, CD11b⁺Ly6G⁺, CD11b⁺F4/80⁺, and CD11c⁺MHCII⁺ myeloid subsets in the spleen (B) and tumor site (C) were determined. (D) Mean percentages \pm SEM of RORC- and IRF8-expressing CD11b⁺Ly6C⁺, CD11b⁺Ly6G⁺, CD11b⁺F4/80⁺, and CD11c⁺MHCII⁺ myeloid cells and (E) mean percentages \pm SEM of ARG1, IL-4Ra, CD88, and CD80 cells within the same myeloid subsets in the spleen. (F and G) Representative flow cytometry plots for RORC and IRF8 expression. (H) Mean percentages \pm SEM and (I) representative flow cytometry plots of IFN-γ- and ARG1-expressing CD11b⁺Ly6C⁺ and CD11b⁺Ly6G⁺ myeloid cells at the tumor site. (J) to (L) Mean percentages \pm SEM of CD4⁺ and CD8⁺ T_{CM} and T_{EM} cells (J) and IFN-γ-expressing CD4⁺ and CD8⁺ T_{EM} and T_{CM} at the tumor site (K) and respective contour plots (L). Data are from one representative of three experiments with six mice per group (*P < 0.05, **P < 0.01, and ***P < 0.001).

protein 1 (SREBP1), which regulates transcription of enzymes involved in cholesterol synthesis (47, 48). Because acetyl-coA was elevated (Fig. 7I and fig. S17) and mTORC1 activation was enhanced in PD-1-deficient myeloid progenitors in response to growth factors driving emergency myelopoiesis (fig. S15), we examined whether activation of the mevalonate pathway that induces cholesterol synthesis (fig. S18A) might be involved. In PD-1-deficient myeloid progenitors cultured with growth factors of emergency myelopoiesis, mRNA of genes regulating cholesterol synthesis and uptake was increased, mRNA of genes promoting cholesterol metabolism was decreased (Fig. 7J and fig. S18B), whereas cellular cholesterol and neutral lipid content was elevated (Fig. 7, K to M). PD-1-deficient DC not only differentiated in vitro in the presence of B16-F10 tumor supernatant but also had a significant increase of cholesterol and neutral lipids compared with similarly differentiated DC from control mice (Fig. 7N). Consistent with these in vitro findings, glucose uptake and content of cholesterol and neutral lipids were elevated in GMPs of tumor-bearing PD-1 KO mice compared with control

mice at days 7 or 9 after tumor inoculation, respectively, when tumors were not yet detectable or tumors in WT and PD-1 mice had equal size (fig. S19). Thus, features associated with metabolism-driven differentiation of myeloid progenitors are enhanced early in tumor-bearing PD-1 KO mice.

In addition to cholesterol synthesis, mevalonate also leads to the synthesis of isoprenoids, including geranylgeranyl pyrophosphate (GGPP) (fig. S17), which is required for protein geranylgeranylation catalyzed by geranylgeranyltransferase and has an active role in the up-regulation of RORC expression (49). Our metabolite analysis showed increased GGPP (Fig. 7I), providing a mechanistic explanation for the up-regulation of RORC in PD-1-deficient myeloid cells. Cholesterol accumulation is associated with skewing of hematopoiesis toward myeloid lineage and monocytosis, induces a proinflammatory program in monocytes/macrophages and DC, and amplifies TLR signaling (50–52). Together, these results unravel a previously unidentified role of PD-1 targeting in regulating myeloid lineage fate commitment and proinflammatory differentiation of monocytes,

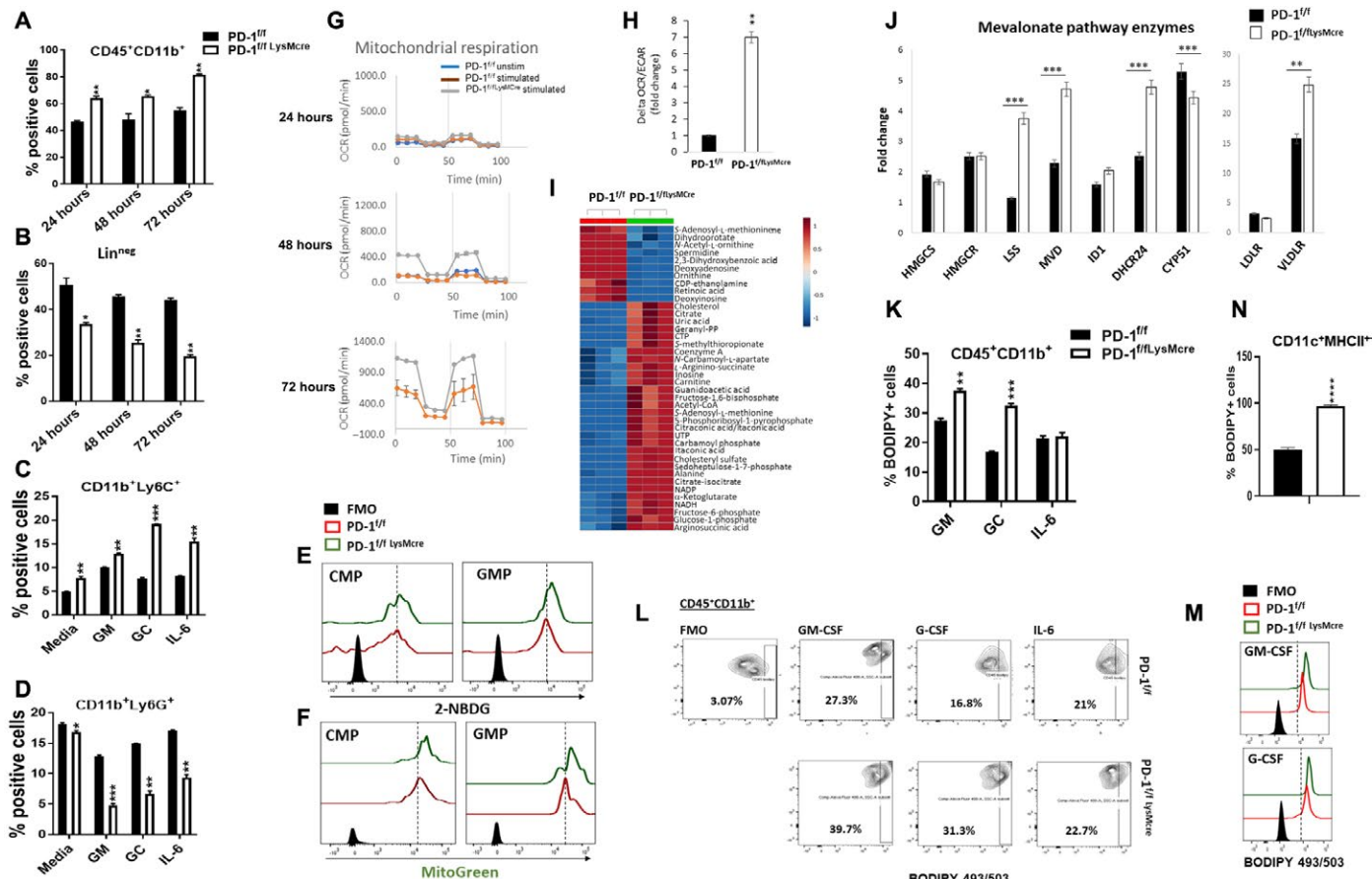


Fig. 7. Myeloid-specific PD-1 ablation reprograms myeloid cell signaling and metabolism and induces cholesterol synthesis. (A and B) Lin^{neg} bone marrow from PD-1^{f/f} and PD-1^{f/f}LysMcre mice was cultured with GM-CSF, G-CSF, and IL-6 for the indicated time intervals. Mean percentages ± SEM of CD11b⁺CD45⁺ (A) and Lin^{neg} cells (B) are shown. (C and D) Bone marrow cells purified as in (A) and (B) were cultured with the indicated growth factors, and mean percentages ± SEM of CD11b⁺Ly6C⁺ and CD11b⁺Ly6G⁺ cells were examined after 48 hours of culture. (E to H) Bone marrow cells were prepared and cultured as in (A) and (B), and at 48 hours of culture, glucose uptake was assessed using 2-[N-(7-Nitrobenz-2-oxa-1,3-diazol-4-yl)Amino]-2-Deoxyglucose (2-NBDG) (E), and mitochondrial biogenesis was assessed by MitoGreen staining and flow cytometry (F). (G) At 24, 48, and 72 hours of culture, OCR and ECAR were measured by a Seahorse extracellular flux analyzer, and mitostress responses at each time point of culture were examined. (H) OCR/ECAR ratio was measured at these time points, and the increase of OCR/ECAR ratio during stimulation was calculated. (I) Lin^{neg} bone marrow cells from PD-1^{f/f} and PD-1^{f/f}LysMcre mice were cultured with G-CSF and GM-CSF for 48 hours, and metabolite analysis was performed by mass spectrometry. The unsupervised hierarchical clustering heat map of the top 50 metabolites is shown. (J) At 24, 48, and 72 hours of culture with G-CSF and GM-CSF, mRNA was extracted and analyzed for the expression of the indicated genes by qPCR. Results of the 48-hour culture are shown and are presented as the fold increase over the mRNA level expressed by PD-1^{f/f} cells. Results are from one of three independent experiments. (K to M) At 24 hours of culture with GM-CSF, G-CSF, or IL-6, the content of neutral lipid droplets, including triglycerides and cholesterol esters, was assessed by flow cytometry using boron-dipyrromethene (BODIPY) 493/503. Mean percentages ± SEM (K) of BODIPY 493/503-positive cells within the CD11b⁺CD45⁺ gate, representative contour plots (L), and histograms of FACS analysis (M) are shown. (N) PD-1^{f/f} and PD-1^{f/f}LysMcre DC were differentiated in the presence of B16-F10 tumor supernatant, and the content of neutral lipids was assessed. Mean percentage ± SEM of BODIPY 493/503-positive DC within the CD45⁺CD11b⁺ gate is shown. Results are representative of three experiments. *P < 0.05, **P < 0.01, and ***P < 0.005.

macrophages, and DC during tumor-driven emergency myelopoiesis, through metabolic reprogramming.

Myeloid-specific PD-1 ablation induces improved T cell functionality

Previously, it was determined that monocyte/macrophage terminal differentiation is controlled by the combined actions of retinoid receptors and the nuclear receptor peroxisome proliferator-activated receptor γ (PPAR γ), which is regulated by cholesterol and promotes gene expression and lipid metabolic processes, leading to terminal macrophage differentiation (26, 53). Because our in vitro studies showed that PD-1-deficient myeloid progenitors developed a distinct

metabolic program with elevated cholesterol metabolism, we examined whether PD-1 ablation might alter the expression of PPAR γ in addition to RORC. We found that the expression of PPAR γ was elevated in CD11b⁺Ly6C⁺ monocytic cells and M Φ isolated from tumors of PD-1^{-/-} and PD-1^{f/f}LysMcre mice (Fig. 8, A to C). Because PD-1-deficient myeloid progenitors developed robust mitochondrial activity during culture in vitro (Fig. 7, G and H) and PPAR γ is involved in mitochondrial function (53), we examined whether myeloid cells in tumor-bearing mice have improved mitochondrial metabolism, a feature that has an important role in supporting antitumor function of other immune cells (54). Monocytes, M Φ , and DC isolated from tumor of PD-1^{-/-}, and PD-1^{f/f}LysMcre mice had increased mitochondrial

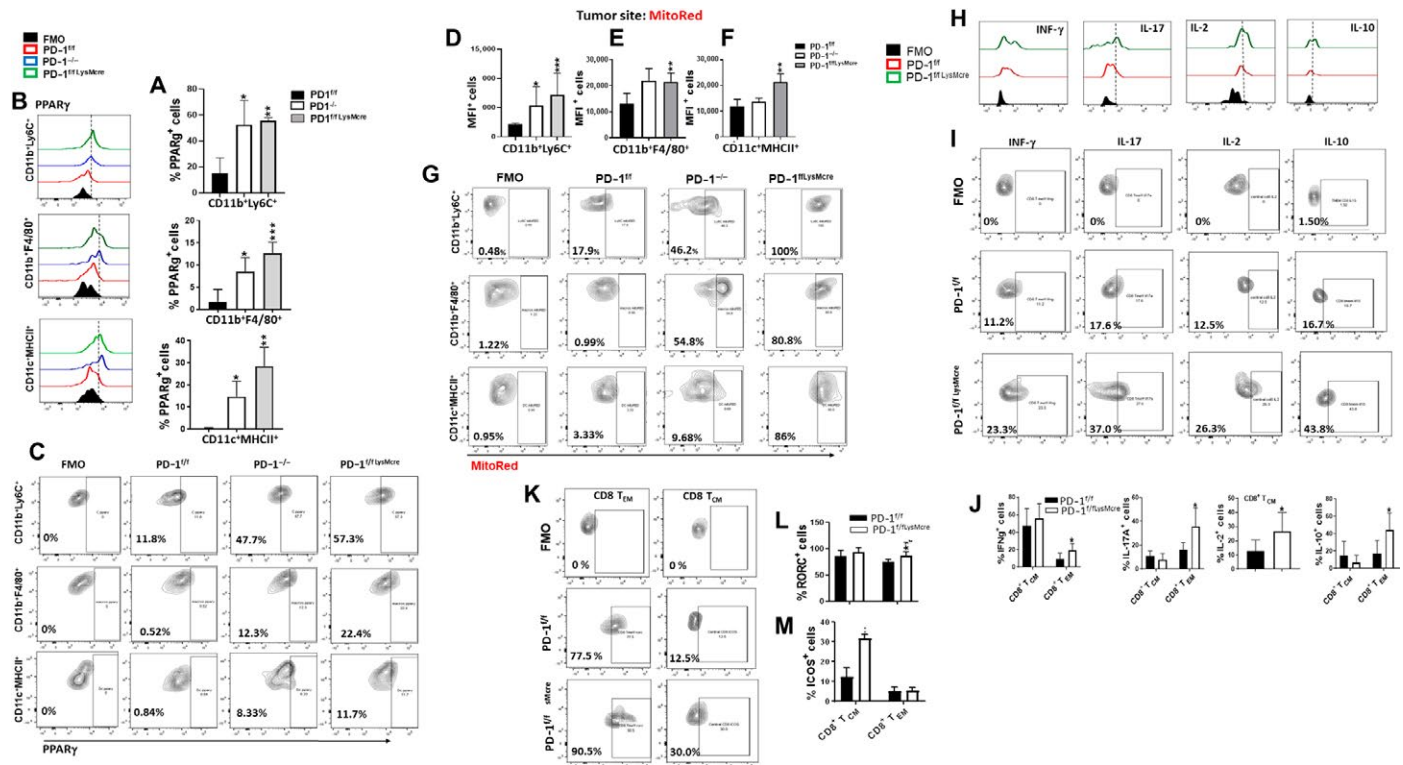


Fig. 8. PD-1 ablation induces enhanced mitochondrial metabolism of myeloid cells in tumor-bearing mice and improved T cell function. (A to C) Expression of PPAR γ in myeloid cells at the B16-F10 site in PD-1 ff , PD-1 ffLysMcre , and PD-1 $^{-/-}$ mice was examined by flow cytometry. Mean percentages \pm SEM (A), representative histograms (B), and contour plots (C) of PPAR γ -expressing CD11b+Ly6C $^+$, CD11b+F4/80 $^+$, and CD11c+MHCII $^+$ subsets. (D to G) Mitochondrial metabolic activity of myeloid cells at the B16-F10 tumor site in PD-1 ff , PD-1 ffLysMcre , and PD-1 $^{-/-}$ mice was examined by assessing mitochondrial membrane potential using MitoRed. Mean fluorescence intensity (MFI) \pm SEM of MitoRed-positive CD11b+Ly6C $^+$, CD11b+F4/80 $^+$, and CD11c+MHCII $^+$ subsets within the CD45 $^+$ CD11b $^+$ gate (D to F) and representative plots of FACS analysis (G) are shown. (H to L) In parallel, expression of IFN- γ , IL-17A, IL-2, IL-10, RORC, and ICOS in CD8 $^+$ T_{CM} and T_{EM} isolated from B16-F10-bearing PD-1 ff and PD-1 ffLysMcre mice was assessed by flow cytometry. Representative histograms (H), contour plots (I and K), and mean percentages \pm SEM (J, L, and M) within the CD44 hi CD62L hi gate (for T_{CM}) and CD44 hi CD62L lo gate (for T_{EM}) are shown. Data are from one representative of four independent experiments (*P < 0.05, **P < 0.01, and ***P < 0.005).

membrane potential compared with myeloid cells from control tumor-bearing mice, consistent with enhanced mitochondrial metabolism (Fig. 8, D to G).

We investigated whether these significant immunometabolic changes of myeloid cells, induced by myeloid-specific PD-1 targeting, affected immunological properties of T cells that have key roles in their antitumor function. Compared with control PD-1 ff tumor-bearing mice, PD-1 ffLysMcre tumor-bearing mice had no quantitative differences in CD4 $^+$ or CD8 $^+$ T_{EM} and T_{CM} cells (fig. S20A) but had significant functional differences. There was an increase of IFN- γ -, IL-17-, and IL-10-producing CD8 $^+$ T_{EM} cells and IL-2-producing CD8 $^+$ T_{CM} cells (Fig. 8, H to J). Inducible T cell costimulator (ICOS) and lymphocyte-activation gene 3 (Lag3) were elevated in T cells from PD-1 ffLysMcre tumor-bearing mice but cytotoxic T-lymphocyte-associated protein 4 (CTLA4), T cell immunoglobulin and mucin domain 3 (Tim3), CD160, and PD-1/PD-L1 were comparable in T cells from PD-1 ff and PD-1 ffLysMcre tumor-bearing mice (Fig. 8, K to M, and fig. S20B). These findings are significant because IL-17-producing T helper cell 17 (T_H17)/T cytotoxic cell 17 (Tc17) cells have enhanced antitumor function and mediate durable tumor growth inhibition (55). Moreover, T cells with a “hybrid” phenotype producing

both IFN- γ and IL-17 might have superior antitumor properties by combining the enhanced effector function of T_H1/Tc1 and the longevity and stemness of T_H17/Tc17 cells (56). In our studies, these properties of T_{EM} cells correlated with improved antitumor function in PD-1 ffLysMcre mice.

To examine experimentally whether PD-1-deficient myeloid cells differentiated in tumor-bearing mice in vivo have improved capacity of inducing antigen-specific T cell responses, we assessed responses of the same primary CD4 $^+$ or CD8 $^+$ T cells to antigen-loaded DCs isolated from PD-1 $^{-/-}$ or control mice bearing B16-F10 tumors (fig. S21A). DCs isolated from the spleen of tumor-bearing WT and PD-1 $^{-/-}$ mice were pulsed with ovalbumin (OVA) and cocultured with OVA-specific CD4 $^+$ or CD8 $^+$ T cells from OTI or OTII T cell receptor (TCR)-transgenic mice. DCs from tumor-bearing PD-1 $^{-/-}$ mice had superior ability to induce OTI and OTII T cell proliferation and IFN- γ expression (fig. S21, B and C). Together, our data provide evidence that myeloid cell-intrinsic PD-1 ablation induces potent antitumor immunity by decreasing accumulation of MDSC and promoting proinflammatory and effector monocytic/macrophage and DC differentiation, thereby leading to enhanced effector T cell responses.

DISCUSSION

Our present studies reveal a previously unidentified role of the PD-1 pathway in regulating lineage fate commitment and function of myeloid cells that arise from tumor-driven emergency myelopoiesis. These outcomes are mediated by myeloid-intrinsic effects of PD-1 ablation, leading to altered signaling and metabolic reprogramming of myeloid progenitors characterized by enhanced differentiation and elevated cholesterol synthesis. Consequently, the accumulation of immature immunosuppressive and tumor-promoting MDSC is diminished, and the output of differentiated, inflammatory effector monocytes, MΦ, and DC is enhanced. These immunometabolic changes of myeloid cells promote the differentiation of T_{EM} cells and systemic antitumor immunity *in vivo* despite preserved PD-1 expression in T cells.

We found that PD-1-deficient myeloid progenitors had enhanced activation of Erk1/2 and mTORC1 in response to G-CSF. These results indicate that Erk1/2 and mTORC1, a downstream mediator of phosphatidylinositol 3-kinase (PI3K)/Akt signaling, which are major targets of PD-1 in T cells (2), are subjected to PD-1-mediated inhibition in myeloid cells. These results are revealing because Erk1/2 phosphorylation subverts MDSC-mediated suppression by inducing M-MDSCs differentiation to APC (39). Erk and PI3K regulate glycolysis in response to G-CSF (57). PI3K/Akt/mTORC1 signaling is critical in myeloid lineage commitment. Expression of constitutively active Akt in CD34⁺ cells induces enhanced monocyte and neutrophil development, whereas a dominant negative Akt has the opposite effect (58). mTORC1 is necessary for the transition of hematopoietic cells from a quiescent state to a prepared “alert” state in response to injury-induced systemic signals (59), for G-CSF-mediated differentiation of myeloid progenitors (40), and for M-CSF-mediated monocyte/macrophage generation (41). mTORC1 stimulates translation initiation through phosphorylation of 4E (eIF4E)-binding protein 1 (4E-BP1) and ribosomal S6 kinases and has a decisive role in the expression of glucose transporters and enzymes of glycolysis and PPP (47). Consistent with these, our studies showed that PD-1-deficient myeloid progenitors had elevated expression of glycolysis and PPP intermediates after culture with emergency cytokines *in vitro* and enhanced monocytic differentiation in tumor-bearing mice *in vivo*. Together, our findings indicate that PD-1 might affect the differentiation of myeloid cells by regulating the fine tuning of signaling responses of myeloid progenitors to hematopoietic growth factors that induce myeloid cell differentiation and lineage fate determination during emergency myelopoiesis. Further studies will identify how receptor-proximal signaling events mediated by hematopoietic growth factors are targeted by PD-1 in a manner comparable to PD-1-mediated targeting of signaling pathways in T cells (2, 34, 35).

Our metabolite analysis showed that a notable difference of PD-1-deficient myeloid progenitors was the increased expression of mevalonate metabolism enzymes and the elevated cholesterol. mTORC1 activates SREBP1, which induces transcription of enzymes involved in fatty acid and cholesterol synthesis (48), thereby leading to glycolysis-regulated activation of the mevalonate pathway. Our signaling studies showing enhanced mTORC1 activation and our metabolic studies showing enhanced mitochondrial metabolism and increased cholesterol content in PD-1-deficient myeloid cells provide a mechanistic link between the altered differentiation of PD-1-deficient myeloid progenitors and the altered immunophenotypic and functional program of PD-1-deficient monocytes, MΦ, and DC in tumor-bearing mice. Cholesterol drives myeloid cell expansion

and differentiation of macrophages and DC (50, 51, 60) and promotes antigen-presenting function (61). These properties are consistent with the metabolic profile and the increased cholesterol of PD-1-deficient myeloid progenitors; the inflammatory and effector features of differentiated monocytes, MΦ, and DC; and the enhanced T effector cell activation in tumor-bearing mice with myeloid-specific PD-1 ablation that we identified in our studies. By such mechanism, PD-1 might centrally regulate antitumor immunity, independently of the expression of PD-1 and its ligands in the TME. Our studies showed that PD-1 expression on myeloid progenitors is an early event during tumor-mediated emergency myelopoiesis and indicate that PD-1 blockade at early stages of cancer might have a decisive effect on antitumor immunity by preventing MDSC generation from myeloid progenitors and inducing the systemic output of effector myeloid cells that drive antitumor T cell responses.

In addition to its expression in myeloid progenitors, in the bone marrow, we found that PD-1 is expressed in all myeloid subsets including M-MDSC, PMN-MDSC, CD11b⁺F4/80⁺ MΦ, and CD11c⁺MHCII⁺ DC in the tumor and the spleen of tumor-bearing mice, albeit at different levels. This difference might be related to gradient of tumor-derived factors responsible for PD-1 induction such as G-CSF and GM-CSF that we found to induce PD-1 transcription in myeloid progenitors. This possibility would be consistent with the gradual up-regulation of PD-1 expression in splenic myeloid cells, determined by our kinetics studies, which correlates with tumor growth that might be responsible for the increase of systemic levels of tumor-derived soluble factors that induce PD-1. Other cues of the TME known to mediate the activation step of MDSC (14) might also be responsible for the induction of higher PD-1 expression level in the tumor versus the splenic myeloid cells. Our findings unravel a previously unidentified role of PD-1 in myeloid cell fate commitment during emergency myelopoiesis, a process that is involved not only in antitumor immunity but also in the control of pathogen-induced innate immune responses and sterile inflammation (62).

An additional important finding of our studies is that the nuclear receptors RORC and PPAR γ are up-regulated in myeloid cells by PD-1 ablation. RORs were initially considered retinoic acid receptors but were subsequently identified as sterol ligands. RORC not only is induced by sterols and isoprenoid intermediates (49) but also serves as the high-affinity receptor of the cholesterol precursor desmosterol (63, 64), a metabolic intermediate of cholesterol synthesis via the mevalonate pathway that regulates inflammatory responses of myeloid cells (52, 60). Desmosterol and its sterol sulfates function as endogenous RORC agonists and induce expression of RORC target genes (63, 64). Our studies showed that, in addition to cholesterol, the mevalonate metabolism product GGPP that has an active role in the up-regulation of RORC expression (49) was elevated in PD-1-deficient myeloid cells, providing a mechanistic basis for our finding of the elevated RORC expression. Retinoid receptors and PPAR γ together regulate monocyte/macrophage terminal differentiation (26). Although initially thought to be involved in proinflammatory macrophage differentiation, it was subsequently understood that PPAR γ predominantly promotes macrophage-mediated resolution of inflammation by inducing expression of the nuclear receptor liver X receptor and the scavenger receptor CD36, thereby regulating tissue remodeling (65). PPAR γ also regulates macrophage-mediated tissue remodeling by efferocytosis and production of proresolving cytokines (66), which can suppress cancer growth (67). The combined actions of RORC and PPAR γ induced by myeloid-specific PD-1 ablation

might be involved in the antitumor function by promoting both proinflammatory and tissue remodeling properties of myeloid cells. Future studies will dissect the specific role of each of these nuclear receptors on the antitumor immunity induced by myeloid cell–specific ablation of PD-1.

In conclusion, our results provide multiple levels of evidence that myeloid-specific PD-1 targeting mediates myeloid cell–intrinsic effects, which have a decisive role on systemic antitumor responses. This might be a key mechanism by which PD-1 blockade induces antitumor function. Recapitulating this immunometabolic program of myeloid cells will improve the outcome of cancer immunotherapy.

MATERIALS AND METHODS

Animals

All procedures were in accordance with the National Institutes of Health Guidelines for the Care and Use of Animals and approved by the Institutional Animal Care and Use Committee at Beth Israel Deaconess Medical Center (Boston, MA). C57BL/6 WT mice were purchased from Charles River Laboratories (Franklin, MA). PD-1^{−/−} mice were provided by T. Honjo (Kyoto University, Japan). PD-1^{−/−} mice (B6.Cg-Pdcd1^{tm1.1Shr}/J) were also purchased from the Jackson laboratory (Bar Harbor, ME). All the studies requiring the use of PD-1^{−/−} mice were performed with both PD-1-deficient strains and resulted in similar outcomes. *Pdcd1*^{fl/fl} (PD-1^{fl/fl}) mice on a C57BL/6 background were generated by Ozone (Australia) using goGermline technology. Briefly, a targeting vector was prepared containing LoxP sites in introns 1 and 3, closely flanking exons 2 and 3, respectively, of the *Pdcd1* (fig. S12A). The genomic 5' and 3' arms of homology and the floxed genomic region were generated by PCR amplification of C57BL/6 genomic DNA. An FRT-PGK-Neo^R-Frt selection cassette was placed immediately 5' of the LoxP site in intron 3. Homologous recombination of the targeting vector was carried out by electroporation of embryonic stem (ES) cells, and clones were selected for neomycin resistance. Correctly targeted ES clones were identified by Southern blot restriction fragment length polymorphism (RFLP) analysis and microinjected into goGermline blastocysts to generate germline chimeras. After germline transmission, the FRT-PGK-Neo^R-FRT cassette was deleted by mating to a transgenic line containing FLP recombinase. The *Flo* gene was removed by segregation in subsequent crosses. PD-1^{fl/fl} mice were mated with LysMcre mice [B6.129P2[−] *Lyz2*^{tm1(cre)If0}/J] or CD4cre mice [B6.Cg-Tg(Cd4-cre)1Cwi/Bflu], obtained from the Jackson laboratory. Selective ablation of PD-1 protein expression in T cells versus myeloid cells in each strain was confirmed by flow cytometry (fig. S12, B and C). Rag2-deficient mice [B6(Cg)-Rag2^{tm1.1Cgn}/J], OTI TCR transgenic mice [C57BL/6[−] Tg(TcrαTcrβ)1100Mjb/J], and OTII TCR transgenic mice [B6.Cg-Tg(TcrαTcrβ)425Cbn/J] were purchased from the Jackson laboratory (Bar Harbor, ME).

Tumor cell lines and tumor experiments

MC17-51 and B16-F10 cell lines were purchased from the American Type Culture Collection. The B16-F10 cell line was subcloned, and subclones with intermediate growth rate were selected for use. The MC38 cell line was purchased from Kerafast. For tumor implantation, 10⁵ murine fibrosarcoma (MC17-51) were injected intramuscularly in the left hindlimb, whereas 2.5 × 10⁵ murine colon carcinoma (MC38) or 5 × 10⁵ murine melanoma (B16-F10) cells were injected subcutaneously in the left flank. Tumor growth was monitored daily

with a caliper fitted with a vernier scale, starting from day 9. Tumor volume was calculated on the basis of three perpendicular measurements. At days 15 to 16 for B16-F10 tumors, at days 12 to 14 for MC17-51 tumors, and at days 15 to 21 for MC38 after tumor inoculation, mice were euthanized, and tumor, spleen, small intestine, and bone marrow were harvested. Eight- to 12-week-old male mice were used for MC17-51 inoculations, and 8- to 12-week-old male or female mice were used for MC38 and B16-F10 inoculations. For studies at various time points after tumor implantation, a large cohort of mice of each strain was used for simultaneous tumor inoculation, and at the indicated times, equal numbers of mice were euthanized and assessment of the indicated end points was performed. For treatment with anti-PD-1-blocking antibody, 250 µg of either anti-PD-1 (clone RMP1-14, Bio X Cell) or immunoglobulin G2a control (clone 2A3, Bio X Cell) diluted in sterile phosphate-buffered saline were administered intraperitoneally in a volume of 100 µl per dose on days 9, 12, and 15 after tumor inoculation.

Statistics

Statistical significance for comparison between two groups was determined by two-tailed Student's *t* test or Mann-Whitney *U* test. Statistical significance for comparison among three or more groups was determined by analysis of variance (ANOVA). **P* < 0.05, ***P* < 0.01, ****P* < 0.005, and *****P* < 0.0001.

SUPPLEMENTARY MATERIALS

immunology.science.org/cgi/content/full/5/43/eaay1863/DC1

Materials and Methods

- Fig. S1. Gating strategy of hematopoietic and myeloid precursors in the bone marrow.
- Fig. S2. Gating strategy of myeloid subsets in the spleen and tumor site.
- Fig. S3. Cancer-induced emergency myelopoiesis in three different mouse tumor models.
- Fig. S4. PD-1 expression is induced on myeloid progenitors by emergency cytokines.
- Fig. S5. Gating strategy for identification of MDSC in human blood samples.
- Fig. S6. PD-1 expression in human MDSC.
- Fig. S7. PD-1 ablation alters tumor-driven emergency myelopoiesis.
- Fig. S8. PD-1 ablation induces expression of RORC and IRF8 in myeloid cells expanding in response to tumor-driven emergency myelopoiesis.
- Fig. S9. PD-1 ablation induces expression of RORC and IRF8 in myeloid cells expanding in mice-bearing MC38 or MC17-51 tumors.
- Fig. S10. PD-1 ablation increases the output of RORC^{hi} effector-like myeloid cells at early stages of tumor growth.
- Fig. S11. Therapeutic targeting of PD-1 increases effector features of myeloid cells and decreases tumor growth.
- Fig. S12. Myeloid-specific and T cell–specific PD-1 deletion.
- Fig. S13. Myeloid-specific PD-1 ablation promotes expansion of IRF8^{hi} and RORC^{hi} monocytes and IFN-γ-producing monocytes and macrophages in the tumor site.
- Fig. S14. Tumor-induced emergency myelopoiesis and myeloid effector differentiation in Rag2-deficient mice treated with PD-1 antibody.
- Fig. S15. PD-1 ablation reduces the threshold of growth factor-mediated signaling in GMP.
- Fig. S16. Myeloid-specific PD-1 ablation induces a distinct metabolic profile characterized by elevated cholesterol.
- Fig. S17. Metabolic pathways linking glycolysis to PPP, fatty acid, and cholesterol synthesis.
- Fig. S18. Schematic presentation of the mevalonate pathway.
- Fig. S19. Increase of glucose uptake and neutral lipid content in PD-1-deficient myeloid progenitors early after tumor implantation.
- Fig. S20. Myeloid-specific PD-1 deletion alters the immunological profile of CD8⁺ T_{EM} cells.
- Fig. S21. PD-1 ablation enhances antigen presentation *ex vivo* by tumor-matured DC.
- Table S1. List of significantly different metabolites.
- Table S2. List of antibodies used for surface staining.
- Table S3. List of antibodies used for intracellular staining.
- Table S4. List of antibodies used for phenotype of human MDSC.
- Table S5. Raw data in Excel spreadsheet.
- References (68–71)

[View/request a protocol for this paper from Bio-protocol.](#)

REFERENCES AND NOTES

- T. Okazaki, S. Chikuma, Y. Iwai, S. Fagarasan, T. Honjo, A rheostat for immune responses: The unique properties of PD-1 and their advantages for clinical application. *Nat. Immunol.* **14**, 1212–1218 (2013).
- V. A. Boussiotis, Molecular and biochemical aspects of the PD-1 checkpoint pathway. *N. Engl. J. Med.* **375**, 1767–1778 (2016).
- N. A. Rizvi, M. D. Hellmann, A. Snyder, P. Kvistborg, V. Makarov, J. J. Havel, W. Lee, J. Yuan, P. Wong, T. S. Ho, M. L. Miller, N. Rekhtman, A. L. Moreira, F. Ibrahim, C. Bruggeman, B. Gasmi, R. Zappasodi, Y. Maeda, C. Sander, E. B. Garon, T. Merghoub, J. D. Wolchok, T. N. Schumacher, T. A. Chan, Cancer immunology. Mutational landscape determines sensitivity to PD-1 blockade in non-small cell lung cancer. *Science* **348**, 124–128 (2015).
- W. Chen, J. Wang, L. Jia, J. Liu, Y. Tian, Attenuation of the programmed cell death-1 pathway increases the M1 polarization of macrophages induced by zymosan. *Cell Death Dis.* **7**, e2115 (2016).
- X. Huang, F. Venet, Y. L. Wang, A. Lepape, Z. Yuan, Y. Chen, R. Swan, H. Kherouf, G. Monneret, C. S. Chung, A. Ayala, PD-1 expression by macrophages plays a pathologic role in altering microbial clearance and the innate inflammatory response to sepsis. *Proc. Natl. Acad. Sci. U.S.A.* **106**, 6303–6308 (2009).
- L. Shen, Y. Gao, Y. Liu, B. Zhang, Q. Liu, J. Wu, L. Fan, Q. Ou, W. Zhang, L. Shao, PD-1/PD-L pathway inhibits M.tb-specific CD4⁺ T-cell functions and phagocytosis of macrophages in active tuberculosis. *Sci. Rep.* **6**, 38362 (2016).
- M. Qorraj, H. Bruns, M. Böttcher, L. Weigand, D. Saul, A. Mackensen, R. Jitschin, D. Mougiakakos, The PD-1/PD-L1 axis contributes to immune metabolic dysfunctions of monocytes in chronic lymphocytic leukemia. *Leukemia* **31**, 470–478 (2017).
- S. R. Gordon, R. L. Maute, B. W. Dulken, G. Hutter, B. M. George, M. N. McCracken, R. Gupta, J. M. Tsai, R. Sinha, D. Corey, A. M. Ring, A. J. Connolly, I. L. Weissman, PD-1 expression by tumour-associated macrophages inhibits phagocytosis and tumor immunity. *Nature* **545**, 495–499 (2017).
- D. I. Gabrilovich, S. Ostrand-Rosenberg, V. Bronte, Coordinated regulation of myeloid cells by tumours. *Nat. Rev. Immunol.* **12**, 253–268 (2012).
- V. Bronte, S. Brandau, S.-H. Chen, M. P. Colombo, A. B. Frey, T. F. Greten, S. Mandruzzato, P. J. Murray, A. Ochoa, S. Ostrand-Rosenberg, P. C. Rodriguez, A. Sica, V. Umansky, R. H. Vonderheide, D. I. Gabrilovich, Recommendations for myeloid-derived suppressor cell nomenclature and characterization standards. *Nat. Commun.* **7**, 12150 (2016).
- L. Dolcetti, E. Peranzoni, S. Ugel, I. Marigo, A. F. Gomez, C. Mesa, M. Geilich, G. Winkels, E. Traggiai, A. Casati, F. Grassi, V. Bronte, Hierarchy of immunosuppressive strength among myeloid-derived suppressor cell subsets is determined by GM-CSF. *Eur. J. Immunol.* **40**, 22–35 (2010).
- J. I. Youn, S. Nagaraj, M. Collazo, D. I. Gabrilovich, Subsets of myeloid-derived suppressor cells in tumor-bearing mice. *J. Immunol.* **181**, 5791–5802 (2008).
- K. Movahedi, M. Guilliams, J. Van den Bossche, R. Van den Berg, C. Gysemans, A. Beschin, P. De Baetselier, J. A. Van Genderachter, Identification of discrete tumor-induced myeloid-derived suppressor cell subpopulations with distinct T cell-suppressive activity. *Blood* **111**, 4233–4244 (2008).
- V. Kumar, S. Patel, E. Tcyganov, D. I. Gabrilovich, The nature of myeloid-derived suppressor cells in the tumor microenvironment. *Trends Immunol.* **37**, 208–220 (2016).
- P. H. Feng, K.-Y. Lee, Y.-L. Chang, Y.-F. Chan, L.-W. Kuo, T.-Y. Lin, F.-T. Chung, C.-S. Kuo, C.-T. Yu, S.-M. Lin, C.-H. Wang, C.-L. Chou, C.-D. Huang, H.-P. Kuo, CD14⁺S100A⁺ monocytic myeloid-derived suppressor cells and their clinical relevance in non-small cell lung cancer. *Am. J. Respir. Crit. Care Med.* **186**, 1025–1036 (2012).
- C. Iclozan, S. Antonia, A. Chiappori, D. T. Chen, D. Gabrilovich, Therapeutic regulation of myeloid-derived suppressor cells and immune response to cancer vaccine in patients with extensive stage small cell lung cancer. *Cancer Immunol. Immunother.* **62**, 909–918 (2013).
- C. Meyer, L. Cagnon, C. M. Costa-Nunes, P. Baumgaertner, N. Montandon, L. Leyvraz, O. Michielin, E. Romano, D. E. Speiser, Frequencies of circulating MDSC correlate with clinical outcome of melanoma patients treated with ipilimumab. *Cancer Immunol. Immunother.* **63**, 247–257 (2014).
- I. Azzaoui, F. Uhel, D. Rossille, C. Pangault, J. Dulong, J. L. Priol, T. Lamy, R. Houot, S. L. Gouill, G. Cartron, P. Godmer, K. Bouabdallah, N. Milpied, G. Damaj, K. Tarte, T. Fest, M. Roussel, T-cell defect in diffuse large B-cell lymphomas involves expansion of myeloid-derived suppressor cells. *Blood* **128**, 1081–1092 (2016).
- R. Weber, V. Fleming, X. Hu, V. Nagibin, C. Groth, P. Altevogt, J. Utikal, V. Umansky, Myeloid-derived suppressor cells hinder the anti-cancer activity of immune checkpoint inhibitors. *Front. Immunol.* **9**, 1310 (2018).
- D. Pan, A. Kobayashi, P. Jiang, L. F. de Andrade, R. E. Tay, A. M. Luoma, D. Tsoucas, X. Qiu, K. Lim, P. Rao, H. W. Long, G.-C. Yuan, J. Doench, M. Brown, X. S. Liu, K. W. Wucherpfennig, A major chromatin regulator determines resistance of tumor cells to T cell-mediated killing. *Science* **359**, 770–775 (2018).
- L. Strauss, S. Sangaletti, F. M. Consonni, G. Szelenyi, S. Morlacchi, M. G. Totaro, C. Porta, A. Anselmo, S. Tartari, A. Doni, F. Zitelli, C. Tripodo, M. P. Colombo, A. Sica, RORC1 regulates tumor-promoting “emergency” granulo-monocytopoiesis. *Cancer Cell* **28**, 253–269 (2015).
- D. Sichien, C. L. Scott, L. Martens, M. Vanderkerken, S. Van Gassen, M. Plantinga, T. Joeris, S. De Prijck, L. Vanhoufte, M. Vanheeswyngels, G. Van Isterdael, W. Toussaint, F. B. Madeira, K. Vergote, W. W. Agace, B. E. Clausen, H. Hammam, M. Dalod, Y. Saeyns, B. N. Lambrecht, M. Guilliams, IRF8 transcription factor controls survival and function of terminally differentiated conventional and plasmacytoid dendritic cells, respectively. *Immunity* **45**, 626–640 (2016).
- A. Yanez, M. Y. Ng, N. Hassanzadeh-Kiabi, H. S. Goodridge, IRF8 acts in lineage-committed rather than oligopotent progenitors to control neutrophil vs monocyte production. *Blood* **125**, 1452–1459 (2015).
- C. S. Netherby, M. N. Messmer, L. Burkard-Mandel, S. Colligan, A. Miller, E. C. Gomez, J. Wang, M. J. Nemeth, S. I. Abrams, The granulocyte progenitor stage is a key target of IRF8-mediated regulation of myeloid-derived suppressor cell production. *J. Immunol.* **198**, 4129–4139 (2017).
- J. D. Waight, C. Netherby, M. L. Hensen, A. Miller, Q. Hu, S. Liu, P. N. Bogner, M. R. Farren, K. P. Lee, K. Liu, S. I. Abrams, Myeloid-derived suppressor cell development is regulated by a STAT1/IRF8 axis. *J. Clin. Invest.* **123**, 4464–4478 (2013).
- A. Szanto, L. Nagy, Retinoids potentiate peroxisome proliferator-activated receptor γ action in differentiation, gene expression, and lipid metabolic processes in developing myeloid cells. *Mol. Pharmacol.* **67**, 1935–1943 (2005).
- P. L. Raber, P. Thevenot, R. Sierra, D. Wyczewowska, D. Halle, M. E. Ramirez, A. C. Ochoa, M. Fletcher, C. Velasco, A. Wilk, K. Reiss, P. C. Rodriguez, Subpopulations of myeloid-derived suppressor cells impair T cell responses through independent nitric oxide-related pathways. *Int. J. Cancer* **134**, 2853–2864 (2014).
- S. Mandruzzato, S. Solito, E. Falisi, S. Francescato, V. Chiarion-Sileni, S. Mocellin, A. Zanon, C. R. Rossi, D. Nitti, V. Bronte, P. Zanovello, IL4R α ⁺ myeloid-derived suppressor cell expansion in cancer patients. *J. Immunol.* **182**, 6562–6568 (2009).
- V. Bronte, P. Serafini, C. De Santo, I. Marigo, V. Tosello, A. Mazzoni, D. M. Segal, C. Staib, M. Lowell, G. Sutter, M. P. Colombo, P. Zanovello, IL-4-induced arginase 1 suppresses alloreactive T cells in tumor-bearing mice. *J. Immunol.* **170**, 270–278 (2003).
- C. Giallongo, N. Parrinello, D. Tibullo, P. L. Cava, A. Romano, A. Chiarenza, I. Barbagallo, G. A. Palumbo, F. Stagno, P. Vigneri, F. D. Raimondo, Myeloid derived suppressor cells (MDSCs) are increased and exert immunosuppressive activity together with polymorphonuclear leukocytes (PMNs) in chronic myeloid leukemia patients. *PLOS ONE* **9**, e101848 (2014).
- J. M. Zou, J. Qin, Y. C. Li, Y. Wang, D. Li, Y. Shu, C. Luo, S. S. Wang, G. Chi, F. Guo, G. M. Zhang, Z. H. Feng, IL-35 induces N2 phenotype of neutrophils to promote tumor growth. *Oncotarget* **8**, 33501–33514 (2017).
- J. Woytschak, N. Keller, C. Krieg, D. Impellizzieri, R. W. Thompson, T. A. Wynn, A. S. Zinkernagel, O. Boyman, Type 2 interleukin-4 receptor signaling in neutrophils antagonizes their expansion and migration during infection and inflammation. *Immunity* **45**, 172–184 (2016).
- G. Mondanelli, R. Bianchi, M. T. Pallotta, C. Orabona, E. Albini, A. Iacono, M. L. Belladonna, C. Vacca, F. Fallarino, A. Macchiarulo, S. Ugel, V. Bronte, F. Gevi, L. Zolla, A. Verhaar, M. Peppelenbosch, E. M. C. Mazza, S. Bicciato, Y. Laouar, L. Santambrogio, P. Puccetti, C. Volpi, U. Grohmann, A relay pathway between arginine and tryptophan metabolism confers immunosuppressive properties on dendritic cells. *Immunity* **46**, 233–244 (2017).
- R. V. Parry, J. M. Chemnitz, K. A. Frauwirth, A. R. Lanfranco, I. Braunstein, S. V. Kobayashi, P. S. Linsley, C. B. Thompson, J. L. Riley, CTLA-4 and PD-1 receptors inhibit T-cell activation by distinct mechanisms. *Mol. Cell. Biol.* **25**, 9543–9553 (2005).
- N. Patsoukis, J. Brown, V. Petkova, F. Liu, L. Li, V. A. Boussiotis, Selective effects of PD-1 on Akt and Ras pathways regulate molecular components of the cell cycle and inhibit T cell proliferation. *Sci. Signal.* **5**, ra46 (2012).
- M. Ye, H. Iwasaki, C. V. Laiosa, M. Stadtfeld, H. Xie, S. Heck, B. Clausen, K. Akashi, T. Graf, Hematopoietic stem cells expressing the myeloid lysozyme gene retain long-term, multilineage repopulation potential. *Immunity* **19**, 689–699 (2003).
- G. J. Lieschke, D. Grail, G. Hodgson, D. Metcalf, E. Stanley, C. Cheers, K. J. Fowler, S. Basu, Y. F. Zhan, A. R. Dunn, Mice lacking granulocyte colony-stimulating factor have chronic neutropenia, granulocyte and macrophage progenitor cell deficiency, and impaired neutrophil mobilization. *Blood* **84**, 1737–1746 (1994).
- F. Liu, H. Y. Wu, R. Wesselschmidt, T. Kornaga, D. C. Link, Impaired production and increased apoptosis of neutrophils in granulocyte colony-stimulating factor receptor-deficient mice. *Immunity* **5**, 491–501 (1996).
- S. H. Albeituni, C. Ding, M. Liu, X. Hu, F. Luo, G. Kloecker, M. Bousamra II, H.-g. Zhang, J. Yan, Yeast-derived particulate β -glucan treatment subverts the suppression of myeloid-derived suppressor cells (MDSC) by inducing polymorphonuclear MDSC apoptosis and monocytic MDSC differentiation to APC in cancer. *J. Immunol.* **196**, 2167–2180 (2016).
- D. Li, H. Yang, H. Nan, P. Liu, S. Pang, Q. Zhao, R. Karni, M. P. Kamps, Y. Xu, J. Zhou, T. Wiedmer, P. J. Sims, F. Wang, Identification of key regulatory pathways of myeloid

- differentiation using an mESC-based karyotypically normal cell model. *Blood* **120**, 4712–4719 (2012).
41. P. W. F. Karmaus, A. A. Herrada, C. Guy, G. Neale, Y. Dhungana, L. Long, P. Vogel, J. Avila, C. B. Clish, H. Chi, Critical roles of mTORC1 signaling and metabolic reprogramming for M-CSF-mediated myelopoiesis. *J. Exp. Med.* **214**, 2629–2647 (2017).
 42. E. M. Coccia, N. D. Russo, E. Stellacci, U. Testa, G. Marziali, A. Battistini, STAT1 activation during monocyte to macrophage maturation: Role of adhesion molecules. *Int. Immunopharmacol.* **11**, 1075–1083 (1999).
 43. A. Moussaieff, M. Rouleau, D. Kitsberg, M. Cohen, G. Levy, D. Barasch, A. Nemirovski, S. Shen-Orr, I. Laevsky, M. Amit, D. Bornze, B. Elena-Herrmann, T. Scherf, M. Nissim-Rafinia, S. Kempa, J. Itskovitz-Eldor, E. Meshorer, D. Aberdam, Y. Nahmias, Glycolysis-mediated changes in acetyl-CoA and histone acetylation control the early differentiation of embryonic stem cells. *Cell Metab.* **21**, 392–402 (2015).
 44. T. TeSlaa, A. C. Chaikovsky, I. Lipchina, S. L. Escobar, K. Hochedlinger, J. Huang, T. G. Graeber, D. Braas, M. A. Teitel, α -Ketoglutarate accelerates the initial differentiation of primed human pluripotent stem cells. *Cell Metab.* **24**, 485–493 (2016).
 45. W. M. Yu, X. Liu, J. Shen, O. Jovanovic, E. E. Pohl, S. L. Gerson, T. Finkel, H. E. Broxmeyer, C.-K. Qu, Metabolic regulation by the mitochondrial phosphatase PTPTM1 is required for hematopoietic stem cell differentiation. *Cell Stem Cell* **12**, 62–74 (2013).
 46. K. Ito, K. Ito, Hematopoietic stem cell fate through metabolic control. *Exp. Hematol.* **64**, 1–11 (2018).
 47. K. Duvel, J. L. Yecies, S. Menon, P. Raman, A. I. Lipovsky, A. L. Souza, E. Triantafellow, Q. Ma, R. Gorski, S. Cleaver, M. G. Vander Heiden, J. P. Mac Keigan, P. M. Finan, C. B. Clish, L. O. Murphy, B. D. Manning, Activation of a metabolic gene regulatory network downstream of mTOR complex 1. *Mol. Cell* **39**, 171–183 (2010).
 48. T. Porstmann, B. Griffiths, Y.-L. Chung, O. Delpuech, J. R. Griffiths, J. Downward, A. Schulze, PKB/Akt induces transcription of enzymes involved in cholesterol and fatty acid biosynthesis via activation of SREBP. *Oncogene* **24**, 6465–6481 (2005).
 49. S. Kagami, T. Owada, H. Kanari, Y. Saito, A. Suto, K. Ikeda, K. Hirose, N. Watanabe, I. Iwamoto, H. Nakajima, Protein geranylgeranylation regulates the balance between Th17 cells and Foxp3⁺ regulatory T cells. *Int. Immunopharmacol.* **21**, 679–689 (2009).
 50. A. J. Murphy, M. Akhtari, S. Tolani, T. Pagler, N. Bijl, C.-L. Kuo, M. Wang, M. Sanson, S. Abramowicz, C. Welch, A. E. Boehm, J. A. Kuivenhoven, L. Yvan-Charvet, A. R. Tall, ApoE regulates hematopoietic stem cell proliferation, monocytosis, and monocyte accumulation in atherosclerotic lesions in mice. *J. Clin. Invest.* **121**, 4138–4149 (2011).
 51. M. Westerterp, E. L. Gautier, A. Ganda, M. M. Molusky, W. Wang, P. Fotakis, N. Wang, G. J. Randolph, V. D. D'Agati, L. Yvan-Charvet, A. R. Tall, Cholesterol accumulation in dendritic cells links the inflammasome to acquired immunity. *Cell Metab.* **25**, 1294–1304.e6 (2017).
 52. A. R. Tall, L. Yvan-Charvet, Cholesterol, inflammation and innate immunity. *Nat. Rev.* **15**, 104–116 (2015).
 53. P. Tontonoz, L. Nagy, J. G. Alvarez, V. A. Thomazy, R. M. Evans, PPAR γ promotes monocyte/macrophage differentiation and uptake of oxidized LDL. *Cell* **93**, 241–252 (1998).
 54. N. E. Scharping, A. V. Menk, R. S. Moreci, R. D. Whetstone, R. E. Dadey, S. C. Watkins, R. L. Ferris, G. M. Delgoffe, The tumor microenvironment represses T cell mitochondrial biogenesis to drive intratumoral T cell metabolic insufficiency and dysfunction. *Immunity* **45**, 374–388 (2016).
 55. J. S. Bowers, M. H. Nelson, K. Majchrzak, S. R. Bailey, B. Rohrer, A. D. M. Kaiser, C. Atkinson, L. Gattinoni, C. M. Paulos, Th17 cells are refractory to senescence and retain robust antitumor activity after long-term ex vivo expansion. *JCI Insight* **2**, e90772 (2017).
 56. S. Chatterjee, A. Daenthanasanmak, P. Chakraborty, M. W. Wyatt, P. Dhar, S. P. Selvam, J. Fu, J. Zhang, H. Nguyen, I. Kang, K. Toth, M. Al-Homrani, M. Husain, G. Beeson, L. Ball, K. Helke, S. Husain, E. Garrett-Mayer, G. Hardiman, M. Mehrotra, M. I. Nishimura, C. C. Beeson, M. G. Bupp, J. Wu, B. Ogretmen, C. M. Paulos, J. Rathmell, X. Z. Yu, S. Mehrotra, CD38-NAD⁺axis regulates immunotherapeutic anti-tumor T cell response. *Cell Metab.* **27**, 85–100.e8 (2018).
 57. A. W.-M. Lee, D. J. States, Colony-stimulating factor-1 requires PI3-kinase-mediated metabolism for proliferation and survival in myeloid cells. *Cell Death Differ.* **13**, 1900–1914 (2006).
 58. M. Buitenhuis, L. P. Verhagen, H. W. M. van Deutkom, A. Castor, S. Verploegen, L. Koenderman, S.-E. W. Jacobsen, P. J. Coffer, Protein kinase B (c-akt) regulates hematopoietic lineage choice decisions during myelopoiesis. *Blood* **111**, 112–121 (2008).
 59. J. T. Rodgers, K. Y. King, J. O. Brett, M. J. Cromie, G. W. Charville, K. K. Maguire, C. Brunson, N. Mastey, L. Liu, C.-R. Tsai, M. A. Goodell, T. A. Rando, mTORC1 controls the adaptive transition of quiescent stem cells from G0 to G_{Alert}. *Nature* **510**, 393–396 (2014).
 60. N. J. Spann, L. X. Garmire, J. G. McDonald, D. S. Myers, S. B. Milne, N. Shibata, D. Reichart, J. N. Fox, I. Shaked, D. Heubodler, C. R. H. Raetz, E. W. Wang, S. L. Kelly, M. C. Sullards, R. C. Murphy, A. H. Merrill Jr., H. A. Brown, E. A. Dennis, A. C. Li, K. Ley, S. Tsimikas, E. Fahy, S. Subramaniam, O. Quehenberger, D. W. Russell, C. K. Glass, Regulated accumulation of desmosterol integrates macrophage lipid metabolism and inflammatory responses. *Cell* **151**, 138–152 (2012).
 61. H. A. Anderson, P. A. Roche, MHC class II association with lipid rafts on the antigen presenting cell surface. *Biochim. Biophys. Acta* **1853**, 775–780 (2015).
 62. K. Y. King, M. A. Goodell, Inflammatory modulation of HSCs: Viewing the HSC as a foundation for the immune response. *Nat. Rev. Immunol.* **11**, 685–692 (2011).
 63. X. Hu, Y. Wang, L.-Y. Hao, X. Liu, C. A. Lesch, B. M. Sanchez, J. M. Wendling, R. W. Morgan, T. D. Aicher, L. L. Carter, P. L. Toogood, G. D. Glick, Sterol metabolism controls T_H17 differentiation by generating endogenous ROR γ agonists. *Nat. Chem. Biol.* **11**, 141–147 (2015).
 64. F. R. Santori, P. Huang, S. A. van de Pavert, E. F. Douglass Jr., D. J. Leaver, B. A. Haubrich, R. Keber, G. Lorbeck, T. Konijn, B. N. Rosales, D. Rozman, S. Horvat, A. Rahier, R. E. Mebius, F. Rastinejad, W. D. Nes, D. R. Littman, Identification of natural ROR γ ligands that regulate the development of lymphoid cells. *Cell Metab.* **21**, 286–297 (2015).
 65. A. Chawla, W. A. Boisvert, C.-H. Lee, B. A. Laffitte, Y. Barak, S. B. Joseph, D. Liao, L. Nagy, P. A. Edwards, L. K. Curtiss, R. M. Evans, P. Tontonoz, A PPAR γ -LXR-ABCA1 pathway in macrophages is involved in cholesterol efflux and atherogenesis. *Mol. Cell* **7**, 161–171 (2001).
 66. Y. S. Yoon, S.-Y. Kim, M.-J. Kim, J.-H. Lim, M.-S. Cho, J. L. Kang, PPAR γ activation following apoptotic cell instillation promotes resolution of lung inflammation and fibrosis via regulation of efferocytosis and proresolving cytokines. *Mucosal Immunol.* **8**, 1031–1046 (2015).
 67. M. L. Sulciner, C. N. Serhan, M. M. Gilligan, D. K. Mudge, J. Chang, A. Gartung, K. A. Lehner, D. R. Bielenberg, B. Schmidt, J. Dalli, E. R. Greene, Y. Gus-Brautbar, J. Piwowarski, T. Mammodo, D. Zurakowski, M. Perretti, V. P. Sukhatme, A. Kaipainen, M. W. Kieran, S. Huang, D. Panigrahy, Resolvin s suppress tumor growth and enhance cancer therapy. *J. Exp. Med.* **215**, 115–140 (2018).
 68. I. Zanoni, R. Ostuni, G. Capuano, M. Collini, M. Caccia, A. E. Ronchi, M. Rocchetti, F. Mingozzi, M. Foti, G. Chirico, B. Costa, A. Zaza, P. Ricciardi-Castagnoli, F. Granucci, CD14 regulates the dendritic cell life cycle after LPS exposure through NFAT activation. *Nature* **460**, 264–268 (2009).
 69. B. Weigmann, I. Tubbe, D. Seidel, A. Nicolaev, C. Becker, M. F. Neurath, Isolation and subsequent analysis of murine lamina propria mononuclear cells from colonic tissue. *Nat. Protoc.* **2**, 2307–2311 (2007).
 70. C. A. Dumitru, K. Moses, S. Trellakis, S. Lang, S. Brandau, Neutrophils and granulocytic myeloid-derived suppressor cells: Immunophenotyping, cell biology and clinical relevance in human oncology. *Cancer Immunol. Immunother.* **61**, 1155–1167 (2012).
 71. M. Yuan, S. B. Breitkopf, X. Yang, J. M. Asara, A positive/negative ion-switching, targeted mass spectrometry-based metabolomics platform for bodily fluids, cells, and fresh and fixed tissue. *Nat. Protoc.* **7**, 872–881 (2012).

Acknowledgments

Funding: This work was supported by NIH grants CA183605, CA18360551, and AI098129-01 and by the DoD grant PC140571. **Author contribution:** L.S. participated in the conceptualization of the project and experimental design, performed experiments and the analysis and validation of the data, prepared figures, and participated in the preparation of the manuscript. M.A.A.M. performed experiments and the analysis and validation of the data, prepared figures, and participated in the preparation of the manuscript. J.D.W., N.M.T.-O., A.C., R.P., Q.W., and M.Y. participated in various steps of the experimental studies. J.A. participated in the experimental design of metabolite studies and the formal analysis and the validation of the data and participated in the preparation of the manuscript. N.P. participated in the conceptualization of the project, designed and performed the bioenergetics studies, and participated in experiments, the analysis and validation of the data, and the preparation of the manuscript. V.A.B. had the overall responsibility of project conceptualization, experimental design, investigation, data analysis and validation, and preparation of the manuscript and figures. **Competing interests:** V.A.B. has patents on the PD-1 pathway licensed by Bristol-Myers Squibb, Roche, Merck, EMD-Serono, Boehringer Ingelheim, AstraZeneca, Novartis, and Dako. The authors declare no other competing interests. **Data and materials availability:** All data needed to evaluate the conclusions in the paper are present in the paper or the Supplementary Materials.

Submitted 29 May 2019

Accepted 13 November 2019

Published 3 January 2020

10.1126/sciimmunol.aay1863

Citation: L. Strauss, M. A. A. Mahmoud, J. D. Weaver, N. M. Tijaro-Ovalle, A. Christofides, Q. Wang, R. Pal, M. Yuan, J. Asara, N. Patsoukis, V. A. Boussiotis, Targeted deletion of PD-1 in myeloid cells induces antitumor immunity. *Sci. Immunol.* **5**, eaay1863 (2020).

IMMUNOTHERAPY

Gasdermin E-mediated target cell pyroptosis by CAR T cells triggers cytokine release syndrome

Yuying Liu^{1,2*}, **Yiliang Fang**^{1*}, **Xinfeng Chen**^{3*}, **Zhenfeng Wang**¹, **Xiaoyu Liang**¹,
Tianzhen Zhang¹, **Mengyu Liu**¹, **Nannan Zhou**¹, **Jiadi Lv**¹, **Ke Tang**⁴, **Jing Xie**¹,
Yunfeng Gao¹, **Feiran Cheng**¹, **Yabo Zhou**¹, **Zhen Zhang**³, **Yu Hu**⁵, **Xiaohui Zhang**⁶,
Quanli Gao⁷, **Yi Zhang**³, **Bo Huang**^{1,2,4†}

Cytokine release syndrome (CRS) counteracts the effectiveness of chimeric antigen receptor (CAR) T cell therapy in cancer patients, but the mechanism underlying CRS remains unclear. Here, we show that tumor cell pyroptosis triggers CRS during CAR T cell therapy. We find that CAR T cells rapidly activate caspase 3 in target cells through release of granzyme B. The latter cleaves gasdermin E (GSDME), a pore-forming protein highly expressed in B leukemic and other target cells, which results in extensive pyroptosis. Consequently, pyroptosis-released factors activate caspase 1 for GSDMD cleavage in macrophages, which results in the release of cytokines and subsequent CRS. Knocking out GSDME, depleting macrophages, or inhibiting caspase 1 eliminates CRS occurrence in mouse models. In patients, GSDME and lactate dehydrogenase levels are correlated with the severity of CRS. Notably, we find that the quantity of perforin/granzyme B used by CAR T cells rather than existing CD8⁺ T cells is critical for CAR T cells to induce target cell pyroptosis.

INTRODUCTION

Despite the success of clinical applications of genetically engineered T cells modified with chimeric antigen receptors (CARs) against B cell malignancies (1–3), cytokine release syndrome (CRS) hinders the effectiveness of this treatment in patients (4, 5). It is known that CRS is triggered by acute inflammatory responses and characterized by fever, hypotension, and respiratory insufficiency associated with elevated serum cytokines (5–7). Although macrophages have been reported to be involved in the pathogenesis of CRS in the CAR T cell–treated humanized mouse model (8, 9), the mechanisms triggering CRS are unclear. CAR T cells undergo activation and expansion in patients after their infusion (5, 10, 11), and rapidly expanded CAR T cells may result in a rapid and massive death of B leukemic cells within a brief period. Coincidentally, disease burden in patients with acute lymphoblastic leukemia is also strongly correlated with the incidence and severity of CRS (5, 10–12). The manner by which such a massive malignant B cell death is involved in CRS pathogenesis remains elusive.

Cells can undergo distinct types of death. Apoptosis was originally considered the only form of controlled and programmed death. However, recent studies have demonstrated a previously unidentified form of programmed necrosis, characterized by rapid cellular swelling, large bubbles emerging from the plasma membrane, and the release of pro-

inflammatory factors (13, 14). At least two programmed necrotic cell death pathways have been identified, including a mixed lineage kinase domain-like (MLKL)–mediated necroptosis (15, 16) and gasdermin D (GSDMD)– or GSDME-mediated pyroptosis (17, 18). Recruitment of receptor-interacting protein kinase 1 (RIPK1) to the tumor necrosis factor- α (TNF- α) receptor forms a death complex with RIP3 and subsequently activates MLKL to generate membrane nan pores, thus causing necroptotic cell death (19). Unlike MLKL, GSDMD or GSDME is activated by inflammatory caspases (caspases 1, 4, and 5 and murine caspase 11) or caspase 3 (17, 20) and can form oligomers that insert into the cell membranes to form pores, thus mediating pyroptotic cell death. In this study, we provide evidence that human B leukemic cells and other target tumor cells express a sufficient amount of GSDME, which is efficiently activated by CAR T cell–released granzyme B–activated caspase 3, leading to target cell pyroptosis. Pyroptosis-released factors stimulate macrophages to produce proinflammatory cytokines, which is likely triggering CRS in CAR T cell–treated patients.

RESULTS

CAR T cells induce target cell pyroptosis

When we incubated CD19-recognizing CAR T cells with CD19⁺ primary leukemic cells isolated from B cell acute lymphoblastic leukemia (B-ALL) patients, we found that the viability of B leukemic cells markedly decreased, whereas human epidermal growth factor receptor 2 (HER2)–specific CAR T cells did not have such an effect (Fig. 1A). We observed that the dying cells appeared to have a swollen appearance with large bubbles arising from the plasma membrane (Fig. 1B). Flow cytometric analysis showed that more than 30% of CAR T cell–treated CD19⁺ B leukemic cells were annexin V⁺ and propidium iodide (PI)⁺ (Fig. 1C). High levels of lactate dehydrogenase (LDH) were present in the supernatants (Fig. 1D), suggesting that CAR T cells induce pyroptosis in CD19⁺ B leukemic cells. We also found that CD19-CAR T cells induced pyroptosis in CD19⁺ Raji and NALM-6 leukemic cell lines in a time- and effector/target ratio–dependent manner, as indicated by decreased cell viability, cellular swelling with bubbles,

¹Department of Immunology and National Key Laboratory of Medical Molecular Biology, Institute of Basic Medical Sciences, Chinese Academy of Medical Sciences (CAMS) and Peking Union Medical College, Beijing 100005, China. ²Clinical Immunology Center, CAMS, Beijing 100005, China. ³Biotherapy Center and Cancer Center, First Affiliated Hospital of Zhengzhou University, Zhengzhou 450052, Henan, China.

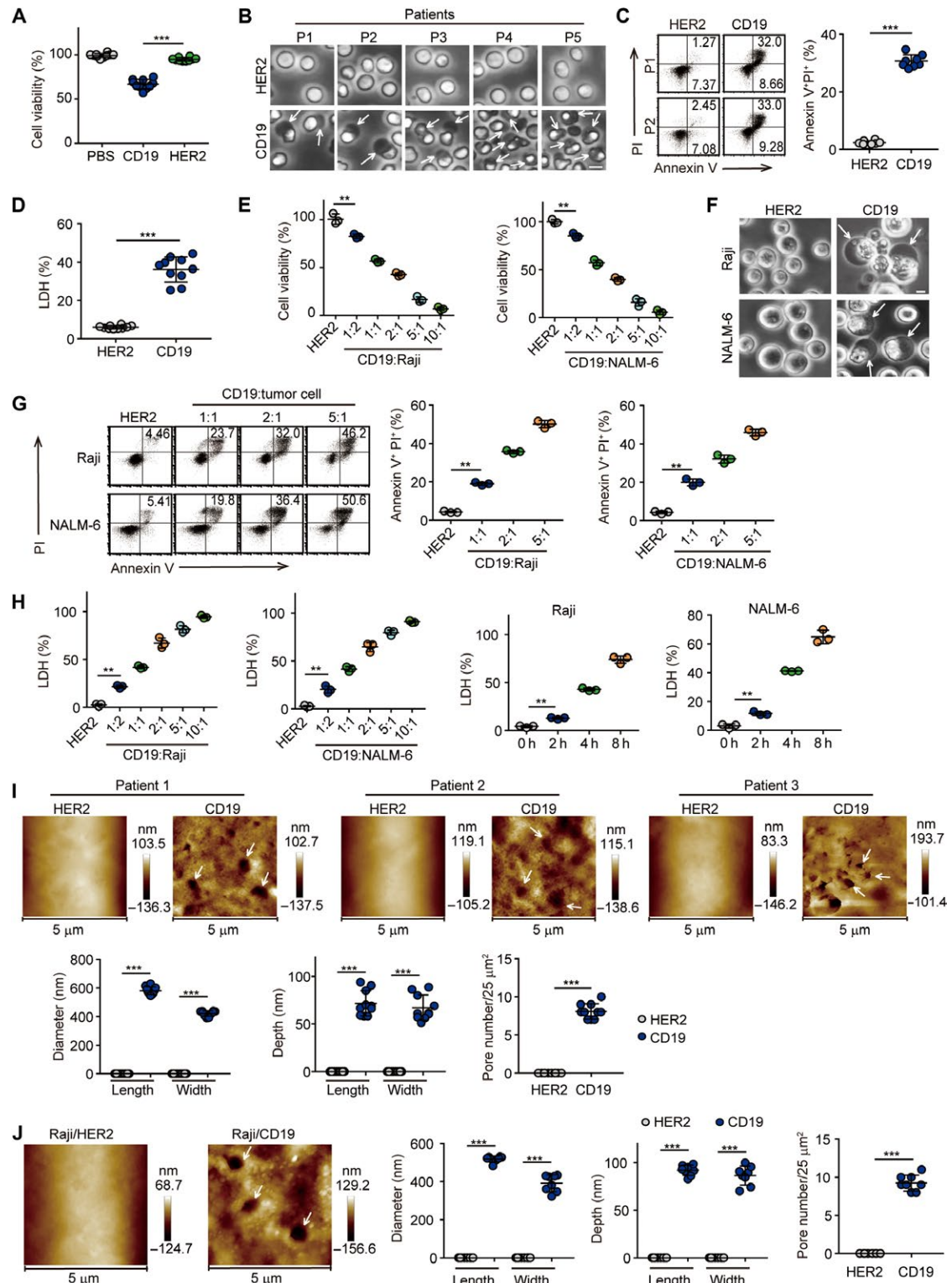
⁴Department of Biochemistry and Molecular Biology, Tongji Medical College, Huazhong University of Science and Technology, Wuhan 430030, China. ⁵Institute of Hematology, Union Hospital, Tongji Medical College, Huazhong University of Science and Technology, Wuhan 430022, China. ⁶Peking University People's Hospital, Peking University Institute of Hematology, Beijing 100044, China. ⁷Department of Immunology, Affiliated Cancer Hospital of Zhengzhou University and Henan Cancer Hospital, Zhengzhou, Henan 450008, China.

*These authors contributed equally to this work.

†Corresponding author. Email: tjhhuangbo@hotmail.com

Copyright © 2020
The Authors, some
rights reserved;
exclusive licensee
American Association
for the Advancement
of Science. No claim
to original U.S.
Government Works

Fig. 1. CAR T cells induced tumor cell pyroptosis. (A to D) Primary B leukemic cells were cocultured with CD19 or HER2-CAR T cells at an effector/target ratio (E/T) of 2:1 for 6 hours. Tumor cell viability was measured by using the CellTiter-Glo Luminescent Cell Viability Assay Kit [(A), $n = 10$]. The representative images were shown (B). Cell death was determined by flow cytometry [(C), $n = 6$], and LDH level in the supernatants was measured [(D), $n = 10$]. Scale bar, 20 μ m. White arrows indicate pyroptotic cells. (E to H) Luc-Raji or NALM-6 cells were cocultured with CD19- or HER2-CAR T cells at different ratios as indicated for 4 hours or at the ratio of 1:1 for the indicated time. Cell viability was measured (E), and the representative images were shown (F). The percentage of annexin V⁺/PI⁺ tumor cells was determined by flow cytometry (G). LDH levels in the supernatants were measured (H). Scale bar, 10 μ m. (I) The same as (A), except that primary B leukemic cells were imaged by AFM. Pore diameter and depth were calculated within a cellular membrane area of 5 μ m by 5 μ m from 10 cells. Pore number was quantified from three areas of 5 μ m by 5 μ m per cell. A pore was defined as a cavity deeper than 10 nm in the plasma membrane. White arrows indicate pores. (J) Raji cells were cocultured with CD19-CAR T cells for 1 hour. Pore size and number were measured and counted. ** $P < 0.01$, *** $P < 0.001$, by Student's *t* test (C, D, I, and J) or one-way ANOVA (A, E, G, and H). Data are means \pm SD of three independent experiments.



an increased percentage of annexin V⁺/PI⁺ cells, and high levels of LDH (Fig. 1, E to H, and fig. S1A). Pyroptosis is known to be mediated by gasdermins such as GSDMD and GSDME, which form pores in the plasma membrane (17, 20, 21). Recently, we developed an atomic force microscopy (AFM)-based technology to visualize pore forma-

tion in true cellular membranes (22). Using this method, we observed that many pores were formed in the membrane of the B leukemic cells after coculture with CD19-CAR T cells (Fig. 1, I and J, and fig. S1B), further supporting the idea that B leukemic cells underwent pyroptosis. Other CAR T cells such as HER2-recognition CAR, incubated with

HER2⁺ solid tumor cells (MCF-7 and SGC-7901), also caused decreased cell viability, swelling with bubbles, LDH release, and pore formation in tumor cells (fig. S1, C to F, and movies S1 and S2). Together, these results suggest that CAR T cell therapy may induce target tumor cells to enter pyroptosis.

CAR T cells activate GSDME to mediate target cell pyroptosis

It is known that activated inflammatory caspases (caspases 1, 4, 5, and 11) or caspase 3 can cleave GSDMD or GSDME to generate its active form, which inserts into the cellular membranes causing pore formation and subsequent cellular pyroptosis (17, 21). GSDME, but

not GSDMD, was ubiquitously expressed in the CD19⁺ malignant B cells of patients (Fig. 2A). In addition, CD19⁺ Raji and NALM-6 cells and HER2⁺ SGC-7901 and MCF-7 tumor cells also expressed high levels of GSDME (Fig. 2A), and the active form of GSDME was induced by CAR T cells in CD19⁺ or HER2⁺ tumor cells (Fig. 2B and fig. S2A). MLKL is also able to form pores in the cell membrane and induce necroptosis (16), but the phosphorylated form of MLKL and RIPK1/3 was not detectable in tumor cells (fig. S2A). These results suggest that GSDME rather than other molecules mediates CAR T cell-triggered tumor cell pyroptosis. To verify this, we knocked out GSDME in four types of target cells (Raji, NALM-6, SGC-7901,

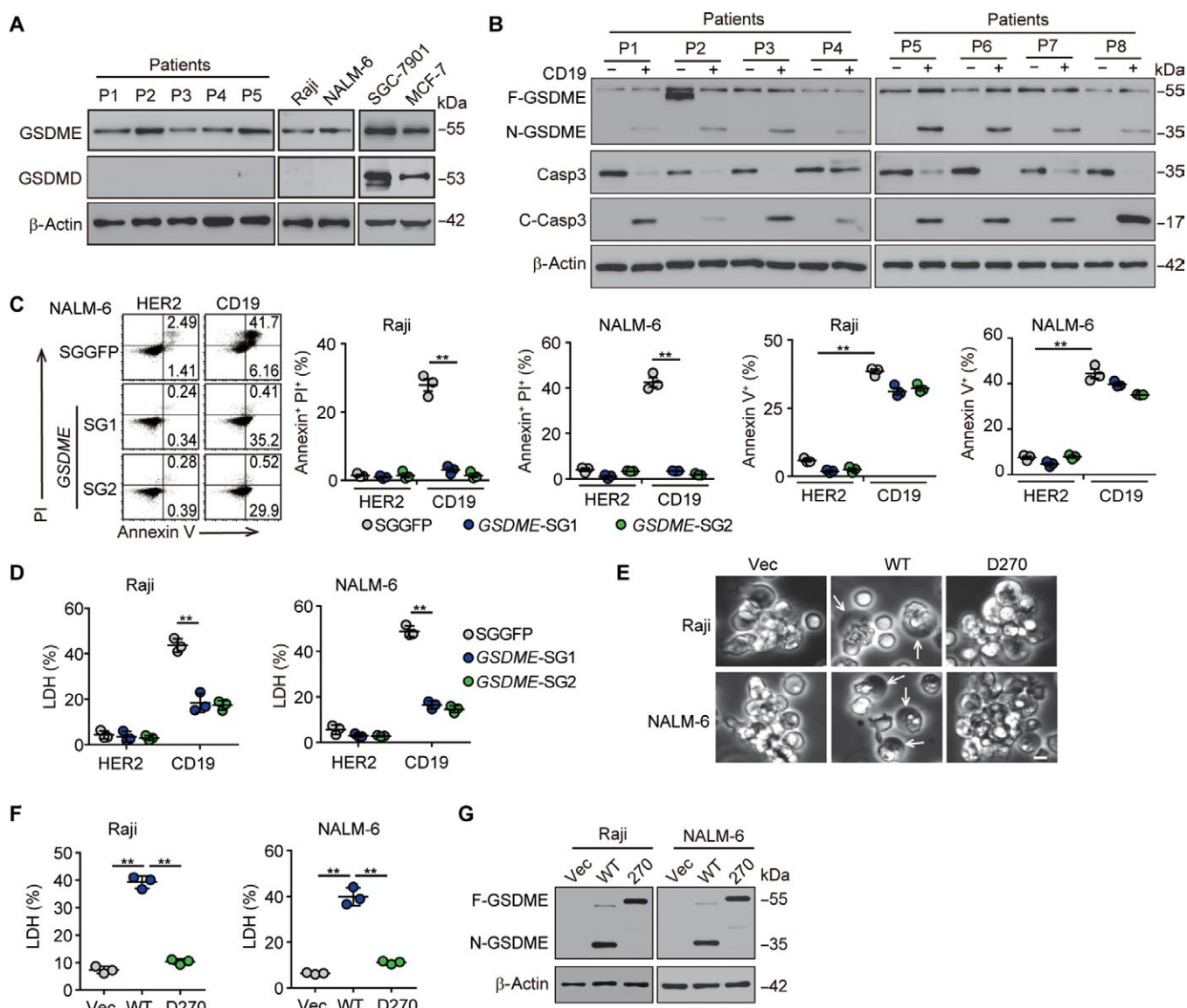


Fig. 2. Tumor cell pyroptosis by CAR T cells is mediated by GSDME. (A) GSDME and GSDMD in primary B leukemic cells isolated from B-ALL patients ($n = 5$) or cell lines were determined by Western blot. (B) CD19⁺ B leukemic cells from B-ALL patients ($n = 8$) were cocultured with or without CD19-CAR T cells for 6 hours. GSDME, caspase 3 (Casp3), and cleaved caspase 3 (C-Casp3) were analyzed by Western blot. (C and D) SGGFP or GSDME-SGs[−] Raji or NALM-6 cells were cocultured with HER2 or CD19-CAR T cells for 4 hours. The percentage of annexin V⁺/PI⁺ or annexin V⁺ cells (C) and the LDH level from the supernatant (D) were measured. (E to G) GSDME-deficient Raji or NALM-6 cells with overexpressed vector, WT-GSDME, or D270-GSDME were cocultured with CD19-CAR T cells at an E/T ratio of 2:1 for 4 hours. Cell morphology was observed under a microscope (E). The LDH level from the supernatant was detected (F). The expression of GSDME was determined by Western blot (G). Scale bar, 20 μ m. White arrows indicate the pyroptotic cell. ** $P < 0.01$, by one-way ANOVA (C, D, and F). Data are means \pm SD of three independent experiments.

and MCF-7) and found that GSDME deficiency, which did not affect tumor cell growth (fig. S2, B and C), abrogated CAR T cell-induced target cell pyroptosis, as indicated by the decreased percentage of annexin V⁺/PI⁺ cells and reduced levels of LDH in supernatants (Fig. 2, C and D, and fig. S2, D and E). However, overexpression of GSDME increased pyroptosis of target cells (fig. S2, F and G), suggesting that CAR T cells trigger tumor cell pyroptosis by activating GSDME. Despite the pyroptosis mediated by GSDME, the blockade of GSDME actually resulted in target cell death switching from pyroptosis to apoptosis (Fig. 2C and fig. S2D). In line with this observation, normal B cells did not express GSDME (fig. S2H) and could also be triggered to undergo apoptosis by CD19-CAR T cells (fig. S2, I and J). To validate this idea, we introduced GSDME-expressing vectors to the GSDME-deficient tumor cells and found that the re-expression of GSDME restored CAR T cell-induced pyroptosis (Fig. 2, E and F). However, the reexpression of mutant GSDME (D270A) could not restore the pyroptosis from the apoptosis (Fig. 2, E and F). Consistent with this observation, the active form of GSDME was not found in GSDME (D270A)-expressing cells (Fig. 2G). Together,

these results suggest that CAR T cells can mobilize GSDME to induce target cell pyroptosis.

CAR T cell-released granzyme B triggers the cleavage of GSDME

To better understand the molecular mechanism that CAR T cells use to activate GSDME in tumor cells, we measured caspase 3 cleavage by Western blot (17). As expected, caspase 3, but not caspase 1 or caspase 4, was cleaved and activated in co-incubated tumor cells (Figs. 2B and 3A and fig. S3A). Moreover, the addition of the caspase 3 inhibitor DEVD or the pan-caspase inhibitor zVAD inhibited the cleavage of GSDME and prevented tumor cell pyroptosis (fig. S3, B to D). In contrast, we found that GSDME knockout did not affect caspase 3 activation, suggesting that GSDME functions downstream of caspase 3 (fig. S3E). Granzyme B, which is released from cytolytic T cells, is a key effector molecule that cleaves caspases 3 and 7 to generate their active forms (23, 24). We found that inhibition of granzyme B in CAR T cells by small interfering RNA (siRNA) or a chemical compound (GrBI) blocked the activation of caspases 3 and

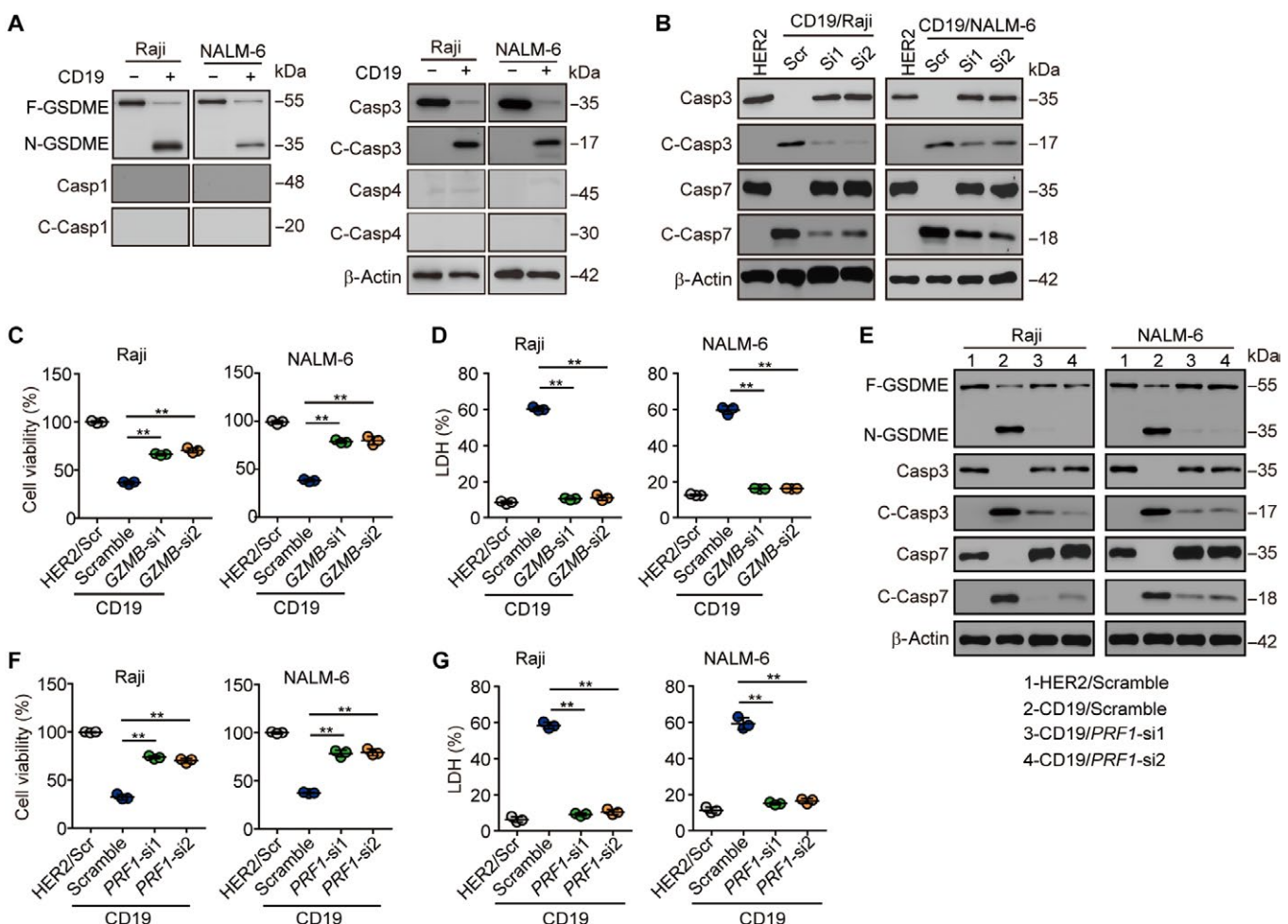


Fig. 3. CAR T cell-released granzyme B triggers the activation of GSDME. (A) CD19⁺ Raji or NALM-6 cells were cocultured with or without CD19-CART cells for 4 hours. GSDME, Casp1, C-Casp1, Casp3, C-Casp3, Casp4, and C-Casp4 were analyzed by Western blot. (B to D) Scramble (Scr) or GZMB-siRNAs⁻ CD19-CART cells were cocultured with Luc-Raji or NALM-6 cells for 4 hours. Casp3, C-Casp3, Casp7, and C-Casp7 were analyzed by Western blot (B). Cell viability (C) and LDH levels in the supernatants (D) were measured. (E to G) The same as (B) to (D), except that PRF1-siRNAs⁻ CD19-CART cells were used. **P < 0.01, by one-way ANOVA (C, D, F, and G). Data are means ± SD of three independent experiments.

7 in tumor cells, thus inhibiting pyroptosis (Fig. 3, B to D, and fig. S3, F to I). Perforin pore formation allows granzyme B to enter the cytosol of target cells (25), and perforin knockdown prevented the activation of caspases 3 and 7, cleavage of GSDME, and subsequent pyroptosis (Fig. 3, E to G, and fig. S3F). These results suggest that CAR T cells release perforin to form pores, leading to the entry of granzyme B into target tumor cells, which causes the subsequent activation of GSDME and pyroptosis.

Superior affinity to target cells is critical for CAR T cells to trigger pyroptosis

The above data indicated that CAR T cells used perforin/granzyme B to induce tumor cell pyroptosis. However, nontransduced CD8⁺ T cells can use the same perforin and granzyme B mechanism to attack target cells, leading to tumor cell apoptosis rather than pyroptosis (26). To better define this mechanism, we constructed human CD19-recognizing mouse CAR (hCD19-mCAR) in murine OT-I T cells and human CD19- or human HER2-expressing B16 melanoma cells. Incubation of OT-I hCD19-mCAR T cells with CD19-B16 cells triggered pyroptosis, but this was not observed in HER2-B16 cells or vector-B16 cells, and ovalbumin (OVA) peptide-pulsed B16 cells underwent apoptosis (Fig. 4, A to C). In addition, we found that, even when the incubation time was prolonged, the pulsed B16 cells did not display cellular swelling or membrane bubbles (fig. S4A), suggesting that nontransduced tumor-specific T cells do not induce target tumor cell pyroptosis. Consistently, unmodified OT-I T cells released perforin/granzyme B to induce OVA-B16 apoptosis rather than pyroptosis (fig. S4, B and C). Similarly, allogeneic CD8⁺ T cells isolated from donors also used perforin/granzyme B to induce apoptosis in MCF-7 or SGC-7901 cells rather than pyroptosis (fig. S4, D and E). Knockdown of either perforin or granzyme B inhibited the killing of OVA-B16 or B16 tumor cells by OT-I or pmel T cells (fig. S4F), raising a question as to why CAR T cell- but not tumor-specific T cell-derived perforin/granzyme B induced pyroptosis. One explanation is that the quantity of perforin/granzyme B released from CAR T cells and from unmodified CD8⁺ T cells may be different. It is known that the affinity of CAR and its antigen may be 100-fold higher than that of T cell receptor (TCR) and major histocompatibility complex (MHC)-peptide complex (27, 28). We speculated that the CAR-antigen interaction resulted in more perforin/granzymes being released by CAR T cells. OT-I hCD19-mCAR T cells released more perforin/granzyme B after coculture with hCD19-B16 cells, as compared with HER2-B16 or OVA peptide-pulsed B16 cells (Fig. 4D). Although allogeneic CD8⁺ T cells could kill MCF-7 or SGC-7901 tumor cells in the presence of a CD28 antibody (fig. S4D), these CD8⁺ T cells expressed much lower levels of CD107a than the corresponding CAR T cells (fig. S4G), and less granzyme B was present in the target tumor cells during incubation with allogeneic T cells (fig. S4H). Moreover, we found that tumor-specific T cells induced a small amount of GSDME cleavage and did not activate GSDMD or MLKL, regardless of the cleavage of caspases 3 and 7 in tumor cells (fig. S4I). Cells have the ability to rapidly repair the formed membrane pore (22, 29), thus preventing cell pyroptosis induced by a small amount of GSDME activated by caspase 3. Therefore, only a large amount of active GSDME can surpass the pore-repairing ability of the cell and lead to pyroptosis. As expected, high levels of cleaved GSDME was present in CD19-B16 cells after incubation with CD19-CAR T cells (Fig. 4E), and a GSDME knockout abolished the effect of CAR T cells on CD19-B16 cell pyroptosis (Fig. 4, F and G). However,

the knockout of GSDME had less influence on B16 cell apoptosis induced by OT-I T cells (Fig. 4, F and H). The addition of exogenous perforin/granzyme B to the medium led to OVA-B16 or B16 cell pyroptosis by tumor-specific T cells (Fig. 4, I to K). In addition, the use of recombinant perforin and granzyme B to treat tumor cells induced tumor cell death by either apoptosis or pyroptosis dependent on the dosage (low or high) (fig. S5, A to C). In addition to the superior affinity of CAR to tumor cell antigen, we also investigated whether the co-signaling domains in CD19-CAR played a role in regulating target cell pyroptosis. We constructed CD19-CAR with CD3ζ domains, but without CD28 signaling domains, and cocultured with CD19-expressing B16 cells in the presence of a CD28 antibody. We found that compared with CD3ζ-CD28-CAR T cells, CD3ζ-CAR T cells had much less of an effect on the decreased cell viability, increased LDH levels, and the induction of annexin V⁺/PI⁺ cells (Fig. 5, A to C). CD3ζ-CAR T cells appeared to not induce tumor cell pyroptosis, as evidenced by the lack of cellular swelling and membrane bubbles (Fig. 5D). In addition, we found that CD19-CAR T cells with different co-signaling domains (CD3ζ-CD28, CD3ζ-4-1BB, or CD3ζ-CD28-4-1BB) could induce CD19-B16 cells to enter pyroptosis (Fig. 5, E to G). Among them, CD3ζ-CD28-4-1BB-CD19-CAR T cells exerted the strongest effect on pyroptosis, whereas CD3ζ-CD28 and CD3ζ-4-1BB-CD19-CAR T cells had a similar effect (Fig. 5, E to G). Together, these results suggest that superior tumor antigen affinity and the co-signaling domains confer CAR T cells with the ability to release large amounts of perforin/granzyme B required for CAR T cell-mediated tumor cell pyroptosis.

Target cell pyroptosis stimulates macrophages to release CRS-related cytokines

Pyroptotic cells release large amounts of damage-associated molecular pattern molecules (DAMPs), which can trigger strong inflammatory responses like CRS, prompting us to hypothesize that GSDME-mediated pyroptosis triggers CRS during CAR T cell therapy. Macrophages are involved in inflammatory responses and have been reported to play an important role in CAR T cell therapy-induced CRS (8, 9). When cocultured supernatants (CD19-CAR T cells and NALM-6, Raji, or primary B leukemic cells) were used to treat macrophages derived from the peripheral blood mononuclear cells (PBMCs) of healthy donors, we observed a marked release of interleukin-1β (IL-1β) and IL-6, two markers of CRS (Fig. 6, A and B, and fig. S6A). Supernatants from HER2-CAR T/SGC-7901 cells also resulted in the release of these two cytokines by treated macrophages (fig. S6B), indicating that CRS can be triggered by products of tumor cell pyroptosis. However, supernatants from nontransduced tumor-specific CD8⁺ T cells that killed target tumor cells did not stimulate macrophages to secrete IL-1β or to up-regulate the expression of IL-6 (fig. S6C). To validate these results, we used CD19 or HER2⁻ CAR T cells to coculture with GSDME^{-/-} target cells (NALM-6, Raji, or SGC-7901). Under this condition, the supernatants were not able to stimulate macrophages to produce IL-1β or IL-6 (Fig. 6C and fig. S6D). It is known that macrophages release IL-1β through the activation of the inflammasome pathway. Caspase 1, the effector molecule of inflammasomes that cleaves pro-IL-1β, was activated in macrophages by the above pyroptotic supernatants, whereas supernatants from the GSDME knockout groups did not cause the cleavage of caspase 1 in macrophages (Fig. 6D). In addition to IL-1β, caspase 1 also cleaves and generates the active form of GSDMD, the membrane pore-forming molecule, which leads to the release of IL-1β and other

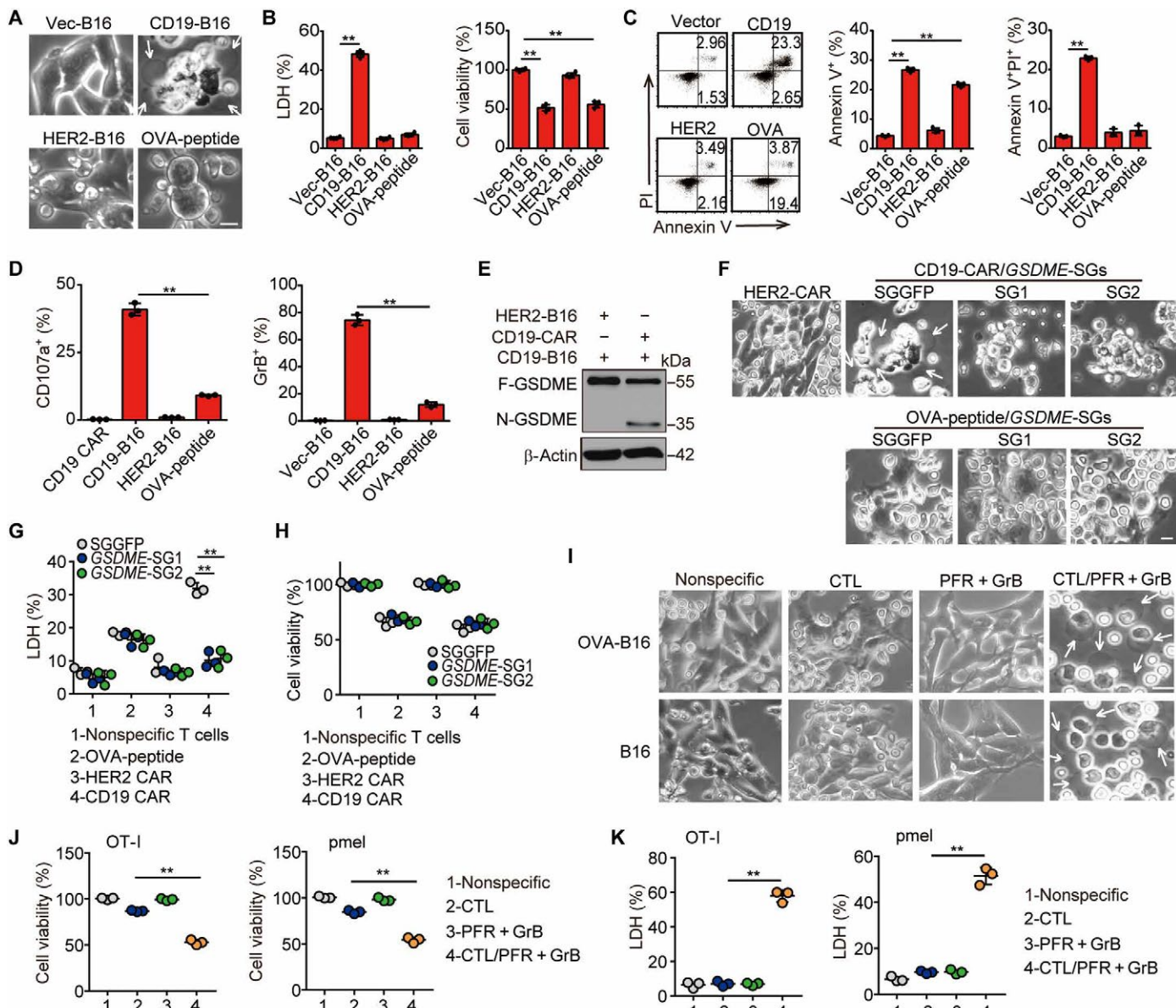


Fig. 4. Superior affinity is critical for CAR T cell-mediated tumor cell pyroptosis. (A to D) hCD19-mCAR T cells were cocultured with CD19-B16 (E/T = 2:1), HER2-B16 (E/T = 2:1), or vector-B16 pulsed with OVA peptide (E/T = 20:1) for 6 hours. Representative cell morphology was shown (A). LDH levels in supernatants, cell viability (B), and the annexin V⁺ or annexin V⁺/PI⁺ cells (C) were measured. The CD107a⁺ or GrB⁺ cells were determined by flow cytometry (D). White arrows indicate pyroptotic cells. (E) CD19-recognizing CAR OT-I T cells were cocultured with CD19 or HER2-B16 cells for 6 hours at a 2:1 E/T ratio. The expression of GSDME was determined by Western blot. (F to H) The same as (A), except that SGGFP or GSDME-SGs-CD19-B16 cells were used. Cell morphology was observed by microscopy (F). The LDH level from the supernatant (G) was measured, and cell viability (H) was detected by a microplate luminometer. Scale bar, 20 μ m. (I to K) Luc-OVA-B16 or B16 cells were cocultured with tumor-specific CD8⁺ T cells in the presence or absence of 10 nM perforin and granzyme B. A representative image of cell death is shown (I). Six hours later, cell viability (J) and LDH levels (K) were measured. White arrows indicate the pyroptotic cells. **P < 0.01, by one-way ANOVA (B to D, G, J, and K). Data are means \pm SD of three independent experiments.

proinflammatory factors. We found that pyroptosis supernatants rather than GSDME^{-/-} supernatants caused the cleavage and activation of GSDMD (Fig. 6D). In addition, supernatants from nontransduced tumor-specific CD8⁺ T cell that killed target tumor cells did not induce cleavage of GSDMD or caspase 1 (fig. S6E). In addition, knockout of either GSDMD or caspase 1 abolished the up-regulation of IL-1 β and IL-6 in macrophages caused by pyroptosis supernatants (Fig. 6E and fig. S6, F to H). NACHT, LRR, and PYD domains-containing

protein 3 (NLRP3) is an inflammasome form that cleaves caspase 1 in macrophages. We found that pyroptotic supernatants could not effectively induce caspase 1 cleavage and subsequent mature IL-1 β production in NLRP3^{-/-} macrophages (fig. S7, A and B). Various factors such as reactive oxygen species (ROS), ions, and adenosine 5'-triphosphate (ATP) are able to activate the NLRP3 inflammasome (30). CD19 or HER2⁺ CAR T cell treatment led to a 14- to 26-fold increase of ATP concentration in the pyroptotic supernatants (fig. S7C). However,

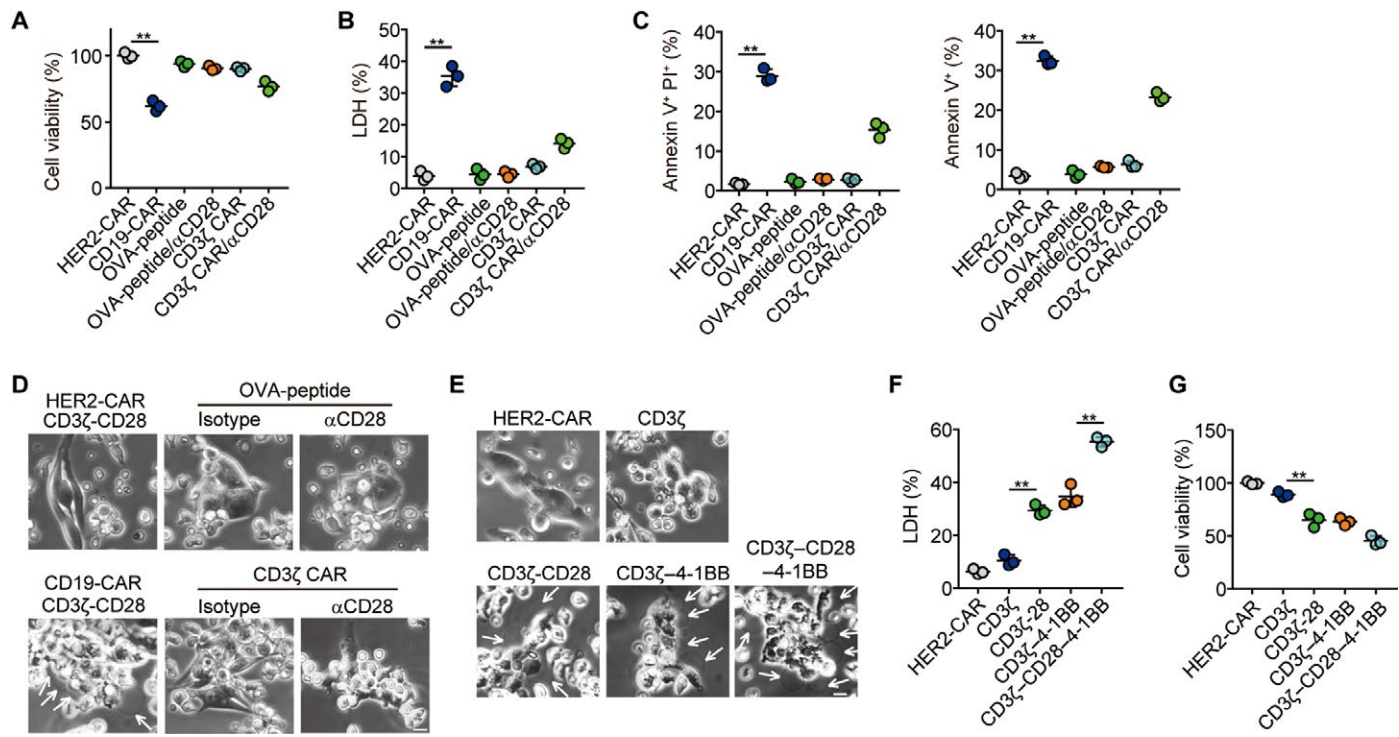


Fig. 5. Co-signaling domain(s) is important for pyroptosis by CAR T cells. (A to D) CD19-recognizing CD3ζ-CAR T cells were cocultured with CD19-expressing B16 cells in the presence of a CD28 antibody. Meanwhile, OT-I T cells were cocultured with OT-I peptide-pulsed, CD19-expressing B16 cells. CD3ζ-CD28-CAR T cells were used as a positive control. Cell viability was measured by a microplate luminometer (A), and the LDH level from the supernatant was detected (B). The percentage of annexin V⁺/PI⁺ or annexin V⁺ cells was determined by flow cytometry (C). Cell morphology was observed by microscopy (D). Scale bar, 20 μm. (E to G) CD19-B16 cells were cocultured with HER2-CAR T cells or CD3ζ, CD3ζ-CD28, CD3ζ-4-1BB, or CD3ζ-CD28-4-1BB-CD19-CAR T cells for 4 hours. Cell morphology was observed under a microscope (E). The LDH level (F) and cell viability (G) were also measured. Scale bar, 20 μm. **P < 0.01, by one-way ANOVA (A to C, F, and G). Data are means ± SD of three independent experiments.

such an increase in ATP was abrogated by the inhibition of caspase 3 or granzyme B or by the knockdown of GSDME, perforin, or granzyme B (fig. S7, D to G). Apyrase is known to effectively degrade ATP (31), and treatment of pyroptotic supernatants with apyrase degraded ATP molecules in pyroptotic supernatants (fig. S7C), and this prevented pyroptotic supernatant-treated macrophages from cleaving caspase 1, GSDMD, or IL-1β (fig. S7, H and I). A similar result was obtained in supernatants treated with Brilliant Blue G (BBG), an antagonist of the ATP-recognizing receptor P2X7 (fig. S7, H and I). Therefore, ATP from pyroptotic supernatants is sufficient to promote the release of the CRS-related cytokine IL-1β by macrophages. Cell death can cause the release of DAMPs such as heat shock proteins (HSPs) and high-mobility group box 1 (HMGB1), and these can stimulate macrophages to produce IL-6 by activating mitogen-activated protein kinase (MAPK) and nuclear factor κB (NF-κB). We found much higher levels of HMGB1 in pyroptotic supernatants, compared with the non-pyroptotic supernatants, but levels of HSP70 were not altered (fig. S7J). Stimulation of macrophages with HMGB1 up-regulated the expression of IL-6 (fig. S7, K and L). In contrast, knockdown of HMGB1 in tumor cells disrupted the effect of the pyroptotic supernatant on IL-6 expression at both the mRNA and protein levels (fig. S7, M and N), suggesting that HMGB1 induces the IL-6 production in macrophages after tumor cell pyroptosis. Thus, HMGB1 in the pyroptotic supernatants may promote IL-6 expression in macrophages. Together, these results suggest that tumor cell pyroptosis activates the GSDMD-

mediated inflammatory pathway in macrophages, leading to the release of CRS-related cytokines.

CAR T cell therapy induces CRS through GSDME-mediated pyroptosis in vivo

Last, we tried to demonstrate that GSDME-mediated pyroptosis triggers CAR T cell therapy–caused CRS in vivo. We used a CAR T cell-induced CRS mouse model that used intraperitoneal injection of Raji or NALM-6 cells into severe combined immunodeficient (SCID)-beige mice, followed by an intraperitoneal injection of human CAR T cells, as described previously (8). An acute systemic inflammatory response, highly similar to human CRS, as depicted by high fever, weight loss, and increased levels of acute-phase proteins, such as serum amyloid A3 (SAA3), IL-1β, and IL-6, was present (Fig. 7, A to E, and fig. S8, A to E). However, injection of GSDME^{-/-} Raji or NALM-6 cells in SCID-beige mice abrogated CRS symptoms upon CD19-CAR T cell treatment, as indicated by reduced weight loss, diminished fever, decreased blood levels of IL-1β, IL-6, and SAA (Fig. 7, F to H, and fig. S8, F to H), and the prevention of CRS-related mortality (Fig. 7I and fig. S8I). We also examined intravenous injection of GSDME^{-/-} Raji cells into the non-obese diabetic SCID gamma (NSG) mice, and CRS symptoms and CRS-related mortality were also abrogated by GSDME deficiency (fig. S8, J to L), suggesting that GSDME-mediated pyroptosis may contribute to CRS during CAR T cell therapy. In line with these results, the knockout of GSDME in target tumor cells resulted

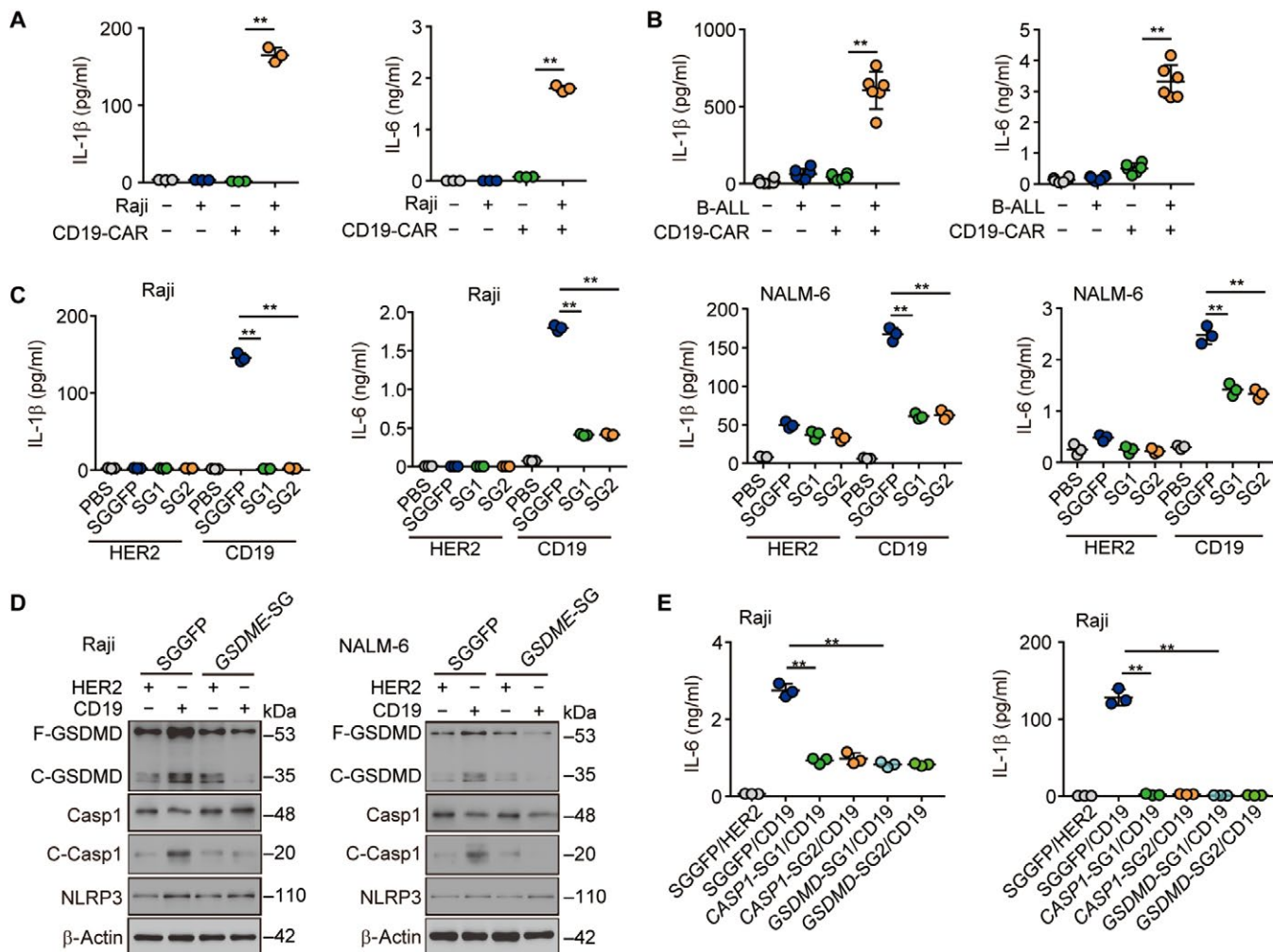


Fig. 6. Tumor cell pyroptosis triggered macrophages to release proinflammatory cytokines. (A) Macrophages isolated from healthy volunteers were treated with control or pyroptotic Raji supernatants. IL-1 β and IL-6 in the culture medium were determined by enzyme-linked immunosorbent assay (ELISA). (B) The same as (A), except that pyroptotic primary B leukemic cell supernatants were used. (C and D) Human macrophages were treated with supernatants from coculturing SGGFP or GSDME-SGs[−] Raji or NALM-6 cells with or without CD19-CAR T cells. IL-1 β and IL-6 were determined by ELISA (C), and GSDMD, Casp1, C-Casp1, and NLRP3 were analyzed by Western blot (D). (E) SGGFP, CASP1-SGs, or GSDMD-SGs[−] THP-1 cells were treated with supernatants from coculturing Raji cells and CART cells. IL-1 β and IL-6 were determined by ELISA. ** $P < 0.01$, by one-way ANOVA (A to C and E). Data are means \pm SD of three independent experiments.

in a decreased serum ATP level in the CAR T cell–treated mice (fig. S8M). In addition, we found that the use of apyrase or BBG also abrogated the above CAR T cell therapy–induced CRS and prolonged survival (fig. S9, A to D), further suggesting that the CAR T cell–induced CRS is mediated through the GSDME-ATP pathway. The analysis of peritoneal macrophages confirmed the activation of caspase 1 and GSDMD (Fig. 7J) and the up-regulation of IL-1 β , IL-6, and SAA (Fig. 7, C to E) in the CAR T cell–treated mice. In contrast, the depletion of macrophages or the administration of a caspase 1 inhibitor prevented CAR T cell–associated CRS, as evidenced by decreased levels of SAA, IL-6, and IL-1 β ; reduced weight loss; diminished fever; and prolonged survival (Fig. 7, K to M). However, this prevention of CRS could be abolished by the intraperitoneal injection of exogenous wild-type (WT) macrophages but not *Gsdmd*^{−/−} or *Casp1*^{−/−} macrophages (fig. S9, E to H). To further validate these results in patients, we analyzed the GSDME levels in primary B-ALL leukemia cells isolated

from 11 patients before CD19-CAR T cell treatment. Although B leukemic cells from patients ubiquitously expressed GSDME (Fig. 7N), a higher level of GSDME was associated with a more severe case of CRS in those patients (Fig. 7O). ATP levels were found to be much higher in CRS patients than in healthy volunteers (fig. S9I). Moreover, patients with a high grade of CRS ($n = 7$) had higher blood LDH levels, compared with those with low grade of CRS ($n = 4$) (fig. S9J), and LDH levels positively correlated to the severity of CRS (Fig. 7P). Together, these results suggest that B leukemic cell pyroptosis induced by CAR T cell therapy triggers CRS in patients.

DISCUSSION

Genetic modification confers CAR T cells an enhanced ability to kill target tumor cells. The effects of the resulting massive tumor cell death on patients remain unclear. In this study, we show that CAR

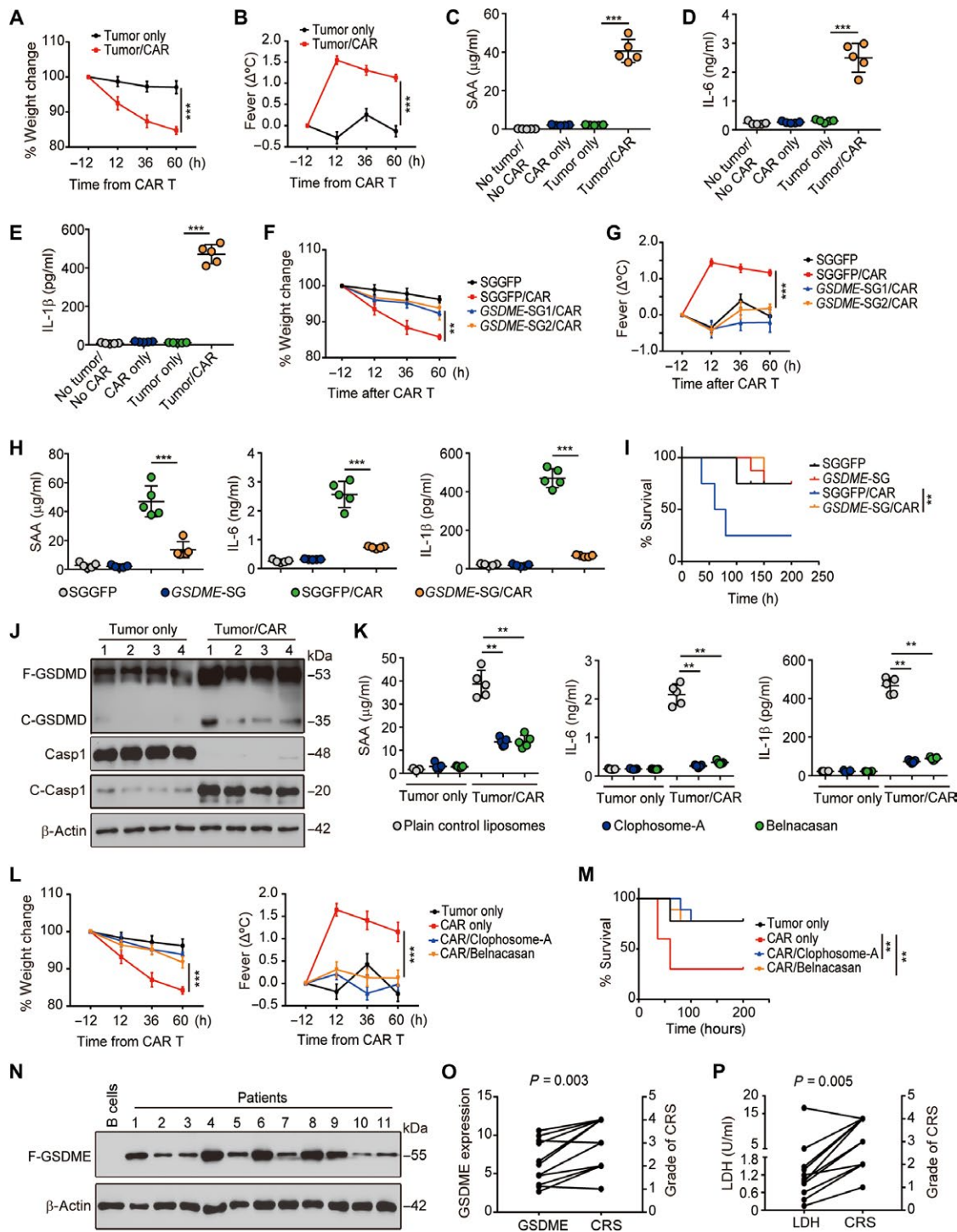


Fig. 7. Tumor cell pyroptosis triggers CRS in CAR T cell-treated mice. (A to E) CD19-CAR T cells were transferred to SCID-beige mice with a high Raji tumor burden. The change of weight [(A), $n = 6$] and body temperature [(B), $n = 6$] was calculated. The serum levels of SAA (C), IL-6 (D), and IL-1 β (E) were measured by ELISA ($n = 5$). (F to I) SGGFP $^+$ or GSDME-SGs-Luc-Raji cells were intraperitoneally injected into mice for 3 weeks, followed by the intravenous injection of CD19-CAR T cells. Weight [(F), $n = 6$] and temperature [(G), $n = 6$] changes were calculated. Serum levels of SAA, IL-6, and IL-1 β were measured by ELISA [(H), $n = 5$]. Mice survival was analyzed [(I), $n = 10$]. (J) The same as (A), except that intraperitoneal macrophages were isolated to perform Western blot with anti-GSDMD, Casp1, and C-Casp1 ($n = 4$). (K to M) Mice with high Raji tumor burden were treated with a control liposome, clophosome-A (intravenous, 200 μ l), or belnacasan (100 mg/kg) once daily for 3 days, followed by CD19-CAR T cell injection. Thirty-six hours later, serum levels of SAA, IL-6, and IL-1 β were measured by ELISA [(K), $n = 5$]. Weight and temperature changes were calculated [(L), $n = 6$]. Mouse survival was recorded [(M), $n = 10$]. (N) Primary B leukemic cells isolated from B-ALL patients ($n = 11$) were lysed for Western blot against GSDME. (O) Correlation between GSDME expression and grade of CRS ($n = 11$). (P) Correlation between LDH level and CRS grade ($n = 11$). ** $P < 0.01$, *** $P < 0.001$, by Student's t test (A and B), one-way ANOVA (C to H, K, and L) or by log-rank survival analysis (I and M). Data are means \pm SD.

T cells, by virtue of their release of a large amount of perforin and granzyme B, activate the caspase 3–GSDME pathway in B leukemic cells, leading to cell pyroptosis and subsequent CRS. CAR T cells have been observed to undergo an expansion process and reach an extremely high frequency at a certain time point *in vivo*. Thus, within a relatively short time, most targeted cells could undergo pyroptosis, causing stimulated macrophages to produce IL-6 and IL-1 β via activated caspase 1 and thus triggering CRS. The elucidation of this molecular mechanism provides an insight into the clinical observation that CRS severity is associated with the CAR T cell number and B leukemic cell burden during the CAR T cell therapy (5, 10–12).

The detection of GSDME expression in human B leukemic, MCF-7 breast cancer, and murine B16 melanoma cells is unexpected because it functions as a pore-forming protein, and its activation is potentially dangerous and may result in cell death. It has been reported that GSDME is not expressed in many detected tumor cell lines (17). In line with this, the promoter region of the *GSDME* gene displays a hypermethylation state (32, 33), thus indicating that the *GSDME* gene is silenced epigenetically in cells. GSDME is considered a tumor suppressor gene capable of inducing programmed cell death as a result of caspase 3 cleavage, and tumor cells may have evolved epigenetic means to silence GSDME expression to allow tumorigenesis. However, the high expression of GSDME in B leukemic cells and other tumor cells hints that GSDME probably exerts an alternative function to pore formation in tumor cells. The manner by which GSDME expression overcomes hypermethylation regulation and whether GSDME has a conventional function apart from pore formation are currently being investigated.

An important finding in this study is that CAR T cells release more perforin/granzyme B than nontransduced natural T cells. The release of cytolytic effector molecules by T cells relies on activation by two signals, MHC-antigenic peptide-TCR (signal 1) and CD80/CD86-CD28 (signal 2). Full activation of signal 2 relies on the activation strength of the TCR signaling. TCR signaling-activated LCK (light chain kinase) phosphorylates CD28 tyrosine residues; meanwhile, TCR signaling-activated LAT (linker of activated T cells) and SLP-76 phosphorylate and activate the key CD28 downstream signal molecule PLC- γ (phospholipase C- γ), thus degrading PIP₂ (phosphatidylinositol 4,5-bisphosphate) into DAG (diacylglycerol) and IP₃ (inositol 1,4,5-trisphosphate). On the basis of the understanding of T cell activation and the advances in genetic engineering, synthetic CARs are designed for human T cells. The basic concept for designing a CAR is to link a single-chain variable fragment (scFv) to CD3 ζ intracellular signaling module to induce T cell activation upon antigen binding. Currently, this modular structure has been extended from a single CD3 ζ signaling domain to the CD3 ζ -CD28, CD3 ζ -4-1BB, or CD3 ζ -CD28-4-1BB signaling domains to mimic both signal 1 and signal 2 (3). Because the affinity of CAR and its antigen may be 100-fold higher than that of the TCR and MHC-peptide complex (27, 28), this superior affinity plus the costimulatory signal confers CAR T cells the ability to release a large amount of perforin/granzyme B, which is required for CAR T cell-mediated target cell pyroptosis. Upon entering the cytoplasm, granzyme B may cleave procaspease 3 into its active form. Activated caspase 3 either induces apoptosis or cleaves GSDME to trigger pyroptosis through membrane pore formation. However, cells have the ability to rapidly heal pores in the plasma membrane. Whether GSDME triggers pyroptosis depends on the balance between membrane pore formation and membrane repair. Despite having the same amount of GSDME in target cells, natural TCR CD8 $^{+}$

T cells cause only low levels of cleaved GSDME, but CAR T cells release higher levels of perforin/granzyme B and result in a more activated GSDME.

Pyroptotic lysis is highly proinflammatory due to the release of cytosolic contents that are enriched in DAMPs. In this study, we demonstrate that tumor cell pyroptosis leads to the activation of caspase 1 and GSDMD in macrophages, leading to the release of a large amount of proinflammatory cytokines and the occurrence of CRS. Among proinflammatory cytokines, IL-6 and IL-1 β are especially important. Clinically, IL-6-neutralizing antibody is widely used to prevent and/or treat the CRS in CAR T cell-treated patients (34). As a pleiotropic cytokine, IL-6 is mainly regulated at the transcriptional level by transcription factors such as NF- κ B, AP-1 (activator protein 1), and STAT3 (signal transducer and activator of transcription 3) (35). Pathogen-associated molecular patterns (PAMPs), such as lipopolysaccharide (LPS), and DAMPs, such as HSPs and HMGB1, can stimulate macrophages to produce IL-6 through activation of these transcription factors (35, 36). We found that HMGB1 is present in pyroptotic supernatants, thus directly activating IL-6 in macrophages. IL-1 β is synthesized as a precursor form, and its release depends on activation of caspase 1, which is a proinflammatory caspase that is tightly regulated by inflammasomes. Inflammasome NLRP3 has been known to be widely activated by various stimuli, including microbial toxins, particulate matter, crystals, aggregated β -amyloid, or extracellular ATP (30). In this study, we found that pyroptotic supernatants contain ATP, and treatment with a P2X7 receptor antagonist or degradation of ATP inhibited the ability of pyroptotic supernatants to activate caspase 1 in macrophages. With the help of our mouse CRS model, we further demonstrated that the knockout of GSDME in target tumor cells, depleting macrophages or inhibiting caspase 1/GSDMD, can each block the occurrence of CRS. The elucidation of this molecular pathway is fundamental to better understand toxicity associated with CAR T cell therapy. A recent study by Staedtke *et al.* (37) showed that a catecholamine blocker can inhibit macrophages from releasing proinflammatory cytokines. Thus, a combined blockade of GSDME and catecholamine may result in a better treatment of CRS without diminishing tumor clearance.

Although this study reports that CAR T cells induce target tumor cell pyroptosis through a GSDME-dependent pathway, alternative pathway(s) might exist to mediate target cell pyroptosis by CAR T cells. Recent studies have reported that CAR T cells may mobilize TNF- α to mediate the killing process, which might be independent of granzyme B and perforin (38, 39). One possibility for this finding is that CAR T cells could use a two-step strategy to attack target cells. Granzyme B and perforin launch the first wave of killing, which could be followed by TNF- α if the target cells escape the first attack. This may also explain why pyroptosis can be blocked without considerably affecting CAR T cell-mediated killing. Our present study reveals the mechanistic difference between the type of cellular death caused by CAR and natural TCR T cells, which provides an opportunity to modify CAR to reduce CRS by switching target tumor cell death from pyroptosis to apoptosis.

Study design

The primary objective of the study was to elucidate the underlying mechanism of CRS occurrence. This study is a continuation of a previous investigation (40), in which we conducted a phase 1 clinical trial to evaluate the safety and efficacy of autologous CD19-CAR T cell treatment in patients with relapsed or refractory B-ALL (R/R ALL).

CD19-CAR T cells were generated ex vivo with the use of autologous T cells transduced with CD19 TCR- ζ /4-1BB lentiviral vector to express a CAR containing a CD3 ζ domain to provide a T cell activation signal and a 4-1BB domain to provide a costimulatory signal. Patients with R/R ALL were administered CD19-CAR T cells (1×10^6 to 1×10^7 /kg) intravenously on days 0, 1, and 2 in the absence of disease progression or unacceptable toxicity. The clinical study protocol (ClinicalTrials.gov number NCT03156101) was approved by the First Affiliated Hospital of Zhengzhou University Institutional Review Board. The clinical investigation was conducted by the investigators in the First Affiliated Hospital of Zhengzhou University, and data were collected and analyzed at Institute of Basic Medical Science of Chinese Academy of Medical Sciences. All participants provided written informed consent before being enrolled in this study. For the in vitro study, CAR T or unmodified T cells were used to coculture with different tumor cells to determine tumor cell pyroptosis or apoptosis. We also used Cas9 technology to knock out different genes to elucidate how pyroptosis triggered CRS through a macrophage-dependent pathway in mouse models.

MATERIALS AND METHODS

Patients

To be eligible for participation in the study, patients had to be at least 4 years old at screening and no older than 70 years old and had been diagnosed as CD19 $^+$ relapsed or refractory B cell leukemia, who were not eligible for autologous or allogeneic stem cell transplantation and had limited prognosis (several months to <2-year survival) with currently available therapies; an Eastern Cooperative Oncology Group (ECOG) result of 0, 1, or 2; and stable vital signs. Other eligibility criteria were adequate heart, liver, and kidney function.

Human specimens

Human peripheral blood or bone marrow was obtained from patients at the First Affiliated Hospital of Zhengzhou University. Ethical permission was granted by the Clinical Trial Ethics Committee of the First Affiliated Hospital of Zhengzhou University. All patients provided written informed consent to participate in the study. The clinical features of the patients are listed in tables S1 to S5.

Animals and cell lines

Female SCID-beige or NSG mice, 6 to 8 weeks old, were purchased from the Center of Medical Experimental Animals of the Chinese Academy of Medical Science (Beijing, China). OT-I transgenic mice were gifted by H. Zhang (Sun Yat-sen University). Pmel-1 transgenic mice were presented by Y. Wan (Third Military Medical University). These animals were maintained in the Animal Facilities of Chinese Academy of Medical Science under pathogen-free conditions. THP-1 (acute monocytic leukemia cell line), SGC-7901 (gastric adenocarcinoma cell line), and MCF-7 (breast cancer cell line) and mouse tumor cell lines B16 and OVA-B16 (melanoma) were purchased from the China Center for Type Culture Collection (Beijing, China). Human tumor cell lines Raji (Burkitt's lymphoma cell line) and Nalm6 (acute lymphocytic leukemia cell line) were gifted by M. Wang (Chinese Academy of Medical Sciences and Peking Union Medical College). These cells were cultured in RPMI 1640 medium (Thermo Fisher Scientific) with 10% fetal bovine serum (FBS) (Gibco, USA), 2 mM L-glutamine (Gibco, USA), and 1% penicillin-streptomycin in a humidified atmosphere containing 5% CO₂ at 37°C.

Construction of human CD19 or HER2 $^-$ CAR T cells

The CAR for HER2 and CD19 was constructed as previously described (41, 42). In brief, the scFv fragment of HER2 from monoclonal antibody 4D5 or the scFv fragment of CD19 from clone FMC63 linked the CD8 α -chain hinge and transmembrane region with CD3 ζ and CD28 intracellular signaling domains, and this cassette was inserted into the lentiviral vector provided by the Obiooo Bioscience Company. The transduction procedure was initiated by stimulating CD8 $^+$ T cells with CD3/CD28 activator beads (Invitrogen) according to the instruction provided by the manufacturer with recombinant human IL-2 at a final concentration of 100 U/ml in X-VIVO 15 medium (Lonza) containing 5% FBS. Cells were harvested for lentiviral transduction on day 2 and resuspended in the same medium. The supernatants containing leviviruses were added to the medium at the multiplicity of infection of 1:10, and the plates were coated with RetroNectin [CH-296; Takara Bio, Otsu, Japan; coated using CH-296 (10 mg/ml)] according to the manufacturer. Then, cells were centrifuged at 1000g for 2 hours at 32°C and incubated at 37°C for 6 hours. The infection rates were quantified with flow cytometry after 2 days. In this study, the amount of CD19-CAR T cells was used according to the ratio of effector to target cells (2:1) or as indicated in the in vitro experiments. The T cells were transfected with lentivirus-CAR and cultured for 10 days for in vivo experiments. The transfection efficiency was evaluated by flow cytometry on days 3 and 5 after lentivirus transduction and at the end of culture. The transfection efficiency was around 40%. For in vitro experiments, we cultured CAR T cells for 5 to 7 days. These T cells grew logarithmically during the period of expansion. For clinical trial, we used CD3 ζ -4-1BB-CAR T. Otherwise, CD3 ζ -CD28-CAR T cells were used.

Construction of mCAR-hCD19

The sequences for mCAR-hCD19 contained the antigen receptor of human CD19 or HER2 scFv; the murine CD3 ζ , CD28, and/or 4-1BB; and the myc tag on the N terminus, as described before (43), and were synthesized by SygenTech. This chimeric antigen construct was then cloned into a murine stem cell virus-green fluorescent protein (MSCV-GFP) (Clontech) murine retroviral vector (MSCV-myc-CAR-2A). Then, the Platinum-E (Plat-E) Retroviral Packaging Cell Line, Ecotropic cells (Cell Biolabs, RV-101) were transfected with mCAR-hCD19 plasmid and pCL-Eco retrovirus packaging plasmid to obtain retrovirus containing mCAR-hCD19. OT-I CD8 $^+$ T cells were activated with anti-CD3/CD28 beads (Gibco, 11453D), IL-2 (PerproTech, 212-12), and 55 μ M β -mercaptoethanol (Gibco, 21985-023) for 24 hours. Then, OT-I CD8 $^+$ T cells were infected with the above virus in the presence of RetroNectin (Takara Bio) for 8 hours. Twenty-four hours later, the GFP-positive cells were sorted by flow cytometry using the BD Biosciences FACSAria II to obtain cells expressing high levels of hCD19 or hHER2.

CRS grades

The grading system of CRS is performed based on the clinical classification (44). In brief, grade 1 is that symptoms are not life threatening, such as fever, headache, myalgias, malaise, nausea, or fatigue; grade 2 includes symptoms that require and respond to intravenous fluids or low-dose vasopressors, grade 2 organ toxicity, or fraction of inspired oxygen less than 40%; grade 3 includes symptoms that require and respond to aggressive intervention (high-dose or multiple vasopressors), grade 3 organ toxicity or grade 4 transaminitis, or fraction of inspired oxygen equal or more than 40%; grade 4 can

manifest as life-threatening symptoms, grade 4 organ toxicity (excluding grade 4 transaminitis), or needing ventilator support; grade 5 is death. Grading of organ toxicities is performed based on CTCAE (Common Terminology Criteria for Adverse Events) v4.03 (45).

Quantification and statistical analysis

All experiments were performed at least three times. Results are expressed as means \pm SEM or means \pm SD, as indicated, and analyzed by two-tailed unpaired Student's *t* test or one-way analysis of variance (ANOVA), followed by Bonferroni's test. $P < 0.05$ was considered statistically significant. The analysis was conducted using the GraphPad 6.0 software. To analyze the correlation between the level of GSDME or LDH and the degradation of CRS, Pearson's correlation test was applied. The survival rates were performed by the log-rank test.

SUPPLEMENTARY MATERIALS

immunology.scienmag.org/cgi/content/full/5/43/eaax7969/DC1

Materials and Methods

Fig. S1. CAR T cells induced tumor cells to enter pyroptosis.

Fig. S2. GSDME-mediated CAR T cell induced tumor cell pyroptosis.

Fig. S3. Perforin/granzyme B–caspase 3–GSDME pathway–mediated CAR T cell induced tumor cell pyroptosis.

Fig. S4. Tumor-specific CD8⁺ T cells induced tumor cells to enter apoptosis, not pyroptosis.

Fig. S5. High levels of perforin and granzyme B induce tumor cell pyroptosis.

Fig. S6. Tumor cell pyroptosis activated macrophages to release inflammatory cytokines.

Fig. S7. Pyroptotic tumor cells released ATP to activate macrophages.

Fig. S8. Tumor cell pyroptosis initiated CRS induced by CAR T cell therapy *in vivo*.

Fig. S9. ATP-Casp1-GSDMD pathway regulated the CRS induced by CAR T cell therapy *in vivo*.

Table S1. The general information from patients enrolled.

Table S2. Body temperature (°C) from B-ALL patients after CD19 CAR T cell therapy.

Table S3. Serum level of IL-6 (pg/ml) from patients after CART T cell therapy.

Table S4. Serum level of IFN-γ (pg/ml) from patients after CART T cell therapy.

Table S5. Serum level of IL-10 (pg/ml) from patients after CAR T cell therapy.

Movie S1. HER2⁺ m-Cherry–MCF-7 cells were cocultured with HER2-CAR T cells.

Movie S2. HER2⁺ m-Cherry–SGC-7901 cells were cocultured with HER2-CAR T cells.

[View/request a protocol for this paper from Bio-protocol.](#)

REFERENCES AND NOTES

- S. S. Neelapu, F. L. Locke, N. L. Bartlett, L. J. Lekakis, D. B. Miklos, C. A. Jacobson, I. Braunschweig, O. O. Oluwole, T. Siddiqi, Y. Lin, J. M. Timmerman, P. J. Stiff, J. W. Friedberg, I. W. Flinn, A. Goy, B. T. Hill, M. R. Smith, A. Deol, U. Farooq, P. McSweeney, J. Munoz, I. Avivi, J. E. Castro, J. R. Westin, J. C. Chavez, A. Ghobadi, K. V. Komanduri, R. Levy, E. D. Jacobsen, T. E. Witzig, P. Reagan, A. Bot, J. Rossi, L. Navale, Y. Jiang, J. Aycock, M. Elias, D. Chang, J. Wiezorek, W. Y. Go, Axicabtagene ciloleucel CAR T-cell therapy in refractory large B-cell lymphoma. *N. Engl. J. Med.* **377**, 2531–2544 (2017).
- S. L. Maude, T. W. Laetsch, J. Buechner, S. Rives, M. Boyer, H. Bittencourt, P. Bader, M. R. Verneris, H. E. Stefanski, G. D. Myers, M. Qayed, B. De Moerloose, H. Hiramatsu, K. Schlis, K. L. Davis, P. L. Martin, E. R. Nemecek, G. A. Yanik, C. Peters, A. Baruchel, N. Boissel, F. Mechinaud, A. Baldazzi, J. Krueger, C. H. June, B. L. Levine, P. Wood, T. Tarhan, M. Leung, K. T. Mueller, Y. Zhang, K. Sen, D. Lebwohl, M. A. Pulsipher, S. A. Grupp, Tisagenlecleucel in children and young adults with B-cell lymphoblastic leukemia. *N. Engl. J. Med.* **378**, 439–448 (2018).
- M. Sadelain, I. Rivière, S. Riddell, Therapeutic T cell engineering. *Nature* **545**, 423–431 (2017).
- C. L. Bonifant, H. J. Jackson, R. J. Brentjens, K. J. Curran, Toxicity and management in CAR T-cell therapy. *Mol. Ther. Oncolytics* **3**, 16011 (2016).
- M. L. Davila, I. Riviere, X. Wang, S. Bartido, J. Park, K. Curran, S. S. Chung, J. Stefanski, O. Borquez-Ojeda, M. Olszewska, J. Ou, T. Wasieleswska, Q. He, M. Fink, H. Shinglot, M. Youssif, M. Satter, Y. Wang, J. Hosey, H. Quintanilla, E. Halton, Y. Bernal, D. C. Bouhassira, M. E. Arcila, M. Gonen, G. J. Roboz, P. Maslak, D. Douer, M. G. Frattini, S. Giralt, M. Sadelain, R. Brentjens, Efficacy and toxicity management of 19-28z CART cell therapy in B cell acute lymphoblastic leukemia. *Sci. Transl. Med.* **6**, 224ra225 (2014).
- N. Frey, Cytokine release syndrome: Who is at risk and how to treat. *Best Pract. Res. Clin. Haematol.* **30**, 336–340 (2017).
- D. T. Teachey, S. F. Lacey, P. A. Shaw, J. J. Melenhorst, S. L. Maude, N. Frey, E. Pequignot, V. E. Gonzalez, F. Chen, J. Finklestein, D. M. Barrett, S. L. Weiss, J. C. Fitzgerald, R. A. Berg, R. Aplenc, C. Callahan, S. R. Rheingold, Z. Zheng, S. Rose-John, J. C. White, F. Nazimuddin, G. Wertheim, B. L. Levine, C. H. June, D. L. Porter, S. A. Grupp, Identification of predictive biomarkers for cytokine release syndrome after chimeric antigen receptor T-cell therapy for acute lymphoblastic leukemia. *Cancer Discov.* **6**, 664–679 (2016).
- T. Giavridis, S. J. C. van der Stegen, J. Eyquem, M. Hamieh, A. Piersigilli, M. Sadelain, CAR T cell-induced cytokine release syndrome is mediated by macrophages and abated by IL-1 blockade. *Nat. Med.* **24**, 731–738 (2018).
- M. Norelli, B. Camisa, G. Barbiera, L. Falcone, A. Purevdorj, M. Genua, F. Sanvito, M. Ponzoni, C. Doglioni, P. Cristofori, C. Traversari, C. Bordignon, F. Ciceri, R. Ostuni, C. Bonini, M. Casucci, A. Bondanza, Monocyte-derived IL-1 and IL-6 are differentially required for cytokine-release syndrome and neurotoxicity due to CAR T cells. *Nat. Med.* **24**, 739–748 (2018).
- S. L. Maude, N. Frey, P. A. Shaw, R. Aplenc, D. M. Barrett, N. J. Bunin, A. Chew, V. E. Gonzalez, Z. Zheng, S. F. Lacey, Y. D. Mahnke, J. J. Melenhorst, S. R. Rheingold, A. Shen, D. T. Teachey, B. L. Levine, C. H. June, D. L. Porter, S. A. Grupp, Chimeric antigen receptor T cells for sustained remissions in leukemia. *N. Engl. J. Med.* **371**, 1507–1517 (2014).
- D. W. Lee, J. N. Kochenderfer, M. Stetler-Stevenson, Y. K. Cui, C. Delbrook, S. A. Feldman, T. J. Fry, R. Orentas, M. Sabatino, N. N. Shah, S. M. Steinberg, D. Stroncek, N. Tscherneia, C. Yuan, H. Zhang, L. Zhang, S. A. Rosenberg, A. S. Wayne, C. L. Mackall, T cells expressing CD19 chimeric antigen receptors for acute lymphoblastic leukaemia in children and young adults: A phase 1 dose-escalation trial. *Lancet* **385**, 517–528 (2015).
- J. H. Park, I. Rivière, M. Gonen, X. Wang, B. Senechal, K. J. Curran, C. Sauter, Y. Wang, B. Santomasso, E. Mead, M. Roshal, P. Maslak, M. Davila, R. J. Brentjens, M. Sadelain, Long-term follow-up of CD19 CAR therapy in acute lymphoblastic leukemia. *N. Engl. J. Med.* **378**, 449–459 (2018).
- J. Shi, W. Gao, F. Shao, Pyroptosis: Gasdermin-mediated programmed necrotic cell death. *Trends Biochem. Sci.* **42**, 245–254 (2017).
- D. Wallach, T.-B. Kang, C. P. Dillon, D. R. Green, Programmed necrosis in inflammation: Toward identification of the effector molecules. *Science* **352**, aaf2154 (2016).
- J. Lin, S. Kumar, C. Kim, T.-M. Van, L. Wachsmuth, A. Polykratis, M. Pasparakis, RIPK1 counteracts ZBP1-mediated necroptosis to inhibit inflammation. *Nature* **540**, 124–128 (2016).
- J. Yuan, P. Amin, D. Ofengheim, Necroptosis and RIPK1-mediated neuroinflammation in CNS diseases. *Nat. Rev. Neurosci.* **20**, 19–33 (2019).
- Y. Wang, W. Gao, X. Shi, J. Ding, W. Liu, H. He, K. Wang, F. Shao, Chemotherapy drugs induce pyroptosis through caspase-3 cleavage of a gasdermin. *Nature* **547**, 99–103 (2017).
- S. Rühl, K. Shkarina, B. Demarco, R. Heilig, J. C. Santos, P. Broz, ESCRT-dependent membrane repair negatively regulates pyroptosis downstream of GSDMD activation. *Science* **362**, 956–960 (2018).
- U. Ros, A. Peña-Blanco, K. Hänggi, U. Kunzendorf, S. Krautwald, W. W.-L. Wong, A. J. García-Sáez, Necroptosis execution is mediated by plasma membrane nanopores independent of calcium. *Cell Rep.* **19**, 175–187 (2017).
- J. Ding, K. Wang, W. Liu, Y. She, Q. Sun, J. Shi, H. Sun, D.-C. Wang, F. Shao, Pore-forming activity and structural autoinhibition of the gasdermin family. *Nature* **535**, 111–116 (2016).
- J. Shi, Y. Zhao, K. Wang, X. Shi, Y. Wang, H. Huang, Y. Zhuang, T. Cai, F. Wang, F. Shao, Cleavage of GSDMD by inflammatory caspases determines pyroptotic cell death. *Nature* **526**, 660–665 (2015).
- Y. Liu, T. Zhang, Y. Zhou, J. Li, X. Liang, N. Zhou, J. Lv, J. Xie, F. Cheng, Y. Fang, Y. Gao, N. Wang, B. Huang, Visualization of perforin/gasdermin/complement-formed pores in real cell membranes using atomic force microscopy. *Cell. Mol. Immunol.* **16**, 611–620 (2019).
- X. Yang, H. R. Stennicke, B. Wang, D. R. Green, R. U. Janicke, A. Srinivasan, P. Seth, G. S. Salvesen, C. J. Froelich, Granzyme B mimics apical caspases. Description of a unified pathway for trans-activation of executioner caspase-3 and -7. *J. Biol. Chem.* **273**, 34278–34283 (1998).
- S. S. Metkar, B. Wang, M. L. Ebbs, J. H. Kim, Y. J. Lee, S. M. Raja, C. J. Froelich, Granzyme B activates procaspase-3 which signals a mitochondrial amplification loop for maximal apoptosis. *J. Cell Biol.* **160**, 875–885 (2003).
- I. Voskoboinik, J. C. Whisstock, J. A. Trapani, Perforin and granzymes: Function, dysfunction and human pathology. *Nat. Rev. Immunol.* **15**, 388–400 (2015).
- A. H. Greenberg, Activation of apoptosis pathways by granzyme B. *Cell Death Differ.* **3**, 269–274 (1996).
- J. D. Stone, A. S. Chervin, D. M. Kranz, T-cell receptor binding affinities and kinetics: Impact on T-cell activity and specificity. *Immunology* **126**, 165–176 (2009).
- M. Chmielewski, A. Hombach, C. Heuser, G. P. Adams, H. Abken, T cell activation by antibody-like immunoreceptors: Increase in affinity of the single-chain fragment domain above threshold does not increase T cell activation against antigen-positive target cells but decreases selectivity. *J. Immunol.* **173**, 7647–7653 (2004).
- J. A. Lopez, O. Susanto, M. R. Jenkins, N. Lukyanova, V. R. Sutton, R. H. Law, A. Johnston, C. H. Bird, P. I. Bird, J. C. Whisstock, J. A. Trapani, H. R. Saibil, I. Voskoboinik, Perforin forms

- transient pores on the target cell plasma membrane to facilitate rapid access of granzymes during killer cell attack. *Blood* **121**, 2659–2668 (2013).
30. O. Gross, C. J. Thomas, G. Guarda, J. Tschopp, The inflammasome: An integrated view. *Immunol. Rev.* **243**, 136–151 (2011).
 31. F. Ghiringhelli, L. Apetoh, A. Tesniere, L. Aymeric, Y. Ma, C. Ortiz, K. Vermaelen, T. Panaretakis, G. Mignot, E. Ullrich, J.-L. Perfettini, F. Schlemmer, E. Tasdemir, M. Uhl, P. Génin, A. Civas, B. Ryffel, J. Kanellopoulos, J. Tschopp, F. André, R. Lidereau, N. M. McLaughlin, N. M. Haynes, M. J. Smyth, G. Kroemer, L. Zitvogel, Activation of the NLRP3 inflammasome in dendritic cells induces IL-1 β -dependent adaptive immunity against tumors. *Nat. Med.* **15**, 1170–1178 (2009).
 32. M. S. Kim, X. Chang, K. Yamashita, J. K. Nagpal, J. H. Baek, G. Wu, B. Trink, E. A. Ratovitski, M. Mori, D. Sidransky, Aberrant promoter methylation and tumor suppressive activity of the DFNA5 gene in colorectal carcinoma. *Oncogene* **27**, 3624–3634 (2008).
 33. K. Akino, M. Toyota, H. Suzuki, T. Imai, R. Maruyama, M. Kusano, N. Nishikawa, Y. Watanabe, Y. Sasaki, T. Abe, E. Yamamoto, I. Tarasawa, T. Sonoda, M. Mori, K. Imai, Y. Shinomura, T. Tokino, Identification of DFNA5 as a target of epigenetic inactivation in gastric cancer. *Cancer Sci.* **98**, 88–95 (2007).
 34. C. H. June, M. Sadelain, Chimeric antigen receptor therapy. *N. Engl. J. Med.* **379**, 64–73 (2018).
 35. S. Kang, T. Tanaka, M. Narazaki, T. Kishimoto, Targeting interleukin-6 signaling in clinic. *Immunity* **50**, 1007–1023 (2019).
 36. U. Andersson, H. Wang, K. Palmblad, A. C. Aveberger, O. Bloom, H. Erlandsson-Harris, A. Janson, R. Kokkola, M. Zhang, H. Yang, K. J. Tracey, High mobility group 1 protein (HMG-1) stimulates proinflammatory cytokine synthesis in human monocytes. *J. Exp. Med.* **192**, 565–570 (2000).
 37. V. Staedtke, R.-Y. Bai, K. Kim, M. Darvas, M. L. Davila, G. J. Riggins, P. B. Rothman, N. Papadopoulos, K. W. Kinzler, B. Vogelstein, S. Zhou, Disruption of a self-amplifying catecholamine loop reduces cytokine release syndrome. *Nature* **564**, 273–277 (2018).
 38. J. Michie, P. A. Beavis, A. J. Freeman, S. J. Vervoort, K. M. Ramsbottom, V. Narasimhan, E. J. Lelliott, N. Lalaoui, R. G. Ramsay, R. W. Johnstone, J. Silke, P. K. Darcy, I. Voskoboinik, C. J. Kearney, J. Oliaro, Antagonism of IAPs enhances CAR T-cell efficacy. *Cancer Immunol. Res.* **7**, 183–192 (2019).
 39. C. J. Kearney, S. J. Vervoort, S. J. Hogg, K. M. Ramsbottom, A. J. Freeman, N. Lalaoui, L. Pijpers, J. Michie, K. K. Brown, D. A. Knight, V. Sutton, P. A. Beavis, I. Voskoboinik, P. K. Darcy, J. Silke, J. A. Trapani, R. W. Johnstone, J. Oliaro, Tumor immune evasion arises through loss of TNF sensitivity. *Sci. Immunol.* **3**, eaar3451 (2018).
 40. Y. Liu, X. Chen, D. Wang, H. Li, J. Huang, Z. Zhang, Y. Qiao, H. Zhang, Y. Zeng, C. Tang, S. Yang, X. Wan, Y. H. Chen, Y. Zhang, Hemofiltration successfully eliminates severe cytokine release syndrome following CD19 CAR-T-cell therapy. *J. Immunother.* **41**, 406–410 (2018).
 41. R. A. Morgan, J. C. Yang, M. Kitano, M. E. Dudley, C. M. Laurencot, S. A. Rosenberg, Case report of a serious adverse event following the administration of T cells transduced with a chimeric antigen receptor recognizing ERBB2. *Mol. Ther.* **18**, 843–851 (2010).
 42. M. C. Milone, J. D. Fish, C. Carpenito, R. G. Carroll, G. K. Binder, D. Teachey, M. Samanta, M. Lakhal, B. Gloss, G. Danet-Desnoyers, D. Campana, J. L. Riley, S. A. Grupp, C. H. June, Chimeric receptors containing CD137 signal transduction domains mediate enhanced survival of T cells and increased antileukemic efficacy in vivo. *Mol. Ther.* **17**, 1453–1464 (2009).
 43. J. Chen, I. F. López-Moyado, H. Seo, C.-J. Lio, L. J. Hemplerman, T. Sekiya, A. Yoshimura, J. P. Scott-Browne, A. Rao, NR4A transcription factors limit CAR T cell function in solid tumours. *Nature* **567**, 530–534 (2019).
 44. S. S. Neelapu, S. Tummala, P. Kebrabaei, W. Wierda, C. Gutierrez, F. L. Locke, K. V. Komanduri, Y. Lin, N. Jain, N. Daver, J. Westin, A. M. Gulbis, M. E. Loghin, J. F. de Groot, S. Adkins, S. E. Davis, K. Rezvani, P. Hwu, E. J. Shpall, Chimeric antigen receptor T-cell therapy—Assessment and management of toxicities. *Nat. Rev. Clin. Oncol.* **15**, 47–62 (2017).
 45. U.S. Department of Health and Human Services, *Common Terminology Criteria for Adverse Events (CTCAE) Version 5.0* (U.S. Department of Health and Human Services, 2010).

Acknowledgments: We would like to thank all the participants and the staff at the First Affiliated Hospital of Zhengzhou University, Affiliated Cancer Hospital of Zhengzhou University, Peking University People's Hospital, and Union Hospital of Tongji Medical College for their support and aid during our study. **Funding:** This work was supported by the National Natural Science Foundation of China (817788101, 81661128007, 81530080, 81773062, 91942314) and Chinese Academy of Medical Sciences (CAMS) Initiative for Innovative Medicine (CAMS-I2M) 2017-I2M-1-001 and 2016-I2M-1-007. **Author contributions:** B.H. conceived the project. Y.L., Y.F., X.C., Z.W., X.L., T.Z., M.L., N.Z., J.L., K.T., J.X., Y.G., F.C., Y.Zhou, Z.Z., and Y.H. performed the experiments. B.H., Y.L., Y.F., X.C., X.Z., Q.G., and Y.Zhang developed methodology. B.H., Y.L., and Y.F. performed data analysis. Y.L. and Y.F. did the statistical analysis. B.H. and Y.L. wrote the manuscript. **Competing interests:** The authors declare that they have no competing financial interests. **Data and materials availability:** All data needed to evaluate the conclusions in the paper are present in the paper or the Supplementary Materials. Materials described in the study are either commercially available or on request from the corresponding author.

Submitted 23 April 2019
Resubmitted 28 August 2019
Accepted 19 December 2019
Published 17 January 2020
10.1126/sciimmunol.aax7969

Citation: Y. Liu, Y. Fang, X. Chen, Z. Wang, X. Liang, T. Zhang, M. Liu, N. Zhou, J. Lv, K. Tang, J. Xie, Y. Gao, F. Cheng, Y. Zhou, Z. Zhang, Y. Hu, X. Zhang, Q. Gao, Y. Zhang, B. Huang, Gasdermin E-mediated target cell pyroptosis by CAR T cells triggers cytokine release syndrome. *Sci. Immunol.* **5**, eaax7969 (2020).

CANCER THERAPY

A systems mechanism for KRAS mutant allele-specific responses to targeted therapy

Thomas McFall¹, Jolene K. Diedrich^{2,3}, Meron Mengistu⁴, Stacy L. Littlechild¹, Kendra V. Paskvan¹, Laura Sisk-Hackworth¹, James J. Moresco², Andrey S. Shaw⁴, Edward C. Stites^{1*}

Cancer treatment decisions are increasingly guided by which specific genes are mutated within each patient's tumor. For example, agents inhibiting the epidermal growth factor receptor (EGFR) benefit many colorectal cancer (CRC) patients, with the general exception of those whose tumor includes a KRAS mutation. However, among the various KRAS mutations, that which encodes the G13D mutant protein (KRAS^{G13D}) behaves differently; for unknown reasons, KRAS^{G13D} CRC patients benefit from the EGFR-blocking antibody cetuximab. Controversy surrounds this observation, because it contradicts the well-established mechanisms of EGFR signaling with regard to RAS mutations. Here, we identified a systems-level, mechanistic explanation for why KRAS^{G13D} cancers respond to EGFR inhibition. A computational model of RAS signaling revealed that the biophysical differences between the three most common KRAS mutants were sufficient to generate different sensitivities to EGFR inhibition. Integrated computation with experimentation then revealed a nonintuitive, mutant-specific dependency of wild-type RAS activation by EGFR that is determined by the interaction strength between KRAS and the tumor suppressor neurofibromin (NF1). KRAS mutants that strongly interacted with and competitively inhibited NF1 drove wild-type RAS activation in an EGFR-independent manner, whereas KRAS^{G13D} weakly interacted with and could not competitively inhibit NF1 and, thus, KRAS^{G13D} cells remained dependent on EGFR for wild-type RAS activity. Overall, our work demonstrates how systems approaches enable mechanism-based inference in genomic medicine and can help identify patients for selective therapeutic strategies.

INTRODUCTION

Cancer treatment decisions are increasingly influenced by which specific genes are mutated within each patient. This has been referred to as personalized medicine, precision medicine, and genomic medicine. One example of personalized medicine in cancer involves the use of epidermal growth factor receptor (EGFR)-blocking antibodies and inhibitors in colorectal cancer (CRC) patients. Clinical trials have shown that humanized therapeutic antibodies that target EGFR, like cetuximab and panitumumab, provide a survival benefit to CRC patients (1, 2). These drugs are now approved for CRC patients, except for those with KRAS mutations.

About 40% of patients with CRC have an acquired KRAS mutation within their tumor (3). The Ras family of guanosine triphosphatases (GTPases)—HRAS, NRAS, and KRAS—serve as key nodes in the EGFR signaling network (Fig. 1A). The signals that propagate from Ras to its effectors, like the RAF family of kinases, during the course of EGFR signaling can also be initiated by constitutively active mutant KRAS proteins. These mutant KRAS proteins are not dependent on EGFR for their activation (4). Thus, it seemed logical that the presence of a constitutively active mutant KRAS would indicate resistance to anti-EGFR agents. Clinical trials concluded that CRC patients with constitutively active mutant KRAS do not benefit from anti-EGFR agents (5, 6). This relationship between EGFR inhibitors, KRAS mutations, and CRC appears consistent with the conventional understanding of EGFR signaling.

However, multiple studies that evaluated whether there were differences between the common, constitutively active KRAS mutants

suggest that the relationship between oncogenic KRAS mutants and the response to EGFR inhibitors is more complicated. Initially, a retrospective analysis of phase 3 clinical trial data found that the anti-EGFR agent cetuximab benefited CRC patients with a KRAS G13D mutation, but not patients with any other KRAS mutation (7). Although this claim has been further supported with additional clinical trials and experimental model systems (7–9), the finding remains controversial because it is difficult to reconcile known principles of Ras biology with KRAS G13D patients responding differently (4, 10–12). Without a mechanism, expert opinion has been to consider the KRAS G13D mutation equivalent to other KRAS mutations and to assume that patients with the KRAS G13D mutation would not benefit from anti-EGFR agents, despite the evidence to the contrary. Resolving this problem has the potential to benefit a large number of cancer patients. For example, there are about 10,000 new cases of KRAS G13D CRC in the United States alone (13, 14).

Here, we performed a computational and experimental investigation of this problem. Applying our previously described computational systems biology methods for studying Ras mutant proteins (15) revealed that the controversial KRAS G13D behavior that has been interpreted to be inconsistent with known mechanisms of Ras biology is actually fully consistent with known mechanisms of Ras biology. Our model suggests that cancers with the G13D mutant are more sensitive to EGFR inhibition because the amount of active, cellular, wild-type (WT) guanosine triphosphate (GTP)-bound Ras (RasGTP) decreases in G13D cancers much more than in cancers with other Ras mutations. The model also suggests that the key difference between G13D and the other common Ras mutants is that G13D does not bind well to the tumor suppressor neurofibromin (NF1) and that a strong interaction with NF1 leads to the competitive inhibition of its GTPase activating protein (GAP) activity and increased WT RasGTP levels in an EGFR-independent manner, whereas a weak interaction with NF1 does not result in competitive inhibition of NF1 and WT RasGTP

Copyright © 2019
The Authors, some
rights reserved;
exclusive licensee
American Association
for the Advancement
of Science. No claim
to original U.S.
Government Works

¹Integrative Biology Laboratory, Salk Institute for Biological Studies, La Jolla, CA 92037, USA. ²Mass Spectrometry Core for Proteomics and Metabolomics, Salk Institute for Biological Studies, La Jolla, CA 92037, USA. ³Department of Molecular Medicine, The Scripps Research Institute, La Jolla, CA 92037, USA. ⁴Department of Research Biology, Genentech, South San Francisco, CA 94080, USA.

*Corresponding author. Email: estites@salk.edu

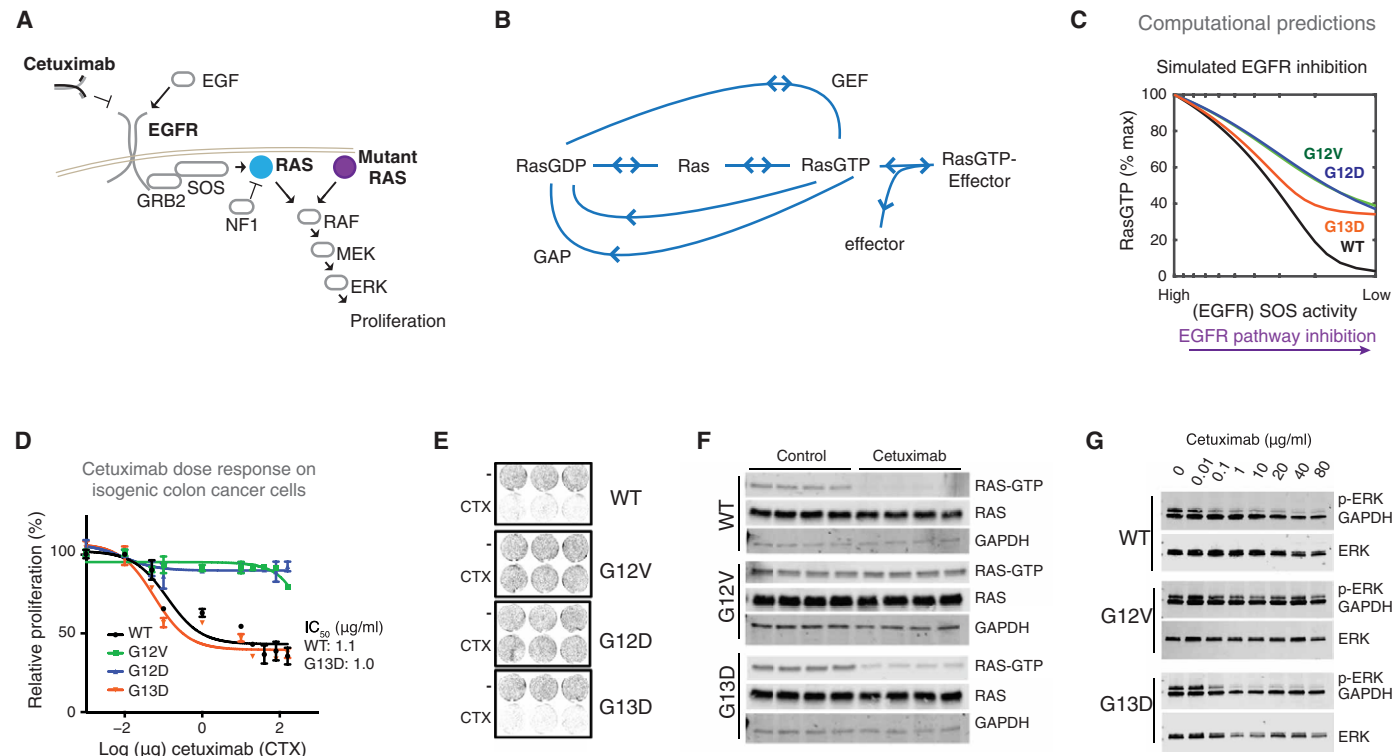


Fig. 1. The KRAS mutant-specific response to anti-EGFR agent cetuximab in CRC. (A) EGFR signals through the RASGTPases to drive proliferation. Constitutively active Ras mutants are active in an EGFR-independent manner and are known to cause resistance to EGFR inhibitors. (B) Biochemical processes that influence Ras nucleotide binding for both WT and mutant Ras proteins and that are the focus of the mathematical model. (C) Simulated anti-EGFR dose response from the computational Ras model. (D) MTT proliferation assays to assess dose responses of KRAS WT SW48 (WT) colon cancer cells and three derivative isogenic cell lines, each with one of the three most common KRAS mutants in colon cancer (G12D, G12V, and G13D), to the EGFR-blocking antibody cetuximab (CTX; at doses indicated for 48 hours). Data are means \pm SD of seven biological replicates and are representative of three experiments. (E) Two-dimensional colony formation assay for each cell line in the isogenic panel treated without or with cetuximab (20 μ g/ml) for 7 days. Images are representative of six independent experiments. (F) Ras binding domain (RBD) pull-down Ras activation assays for isogenic SW48 cells cultured without and with cetuximab [as in (E)]. Four biological replicates for each condition were included in each of three independent experiments. (G) Immunoblots of ERK phosphorylation (p-ERK) in whole-cell lysates from isogenic SW48 cells cultured in the presence of increasing concentrations of cetuximab. Blots are representative of three independent experiments.

levels remain EGFR dependent. Our experiments confirm these model predictions. Overall, this work demonstrates the power of computational systems biology approaches to address problems in personalized medicine, and it also highlights the necessity of mathematical models based on fundamental biochemistry as a tool for understanding the behaviors of biological networks that are important to disease.

RESULTS

Systems modeling of oncogenic KRAS mutants

We previously developed a mathematical model of the processes that regulate Ras signaling (15). This model is based on the well-established architecture of the Ras signaling module and the readily available biochemical rate constants of WT and mutant proteins (text S1 and fig. S1). These processes—nucleotide exchange, GTP hydrolysis, and effector binding—can be considered the “central dogma of Ras signaling.” A Ras mutant is incorporated into the computational model through the inclusion of its specific biochemical rate constants. We then simulate the reactions between Ras and its interaction partners in accordance with the accepted biochemical understanding of these processes. That is, we simulate Ras signaling in silico at the level of chemical mass action kinetics. We use model simulations to find the behaviors that logically follow from this well-accepted information

but may nevertheless be nonobvious due to the complexity and scope of the system (15, 16).

Here, we use our mathematical model to computationally investigate how Ras mutations should influence the response to EGFR inhibition. The three most common Ras mutants in CRC are G12D, G12V, and G13D (3). We updated our model, which already included G12D and G12V mutants (15), to also include the G13D mutant by incorporating the known biochemical differences between each mutant and WT Ras, as has been previously measured experimentally (fig. S1) (17, 18). We found that the available data for the G13D mutant were sufficient to result in its constitutive activation, just as the available data for G12D and G12V have been shown to be sufficient to explain these mutants’ constitutive activation (figs. S2 and S3, A and B).

We then used the model to investigate how Ras signaling networks containing each mutant would respond to EGFR inhibition. We did this by using the computational model to find the abundance of total cellular, active RasGTP that should occur for conditions of high EGFR activation [which leads to Ras activation through the Ras guanine exchange factors (GEFs) son of sevenless 1 (SOS1) and SOS2] to conditions of low EGFR activation (where low amounts of Ras activation by Ras GEFs would occur). Unexpectedly, our simulations of EGFR inhibition, which were based on the biochemical properties of these mutants, found that the G13D-containing network displayed

larger reductions in Ras signals than the G12D- and G12V-containing networks (Fig. 1B and fig. S3C). This was notable, because expert opinion had been that it did not make sense for different Ras mutants to respond differently to EGFR inhibition. Our analysis revealed that it is fully consistent with Ras central dogma for some mutants to respond more strongly to EGFR inhibition. Moreover, our analysis suggests that the available biochemical data are sufficient to explain a mechanism by which G13D would be the most sensitive of the most common KRAS mutants in CRC.

Evaluation of an experimental model system for this phenomenon

To experimentally study KRAS allele-specific differences and model predictions, we obtained a panel of isogenic CRC cells that was previously derived from the SW48 CRC cell line and was used to study the KRAS G13D response to cetuximab (7). We obtained isogenic cells with the following KRAS genotypes: G12D/WT (G12D cells), G12V/WT (G12V cells), G13D/WT (G13D cells), and WT/WT (WT cells) (fig. S4A). The mutant isogenic cells display constitutively increased amounts of active RasGTP when compared to the parental WT cells (fig. S4B), consistent with all three of these mutants being constitutively active. No statistically significant changes in extracellular signal-regulated kinase (ERK) phosphorylation were noted with the Ras mutant isogenic lines, which is consistent with other recent work on signaling within Ras mutant isogenic SW48 cells (19).

We performed dose-response experiments with the EGFR-blocking antibody cetuximab to evaluate the described difference for these cells. When treated with increasing doses of cetuximab, both the G13D and WT cells displayed reduced proliferation (Fig. 1C) and reduced colony formation (Fig. 1D and fig. S4C), whereas each in the G12D and G12V cells were not noticeably affected. We also evaluated dose responses to mitogen-activated protein kinase (MAPK) kinase (MEK) inhibitors to evaluate whether these cells were more sensitive to any inhibition of the pathway. We observed that all cell lines responded similarly to MEK inhibition (fig. S5A), suggesting that the G13D cells are not simply more sensitive to all agents that target the EGFR-RAS-ERK pathway.

We hypothesized that if there was a difference in how these cells depended on EGFR signals, then we should be able to detect net proliferation differences when these cells are cultured in medium containing low amounts of serum. Consistent with our hypothesis, we observed that G13D and WT cells proliferated more slowly than G12D and G12V cells when grown in low-serum medium, but that all cells proliferated at a similar rate when supplemental EGF was added to the medium (fig. S4D). This further suggests that G13D cells display an increased dependency on EGFR signaling compared to G12D and G12V cells. In addition, because the patterns of response appeared analogous to the clinical observations regarding KRAS genotype and response (7), the data suggest that this cell line would be useful to test our experimental model.

An alternative experimental model for this phenomenon

We desired an additional experimental system for comparing mutant-specific responses to treatment. We hypothesized that the introduction of mutant KRAS G12D or G12V into the WT Ras cells should reduce sensitivity to cetuximab, whereas the introduction of KRAS G13D would have a minimal effect on sensitivity. In our experiments, we observed that transfected KRAS G12D or G12V, but not G13D or WT, promoted resistance to cetuximab, consistent with our hypothesis

and consistent with the G13D mutant being comparably more sensitive to EGFR inhibition (fig. S6).

Experimental evaluation of predicted signaling differences

Our model suggests that there should be signaling differences between G13D cells and cells with one of the other common KRAS mutations (G12D and G12V cells). We measured the abundance of active RasGTP in cells treated with or without cetuximab, and we detected a reduction in RasGTP only in G13D and WT cells, but not in G12V cells (Fig. 1E). As RasGTP signals are transmitted downstream through the ERK MAPK cascade (Fig. 1A), we also measured phosphorylated ERK for cells treated with different doses of cetuximab. We detected reductions in the abundance of phosphorylated ERK in both the sensitive G13D and WT cells upon treatment with cetuximab but not in the resistant G12V cells (Fig. 1F). All cells displayed reductions in phosphorylated ERK when treated with a MEK inhibitor (fig. S5B). In contrast to the observed changes in ERK phosphorylation, we did not detect changes in AKT phosphorylation under treatment with cetuximab (fig. S7), consistent with little to no change in AKT phosphorylation after EGFR inhibition in nine other CRC cell lines (20).

Experimental confirmation of EGFR dependence

We performed additional experiments to confirm that the response of these isogenic SW48 cells to cetuximab was EGFR dependent. First, we used small interfering RNA (siRNA) to knock down EGFR expression in these four different isogenic cell lines (fig. S8A). We observed reduced ERK phosphorylation and reduced proliferation of the WT cells and of the G13D cells with EGFR knockdown, but no difference in the G12V or G12D cells (fig. S8, A and B). We then performed dose-response experiments with the EGFR-blocking antibody panitumumab to complement the studies with the EGFR-blocking antibody cetuximab. As with cetuximab, we observed that G13D and WT cells both displayed reduced proliferation when treated with panitumumab, whereas G12V and G12D cells were insensitive to panitumumab (fig. S9A). Immunoblots similarly observed reduced ERK phosphorylation for WT and G13D cells, but not for G12V cells (fig. S9B). To more broadly evaluate the response to agents that target EGFR, we also performed dose-response experiments using the tyrosine kinase inhibitor erlotinib, which is a small-molecule compound that targets the kinase domain of EGFR. We found G13D and WT cells to be more sensitive to erlotinib than G12V and G12D cells (fig. S10A). In contrast to our experiments with cetuximab and panitumumab (Fig. 1C and fig. S9A), G12V and G12D cells here appeared to be slightly sensitive to erlotinib (fig. S10A). Immunoblots observed reduced ERK phosphorylation for WT and G13D cells, but not G12V cells (fig. S10B), raising the possibility that the partial sensitivity of G12V (and G12D) cells may come from off-target effects.

Model prediction of differences in WT Ras activation

Our computational model includes both mutant (KRAS) and WT (KRAS, NRAS, and HRAS) pools of Ras because CRC cells express all three Ras proteins (21). The differences in total RasGTP that our model predicts (as in Fig. 1B) are accordingly distributed between GTP-bound mutant Ras proteins and GTP-bound WT Ras proteins. We queried our model to determine whether the predicted changes in signal were coming from mutant Ras, WT Ras, or both. Our simulations suggest that EGFR inhibition should cause no appreciable changes in the amount of mutant Ras bound to GTP (Fig. 2A and fig. S3D). This is consistent with the conventional wisdom that anti-EGFR

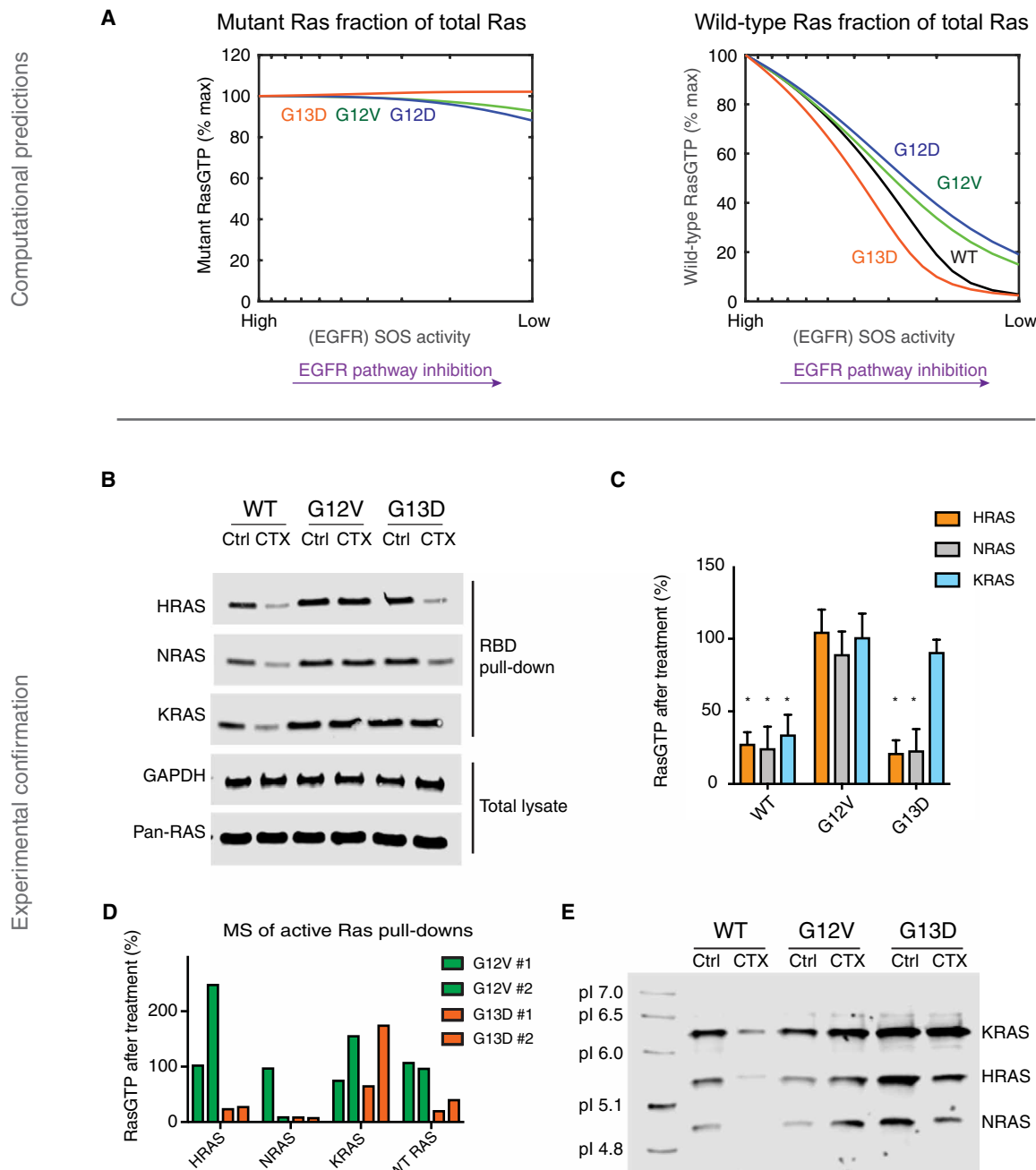


Fig. 2. The Ras model predicts, and experiments confirm, that WT Ras activation distinguishes sensitive from nonsensitive cancer cells. (A) Simulated anti-EGFR dose response for the Ras model, further subdivided to reveal the change in active, GTP-bound mutant Ras (left) and the change in active, GTP-bound WT Ras (right), within each modeled genotype. (B) RBD pull-down Ras activation assays for isogenic SW48 cells (WT, KRAS G12V, and KRAS G13D) cultured without or with cetuximab (20 µg/ml) or without cetuximab for 48 hours. Blots are representative of four independent experiments. (C) Densitometry-based quantification of the ratio of RasGTP between cetuximab-treated and untreated cells from three independent assays represented in (B). The quantified data are means \pm SD. * P < 0.05, one-way ANOVA (F = 35.22) with post hoc Tukey's test for multiple comparisons between WT or G13D cells versus G12V cells for each RAS isoform. (D) MS-based quantification of the GTP-bound WT HRAS, WT NRAS, total (both WT and mutant) KRAS, and WT H/N/KRAS in cetuximab-treated KRAS^{G12V} or KRAS^{G13D} cells relative to untreated counterparts (20 µg/ml for 48 hours). Data from two independent experiments are presented. (E) IEF of excised gel bands from RBD pull-down lysates, performed upon excised gel bands. Lysates are from isogenic SW48 cells (WT, KRAS G12V, and KRAS G13D) cultured without or with cetuximab (20 µg/ml for 48 hours). Blot is representative of three independent experiments.

agents should not influence mutant Ras signaling. However, our simulations predicted that EGFR inhibition should result in large changes in WT RasGTP (Fig. 2A and fig. S3D). This suggests that the nonobvious response to anti-EGFR agents may have a basis in WT Ras signaling.

Experimental confirmation of differences in WT Ras activation
We returned to our experimental system to test the model-based hypothesis that EGFR inhibition causes a larger drop in WT RasGTP in G13D cells than in cells with one of the other common Ras mutants. We measured Ras activation in the presence and absence of cetuximab

for each of the Ras proteins (HRAS, NRAS, and KRAS) (Fig. 2, B and C) by using antibodies specific for each form of Ras (fig. S11). We observed a large reduction in GTP-bound WT HRAS and GTP-bound WT NRAS after cetuximab treatment only in *G13D* and *WT* cells, consistent with our model's predictions. We also observed a larger reduction in GTP-bound KRAS in *WT* cells than in *G12V* and *G13D* cells, consistent with the presence of one constitutively active *KRAS* allele for the two mutant cell lines.

To complement these studies, we developed a mass spectrometry (MS) assay that could quantify the amount of active HRAS, NRAS, KRAS, and WT H/N/KRAS through the use of isotopically labeled peptides unique to HRAS, NRAS, KRAS, WT H/N/KRAS, and the *G12V* and *G13D* Ras mutants. This approach revealed greater reductions in active (GTP-bound) WT HRAS, WT NRAS, and WT H/N/KRAS in *G13D* cells treated with cetuximab than in *G12V* cells treated with cetuximab (Fig. 2D and data file S1). In addition, total (WT and mutant) KRAS in *G13D* cells displayed a partial reduction in GTP binding, consistent with one KRAS allele being WT and one KRAS allele being mutant.

We also developed an approach to differentiate between HRAS, KRAS, and NRAS through isoelectric focusing (IEF). Analysis of Ras binding domain (RBD) lysates that were further separated by IEF before immunoblotting revealed decreased relative levels of active NRAS and HRAS in isogenic *WT* and *G13D* cells treated with cetuximab, but not in *G12V* cells treated with cetuximab (Fig. 2E). In addition, active KRAS levels were most strongly reduced in *WT* cells treated with cetuximab, but did not demonstrate any reduction in the (KRAS) *G12V* and (KRAS) *G13D* cells treated with cetuximab. We also note that, in several experiments, there was an increased level of RasGTP detected within *G12V* cells treated with cetuximab. We hypothesize that this may be a temporary, rebound, increase in signal after a partial loss of negative feedback (22, 23). Together, the immunoblots, MS, and IEF demonstrate reductions in WT HRAS and NRAS GTP levels in both *WT* and *G13D* cells, but not the *G12V* cells.

Model-based identification of a determinative interaction with NF1

The behavior of each mutant in our computational model is determined by its parameter values (fig. S1). We set out to determine which specific parameter value(s) is responsible for the *G13D* mutant being more sensitive to modeled EGFR inhibition. We reasoned that it may be possible to determine which parameter(s) is responsible for sensitivity by systematically considering synthetic Ras mutants that were built from combinations of the *G12V*, *G12D*, and *G13D* parameter values. We therefore created 648 such computational Ras mutants by considering all combinations of the parameters from the *G13D*, *G12V*, and *G12D* mutants, effectively creating computational hybrid Ras mutants (Fig. 3A). We used our model to simulate dose responses to EGFR inhibition for each of 648 different computational hybrids, and then we determined whether any single parameter could distinguish between the sensitive and resistant hybrid mutant networks. Our analysis found that all hybrids that were sensitive to simulated EGFR inhibition contained the K_m value (or the enzymatic Michaelis constant) that characterizes the interaction between KRAS *G13D* and the RasGTPase activating protein (Ras GAP) NF1, and also that all mutants that were insensitive to simulated EGFR inhibition had the K_m value that applied to the *G12D* and *G12V* mutants (Fig. 3B and fig. S3E). Thus, this demonstrates that that this parameter is necessary and sufficient for sensitivity to EGFR inhibition in our systems model of Ras signaling.

Experimental confirmation of a determinative interaction with NF1

Ras GAPs like NF1 facilitate the inactivation of WT RasGTP to RasGDP, and oncogenic Ras mutants are insensitive to Ras GAPs. An increased K_m essentially indicates that the GAP cannot bind well to the mutant Ras protein. It was initially unclear to us why reduced binding to GAP would influence the response to anti-EGFR agents as we modeled all three Ras mutants to have no increase in GTP hydrolysis once bound, so binding to GAP would intuitively be inconsequential.

We set out to test these computational results that suggest that the strength of the interaction with NF1 can determine whether a cell line with a given mutation is sensitive or resistant to cetuximab. It has previously been reported that *G13D* Ras binds much less well to NF1 (17). We reproduced this impaired binding with a coimmunoprecipitation study (fig. S12A) and with bioluminescence resonance energy transfer (BRET) (fig. S12B). We hypothesized that a KRAS *G12V/G13D* hybrid mutant (GG/VD), where the glycine residues at codons 12 and 13 were replaced with a valine and aspartic acid, respectively, would be constitutively active and bind poorly to NF1. We created this mutant and, when it was transfected into parental SW48 cells, we found it to be constitutively active, as demonstrated by the presence of increased ERK phosphorylation (Fig. 3C and fig. S12C). We also found that this GG/VD combination mutant bound much less well to NF1 than KRAS *G12V* (Fig. 3C and fig. S12B).

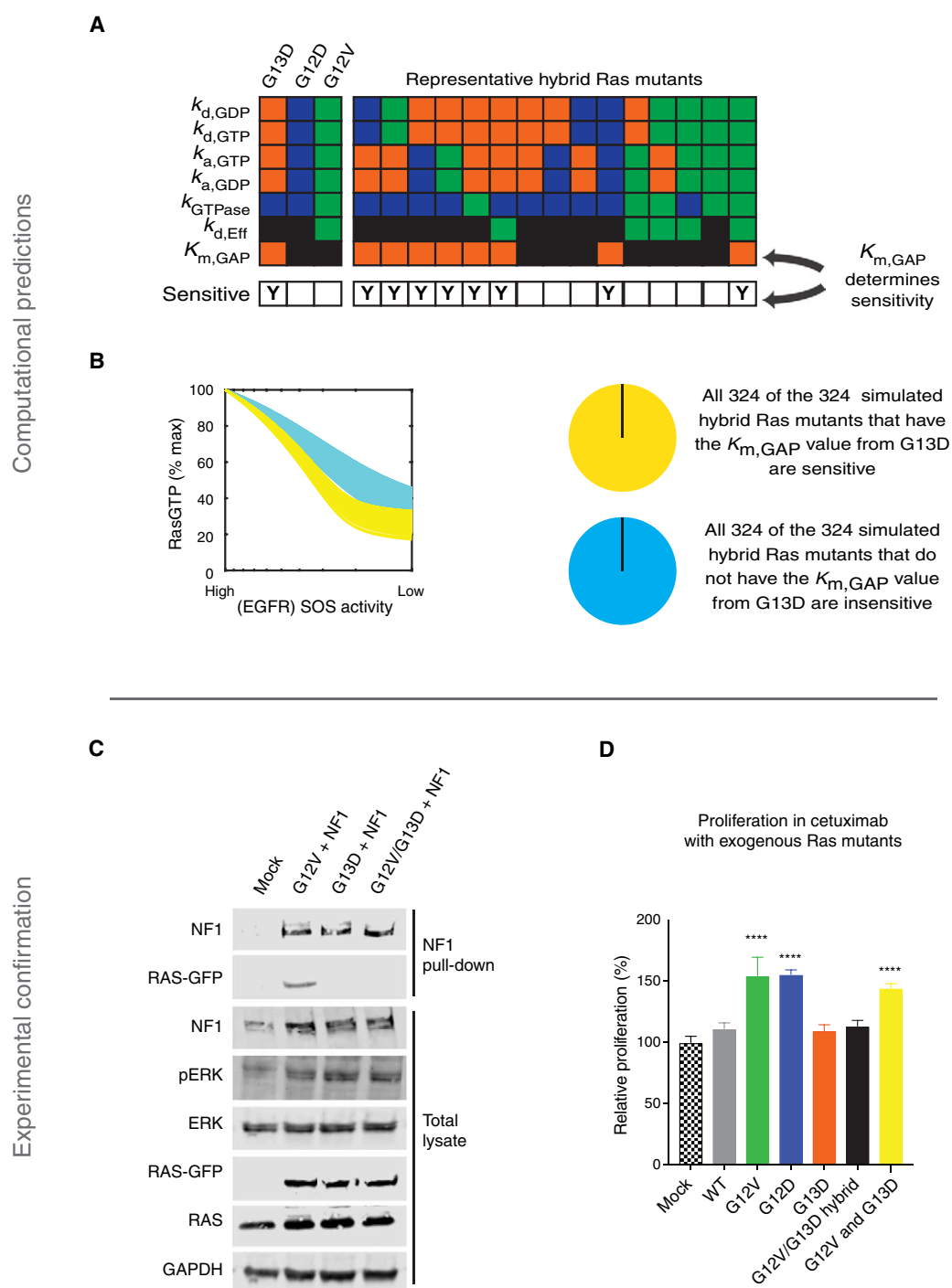
If the ability to bind NF1 is the critical factor that determines whether or not a mutant promotes resistance to cetuximab, as suggested by our model, we reasoned that the KRAS *G12V/G13D* mutant would not promote resistance to cetuximab. We used our transfection-based assay (as shown in fig. S6) to evaluate the ability of transfected Ras mutants to alter *WT* cell sensitivity to cetuximab. Consistent with our hypothesis, we observed that the *G12V/G12D* double mutant did not promote resistance, despite being constitutively active (Fig. 3D).

A mechanism for KRAS mutant allele-specific responses to EGFR inhibition

We considered how differences in the interaction between KRAS and NF1 might result in differences in network signal output. Our previous systems analysis of oncogenic Ras found that the reversible and nonproductive binding interaction between a Ras mutant and a Ras GAP can promote WT Ras activation (15), because the GAP-insensitive Ras mutant can effectively behave as a competitive inhibitor of Ras GAPs (24). Several other studies have also observed increased WT Ras when mutant Ras is present (25–27). Our new study suggests that *G13D* is an exception to this process because it binds much less well to NF1 and therefore cannot lead to WT Ras activation through the competitive inhibition of NF1 Ras GAP activity.

We therefore propose a mechanism that explains why KRAS *G13D*, but not other common KRAS mutants like *G12D* and *G12V*, responds to cetuximab (Fig. 4A). In a *WT* cell, Ras activation is dependent on EGFR and can be counteracted with EGFR inhibitors. In a *G12D* or *G12V* cell, the mutant KRAS is constitutively active. Through the competitive inhibition of the Ras GAP NF1, WT Ras is also active in an EGFR-independent manner, and the cells will be insensitive to therapeutic EGFR inhibition. In a *G13D* cell, the mutant KRAS is constitutively active and WT Ras activation is dependent on EGFR because the *G13D* mutant cannot drive WT Ras activation through the competitive inhibition of NF1. Assuming that the activation of proliferative signals downstream from Ras requires a

Fig. 3. The Ras model predicts, and experiments confirm, that mutant-specific interactions with tumor suppressor NF1 determine whether or not cells respond to anti-EGFR agents. (A) Schematic to explain computational Ras hybrid mutants. G13D, G12D, and G12V have been described to differ in seven biochemical parameters. A total of 648 different computational hybrids were generated by considering all of the possible combinations of these differentiating parameters. For each mutant, the model was evaluated to determine whether the computational hybrid was sensitive ("Y" in bottom row) or resistant to simulated EGFR inhibition. Orange indicates a parameter value specific to KRAS G13D, blue indicates a parameter value specific to G12D, green indicates a value specific to G12V, and black indicates a value specific to KRAS WT that is also used for a mutant when specific data are available. Fifteen representative hybrid mutants are shown from the 648 total hybrid mutants to visualize how they hybrid mutants contain combinations of the individual parameters used to model a G13D, G12D, or G12V mutant. (B) Simulated dose responses for all 648 hybrids, color-coded on the basis of whether the hybrid had the Ras/NF1 K_m value of the G13D mutant or that of the G12V or G12D mutant. (C) Coimmunoprecipitation of NF1 with KRAS G12V, G13D, and G12V/G13D (GG/VD) from mixtures of lysates from NF1-transfected cells with lysates from RAS-transfected cells. Blots are representative of three independent experiments. (D) MTT proliferation assays of cetuximab-treated KRAS WT SW48 cells transfected with WT, G12V, G12D, G13D, G12V/G13D double mutant (GG/VD), or both G12V and G13D KRAS (20 μ g/ml for 48 hours). Data are means \pm SD of eight biological replicates and are representative of three experiments. Significance was determined with a cutoff of 25% induced growth and *** $P < 0.001$ when compared to mock transfection by one-way ANOVA ($F = 90.69$) with post hoc Tukey's test for multiple comparisons.



quantity of Ras signal that is greater than the mutant alone can typically provide, inhibition of WT Ras through EGFR inhibition should negatively affect proliferation signals within the G13D cell. This assumption that WT Ras signaling is required in addition to mutant Ras signaling is consistent with emerging data that cancer promotion requires both WT and mutant Ras signals (15, 22, 25–27).

Experimental confirmation of our mechanism

We desired to test and confirm this proposed mechanism. We hypothesized that reduced expression of NF1 would make both G13D

and WT cells less sensitive to cetuximab but would not largely affect G12V cells. This is because we reasoned that reduced NF1 should result in increased WT RasGTP, thereby making these cells less dependent on EGFR for WT Ras activation. We performed siRNA-mediated knockdown experiments of NF1 in WT, G13D, and G12V cells and compared proliferation in the presence and absence of cetuximab. As hypothesized, NF1 knockdown reduced the sensitivity of G13D and WT cells to cetuximab with minimal effect on G12V cells (Fig. 4B). We also hypothesized that increased expression of NF1 should make G12V cells more sensitive to cetuximab. This is because

A

Mechanism revealed through computational analysis of Ras biochemistry

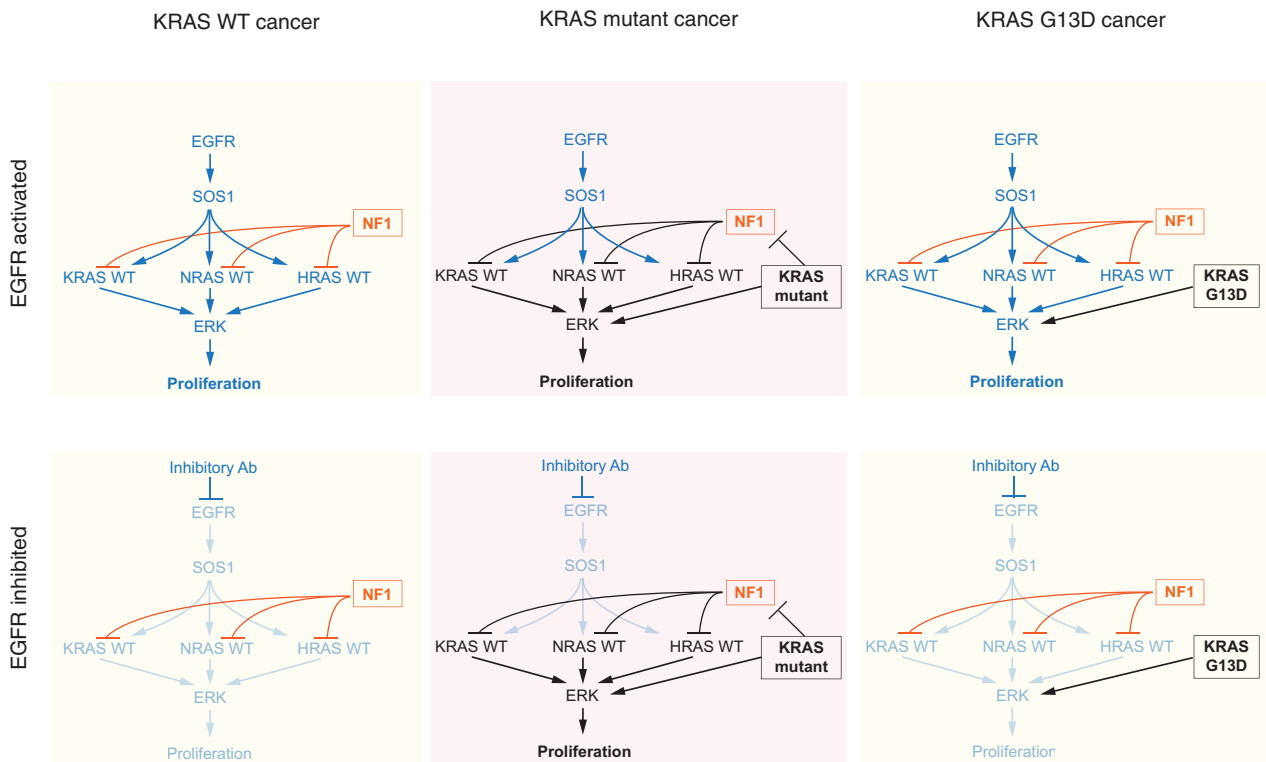
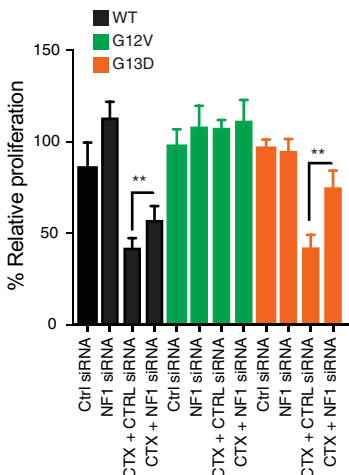
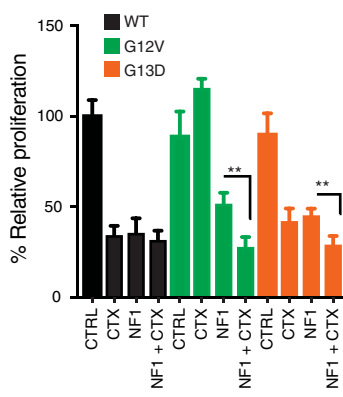
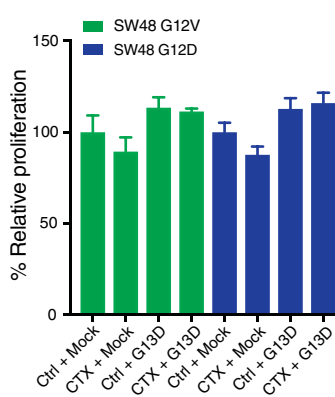
**B****C****D**

Fig. 4. A mechanism for KRAS allele-specific response to anti-EGFR agents with experimental validation. (A) In a KRAS WT cancer, NF1 ensures that there are low levels of RasGTP when EGFR is not active (or is inhibited). In KRAS G12D and KRAS G12V cancers, mutant Ras is active. WT Ras is also active through the competitive inhibition of NF1 through the nonproductive interaction between these Ras mutants and NF1. In a KRAS G13D cancer, mutant Ras is active but WT Ras remains dependent on EGFR for activation due to the inability of KRAS G13D to bind NF1. (B) MTT proliferation assays for isogenic SW48 cells with siRNA knockdown of NF1 and/or with cetuximab treatment. (C) MTT proliferation assays for isogenic SW48 cells with NF1 transfection and/or with cetuximab treatment. (D) MTT proliferation assays of cetuximab-treated KRAS G12D SW48 cells (left) and KRAS G13D SW48 cells (right) transfected with KRAS WT, G12V, G12D, or G13D. (B to D) Cetuximab, 20 µg/ml for 72 hours. Data are means ± SD of eight biological replicates and are representative of three experiments. *P < 0.05 and **P < 0.01 by one-way ANOVA (F > 27 for all three graphs) with post hoc Tukey's test.

we reasoned that these cells would become more dependent on EGFR for WT Ras activation as NF1 levels increased. To test, we transfected WT, G13D, and G12V cells with NF1 and then treated them with cetuximab. As hypothesized, increased NF1 expression made the G12V cells significantly more sensitive to cetuximab (Fig. 4C). Last, we reasoned that this mechanism also suggests that the introduction of KRAS G13D into a G12V or G12D cell would not cause the G12V or G12D to become sensitive to cetuximab, because the codon 12 KRAS mutant can still competitively inhibit NF1. We experimentally tested this hypothesis by transfecting G12V and G12D cells with KRAS G13D and found that the introduction of the KRAS G13D mutant did not cause the cells to become sensitive to cetuximab (Fig. 4D), consistent with our proposed mechanism.

Validation of our mechanism in additional CRC cell lines

We lastly set out to determine whether the patterns of EGFR sensitivity and WT RAS activation in relation to KRAS mutation status that we first predicted with a mathematical model and then observed in an isogenic panel of SW48 CRC cell lines would be more generally observable in other CRC cell lines. We obtained three hemizygous KRAS G13D CRC cell lines (LoVo, HCT116, and HCT-15), one CRC cell line for each of KRAS WT (CaCo2), KRAS G12V (SW403), and KRAS G12D (LS180). Of note, all three of these KRAS G13D CRC cell lines have an NF1 mutation, whereas the other three CRC cell lines do not. We evaluated whether the NF1 mutations result in reduced NF1 protein expression with immunoblots, and we did not detect NF1 expression in the three KRAS G13D cell lines (Fig. 5A). Consistent with our finding that reduced NF1 expression can convert a KRAS G13D SW48 cell line from being sensitive to cetuximab to insensitive to cetuximab (Fig. 4D), we observed that the cell lines that both had an NF1 mutant and the KRAS G13D mutant (LoVo, HCT116, and HCT-15) were insensitive to cetuximab (Fig. 5B). We also observed that the KRAS WT (CaCo2) CRC cell line was sensitive to cetuximab and that the KRAS G12V (SW403) and KRAS G12D (LS180) CRC cell lines were insensitive to cetuximab, consistent with the data from the isogenic SW48 cell lines.

The mechanism we have proposed (Fig. 4A) assumes that NF1 is present. We therefore hypothesized that if we reintroduced NF1 protein expression to the KRAS G13D and NF1 mutant CRC cell lines, they would gain sensitivity to cetuximab. We used lentiviral transduction to express full-length NF1 in these three cell lines (Fig. 5C). We observed that the reintroduction of NF1 caused a reduction in proliferation for these cells (fig. S13). Cetuximab dose responses found that these three KRAS G13D mutant cell lines with exogenous NF1 expression (LoVo + NF1, HCT116 + NF1, and HCT-15 + NF1) were now sensitive to cetuximab (Fig. 5B), fully consistent with our proposed mechanism. In addition, we performed immunoblots on RBD lysates and whole-cell lysates to evaluate RAS-GTP levels and ERK phosphorylation. We observed changes in RasGTP levels and in ERK phosphorylation with cetuximab treatment for KRAS WT CaCo2 cells, but not in the CRC cells with a KRAS G12D mutation, a KRAS G12V mutation, or a KRAS G13D mutation with a co-occurring NF1 mutation (Fig. 5D). In addition, we observed reductions in RAS-GTP and ERK phosphorylation in the KRAS G13D cells when NF1 protein had been reintroduced, but not in their NF1 mutant state (Fig. 5D). Together, these experiments suggest that the mechanism we identified through computational modeling and with SW48 isogenic cells is more general. It also highlights that NF1 mutations that co-occur with a KRAS G13D mutation may confer resistance to cetuximab.

DISCUSSION

Every year, there are about 10,000 new cases of KRAS G13D CRC in the United States alone. Despite the phase 3 clinical trial evidence that these patients would benefit from U.S. Food and Drug Administration-approved EGFR inhibitors, the apparent discrepancy between the known mechanisms of Ras signaling and these clinical effects has been seen as problematic. The field has chosen to favor intuition over empirical data and has considered KRAS G13D equivalent to other codon 12, 13, and 61 KRAS mutations. This practice should be reconsidered; our mathematical work has identified a mechanism that is fully consistent with fundamental Ras biology and the idea that the KRAS G13D mutant can be more sensitive to EGFR inhibition.

Our mathematical model describes the “central dogma” of Ras biology. That is, Ras GEFs activate Ras, Ras GAPs inactivate Ras, active Ras binds to Ras effectors, and Ras has very slow GTPase activity and very slow GEF-independent nucleotide exchange activity. Our model is based on peer-reviewed data that biochemically and biophysically characterize each of these reactions. Our simulations find that Ras central dogma permits different mutations to respond differently to the same upstream inhibitor. In addition, our computational analysis finds that the available biochemical data for the KRAS G13D mutant are sufficient to provide a mechanistic explanation for why KRAS G13D patients benefit from EGFR inhibition.

Differences in WT Ras activation between these KRAS mutant cells as they are treated with EGFR inhibitors are the critical aspects that we uncovered with our model. Our experiments tested and confirmed this mechanism. Of note, the mathematical model, its analysis, and these hypotheses were posted to bioRxiv before the experimental work in this study began (28). This helps demonstrate that these were true, prospective, predictions.

Our study also suggests one mechanism by which KRAS G13D cancers may become resistant to EGFR agents. We demonstrated that decreased NF1 expression makes KRAS G13D mutant cancer cells more resistant to EGFR inhibition. Accordingly, we would hypothesize that CRC patients who have both NF1 and KRAS G13D mutations will be less likely to receive benefit and/or will receive a smaller benefit. We queried colorectal genomics studies to ask how often NF1 and KRAS G13D mutations co-occur (13). We found that KRAS G13D CRC patients had a co-occurring NF1 mutation less than 4% of the time, suggesting that a very large proportion of KRAS G13D CRC patients may be able to benefit from anti-EGFR agents that have been approved for CRC like cetuximab and panitumumab.

The fact that KRAS G13D CRC cell lines commonly have NF1 mutations, whereas patients do not, is intriguing. We hypothesize that a requirement for WT Ras activation in CRC limits the KRAS G13D CRC that can yield cell lines to only the cells that harbor an additional mutation that promotes an increase in WT RasGTP. Within actual KRAS G13D CRC patients, we hypothesize that WT Ras is promoted by extracellular signals that activate receptor tyrosine kinases like EGFR.

There are likely additional mechanisms that can lead to resistance to EGFR inhibition, just as there are multiple mechanisms for resistance to other targeted therapies. Future work will attempt to uncover these relationships. It is also possible that there are additional Ras mutants that respond to EGFR inhibition through similar mechanisms involving reduced binding to NF1. Future work will attempt to identify additional exceptional responder Ras mutants.

Our focus on the central dogma of Ras signal regulation has allowed us to construct a model for which there are readily available,

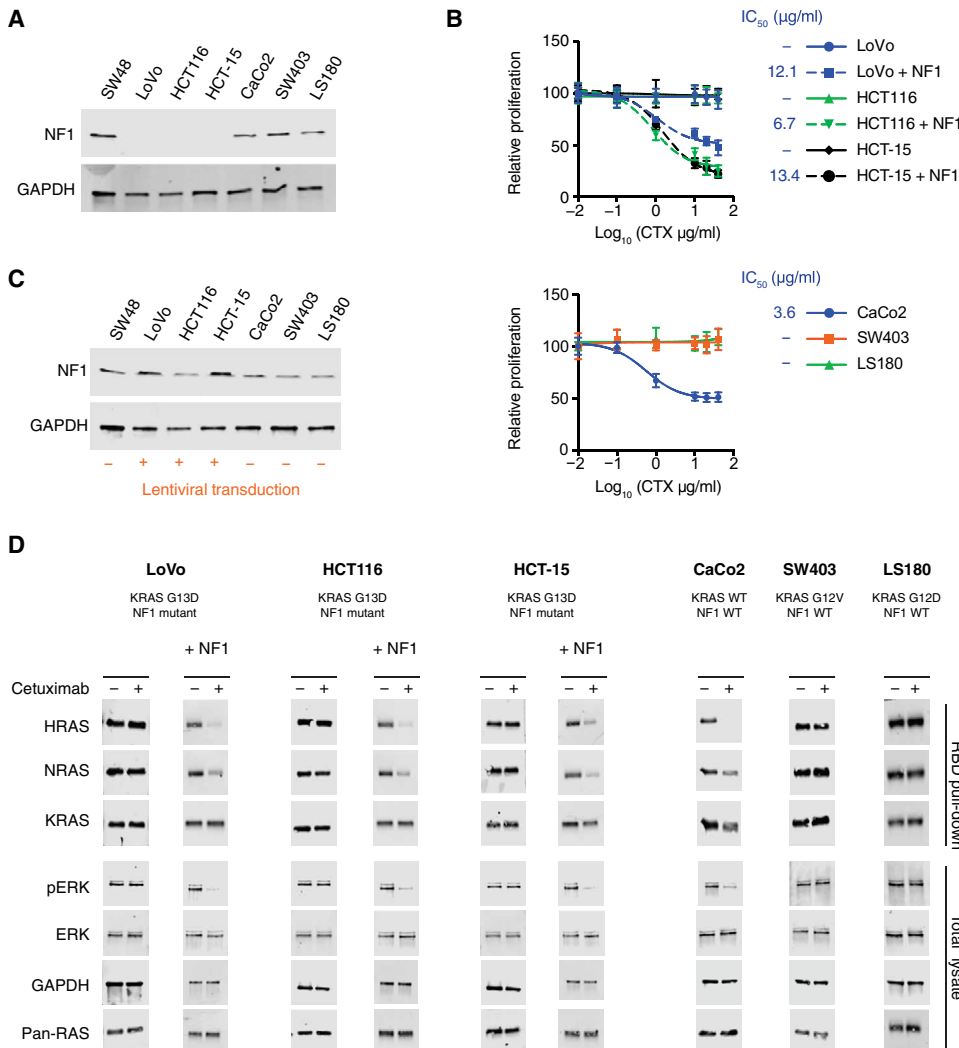


Fig. 5. Evaluation of proposed mechanism in additional CRC cell lines. (A) Immunoblot of NF1 expression in an extended panel of CRC cell lines that includes three KRAS G13D, NF1 mutant, CRC cell lines (LoVo, HCT116, and HCT-15); KRAS WT, NF1 WT, CaCo2 cells; KRAS G12V, NF1 WT, SW403 cells; and KRAS G12D, NF1 WT, LS180 cells. Parental, KRAS WT, NF1 WT, SW48 cells are included for comparison. Blots are representative of three independent experiments. (B) MTT proliferation assays to assess dose responses of the extended panel of CRC cell lines. Top: Dose responses for the three KRAS G13D, NF1 mutant, cell lines and for the same three cell lines that have been transduced to express NF1. Bottom: Dose responses from the three NF1 WT cell lines (cetuximab at doses indicated for 48 hours). Data are means \pm SD of eight biological replicates and are representative of three experiments. Median inhibitory concentration (IC_{50}) values are presented for sensitive cell lines; (—) indicates a resistant cell line. (C) Immunoblot of NF1 expression in the KRAS G13D, NF1 mutant, CRC cell lines (LoVo, HCT116, and HCT-15) after lentiviral transduction with NF1. Nontransduced SW48, CaCo2, SW403, and LS180 cells are included for comparison. Blots are representative of three independent experiments. (D) RBD pull-down Ras activation assays and ERK phosphorylation immunoblots for CRC cell lines LoVo, HCT116, HCT-15, CaCo2, SW403, and LS180, cultured without or with cetuximab (20 $\mu\text{g/ml}$ for 48 hours). The NF1 mutant cell lines were investigated both in native form and after transduction with NF1 (+NF1). Blots are representative of three independent experiments.

high-quality, biochemical data for WT and mutant Ras. Although our model is limited in scope, it has been able to uncover multiple unappreciated aspects of Ras biology (15, 16). Many systems models extend to larger considerations of networks. There is a clear appreciation that features beyond the scope of our model, such as positive and negative feedback (19, 22, 26, 27, 29), play important contributions to Ras signaling. Once processes like the positive feedback of RasGTP

on SOS1 (29) and the differences in the regulation of SOS1 and SOS2 (30) are biophysically characterized to the level of the different KRAS mutant alleles, it would be possible to determine whether there are additional differences between KRAS G13D, G12D, and G12V that further contribute to cancers with the KRAS G13D mutant being more sensitive to EGFR inhibition.

Our work demonstrates how systems approaches can uncover nonobvious, mechanistic bases for clinical observations that otherwise defy expert-level explanation. Many genes associated with cancer and other diseases have multiple pathological variants. Our work is relevant to these other genes and diseases, as we have demonstrated how apparently similar variants can exhibit different responses to the same pharmacological treatment. As clinical genomics becomes more common, and as the number of targeted therapies approved and in development continues to grow, we believe that it will be increasingly necessary to perform integrated mathematical analysis of biomolecular systems to understand how mutant allele-specific behaviors emerge and influence response to treatment.

MATERIALS AND METHODS

Mathematical model and analysis

Details of the model and its development have been published previously (15, 31–34) and are summarized here and further described in Supplementary Text. The model focuses on Ras and the types of proteins that directly interact with Ras to regulate RasGTP levels: Ras GEFs (such as SOS1), Ras GAPs (such as NF1), and Ras effector proteins (such as the RAF kinases). The model includes (i) GEF-mediated nucleotide exchange, (ii) intrinsic nucleotide exchange, (iii) GAP-mediated nucleotide hydrolysis, (iv) intrinsic nucleotide hydrolysis, and (v) effector binding. GEF and GAP reactions, (i) and (iii) above, are described mathematically with reversible and irreversible Michaelis-Menten kinetics,

respectively. We consider only the subset of total GEFs and GAPs that are active within our model. The other reactions are described with first- and/or second-order mass action kinetics. It is assumed that WT and Ras mutant proteins have identical reaction mechanisms as indicated above and that differences in rate constants (or enzymatic parameters) for the reactions account for described differences. For example, Ras mutant protein G12V hydrolyzes GTP more slowly

than does WT Ras. In this case, the rate constant for this reaction $k_{\text{GTPase},\text{G12V}}$ is smaller than the rate constant for the same reaction with WT Ras, $k_{\text{GTPase},\text{WT}}$. All reactions are grouped into a set of differential equations, and the steady-state quantity of RasGTP–effector complexes (and RasGTP) is solved for the specified conditions.

Parameters of the model for proteins correspond to biochemically observable properties. Rate constants, enzymatic properties (V_{max} and K_m), and protein abundances for WT Ras proteins have been previously obtained, used, and published (listed in Supplementary Text) (15). Mutant proteins can be characterized by their difference from WT proteins in terms of a multiplicative factor, α . Values for α are determined from previous experimental studies that measured the desired property for both WT and mutant Ras proteins (35, 36). For G12V and G12D, we use the same α values that were previously obtained and used in our model (15). For G13D, previous experiments described this mutant to have an elevated nucleotide dissociation rate compared to WT Ras ($\alpha = 3.6625$) (18). Previous studies have also described Ras G13D to be insensitive to Ras GAP (37) and to have no appreciable binding to the Ras GAP NF1 (17). A 100-fold increase in the K_m value of GAP on Ras G13D is used to model the immeasurable binding to the Ras GAP NF1. We estimated that the change must be at least 100 times large because changes of about 50-fold have previously been measured for other Ras mutants (38), so we assumed that the difference must be larger to be undetectable. The decreased GTPase activity of the G12D mutant is used for the G13D mutant, because we could not find an α factor at the time we began our study; using the same value as G12D allowed us to introduce impaired GTPase activity while also allowing us to focus on the known biochemical differences.

Computational “hybrid” mutants are modeled mutants that have properties of two distinct Ras mutants. For example, a hybrid Ras mutant may be modeled with all of the properties of Ras G12D, except for the faster intrinsic nucleotide dissociation properties of G13D. Such a hybrid could be used to evaluate how faster nucleotide dissociation would influence signaling through the comparison of this hybrid’s behavior with that of the G12D mutant.

The Ras network within the CRC context is assumed to be EGFR driven, and EGFR is assumed to activate Ras through increased activation of Ras GEFs like SOS1 and SOS2. We use a 10-fold increase in V_{max} for GEF reactions to indicate EGFR activation, just as we have done previously to model receptor tyrosine kinase–mediated Ras activation (15). To simulate an EGFR inhibition dose response, we considered levels of GEF activity between the “high” (10 \times increase) case and the basal “low” (1 \times) level and we determined the resulting level of RasGTP by model simulation. We assume that the three Ras proteins—HRAS, NRAS, and KRAS—share similar biochemistry and can be modeled with the same set of biochemical properties; such an assumption is consistent with measurements of the three Ras proteins (39, 40). We assume that measurements that provide α for one Ras protein are good approximations for the same mutant to the other Ras proteins. We assume that more than one Ras gene is expressed in CRC cells. This is consistent with many data (21, 41). We here model Ras mutants as being heterozygous such that, for a KRAS mutant, one-half of total KRAS will be mutant and one-half of total KRAS will be WT. Here, we assume that 50% of total Ras is KRAS (and that 25% of total Ras is mutant). This assumption is consistent with MS quantification of KRAS, NRAS, and HRAS levels (21).

RasGTP and RasGTP–effector complex are considered as measures of Ras pathway activation. Model simulations are used to determine

steady-state levels of RasGTP and RasGTP effector. Simulations and analysis are performed in MATLAB (9.1.0.441655, MathWorks).

Cell line models and culture method

SW48 cells and isogenic counterparts were cultured in RPMI 1640 medium supplemented with fetal bovine serum (FBS) (10%), penicillin (100 U/ml), streptomycin (100 μ g/ml), and L-glutamine (2 mM). SW403 cells were cultured in L-15 medium with FBS (10%), penicillin (100 U/ml), streptomycin (100 μ g/ml), and L-glutamine (2 mM). LS-180 cells were cultured in Eagle’s minimum essential medium (EMEM) with FBS (10%), penicillin (100 U/ml), streptomycin (100 μ g/ml), and L-glutamine (2 mM). LoVo cells were cultured in F12-K medium with FBS (10%), penicillin (100 U/ml), streptomycin (100 μ g/ml), and L-glutamine (2 mM). HCT116 cells were grown in McCoy’s 5A medium with FBS (10%), penicillin (100 U/ml), streptomycin (100 μ g/ml), and L-glutamine (2 mM). HCT-15 cells were grown in RPMI 1640 medium supplemented with FBS (10%), penicillin (100 U/ml), streptomycin (100 μ g/ml), and L-glutamine (2 mM). CaCo2 cells were grown in DMEM with FBS (20%), penicillin (100 U/ml), streptomycin (100 μ g/ml), and L-glutamine (2 mM). All cells were grown in indicated medium and incubated at 37°C in 5% CO₂ unless indicated otherwise in experimental methods. SW48 cells were obtained from Horizon Discovery. SW403, HCT116, HCT-15, CaCo2, SW48, and LoVo were obtained from the American Type Culture Collection.

Western blot analysis

Cell lysates were generated using radioimmunoprecipitation assay buffer [150 mM NaCl, 1% NP-40, 0.5% sodium deoxycholate, 0.1% SDS, 50 mM tris (pH 8.0)] containing protease inhibitor cocktail (Cell Signaling Technology) and incubated on ice for 1 hour. The total protein concentration was determined by Pierce Protein assay (Thermo Fisher Scientific). Protein samples (20 μ g) were resolved by electrophoresis on 10 to 12% SDS–polyacrylamide gels and electrokinetically transferred to polyvinylidene difluoride (PVDF) membranes (Millipore Corporation) for 20 min at 25 V. The blots were probed with the appropriate primary antibody and the appropriate fluorophore-conjugated secondary antibody. The protein bands were visualized using the Licor CLx Odyssey imaging station (Licor Biosystems). Comparative changes were measured with Licor Image Studio software.

Cell proliferation assay

Cells (5000 per well) were seeded in 96-well plates in phenol red–free medium supplemented with charcoal-stripped FBS. Treatments were initiated after the cells were attached. At the appropriate time points, cell viability was determined by MTT assay (3-(4,5-dimethylthiazol-2-yl)-2,5-diphenyltetrazolium bromide); 10 μ l of MTT (5 mg/ml in phosphate-buffered saline) was added to each well followed by incubation at 37°C for 2 hours. The formazan crystal sediments were dissolved in 100 μ l of dimethyl sulfoxide, and absorbance was measured at 590 nm using a Tecan Infinite 200 PRO plate reader. Each treatment was performed in seven replicate wells and repeated three times.

siRNA-mediated gene knockdown

The appropriate recombinant SW48 cells were plated in a 10-cm plate in DMEM supplemented with 10% FBS 24 hours before transfection. The following day, cells were transfected with siRNAs against NF1 (2 μ g) or control siRNA (2 μ g) using Lipofectamine 2000. For

EGFR knockdown, cells were plated in a 96-well format in 100 μ l of Opti-MEM (10% FBS) with 0.1 μ g of siRNA mixed with 0.5 μ l of Lipofectamine 2000 per well. Twenty-four hours after EGFR siRNA delivery, cells were treated with cetuximab for 48 hours, and proliferation was measured by MTT assay. Silencer Select siRNAs were purchased from Thermo Fisher Scientific. Silencer Select-NF1 (s56534) was composed of pooled RNAs targeting exons 2, 10, 16, 18, and 19 in the NF1 mRNA. Silencer Select-EGFR (s565) was composed of pooled siRNA targeting five unique sequences within exon 2 of the EGFR mRNA. Silencer Select Control siRNA (4390843) was used as negative control. All siRNAs were reconstituted in ribonuclease-free molecular-grade water upon arrival from vendor at a concentration of 5 mM.

Expression plasmid transfection

Cells were plated in a 96-well plate at 5000 cells per well in antibiotic-free medium. Twenty-four hours later, cells were transfected with expression plasmids with duplex containing 0.2 μ g of DNA and 0.25 μ l of Lipofectamine 2000 per well. Cell proliferation was assayed within at least 48 hours.

Ras expression constructs from the NCI Ras Initiative clone collection for KRAS4B-WT (Addgene #83129), NRAS-WT (Addgene #83173), HRAS-WT (Addgene #83181), KRAS-G13D (Addgene #83133), KRAS-G12V (Addgene #83132), and KRAS-G12D (Addgene #83131) were Gateway-cloned into enhanced green fluorescent protein (EGFP) expression vector pEZYegfp (Addgene #18671). KRAS G13D was used to create G12V/G13D (GG/VD) through site-directed mutagenesis. NF1 expression construct (Addgene #70423) was Gateway-cloned into pEZYflag (Addgene #18700), and NF1 expression construct (Addgene #70424) was Gateway-cloned into pcDNA3.1-ccdB-Nanoluc (Addgene #87067) and pLenti6.2-ccdB-Nanoluc (Addgene #87075). The RAS Clone Collection was a gift from D. Esposito (Addgene kit #1000000070 and kit #1000000089). pEZYegfp and pEZYflag were gifts from Y.-Z. Zhang (Addgene plasmid #18671; <http://n2t.net/addgene:18671>; RRID: Addgene_18671 and Addgene plasmid #18700; <http://n2t.net/addgene:18700>; RRID: Addgene_18700). pLenti6.2-ccdB-Nanoluc and pcDNA3.1-ccdB-Nanoluc were gifts from M. Taipale (Addgene plasmid #87075; <http://n2t.net/addgene:87075>; RRID: Addgene_87075 and Addgene plasmid #87067; <http://n2t.net/addgene:87067>; RRID: Addgene_87067).

Colony formation assay

Cells were trypsinized, and 4000 cells per well were plated in triplicate six-well plates in DMEM supplemented with FBS. Colonies were formed after 7 days. The cells were fixed with ice-cold methanol and stained with crystal violet. Images were obtained using the Licor CLX Odyssey imaging station (Licor Biosystems). Colony formation was quantified by measuring absorbance per well. Comparison was made by normalizing to control wells. A total of five experimental replicates were performed, with each containing three biological replicates.

Active Ras pull-down assay

Isolation of active RasGTP was performed using the Active Ras Pull-Down and Detection Kit (Thermo Fisher Scientific) following the manufacturer's protocol. Ras abundance was measured by Western blot and/or MS. Western blot analysis of RBD pull-down lysates was performed with mouse anti-KRAS antibody (WH0003841, Sigma), rabbit anti-NRAS (ab16713, Abcam), rabbit anti-HRAS (18295, Proteintech), mouse anti-pan-RAS antibody (1862335, Thermo

Fisher Scientific), and mouse anti-GAPDH (sc-4772, Santa Cruz Biotechnology).

Mass spectrometry

RBD lysates from cetuximab-treated and nontreated cells (20 μ g/ml for 48 hours) were precipitated using methanol-chloroform. Dried pellets were dissolved in 8 M urea, reduced with 5 mM tris (2-carboxyethyl) phosphine hydrochloride, and alkylated with 50 mM chloroacetamide. Proteins were then trypsin-digested overnight at 37°C. Samples were digested at a final volume of 50 μ l. Heavy-labeled peptides were spiked in to the digested samples at appropriate concentrations so that a single liquid chromatography-MS injection contained 10 μ l of digested sample with 500 fmol of heavy-labeled peptides. Peptides used were SFEDIHQYR for HRAS, SFADINLYR for NRAS, SFEDIHHYR for KRAS, LVVVGAGGVGK for WT H/N/KRAS, LVVVGAGDVGK for G13D mutant H/N/KRAS, and LVVVGAVGVGK for G12V mutant H/N/KRAS, and the same peptide sequences were previously used for quantification of endogenous RAS and mutant RAS genes in similar isogenic SW48 cells (21).

The samples were analyzed on a Fusion mass spectrometer (Thermo Fisher Scientific). Samples were injected directly onto a 25-cm, 100- μ m inside diameter column packed with BEH 1.7 μ m C18 resin (Waters). Samples were separated at a flow rate of 300 nl/min on an nLC 1200 (Thermo Fisher Scientific). Buffer A and B were 0.1% formic acid in water and 90% acetonitrile, respectively. A gradient of 1 to 25% B over 110 min, an increase to 40% B over 10 min, an increase to 100% B over another 10 min and held at 90% B for a final 10 min of washing was used for 140 min total run time. Peptides were eluted directly from the tip of the column and nanosprayed directly into the mass spectrometer by application of 2.8 kV at the back of the column. The Fusion was operated in a data-dependent mode. Full MS1 scans were collected in the Orbitrap at 120,000 resolution. The cycle time was set to 3 s, and within this 3 s, the most abundant ions per scan were selected for collision-induced dissociation MS/MS in the ion trap. Monoisotopic precursor selection was enabled, and dynamic exclusion was used with an exclusion duration of 5 s.

Peak area quantitation of the heavy peptides and corresponding light peptides from the samples was extracted by Skyline (42). Within each sample, we used mutant Ras as a standard to normalize against. We then compared the ratio of normalized WT peptide levels in cetuximab-treated conditions to normalized WT peptide levels in non-cetuximab-treated conditions.

IEF of active RAS isoforms

SW48-WT RAS, SW48-KRAS G12V, and SW48 KRAS G13D cells were cultured in T-75 adherent culture flasks. Cells were grown in growth medium alone or growth medium with cetuximab (20 μ g/ml) for 48 hours. Medium was removed, and cells were washed with ice-cold tris-buffered saline. Cells were scraped in 1 ml of lysis wash buffer [25 mM tris-HCl (pH 7.2), 150 mM NaCl, 5 mM MgCl₂, 1% NP-40, and 5% glycerol]. Cells were lysed on ice and vortexed every 10 s. Cell lysates were subjected to RBD coimmunoprecipitation as previously described above. RBD coimmunoprecipitation product was resolved by SDS-polyacrylamide gel electrophoresis in a 12% polyacrylamide gel. Bands were excised from the 21-kDa region of the gel. Gel products were liquified at 95°C for 5 min. Protein was extracted and purified using the ReadyPrep 2-D Cleanup Kit (Bio-Rad Laboratories) following the manufacturer's protocol. Protein samples were added to 50% glycerol loading buffer and incubated at room

temperature for 20 min. Samples and IEF Ladder were resolved on Criterion Bio-Lyte IEF Gel with a 3 to 10 pH range (Bio-Rad Laboratories). Gels were run at the following power conditions with constant voltage: 100 V for 60 min, 250 V for 60 min, and 500 V for 30 min in a stepwise fashion with a total run time of 150 min. The IEF gel was then soaked in 5% SDS buffer for 24 hours with gentle rocking at 4°C. Protein was electrophoretically transferred to PVDF membranes (Millipore Corporation) for 1 hour at a constant 25 V. The PVDF blots were probed with the anti-pan-RAS primary antibody from the Active Ras Pull-Down and Detection Kit (Thermo Fisher Scientific) and the anti-mouse DyLight 800 fluorophore-conjugated secondary antibody (Invitrogen). The protein bands were visualized using the Licor CLx Odyssey imaging station (Licor Biosystems). Comparative changes were measured with Licor Image Studio software.

Coimmunoprecipitation

H293T cells were individually transfected with the expression plasmid for NF1-Flag, WT KRAS-GFP, G12V KRAS-GFP, G12D KRAS-GFP, or KRAS G13D-GFP. Cells were harvested in IP Lysis/Wash Buffer (0.025 M tris-HCl, 0.15 M NaCl, 0.001 M EDTA, 1% NP-40, and 5% glycerol; pH 7.4 and 1× protease inhibitor) 24 hours after transfection. Whole-cell lysates (500 µg) were precleared for 0.5 hours using Control Agarose Resin slurry (Thermo Fisher Scientific). Immunoprecipitation was performed by first incubating 800 µl of H293T NF1-Flag precleared lysate with 200 µl of either WT KRAS-GFP, G12V KRAS-GFP, G12D KRAS-GFP, or G13D KRAS-GFP precleared cell lysate. Each cell lysate mixture had EDTA (pH 8.0) added to make a final concentration of 10 mM. GTP-γ-S was added to the solution to a final concentration of 100 nM. This solution was incubated at room temperature for 20 min with gentle rocking. The reaction was terminated by adding MgCl₂ to the solution at a final concentration of 50 mM. The final steps of the coimmunoprecipitation were performed using the Pierce Immunoprecipitation Kit (Thermo Fisher Scientific) with immobilized anti-NF1 antibody (Santa Cruz Biotechnology, CA). A total of 500 µg of the cell lysate was added and incubated at room temperature under rotary agitation for 2 hours. At the end of the incubation, the complexes were washed five times with lysis buffer. Western blotting was probed with mouse monoclonal NF1 antibody (Santa Cruz Biotechnology) and mouse monoclonal RAS antibody (Thermo Fisher Scientific).

Lentiviral transduction

293FT cells were used to generate lentiviral particles by transfection using Lipofectamine 2000 (Life Technologies Corporation). Packaging plasmids pMD2G, PMDLg/RRE, and pRSV/Rev were cotransfected with pCDH NF1-NanoLuc C-term expression plasmid. Lentivirus containing supernatant was harvested at 48 and 72 hours after transfection. LoVo, HCT116, and HCT-15 cells were plated in respective medium with heat-inactivated FBS (10%) and 2 mM L-glutamine 2 days before infection. For infection, LoVo, HCT116, and HCT-15 cells were transduced with pCDH NF1-nanoLuc lentivirus with polybrene (8 µg/ml) for 10 hours. The cells were washed, medium was replenished, and cells were incubated for 48 hours. After this, cells were placed in puromycin selection (1 µg/ml) for 7 days. Cells were harvested for Western blots and MTT assays as described previously.

AKT phosphorylation

The pAKT antibodies were validated by starving WT SW48 cells in RPMI 1640/penicillin/streptomycin medium for 12 hours, and cells

were stimulated with EGF (50 ng/ml) for 5 min. Whole-cell lysates were prepared and resolved on 12% polyacrylamide gel. Gels were transferred to PVDF membranes and probed with anti-phospho-T308 AKT1 rabbit antibody (AB13038, Cell Signaling Technology), anti-phospho-S473 AKT1 rabbit monoclonal antibody (AB4060, Cell Signaling Technology), and anti-pan-AKT mouse monoclonal antibody (AB2920, Cell Signaling Technology) in 3% bovine serum albumin solution. Cell lines indicated were treated with either vehicle control or cetuximab (20 µg/ml) for 48 hours. Whole-cell lysates were prepared and analyzed by Western blot analysis as previously described.

Bioluminescence resonance energy transfer assay

Human embryonic kidney (HEK)-293T cells were grown in DMEM/10% FBS without antibiotic. Cells were seeded at 5×10^3 cells per well in a 96-well white opaque Perkin Elmer microplate. Twenty-four hours after seeding, cells were cotransfected with a constant concentration of 0.1 µg of NF1-NanoLuc pcDNA expression plasmid and increasing concentrations of RAS-EGFP pcDNA expression plasmid (0, 0.05, 0.1, 0.2, 0.4, 0.6, 0.8, and 1.2 µg) with 0.25 µl of Lipofectamine 2000 per well following the manufacturer's protocol (Thermo Fisher Scientific). Twenty-four hours later, medium was aspirated from each well and 25 µl of Nano-Glo Live Cell Reagent was added to each well per the manufacturer's protocol (Promega). Plates were placed on orbital shaker for 1 min at 300 rpm. After incubation, the plate was read on the Tecan Infinite M200 PRO with LumiColor Dual Setting with an integration time of 1000 ms. BRET ratio was calculated from the dual emission readings. BRET ratio was plotted as a function of the RAS-GFP/NF1-NanoLuc plasmid ratio. BRET assays were repeated five times, each with eight biological replicates.

Statistical analysis

Significant differences among sample groups of greater than or equal to three were determined by one-way analysis of variance (ANOVA) followed by post hoc Tukey's test for multiple comparisons with GraphPad Prism7 software. Significant differences among two sample groups were determined by one-tailed unpaired *t* test. MS was performed twice. Every other experiment was performed at least three times, and *P* values are indicated in each figure.

SUPPLEMENTARY MATERIALS

stke.sciencemag.org/cgi/content/full/12/600/eaaw8288/DC1

Text S1. Extended description of the Ras model

Fig. S1. Schematic of the reactions of the Ras model.

Fig. S2. Available parameters for the Ras G13D mutant are sufficient to account for its constitutive activation.

Fig. S3. Ras model predictions when level of RasGTP-effector complex is used as a readout of signal strength instead of RasGTP.

Fig. S4. Isogenic colon cancer cells display a KRAS mutant-specific response to cetuximab.

Fig. S5. Evaluation of the response of the isogenic panel to MEK inhibitor.

Fig. S6. Transfection-based cetuximab sensitivity assay.

Fig. S7. Evaluation of AKT phosphorylation upon cetuximab treatment.

Fig. S8. Evaluation of EGFR knockdown in isogenic SW48 cells.

Fig. S9. Evaluation of panitumumab treatment of isogenic SW48 cells.

Fig. S10. Evaluation of erlotinib treatment of isogenic SW48 cells.

Fig. S11. Evaluation of Ras antibodies.

Fig. S12. Detection of impaired binding between KRAS G13D and NF1.

Fig. S13. Evaluation of KRAS G13D CRC cell lines that have been transduced with NF1.

Data file S1. MS data and analysis of untreated and cetuximab-treated isogenic SW48 cells.

References (43, 44)

REFERENCES AND NOTES

- D. J. Jonker, C. J. O'Callaghan, C. S. Karapetis, J. R. Zalcberg, D. Tu, H. J. Au, S. R. Berry, M. Krahm, T. Price, R. J. Simes, N. C. Tebbutt, G. van Hazel, R. Wierzbicki, C. Langer, M. J. Moore, Cetuximab for the treatment of colorectal cancer. *N. Engl. J. Med.* **357**, 2040–2048 (2007).
- E. Van Cutsem, M. Peeters, S. Siena, Y. Humblet, A. Hendrlisz, B. Neyns, J. L. Canon, J. L. Van Laethem, J. Maurel, G. Richardson, M. Wolf, R. G. Amado, Open-label phase III trial of panitumumab plus best supportive care compared with best supportive care alone in patients with chemotherapy-refractory metastatic colorectal cancer. *J. Clin. Oncol.* **25**, 1658–1664 (2007).
- Cancer Genome Atlas Network, Comprehensive molecular characterization of human colon and rectal cancer. *Nature* **487**, 330–337 (2012).
- A. G. Stephen, D. Esposito, R. K. Bagni, F. McCormick, Dragging ras back in the ring. *Cancer Cell* **25**, 272–281 (2014).
- C. S. Karapetis, S. Khambata-Ford, D. J. Jonker, C. J. O'Callaghan, D. Tu, N. C. Tebbutt, R. J. Simes, H. Chalchal, J. D. Shapiro, S. Robitaille, T. J. Price, L. Shepherd, H. J. Au, C. Langer, M. J. Moore, J. R. Zalcberg, K-ras mutations and benefit from cetuximab in advanced colorectal cancer. *N. Engl. J. Med.* **359**, 1757–1765 (2008).
- R. G. Amado, M. Wolf, M. Peeters, E. Van Cutsem, S. Siena, D. J. Freeman, T. Juan, R. Sikorski, S. Suggs, R. Radinsky, S. D. Patterson, D. D. Chang, Wild-type KRAS is required for panitumumab efficacy in patients with metastatic colorectal cancer. *J. Clin. Oncol.* **26**, 1626–1634 (2008).
- W. De Roock, D. J. Jonker, F. Di Nicolantonio, A. Sartore-Bianchi, D. Tu, S. Siena, S. Lamba, S. Arena, M. Frattini, H. Piessevaux, E. Van Cutsem, C. J. O'Callaghan, S. Khambata-Ford, J. R. Zalcberg, J. Simes, C. S. Karapetis, A. Bardelli, S. Tejpar, Association of KRAS p.G13D mutation with outcome in patients with chemotherapy-refractory metastatic colorectal cancer treated with cetuximab. *JAMA* **304**, 1812–1820 (2010).
- S. Tejpar, I. Celik, M. Schlichting, U. Sartorius, C. Bokemeyer, E. Van Cutsem, Association of KRAS G13D tumor mutations with outcome in patients with metastatic colorectal cancer treated with first-line chemotherapy with or without cetuximab. *J. Clin. Oncol.* **30**, 3570–3577 (2012).
- M. Nakamura, T. Aoyama, K. Ishibashi, A. Tsuji, Y. Takinishi, Y. Shindo, J. Sakamoto, K. Oba, H. Mishima, Randomized phase II study of cetuximab versus irinotecan and cetuximab in patients with chemo-refractory KRAS codon G13D metastatic colorectal cancer (G13D-study). *Cancer Chemother. Pharmacol.* **79**, 29–36 (2017).
- E. Segelov, S. Thavaneswaran, P. M. Waring, J. Desai, K. P. Robledo, V. J. Gebski, E. Elez, L. M. Nott, C. S. Karapetis, S. Lunke, L. A. Chantrill, N. Pavlakis, M. Khasraw, C. Underhill, F. Ciardiello, M. Jefford, H. Wasan, A. Haydon, T. J. Price, G. van Hazel, K. Wilson, J. Simes, J. D. Shapiro, Response to cetuximab with or without irinotecan in patients with refractory metastatic colorectal cancer harboring the KRAS G13D mutation: Australasian Gastro-Intestinal Trials Group ICECREAM Study. *J. Clin. Oncol.* **34**, 2258–2264 (2016).
- M. Peeters, J. Y. Douillard, E. Van Cutsem, S. Siena, K. Zhang, R. Williams, J. Wiezorek, Mutant KRAS codon 12 and 13 alleles in patients with metastatic colorectal cancer: Assessment as prognostic and predictive biomarkers of response to panitumumab. *J. Clin. Oncol.* **31**, 759–765 (2013).
- M. P. Morelli, S. Kopetz, Hurdles and complexities of codon 13 KRAS mutations. *J. Clin. Oncol.* **30**, 3565–3567 (2012).
- J. Gao, B. A. Aksoy, U. Dogrusoz, G. Dresdner, B. Gross, S. O. Sumer, Y. Sun, A. Jacobsen, R. Sinha, E. Larsson, E. Cerami, C. Sander, N. Schultz, Integrative analysis of complex cancer genomics and clinical profiles using the cBioPortal. *Sci. Signal.* **6**, p1 (2013).
- R. L. Siegel, K. D. Miller, A. Jemal, Cancer statistics, 2018. *CA Cancer J. Clin.* **68**, 7–30 (2018).
- E. C. Stites, P. C. Trampont, Z. Ma, K. S. Ravichandran, Network analysis of oncogenic Ras activation in cancer. *Science* **318**, 463–467 (2007).
- E. C. Stites, P. C. Trampont, L. B. Haney, S. F. Walk, K. S. Ravichandran, Cooperation between noncanonical Ras network mutations. *Cell Rep.* **10**, 307–316 (2015).
- L. Gremer, B. Gilsbach, M. R. Ahmadian, A. Wittinghofer, Fluoride complexes of oncogenic Ras mutants to study the Ras-RasGap interaction. *Biol. Chem.* **389**, 1163–1171 (2008).
- A. Palmioli, E. Sacco, C. Airoldi, F. Di Nicolantonio, A. D'Urzo, S. Shirasawa, T. Sasazuki, A. Di Domizio, L. De Gioia, E. Martegani, A. Bardelli, F. Peri, M. Vanoni, Selective cytotoxicity of a bicyclic Ras inhibitor in cancer cells expressing K-Ras(G13D). *Biochem. Biophys. Res. Commun.* **386**, 593–597 (2009).
- F. E. Hood, B. Klinger, A. U. Newlaczyk, A. Sieber, M. Dorel, S. P. Oliver, J. M. Coulson, N. Bluthgen, I. A. Prior, Isoform-specific Ras signaling is growth factor dependent. *Mol. Biol. Cell* **30**, 1108–1117 (2019).
- H. Ebi, R. B. Corcoran, A. Singh, Z. Chen, Y. Song, E. Lifshits, D. P. Ryan, J. A. Meyerhardt, C. Benes, J. Settleman, K. K. Wong, L. C. Cantley, J. A. Engelmann, Receptor tyrosine kinases exert dominant control over PI3K signaling in human KRAS mutant colorectal cancers. *J. Clin. Invest.* **121**, 4311–4321 (2011).
- C. J. Mageean, J. R. Griffiths, D. L. Smith, M. J. Clague, I. A. Prior, Absolute quantification of endogenous Ras isoform abundance. *PLOS ONE* **10**, e0142674 (2015).
- A. Young, D. Lou, F. McCormick, Oncogenic and wild-type Ras play divergent roles in the regulation of mitogen-activated protein kinase signaling. *Cancer Discov.* **3**, 112–123 (2013).
- P. Lito, N. Rosen, D. B. Solit, Tumor adaptation and resistance to RAF inhibitors. *Nat. Med.* **19**, 1401–1409 (2013).
- G. Bollag, F. McCormick, Differential regulation of rasGAP and neurofibromatosis gene product activities. *Nature* **351**, 576–579 (1991).
- J. W. Keller, K. M. Haigis, J. L. Franklin, R. H. Whitehead, T. Jacks, R. J. Coffey, Oncogenic K-RAS subverts the antiapoptotic role of N-RAS and alters modulation of the N-RAS:gelsolin complex. *Oncogene* **26**, 3051–3059 (2007).
- K. H. Lim, B. B. Ancliffe, D. F. Kashatus, C. M. Counter, Tumour maintenance is mediated by eNOS. *Nature* **452**, 646–649 (2008).
- E. Grabocka, Y. Pylayeva-Gupta, M. J. Jones, V. Lubkov, E. Yemanaberhan, L. Taylor, H. H. Jeng, D. Bar-Sagi, Wild-type H- and N-Ras promote mutant K-Ras-driven tumorigenesis by modulating the DNA damage response. *Cancer Cell* **25**, 243–256 (2014).
- E. C. Stites, Differences in sensitivity to EGFR inhibitors could be explained by described biochemical differences between oncogenic Ras mutants. *bioRxiv* 005397 [Preprint]. 21 May 2014. <https://doi.org/10.1101/005397>.
- H. H. Jeng, L. J. Taylor, D. Bar-Sagi, Sos-mediated cross-activation of wild-type Ras by oncogenic Ras is essential for tumorigenesis. *Nat. Commun.* **3**, 1168 (2012).
- S. Corbalan-Garcia, S. S. Yang, K. R. Degenhardt, D. Bar-Sagi, Identification of the mitogen-activated protein kinase phosphorylation sites on human Sos1 that regulate interaction with Grb2. *Mol. Cell. Biol.* **16**, 5674–5682 (1996).
- E. C. Stites, Modeling membrane localization: Case study of a Ras signaling model. *Adv. Exp. Med. Biol.* **680**, 661–667 (2010).
- E. C. Stites, K. S. Ravichandran, Mathematical investigation of how oncogenic ras mutants promote ras signaling. *Methods Mol. Biol.* **880**, 69–85 (2012).
- E. C. Stites, K. S. Ravichandran, Mechanistic modeling to investigate signaling by oncogenic Ras mutants. *Wiley Interdiscip. Rev. Syst. Biol. Med.* **4**, 117–127 (2012).
- E. C. Stites, A. S. Shaw, Quantitative systems pharmacology analysis of KRAS G12C covalent inhibitors. *CPT Pharmacometrics Syst. Pharmacol.* **7**, 342–351 (2018).
- J. F. Eccleston, K. J. Moore, G. G. Brownbridge, M. R. Webb, P. N. Lowe, Fluorescence approaches to the study of the p21ras GTPase mechanism. *Biochem. Soc. Trans.* **19**, 432–437 (1991).
- E. Chuang, D. Barnard, L. Hettich, X. F. Zhang, J. Avruch, M. S. Marshall, Critical binding and regulatory interactions between Ras and Raf occur through a small, stable N-terminal domain of Raf and specific Ras effector residues. *Mol. Cell. Biol.* **14**, 5318–5325 (1994).
- M. A. Fischbach, J. Settleman, Specific biochemical inactivation of oncogenic Ras proteins by nucleoside diphosphate kinase. *Cancer Res.* **63**, 4089–4094 (2003).
- S. Donovan, K. M. Shannon, G. Bollag, GTPase activating proteins: Critical regulators of intracellular signaling. *Biochim. Biophys. Acta* **1602**, 23–45 (2002).
- C. Lenzen, R. H. Cool, H. Prinz, J. Kuhlmann, A. Wittinghofer, Kinetic analysis by fluorescence of the interaction between Ras and the catalytic domain of the guanine nucleotide exchange factor Cdc25Mm. *Biochemistry* **37**, 7420–7430 (1998).
- M. R. Ahmadian, U. Hoffmann, R. S. Goody, A. Wittinghofer, Individual rate constants for the interaction of Ras proteins with GTPase-activating proteins determined by fluorescence spectroscopy. *Biochemistry* **36**, 4535–4541 (1997).
- J. Omerovic, D. E. Hammond, M. J. Clague, I. A. Prior, Ras isoform abundance and signalling in human cancer cell lines. *Oncogene* **27**, 2754–2762 (2008).
- B. MacLean, D. M. Tomazela, N. Shulman, M. Chambers, G. L. Finney, B. Frewen, R. Kern, D. L. Tabb, D. C. Liebler, M. J. MacCoss, Skyline: An open source document editor for creating and analyzing targeted proteomics experiments. *Bioinformatics* **26**, 966–968 (2010).
- J. R. Sydor, M. Engelhard, A. Wittinghofer, R. S. Goody, C. Herrmann, Transient kinetic studies on the interaction of Ras and the Ras-binding domain of c-Raf-1 reveal rapid equilibration of the complex. *Biochemistry* **37**, 14292–14299 (1998).
- M. G. Rudolph, T. Linnemann, P. Grunewald, A. Wittinghofer, I. R. Vetter, C. Herrmann, Thermodynamics of Ras/effectors and Cdc42/effectors interactions probed by isothermal titration calorimetry. *J. Biol. Chem.* **276**, 23914–23921 (2001).

Acknowledgments: We thank S. Kato for providing cetuximab, and M. Elliott, C. Wilen, A. Saghatelyan, and members of the Salk Institute Cancer Center for helpful conversations and feedback. **Funding:** Support for this work was provided by NIH K22CA216318, NIH T32CA009370, and the Mass Spectrometry Core of the Salk Institute with funding from NIH P30CA014195 and the Helmsley Center for Genomic Medicine. **Author contributions:** T.M., J.J.M., A.S.S., and E.C.S. designed the experiments. T.M., M.M., J.K.D., S.L.L., K.V.P., and L.S.-H.

performed the experiments. T.M., J.K.D., and E.C.S. analyzed the experimental data. E.C.S. performed the computational analysis and wrote the manuscript with input from the other authors. **Competing interests:** The authors declare that they have no competing interests. **Data and materials availability:** All data needed to evaluate the conclusions in the paper are present in the paper or the Supplementary Materials. The MS proteomics data have been deposited to the ProteomeXchange Consortium through the PRIDE partner repository with the dataset identifier PXD014755. All materials are available upon request from the corresponding author.

Submitted 29 January 2019
Accepted 27 August 2019
Published 24 September 2019
10.1126/scisignal.aaw8288

Citation: T. McFall, J. K. Diedrich, M. Mengistu, S. L. Littlechild, K. V. Paskvan, L. Sisk-Hackworth, J. J. Moresco, A. S. Shaw, E. C. Stites, A systems mechanism for KRAS mutant allele-specific responses to targeted therapy. *Sci. Signal.* **12**, eaaw8288 (2019).

FORCEFORSCIENCE.ORG

STAND TOGETHER Be a Force for Science

GET THE FACTS

Understand the science behind the issues that matter.

FOLLOW AAAS ADVOCACY

Champion public discussion and evidence-based policy.

TAKE ACTION

Learn ways you can become an advocate and stand up for science.

AMERICAN ASSOCIATION FOR THE ADVANCEMENT OF SCIENCE



CANCER

Adipocytes sensitize melanoma cells to environmental TGF- β cues by repressing the expression of miR-211

Tamar Golan¹, Roma Parikh¹, Etaí Jacob^{2,3,4,5}, Hananya Vaknine⁶, Valentina Zemser-Werner⁷, Dov Hershkovitz^{7,8}, Hagar Malcov¹, Stav Leibou¹, Hadar Reichman¹, Danna Sheinboim¹, Ruth Percik^{8,9}, Sarah Amar⁶, Ronen Brenner⁶, Shoshana Greenberger¹⁰, Andrew Kung¹¹, Mehdi Khaled¹², Carmit Levy^{1*}

Copyright © 2019
The Authors, some
rights reserved;
exclusive licensee
American Association
for the Advancement
of Science. No claim
to original U.S.
Government Works

Transforming growth factor- β (TGF- β) superfamily members are critical signals in tissue homeostasis and pathogenesis. Melanoma grows in the epidermis and invades the dermis before metastasizing. This disease progression is accompanied by increased sensitivity to microenvironmental TGF- β . Here, we found that skin fat cells (adipocytes) promoted metastatic initiation by sensitizing melanoma cells to TGF- β . Analysis of melanoma clinical samples revealed that adipocytes, usually located in the deeper hypodermis layer, were present in the upper dermis layer within proximity to *in situ* melanoma cells, an observation that correlated with disease aggressiveness. In a coculture system, adipocytes secreted the cytokines IL-6 and TNF- α , which induced a proliferative-to-invasive phenotypic switch in melanoma cells by repressing the expression of the microRNA miR-211. In a xenograft model, miR-211 exhibited a dual role in melanoma progression, promoting cell proliferation while inhibiting metastatic spread. Bioinformatics and molecular analyses indicated that miR-211 directly targeted and repressed the translation of *TGFB1* mRNA, which encodes the type I TGF- β receptor. Hence, through this axis of cytokine-mediated repression of miR-211, adipocytes increased the abundance of the TGF- β receptor in melanoma cells, thereby enhancing cellular responsiveness to TGF- β ligands. The induction of TGF- β signaling, in turn, resulted in a proliferative-to-invasive phenotypic switch in cultured melanoma cells. Pharmacological inhibition of TGF- β prevented these effects. Our findings further reveal a molecular link between fat cells and metastatic progression in melanoma that might be therapeutically targeted in patients.

INTRODUCTION

Cellular plasticity, defined as the ability of cells to interconvert between phenotypic states, enables rapid adaption to a dynamically changing multicellular microenvironment (1, 2). Phenotypic plasticity has a particular relevance to cancer progression as it increases tumorigenic potential and accounts for high metastatic abilities and resistance to therapy (3, 4). As imposed by microenvironmental cues, melanoma cells are able to reversibly switch between two phenotypic states: a proliferative, weakly metastatic state and a less proliferative, highly metastatic state (5–7). These switches enable circulating metastatic cells to proliferate in favorable, secondary metastatic sites (1, 2). These proliferative and metastatic states are controlled by distinct transcriptional programs. One of the major factors responsible for regulating the transcriptional switch is the microphthalmia-associated transcription factor (MITF) (5, 8, 9), which plays a central role in melanoma progression (10, 11). MITF is the master regulator of the melanocyte lineage (11, 12) and regulates the expression of several

microRNAs (miRNAs) including miR-211 (13) and miR-222/221 (14). It was previously suggested by us (15) and others (16, 17) that miR-211 mediates melanoma phenotypic plasticity. Microenvironmental conditions such as hypoxia (18) and inflammation (19) also influence melanoma plasticity; however, the cell types in the melanoma microenvironment that induce the phenotypic switch have not yet been identified.

It has been well established by us (15, 20) and others (21) that interactions between melanoma cells and the surrounding stroma play major roles in melanoma initiation, progression, metastatic potential, determination of metastasis location, and clinical outcome. Among the different components of the melanoma microenvironment are adipocytes, located in the deepest layer of the skin, and the hypodermis, which is mainly composed of differentiated adipocytes and adipose progenitors (22). Adipocytes promote melanoma growth and metastases (23–30). However, as melanoma progresses, the melanoma cells encounter continuously changing microenvironments (14) that vary in adipocyte composition (31–33). Previous studies have not investigated how the dynamic changes in the cellular microenvironment influence melanoma progression.

Transforming growth factor- β (TGF- β) superfamily members have prominent roles in embryonic development and adult tissue homeostasis (34, 35). Canonical TGF- β signaling is induced by ligand binding to the type II transmembrane receptor serine/threonine kinase TGF- β receptor II (TGFB2), which, in turn, recruits and phosphorylates the type I receptor (TGFB1; also known as ALK5) (36). Activated TGFB1 phosphorylates the cytoplasmic receptor-regulated SMADs, SMAD2 and SMAD3, after hetero-oligomerization with SMAD4 (37). The SMAD complex accumulates in the nucleus, where it binds to SMAD-binding elements and regulates the transcription

¹Department of Human Genetics and Biochemistry, Sackler Faculty of Medicine, Tel Aviv University, Tel Aviv 69978, Israel. ²The Mina and Everard Goodman Faculty of Life Sciences, Bar-Ilan University, Ramat Gan 5290002, Israel. ³Department of Structural Biology, Weizmann Institute of Science, Rehovot 7610001, Israel. ⁴Department of Biostatistics and Computational Biology, Dana-Farber Cancer Institute, Boston, MA 02115, USA. ⁵Broad Institute of MIT and Harvard, Cambridge, MA 02142, USA. ⁶Institute of Pathology, E. Wolfson Medical Center, Holon 58100, Israel. ⁷Institute of Pathology, Tel Aviv Sourasky Medical Center, Tel Aviv 6423906, Israel. ⁸Sackler School of Medicine, Tel Aviv University, Tel Aviv 69978, Israel. ⁹Institute of Endocrinology, Chaim Sheba Medical Center, Tel Hashomer, Israel. ¹⁰Department of Dermatology, Sheba Medical Center, Tel Hashomer 52621, Israel. ¹¹Department of Pediatrics, Memorial Sloan Kettering Cancer Center, 1275 York Avenue, New York, NY 10065, USA. ¹²INSERM 1186, Gustave Roussy, Université Paris-Saclay, Villejuif 94805, France.

*Corresponding author. Email: carmitlevy@post.tau.ac.il

of target genes in a cell-specific manner (37). TGF- β signaling can act in autocrine and in paracrine manners and has two opposing roles in human cancer progression by promoting cytostatic effects or the epithelial-mesenchymal transition (38–40).

Here, we found that the dynamic plasticity of melanoma is regulated by adipocyte cells at an earlier than previously reported phase, before melanoma invasion into the dermis, through an intercellular mechanism that sensitizes melanoma cells to environmental TGF- β . Moreover, we found that the phenotypic plasticity depends on proximity of adipocytes and is reversible—and thereby therapeutically targetable.

RESULTS

Subcutaneous adipocytes in proximity to *in situ* melanoma correlate with advanced disease

Melanoma initiates in the epidermis, and upon disease progression, cancer cells invade into the dermis (14, 20). From the dermis, cells can metastasize through the lymph system (41). We examined melanoma pathological specimens that had been staged using Clark's system, which classifies the depth of melanoma invasion through the dermis into five levels. The highest staging level corresponds to the deepest invasion. Staging is reflective of aggressiveness and poor prognosis (42). Hematoxylin and eosin (H&E) staining demonstrated that, at higher Clark's levels and in cases of lymph node metastases, melanoma cells are in closer proximity to the adipose cells than in lower stages (Fig. 1A). In samples of *in situ*, melanoma cells with characteristics of adipocytes were present in the upper dermis layer in proximity to melanoma cells (Fig. 1B and fig. S1B). Normal skin samples had well-defined adipose tissue located at the hypodermis layer of the skin (Fig. 1B and fig. S1B) (22). In vertical melanoma samples, tumor cells had invaded the adipocyte microenvironment (Fig. 1B and fig. S1B). These results were validated by immunostaining of these specimens for a melanoma marker (HMB-45 and S100) and an adipocyte-specific marker (perilipin) (Fig. 1C and fig. S1, C and D). To exclude the possibility that the dermal perilipin1-positive cells are fibroblasts (43), we stained specimens for a fibroblast marker FSP1. Perilipin1-positive cells located in the dermis near the melanoma cells did not express FSP1, whereas the surrounding dermal fibroblast cells were FSP1 positive (Fig. 1D).

To further examine the clinical relevance of the adipocyte cells to melanoma progression, we analyzed nine additional *in situ* melanoma specimens. In most samples, adipocytes were present in the upper dermis in close proximity to melanoma cells (Figs. 1, B and C, and 2A and fig. S1, B and C); however, in a few samples, adipocytes were found in the hypodermis (Fig. 2A). Multiple nests indicate a rapid disease progression (44), and we therefore measured the numbers and sizes of melanoma nests in the melanoma *in situ* samples (Fig. 2, B and C, and fig. S2). In samples in which adipocytes were in close proximity to melanoma, there were substantially more melanoma nests than in specimens without adipocytes (Fig. 2C). No notable difference was observed in nest size (Fig. 2C). Therefore, our findings suggest that if lesions are not removed, they progress more rapidly toward malignancy when adipocytes are in proximity to the melanoma cells. The interactions between adipocytes and melanoma cells occur earlier than previously reported, beginning at the primary radial stage before melanoma invasion into the dermis, supporting disease progression.

Adipocytes induce melanoma plasticity in a reversible manner by inhibiting miR-211 expression

To gain insight into the effect of adipocytes on melanoma cells in the radial phase, we used an *in situ* melanoma model (14, 20). We chose WM3682 melanoma cells, which are highly proliferative and have no intrinsic invasive abilities and therefore resemble melanoma cells in the *in situ* state (table S1) (13). WM3682 melanoma cells were cocultured with primary human subcutaneous differentiated adipocytes (fig. S3A) in a system that enables free flux of medium without direct cell-cell contact (experimental design scheme in Fig. 3A, left). Monocultured melanoma cells were used as a control. After coculture for 5 days, melanoma cell migration (Fig. 3B) and invasion (Fig. 3C) abilities were substantially enhanced compared to monocultured cells. In contrast, coculture with adipocytes led to a decrease in melanoma cell proliferation compared to monocultured cells (Fig. 3, D and E).

Cancer plasticity is characterized by reversible alternations between two phenotypic states (5–7, 45). Therefore, we next examined whether the effects of adipocytes on melanoma cells are reversible. To this end, we used what we refer to as a reverse coculture system: After 5 days in coculture, the adipocytes were removed, the medium was replaced with unconditioned medium, and the remaining melanoma cells were grown as a monoculture for 5 days and then subjected to further analysis (experimental design scheme in Fig. 3A, right). After reverse coculture, adipocyte-induced migratory (Fig. 3B) and invasive (Fig. 3C) capacities were abrogated, and the cells proliferated similarly to melanoma cells in monoculture (Fig. 3, D and E). Together, these results suggest that adipocytes reversibly switch melanoma phenotype from a proliferative to an invasive state.

Because a single miRNA is able to target multiple genes and thereby regulate several phenotypic outcomes simultaneously (46), we next examined whether miRNAs are the downstream effectors of adipocytes. By miRNA profiling using a microarray, we identified 24 significantly differentially expressed miRNAs ($1.5 < \text{fold}, P < 0.05$) between melanoma cells cocultured with adipocytes and monocultured melanoma cells (Fig. 3F and data file S1). One of the most highly down-regulated miRNAs was miR-211, which was previously suggested to be a regulator of melanoma phenotypic plasticity (15–17, 47).

To test whether miR-211 mediates adipocyte-driven melanoma phenotypic plasticity, we first validated the microarray results. Upon coculturing with adipocytes, reductions in both mature miR-211 and pre-miR-211 abundance were observed compared to monocultured cells (Fig. 3G), implying regulation at the transcriptional level. The inhibitory effect of adipocytes on miR-211 expression by melanoma cells was abolished upon adipocyte removal, indicative of reversibility (Fig. 3G). Notably, the decrease in miR-211 expression was reproduced upon coculture with differentiated NIH3T3-L1 adipocytes, a well-established murine fibroblast-origin model for adipose tissue (fig. S3, A and B) (48). This suggests that adipocyte-mediated hindrance of miR-211 expression is not limited to subcutaneous adipocytes. Moreover, incubation of melanoma cells with conditioned medium obtained from a differentiated adipocyte culture reversibly decreased expression of miR-211 produced by melanoma cells compared with cells grown in unconditioned medium (fig. S3C). This suggests that adipocytes exerted these actions through soluble factors.

To further explore how miR-211 contributes to the adipocyte-derived phenotypic plasticity of melanoma cells, we first determined

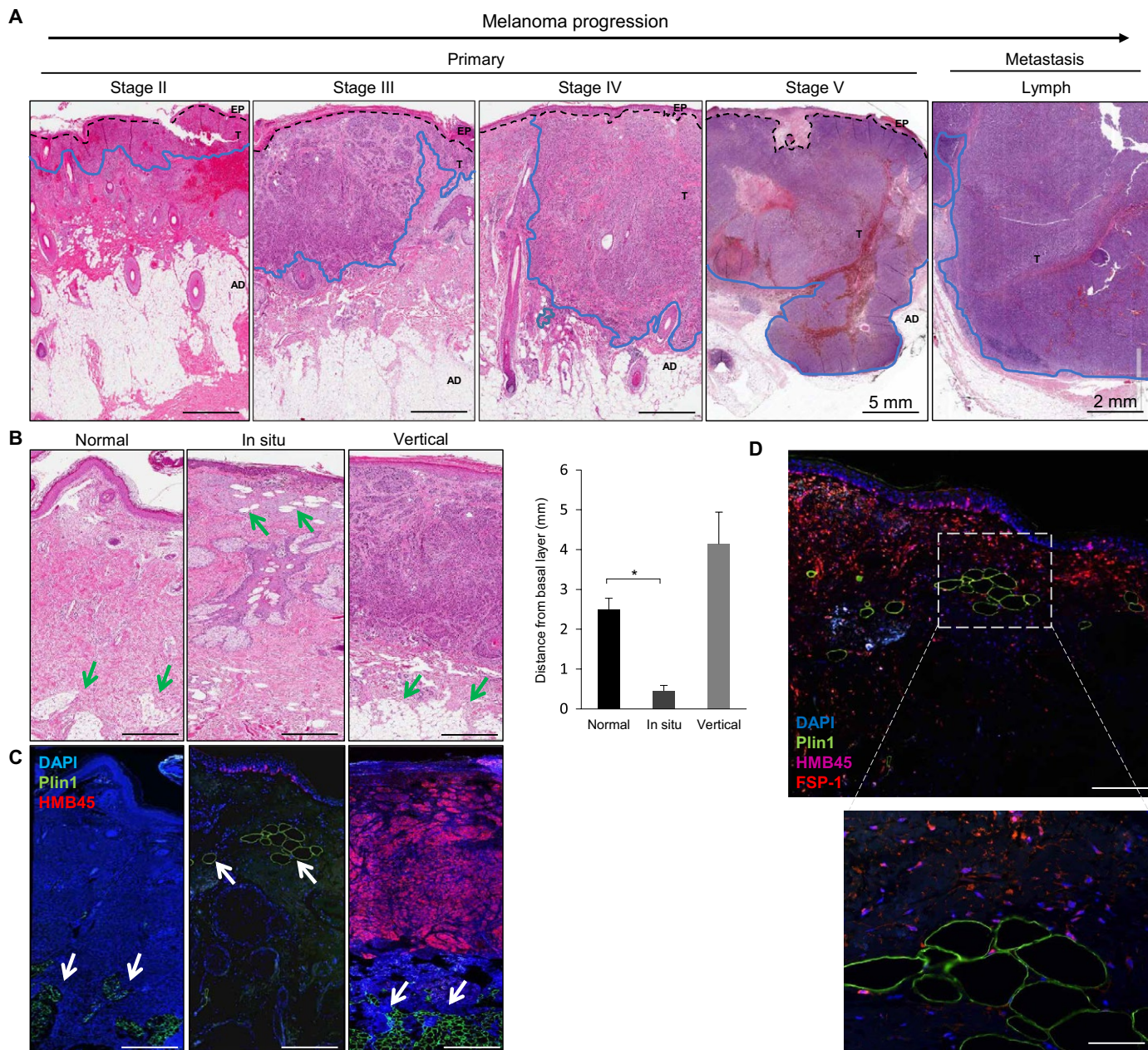
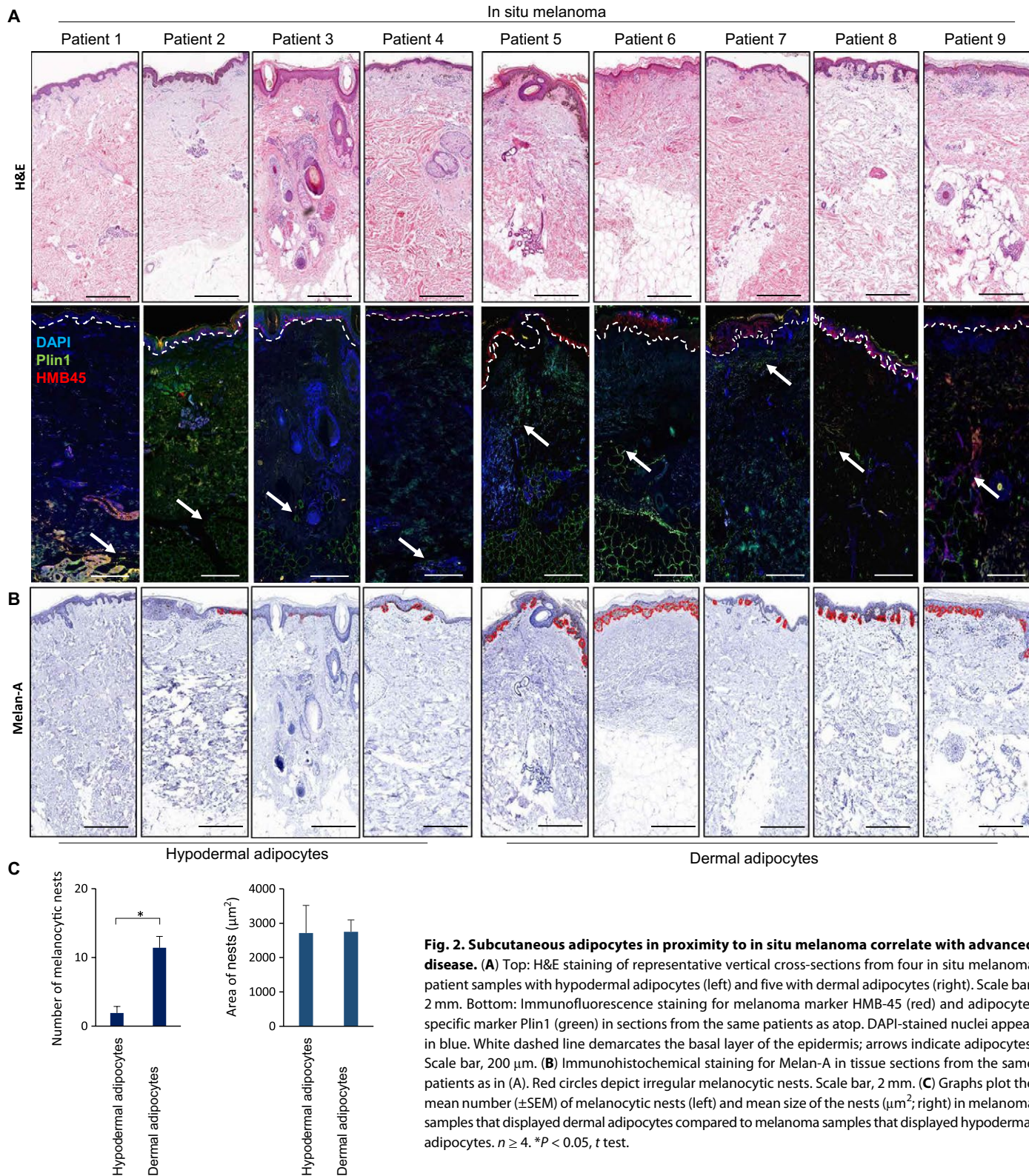


Fig. 1. Subcutaneous adipocytes are observed in proximity to in situ melanoma. (A) Hematoxylin and eosin (H&E) staining of representative vertical cross-sections of melanoma patient samples ($n = 5$) categorized by Clark's staging system (stages II to V) and a melanoma metastasis in the lymph node. Scale bars, 2 mm (stages II to IV and lymph) and 5 mm (stage V). Black dashed lines indicate epidermal-dermal junctions; blue lines indicate tumor margins. T, tumor; AD, adipocytes. (B) H&E staining of typical vertical cross-sections from a healthy skin sample (left) and from two melanoma patient samples at different progression stages (right). Scale bar, 2 mm. Arrows indicate adipocytes. Graph plots the mean (\pm SEM) distance of the adipocytes from the epidermal basal layer from three independent experiments. * $P < 0.05$, t test. (C) Immunofluorescence analysis of consecutive slices from similar sections described and shown in (B) with melanoma marker HMB-45 (red) and adipocyte-specific marker Plin1 (green). DAPI-stained nuclei appear in blue. Scale bar, 2 mm. (D) Additional immunofluorescence analysis of the patient melanoma sections, represented with the in situ section shown in (C), with fibroblast marker FSP1 (pink) as well as HMB-45 (red) and Plin (green). Scale bars, 50 μ m (top) and 20 μ m (inset/bottom).

whether miR-211 alters the melanoma transcriptome. To this end, we chose WM1716 melanoma cells, which express low levels of miR-211 and are highly invasive with weak proliferative potential (13). WM1716 cells were stably transfected with a miR-211 mimic or with a scrambled control (fig. S3D) and subjected to mRNA profiling. In cells stably transfected with miR-211, there was a notable increase in expression of genes associated with proliferation and down-regulation

of genes associated with an invasive phenotype (fig. S3E) (6, 15). To validate these results, we generated an additional melanoma cell line, WM3314 cells, which have high invasive potential, low proliferation ability, and low levels of miR-211 (13), were engineered to stably express a miR-211 mimic or the scrambled control (fig. S3A). For consistency with the proliferative transcriptome, both WM1716 and WM3314 cells had higher proliferation rates upon miR-211 mimic



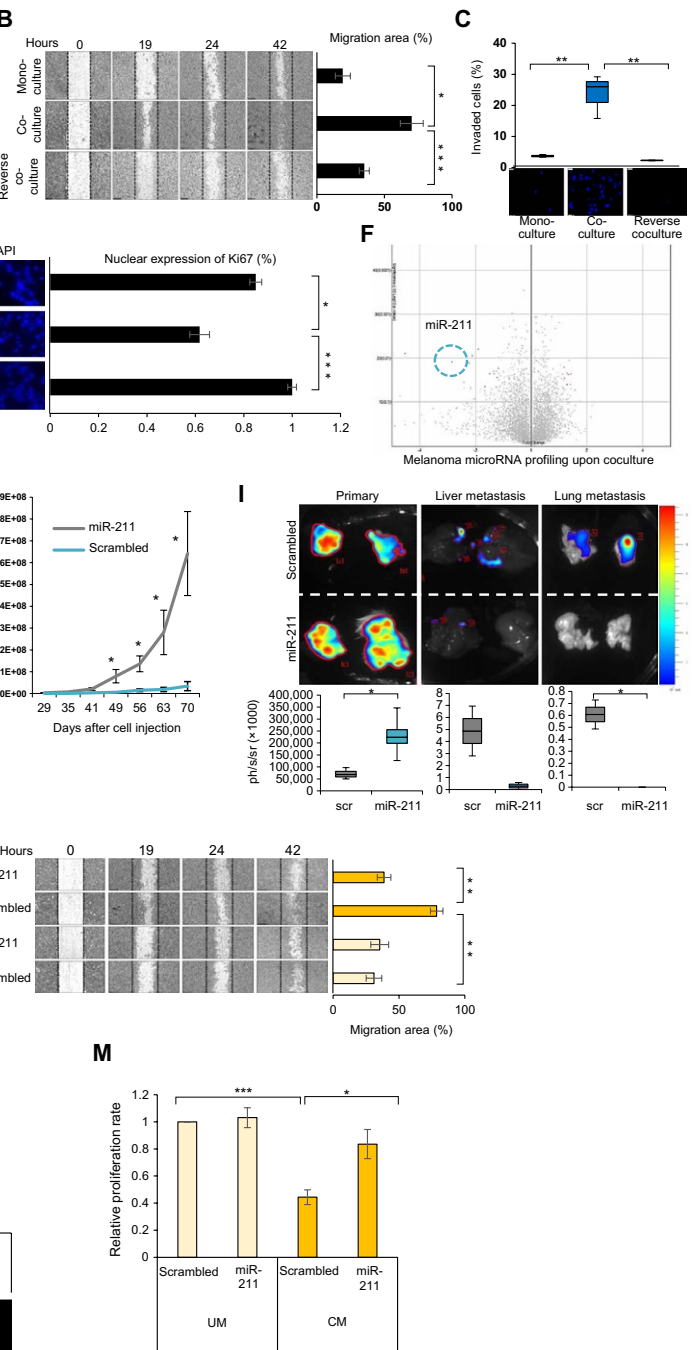
expression compared to the slowly proliferating control cells (fig. S3F). Consistent with these results, antagomiR-mediated depletion of miR-211 from WM3526 cells (fig. S3G), which are highly proliferative and poorly invasive and express relatively high miR-211 levels (13),

resulted in attenuated cell growth (fig. S3H). Furthermore, miR-211 expression in WM1716 and WM3314 cells resulted in enhanced progression through the cell cycle compared to control cells (fig. S3I), and the invasive potential of these cell lines was considerably reduced

Fig. 3. Adipocytes drive melanoma plasticity in a reversible manner by miR-211 repression. (A) Scheme of experimental design coculture and reverse coculture assays. (B to D) Analysis of migration (B), invasion (C), and XTT [2,3-bis(2-methoxy-4-nitro-5-sulfophenyl)-2H-tetrazolium-5-carboxanilide] proliferation (D) assays using WM3682 melanoma cells in the indicated conditions, described in (A). Images are representative. Scale bars, 100 μ m (B) and 50 μ m (C) (DAPI-stained nuclei are blue). Graphs plot means (\pm SEM from three or more independent experiments; * $P < 0.05$, ** $P < 0.01$, and *** $P < 0.005$, *t* test). (E) Representative Ki67 immunostaining (green) and DAPI nuclear staining (blue) in WM3682 cells in the indicated conditions, described in (A). Scale bars, 50 μ m. Graph plots mean \pm SEM from three independent experiments; statistical analyses as in (B) to (D). (F) Volcano plot representing the distribution of significantly (fold >1.5 , $P < 0.05$ by *t* test) differentially expressed miRNAs, noting miR-211, between cocultured and monocultured WM3682 melanoma cells in two independent gene profiling experiments. (G) qRT-PCR analysis of mature and pre-miR-211 expression in WM3682 melanoma cells grown under the indicated conditions, described in (A). Graph plots mean \pm SEM from three independent experiments; statistical analyses as in (B) to (D). (H) Representative *in vivo* bioluminescent images of mice injected with WM1716 cells stably expressing miR-211 or a scrambled control at day 70 after injection. Graph shows mean bioluminescence \pm SEM from five mice per group; statistical analyses as in (B) to (D). (I) Representative ex vivo bioluminescence images of local xenografts, livers, and lungs isolated from mice injected with WM1716 cells stably transfected with miR-211 or scrambled control at 70 days after injection. Graph shows mean bioluminescence \pm SEM from four mice per group; statistical analyses as in (B) to (D). (J) Schematic of experimental design to assess the effects of miR-211 expression in melanoma cells cultured with or without adipocyte-conditioned medium. (K to M) Migration (K), invasion (L), and proliferation (M) assays using WM3682 melanoma cells in the indicated conditions, described in (J). Scale bars, 100 μ m (K) and 50 μ m (L). Graphs, *n*, and statistical analyses are as described in (B) to (D).

upon miR-211 expression (fig. S3J). These results are in agreement with our own (13) and others' (47, 49) previous observations and support the hypothesis that miR-211 maintains melanoma cells in a proliferative state.

We next used a melanoma xenograft mouse model whereby WM1716 and WM3314 cells that constitutively expressed miR-211



or scrambled control as well as a gene encoding luciferase were subcutaneously injected into immunocompromised mice. Mice injected with miR-211-expressing cells displayed higher local tumor growth rates compared to mice injected with cells that expressed the scrambled control (Fig. 3H and fig. S3K). Further, ex vivo quantifications demonstrated that larger local tumors that resulted from cells that

overexpressed the miR-211 mimic were larger than those that resulted from cells that expressed the scrambled control (Fig. 3I and fig. S3L). No metastases were observed in lungs and liver upon miR-211 expression, whereas massive metastatic formation resulted from scrambled control-expressing cells (Fig. 3I and fig. S3L). This demonstrates that miR-211 suppresses melanoma metastatic potential. Metastatic lesions were verified by H&E staining (fig. S3M). Together, these observations demonstrate that miR-211 augments cell growth and suppresses metastatic capacities of melanoma cells, as previously reported (16, 17).

We next examined whether the effect of adipocytes on melanoma phenotype is miR-211 dependent and whether miR-211 reexpression hinders these effects (experimental design scheme in Fig. 3J). To avoid collateral influence of miR-211 mimic transfection, these experiments were conducted by incubation of melanoma cells with conditioned medium from an adipocyte culture. Introduction of miR-211 mimic into WM3682 melanoma cells (fig. S3N) conditioned with adipocyte medium completely abolished the adipocyte-induced migration (Fig. 3K) and invasion (Fig. 3L) abilities observed in scrambled control-transfected cells. The suppressive effect of adipocytes on cell proliferation was reversed upon transfection of melanoma cells with a miR-211 mimic (Fig. 3M). Introduction of the miR-211 mimic into WM3682 melanoma cells not grown in adipocyte-conditioned medium had little effect on cell proliferation (Fig. 3M), likely due to the high basal miR-211 expression in these cells (13). These results demonstrate that adipocytes drive melanoma plasticity by inhibition of miR-211 expression.

Adipocytes decrease miR-211 expression through secretion of IL-6 and TNF- α

The secreted cytokines interleukin-6 (IL-6) and tumor necrosis factor- α (TNF- α) are components of the adipocyte secretome (50) and are known to mediate pro-invasive propensities of cancer cells (51). Moreover, IL-6 and TNF- α decrease the abundance and transcriptional activity of MITF (52, 53), a regulator of melanoma phenotypic switch (16), which transcriptionally promotes miR-211 expression (13). To test whether adipocytes exert their effects on melanoma cells by secretion of these two cytokines, we first examined whether subcutaneous adipocytes secrete IL-6. Medium conditioned with adipocytes had substantially higher amounts of IL-6 compared to unconditioned medium (Fig. 4A). Further, treatment of WM3682 cells with both IL-6 and TNF- α mimicked the effect of culture with adipocytes: It resulted in reduced miR-211 expression (Fig. 4B), increased invasion capacity (Fig. 4C), and decreased proliferation (Fig. 4D) in WM3682 melanoma cells.

We next asked whether the adipocyte-induced melanoma phenotypic plasticity is IL-6 and TNF- α dependent. To this end, we examined the influence of adipocyte-conditioned medium on miR-211 expression in WM3682 melanoma cells in the presence of curcubitacin I, an inhibitor of IL-6 signaling (54), and R7050, a specific inhibitor of TNF- α (experimental design scheme in Fig. 4E, left) (55). Treatment of WM3682 melanoma cells, conditioned with adipocyte medium, with either curcubitacin I or R7050 restored miR-211 expression (Fig. 4F). The inhibitors also abolished the effect of adipocytes on the melanoma phenotypic switch, as demonstrated by reductions in melanoma invasion capacity (Fig. 4G) and proliferation (Fig. 4H).

In immunofluorescence data of melanoma patient samples, IL-6 was detected in upper dermal regions only when adipocytes were present in that region; IL-6 was not detected in adipocyte-free areas (Fig. 4I). To clinically examine the relevance of IL-6, we performed

Kaplan-Meier analysis on melanoma patient survival using data from the cBioPortal for Cancer Genomics (56). There was a notable increase in survival in the group of melanoma patients with no amplification of the mRNA encoding the IL-6 receptor (IL-6R) compared to those with amplification (Fig. 4J). These results suggest that TNF- α and IL-6 secreted by adipocytes induce a phenotypic switch in melanoma cells by inhibition of miR-211 expression.

Notably, treatment of melanoma with IL-6, TNF- α , or adipocyte-conditioned medium reduced the expression of MITF at the mRNA level (fig. S4, A and B) and substantially reduced the activity of a reporter gene driven by the MITF promoter (fig. S4C). Moreover, in the presence of IL-6 and TNF- α inhibitors, adipocytes failed to repress MITF expression in melanoma cells (fig. S4D). This suggests that adipocytes, through the secretion of IL-6 and/or TNF- α , cause a decrease in MITF abundance, which leads to the down-regulation of the miR-211 and disease progression.

miR-211 attenuates TGF- β signaling and reduces melanoma sensitivity to TGF- β

In a search for a cancer-related signaling pathway that might account for miR-211 actions, we identified the genes that were differentially expressed upon stable expression of the miR-211 mimic in WM1716 cells compared to cells expressing a scrambled control (Fig. 5A). Gene set enrichment analysis (GSEA) identified a single set of genes related to TGF- β signaling that are down-regulated in cells that express miR-211 (data file S2 and fig. S5A). Further, we separately calculated the mean log fold ratio of up- and down-regulated genes of 10 additional cancer-related pathways [inferred from Kyoto Encyclopedia of Genes and Genomes (KEGG) database] and found that the TGF- β -mediated signaling was the most significantly altered pathway in cells that express miR-211 mimic (Fig. 5A). Furthermore, of genes known to be involved in the TGF- β pathway, the down-regulated genes were a more prominent group than the up-regulated genes (Fig. 5A and data file S3). Melanoma cells with a proliferative gene expression signature were previously shown to be more susceptible to TGF- β -mediated growth inhibition than cells with an invasive signature (6), whereas MITF depletion was demonstrated to reduce the susceptibility of the proliferative cells to TGF- β -mediated growth inhibition (6, 57).

To confirm that miR-211 attenuates the canonical TGF- β pathway in melanoma, we first examined its effect on a TGF- β -responsive luciferase reporter gene. miR-211 overexpression in both WM1716 and WM3314 cells resulted in reduced TGF- β -responsive reporter activity compared to control cells (Fig. 5B). Conversely, antagonism-mediated depletion of miR-211 from WM3526 cells led to increased TGF- β -responsive reporter activity (fig. S5B). Notably, the ability of miR-211 antagonism to induce TGF- β activity was abolished in the presence of small interfering RNA (siRNA) targeting SMAD4 (Fig. 5C and fig. S5, C and D), indicating that TGF- β operates through SMAD4-mediated signaling. Further, miR-211-expressing cells exhibited markedly lower phosphorylation of the TGF- β signaling cytoplasmic transducer SMAD2 (58) than that observed in control cells (Fig. 5D). Moreover, SMAD4 nuclear translocation was abrogated upon miR-211 expression compared to control cells (Fig. 5E). miR-211 induced the expression of pro-proliferative genes (*ID3*, *ID1*, and *c-MYC*) and reduced levels of pro-invasive TGF- β -driven genes (*SNAI1*, *HMGA2*, *ZEB2*, *ZEB1*, and *TWIST*) (Fig. 5F) (39). These results suggest that miR-211 represses the canonical TGF- β pathway, which, in turn, alters the cellular transcriptome in favor of a proliferative phenotype.

Fig. 4. Adipocytes decrease miR-211 expression through secretion of IL-6 and TNF- α .

(A) Amount of IL-6 in medium conditioned by adipocytes compared to that in control medium. Data are means \pm SEM from three independent experiments. *** $P < 0.005$, t test. (B to D) Analysis of miR-211 expression by qRT-PCR (B), invasion (C), and proliferation by XTT assay (D) in WM3682 melanoma cells treated for 48 hours with IL-6 (40 ng/ml) or TNF- α (15 ng/ml) relative to each in vehicle-treated cells. Images (C) are representative; DAPI-stained nuclei are blue. Scale bar, 50 μ m. Relative proliferation (D) was assessed at day 3. Data are means \pm SEM from three independent experiments. * $P < 0.05$ and *** $P < 0.005$, t test. (E to H) Experimental schematic (E) used to assess miR-211 expression by qRT-PCR (F), invasion (G), and relative proliferation by XTT assay (H) in WM3682 melanoma cells cultured in adipocyte-conditioned medium and treated with an IL-6 inhibitor (IL-6-i) (cucurbitacin I, 0.1 μ M) or a TNF- α inhibitor (TNF- α -i) (R7050, 0.5 μ M) for 48 hours. Graph plots, n , statistical analyses, images, and scale bars are as described in (B) to (D). (I) Representative images and analysis of healthy donor normal skin and *in situ* melanoma patient sections (examined in proximity of adipocytes or not) immunofluorescently stained for melanoma marker HMB-45 (pink), IL-6 (red), and adipocyte-specific marker Plin1 (green) and counterstained with DAPI (blue). Scale bars, 50 μ m (top) and 20 μ m (insets/bottom). Arrows indicate IL-6. (J) Kaplan-Meier survival plot of patients bearing melanoma with no overexpression (blue) or with overexpression of the IL-6 receptor (IL-6R) (red). Data were obtained from the Cancer Genome Atlas ($n = 550$; $P = 0.00971$).

Next, we determined whether miR-211 confers TGF- β -resistance to melanoma cells. TGF- β stimulation failed to increase the TGF- β -responsive reporter activity in both WM1716 and WM3314 miR-211-expressing cells, in contrast to enhanced reporter activity observed in TGF- β -sensitive control cells (Fig. 5G). Both WM1716 and WM3314 cells lost their susceptibility to TGF- β -mediated growth inhibition upon miR-211 expression compared to control cells (Fig. 5H). As expected, the level of endogenous miR-211 inversely correlated with TGF- β susceptibility, as highly proliferative WM3526

cells, which express high levels of endogenous miR-211 (13), were less responsive to TGF- β (fig. S5E) than were WM1716 and WM3314 cells, which express low amounts of miR-211 (Fig. 5H) (13). The effect of miR-211 on melanoma sensitivity to TGF- β -mediated invasion could not be evaluated because of the high intrinsic invasive abilities of WM1716 and WM3314 cells (13).

To identify the cell type in the melanoma environment that is the source of TGF- β , we examined the amount of TGF- β in primary human skin cells that are the major components of the epidermis

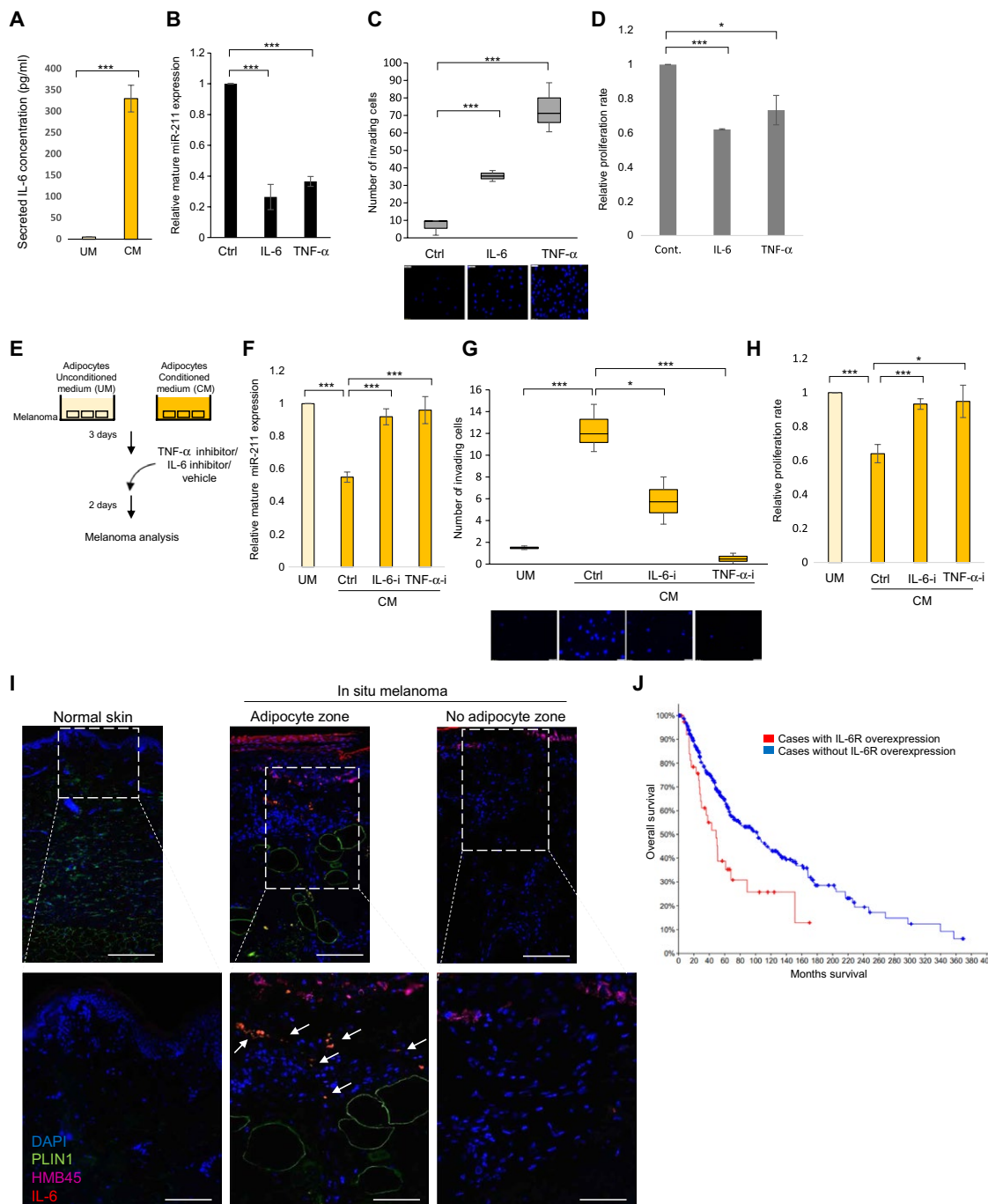
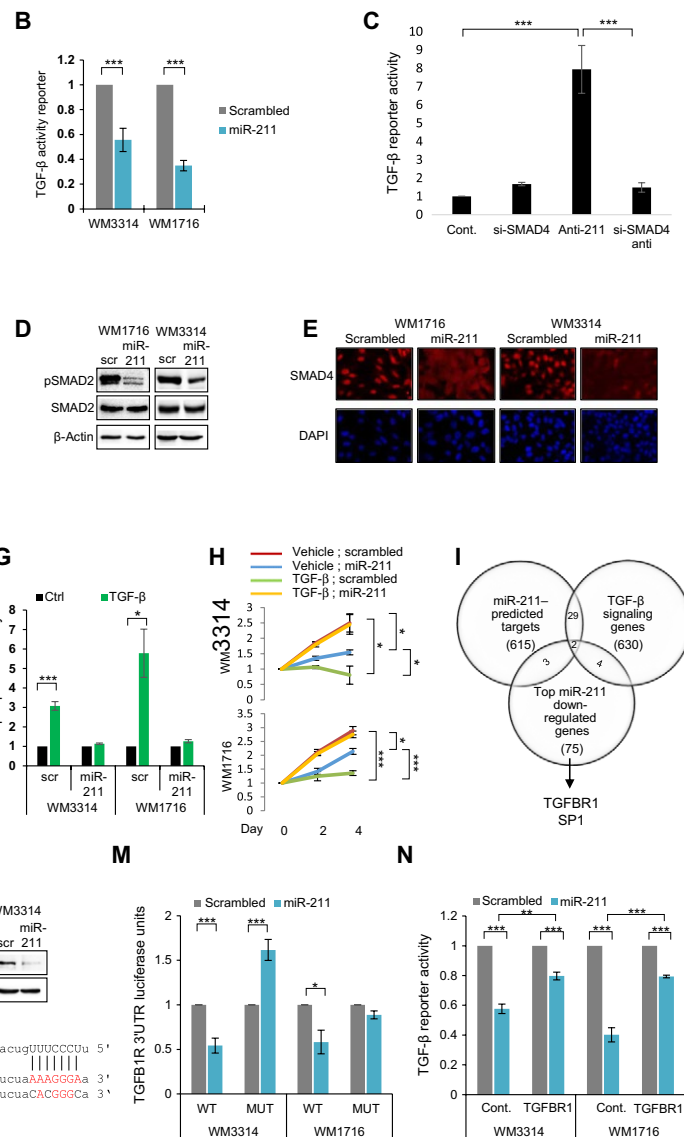


Fig. 5. miR-211 attenuates TGF- β signaling and reduces the sensitivity of melanoma cells to TGF- β . (A) Cell signaling pathway analysis based on transcriptome profiling of WM1716 melanoma cells stably expressing miR-211 or scrambled control. TGF- β pathway score, $P < 0.0056$; down-regulated TGF- β genes, $P < 0.037$; up-regulated TGF- β genes, $P < 0.157$. See also data files S2 and S3. (B) Luciferase activity assay of a TGF- β -responsive reporter in WM1716 and WM3314 cells stably expressing miR-211 or a scrambled control. Data are means \pm SEM from three independent experiments. *** $P < 0.005$, t test.

(C) Luciferase activity assay of TGF- β -responsive reporter in WM3682 cells cotransfected with antagoniR-miR-211 or a scrambled control and either siSMAD4 or scrambled siRNA. Data are means \pm SEM from three independent experiments; statistical analyses as in (B). (D and E) Western blot analysis of phosphorylated and total SMAD2 abundance (D) and SMAD4 immunostaining (red; E) in the indicated cells. β -Actin served as loading control (D); DAPI counterstained the nuclei (blue; E). Scale bar, 20 μ m. (F) qRT-PCR analysis of the expression of a panel of TGF- β signaling-related genes in WM3314 cells stably expressing miR-211 relative to those expressing a scrambled control. Data are means \pm SEM from four independent experiments. * $P < 0.05$ and *** $P < 0.005$, t test. (G) Luciferase activity assay of TGF- β -responsive reporter in the indicated cells upon treatment with recombinant TGF- β (2 ng/ml) or dimethyl sulfoxide (DMSO) (ctrl). Data are means \pm SEM from three independent experiments; statistical analyses as in (F). (H) XTT proliferation assay of cells described and treated as in (G). Data are mean fold change relative to day 0 \pm SEM from three independent experiments; statistical analyses as in (F). (I) Venn diagram showing the overlap between the top 20% of down-regulated genes in WM1716 melanoma cells upon miR-211 introduction, the miR-211-predicted targets, and the genes identified as involved in TGF- β signaling ($n = 2$). (J) qRT-PCR analysis of *TGFBR1* mRNA expression in the indicated cells. Data are means \pm SEM from three independent experiments; statistical analyses as in (B). (K) Western blot analysis of *TGFBR1* protein abundance in the indicated cells. β -Tubulin served as a loading control. Blots are representative of three independent experiments. (L) Predicted miR-211 target site identified in *TGFBR1* 3' UTR (red). Wild-type (WT) and mutated (MUT) miR-211 binding site sequences. (M) Luciferase activity assay of WT or MUT *TGFBR1* 3' UTR reporter constructs in WM3314 and WM1716 cells stably expressing miR-211 or scrambled control. Graphs and statistical analyses are as described in (G). (N) Luciferase activity assay of TGF- β -responsive reporter in WM3314 and WM1716 cells stably expressing miR-211 or scrambled control, which were transfected with either *TGFBR1* complementary DNA (cDNA) that lacks the 3' UTR or an empty vector (ctrl). Data are means \pm SEM from three independent experiments. ** $P < 0.01$ and *** $P < 0.005$, t test.

(differentiated and undifferentiated keratinocytes), the dermis (fibroblasts and endothelial cells), and the hypodermis (adipocytes). TGF- β was highly expressed in the dermis cells compared to cells that compose the epidermis or the hypodermis. This suggests that the dermis layer is the main source of TGF- β in the melanoma environment (fig. S5F).

Melanoma cells are resistant to the activation of TGF- β signaling (6, 59), and our findings suggest that miR-211 attenuates TGF- β



mediated signaling in melanoma cells and reduces their sensitivity to extrinsic TGF- β . To identify miR-211 downstream targets, we overlapped the top 20% of genes down-regulated upon miR-211 expression, potential miR-211 targets obtained from TargetScan prediction algorithms, and TGF- β signaling-related genes inferred from KEGG database (Fig. 5I and data file S4). *TGFBR1* and *SP1* were present in all three sets. The crucial role of *TGFBR1* in transducing TGF- β signaling has been established (36). The transcription

factor SP1 regulates multiple signaling and cellular pathways (60). *TGFBR1* expression in WM3314 and WM1716 cells was reduced upon miR-211 expression at both mRNA (Fig. 5J) and protein levels (Fig. 5K). AntagomiR-211 introduction into WM3526 cells increased expression of *TGFBR1* mRNA (fig. S5G) and TGFBR1 protein (fig. S5H). However, *SP1* expression was not decreased by miR-211 (fig. S5I). The activity of a luciferase reporter gene fused to the *TGFBR1* 3' untranslated region (3' UTR) was decreased upon miR-211 expression in WM3314 and WM1716 cells, and specific mutations in the miR-211 binding sites resulted in derepression (Fig. 5, L and M). Last, in rescue experiments, overexpression of TGFBR1 in WM1716 and WM3314 cells stably transfected with miR-211 blocked the inhibitory effect of miR-211 on TGF- β -responsive reporter activity (Fig. 5N). Together, these findings suggest that miR-211 suppresses endogenous TGF- β signaling in melanoma cells and confers TGF- β resistance, at least, in part, by directly suppressing the expression of *TGFBR1*.

Adipocytes sensitize melanoma cells to TGF- β by repressing miR-211 expression

Adipocytes switch the melanoma cell phenotype from proliferative to invasive by down-regulating miR-211 expression. Given the parallels between miR-211 expression and TGF- β resistance in melanoma cells, we reasoned that adipocytes enhance melanoma cell sensitivity to environmental TGF- β . First, we investigated whether adipocytes could reversibly induce endogenous TGF- β signaling in melanoma cells. WM3682 melanoma cells had higher levels of SMAD2 phosphorylation upon coculture with adipocytes than did monocultured melanoma cells, and SMAD2 phosphorylation was diminished upon coculture reversal (Fig. 6A). Notably, culture of WM3682 cells with conditioned medium from an adipocyte culture resulted in increased expression of *TGFBR1* (Fig. 6A). Moreover, cocultured WM3682 cells had higher expression of the pro-invasive TGF- β -driven genes (*TWIST*, *ZEB2*, *MDM2*, and *HMGH2*) (39) and lower expression of genes more characteristic of the proliferative phenotype (*c-MYC*, *ID3*, and *ID1*) (39) in comparison to monocultured cells (Fig. 6B). These effects were reversed upon adipocyte removal from the culture (Fig. 6B). The adipocyte-induced transcriptional signature of the invasive phenotype was the inverse of that of the miR-211-induced transcriptome (Fig. 5F).

Next, rescue experiments were performed to confirm that adipocytes increase TGF- β signaling in melanoma cells through miR-211 repression (experimental design scheme in Fig. 6C). Using a TGF- β -responsive reporter gene, we demonstrated that miR-211 mimic introduction into WM3682 melanoma cells treated with adipocyte-conditioned medium completely abolished the adipocyte-derived induction of TGF- β reporter activity (Fig. 6D).

Next, we aimed to determine whether adipocytes could reversibly sensitize melanoma cells to TGF- β . Melanoma cells treated with adipocyte-conditioned medium displayed higher TGF- β -responsive reporter activity upon treatment with external TGF- β compared to cells treated with vehicle control (Fig. 6E). No substantial change in TGF- β -responsive reporter activity was detected in cells incubated in unconditioned medium (Fig. 6E). The adipocyte-driven TGF- β sensitivity was abolished upon conditioned medium removal (Fig. 6E), indicative of reversibility. Further, melanoma cells grown in conditioned medium from adipocytes exhibited a reversible susceptibility to TGF- β -mediated invasion, whereas TGF- β resistance was observed in cells grown in unconditioned medium (Fig. 6F).

Together, these results suggest that adipocytes reversibly evoke TGF- β sensitivity in melanoma cells.

We next asked whether adipocyte-induced melanoma phenotypic plasticity is TGF- β signaling dependent. To this end, we examined the influence of SB431542, a specific inhibitor of TGFBR1 (33), on adipocyte-mediated invasion of WM3682 melanoma cells. SB431542 treatment resulted in complete loss of adipocyte-driven invasion (Fig. 6G). These results indicate that adipocytes elicit their effects on melanoma cells in a TGF- β signaling-dependent manner.

DISCUSSION

Cancer research has traditionally focused on cancer cell mutagenesis per se or on its effect on tumor stroma (1). Recently, accumulating evidence, however, highlights the role of the reciprocal cross-talk between the microenvironment and the tumor in establishing the tumor phenotype (1, 14, 61). The cross-talk between melanocytes and their neighboring cells is a classic example of the continuous communication that occurs during normal and disease conditions. Melanoma is a neoplasm of melanocyte origin. Melanocytes produce the pigment melanin, which is stored in melanosomes (20). In normal skin, melanosomes are transferred to the epidermis in response to ultraviolet (UV) exposure providing protection against UV-induced DNA damage (62). Melanoma maintains melanosome production and trafficking functions for reasons that are mostly unknown. We found that melanoma cells communicate with the microenvironment by miRNA trafficking through melanosomes, prompting dermal metastatic niche generation (20). It will be interesting to learn whether there are additional cases of cancer cells that keep their seemingly unnecessary cell of origin functions and whether this might predispose characterization of tumor initiation.

Over the course of progression, the cancer encounters different microenvironments. In the case of cutaneous melanoma during the radial growth phase, proliferation begins from the basal epidermis and advances toward the upper epidermis, which is populated by differentiated keratinocytes (14). Subsequently, in the vertical growth phase, the melanoma invades the dermis, which consists of blood vessels and mesenchymal factors such as fibroblasts (63). It then spreads to the subcutaneous tissue, which is mainly composed of adipocytes (29). The intercommunication between melanoma cells and the neighboring cells is mostly based on direct cell contact, growth factor secretion, circulating extracellular miRNAs, and extracellular vesicle exchange, all leading to the activation of specific pro-cancer signaling pathways (14, 20). Here, we report that, in the presence of *in situ* melanoma, subcutaneous adipocytes translocate from their usual location in the hypodermis layer of the skin to the upper dermal layer. We also found that the translocated adipocytes' proximity to the melanoma cells correlates with disease aggressiveness. It will be interesting to further explore *de novo* melanoma microenvironments that are characterized on the basis of not only molecular changes within the cells but also changes in their location. For example, is there an immune cell that appears specifically in close proximity to *in situ* melanoma? Because the identification of *de novo* cell location depends on immunostaining with specific antibodies as we did here, this presented a technical challenge for us, which we hope future studies will overcome.

The proliferative-to-invasive phenotypic switch model for melanoma progression proposes that tumor plasticity is driven by

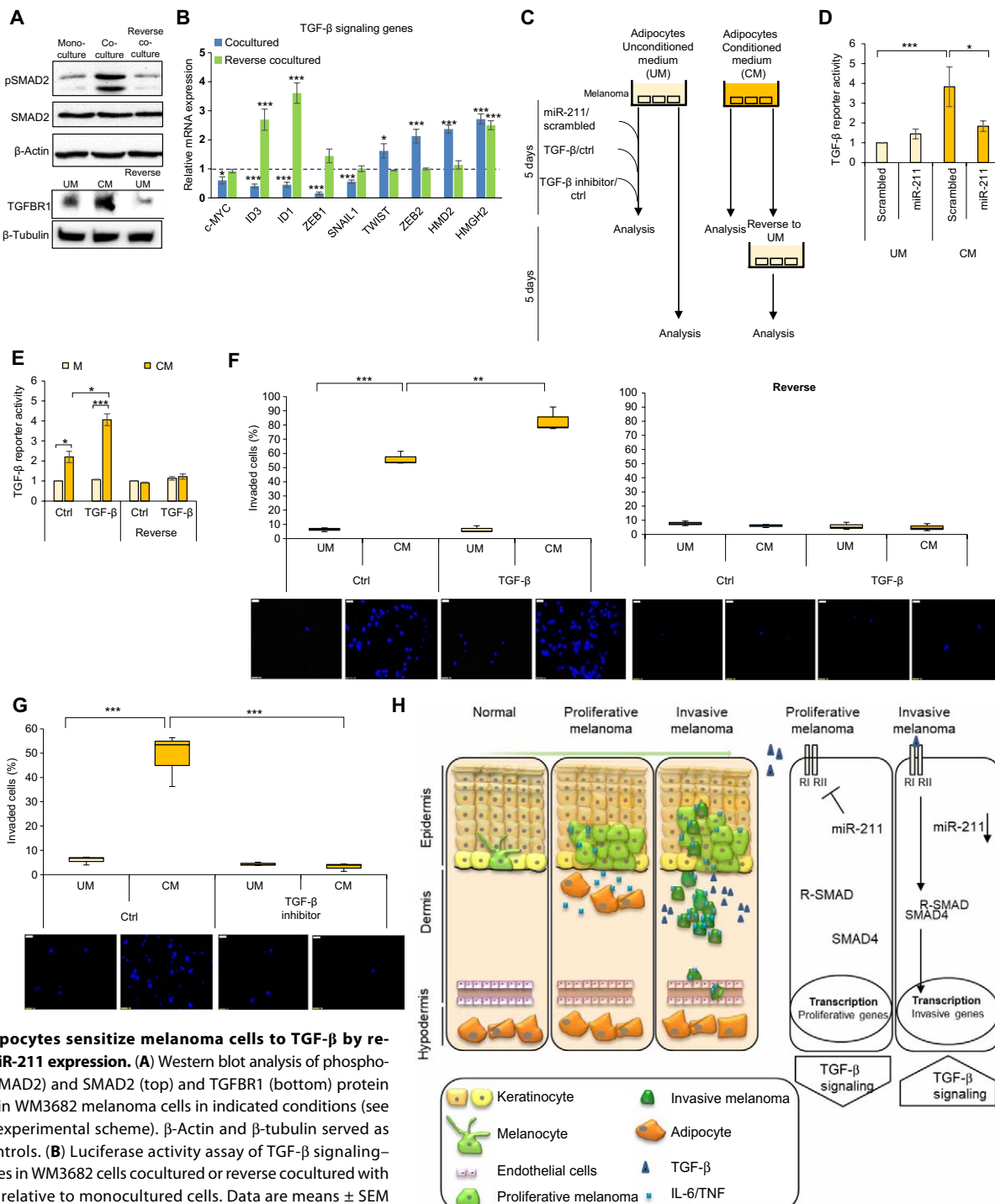


Fig. 6. Adipocytes sensitize melanoma cells to TGF- β by repressing miR-211 expression. (A) Western blot analysis of phospho-SMAD2 (pSMAD2) and SMAD2 (top) and TGFBR1 (bottom) protein expression in WM3682 melanoma cells in indicated conditions (see Fig. 2A for experimental scheme). β -Actin and β -tubulin served as loading controls. (B) Luciferase activity assay of TGF- β signaling-related genes in WM3682 cells cocultured or reverse cocultured with adipocytes relative to monocultured cells. Data are means \pm SEM from three independent experiments; * $P < 0.05$ and *** $P < 0.005$.

(C) Experimental schematic in (D) to (G). **(D and E)** Luciferase activity of a TGF- β -responsive reporter in WM3682 cells either transfected with a miR-211 mimic or scrambled control (D) or treated with TGF- β (2 ng/ml) or DMSO (ctrl) (E). **(F and G)** Invasion assay of WM3682 melanoma cell grown in adipocyte-conditioned medium, followed by conditioned medium removal (reverse) in the indicated conditions, upon treatment with TGF- β (2 ng/ml; F) or TGF- β inhibitor SB431542 (5 μ M; G), each compared with those treated with DMSO. Images are representative; DAPI-stained nuclei are blue. Scale bars, 50 μ m. Data in (D) to (G) are means \pm SEM from three independent experiments. * P < 0.05, ** P < 0.01, and *** P < 0.005, *t* test. **(H)** Proposed mechanism of adipocyte-mediated regulation of TGF- β signaling in melanoma cells. In proliferative melanoma (melanoma *in situ*), miR-211 represses the expression of both TGFBR1 (RI) and TGFBR2 (RII), suppressing endogenous TGF- β signaling in melanoma cells and conferring TGF- β resistance. As a result, cells are highly proliferative and weakly metastatic. When adipocytes are present in the melanoma microenvironment, IL-6 and TNF- α released from the adipocytes suppress miR-211 expression. The subsequent expression of TGF- β receptors enhances sensitivity to environmental TGF- β and therefore promotes the melanoma phenotypic switch from the proliferative to the highly invasive state.

microenvironmental changes, rather than by the accumulation of genetic events (5, 6). Although several microenvironmental conditions induce this phenotypic switch, the cell type(s) in the melanoma microenvironment that induces this crucial phenomenon was hitherto not described. Here, we show that skin adipocytes serve as the cellular inducer of melanoma plasticity. They do so by secreting IL-6 and TNF- α , which decrease miR-211 expression in melanoma, thereby leading to the proliferative-to-invasive phenotypic switch. We further demonstrate that miR-211 inhibition enhances endogenous TGF- β signaling and sensitizes melanoma cells to environmental TGF- β . According to this phenotypic switch model (5, 6), tumor cells are at the invasive stage while in the blood (45). To establish metastases, tumor cells travel via the bloodstream to the destination organ and subsequently revert into the proliferative stage again (5, 6). It will be interesting to learn what the environmental cues in the distant metastatic niche that trigger this phenotypic switch are and whether it can be used to block the formation of metastases.

Our findings are also of relevance to epidemiological and experimental studies, suggesting that obesity increases the risk of developing subcutaneous melanoma (64–68). However, it is still not fully understood whether local changes in the subcutaneous adipose layer contribute to these phenotypes or whether the phenotypes result from a systemic effect. It is possible that obesity alters the subcutaneous adipose tissue and changes the skin microenvironment (67). Obesity is known to be associated with a wide spectrum of dermatologic diseases, such as psoriasis, ulcerations, infections, poor wound healing, and insulin resistance syndrome (67, 69). Furthermore, obesity increases the expression of IL-6 and the IL-6R in subcutaneous adipocytes (70), and obese patients have high serum concentrations of IL-6 compared to patients who are not overweight (71). Increased serum IL-6 is also observed in patients with metastatic melanoma (72, 73). Although most of the studies that link melanoma development to obesity have focused on the systemic effects of visceral adiposity and insulin resistance mechanisms (74), there are substantial changes in the skin microenvironment due to obesity that may contribute to melanoma development. Therefore, obesity might increase the risk of melanoma development due to the alterations in the skin microenvironment.

MATERIALS AND METHODS

Cell culture

Primary human white subcutaneous pre-adipocytes (HWP; PromoCell) were cultured in pre-adipocyte growth medium (C-27410; PromoCell). At 80 to 90% confluence, differentiation was induced by culturing the cells in differentiation medium (C-27436; PromoCell) for 3 days, followed by culturing in nutrition medium (C-27438; PromoCell) that was renewed every 2 days for 6 to 8 days. NIH3T3-L1 cells were provided by A. Munitz (Department of Microbiology and Clinical Immunology, Sackler School of Medicine, Tel Aviv University). Cells were cultured in complete Dulbecco's modified Eagle's medium (DMEM) supplemented with 10% fetal bovine serum (Sigma-Aldrich) and 1% penicillin/streptomycin/glutamine (Invitrogen). Differentiation was induced at 80% confluence using 3T3-L1 differentiation kit (DIF001; Sigma-Aldrich) containing insulin (1.5 μ g/ml), 500 μ M 3-isobutyl-1-methylxanthine (IBMX), and 1 μ M dexamethasone for 3 days followed by culturing in complete DMEM supplemented with insulin (1.5 μ g/ml) (I0516; Sigma-Aldrich) for an additional 8 days. Medium was renewed every 2 days. Differentiation was validated at day 10 after induction by oil red O staining.

Primary normal human epidermal keratinocytes (NHEK; PromoCell) were cultured in growth medium (C-20011; PromoCell) and were induced to differentiate with high calcium (1.2 mM) for 5 days. Primary normal human dermal fibroblasts (NHDF; PromoCell) were cultured in DMEM. Primary human endothelial cells (HUVEC; PromoCell) were grown in endothelial cell growth medium (C-22011; PromoCell). WM3314, WM3526, WM3682, and WM1716 melanoma cell lines were provided by L. A. Garraway (Department of Medical Oncology and Center for Cancer Genome Discovery, Dana-Farber Cancer Institute, Boston, MA). Cells were cultured in complete DMEM. To establish stable cell lines, cells were selected with puromycin (1 μ g/ml) (Sigma-Aldrich). Polymerase chain reaction (PCR) detection kit (Sigma-Aldrich) tested cells for mycoplasma. Characteristics of the melanoma lines are summarized in table S1.

Reagents

TGF- β 1 (T7039; Sigma-Aldrich) was added to culture medium at a final concentration of 2 ng/ml 48 hours before analyses unless indicated differently. A TGF- β inhibitor, SB431542 (Sigma-Aldrich), was added at a final concentration of 5 μ M at 24 hours before analysis. IL-6 (final concentration, 40 ng/ml; Abcam), TNF- α (final concentration, 15 ng/ml; Abcam), IL-6 inhibitor cucurbitacin I (final concentration, 0.1 μ M; Tocris), and TNF- α inhibitor R7050 (final concentration, 0.5 μ M; Tocris) were added 48 hours before analysis.

RNA purification and quantitative reverse transcription PCR

Total RNA was extracted using TRIzol (Invitrogen) according to the manufacturer's instructions. RNA was quantified by measuring OD260/280. For quantitative reverse transcription PCR (qRT-PCR) analysis of mature miR-211, 20 ng of total RNA was subjected to a TaqMan mRNA assay (Applied Biosystems). Mature miR-211 levels were normalized to levels of RNU48. For mRNA analysis, cDNA prepared using the qScript cDNA Synthesis Kit (Quantabio) was subjected to qRT-PCR using the PerfeCTa SYBR Green FastMix (Quantabio). Data are presented as fold changes relative to control. Primer sequences and manufacturers are listed in table S2.

Oligonucleotide transfection

miR-211 mimic, antagomiR-211, scrambled control, and antagomiR control were transfected into melanoma cells using HiPerFect (Qiagen) according to the manufacturer's instructions. Cells were transfected twice, at 24-hour intervals, with 100 pmol of oligonucleotide per 0.5×10^6 cells. Transfected cells were analyzed 48 hours after the first transfection. For data shown in Fig. 3 (K to M), transfections were conducted 3 days after incubation with conditioned medium. Sequences and manufacturers are listed in table S2.

Melanoma coculture with adipocytes

Coculture analysis was performed in 6- or 12-well Millicell Hanging cell culture inserts (1.0 μ m of polyethylene terephthalate; MCRP06, MCRP12; Millipore). Pre-adipocytes were either seeded (coculture) or not seeded (monoculture; control) into hanging inserts and induced to differentiation for 9 to 11 days. At differentiation, WM3682 cells were seeded into the lower compartment of the transwell, and the cells were cocultured for 5 days in nutrition medium. For reverse coculture analysis, the hanging inserts, containing adipocytes, were removed after 5 days of coculture, medium was replaced to unconditioned medium, and cells were allowed to grow for an additional 5 days. Cells were trypsinized to maintain 70% confluence.

For assays with adipocyte-conditioned medium, medium from culture of differentiated adipocytes was replaced 8 days after differentiation induction, and after an additional 2 to 3 days, supernatants were collected on ice. Cells and cellular debris were excluded from the medium by centrifugation at 12,000 rpm for 5 min.

Invasion assays

Melanoma cells (5×10^4) were seeded in duplicate in serum-free DMEM into an 8- μm pore Transwell membrane (Corning) coated with Matrigel (BD Biosciences). Invasion analysis was performed as previously described (13). Images of fixed cells from the invasion chambers were taken using an Olympus IX81 microscope and the cellSens Dimension software. In all assays, three fields per insert were photographed. The number of invaded cells was normalized to the number of total seeded cells.

Quantification of IL-6

IL-6 was quantified in adipocyte-conditioned medium using the Quantikine ELISA Kit (R&D Systems) according to the manufacturer's instructions.

Immunofluorescence

Cells were seeded onto glass slides. After 24 hours, the cells were fixed with 4% paraformaldehyde for 10 min at room temperature, permeabilized with 0.1% Triton X-100, and incubated with 5% bovine serum albumin. The cells were stained with SMAD4 (1:50, D3R4N; Cell Signaling Technology) for 2 hours at room temperature followed by incubation with Alexa Fluor 488-conjugated secondary antibody (1:1000, Invitrogen) or with Ki67 Alexa Fluor 488-conjugated antibody (1:100, D3B5; Cell Signaling Technology) for 2 hours at room temperature. Nuclei were labeled with 4',6-diamidino-2-phenylindole (DAPI; Vector Laboratories). Staining was analyzed using an Olympus IX81 fluorescence microscope and the cellSens Dimension software.

Plasmids and site-directed mutagenesis

For construction of miR-211 and scrambled control, expression vectors, miR-211, and scrambled sequences were cloned into modified PLKO.1 vector containing a cassette coding for luciferase, mCherry, and puromycin as previously described (13). The TGF- β -responsive luciferase construct and *TGFB1* expression plasmid were provided by Y. Henis (Neurobiology Department, The George S. Wise Faculty of Life Sciences, Tel Aviv University). pcDNA3-MITF was described in previous publications (75). The plasmid containing luciferase fused to the *TGFB1* 3' UTR was a gift from E. Galun (The Goldyne Savad Institute of Gene Therapy, Hadassah University Hospital, Jerusalem). Site-directed mutagenesis was performed on the miR-211 binding sites in the *TGFB1* 3' UTR using the QuikChange method (Stratagene) according to the supplier's protocols. Primer sequences for site-directed mutagenesis are listed in table S2.

Transfection and luciferase reporter assay

For establishment of stable cell lines, WM3314 and WM1716 cells were transfected with PLKO.1-miR-211 or PLKO.1-scrambled control vectors using jetPEI kit (Polyplus-transfection) according to the manufacturer's instructions. For luciferase assays, 1 μg of reporter plasmid (TGF- β -responsive reporter, *TGFB1* 3' UTR reporter, mutated *TGFB1* 3' UTR reporter, or MITF reporter) was cotransfected into cells with 40 ng of *Renilla* control plasmid using jetPEI

(Polyplus-transfection). At 48 hours after transfection, luciferase assays were performed using the Dual Luciferase Kit (Promega) according to the manufacturer's recommendations. For data shown in Fig. 5 (M and N), cells were transfected first with oligonucleotides, and then at 24 hours after transfection, the cells were transfected again with oligonucleotides and luciferase reporter plasmids. Luciferase assays were performed 24 hours after reporter plasmid transfection.

Western blot analyses

Equal amounts of extracted proteins (20 to 40 μg) were resolved on 10% SDS-polyacrylamide gel electrophoresis gels, and the proteins were transferred to nitrocellulose membranes (Whatman). The membranes were incubated with *TGFB1* (1:1000, 3712; Cell Signaling Technology), SMAD2 (1:1000, 3102; Cell Signaling Technology), pSMAD2 Ser^{465/467} (1:1000, 138D4; Cell Signaling Technology), SMAD4 (1:1000, 46535; Cell Signaling Technology), and β -actin (1:5000, 3700; Cell Signaling Technology) or β -tubulin (1:5000, 2146; Cell Signaling Technology) followed by incubation with appropriate horseradish peroxidase-conjugated antibodies at room temperature for 1 hour. Proteins were detected by an enhanced chemiluminescence solution (Thermo Fisher Scientific).

Wound scratch assay/migration assay

WM3682 melanoma cells were cocultured or treated with adipocyte-conditioned medium in six-well plates for 3 days. At confluence, the monolayer was wounded by scratching with a plastic pipette tip to create an about 450- μm -diameter strip. Images of wound closure were taken at 0, 19, 24, and 42 hours using an Olympus IX81 microscope and cellSens Dimension software and were analyzed by ImageJ software. Percentage of migration area was calculated by dividing the healed area by the wounded area. Five scratch areas per sample were analyzed.

Oil red O staining

Lipid droplets were stained as previously described (76). Cells were fixed with 4% paraformaldehyde at room temperature for 20 min, incubated with 60% isopropanol at room temperature for 5 min, and stained with 0.3% oil red O (O1391, Sigma-Aldrich) at room temperature for 20 min. After staining, cells were counterstained with Harris hematoxylin solution (HHS16; Sigma-Aldrich) for 45 s. Lipid droplets were photographed using an Olympus BX61 microscope.

Cell cycle analysis by flow cytometry

Cells were synchronized by serum starvation for 18 hours and then released for 10 hours. Cells (1×10^5 cells per sample) were fixed in cold 70% ethanol at 4°C overnight and permeabilized with 0.1% Triton X-100. To analyze DNA content, samples were treated with propidium iodide (0.05 mg/ml) (P4170; Sigma-Aldrich) and RNase A (ribonuclease A) solution (0.1 mg/ml) (R4642; Sigma-Aldrich) at room temperature for 30 min and were analyzed immediately by flow cytometry using a BD FACSCalibur flow cytometer. Data were gated by using Kaluza analysis software.

XTT cell proliferation assay

Aliquots of 2×10^3 WM3682 cells were seeded into 96-well plate in duplicate. Cell proliferation was determined every 24 hours for a period of 4 days, unless indicated differently, using the XTT Cell Proliferation Kit (Biological Industries) according to the manufacturer's instructions. Absorbance intensity was normalized to samples at time 0.

Mice and histopathology analysis

Animal experiments were approved by the University of Tel Aviv Institutional Animal Care and Use Committee (M-11-053). WM3314 or WM1716 cells stably expressing the firefly luciferase reporter and miR-211 or scrambled control were mixed 1:1 with Matrigel (356231; BD Biosciences) and subcutaneously injected into 10-week-old NOD-SCID-IL2 γ null mice (The Jackson Laboratory). Bioluminescence intensities of luciferase-expressing cells in mice were quantified at 29, 35, 41, 49, 56, 63, and 70 days after injection using an IVIS Spectrum system (Caliper Life Sciences, PerkinElmer). Mice were injected with 150 μ l of d-luciferin (Promega) and then gas-anesthetized with isoflurane. A total of 20 mice were used. For ex vivo experiments, mice were sacrificed at 6 to 10 weeks after xenografting. Local xenografts, lungs, and livers were surgically removed and individually imaged. Regions of interest from displayed images were quantified as photons per second (p/s). Internal organs were fixed with 10% formalin and were paraffin-embedded followed by hematoxylin (HHS16, Sigma-Aldrich) and eosin (HT110232, Sigma-Aldrich) staining according to the manufacturer's instruction.

Human samples and histopathology analysis

Human melanoma specimens were from the Sheba Medical Center (Helsinki ethical approval Smc-8333-10) and the Wolfson Medical Center (Helsinki ethical approval 0015-16-WOMC). Melanoma margins were determined by pathologists. The distance between the epidermis (stratum corneum) and the dermal adipocytes was measured using the ruler tool in the Aperio ImageScope software (unit: μ m) at five random places throughout the tissue section, and these distances were averaged. Melanocytic nest numbers and sizes (in μm^2) were calculated by analysis of Melan-A-stained patient samples within a 6-mm range. H&E staining was conducted as described in the previous section. Immunostaining was performed as previously described (14). In brief, slides were incubated, according to the manufacturer's instructions, with FSP1 (ab27957, Abcam), perilipin1 (ab61682, Abcam), IL-6 (ab6672, Abcam), HMB45 (ab732, Abcam or Dako), MART-1/Melan-A (A103, BioSB), and S100 (ab52642, Abcam) antibodies, followed by incubating with the associated fluorophore-conjugated secondary antibodies: Alexa Fluor 488 (A11055, Invitrogen), Alexa Fluor 594 (8889, Cell Signaling), Alexa Fluor 594 (A21203, Invitrogen), or Alexa Fluor 647 (A31571, Invitrogen). Images were obtained at $\times 4$, $\times 10$, and $\times 20$ magnification using fluorescence microscopy (Nikon).

mRNA profiling analysis

Total RNA from WM3682 melanoma cells that were monocultured or cocultured with adipocytes was extracted using TRIzol (Invitrogen). RNA quality was analyzed on Bioanalyzer, and RNA concentrations were determined with NanoDrop. Single-stranded cDNA was generated from the amplified complementary RNA (cRNA) with the WT cDNA Synthesis Kit (Affymetrix) and then fragmented and labeled with the WT Terminal Labeling Kit (Affymetrix). Samples were hybridized with Clarioum S Human Arrays (Affymetrix) and scanned at the Hebrew University Microarray Core Facility. Array scanning was performed according to the manufacturer's instructions. Raw data were processed using Transcriptome Analysis Console (Thermo Fisher Scientific).

Proliferation and invasion gene signature analysis

Log fold ratio of the two genes sets (7) was used after excluding all genes with log fold change of less than 25%. *P* values based on two-

sided Wilcoxon rank sum test that the two distributions are different were calculated using R version 3.5.1.

Signaling pathway analysis for WM1716 *P* value calculations

The probability that a given pathway with certain mean up- and down-regulated genes would be identified by chance was calculated using simulations as follows: The up- or down-regulation was represented as a mean log fold ratio and was calculated separately for each pathway after noise filtering (genes with fold change of less than 0.25 were not considered; other thresholds resulted in the same trend). In cases where multiple probes existed for a gene, their average were taken. *P* values were determined after 5000 repeated calculations of the same measurements of mean log fold ratios for each pathway after shuffling all genes in the pathways in the analysis while keeping pathway size and gene expression distributions intact. The fraction of times the mean log fold change of the down-regulated genes exceeded that of the down-regulated genes in a pathway was considered the *P* value of down-regulation. *P* values for up-regulated genes were calculated in the same manner, and the *P* values for both pathways were the joint probability. KEGG pathway genes were downloaded using the package "EnrichmentBrowser" version 2.10.6 (77).

Gene expression analysis

CEL files (annotation: pd.hugene.1.1.st.v1) for data from WM1716 cells were processed in R version 3.5.1 using the package "oligo" version 1.44.0 (78) with default parameters. Differential expression was calculated by the log (base 2) fold ratio of control to transfected samples after the exclusion of genes with expression of less than 6 (log 2 base).

Gene set enrichment analysis

GSEA for WM1716 cell data was done using GSEA v3.0 (79) from the Broad Institute using c2.cp.kegg.v6.2.symbols gene sets, permutation type "gene set," and all the other parameters as default. False discovery rate of 25% was considered for significance.

Kaplan-Meier analysis

The information analyzed was taken from the Cancer Genome Atlas database, which contains data on 550 patients with melanoma. These data were generated by the TCGA Research Network (<http://cancergenome.nih.gov/>). The Kaplan-Meier graph was generated by using the "survival" tab of cBioPortal for Cancer Genomics (56). Patients were divided into two groups: with and without amplifications of *IL6R* mRNA.

SUPPLEMENTARY MATERIALS

[stke.science.org/cgi/content/full/12/591/eaav6847/DC1](https://stke.sciencemag.org/cgi/content/full/12/591/eaav6847/DC1)

Fig. S1. Subcutaneous adipocytes are observed in proximity to *in situ* melanoma.

Fig. S2. Subcutaneous adipocytes approximate to *in situ* melanoma correlate with advanced disease.

Fig. S3. Adipocytes drive melanoma plasticity in a reversible manner by miR-211 repression.

Fig. S4. Adipocytes decrease miR-211 expression through secretion of IL-6 and TNF- α .

Fig. S5. miR-211 attenuates TGF- β signaling and reduces melanoma sensitivity to TGF- β .

Table S1. Characteristics of melanoma cell lines.

Table S2. Sequence data for oligonucleotides.

Data file S1. Differentially expressed miRNAs in melanoma upon coculture with adipocytes.

Data file S2. Gene set enrichment upon miR-211 expression in melanoma.

Data file S3. Pathway enrichment upon miR-211 expression in melanoma.

Data file S4. Venn diagram data.

REFERENCES AND NOTES

- D. Hanahan, R. A. Weinberg, Hallmarks of cancer: The next generation. *Cell* **144**, 646–674 (2011).
- D. Hanahan, R. A. Weinberg, The hallmarks of cancer. *Cell* **100**, 57–70 (2000).
- K. Kemper, P. L. de Goeje, D. S. Peepoer, R. van Amerongen, Phenotype switching: Tumor cell plasticity as a resistance mechanism and target for therapy. *Cancer Res.* **74**, 5937–5941 (2014).
- C. E. Meacham, S. J. Morrison, Tumour heterogeneity and cancer cell plasticity. *Nature* **501**, 328–337 (2013).
- K. S. Hoek, O. M. Eichhoff, N. C. Schlegel, U. Dobbeling, N. Kober, L. Schaerer, S. Hemmi, R. Dummer, In vivo switching of human melanoma cells between proliferative and invasive states. *Cancer Res.* **68**, 650–656 (2008).
- K. S. Hoek, N. C. Schlegel, P. Brafford, A. Sucker, S. Ugurel, R. Kumar, B. L. Weber, K. L. Nathanson, D. J. Phillips, M. Herlyn, D. Schadendorf, R. Dummer, Metastatic potential of melanomas defined by specific gene expression profiles with no BRAF signature. *Pigment Cell Res.* **19**, 290–302 (2006).
- K. S. Hoek, C. R. Goding, Cancer stem cells versus phenotype-switching in melanoma. *Pigment Cell Melanoma Res.* **23**, 746–759 (2010).
- M. Bittner, P. Meltzer, Y. Chen, Y. Jiang, E. Seftor, M. Hendrix, M. Radmacher, R. Simon, Z. Yakhini, A. Ben-Dor, N. Sampas, E. Dougherty, E. Wang, F. Marincola, C. Gooden, J. Lueders, A. Glatfelter, P. Pollock, J. Carpten, E. Gillanders, D. Leja, K. Dietrich, C. Beaudry, M. Berens, D. Alberts, V. Sondak, N. Hayward, J. Trent, Molecular classification of cutaneous malignant melanoma by gene expression profiling. *Nature* **406**, 536–540 (2000).
- S. Carrreira, J. Goodall, L. Denat, M. Rodriguez, P. Nuciforo, K. S. Hoek, A. Testori, L. Larue, C. R. Goding, Mitf regulation of Dia1 controls melanoma proliferation and invasiveness. *Genes Dev.* **20**, 3426–3439 (2006).
- H. R. Widlund, D. E. Fisher, Microphthalmia-associated transcription factor: A critical regulator of pigment cell development and survival. *Oncogene* **22**, 3035–3041 (2003).
- C. Levy, M. Khaled, D. E. Fisher, MITF: Master regulator of melanocyte development and melanoma oncogene. *Trends Mol. Med.* **12**, 406–414 (2006).
- D. Sheinboim, I. Mazza, I. Dror, S. Parikh, V. Krupalnik, R. E. Bell, A. Zviran, Y. Saita, O. Hakim, Y. Mandel-Gutfreund, M. Khaled, J. H. Hanna, C. Levy, OCT4 impedes cell fate redirection by the melanocyte lineage master regulator MITF in mouse ESCs. *Nat. Commun.* **8**, 1022 (2017).
- C. Levy, M. Khaled, D. Iliopoulos, M. M. Janas, S. Schubert, S. Pinner, P. H. Chen, S. Li, A. L. Fletcher, S. Yokoyama, K. L. Scott, L. A. Garraway, J. S. Song, S. R. Granter, S. J. Turley, D. E. Fisher, C. D. Novina, Intronic miR-211 assumes the tumor suppressive function of its host gene in melanoma. *Mol. Cell* **40**, 841–849 (2010).
- T. Golan, A. R. Messer, A. Amitai-Lange, Z. Melamed, R. Ohana, R. E. Bell, O. Kapitansky, G. Lerman, S. Greenberger, M. Khaled, N. Amar, J. Albrengues, C. Gaggioli, P. Gonen, Y. Tabach, D. Sprinzak, R. Shalom-Fuerstein, C. Levy, Interactions of melanoma cells with distal keratinocytes trigger metastasis via notch signaling inhibition of MITF. *Mol. Cell* **59**, 664–676 (2015).
- R. E. Bell, M. Khaled, D. Netaneli, S. Schubert, T. Golan, A. Buxbaum, M. M. Janas, B. Postolsky, M. S. Goldberg, R. Shamir, C. Levy, Transcription factor/microRNA axis blocks melanoma invasion program by miR-211 targeting NUAK1. *J. Invest. Dermatol.* **134**, 441–451 (2014).
- M. R. Eccles, S. He, A. Ahn, L. J. Slobbe, A. R. Jeffs, H. S. Yoon, B. C. Baguley, MITF and PAX3 play distinct roles in melanoma cell migration; outline of a “genetic switch” theory involving MITF and PAX3 in proliferative and invasive phenotypes of melanoma. *Front. Oncol.* **3**, 229 (2013).
- J. Mazar, F. Qi, B. Lee, J. Marchica, S. Govindarajan, J. Shelley, J. L. Li, A. Ray, R. J. Perera, MicroRNA 211 functions as a metabolic switch in human melanoma cells. *Mol. Cell. Biol.* **36**, 1090–1108 (2016).
- M. P. O’Connell, A. T. Weeraratna, Change is in the air: The hypoxic induction of phenotype switching in melanoma. *J. Invest. Dermatol.* **133**, 2316–2317 (2013).
- K. E. de Visser, A. Eichten, L. M. Coussens, Paradoxical roles of the immune system during cancer development. *Nat. Rev. Cancer* **6**, 24–37 (2006).
- S. Dror, L. Sander, H. Schwartz, D. Sheinboim, A. Barzilai, Y. Dishon, S. Apcher, T. Golan, S. Greenberger, I. Barshack, H. Malcov, A. Zilberman, L. Levin, M. Nessling, Y. Friedmann, V. Igras, O. Barzilay, H. Vaknine, R. Brenner, A. Zinger, A. Schroeder, P. Gonen, M. Khaled, N. Erez, J. D. Hohneisel, C. Levy, Melanoma miRNA trafficking controls tumour primary niche formation. *Nat. Cell Biol.* **18**, 1006–1017 (2016).
- D. Ribatti, G. Mangialardi, A. Vacca, Stephen Paget and the ‘seed and soil’ theory of metastatic dissemination. *Clin. Exp. Med.* **6**, 145–149 (2006).
- R. R. Driskell, C. A. B. Jahoda, C. M. Chuong, F. M. Watt, V. Horsley, Defining dermal adipose tissue. *Exp. Dermatol.* **23**, 629–631 (2014).
- E. Clement, I. Lazar, C. Muller, L. Nieto, Obesity and melanoma: Could fat be fueling malignancy? *Pigment Cell Melanoma Res.* **30**, 294–306 (2017).
- P. Coelho, J. Almeida, C. Prudêncio, R. Fernandes, R. Soares, Effect of adipocyte secretome in melanoma progression and vasculogenic mimicry. *J. Cell. Biochem.* **117**, 1697–1706 (2016).
- K. Kushiro, R. A. Chu, A. Verma, N. P. Núñez, Adipocytes promote B16BL6 melanoma cell invasion and the epithelial-to-mesenchymal transition. *Cancer Microenviron.* **5**, 73–82 (2012).
- J. A. Ellerhorst, A. H. Diwan, S. M. Dang, D. G. Uffort, M. K. Johnson, C. P. Cooke, E. A. Grimm, Promotion of melanoma growth by the metabolic hormone leptin. *Oncol. Rep.* **23**, 901–907 (2010).
- I. Lazar, E. Clement, S. Dauvillier, D. Milhas, M. Ducoux-Petit, S. LeGonidec, C. Moro, V. Soldan, S. Dalle, S. Balor, M. Golzio, O. Burlet-Schiltz, P. Valet, C. Muller, L. Nieto, Adipocyte exosomes promote melanoma aggressiveness through fatty acid oxidation: A novel mechanism linking obesity and cancer. *Cancer Res.* **76**, 4051–4057 (2016).
- H. Y. Kwan, X. Fu, B. Liu, X. Chao, C. L. Chan, H. Cao, T. Su, A. K. W. Tse, W. F. Fong, Z. L. Yu, Subcutaneous adipocytes promote melanoma cell growth by activating the Akt signaling pathway: Role of palmitic acid. *J. Biol. Chem.* **289**, 30525–30537 (2014).
- M. Zhang, J. S. di Martino, R. L. Bowman, N. R. Campbell, S. C. Baksh, T. Simon-Vermot, I. S. Kim, P. Haldeman, C. Mondal, V. Yong-Gonzales, M. Abu-Akel, T. Merghoub, D. R. Jones, X. G. Zhu, A. Arora, C. E. Ariyan, K. Birsoy, J. D. Wolchoff, K. S. Panageas, T. Hollmann, J. J. Bravo-Cordero, R. M. White, Adipocyte-derived lipids mediate melanoma progression via FATP proteins. *Cancer Discov.* **8**, 1006–1025 (2018).
- E. Zoico, E. Darra, V. Rizzatti, M. Tebon, G. Franceschetti, G. Mazzali, A. P. Rossi, F. Fantin, M. Zamboni, Role of adipose tissue in melanoma cancer microenvironment and progression. *Int. J. Obes.* **42**, 344–352 (2018).
- N. Escobedo, G. Oliver, The lymphatic vasculature: Its role in adipose metabolism and obesity. *Cell Metab.* **26**, 598–609 (2017).
- K. H. Kwok, K. S. Lam, A. Xu, Heterogeneity of white adipose tissue: Molecular basis and clinical implications. *Exp. Mol. Med.* **48**, e215 (2016).
- G. J. Imman, F. J. Nicolás, J. F. Callahan, J. D. Harling, L. M. Gaster, A. D. Reith, N. J. Laping, C. S. Hill, SB-431542 is a potent and specific inhibitor of transforming growth factor- β superfamily type I activin receptor-like kinase (ALK) receptors ALK4, ALK5, and ALK7. *Mol. Pharmacol.* **62**, 65–74 (2002).
- M. Y. Wu, C. S. Hill, TGF- β superfamily signaling in embryonic development and homeostasis. *Dev. Cell* **16**, 329–343 (2009).
- M. C. Fleisch, C. A. Maxwell, M. H. Barcellos-Hoff, The pleiotropic roles of transforming growth factor beta in homeostasis and carcinogenesis of endocrine organs. *Endocr. Relat. Cancer* **13**, 379–400 (2006).
- J. L. Wrama, L. Attisano, R. Wieser, F. Ventura, J. Massagué, Mechanism of activation of the TGF- β receptor. *Nature* **370**, 341–347 (1994).
- Y. Shi, J. Massagué, Mechanisms of TGF- β signaling from cell membrane to the nucleus. *Cell* **113**, 685–700 (2003).
- B. Bierie, H. L. Moses, Tumour microenvironment: TGF β : The molecular Jekyll and Hyde of cancer. *Nat. Rev. Cancer* **6**, 506–520 (2006).
- J. J. Lebrun, The dual role of TGF β in human cancer: From tumor suppression to cancer metastasis. *ISRN Mol. Biol.* **2012**, 381428 (2012).
- R. Deryck, R. J. Akhurst, A. Balmain, TGF- β signaling in tumor suppression and cancer progression. *Nat. Genet.* **29**, 117–129 (2001).
- A. J. Cochran, Melanoma metastases through the lymphatic system. *Surg. Clin. North Am.* **80**, 1683–1693 (2000).
- W. H. Clark Jr., L. From, E. A. Bernardino, M. C. Mihm, The histogenesis and biologic behavior of primary human malignant melanomas of the skin. *Cancer Res.* **29**, 705–727 (1969).
- F. M. Gregoire, Adipocyte differentiation: From fibroblast to endocrine cell. *Exp. Biol. Med.* **226**, 997–1002 (2016).
- J. Beer, L. Xu, P. Tschanhl, H. Kittler, Growth rate of melanoma in vivo and correlation with dermatoscopic and dermatopathologic findings. *Dermatol. Pract. Concept.* **1**, 59–67 (2011).
- S. Pinner, P. Jordan, K. Sharrock, L. Bazley, L. Collinson, R. Marais, E. Bonvin, C. Goding, E. Sahai, Intravital imaging reveals transient changes in pigment production and Brn2 expression during metastatic melanoma dissemination. *Cancer Res.* **69**, 7969–7977 (2009).
- B. P. Lewis, C. B. Burge, D. P. Bartel, Conserved seed pairing, often flanked by adenosines, indicates that thousands of human genes are microRNA targets. *Cell* **120**, 15–20 (2005).
- G. M. Boyle, S. L. Woods, V. F. Bonazzi, M. S. Stark, E. Hacker, L. G. Auode, K. Dutton-Regester, A. L. Cook, R. A. Sturm, N. K. Hayward, Melanoma cell invasiveness is regulated by miR-211 suppression of the BRN2 transcription factor. *Pigment Cell Melanoma Res.* **24**, 525–537 (2011).
- H. Green, O. Kehinde, An established preadipose cell line and its differentiation in culture. II. Factors affecting the adipose conversion. *Cell* **5**, 19–27 (1975).
- C. Margue, D. Philippidou, S. E. Reinsbach, M. Schmitt, I. Behrmann, S. Kreis, New target genes of MITF-induced microRNA-211 contribute to melanoma cell invasion. *PLOS ONE* **8**, e73473 (2013).
- G. Frühbeck, J. Gómez-Ambrosi, F. J. Muruzábal, M. A. Burrell, The adipocyte: A model for integration of endocrine and metabolic signaling in energy metabolism regulation. *Am. J. Physiol. Endocrinol. Metab.* **280**, E827–E847 (2001).

51. M. N. Duong, A. Geneste, F. Fallone, X. Li, C. Dumontet, C. Muller, The fat and the bad: Mature adipocytes, key actors in tumor progression and resistance. *Oncotarget* **8**, 57622–57641 (2017).
52. S. Riesenbergs, A. Groetchen, R. Siddaway, T. Bald, J. Reinhardt, D. Smorra, J. Kohlmeyer, M. Renn, B. Phung, P. Aymans, T. Schmidt, V. Hornung, I. Davidson, C. R. Goding, G. Jönsson, J. Landsberg, T. Tütting, M. Hözel, MITF and c-Jun antagonism interconnects melanoma dedifferentiation with pro-inflammatory cytokine responsiveness and myeloid cell recruitment. *Nat. Commun.* **6**, 8755 (2015).
53. A. K. Kamaraju, C. Bertollo, J. Chebath, M. Revel, Pax3 down-regulation and shut-off of melanogenesis in melanoma B16/F10.9 by interleukin-6 receptor signaling. *J. Biol. Chem.* **277**, 15132–15141 (2002).
54. M. A. Blaskovich, J. Sun, A. Cantor, J. Turkson, R. Jove, S. M. Sebiti, Discovery of JSI-124 (cucurbitacin I), a selective Janus kinase/signal transducer and activator of transcription 3 signaling pathway inhibitor with potent antitumor activity against human and murine cancer cells in mice. *Cancer Res.* **63**, 1270–1279 (2003).
55. T. L. Gururaja, S. Yung, R. Ding, J. Huang, X. Zhou, J. McLaughlin, S. Daniel-Issakani, R. Singh, R. D. G. Cooper, D. G. Payan, E. S. Masuda, T. Kinoshita, A class of small molecules that inhibit TNF α -induced survival and death pathways via prevention of interactions between TNF α RI, TRADD, and RIP1. *Chem. Biol.* **14**, 1105–1118 (2007).
56. J. Gao, B. A. Aksoy, U. Dogrusoz, G. Dresdner, B. Gross, S. O. Sumer, Y. Sun, A. Jacobsen, R. Sinha, E. Larsson, E. Cerami, C. Sander, N. Schultz, Integrative analysis of complex cancer genomics and clinical profiles using the cBioPortal. *Sci. Signal.* **6**, pl1 (2013).
57. J. Howlin, H. Cirenaivis, B. Lettiero, J. Staaf, M. Lauss, L. Saal, Å. Borg, S. Gruvberger-Saal, G. Jönsson, Loss of CITED1, an MITF regulator, drives a phenotype switch in vitro and can predict clinical outcome in primary melanoma tumours. *PeerJ* **3**, e788 (2015).
58. A. Nakao, T. Imamura, S. Soucheznytskyi, M. Kawabata, A. Ishisaki, E. Oeda, K. Tamaki, J. Hanai, C. H. Heldin, K. Miyazono, P. ten Dijke, TGF- β receptor-mediated signalling through Smad2, Smad3 and Smad4. *EMBO J.* **16**, 5353–5362 (1997).
59. A. Lasfar, K. A. Cohen-Solal, Resistance to transforming growth factor β -mediated tumor suppression in melanoma: Are multiple mechanisms in place? *Carcinogenesis* **31**, 1710–1717 (2010).
60. N. Y. Tan, L. M. Khachigian, Sp1 phosphorylation and its regulation of gene transcription. *Mol. Cell. Biol.* **29**, 2483–2488 (2009).
61. N. A. Bhowmick, E. G. Neilson, H. L. Moses, Stromal fibroblasts in cancer initiation and progression. *Nature* **432**, 332–337 (2004).
62. H. Malcov-Brog, A. Alpert, T. Golan, S. Parikh, A. Nordlinger, F. Netti, D. Sheinboim, I. Dror, L. Thomas, C. Cosson, P. Gonen, Y. Stanevsky, R. Brenner, T. Perlik, J. Frand, S. Elgavish, Y. Nevo, D. Rahat, Y. Tabach, M. Khaled, S. S. Shen-Orr, C. Levy, UV-protection timer controls linkage between stress and pigmentation skin protection systems. *Mol. Cell* **72**, 444–456.e7 (2018).
63. M. Y. Hsu, F. Meier, M. Herlyn, Melanoma development and progression: A conspiracy between tumor and host. *Differentiation* **70**, 522–536 (2002).
64. L. K. Dennis, J. B. Lowe, C. F. Lynch, M. C. Alavanja, Cutaneous melanoma and obesity in the agricultural health study. *Ann. Epidemiol.* **18**, 214–221 (2008).
65. C. Samanic, W. H. Chow, G. Gridley, B. Jarvholm, J. F. Fraumeni Jr., Relation of body mass index to cancer risk in 362,552 Swedish men. *Cancer Causes Control* **17**, 901–909 (2006).
66. M. Dobbins, K. Decorby, B. C. Choi, The association between obesity and cancer risk: A meta-analysis of observational studies from 1985 to 2011. *J. Clin. Prev. Med.* **2013**, 680536 (2013).
67. A. Mori, H. Sakurai, M. K. Choo, R. Obi, K. Koizumi, C. Yoshida, Y. Shimada, I. Saiki, Severe pulmonary metastasis in obese and diabetic mice. *Int. J. Cancer* **119**, 2760–2767 (2006).
68. T. N. Sergentanis, A. G. Antoniadis, H. J. Gogas, C. N. Antonopoulos, H. O. Adam, A. Ekblom, E. T. Petridou, Obesity and risk of malignant melanoma: A meta-analysis of cohort and case-control studies. *Eur. J. Cancer* **49**, 642–657 (2013).
69. G. Rivera-Gonzalez, B. Shook, V. Horsley, Adipocytes in skin health and disease. *Cold Spring Harb. Perspect. Med.* **4**, a015271 (2014).
70. G. Yosipovitch, A. DeVore, A. Dawn, Obesity and the skin: Skin physiology and skin manifestations of obesity. *J. Am. Acad. Dermatol.* **56**, 901–916 (2007).
71. S. Sindhu, R. Thomas, P. Shihab, D. Sriraman, K. Behbehani, R. Ahmad, Obesity is a positive modulator of IL-6R and IL-6 expression in the subcutaneous adipose tissue: Significance for metabolic inflammation. *PLOS ONE* **10**, e0133494 (2015).
72. L. Roytblat, M. Rachinsky, A. Fisher, L. Greengberg, Y. Shapira, A. Douvdevani, S. Gelman, Raised interleukin-6 levels in obese patients. *Obes. Res.* **8**, 673–675 (2000).
73. L. Hoejberg, L. Bastholt, J. S. Johansen, I. J. Christensen, J. Gehl, H. Schmidt, Serum interleukin-6 as a prognostic biomarker in patients with metastatic melanoma. *Melanoma Res.* **22**, 287–293 (2012).
74. R. Kucera, O. Topolcan, I. Treskova, J. Kinkorova, J. Windrichova, R. Fuchsova, S. Svobodova, V. Treska, V. Babuska, J. Novak, J. Smejkal, Evaluation of IL-2, IL-6, IL-8 and IL-10 in malignant melanoma diagnostics. *Anticancer Res.* **35**, 3537–3541 (2015).
75. E. Feige, S. Yokoyama, C. Levy, M. Khaled, V. Igras, R. J. Lin, S. Lee, H. R. Widlund, S. R. Granter, A. L. Kung, D. E. Fisher, Hypoxia-induced transcriptional repression of the melanoma-associated oncogene MITF. *Proc. Natl. Acad. Sci. U.S.A.* **108**, E924–E933 (2011).
76. J. L. Ramirez-Zacarias, F. Castro-Munozledo, W. Kuri-Harcuch, Quantitation of adipose conversion and triglycerides by staining intracytoplasmic lipids with oil red O. *Histochemistry* **97**, 493–497 (1992).
77. L. Geistlinger, G. Csaba, R. Zimmer, Bioconductor's enrichmentbrowser: Seamless navigation through combined results of set- & network-based enrichment analysis. *BMC Bioinformatics* **17**, 45 (2016).
78. B. S. Carvalho, R. A. Irizarry, A framework for oligonucleotide microarray preprocessing. *Bioinformatics* **26**, 2363–2367 (2010).
79. A. Subramanian, P. Tamayo, V. K. Mootha, S. Mukherjee, B. L. Ebert, M. A. Gillette, A. Paulovich, S. L. Pomeroy, T. R. Golub, E. S. Lander, J. P. Mesirov, Gene set enrichment analysis: A knowledge-based approach for interpreting genome-wide expression profiles. *Proc. Natl. Acad. Sci. U.S.A.* **102**, 15545–15550 (2005).

Funding: This work was supported, in part, by the Israel Science Foundation (ISF; 1997/13) and Melanoma Research Alliance (MRA; 402792). **Author contributions:** T.G. developed the hypothesis, designed the experimental approach, performed experimental work, analyzed data, and wrote the manuscript. R. Parikh performed experimental work, including coculture system and pathological experiments, and analyzed data. E.J. conducted bioinformatic analyses. H.V., V.Z.-W., and D.H. provided melanoma specimens and conducted specimen analysis. H.M. helped design the manuscript figures. S.L. performed pathological analysis. S.A. performed pathological experiments. H.R. established miR-211 target genes. D.S. performed the melanoma patient survival analysis. R.B., R. Percik, and S.G. provided melanoma specimens and useful discussion. A.K. performed live imaging experimental work. M.K. designed and constructed the PLKO.1–miR-211 vector and performed *in vivo* experimental work. C.L. developed the hypothesis, designed the experimental approach, analyzed data, wrote the manuscript, and coordinated the project. **Competing interests:** The authors declare that they have no competing financial interests. **Data and materials availability:** mRNA and miRNA profiling data in support of this study have been deposited at the Gene Expression Omnibus (GEO) with primary accession number: GSE119478. All other data needed to evaluate the conclusions in the paper are present in the paper or the Supplementary Materials.

Submitted 15 October 2018

Accepted 18 June 2019

Published 23 July 2019

10.1126/scisignal.aav6847

Citation: T. Golan, R. Parikh, E. Jacob, H. Vaknine, V. Zemser-Werner, D. Hershkovitz, H. Malcov, S. Leibou, H. Reichman, D. Sheinboim, R. Percik, S. Amar, R. Brenner, S. Greenberger, A. Kung, M. Khaled, C. Levy, Adipocytes sensitize melanoma cells to environmental TGF- β cues by repressing the expression of miR-211. *Sci. Signal.* **12**, eaav6847 (2019).

CANCER

Off-target toxicity is a common mechanism of action of cancer drugs undergoing clinical trials

Ann Lin^{1,2*}, Christopher J. Giuliano^{1,2*}, Ann Palladino¹, Kristen M. John^{1,3}, Connor Abramowicz^{1,4}, Monet Lou Yuan^{1,5}, Erin L. Sausville¹, Devon A. Lukow^{1,2}, Luwei Liu^{1,2}, Alexander R. Chait¹, Zachary C. Galluzzo¹, Clara Tucker^{1,2}, Jason M. Sheltzer^{1†}

Ninety-seven percent of drug-indication pairs that are tested in clinical trials in oncology never advance to receive U.S. Food and Drug Administration approval. While lack of efficacy and dose-limiting toxicities are the most common causes of trial failure, the reason(s) why so many new drugs encounter these problems is not well understood. Using CRISPR-Cas9 mutagenesis, we investigated a set of cancer drugs and drug targets in various stages of clinical testing. We show that—contrary to previous reports obtained predominantly with RNA interference and small-molecule inhibitors—the proteins ostensibly targeted by these drugs are nonessential for cancer cell proliferation. Moreover, the efficacy of each drug that we tested was unaffected by the loss of its putative target, indicating that these compounds kill cells via off-target effects. By applying a genetic target-deconvolution strategy, we found that the mischaracterized anticancer agent OTS964 is actually a potent inhibitor of the cyclin-dependent kinase CDK11 and that multiple cancer types are addicted to CDK11 expression. We suggest that stringent genetic validation of the mechanism of action of cancer drugs in the preclinical setting may decrease the number of therapies tested in human patients that fail to provide any clinical benefit.

INTRODUCTION

Substantial progress has been made in the treatment of certain malignancies by targeting cancer “addictions” or genetic dependencies that encode proteins required for the survival and/or proliferation of cancer cells (1). Therapeutic agents that block the function of a cancer dependency—such as the kinase inhibitor lapatinib in HER2⁺ breast cancer—can trigger apoptosis and durable tumor regression (2). Discovering and characterizing druggable cancer dependencies are key goals of preclinical research.

While screening cancer drug targets, we found that maternal embryonic leucine zipper kinase (MELK), a protein previously reported to be essential in multiple cancer types, could be eliminated using CRISPR-mediated gene editing without any detectable loss in cancer cell fitness (3, 4). In addition, we demonstrated that OTS167, a small-molecule inhibitor of MELK undergoing phase 2 clinical trials, continued to kill MELK-knockout (KO) cancer cells with no decrease in potency. These findings suggested that a drug tested in human cancer patients had been designed to target a nonessential cellular protein and that its putative inhibitor killed cells by interacting with proteins other than its reported target. We hypothesized that problems in drug development and inhibitor validation, as exemplified by MELK and OTS167, could potentially contribute to the high failure rate of new cancer therapies. In particular, drugs that target superfluous proteins may display limited efficacy in human patients, and if these drugs are active only via off-target effects, then this could potentially contribute to patient toxicity. Moreover, clinical trials that use a biomarker to select patients for trial inclusion are about twice as likely to succeed as those without one (5). Misidentifying a drug’s mechanism of action (MOA) could

hamper efforts to uncover a biomarker capable of predicting therapeutic responses, further decreasing the success rate of clinical trials. To test whether other cancer drugs had similarly been designed against nonessential targets or had been assigned an incorrect MOA, we set out to systematically analyze multiple cancer drugs and drug targets that have entered clinical trials or are in late-stage pre-clinical development.

RESULTS

CRISPR competition assays to investigate several putative cancer dependencies

Based on an analysis of the literature, we chose drug targets that met several criteria (described in detail in Materials and Methods). Notably, we selected drug targets that had been reported to play a cell-autonomous role in cancer growth, such that their loss or inhibition was reportedly sufficient to block cancer cell proliferation. In addition, we selected drug targets that lacked a known mutation capable of conferring resistance to their targeted inhibitors, which we hypothesized represents the gold standard for proving a drug’s MOA. We identified 10 cancer drugs targeting six proteins that met these criteria (Table 1). Five of these proteins are reported to represent cancer dependencies (HDAC6, MAPK14/p38α, PAK4, PBK, and PIM1) (6–15). One protein (CASP3/caspase-3) is reported to induce apoptosis when activated by a small molecule (16, 17) and is discussed separately. Among the putative dependencies, over 180 different publications indicate that they are required for cancer cell proliferation or fitness (listed in data file S1). For each of these genes, the majority of evidence supporting their designation as cancer dependencies comes from RNA interference (RNAi) studies, in which small interfering RNA (siRNA)—or short hairpin RNA (shRNA)—mediated knockdown was reported to impair cancer cell fitness. In addition, each protein is targeted by one or more small-molecule drugs, which have been described to exhibit potent cell killing in vitro and in vivo. On the basis of these preclinical results, the

¹Cold Spring Harbor Laboratory, Cold Spring Harbor, NY 11724, USA. ²Stony Brook University, Stony Brook, NY 11794, USA. ³Hofstra University, Hempstead, NY 11549, USA. ⁴New York Institute of Technology, Glen Head, NY 11545, USA. ⁵Syosset High School, Syosset, NY 11791, USA.

*These authors contributed equally to this work.

†Corresponding author. Email: sheltzer@cshl.edu

Copyright © 2019
The Authors, some
rights reserved;
exclusive licensee
American Association
for the Advancement
of Science. No claim
to original U.S.
Government Works

Table 1. Anticancer drugs and drug targets.

Target	Drug	No. of cancer clinical trials
CASP3	1541B	Preclinical
	PAC-1	3
HDAC6	Citarinostat	5
	Ricolinostat	10
MAPK14 (p38 α)	Ralimetinib	5
	SCIO-469	3
PAK4	PF-03758309	1
PBK (TOPK)	OTS514	Preclinical
	OTS964	Preclinical
PIM1	SGI-1776	2

drugs listed in Table 1 have been used in at least 29 different clinical trials, with an estimated enrollment of more than 1000 patients.

We first set out to validate the role of the putative dependencies targeted by these drugs in cancer cell fitness. To accomplish this, we applied a CRISPR-Cas9-based cell competition assay, in which cancer cells are infected at a low multiplicity of infection with green fluorescent protein (GFP)-expressing guide RNA (gRNA) vectors targeting a gene of interest (Fig. 1A) (18). If a CRISPR-induced mutation reduces cell fitness, then the untransduced cells within a population should outcompete the gRNA-expressing cells, and the fraction of GFP $^+$ cells should decrease over time. To verify this approach, we designed gRNAs against pan-essential genes and against several confirmed cancer drug targets. In breast cancer, colorectal cancer, lung cancer, and melanoma cell lines, guides targeting the essential replication proteins RPA3 and proliferating cell nuclear antigen (PCNA) dropped out up to 100-fold, and guides targeting the validated pan-cancer dependencies Aurora A, Aurora B, and ERCC3 exhibited similar levels of depletion (Fig. 1B). Mutations in Aurora A (19), Aurora B (20), and ERCC3 (21) confer resistance to the cytotoxic agents MLN8054, ZM447439, and triptolide, respectively, thereby providing genetic evidence that they are required for cancer cell growth. In contrast, gRNAs targeting the nonessential Rosa26 and AAVS1 loci exhibited minimal dropout over five passages in culture. These GFP competition assays were also capable of identifying cell type-specific dependencies: Guides targeting the oncogenic kinase BRAF dropped out in a BRAF-mutant melanoma cell line but not a BRAF-wild-type (WT) colorectal cancer line, whereas guides targeting the gene encoding the estrogen receptor (ESR1) dropped out in an ER-positive breast cancer line but not in a triple-negative breast cancer line (Fig. 1C). We concluded that our CRISPR dropout assay can robustly identify both pan-essential and cancer type-specific genetic dependencies.

We next designed gRNAs against the reported cancer dependencies HDAC6, MAPK14 (p38 α), PAK4, PBK, and PIM1. To maximize the likelihood that a CRISPR-induced mutation results in a non-functional allele, guides were designed to target exons that encode key functional domains within a protein (fig. S1A) (18). We used Western blotting to verify that each guide resulted in strong protein depletion in four separate cell lines (Fig. 1D and fig. S1B), and we then further confirmed target ablation by performing a second set of Western blots with a different antibody that recognizes a distinct

protein epitope (fig. S1C). Next, we conducted GFP competition assays in 32 cell lines from 12 different cancer types, which included multiple cell lines in which each gene had previously been reported to be essential (data file S1). In each experiment, four gRNAs targeting Rosa26 and AAVS1 were used as negative controls, whereas four gRNAs targeting PCNA and RPA3 were used as positive controls. These positive control guides dropped out between ~10- and ~200-fold over five passages in culture, whereas the negative control guides consistently exhibited <2.5-fold dropout. The variation in positive control dropout rates likely reflects cellular differences in Cas9 expression, proliferation, and the spectrum of indel mutations produced by the gRNA. Notably, all guides targeting HDAC6, MAPK14, PAK4, PBK, and PIM1 failed to drop out in every cell line that we tested (Fig. 1E, fig. S2, and data file S2). For instance, HDAC6 has been reported to be a genetic dependency in ARID1A-mutant ovarian cancer (6). However, in ARID1A-mutant ovarian cancer cell lines A2780, OVK18, OVTKO, and TOV-21G, HDAC6-targeting guides failed to deplete above background levels. Similarly, PIM1 has been reported to be a genetic dependency in triple-negative breast cancer (14, 15), but PIM1-targeting guides were not depleted in any of the seven triple-negative breast cancer cell lines that we tested (data file S2). These results called into question whether these putative drug targets are required for cancer cell growth.

Generation and analysis of CRISPR-derived KO clones

To further test the essentiality of these genes in cancer, we derived clones harboring CRISPR-induced KOs in each gene in multiple cancer types. All five genes were knocked out in the triple-negative breast cancer cell line MDA-MB-231 and the melanoma cell line A375. HDAC6, MAPK14, PBK, and PIM1 were knocked out in the colorectal cancer cell line DLD1, whereas PAK4 was knocked out in the colorectal cancer cell line HCT116, because it has previously been reported that PAK4 is not a dependency in DLD1 (11). To minimize the possibility that downstream translational initiation or alternative splicing bypasses the effect of a single CRISPR-induced mutation, clones were made by cotransducing cancer cells with guides that targeted two different exons in a gene of interest (Fig. 2A and fig. S1A). Complete target ablation was then verified by Western blotting using two antibodies that recognized distinct protein epitopes (Fig. 2B and figs. S3 to S5A). We next compared these KO clones to control clones transduced with guides targeting Rosa26 or AAVS1. As a positive control, we confirmed that knocking out the verified drug target MEK1 decreased proliferative capacity in A375 clones (fig. S4). However, we found that clones lacking each putative genetic dependency listed in Table 1 proliferated at levels that were indistinguishable from control A375, DLD1, and HCT116 cancer cells (Fig. 2C). For instance, PAK4-KO melanoma cells underwent an average of 20.3 population doublings over the course of 15 days in culture, compared to 19.9 doublings for the Rosa26 gRNA-transduced clones. To test whether these genes were dispensable for cell division but required for growth in other environments, we also seeded the KO clones in soft agar and assessed their ability to grow in anchorage-independent conditions. Although MEK1-KO clones formed fewer colonies in soft agar (fig. S4E), every HDAC6, MAPK14, PAK4, PBK, and PIM1 KO exhibited WT rates of colony formation, further verifying that these genes are not required for cancer cell fitness (Fig. 2, D and E).

Consistent with previously reported results, Rosa26 and AAVS1 control clones derived from MDA-MB-231 cell populations exhibited

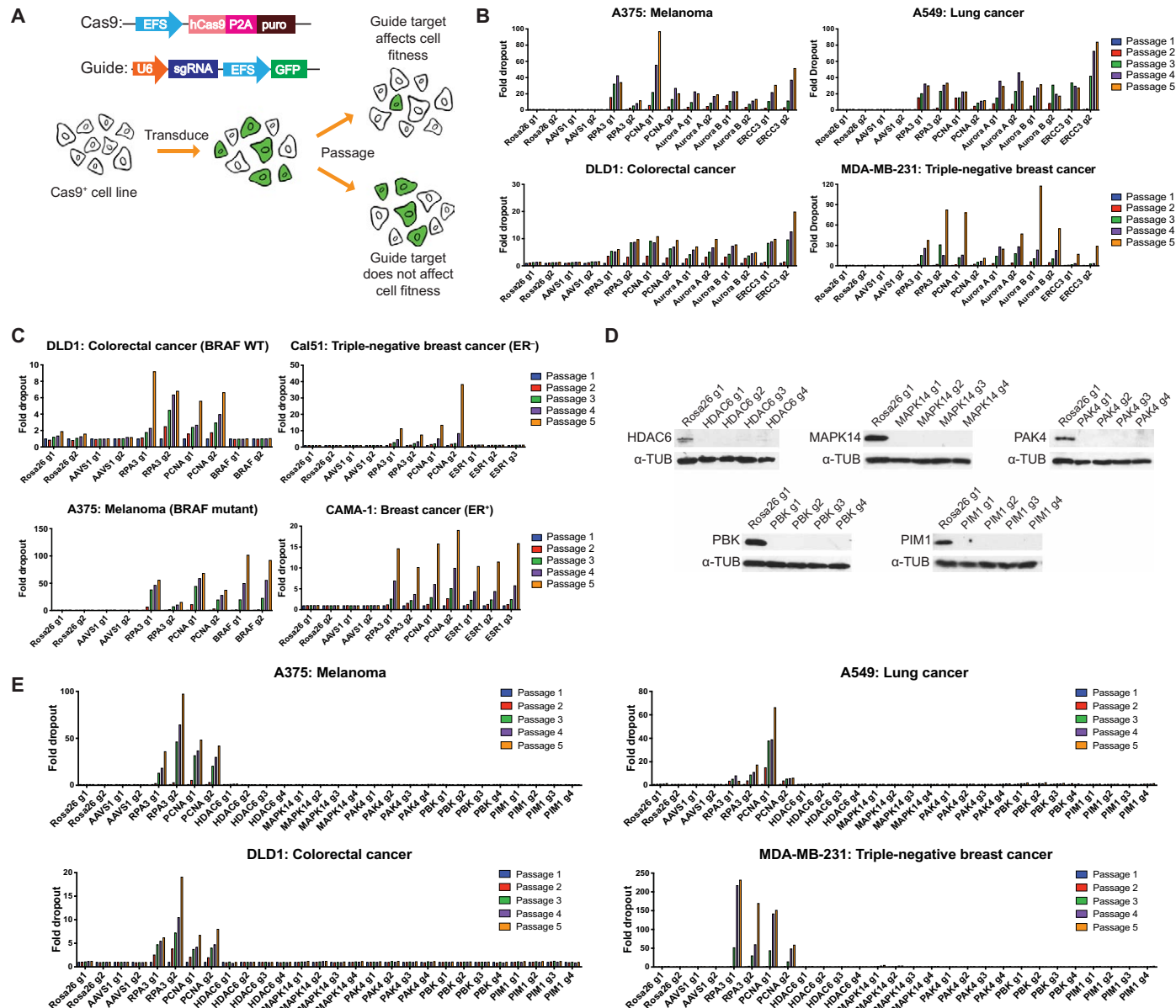


Fig. 1. Cell competition assays to test the essentiality of putative cancer dependencies. (A) Schematic of the CRISPR-based cell competition assays used in this paper (18). (B) Cell competition assays comparing guides targeting *AAVS1* and *ROSA26* (nonessential, negative control genes), *RPA3* and *PCNA* (pan-essential positive control proteins), and *Aurora A*, *Aurora B*, and *ERCC3* (inhibitor-validated cancer dependencies). Full results from these competition experiments are included in data file S2. (C) Cell competition assays for the cell type–specific cancer dependencies *BRAF* and *ESR1*. (D) Western blot analysis of A375 populations transduced with the indicated gRNAs. (E) Cell competition assays with gRNAs targeting *HDAC6*, *MAPK14*, *PAK4*, *PBK*, or *PIM1* in four different cancer cell lines.

some variability in proliferative capacity (3, 4, 22). By analyzing a total of 12 single cell-derived control clones, we established a range of doubling times in which WT MDA-MB-231 cells can divide (fig. S5B). Every *HDAC6*, *MAPK14*, *PAK4*, *PBK*, and *PIM1* KO clone proliferated at a comparable rate to these control clones (fig. S5C). All KO clones were also capable of forming colonies in soft agar at rates comparable to the control clones, further verifying that these putative dependencies are nonessential in breast cancer (fig. S5D).

Lack of homolog up-regulation in KO clones

Null mutations caused by CRISPR may trigger a different cellular response than RNAi-induced gene repression, potentially contributing

to the discrepancies between our results and those that had previously been reported. In particular, a recent study suggested that CRISPR-induced nonsense mutations can trigger the up-regulation of the homologs of a targeted gene, potentially compensating for the effects of the lesion (23). We assessed the expression of the closest homologs of *HDAC6*, *MAPK14*, *PAK4*, *PBK*, and *PIM1* in 33 different KO clones that we generated, but we observed no consistent up-regulation of any target homolog (fig. S6). In addition, we analyzed RNA sequencing (RNA-seq) data from 10 published experiments in gene-edited cancer cells from other laboratories and similarly failed to detect consistent evidence for the up-regulation of target gene homologs (fig. S7). In several experiments, we found that the homologs

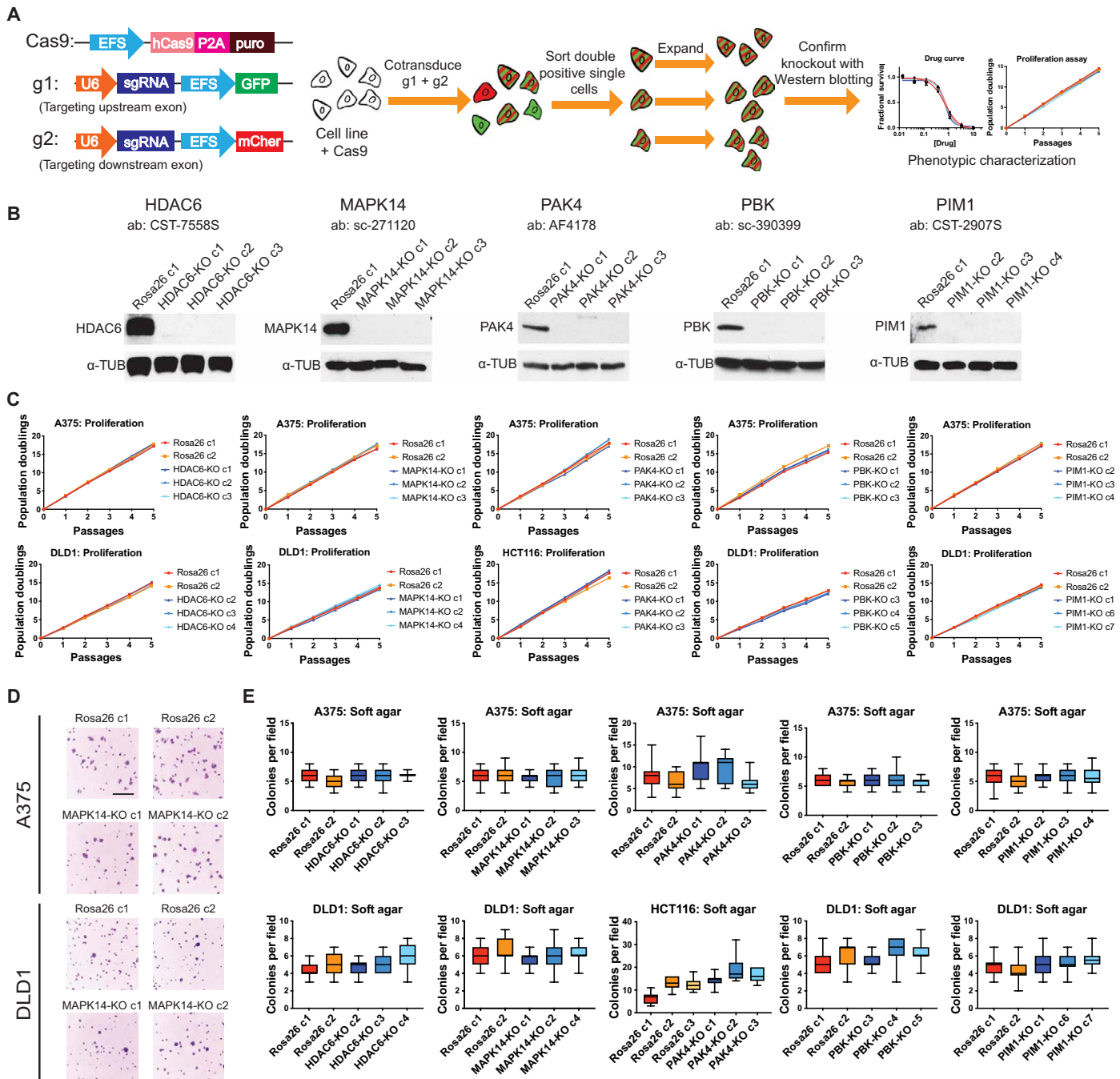


Fig. 2. Generating and analyzing single cell-derived KO clones of putative cancer dependencies. (A) Schematic of the two-guide strategy used to generate clonal KO cell lines. (B) Western blot analysis of single cell-derived A375 KO clones. ab, antibody. (C) Proliferation assays for HDAC6, MAPK14, PAK4, PBK, and PIM1 KO clones. (D) Representative images of A375 and DLD1 Rosa26 or MAPK14-KO clones grown in soft agar. Scale bar, 2 mm. (E) Quantification of colony formation in control or KO A375, DLD1, and HCT116 clones. Boxes represent the 25th, 50th, and 75th percentiles of colonies per field, and the whiskers represent the 10th and 90th percentiles. For each assay, colonies were counted in at least 15 fields under a 10x objective.

of the targeted gene were down-regulated. These results suggest that homolog up-regulation is not a common consequence of CRISPR mutagenesis in human cancer cells and that compensatory homolog overexpression is unlikely to explain the lack of a detectable growth defect in the CRISPR clones that we have analyzed.

Assessing putative cancer dependencies in whole-genome CRISPR and RNAi screens

Cell lines can exhibit interlaboratory variability that affects their response to different genetic and chemical perturbations (24). In addition, although we chose cancer types to study based on the dependency

patterns reportedly exhibited by each gene (data file S1), it remained possible that these genes represent dependencies in a cancer lineage not included among the 32 cell lines that we studied. To test this possibility and to assess whether unique or nonrepresentative features of the cell lines used in our laboratory contributed to our discrepant results, we reanalyzed genetic dependency data from whole-genome CRISPR screens conducted in 485 cancer cell lines (fig. S8A). These screens consistently identified both pan-cancer and cell type–specific genetic dependencies (for example, Aurora B, BRAF, and PIK3CA; fig. S8, B and C). However, in accordance with our earlier results, these experiments also indicated that our chosen dependencies were fully dispensable for cancer cell fitness (fig. S8, A to C). For instance, MAPK14/p38 α has previously been reported to be essential in breast cancer (9), but CRISPR screens conducted in 26 different breast cancer cell lines corroborate that its loss is tolerated without a substantial fitness defect (fig. S8D). Notably, we also reanalyzed 712 genome-wide shRNA screens, and these knockdown experiments similarly failed to identify HDAC6, MAPK14, PAK4, PBK, or PIM1 as cancer-essential genes (fig. S8, E to G). In total, these results indicate that our findings are unlikely to be explained by nonrepresentative features of the cell lines studied in our laboratory, by differences between partial and complete loss-of-function perturbations, or by these genes functioning as genetic dependencies only in certain cancer types. Instead, our data suggest that multiple genes targeted in cancer clinical trials are, in fact, fully dispensable for cancer cell growth.

Knocking down putative cancer dependencies with CRISPR interference

To further investigate whether differences between partial and complete loss-of-function perturbations could explain our discrepant results, we next performed competition experiments using the CRISPR interference (CRISPRi) system. In this approach, catalytically inactive Cas9 is fused to a transcriptional repressor and targeted to a gene's promoter, resulting in down-regulation of gene expression without the generation of a complete loss of function–inducing frameshift mutation (25). We designed three gRNAs that recognized HDAC6, MAPK14, PAK4, PBK, and PIM1 and verified that these constructs blocked the expression of their targets (fig. S9A). We then conducted competition experiments in four different cell lines, and we found that gRNAs targeting the essential replication protein MCM2 exhibited ~10- to ~20-fold dropout, whereas gRNAs targeting HDAC6, MAPK14, PAK4, PBK, and PIM1 failed to deplete (fig. S9B). These assays further verify that our results cannot be explained by the existence of different cellular responses to partial and complete loss-of-function alterations.

Assessing the sensitivity of target-KO clones to chemotherapy agents undergoing combination clinical trials

Several of the proteins listed in Table 1 are currently undergoing combination clinical trials using their targeted inhibitors together with other chemotherapy agents. It is conceivable that a protein could be nonessential under normal conditions but that its loss sensitizes cells to specific chemotherapies. For instance, HDAC6 is capable of deacetylating microtubules (26), and HDAC6 inhibition has been reported to render cells vulnerable to drugs that interfere with microtubule dynamics (27). As a result of this preclinical work, two clinical trials are combining HDAC6 inhibitors with the micro-

tubule stabilizer paclitaxel (NCT02632071 and NCT02661815). We therefore tested whether the KO clones that we had generated were sensitive to various chemotherapy agents (fig. S10, A to C). In contrast to previous results, loss of HDAC6 failed to sensitize cells to paclitaxel or to four other anticancer drugs (fig. S10A). Similarly, p38 α inhibitors have been clinically applied in combination with bortezomib, gemcitabine, carboplatin, and temozolamide (NCT00087867, NCT00095680, NCT01663857, and NCT02364206), but MAPK14/p38 α KO clones in multiple cell lines were as sensitive to these agents as Rosa26 control clones (fig. S10B). These results suggest that, in addition to being nonessential, these putative drug targets do not affect sensitivity to several chemotherapy agents that have been tested in combination trials.

Assessing RNAi promiscuity as a cause of the misidentification of cancer dependencies

If these genes do not drive cancer growth or chemotherapy resistance, then why have inhibitors targeting the proteins that they encode been tested in human patients with cancer? A review of the literature indicates that each of these genes has been described to be essential on the basis of RNAi-induced knockdown phenotypes (data file S1). Off-target toxicity has been reported to be a common problem in the design and interpretation of RNAi-based experiments (28–30), although the impact of these issues on the therapeutic development pipeline is not known. We acquired four different RNAi constructs that were used in these prior studies and then tested their effects on the clones that we had generated. Although we were able to confirm that each construct decreased the expression of its putative target, we also found that these constructs impaired proliferation in both WT clones and clones in which the construct's target had been knocked out (fig. S11, A to C). For example, a recent report found that PAK4-targeting siRNAs blocked cell division in HCT116 colon cancer cells and concluded that PAK4 was a genetic dependency in this cell line (31). However, we found that these same siRNAs induced an equivalent decrease in proliferation in both HCT116 PAK4-KO and HCT116 Rosa26 clones, suggesting that their effects on growth are a consequence of off-target toxicity (fig. S11A). Similarly, while knocking down PIM1 has been reported to block proliferation in the MDA-MB-231 breast cancer cell line (15), this construct had the same effect in MDA-MB-231 PIM1-KO cells (fig. S11B). Our results therefore suggest that these drug targets have advanced to clinical testing due, at least in part, to promiscuous RNAi constructs.

Assessing the specificity of cancer drugs undergoing clinical trials

Off-target toxicity from small-molecule drugs can cause dangerous side effects and is a major cause of clinical trial failure (32, 33). Our results suggested that the drugs listed in Table 1 were designed to target nonessential cellular proteins, raising the possibility that the anticancer effects of these drugs could be due to off-target interactions. We therefore sought to apply CRISPR to differentiate between the on- and off-target effects of each clinical cancer drug. First, we confirmed that CRISPR could be used to verify the MOA for several genetically validated therapies. The natural product rapamycin is reported to bind to the prolyl isomerase FKBP12, and this complex inhibits the essential mTOR (mammalian target of rapamycin) kinase (fig. S12A) (34, 35). We knocked out FKBP12 using CRISPR, and we verified that these KO clones exhibited increased resistance

to rapamycin treatment (fig. S12, B and C). Similarly, knocking out p53 conferred resistance to the experimental p53-activating drug nutlin-3a (fig. S12, D to F). Last, we sought to test whether CRISPR could be used to validate a published resistance-granting point mutation. We used CRISPR-mediated homology-directed repair (HDR) to introduce a missense mutation into the kinase domain of the essential mitotic kinase MPS1, and we verified that this substitution was capable of granting resistance to the small-molecule MPS1 inhibitor AZ3146 (fig. S12, G to I) (36). Thus, CRISPR-derived KO and knock-in cell lines can be used to validate on-target drug activity.

Next, we applied CRISPR to interrogate the MOA of two caspase-3 activating compounds: PAC-1 and 1541B. These drugs are reported to function by catalyzing the conversion of caspase-3 from its inactive, pro caspase state to its active, cleaved form, thereby causing cellular apoptosis (fig. S13A) (16, 17). Currently, PAC-1 is undergoing three different clinical trials in patients with cancer (NCT02355535, NCT03332355, and NCT03927248). We knocked out the CASP3 gene in four different cell lines and then verified protein ablation using two different antibodies (Fig. 3A and fig. S13). However, these CASP3-KO lines exhibited identical sensitivity to PAC-1 and 1541B compared with Rosa26 controls (Fig. 3B and fig. S13, D and F). These results suggest that a putative caspase-3 activator undergoing clinical trials actually kills cancer cells in a caspase-3-independent manner.

We next tested each putative HDAC6, MAPK14, PAK4, PBK, and PIM1 inhibitor in control and KO clones. If these drugs act by specifically inhibiting their reported targets, then cancer cells that totally lack the expression of their targets would be expected to be resistant to these drugs' effects. In contrast, if a drug kills cells in which its reported target has been knocked out, then this drug necessarily kills cells by affecting another protein or proteins. In every instance that we tested, cancer cells in which HDAC6, MAPK14, PAK4, PBK, or PIM1 had been knocked out exhibited WT sensitivity to their putative targeted inhibitors (Fig. 3 and fig. S14, A and B). For example, we found that the PAK4 inhibitor PF-3758309 blocked the growth of both Rosa26 and PAK4-KO melanoma cells with a GI_{50} value of ~9 nM (Fig. 3G). Given that this drug is fully capable of killing cells in which its putative target has been deleted, the ability of PF-3758309 to block cancer cell growth must be through an off-target effect. To further interrogate whether the drugs studied in this manuscript could exhibit an on-target MOA in an additional genetic background, we knocked out HDAC6 in TOV-21G cells, an ARID1A-mutant ovarian cancer cell line in which this gene has been reported to be a dependency (fig. S15A) (6). However, TOV-21G HDAC6-KO cells exhibited WT fitness in vitro and in soft agar (fig. S15, B and C), and these cells remained sensitive to catarinostat and ricolinostat, two putative HDAC6 inhibitors in clinical trials (fig. S15D). In total, all 10 different anticancer agents targeting CASP3, HDAC6, MAPK14, PAK4, PBK, or PIM1 exhibited clear evidence of target-independent cell killing in every KO cell line that we examined.

Last, we applied these putative inhibitors to investigate several combination chemotherapy trials. As described above, HDAC6 inhibitors are currently undergoing testing in cancer patients along with paclitaxel, and p38 α inhibitors have also been combined with several different therapeutic agents. We verified that cotreatment with a targeted inhibitor and a second agent generally caused a greater decrease in cancer cell viability than either agent alone (fig. S14B). However, this synthetic enhancement was observed in

both Rosa26 and target-KO clones, suggesting that these additive effects are also due to an off-target interaction.

Discovering the true target of OTS964

If these clinical anticancer therapies do not kill cells by inhibiting their reported targets, then how do they block cancer growth? We note that, although the MOA of each drug has previously been characterized using biochemical and biophysical approaches, there is little genetic evidence linking each drug to its reported target. We hypothesized that an alternative genetic methodology could shed light on the true target of a therapeutic agent whose MOA was in question.

For this work, we chose to focus on the putative PBK inhibitor OTS964, because it exhibited nanomolar potency in multiple cancer types and our CRISPR experiments had provided clear evidence that PBK was not required for cell proliferation. Moreover, OTS964 has been reported to affect mitotic progression (13), and antimitotic drugs have been historically proven to be highly successful anticancer agents (37). To identify mutations that conferred resistance to OTS964, we used HCT116 colorectal cancer cells, which harbor an increased mutation rate caused by a defect in mismatch repair (38). We cultured HCT116 cells in the presence of a lethal concentration of OTS964 and successfully isolated 12 clones that were capable of growing under these conditions (Fig. 4A). We found that these clones exhibited stable resistance to OTS964, as they failed to revert to OTS964 sensitivity after prolonged growth in normal medium (fig. S16A). Cancer cells commonly acquire chemotherapy resistance by amplifying the P-glycoprotein drug efflux pump (39). However, the OTS964-resistant clones remained sensitive to paclitaxel, a verified P-glycoprotein substrate, suggesting that they had not acquired a multidrug resistance phenotype (fig. S16B) (40). These experiments indicated that our drug-resistant clones could harbor a mutation or mutations that specifically altered OTS964 sensitivity.

To identify genetic alterations capable of conferring OTS964 resistance, we subjected 10 OTS964-resistant clones, 1 Rosa26 control clone, and the parental cell population to whole-exome sequencing (WES). Notably, all 10 resistant clones were found to harbor heterozygous missense mutations in the poorly characterized cyclin-dependent kinase (CDK) CDK11B (fig. S16C). Eight clones harbored two mutations in this gene, H572Y and G579S, in trans, whereas two clones harbored only the G579S substitution. No CDK11B mutations were observed in the parental population or in the Rosa26 control clone. Sanger sequencing verified the presence of the CDK11B mutations in two independent drug-resistant clones that were not subjected to WES (Fig. 4B and fig. S16C). These mutations were also absent from additional control clones that were analyzed (fig. S16C) and have not been previously observed in the Catalog of Somatic Mutations in Cancer database (41).

The human genome encodes two CDK11 proteins, CDK11A and CDK11B, that are 97% identical and that arose from an evolutionarily recent gene duplication event (42). The CDK11 family has been reported to support various cellular processes, including transcription, splicing, and chromosome segregation (43), but its role in cancer is unknown. No drugs have previously been reported to target CDK11, and inhibitors that are specific for single CDKs are difficult to discover due to the sequence similarity among these kinases (44). We aligned the sequences of the human CDKs, and we noted that 19 of 20 of these proteins harbored an alanine residue immediately upstream of the magnesium-coordinating DFG motif (fig. S16D).

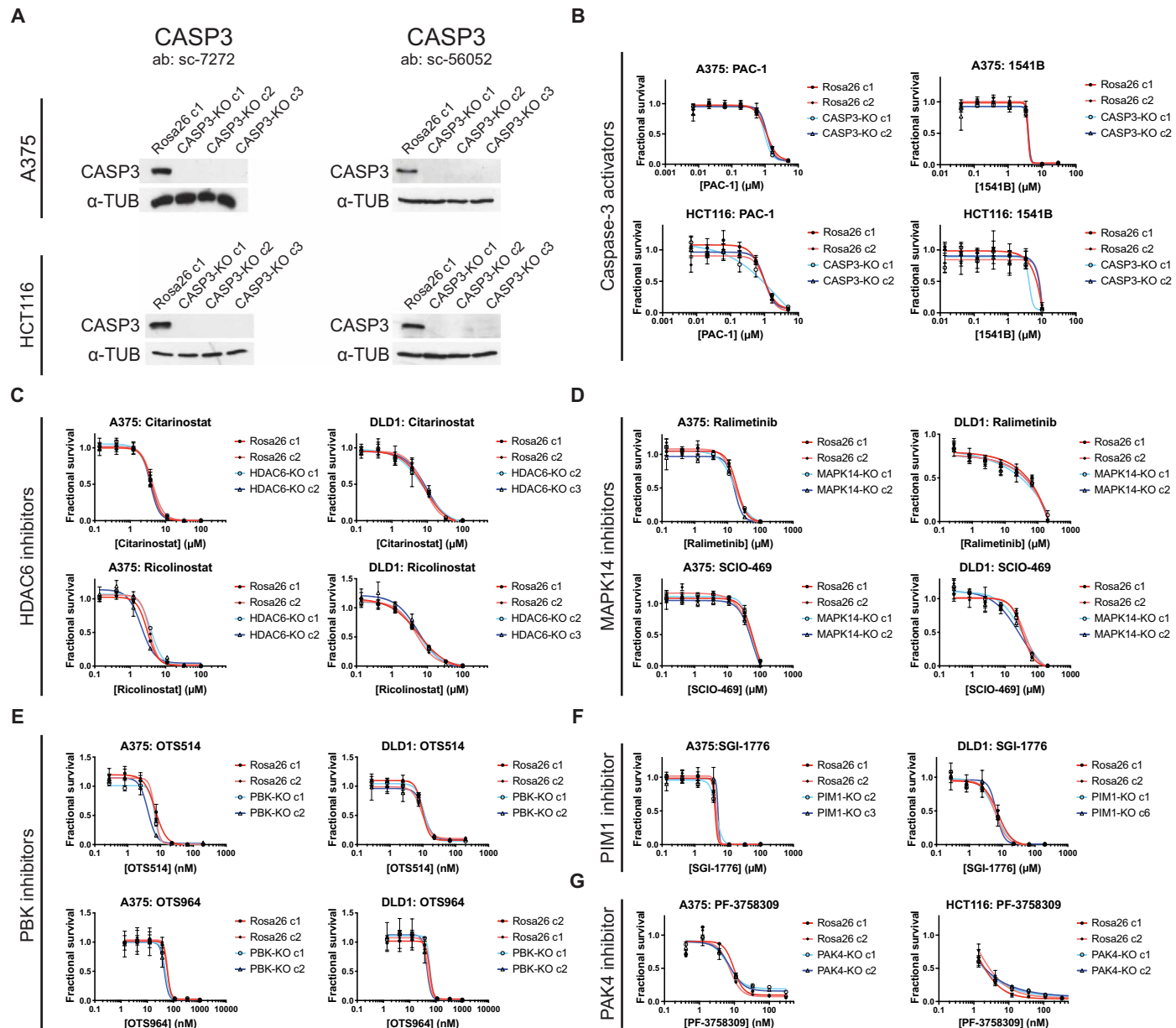


Fig. 3. Target-independent cell killing by multiple anticancer drugs. **(A)** Western blot analysis for caspase-3 in A375 and HCT116 cells. **(B)** Seven-point dose-response curves of Rosa26 and CASP3-KO A375 and HCT116 cells in the presence of two putative caspase-3 activators: 1541B and PAC-1. **(C)** Seven-point dose-response curves of Rosa26 and HDAC6-KO A375 and DLD1 cells in the presence of two putative HDAC6 inhibitors: ricolinostat and citarinostat. **(D)** Seven-point dose-response curves of Rosa26 and MAPK14-KO A375 and DLD1 cells in the presence of two putative MAPK14 inhibitors: ralimetinib and SCIO-469. **(E)** Seven-point dose-response curves of Rosa26 and PBK-KO A375 and DLD1 cells in the presence of two putative PBK inhibitors: OTS514 and OTS964. **(F)** Seven-point dose-response curves of Rosa26 and PIM1-KO A375 and DLD1 cells in the presence of a putative PIM1 inhibitor: SGI-1776. **(G)** Seven-point dose-response curves of Rosa26 and PAK4-KO A375 and HCT116 cells in the presence of a putative PAK4 inhibitor: PF-3758309.

Only CDK11 contained a glycine at this location, and this glycine was mutated to serine in every OTS964-resistant clone that we sequenced (fig. S16, C and D). This amino acid position (called “xDFG”) has previously been identified as a key residue that affects kinase inhibitor binding (45), suggesting a potential basis for CDK11-selective inhibition. To test whether the xDFG Gly→Ser mutation was sufficient to confer resistance to OTS964, we designed a strategy to use CRISPR-mediated HDR to introduce this substitution into the endogenous *CDK11B* gene (Fig. 4C). These experiments revealed

that this point mutation was sufficient to restore viability in A375, A2780, DLD1, and MDA-MB-231 cancer cells grown in a lethal concentration of OTS964 (Fig. 4, D and E). To verify that our results were not an off-target effect of CRISPR, we generated a retrovirus to stably express *CDK11B^{G579S}* cDNA, and we confirmed that this construct was also sufficient to confer OTS964 resistance (fig. S16E). In an HCT116 clone that had spontaneously evolved resistance to OTS964, eliminating mutant *CDK11B* with CRISPR restored OTS964 sensitivity, demonstrating that this alteration is both

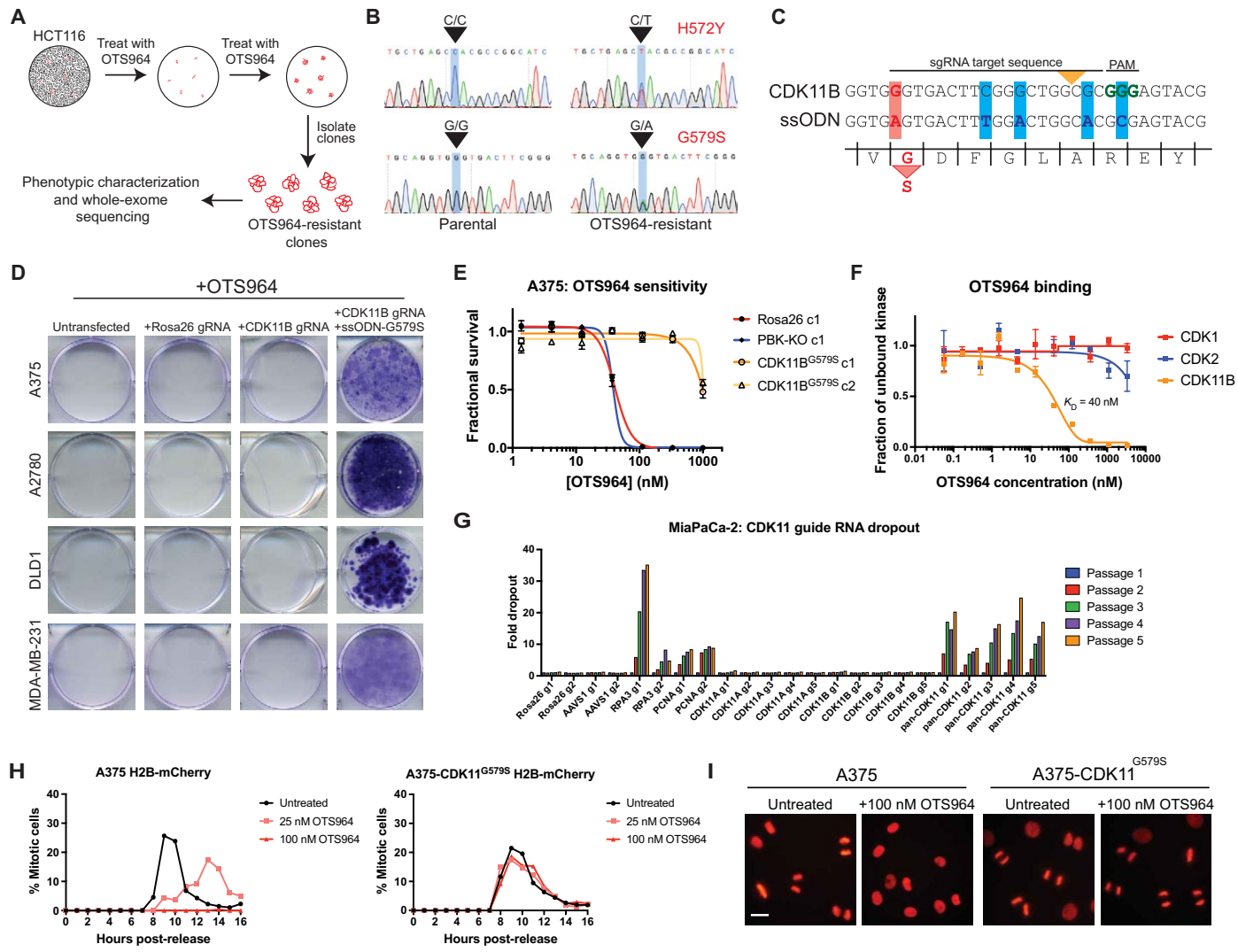


Fig. 4. Discovery of CDK11 as the in cellulo target of the mischaracterized anticancer drug OTS964. (A) A schematic of the strategy to use the highly mutagenic HCT116 cell line to isolate mutations that confer OTS964 resistance. (B) Sanger sequencing validation of two heterozygous mutations in the CDK11B kinase domain. (C) Constructs used to introduce the G579S mutation into CDK11B via CRISPR-mediated HDR. Yellow arrowhead indicates the site of Cas9 cleavage. Red bar indicates the G579S substitution, and blue bars indicate silent mutations introduced to prevent recutting after HDR. (D) Crystal violet staining of cancer cells transfected with the indicated constructs and then cultured in a lethal concentration of OTS964. (E) Seven-point dose-response curves of ROSA26, PBK-KO, and CDK11B^{G579S} clones grown in varying concentration of OTS964. (F) Titration experiments reveal that OTS964 binds to CDK11B with a K_D of 40 nM. (G) Pancreatic cancer cell line MiaPaca-2 was transduced with guides specific for CDK11A, guides specific for CDK11B, or guides that harbored cut sites in both genes. (H) A375 H2B-mCherry cells (left) or A375 H2B-mCherry cells that express CDK11B^{G579S} (right) were arrested at G₁/S with a double-thymidine block and then were released into normal medium or medium containing OTS964. The percentage of mitotic cells in each population was scored every hour. (I) Representative images of the experiments in (H), 9 hours after release from thymidine. Scale bar, 25 μ m.

necessary and sufficient for drug resistance (fig. S16F). Introducing an alanine substitution into residue 579, so that the CDK11B xDFG motif was identical to the other human CDKs, was also sufficient to decrease the efficacy of OTS964 (fig. S16, G and H). Last, to confirm a direct interaction between OTS964 and CDK11B, we assessed the binding of OTS964 to different CDKs. OTS964 bound to CDK11B with a K_D (dissociation constant) of 40 nM, and it displayed greater than 10-fold selectivity for this kinase compared with several other CDKs (Fig. 4F and fig. S16I). In total, these results indicate that the putative PBK inhibitor OTS964 actually functions by targeting CDK11, and its specificity for this kinase is conferred by CDK11's distinct xDFG motif.

Discovering the consequences of CDK11 inhibition in cancer

We next determined the cellular effects of OTS964 treatment and CDK11 ablation with CRISPR. In cell competition assays, cancer cells transduced with gRNAs specific for either CDK11A or CDK11B exhibited minimal dropout. However, guides designed to recognize both isoforms exhibited substantial dropout in every cell line that we tested, including pancreatic cancer and triple-negative breast cancer (Fig. 4G and fig. S17A). Flow cytometry revealed that cells transduced with pan-CDK11 guides accumulated in G₂/M with 4C DNA content, suggesting that CDK11 function is required for mitotic progression (fig. S17B). To test whether OTS964 phenocopies the CDK11 gRNAs, we arrested A375 cells expressing the

chromosomal marker H2B-mCherry at G₁/S with a double-thymidine block and then released them into normal medium or medium containing OTS964. Cells treated with a low concentration of OTS964 exhibited delayed nuclear envelope breakdown and progressed slowly through mitosis (Fig. 4H, fig. S17C, and movies S1 and S2). Cells treated with a lethal concentration of OTS964 arrested in G₂, before mitotic entry (movie S3). OTS964 treatment did not perturb DNA replication, because the arrested cells displayed 4C DNA content and did not accumulate 53BP1 foci, a marker of DNA damage (fig. S17, D and E). Introducing the G579S substitution into A375 cells rescued normal mitotic entry and progression in the presence of a lethal concentration of OTS964 (Fig. 4, H and I, fig. S17C, and movie S4). These results establish CDK11 activity as necessary for mitosis in human cancer and suggest that CDK11 is the key in cellulo target of OTS964.

DISCUSSION

It is generally known that small molecules can exhibit off-target effects that may confound the design of specific chemical inhibitors (46). Our data suggest that, rather than simply being the side effect of a drug, these off-target interactions are frequently the mechanism by which small molecules block cancer growth. Every inhibitor tested in this manuscript that lacked a previously described resistance mutation was found to kill through an off-target effect; these results therefore identify this phenomenon as a common problem that affects cancer clinical trials. As 97% of drug-indication pairs tested in clinical trials fail to receive U.S. Food and Drug Administration (FDA) approval (5), the misidentification of essential genes in cancer and the mischaracterization of reportedly target-specific inhibitors likely contribute to their exceedingly high failure rate. The adoption of more stringent genetic target and activity validation studies may alleviate this problem and decrease the failure rate of new cancer drugs.

Each gene that we studied has been reported to be required in a cell-autonomous manner for cancer proliferation by more than 180 publications, and it is this specific claim that our work sought to test (data file S1). Toward this end, we generated KO clones in at least three cancer cell lines, we performed CRISPR competition assays in 32 cell lines, and we performed CRISPRi-knockdown competition assays in an additional four cell lines, which all consistently demonstrated that HDAC6, MAPK14, PAK4, PBK, and PIM1 are dispensable for cancer cell fitness. Although cancer cells harbor the ability to evolve in response to various perturbations, we do not believe that this adaptability is sufficient to explain the robust growth of the CRISPR-modified cells that we have generated. First, in the competition assays that we conducted, cells are analyzed immediately after gRNA transduction, allowing them no time to adapt to the loss of the targeted gene. For instance, although BRAF-addicted melanoma cells are capable of evolving BRAF independence over time by acquiring secondary mutations in MEK or NRAS (47), we still observed a strong depletion of BRAF-targeting guides in these dropout assays. Second, we knocked out the verified drug target MEK1 and confirmed that MEK1-KO clones grow substantially more slowly than Rosa26 control clones, demonstrating our ability to validate genetic dependencies in CRISPR-modified clones. Third, although each of the genes that we studied has previously been reported to be essential, our experiments provide a mechanism to explain these discrepant results. In particular, we demonstrate that several RNAi constructs previously used to inhibit these genes exhibit identical antiproliferative

effects in target-WT and target-KO cancer cells, suggesting that RNAi promiscuity contributed to the misidentification of these genes as drug targets. Fourth, although it has been proposed that cells can compensate for CRISPR-induced mutations by up-regulating homologs of the targeted gene (23), we failed to detect any evidence of this in our KO clones or in genetically modified cell lines from several independent laboratories. Last, high-throughput screens conducted in hundreds of cancer cell lines using both RNAi and CRISPR technologies have also failed to identify these genes as cancer dependencies. We therefore believe that cellular evolution after CRISPR mutagenesis is unlikely to explain the robust growth of the cancer cells lacking the drug targets that we have studied.

The cell lines studied in this paper were chosen based on the literature on each target, but we have not attempted to recapitulate every individual published result with each drug or drug target. Thus, it remains possible that these drug targets exhibit a cell type-specific dependency pattern not uncovered in this work. To partially address this concern, we analyzed published whole-genome CRISPR and RNAi screening data from >700 cell lines, which consistently revealed that the genes studied in this work could be eliminated without substantially affecting cell fitness. Because of the breadth of cell lines tested both within our laboratory and through high-throughput screening, it is unlikely that these genes are genetic dependencies in a common cancer lineage. Nonetheless, we do not rule out the possibility that these genes are essential in a rare cancer type not included among those studied here. In addition, it remains possible that these genes play a non-cell-autonomous role during tumorigenesis. For instance, whereas MAPK14/p38 α has been reported to be essential for proliferation in breast cancer (9, 48), colon cancer (8), ovarian cancer (49), and several other cancer types, it has also been proposed to mediate inflammatory signaling (50). Thus, although our work provides strong evidence that these proteins are dispensable for cancer proliferation, we do not rule out the possibility that these proteins have some function in other non-cell-autonomous processes related to tumor development *in vivo*.

Our results indicate that many cancer drugs in clinical trials kill cells independently of their reported targets. As the application of a predictive biomarker doubles the likelihood that a clinical trial will succeed (5), the inability to decipher a drug's true target may prevent successful biomarker identification and contribute to trial failure. Moreover, our findings may provide evidence that cancer drug polypharmacology is a common MOA for reportedly target-specific compounds. For example, whereas ricolinostat has been reported to be a selective HDAC6 inhibitor (51), our work shows that HDAC6 expression is fully dispensable for ricolinostat sensitivity. These results are similar to those reported in (52), which found that ricolinostat continued to kill HDAC6-KO HAP1 cells. The human genome harbors 18 different histone deacetylases (53), and it is possible that this drug kills cells by inhibiting HDAC6 and several synthetically redundant HDAC family members. In addition, the invalidation of a drug's putative target does not necessarily mean that a drug will be ineffective in the clinic, as some broadly non-specific inhibitors have been proven efficacious in certain circumstances. In many cases, these successes derive from a thorough understanding of a drug's MOA. For instance, the multitargeted kinase inhibitor midostaurin has received FDA approval for use in FLT3 $^+$ leukemias due to its demonstrated activity against FLT3 (54). Thus, strong validation of on-target drug activity remains essential.

Alternately, these mischaracterized drugs may kill cells by inhibiting single, specific proteins that are not closely related to their reported targets. For instance, our results demonstrate that the putative PBK inhibitor OTS964 functions by blocking CDK11 activity. Several CDK inhibitors have received FDA approval or are in late-stage trials for various malignancies, underscoring the clinical potential for targeting members of the CDK family (55). However, no CDK11-specific inhibitors have been previously described (56). OTS964 and its derivatives could therefore allow us to block cancer growth by inhibiting a previously undruggable mitotic CDK. Furthermore, our work identifies CDK11's distinct xDFG motif as a key determinant of drug sensitivity, suggesting a potential structural basis for CDK11-specific inhibition. Although CDK11 has previously been reported to function in chromosome segregation (57), our results demonstrate that its activity is required for entry into mitosis. It will therefore be crucial to investigate whether CDK11 inhibitors are capable of synergizing with PLK1 inhibitors, Aurora A inhibitors, or any other drugs that similarly target mitotic entry (58). Last, the CDK11 locus on chromosome 1p has been reported to be deleted or translocated in several cancer types, including melanoma and neuroblastoma (43), raising the exciting possibility that alterations in this gene family could serve as predictive biomarkers for CDK11 inhibitor sensitivity.

More broadly, our results underscore the power of genetic approaches to improve the preclinical characterization of cancer drugs and drug targets. In particular, CRISPR-mediated gene editing is a powerful methodology for interrogating the effects of loss-of-function alterations in disease-relevant genes, and head-to-head comparisons have verified that CRISPR is less susceptible to off-target effects than RNAi (59, 60). Although biochemical and biophysical approaches can demonstrate target engagement by a potential therapeutic molecule, these assays alone are insufficient to demonstrate the relevance of this interaction in *cellulo*. Mutagenesis experiments, using either spontaneous or CRISPR-directed approaches, can complement these assays to verify or discover a drug's true MOA and indicate potential biomarkers for sensitivity and resistance. We suggest that the adoption of stringent genetic characterization assays in the preclinical setting will decrease the number of drugs used in human cancer patients that fail to provide any clinical benefit.

MATERIALS AND METHODS

Study design

In this work, we sought to determine whether several drug targets were truly essential for cancer cell fitness. After discovering that many of these drug targets were nonessential, we investigated whether the drugs used to target them killed cells through an off-target effect. The cell lines used in this study were selected based on an analysis of the literature on these drug targets (summarized in data file S1). No predetermined sample sizes were used for this analysis. No randomization or blinding was performed. Cell competition experiments represent single biological replicates. Proliferation assays represent two to three biological replicates. Drug sensitivity curves were generated with three to six technical replicates. Soft agar experiments represent three technical replicates with at least 15 independent fields counted for each experiment. Raw data for the cell competition experiments are included in data file S2.

Selecting drug targets to study

Our laboratory previously investigated the role of MELK in cancer (3, 4). We found that, contrary to previous results obtained with RNAi, cancer cells tolerated CRISPR-induced ablation of MELK with no loss in cell fitness. In addition, we found that OTS167, a small-molecule inhibitor of MELK in clinical trials, killed cells in a MELK-independent manner. These findings led us to investigate whether MELK and OTS167 were aberrations or whether other drugs and drug targets had been similarly mischaracterized.

To begin this project, we generated a list of drugs and drug targets to study. We constructed this list using a few criteria, informed in part by our experience studying MELK. First, we sought to identify cancer genes that reportedly played a cell-autonomous role in cancer growth, so that we could study the most relevant phenotypes that resulted from their ablation in cell culture. Thus, we did not consider drugs that primarily target angiogenesis, the immune checkpoints, or related *in vivo* processes. (Importantly, our work does not rule out *in vivo* roles for the genes studied in this paper.) Second, we only considered drugs that were reported to act by targeting single, specific proteins. If a drug was believed to act by inhibiting multiple proteins, then this would confound our CRISPR experiments, because the genetic ablation of a single gene would not be expected to phenocopy the effects of the inhibitor. Third, we focused on genes that were reported to have broad dependency patterns, allowing us to study the consequences of their inhibition in a wide range of cell lines. Fourth, we focused on genes that had been largely characterized using RNAi, although we did not exclude genes that had been previously studied using CRISPR, transgenic mice, dominant-negative alleles, or other approaches. Fifth, we chose drugs that were in advanced preclinical or clinical testing. Sixth, we posited that the gold standard for showing on-target drug activity was the identification of a mutation that confers resistance to a targeted inhibitor, and we sought to study drugs that lacked known resistance-granting mutations.

Using these criteria, we searched PubMed, the database of American clinical trials (<https://clinicaltrials.gov/>), and other related resources (61) for drugs and drug targets that fit these criteria. We did not aim to comprehensively identify every drug that met the above criteria but instead chose to limit ourselves to a small number of targets such that we could deeply characterize each one. Using these approaches, we chose to study CASP3, HDAC6, MAPK14, PAK4, PBK, and PIM1. We first became aware of the putative PBK inhibitor OTS964 because it was developed by the same company that created the MELK inhibitor that we previously studied. A press release on this drug reported that clinical trials would soon be initiated, although, to our knowledge, these clinical trials have not yet begun (62). In addition, our list of drugs initially included the putative PAK4 inhibitor KPT-9274. However, while performing the research described in this paper, a report was published that identified mutations in NAMPT that granted resistance to KPT-9274; therefore, we did not further pursue this compound (63). After the initial submission of this manuscript, a second group independently demonstrated that the putative HDAC6 inhibitor ricolinostat kills HDAC6-KO HAP1 cancer cells, in accordance with our results (52).

We also chose to study two drugs, PAC-1 and 1541B, that reportedly function by activating the apoptosis protein caspase-3. Although caspase-3 is not considered to be a "cancer dependency," its activation by small molecules has been reported to trigger cancer cell apoptosis (16, 17). The first activator, PAC-1, was introduced in

a publication that used in vitro methods to demonstrate the ability of PAC-1 to induce procaspase-3 cleavage and activation. Furthermore, the group implied specificity of PAC-1 for caspase-3 by showing that it exhibited a higher IC₅₀ (median inhibitory concentration) value in MCF7 cells, a caspase-3-deficient breast cancer cell line, compared with caspase-3-expressing cell lines (16). After this study, however, concerns were raised over whether caspase-3 activation was the true MOA of PAC-1. In a letter to *Nature Chemical Biology*, another laboratory reportedly failed to see substantial activation of procaspase-3 in in vitro studies of PAC-1 (64). In addition, the group stated that the caspase-3-deficient cell line, MCF7, displayed similar sensitivities to the drug as two caspase-3-expressing cell lines. Although this letter raised questions as to the true MOA of PAC-1, the original developers of this compound disputed these concerns, arguing that the different in vitro results were a consequence of different procaspase concentrations and buffer conditions used in the assays (65). In support of this claim, in later publications, the group detailed the in vitro MOA of PAC-1 as a zinc chelator, describing a mechanism where zinc prevents procaspase-3 activation; therefore, the in vitro efficacy of PAC-1 is highly dependent on the concentration of zinc in the buffer (66). This group also argued that the activity of PAC-1 against the MCF7 cell line only occurs under conditions of low cell density and high drug concentration and that the mechanism of death seems to resemble necrosis more than caspase-mediated apoptosis (65). A number of other publications using PAC-1 and second-generation caspase-3 activators reported a similar resistance of MCF7 cells to caspase-3-activating compounds (17, 67). On the basis of this evidence, many in the field have continued to use PAC-1, not only in biological investigations but also in a number of clinical trials, under its listing as a caspase-3 activator (Table 1 and data file S1). In contrast to PAC-1, later caspase-3 activators, namely 1541, were reported to have direct interactions with caspase-3. 1541, the parental compound to the 1541B inhibitor used in our study, was not only able to induce caspase-3 activation in in vitro conditions where PAC-1 exhibited no effect, but 1541 resistance mutations in the CASP3 gene were also described (17). Because caspase-3 deficiencies have been linked with decreased sensitivity to a wide range of chemotherapeutic agents, we considered it possible that this putative resistance could be caused by an indirect effect on apoptosis (68, 69). Thus, because of the controversy and conflicting data concerning the MOA of different caspase-3 activators, we decided to include these compounds in our study.

Cell culture

The sources of each cell line are listed in data file S3. The identities of all human cell lines used in this study were confirmed using STR (short tandem repeat) profiling (University of Arizona Genetics Core). A375, A549, A673, Cal51, Cama1, DLD1, HCT116, HEK293T, MDA-MB-231, PC3, SK-MEL-28, and U87 cell lines were cultured in Dulbecco's modified Eagle's medium (DMEM) (Thermo Fisher Scientific, cat. no. 11995-073) supplemented with 10% fetal bovine serum (FBS) (Sigma-Aldrich, cat. no. F2442), 2 mM glutamine (Lonza, cat. no. 17-605F), and penicillin and streptomycin (100 U/ml; Life Technologies, cat. no. 15140122). A2780, DU-145, HCC1143, HCC38, HT29, K562, LNCaP, MDA-MB-453, MDA-MB-468, NCI-H82, OVK18, OVTKO, SUIT2, SW480, and TOV-21G cell lines were cultured in RPMI 1640 (Lonza, cat. no. 12-115F/12) supplemented with 10% FBS, 2 mM glutamine, and penicillin and streptomycin (100 U/ml). MiaPaCa-2 cells were cultured in DMEM

supplemented with 10% FBS, 2.5% horse serum (Thermo Fisher Scientific, cat. no. 26050088), 2 mM glutamine, and penicillin and streptomycin (100 U/ml). MCF7 cells were cultured in DMEM supplemented with 10% FBS, insulin (0.01 mg/ml; Thermo Fisher Scientific, cat. no. 12585-014), 2 mM glutamine, and penicillin and streptomycin (100 U/ml). T24 cells were cultured in McCoy's 5A medium (Life Technologies, cat. no. 16600-108) supplemented with 10% FBS, 2 mM glutamine, and penicillin and streptomycin (100 U/ml). HepG2 cells were cultured in Eagle's minimum essential medium (American Type Culture Collection; cat. no. 30-2003) supplemented with 10% FBS, 2 mM glutamine, and penicillin and streptomycin (100 U/ml). RPE1 cells were cultured in DMEM/F12 (Thermo Fisher Scientific, cat. no. 11320-033) supplemented with 10% FBS, 2 mM glutamine, and penicillin and streptomycin (100 U/ml). Sum149 cells were cultured in Ham's F12 medium (Lonza, cat. no. 12-615F) supplemented with 5% FBS, insulin (0.01 mg/ml), hydrocortisone (500 ng/ml; STEMCELL Technologies, cat. no. 07926), 2 mM glutamine, and penicillin and streptomycin (100 U/ml). Additional details on the conduct of these studies are included in Supplementary Materials and Methods.

Statistical analysis

For box plots, the boxes represent the 25th, 50th, and 75th percentiles of the colonies per field, whereas the whiskers represent the 10th and 90th percentiles. In fig. S4, a Student's *t* test (two sided) was used to compare control and MEK1-KO colony formation efficiency.

SUPPLEMENTARY MATERIALS

stm.sciencemag.org/cgi/content/full/11/509/eaaw8412/DC1

Materials and Methods

- Fig. S1. Drug target ablation with CRISPR-Cas9.
- Fig. S2. Cell competition assays in multiple cancer types.
- Fig. S3. Verification of drug target-KOs.
- Fig. S4. Knocking out the verified genetic dependency MEK1 in A375 melanoma cells.
- Fig. S5. MDA-MB-231 clonal analysis.
- Fig. S6. Analysis of homolog gene expression in CRISPR-KO clones.
- Fig. S7. Analysis of homolog gene expression in published RNA-seq experiments.
- Fig. S8. Assessing putative cancer dependencies in whole-genome CRISPR and RNAi screens.
- Fig. S9. Targeting several putative cancer dependencies with CRISPRi.
- Fig. S10. Lack of sensitivity to several clinical chemotherapy agents in putative cancer dependency KOs.
- Fig. S11. Target-independent toxicity of RNAi reagents previously used to investigate several putative cancer dependencies.
- Fig. S12. Using CRISPR to validate the MOA of several anticancer drugs.
- Fig. S13. Off-target toxicity of two caspase-3-activating compounds in CASP3-KO clones.
- Fig. S14. Target-independent cancer cell killing in single-agent and combination therapy experiments.
- Fig. S15. Off-target toxicity of two putative HDAC6-inhibiting compounds in HDAC6-KO ovarian cancer clones.
- Fig. S16. A mutation in the xDFG residue of CDK11B in OTS964-resistant clones.
- Fig. S17. Requirement for CDK11 activity for progression through mitosis.
- Data file S1. Literature supporting the designation of HDAC6, MAPK14, PAK4, PBK, and PIM1 as cancer genetic dependencies and CASP3 as a drug target.
- Data file S2. Cell competition assay results.
- Data file S3. Sources of the cell lines used in this manuscript.
- Data file S4. CRISPR gRNA sequences.
- Data file S5. CRISPRi gRNA sequences.
- Data file S6. Quantitative polymerase chain reaction primers.
- Data file S7. Antibody sources and concentrations.
- Data file S8. Drugs and drug sources.
- Movie S1. A375 cells expressing H2B-mCherry released from a double-thymidine block into normal medium.
- Movie S2. A375 cells expressing H2B-mCherry released from a double-thymidine block into medium with 25 nM OTS964.

Movie S3. A375 cells expressing H2B-mCherry released from a double-thymidine block into medium with 100 nM OTS964.

Movie S4. A375^{CDK11B-G579S} cells expressing H2B-mCherry released from a double-thymidine block into medium with 100 nM OTS964.

References (70–257)

REFERENCES AND NOTES

- J. Luo, N. L. Solimini, S. J. Elledge, Principles of cancer therapy: Oncogene and non-oncogene addiction. *Cell* **136**, 823–837 (2009).
- S. V. Sharma, J. Settleman, Oncogene addiction: Setting the stage for molecularly targeted cancer therapy. *Genes Dev.* **21**, 3214–3231 (2007).
- A. Lin, C. J. Giuliano, N. M. Sayles, J. M. Sheltzer, CRISPR/Cas9 mutagenesis invalidates a putative cancer dependency targeted in on-going clinical trials. *eLife* **6**, e24179 (2017).
- C. J. Giuliano, A. Lin, J. C. Smith, A. C. Palladino, J. M. Sheltzer, MELK expression correlates with tumor mitotic activity but is not required for cancer growth. *eLife* **7**, e32838 (2018).
- C. H. Wong, K. W. Siah, A. W. Lo, Estimation of clinical trial success rates and related parameters. *Biostatistics* **20**, 273–286 (2019).
- B. G. Bitler, S. Wu, P. H. Park, Y. Hai, K. M. Aird, Y. Wang, Y. Zhai, A. V. Kossenkov, A. Vara-Ailor, F. J. Rauscher III, W. Zou, D. W. Speicher, D. G. Huntsman, J. R. Conejo-Garcia, K. R. Cho, D. W. Christianson, R. Zhang, *ARID1A*-mutated ovarian cancers depend on HDAC6 activity. *Nat. Cell Biol.* **19**, 962–973 (2017).
- P. Putcha, J. Yu, R. Rodriguez-Barrueco, L. Saucedo-Cuevas, P. Villagrassa, E. Murga-Penas, S. N. Quayle, M. Yang, V. Castro, D. Llobet-Navas, D. Birnbaum, P. Finetti, W. A. Woodward, F. Bertucci, M. L. Alpaugh, A. Califano, J. Silva, HDAC6 activity is a non-oncogene addiction hub for inflammatory breast cancers. *Breast Cancer Res.* **17**, 149 (2015).
- J. Gupta, I. del Barco Barrantes, A. Igea, S. Sakellariou, I. S. Pateras, V. G. Gorgoulis, A. R. Nebreda, Dual function of p38α mapk in colon cancer: Suppression of colitis-associated tumor initiation but requirement for cancer cell survival. *Cancer Cell* **25**, 484–500 (2014).
- B. Cánovas, A. Igea, A. Sartori, R. R. Gomis, T. T. Paull, M. Isoda, H. Pérez-Montoyo, V. Serra, E. González-Suárez, T. H. Stracker, A. R. Nebreda, Targeting p38α increases DNA damage, chromosome instability, and the anti-tumoral response to taxanes in breast cancer cells. *Cancer Cell* **33**, 1094–1110.e8 (2018).
- M. K. Y. Siu, H. Y. Chan, D. S. H. Kong, E. S. Y. Wong, O. G. W. Wong, H. Y. S. Ngan, K. F. Tam, H. Zhang, Z. Li, Q. K. Y. Chan, S. W. Tsao, S. Strömbäld, A. N. Y. Cheung, p21-activated kinase 4 regulates ovarian cancer cell proliferation, migration, and invasion and contributes to poor prognosis in patients. *Proc. Natl. Acad. Sci. U.S.A.* **107**, 18622–18627 (2010).
- B. W. Murray, C. Guo, J. Piraino, J. K. Westwick, C. Zhang, J. Lamerdin, E. Dagostino, D. Knighton, C.-M. Loi, M. Zager, E. Kraynov, I. Popoff, J. G. Christensen, R. Martinez, S. E. Kephart, J. Marakovits, S. Karlicek, S. Bergqvist, T. Smeal, Small-molecule p21-activated kinase inhibitor PF-3758309 is a potent inhibitor of oncogenic signaling and tumor growth. *Proc. Natl. Acad. Sci. U.S.A.* **107**, 9446–9451 (2010).
- J.-H. Park, M.-L. Lin, T. Nishida, Y. Nakamura, T. Katagiri, PDZ-binding kinase/T-LAK cell-originated protein kinase, a putative cancer/testis antigen with an oncogenic activity in breast cancer. *Cancer Res.* **66**, 9186–9195 (2006).
- Y. Matsuo, J.-H. Park, T. Miyamoto, S. Yamamoto, S. Hisada, H. Alachkar, Y. Nakamura, TOPK inhibitor induces complete tumor regression in xenograft models of human cancer through inhibition of cytokinesis. *Sci. Transl. Med.* **6**, 259ra145 (2014).
- D. Horiochi, R. Camarda, A. Y. Zhou, C. Yau, O. Momcilovic, S. Balakrishnan, A. N. Corella, H. Eyob, K. Kessenbrock, D. A. Lawson, L. A. Marsh, B. N. Anderton, J. Rohrberg, R. Kunder, A. V. Bazarov, P. Yaswen, M. T. McManus, H. S. Rugo, Z. Werb, A. Goga, PIM1 kinase inhibition as a targeted therapy against triple-negative breast tumors with elevated MYC expression. *Nat. Med.* **22**, 1321–1329 (2016).
- F. Brásó-Maristany, S. Filosto, S. Catchpole, R. Marlow, J. Quist, E. Francesch-Domenech, D. A. Plumb, L. Zakka, P. Gazinska, G. Liccardi, P. Meier, A. Gris-Olivier, M. C. U. Cheang, A. Perdriz-Rosell, M. Shafat, E. Noél, N. Patel, K. McEachern, M. Scaltriti, P. Castel, F. Noor, R. Buus, S. Mathew, J. Watkins, V. Serra, P. Marra, A. Grigoriadis, A. N. Tutt, PIM1 kinase regulates cell death, tumor growth and chemotherapy response in triple-negative breast cancer. *Nat. Med.* **22**, 1303–1313 (2016).
- K. S. Putt, G. W. Chen, J. M. Pearson, J. S. Sandhorst, M. S. Hoagland, J.-T. Kwon, S.-K. Hwang, H. Jin, M. I. Churchwell, M.-H. Cho, D. R. Doerge, W. G. Helferich, P. J. Hergenrother, Small-molecule activation of procaspase-3 to caspase-3 as a personalized anticancer strategy. *Nat. Chem. Biol.* **2**, 543–550 (2006).
- D. W. Wolan, J. A. Zorn, D. C. Gray, J. A. Wells, Small-molecule activators of a proenzyme. *Science* **326**, 853–858 (2009).
- J. Shi, E. Wang, J. P. Milazzo, Z. Wang, J. B. Kinney, C. R. Vakoc, Discovery of cancer drug targets by CRISPR-Cas9 screening of protein domains. *Nat. Biotechnol.* **33**, 661–667 (2015).
- D. A. Sloane, M. Z. Trifkic, M. L. H. Chu, M. B. A. C. Lamers, C. S. Mason, I. Mueller, W. J. Savory, D. H. Williams, P. A. Eyers, Drug-resistant aurora a mutants for cellular target validation of the small molecule kinase inhibitors MLN8054 and MLN8237. *ACS Chem. Biol.* **5**, 563–576 (2010).
- F. Girdler, F. Sessa, S. Patercoli, F. Villa, A. Musacchio, S. Taylor, Molecular basis of drug resistance in Aurora kinases. *Chem. Biol.* **15**, 552–562 (2008).
- Y. Smurny, M. Cai, H. Wu, E. McWhinnie, J. A. Tallarico, Y. Yang, Y. Feng, DNA sequencing and CRISPR-Cas9 gene editing for target validation in mammalian cells. *Nat. Chem. Biol.* **10**, 623–625 (2014).
- G. N. Khan, E. J. Kim, T. S. Shin, S. H. Lee, Heterogeneous cell types in single-cell-derived clones of MCF7 and MDA-MB-231 cells. *Anticancer Res.* **37**, 2343–2354 (2017).
- M. A. El-Brolosy, Z. Kontarakis, A. Rossi, C. Kuenne, S. Günther, N. Fukuda, K. Kikhi, G. L. M. Boezio, C. M. Takacs, S.-L. Lai, R. Fukuda, C. Gerri, A. J. Giraldez, D. Y. R. Stainier, Genetic compensation triggered by mutant mRNA degradation. *Nature* **568**, 193–197 (2019).
- U. Ben-David, B. Siranosian, G. Ha, H. Tang, Y. Oren, K. Hinohara, C. A. Strathdee, J. Dempster, N. J. Lyons, R. Burns, A. Nag, G. Kugener, B. Cimini, P. Tsvetkov, Y. E. Maruvka, R. O'Rourke, A. Garrity, A. A. Tubelli, P. Bandopadhay, A. Tsherniak, F. Vazquez, B. Wong, C. Birger, M. Ghandi, A. R. Thorner, J. A. Bittker, M. Meyerson, G. Getz, R. Beroukhim, T. R. Golub, Genetic and transcriptional evolution alters cancer cell line drug response. *Nature* **560**, 325–330 (2018).
- L. A. Gilbert, M. A. Horlbeck, B. Adamson, J. E. Villalta, Y. Chen, E. H. Whitehead, C. Guimaraes, B. Panning, H. L. Ploegh, M. C. Bassik, L. S. Qi, M. Kampmann, J. S. Weissman, Genome-scale CRISPR-mediated control of gene repression and activation. *Cell* **159**, 647–661 (2014).
- C. Hubbert, A. Guardiola, R. Shao, Y. Kawaguchi, A. Ito, A. Nixon, M. Yoshida, X.-F. Wang, T.-P. Yao, HDAC6 is a microtubule-associated deacetylase. *Nature* **417**, 455–458 (2002).
- P. Huang, I. Almeida-Pinto, M. Jarpe, J. H. van Duzer, R. Mazitschek, M. Yang, S. S. Jones, S. N. Quayle, Selective HDAC inhibition by ACY-241 enhances the activity of paclitaxel in solid tumor models. *Oncotarget* **8**, 2694–2707 (2016).
- A. L. Jackson, S. R. Bartz, J. Schelter, S. V. Kobayashi, J. Burchard, M. Mao, B. Li, G. Cavet, P. S. Linsley, Expression profiling reveals off-target gene regulation by RNAi. *Nat. Biotechnol.* **21**, 635–637 (2003).
- A. Birmingham, E. M. Anderson, A. Reynolds, D. Ilsley-Tyree, D. Leake, Y. Fedorov, S. Baskerville, E. Maksimova, K. Robinson, J. Karpilow, W. S. Marshall, A. Khvorova, 3' UTR seed matches, but not overall identity, are associated with RNAi off-targets. *Nat. Methods* **3**, 199–204 (2006).
- W. Putzbach, Q. Q. Gao, M. Patel, S. van Dongen, A. Haluck-Kangas, A. A. Sarshad, E. T. Bartom, K.-Y. A. Kim, D. M. Scholtens, M. Hafner, J. C. Zhao, A. E. Murmann, M. E. Peter, Many siRNAs can kill cancer cells by targeting multiple survival genes through an off-target mechanism. *elife* **6**, e29702 (2017).
- H. Tabusa, T. Brooks, A. J. Massey, Knockdown of PAK4 or PAK1 inhibits the proliferation of mutant kras colon cancer cells independently of RAF/MEK/ERK and PI3K/AKT signaling. *Mol. Cancer Res.* **11**, 109–121 (2013).
- R. K. Harrison, Phase II and phase III failures: 2013–2015. *Nat. Rev. Drug Discov.* **15**, 817–818 (2016).
- T. Force, K. L. Kolaja, Cardiotoxicity of kinase inhibitors: The prediction and translation of preclinical models to clinical outcomes. *Nat. Rev. Drug Discov.* **10**, 111–126 (2011).
- J. Heitman, N. R. Movva, M. N. Hall, Targets for cell cycle arrest by the immunosuppressant rapamycin in yeast. *Science* **253**, 905–909 (1991).
- D. M. Sabatini, H. Erdjument-Bromage, M. Lui, P. Tempst, S. H. Snyder, RAFT1: A mammalian protein that binds to FKBP12 in a rapamycin-dependent fashion and is homologous to yeast TORs. *Cell* **78**, 35–43 (1994).
- M. D. Gurden, I. M. Westwood, A. Faisal, S. Naud, K.-M. J. Cheung, C. McAndrew, A. Wood, J. Schmitt, K. Boxall, G. Mak, P. Workman, R. Burke, S. Hoelder, J. Blagg, R. L. M. Van Montfort, S. Linardopoulos, Naturally occurring mutations in the MPS1 gene predispose cells to kinase inhibitor drug resistance. *Cancer Res.* **75**, 3340–3354 (2015).
- A. Janssen, R. H. Medema, Mitosis as an anti-cancer target. *Oncogene* **30**, 2799–2809 (2011).
- W. E. Glaab, K. R. Tindall, Mutation rate at the hprt locus in human cancer cell lines with specific mismatch repair-gene defects. *Carcinogenesis* **18**, 1–8 (1997).
- D. Nielsen, T. Skovsgaard, P-glycoprotein as multidrug transporter: A critical review of current multidrug resistant cell lines. *Biochim. Biophys. Acta* **1139**, 169–183 (1992).
- R. B. Kim, Drugs as P-glycoprotein substrates, inhibitors, and inducers. *Drug Metab. Rev.* **34**, 47–54 (2002).
- S. A. Forbes, D. Bearse, P. Gunasekaran, K. Leung, N. Bindal, H. Boutsalakis, M. Ding, S. Bamford, C. Cole, S. Ward, C. Y. Kok, M. Jia, T. De, J. W. Teague, M. R. Stratton, U. McDermott, P. J. Campbell, COSMIC: Exploring the world's knowledge of somatic mutations in human cancer. *Nucleic Acids Res.* **43**, D805–D811 (2015).
- R. Gururajan, J. M. Lahti, J. Grenet, J. Easton, I. Gruber, P. F. Ambros, V. J. Kidd, Duplication of a genomic region containing the *Cdc2L1-2* and *MMP21-22* genes on human chromosome 1p36.3 and their linkage to D1Z2. *Genome Res.* **8**, 929–939 (1998).
- N. F. Dos Santos, F. C. Paparidis, The emerging picture of CDK11: Genetic, functional and medicinal aspects. *Curr. Med. Chem.* **25**, 880–888 (2018).

44. F. M. Ferguson, N. S. Gray, Kinase inhibitors: The road ahead. *Nat. Rev. Drug Discov.* **17**, 353–377 (2018).
45. D. K. Treiber, N. P. Shah, Ins and outs of kinase DFG motifs. *Chem. Biol.* **20**, 745–746 (2013).
46. S. Klaeger, S. Heinzelmeir, M. Wilhelm, H. Polzer, B. Vick, P.-A. Koenig, M. Reinecke, B. Ruprecht, S. Petzoldt, C. Meng, J. Zecha, K. Reiter, H. Qiao, D. Helm, H. Koch, M. Schoof, G. Caneveri, E. Casale, S. R. Depaolini, A. Feuchtinger, Z. Wu, T. Schmidt, L. Rueckert, W. Becker, J. Huenges, A.-K. Garz, B.-O. Gohlke, D. P. Zolg, G. Kayser, T. Voorder, R. Preissner, H. Hahne, N. Tönissen, K. Kramer, K. Götz, F. Bassermann, J. Schlegl, H.-C. Ehrlich, S. Aiche, A. Walch, P. A. Greif, S. Schneider, E. R. Felder, J. Ruland, G. Médard, I. Jeremias, K. Spiekermann, B. Kuster, The target landscape of clinical kinase drugs. *Science* **358**, eaan4368 (2017).
47. H. Rizos, A. M. Menzies, G. M. Pupo, M. S. Carlino, C. Fung, J. Hyman, L. E. Haydu, B. Mijatov, T. M. Becker, S. C. Boyd, J. Howle, R. Saw, J. F. Thompson, R. F. Kefford, R. A. Scolyer, G. V. Long, BRAF inhibitor resistance mechanisms in metastatic melanoma: Spectrum and clinical impact. *Clin. Cancer Res.* **20**, 1965–1977 (2014).
48. L. Chen, J. A. Mayer, T. I. Krisko, C. W. Speers, T. Wang, S. G. Hilsenbeck, P. H. Brown, Inhibition of the p38 kinase suppresses the proliferation of human ER-negative breast cancer cells. *Cancer Res.* **69**, 8853–8861 (2009).
49. A. Matrone, V. Grossi, F. Chiacchiera, E. Fina, M. Cappellari, A. M. Caringella, E. Di Naro, G. Loverro, C. Simone, p38 α is required for ovarian cancer cell metabolism and survival. *Int. J. Gynecol. Cancer* **20**, 203–211 (2010).
50. C. Kim, Y. Sano, K. Todorova, B. A. Carlson, L. Arpa, A. Celada, T. Lawrence, K. Otsu, J. L. Brissette, J. S. C. Arthur, J. M. Park, p38 MAP kinase serves cell type-specific inflammatory functions in skin injury and coordinates pro- and anti-inflammatory gene expression. *Nat. Immunol.* **9**, 1019–1027 (2008).
51. D. T. Vogl, N. S. Raje, S. Jagannath, P. G. Richardson, P. Hari, R. Z. Orłowski, J. G. Supko, D. Tamang, M. Yang, S. S. Jones, C. Wheeler, R. J. Markelewicz, S. Lonial, Ricolinostat, the first selective histone deacetylase 6 inhibitor, in combination with bortezomib and dexamethasone for relapsed or refractory multiple myeloma. *Clin. Cancer Res.* **23**, 3307–3315 (2017).
52. Y. Depetter, S. Geurs, R. De Vreese, S. Goethals, E. Vandoorn, A. Laevens, J. Steenbrugge, E. Meyer, P. de Tullio, M. Bracke, M. D'hooghe, O. De Wever, Selective pharmacological inhibitors of HDAC6 reveal biochemical activity but functional tolerance in cancer models. *Int. J. Cancer* **145**, 735–747 (2019).
53. E. Seto, M. Yoshida, Erasers of histone acetylation: The histone deacetylase enzymes. *Cold Spring Harb. Perspect. Biol.* **6**, a018713 (2014).
54. M. Lewis, Midostaurin approved for FLT3-mutated AML. *Blood* **129**, 3403–3406 (2017).
55. S. R. Whittaker, A. Mallinger, P. Workman, P. A. Clarke, Inhibitors of cyclin-dependent kinases as cancer therapeutics. *Pharmacol. Ther.* **173**, 83–105 (2017).
56. Y. Zhou, J. K. Shen, F. J. Hornick, Q. Kan, Z. Duan, The emerging roles and therapeutic potential of cyclin-dependent kinase 11 (CDK11) in human cancer. *Oncotarget* **7**, 40846–40859 (2016).
57. D. Hu, M. Valentine, V. J. Kidd, J. M. Lahti, CDK11⁵⁵⁸ is required for the maintenance of sister chromatid cohesion. *J. Cell Sci.* **120**, 2424–2434 (2007).
58. E. Manchado, M. Guillamot, M. Malumbres, Killing cells by targeting mitosis. *Cell Death Differ.* **19**, 369–377 (2012).
59. I. Smith, P. G. Greenside, T. Natoli, D. L. Lahr, D. Wadden, I. Tirosh, R. Narayan, D. E. Root, T. R. Golub, A. Subramanian, J. G. Doench, Evaluation of RNAi and CRISPR technologies by large-scale gene expression profiling in the Connectivity Map. *PLoS Biol.* **15**, e2003213 (2017).
60. B. Evers, K. Jastrzebski, J. P. M. Heijmans, W. Gremmum, R. L. Beijersbergen, R. Bernards, CRISPR knockout screening outperforms shRNA and CRISPRi in identifying essential genes. *Nat. Biotechnol.* **34**, 631–633 (2016).
61. J. Xu, P. Wang, H. Yang, J. Zhou, Y. Li, X. Li, W. Xue, C. Yu, Y. Tian, F. Zhu, Comparison of FDA approved kinase targets to clinical trial ones: Insights from their system profiles and drug-target interaction networks. *Biomed. Res. Int.* **2016**, 2509385 (2016).
62. Highly effective new anti-cancer drug shows few side effects—in mice, *Univ. Chic. News* (2014); <https://news.uchicago.edu/story/highly-effective-new-anti-cancer-drug-shows-few-side-effects-mice>.
63. J. E. Neggers, B. Kwanten, T. Dierckx, H. Noguchi, A. Voet, L. Bral, K. Minner, B. Massant, N. Kint, M. Delforge, T. Vercruyse, E. Baloglu, W. Senapatis, M. Jacquemyn, D. Daelemans, Target identification of small molecules using large-scale CRISPR-Cas mutagenesis scanning of essential genes. *Nat. Commun.* **9**, 502 (2018).
64. J.-B. Denault, M. Drag, G. S. Salvesen, J. Alves, A. B. Heidt, Q. Devereaux, J. L. Harris, Small molecules not direct activators of caspases. *Nat. Chem. Biol.* **3**, 519 (2007).
65. Reply to ‘Small molecules not direct activators of caspases’. *Nat. Chem. Biol.* **3**, 520 (2007).
66. Q. P. Peterson, D. R. Goode, D. C. West, K. N. Ramsey, J. J. Y. Lee, P. J. Hergenrother, PAC-1 activates procaspase-3 in vitro through relief of zinc-mediated inhibition. *J. Mol. Biol.* **388**, 144–158 (2009).
67. F. Wang, L. Wang, Y. Zhao, Y. Li, G. Ping, S. Xiao, K. Chen, W. Zhu, P. Gong, J. Yang, C. Wu, A novel small-molecule activator of procaspase-3 induces apoptosis in cancer cells and reduces tumor growth in human breast, liver and gallbladder cancer xenografts. *Mol. Oncol.* **8**, 1640–1652 (2014).
68. X.-H. Yang, T. L. Sladek, X. Liu, B. R. Butler, C. J. Froelich, A. D. Thor, Reconstitution of caspase 3 sensitizes MCF-7 breast cancer cells to doxorubicin- and etoposide-induced apoptosis. *Cancer Res.* **61**, 348–354 (2001).
69. X. Yang, F. Zheng, H. Xing, Q. Gao, W. Wei, Y. Lu, S. Wang, J. Zhou, W. Hu, D. Ma, Resistance to chemotherapy-induced apoptosis via decreased caspase-3 activity and overexpression of antiapoptotic proteins in ovarian cancer. *J. Cancer Res. Clin. Oncol.* **130**, 423–428 (2004).
70. C. J. Giuliano, A. Lin, V. Girish, J. M. Sheltzer, Generating single cell-derived knockout clones in mammalian cells with CRISPR/Cas9. *Curr. Protoc. Mol. Biol.* **128**, e100 (2019).
71. Y. Tarumoto, B. Lu, T. D. D. Somerville, Y.-H. Huang, J. P. Milazzo, X. S. Wu, O. Klingbeil, O. E. Demerdash, J. Shi, C. R. Vakoc, LKB1, salt-inducible kinases, and MEF2C are linked dependencies in acute myeloid leukemia. *Mol. Cell* **69**, 1017–1027.e6 (2018).
72. O. Shalem, N. E. Sanjana, E. Hartenian, X. Shi, D. A. Scott, T. S. Mikkelsen, D. Heckl, B. L. Ebert, D. E. Root, J. G. Doench, F. Zhang, Genome-scale CRISPR-Cas9 knockout screening in human cells. *Science* **343**, 84–87 (2014).
73. M. A. Horlbeck, L. A. Gilbert, J. E. Villalba, B. Adamson, R. A. Pak, Y. Chen, A. P. Fields, C. Y. Park, J. E. Corn, M. Kampmann, J. S. Weissman, Compact and highly active next-generation libraries for CRISPR-mediated gene repression and activation. *eLife* **5**, e19760 (2016).
74. S. T. Smale, Calcium phosphate transfection of 3T3 fibroblasts. *Cold Spring Harb. Protoc.* **2010**, pdb.prot5372 (2010).
75. J. van den Berg, A. G. Manjón, K. Kielbassa, F. M. Feringa, R. Freire, R. H. Medema, A limited number of double-strand DNA breaks is sufficient to delay cell cycle progression. *Nucleic Acids Res.* **46**, 10132–10144 (2018).
76. R. Edgar, M. Domrachev, A. E. Lash, Gene Expression Omnibus: NCBI gene expression and hybridization array data repository. *Nucleic Acids Res.* **30**, 207–210 (2002).
77. H. Mou, J. Moore, S. K. Malonia, Y. Li, D. M. Ozata, S. Hough, C.-Q. Song, J. L. Smith, A. Fischer, Z. Weng, M. R. Green, W. Xue, Genetic disruption of oncogenic Kras sensitizes lung cancer cells to Fas receptor-mediated apoptosis. *Proc. Natl. Acad. Sci. U.S.A.* **114**, 3648–3653 (2017).
78. G. M. Boratyn, C. Camacho, P. S. Cooper, G. Coulouris, A. Fong, N. Ma, T. L. Madden, W. T. Matten, S. D. McGinnis, Y. Merezukh, Y. Raytselis, E. W. Sayers, T. Tao, J. Ye, I. Zaretskaya, BLAST: A more efficient report with usability improvements. *Nucleic Acids Res.* **41**, W29–W33 (2013).
79. B. DepMap, DepMap Achilles 18Q3 public (2018); doi:10.6084/m9.figshare.6931364.v1.
80. R. M. Meyers, J. G. Bryan, J. M. McFarland, B. A. Weir, A. E. Sizemore, H. Xu, N. V. Dharia, P. G. Montgomery, G. S. Cowley, S. Pantel, A. Goodale, Y. Lee, L. D. Ali, G. Jiang, R. Lubonja, W. F. Harrington, M. Strickland, T. Wu, D. C. Hawes, V. A. Zhivich, M. R. Wyatt, Z. Kalani, J. J. Chang, M. Okamoto, K. Stegmaier, T. R. Golub, J. S. Boehm, F. Vazquez, D. E. Root, W. C. Hahn, A. Tsherniak, Computational correction of copy number effect improves specificity of CRISPR-Cas9 essentiality screens in cancer cells. *Nat. Genet.* **49**, 1779–1784 (2017).
81. DEMETER2 data (2018); doi:10.6084/m9.figshare.6025238.v2.
82. J. M. McFarland, Z. V. Ho, G. Kugener, J. M. Dempster, P. G. Montgomery, J. G. Bryan, J. M. Krill-Burger, T. M. Green, F. Vazquez, J. S. Boehm, T. R. Golub, W. C. Hahn, D. E. Root, A. Tsherniak, Improved estimation of cancer dependencies from large-scale RNAi screens using model-based normalization and data integration. *Nat. Commun.* **9**, 4610 (2018).
83. M. Sadelain, E. P. Papapetrou, F. D. Bushman, Safe harbours for the integration of new DNA in the human genome. *Nat. Rev. Cancer* **12**, 51–58 (2012).
84. T. Cerbini, R. Funahashi, Y. Luo, C. Liu, K. Park, M. Rao, N. Malik, J. Zou, Transcription activator-like effector nuclease (TALEN)-mediated CLYBL targeting enables enhanced transgene expression and one-step generation of dual reporter human induced pluripotent stem cell (iPSC) and neural stem cell (NSC) lines. *PLOS ONE* **10**, e0116032 (2015).
85. M. I. Davis, J. P. Hunt, S. Herrgard, P. Ciceri, L. M. Wodicka, G. Pallares, M. Hocker, D. K. Treiber, P. P. Zarinkar, Comprehensive analysis of kinase inhibitor selectivity. *Nat. Biotechnol.* **29**, 1046–1051 (2011).
86. J. Ai, Y. Wang, J. A. Dar, J. Liu, L. Liu, J. B. Nelson, Z. Wang, HDAC6 regulates androgen receptor hypersensitivity and nuclear localization via modulating Hsp90 acetylation in castration-resistant prostate cancer. *Mol. Endocrinol.* **23**, 1963–1972 (2009).
87. R. A. Rodriguez-Fonsec, Y. Sixto-Lopez, M. J. Fragoso-Vazquez, R. Flores-Mejia, L. C. Cabrera-Perez, I. Vazquez-Moctezuma, M. C. Rosales-Hernandez, M. Bello, M. Martinez-Archundia, J. G. Trujillo-Ferrara, E. Becerra-Martinez, J. Correa-Basurto, Design, synthesis and biological evaluation of a phenyl butyric acid derivative, N-(4-chlorophenyl)-4-phenylbutanamide: A HDAC6 inhibitor with anti-proliferative activity on cervix cancer and leukemia cells. *Anticancer Agents Med Chem.* **17**, 10.2174/1871520617666170103092851, (2017).
88. G. I. Aldana-Masangkay, A. Rodriguez-Gonzalez, T. Lin, A. K. Ikeda, Y.-T. Hsieh, Y.-M. Kim, B. Lomenick, K. Okemoto, E. M. Landaw, D. Wang, R. Mazitschek, J. E. Bradner,

- K. M. Sakamoto, Tubacin suppresses proliferation and induces apoptosis of acute lymphoblastic leukemia cells. *Leuk. Lymphoma* **52**, 1544–1555 (2011).
89. J. E. Amengual, P. Johannet, M. Lombardo, K. Zullo, D. Hoehn, G. Bhagat, L. Scotto, X. Jirau-Serrano, D. Radeski, J. Heinen, H. Jiang, S. Cremers, Y. Zhang, S. Jones, O. A. O'Connor, Dual targeting of protein degradation pathways with the selective HDAC6 inhibitor ACY-1215 and bortezomib is synergistic in lymphoma. *Clin. Cancer Res.* **21**, 4663–4675 (2015).
90. J. Bai, Y. Lei, G.-I. An, L. He, Down-regulation of deacetylase HDAC6 inhibits the melanoma cell line A375.S2 growth through ROS-dependent mitochondrial pathway. *PLOS ONE* **10**, e0121247 (2015).
91. M. Balliu, L. Guandalini, M. N. Romanelli, M. D'Amico, F. Paoletti, HDAC-inhibitor (S)-8 disrupts HDAC6-PP1 complex prompting A375 melanoma cell growth arrest and apoptosis. *J. Cell. Mol. Med.* **19**, 143–154 (2015).
92. J. A. Bergman, K. Woan, P. Perez-Villarroel, A. Villagra, E. M. Sotomayor, A. P. Kozikowski, Selective histone deacetylase 6 inhibitors bearing substituted urea linkers inhibit melanoma cell growth. *J. Med. Chem.* **55**, 9891–9899 (2012).
93. J. Cao, W. Lv, L. Wang, J. Xu, P. Yuan, S. Huang, Z. He, J. Hu, Ricolinostat (ACY-1215) suppresses proliferation and promotes apoptosis in esophageal squamous cell carcinoma via miR-30d/PI3K/AKT/mTOR and ERK pathways. *Cell Death Dis.* **9**, 817 (2018).
94. M.-J. Chuang, S.-T. Wu, S.-H. Tang, X.-M. Lai, H.-C. Lai, K.-H. Hsu, K.-H. Sun, G.-H. Sun, S.-Y. Chang, D.-S. Yu, P.-W. Hsiao, S.-M. Huang, T.-L. Cha, The HDAC inhibitor LBH589 induces ERK-dependent prometaphase arrest in prostate cancer via HDAC6 inactivation and down-regulation. *PLOS ONE* **8**, e73401 (2013).
95. M. Cosenza, M. Civallero, L. Marcheselli, S. Sacchi, S. Pozzi, Ricolinostat, a selective HDAC6 inhibitor, shows anti-lymphoma cell activity alone and in combination with bendamustine. *Apoptosis* **22**, 827–840 (2017).
96. G. Ding, H.-D. Liu, Q. Huang, H.-X. Liang, Z.-H. Ding, Z.-J. Liao, G. Huang, HDAC6 promotes hepatocellular carcinoma progression by inhibiting P53 transcriptional activity. *FEBS Lett.* **587**, 880–886 (2013).
97. J. Dong, N. Zheng, X. Wang, C. Tang, P. Yan, H.-B. Zhou, J. Huang, A novel HDAC6 inhibitor exerts an anti-cancer effect by triggering cell cycle arrest and apoptosis in gastric cancer. *Eur. J. Pharmacol.* **828**, 67–79 (2018).
98. X.-h. Fu, X. Zhang, H. Yang, X.-w. Xu, Z.-l. Hu, J. Yan, X.-l. Zheng, R.-r. Wei, Z.-q. Zhang, S.-r. Tang, M.-y. Geng, X. Huang, CUDC-907 displays potent antitumor activity against human pancreatic adenocarcinoma in vitro and in vivo through inhibition of HDAC6 to downregulate c-Myc expression. *Acta Pharmacol. Sin.* **40**, 677–688 (2019).
99. S. A. Gradilone, B. N. Radtke, P. S. Bogert, B. Q. Huang, G. B. Gajdos, N. F. LaRussa, HDAC6 inhibition restores ciliary expression and decreases tumor growth. *Cancer Res.* **73**, 2259–2270 (2013).
100. B. Hackanson, L. Rimmelm, M. Benkiser, M. Abdelkarim, M. Fliegauf, M. Jung, M. Lübbert, HDAC6 as a target for antileukemic drugs in acute myeloid leukemia. *Leuk. Res.* **36**, 1055–1062 (2012).
101. T. Hidemitsu, J. Qi, R. M. Paranal, W. Tang, E. Greenberg, N. West, M. E. Colling, G. Estiu, R. Mazitschek, J. A. Perry, H. Ohguchi, F. Cottini, N. Mimura, G. Görgün, Y.-T. Tai, P. G. Richardson, R. D. Carrasco, O. Wiest, S. L. Schreiber, K. C. Anderson, J. E. Bradner, Discovery of selective small-molecule HDAC6 inhibitor for overcoming proteasome inhibitor resistance in multiple myeloma. *Proc. Natl. Acad. Sci. U.S.A.* **113**, 13162–13167 (2016).
102. E. S. Inks, B. J. Josey, S. R. Jesinkey, C. J. Chou, A novel class of small molecule inhibitors of HDAC6. *ACS Chem. Biol.* **7**, 331–339 (2012).
103. M. Kaliszczak, S. Trousil, Ö. Åberg, M. Perumal, Q.-D. Nguyen, E. O. Aboagye, A novel small molecule hydroxamate preferentially inhibits HDAC6 activity and tumour growth. *Br. J. Cancer* **108**, 342–350 (2013).
104. M. Kaliszczak, E. van Hechanova, Y. Li, H. Alsadah, K. Parzych, H. W. Auner, E. O. Aboagye, The HDAC6 inhibitor C1A modulates autophagy substrates in diverse cancer cells and induces cell death. *Br. J. Cancer* **119**, 1278–1287 (2018).
105. H.-Y. Lee, A.-C. Tsai, M.-C. Chen, P.-J. Shen, Y.-C. Cheng, C.-C. Kuo, S.-L. Pan, Y.-M. Liu, J.-F. Liu, T.-K. Yeh, J.-C. Wang, C.-Y. Chang, J.-Y. Chang, J.-P. Liou, Azaindolylsulfonamides, with a more selective inhibitory effect on histone deacetylase 6 activity, exhibit antitumor activity in colorectal cancer HCT116 cells. *J. Med. Chem.* **57**, 4009–4022 (2014).
106. J.-H. Lee, A. Mahendran, Y. Yao, L. Ngo, G. Venta-Perez, M. L. Choy, N. Kim, W.-S. Ham, R. Breslow, P. A. Marks, Development of a histone deacetylase 6 inhibitor and its biological effects. *Proc. Natl. Acad. Sci. U.S.A.* **110**, 15704–15709 (2013).
107. Y.-S. Lee, K.-H. Lim, X. Guo, Y. Kawaguchi, Y. Gao, T. Barrientos, P. Ordentlich, X.-F. Wang, C. M. Counter, T.-P. Yao, The cytoplasmic deacetylase HDAC6 is required for efficient oncogenic tumorigenesis. *Cancer Res.* **68**, 7561–7569 (2008).
108. N. Li, X.-J. Tie, P.-J. Liu, Y. Zhang, H.-Z. Ren, X. Gao, Z.-Q. Xu, Effects of down-regulation of HDAC6 expression on proliferation, cell cycling and migration of esophageal squamous cell carcinoma cells and related molecular mechanisms. *Asian Pac. J. Cancer Prev.* **14**, 685–689 (2013).
109. S. Li, X. Liu, X. Chen, L. Zhang, X. Wang, Histone deacetylase 6 promotes growth of glioblastoma through inhibition of SMAD2 signaling. *Tumor Biol.* **36**, 9661–9665 (2015).
110. M. Lienlaf, P. Perez-Villarroel, T. Knox, M. Pabon, E. Sahakian, J. Powers, K. V. Woan, C. Lee, F. Cheng, S. Deng, K. S. M. Smalley, M. Montecino, A. Kozikowski, J. Pinilla-Ibarz, A. Sarnaik, E. Seto, J. Weber, E. M. Sotomayor, A. Villagra, Essential role of HDAC6 in the regulation of PD-L1 in melanoma. *Mol. Oncol.* **10**, 735–750 (2016).
111. J. Liu, J. Gu, Z. Feng, Y. Yang, N. Zhu, W. Lu, F. Qi, Both HDAC5 and HDAC6 are required for the proliferation and metastasis of melanoma cells. *J. Transl. Med.* **14**, 7 (2016).
112. Y.-M. Liu, H.-Y. Lee, M.-J. Lai, S.-L. Pan, H.-L. Huang, F.-C. Kuo, M.-C. Chen, J.-P. Liou, Pyrimidinedione-mediated selective histone deacetylase 6 inhibitors with antitumor activity in colorectal cancer HCT116 cells. *Org. Biomol. Chem.* **13**, 10226–10235 (2015).
113. T. Lwin, X. Zhao, F. Cheng, X. Zhang, A. Huang, B. Shah, Y. Zhang, L. C. Moscinski, Y. S. Choi, A. P. Kozikowski, J. E. Bradner, W. S. Dalton, E. Sotomayor, J. Tao, A microenvironment-mediated c-Myc/miR-548m/HDAC6 amplification loop in non-Hodgkin B cell lymphomas. *J. Clin. Invest.* **123**, 4612–4626 (2013).
114. A. B. Mak, A. M. L. Nixon, S. Kittanakom, J. M. Stewart, G. I. Chen, J. Curak, A.-C. Gingras, R. Mazitschek, B. G. Neel, I. Stagljar, J. Moffat, Regulation of CD133 by HDAC6 promotes β-catenin signaling to suppress cancer cell differentiation. *Cell Rep.* **2**, 951–963 (2012).
115. T. R. Medler, J. M. Craig, A. Fiorillo, Y. B. Feeney, J. C. Harrell, C. V. Clevenger, HDAC6 deacetylates HMGN2 to regulate Stat5a activity and breast cancer growth. *Mol. Cancer Res.* **14**, 994–1008 (2016).
116. J.-T. Pai, C.-Y. Hsu, K.-T. Hua, S.-Y. Yu, C.-Y. Huang, C.-N. Chen, C.-H. Liao, M.-S. Weng, NBM-B-BBX-OS01, semisynthesized from osthole, induced G1 growth arrest through HDAC6 inhibition in lung cancer cells. *Molecules* **20**, 8000–8019 (2015).
117. S. Park, J. K. Kim, H. J. Bae, J. W. Eun, Q. Shen, H. S. Kim, W. C. Shin, H. D. Yang, E. K. Lee, J. S. You, W. S. Park, J. Y. Lee, S. W. Nam, HDAC6 sustains growth stimulation by prolonging the activation of EGFR receptor through the inhibition of rabaptin-5-mediated early endosome fusion in gastric cancer. *Cancer Lett.* **354**, 97–106 (2014).
118. H.-W. Ryu, D.-H. Lee, D.-H. Shin, S. H. Kim, S. H. Kwon, Aceroside VIII is a new natural selective HDAC6 inhibitor that synergistically enhances the anticancer activity of HDAC inhibitor in HT29 cells. *Planta Med.* **81**, 222–227 (2015).
119. L. Santo, T. Hidemitsu, A. L. Kung, J.-C. Tseng, D. Tamang, M. Yang, M. Jarpe, J. H. van Duzer, R. Mazitschek, W. C. Ogier, D. Cirstea, S. Rodig, H. Eda, T. Scullen, M. Canavese, J. Bradner, K. C. Anderson, S. S. Jones, N. Raje, Preclinical activity, pharmacodynamic, and pharmacokinetic properties of a selective HDAC6 inhibitor, ACY-1215, in combination with bortezomib in multiple myeloma. *Blood* **119**, 2579–2589 (2012).
120. C. Seidel, M. Schnekenburger, A. Mazumder, M.-H. Teiten, G. Kirsch, M. Dicato, M. Diederich, 4-Hydroxybenzoic acid derivatives as HDAC6-specific inhibitors modulating microtubular structure and HSP90α chaperone activity against prostate cancer. *Biochem. Pharmacol.* **99**, 31–52 (2016).
121. Y. W. Song, Y. Lim, S. K. Cho, 2,4-Di-tert-butylphenol, a potential HDAC6 inhibitor, induces senescence and mitotic catastrophe in human gastric adenocarcinoma AGS cells. *Biochim. Biophys. Acta* **1865**, 675–683 (2018).
122. C. Subramanian, J. A. Jarzembski, A. W. Opipari Jr., V. P. Castle, R. P. S. Kwok, HDAC6 deacetylates Ku70 and regulates Ku70-Bax binding in neuroblastoma. *Neoplasia* **13**, 726–734 (2011).
123. Y. Tan, S. Zhang, H. Zhu, Y. Chu, H. Zhou, D. Liu, J. Huo, Histone deacetylase 6 selective inhibitor ACY1215 inhibits cell proliferation and enhances the chemotherapeutic effect of 5-fluorouracil in HCT116 cells. *Ann. Transl. Med.* **7**, 2 (2019).
124. S. Valente, D. Trisciuoglio, M. Tardugno, R. Benedetti, L. Labella, D. Secci, C. Mercurio, R. Boggio, S. Tomassi, S. Di Maro, E. Novellino, L. Altucci, D. Del Bufalo, A. Mai, S. Cosconati, tert-Butylcarbamate-containing histone deacetylase inhibitors: Apoptosis induction, cytodifferentiation, and antiproliferative activities in cancer cells. *ChemMedChem* **8**, 800–811 (2013).
125. F. Wang, B.-W. Zhong, Z.-R. Zhao, ACY 1215, a histone deacetylase 6 inhibitor, inhibits cancer cell growth in melanoma. *J. Biol. Regul. Homeost. Agents* **32**, 851–858 (2018).
126. L. Wang, M. Kofler, G. Brosch, J. Melesina, W. Sippl, E. D. Martinez, J. Easmon, 2-Benzazolyl-4-Piperazin-1-Ylsulfonylbenzenecarboxyhydroxamic acids as novel selective histone deacetylase-6 inhibitors with antiproliferative activity. *PLOS ONE* **10**, e0134556 (2015).
127. L. Wang, S. Xiang, K. A. Williams, H. Dong, W. Bai, S. V. Niclosa, S. Khochbin, G. Bepler, X. Zhang, Depletion of HDAC6 enhances cisplatin-induced DNA damage and apoptosis in non-small cell lung cancer cells. *PLOS ONE* **7**, e44265 (2012).
128. X.-C. Wang, Y. Ma, P.-s. Meng, J.-I. Han, H.-Y. Yu, L.-J. Bi, miR-433 inhibits oral squamous cell carcinoma (OSCC) cell growth and metastasis by targeting HDAC6. *Cancer Lett.* **379**, 134–142 (2016).
129. Z. Wang, P. Hu, F. Tang, H. Lian, X. Chen, Y. Zhang, X. He, W. Liu, C. Xie, HDAC6 promotes cell proliferation and confers resistance to temozolamide in glioblastoma. *Cancer Lett.* **379**, 134–142 (2016).
130. Z. Wang, F. Tang, P. Hu, Y. Wang, J. Gong, S. Sun, C. Xie, HDAC6 promotes cell proliferation and confers resistance to gefitinib in lung adenocarcinoma. *Oncol. Rep.* **36**, 589–597 (2016).

131. L.-H. Wei, P.-L. Tornig, S.-M. Hsiao, Y.-M. Jeng, M.-W. Chen, C.-A. Chen, Histone deacetylase 6 regulates estrogen receptor α in uterine leiomyoma. *Reprod. Sci.* **18**, 755–762 (2011).
132. K. V. Woan, M. Lienlaf, P. Perez-Villaroel, C. Lee, F. Cheng, T. Knox, D. M. Woods, K. Barrios, J. Powers, E. Sahakian, H. W. Wang, J. Canales, D. Marante, K. S. M. Smalley, J. Bergman, E. Seto, A. Koziowski, J. Pinilla-Ibarz, A. Sarnai, E. Celis, J. Weber, E. M. Sotomayor, A. Villagra, Targeting histone deacetylase 6 mediates a dual anti-melanoma effect: Enhanced antitumor immunity and impaired cell proliferation. *Mol. Oncol.* **9**, 1447–1457 (2015).
133. W. Xiang, F. Guo, W. Cheng, J. Zhang, J. Huang, R. Wang, Z. Ma, K. Xu, HDAC6 inhibition suppresses chondrosarcoma by restoring the expression of primary cilia. *Oncol. Rep.* **38**, 229–236 (2017).
134. F. Yang, F. Wang, Y. Liu, S. Wang, X. Li, Y. Huang, Y. Xia, C. Cao, Sulforaphane induces autophagy by inhibition of HDAC6-mediated PTEN activation in triple negative breast cancer cells. *Life Sci.* **213**, 149–157 (2018).
135. M. H. Yang, G. Laurent, A. S. Bause, R. Spang, N. German, M. C. Haigis, K. M. Haigis, HDAC6 and SIRT2 regulate the acetylation state and oncogenic activity of mutant K-RAS. *Mol. Cancer Res.* **11**, 1072–1077 (2013).
136. Z. Yang, T. Wang, F. Wang, T. Niu, Z. Liu, X. Chen, C. Long, M. Tang, D. Cao, X. Wang, W. Xiang, Y. Yi, L. Ma, J. You, L. Chen, Discovery of selective histone deacetylase 6 inhibitors using the quinazoline as the cap for the treatment of cancer. *J. Med. Chem.* **59**, 1455–1470 (2016).
137. L. Yuan, W. Lou, J. Sang, Effect of HDAC6 down-regulation on the growth of xenografted human laryngeal carcinoma cell line Hep-2 in nude mice and underlying mechanism. *Zhonghua Er Bi Yan Hou Tou Jing Wai Ke Za Zhi* **47**, 481–486 (2012).
138. I. Zhang, M. Beus, U. Stochaj, P. U. Le, B. Zorc, Z. Rajić, K. Petrecca, D. Maysinger, Inhibition of glioblastoma cell proliferation, invasion, and mechanism of action of a novel hydroxamic acid hybrid molecule. *Cell Death Discov.* **4**, 41 (2018).
139. O. M. Abdelhafez, E. Y. Ahmed, N. A. Abdel Latif, R. K. Arafa, Z. Y. Abd Elmageed, H. I. Ali, Design and molecular modeling of novel P38 α MAPK inhibitors targeting breast cancer, synthesized from oxygen heterocyclic natural compounds. *Bioorg. Med. Chem.* **27**, 1308–1319 (2019).
140. J. W. Antoon, M. R. Bratton, L. M. Guillot, S. Wadsworth, V. A. Salvo, M. E. Burow, Inhibition of p38-MAPK alters SRC coactivation and estrogen receptor phosphorylation. *Cancer Biol. Ther.* **13**, 1026–1033 (2012).
141. R. M. Campbell, B. D. Anderson, N. A. Brooks, H. B. Brooks, E. M. Chan, A. D. Dios, R. Gilmour, J. R. Graff, E. Jambrina, M. Mader, D. McCann, S. Na, S. H. Parsons, S. E. Pratt, C. Shih, L. F. Stancato, J. J. Starling, C. Tate, J. A. Velasco, Y. Wang, X. S. Ye, Characterization of LY2228820 dimesylate, a potent and selective inhibitor of p38 MAPK with antitumor activity. *Mol. Cancer Ther.* **13**, 364–374 (2014).
142. F. Chiacchiera, A. Matrone, E. Ferrari, G. Ingravallo, G. Lo Sasso, S. Murzilli, M. Petruzzelli, L. Salvatore, A. Moschetta, C. Simone, p38 α blockade inhibits colorectal cancer growth in vivo by inducing a switch from HIF1 α - to FoxO-dependent transcription. *Cell Death Differ.* **16**, 1203–1214 (2009).
143. F. Comes, A. Matrone, P. Lastella, B. Nico, F. C. Susca, R. Bagnulo, G. Ingravallo, S. Modica, G. Lo Sasso, A. Moschetta, G. Guanti, C. Simone, A novel cell type-specific role of p38 α in the control of autophagy and cell death in colorectal cancer cells. *Cell Death Differ.* **14**, 693–702 (2007).
144. I. Del Barco Barrantes, C. Stephan-Otto Attolini, K. Slobodnyuk, A. Igea, S. Gregorio, S. Gawrak, R. R. Gomis, A. R. Nebreda, Regulation of mammary luminal cell fate and tumorigenesis by p38 α . *Stem Cell Rep.* **10**, 257–271 (2018).
145. K. Gill, L. Nigam, R. Singh, S. Kumar, N. Subbarao, S. S. Chauhan, S. Dey, The rational design of specific peptide inhibitor against p38 α MAPK at allosteric-site: A therapeutic modality for HNSCC. *PLOS ONE* **9**, e101525 (2014).
146. K. Leelahanichkul, P. Amornphimoltham, A. A. Molinolo, J. R. Basile, S. Koontongkaew, J. S. Gutkind, A role for p38 MAPK in head and neck cancer cell growth and tumor-induced angiogenesis and lymphangiogenesis. *Mol. Oncol.* **8**, 105–118 (2014).
147. M. Limoge, A. Safina, A. M. Truskovsky, I. Aljahdali, J. Zonneville, A. Gruvski, C. L. Arteaga, A. V. Bakin, Tumor p38MAPK signaling enhances breast carcinoma vascularization and growth by promoting expression and deposition of pro-tumorigenic factors. *Oncotarget* **8**, 61969–61981 (2017).
148. A. Matrone, V. Grossi, F. Chiacchiera, E. Fina, M. Cappellari, A. M. Caringella, E. Di Naro, G. Loverro, C. Simone, p38alpha is required for ovarian cancer cell metabolism and survival. *Int. J. Gynecol. Cancer* **20**, 203–211 (2010).
149. S. Medicherla, M. Reddy, J. Ying, T. A. Navas, L. Li, A. N. Nguyen, I. Kerr, N. Hanjarappa, A. A. Prottler, L. S. Higgins, p38 α -selective MAP kinase inhibitor reduces tumor growth in mouse xenograft models of multiple myeloma. *Anticancer Res* **28**, 3827–3833 (2008).
150. A. N. Nguyen, E. G. Stebbins, M. Henson, G. O'Young, S. J. Choi, D. Quon, D. Damm, M. Reddy, J. Y. Ma, E. Haghnazari, A. M. Kapoun, S. Medicherla, A. Prottler, G. F. Schreiner, N. Kurihara, J. Anderson, G. D. Roodman, T. A. Navas, L. S. Higgins, Normalizing the bone marrow microenvironment with p38 inhibitor reduces multiple myeloma cell proliferation and adhesion and suppresses osteoclast formation. *Exp. Cell Res.* **312**, 1909–1923 (2006).
151. D. Planchard, V. Camara-Clayette, N. Dorvault, J.-C. Soria, P. Fouret, p38 mitogen-activated protein kinase signaling, ERCC1 expression, and viability of lung cancer cells from never or light smoker patients. *Cancer* **118**, 5015–5025 (2012).
152. W.-J. Song, Y. Dong, C. Luo, Y.-Y. Chen, p38MAPK family isoform p38 α and activating transcription factor 2 are associated with the malignant phenotypes and poor prognosis of patients with ovarian adenocarcinoma. *Pathol. Res. Pract.* **213**, 1282–1288 (2017).
153. K. Vanderkerken, S. Medicherla, L. Coulton, H. De Raeve, A. Willems, M. Lawson, B. Van Camp, A. A. Prottler, L. S. Higgins, E. Menu, P. I. Croucher, Inhibition of p38 α mitogen-activated protein kinase prevents the development of osteolytic bone disease, reduces tumor burden, and increases survival in murine models of multiple myeloma. *Cancer Res.* **67**, 4572–4577 (2007).
154. H. Zarredar, S. Pashapour, S. Farajnia, K. Ansarin, B. Baradarani, V. Ahmadzadeh, F. Safari, Targeting the KRAS, p38 α , and NF- κ B in lung adenocarcinoma cancer cells: The effect of combining RNA interferences with a chemical inhibitor. *J. Cell. Biochem.* **120**, 10670–10677 (2019).
155. Y. Zhang, X. Wang, X. Qin, X. Wang, F. Liu, E. White, X. F. S. Zheng, PP2AC level determines differential programming of p38-TSC-mTOR signaling and therapeutic response to p38-targeted therapy in colorectal cancer. *EbioMedicine* **2**, 1944–1956 (2015).
156. A. Aboukameel, I. Muqbil, W. Senapedis, E. Baloglu, Y. Landesman, S. Shacham, M. Kauffman, P. A. Philip, R. M. Mohammad, A. S. Azmi, Novel p21-activated kinase 4 (PAK4) allosteric modulators overcome drug resistance and stemness in pancreatic ductal adenocarcinoma. *Mol. Cancer Ther.* **16**, 76–87 (2017).
157. M. G. Callow, F. Clairvoyant, S. Zhu, B. Schryver, D. B. Whyte, J. R. Bischoff, B. Jalla, T. Smeal, Requirement for PAK4 in the anchorage-independent growth of human cancer cell lines. *J. Biol. Chem.* **277**, 550–558 (2002).
158. J. Castillo, J. C. Knol, C. M. Korver, S. R. Piersma, T. V. Pham, R. R. de Goeij-de Haas, A. M. M. van Pelt, C. R. Jimenez, B. J. H. Jansen, Human testis phosphoproteome reveals kinases as potential targets in spermatogenesis and testicular cancer. *Mol. Cell. Proteomics* **18**, S132–S144 (2019).
159. É. Cosset, S. Ilmjärvi, V. Dutoit, K. Elliott, T. von Schalscha, M. F. Camargo, A. Reiss, T. Moroishi, L. Seguin, G. Gomez, J.-S. Moo, O. Preynat-Seauve, K.-H. Krause, H. Cheineweiss, J. N. Sarkaria, K.-L. Guan, P.-Y. Dietrich, S. M. Weis, P. S. Mischel, D. A. Cheresh, Glut3 addiction is a druggable vulnerability for a molecularly defined subpopulation of glioblastoma. *Cancer Cell* **32**, 856–868.e5 (2017).
160. X. Fu, J. Feng, D. Zeng, Y. Ding, C. Yu, B. Yang, PAK4 confers cisplatin resistance in gastric cancer cells via PI3K/Akt- and MEK/ERK-dependent pathways. *Biosci. Rep.* **34**, e00094 (2014).
161. L.-F. He, H.-W. Xu, M. Chen, Z.-R. Xian, X.-F. Wen, M.-N. Chen, C.-W. Du, W.-H. Huang, J.-D. Wu, G.-J. Zhang, Activated-PAK4 predicts worse prognosis in breast cancer and promotes tumorigenesis through activation of PI3K/AKT signaling. *Oncotarget* **8**, 17573–17585 (2017).
162. A. C. Kimmelman, A. F. Hezel, A. J. Aguirre, H. Zheng, J.-H. Paik, H. Ying, G. C. Chu, J. X. Zhang, E. Sahin, G. Yeo, A. Ponugoti, R. Nabuji, S. Deroo, S. Yang, X. Wang, J. P. McGrath, M. Protopopova, E. Ivanova, J. Zhang, B. Feng, M. S. Tsao, M. Redston, A. Protopopov, Y. Xiao, P. A. Futreal, W. C. Hahn, D. S. Klimstra, L. Chin, R. A. DePinho, Genomic alterations link Rho family of GTPases to the highly invasive phenotype of pancreas cancer. *Proc. Natl. Acad. Sci. U.S.A.* **105**, 19372–19377 (2008).
163. H. King, K. Thillai, A. Whale, P. Arumugam, H. Eldaly, H. M. Kocher, C. M. Wells, PAK4 interacts with p85 alpha: Implications for pancreatic cancer cell migration. *Sci. Rep.* **7**, 42575 (2017).
164. N. Li, M. A. Lopez, M. Linares, S. Kumar, S. Oliva, J. Martinez-Lopez, L. Xu, Y. Xu, T. Perini, W. Senapedis, E. Baloglu, M. A. Shamma, Z. Hunter, K. C. Anderson, S. P. Treon, N. C. Munshi, M. Fulciniti, Dual PAK4-NAMPT inhibition impacts growth and survival, and increases sensitivity to DNA-damaging agents in Waldenström macroglobulinemia. *Clin. Cancer Res.* **25**, 369–377 (2019).
165. Q. Li, X. Zhang, N. Wei, S. Liu, Y. Ling, H. Wang, p21-activated kinase 4 as a switch between caspase-8 apoptosis and NF- κ B survival signals in response to TNF- α in hepatocarcinoma cells. *Biochem. Biophys. Res. Commun.* **503**, 3003–3010 (2018).
166. S.-Q. Li, Z.-H. Wang, X.-G. Mi, L. Liu, Y. Tan, MiR-199a/b-3p suppresses migration and invasion of breast cancer cells by downregulating PAK4/MEK/ERK signaling pathway. *IUBMB Life* **67**, 768–777 (2015).
167. Z. Li, X. Li, L. Xu, Y. Tao, C. Yang, X. Chen, F. Fang, Y. Wu, X. Ding, H. Zhao, M. Li, G. Qian, Y. Xu, J. Ren, W. Du, J. Wang, J. Lu, S. Hu, J. Pan, Inhibition of neuroblastoma proliferation by P-3758309, a small-molecule inhibitor that targets p21-activated kinase 4. *Oncol. Rep.* **38**, 2705–2716 (2017).
168. H. Lu, S. Liu, G. Zhang, W. Bin, Y. Zhu, D. T. Frederick, Y. Hu, W. Zhong, S. Randell, N. Sadek, W. Zhang, G. Chen, C. Cheng, J. Zeng, L. W. Wu, J. Zhang, X. Liu, W. Xu, C. Krepler, K. Sproesser, M. Xiao, B. Miao, J. Liu, C. D. Song, J. Y. Liu, G. C. Karakousis, L. M. Schuchter, Y. Lu, G. Mills, Y. Cong, J. Chernoff, J. Guo, G. M. Boland, R. J. Sullivan, Z. Wei, J. Field, R. K. Amaravadi, K. T. Flaherty, M. Herlyn, X. Xu, W. Guo, PAK signalling drives acquired drug resistance to MAPK inhibitors in BRAF-mutant melanomas. *Nature* **550**, 133–136 (2017).

169. S.-X. Lu, C. Z. Zhang, R.-Z. Luo, C.-H. Wang, L.-L. Liu, J. Fu, L. Zhang, H. Wang, D. Xie, J.-P. Yun, Zic2 promotes tumor growth and metastasis via PAK4 in hepatocellular carcinoma. *Cancer Lett.* **402**, 71–80 (2017).
170. M.-H. Park, H.-S. Lee, C.-S. Lee, S. T. You, D.-J. Kim, B.-H. Park, M. J. Kang, W. D. Heo, E.-Y. Shin, M. A. Schwartz, E.-G. Kim, p21-activated kinase 4 promotes prostate cancer progression through CREB. *Oncogene* **32**, 2475–2482 (2013).
171. N. Tyagi, A. Bhardwaj, A. P. Singh, S. McClellan, J. E. Carter, S. Singh, p21 activated kinase 4 promotes proliferation and survival of pancreatic cancer cells through AKT- and ERK-dependent activation of NF- κ B pathway. *Oncotarget* **5**, 8778–8789 (2014).
172. L. E. Wong, N. Chen, V. Karantza, A. Minden, The Pak4 protein kinase is required for oncogenic transformation of MDA-MB-231 breast cancer cells. *Oncogene* **2**, e50 (2013).
173. T. Wu, Y. Pang, J. Guo, W. Yin, M. Zhu, C. Hao, K. Wang, J. Wang, D. Zhao, M. Cheng, Discovery of 2-(4-substituted-piperidin/piperazine-1-yl)-N-(5-cyclopropyl-1H-pyrazol-3-yl)-quinazoline-2,4-diamines as PAK4 inhibitors with potent A549 cell proliferation, migration, and invasion inhibition activity. *Molecules* **23**, E417 (2018).
174. B. Zeng, W. Shi, G. Tan, MIR-199a/b-3p inhibits gastric cancer cell proliferation via down-regulating PAK4/MEK/ERK signaling pathway. *BMC Cancer* **18**, 34 (2018).
175. H.-Y. Zhang, J. Zhang, C.-Z. Hao, Y. Zhou, J. Wang, M.-S. Cheng, D.-M. Zhao, F. Li, LC-0882 targets PAK4 and inhibits PAK4-related signaling pathways to suppress the proliferation and invasion of gastric cancer cells. *Am. J. Transl. Res.* **9**, 2736–2747 (2017).
176. J. Zhang, J. Wang, Q. Guo, Y. Wang, Y. Zhou, H. Peng, M. Cheng, D. Zhao, F. Li, LCH-7749944, a novel and potent p21-activated kinase 4 inhibitor, suppresses proliferation and invasion in human gastric cancer cells. *Cancer Lett.* **317**, 24–32 (2012).
177. H. Alachkar, M. Mutonga, G. Malnassy, J.-H. Park, N. Fulton, A. Woods, L. Meng, J. Kline, G. Raca, O. Odenike, N. Takamatsu, T. Miyamoto, Y. Matsuo, W. Stock, Y. Nakamura, T-LAK cell-originated protein kinase presents a novel therapeutic target in FLT3-ITD mutated acute myeloid leukemia. *Oncotarget* **6**, 33410–33425 (2015).
178. V. Ayllón, R. O'Connor, PBK/TOPK promotes tumour cell proliferation through p38 MAPK activity and regulation of the DNA damage response. *Oncogene* **26**, 3451–3461 (2007).
179. Y. Chai, H. Xue, Y. Wu, X. Du, Z. Zhang, Y. Zhang, L. Zhang, S. Zhang, Z. Zhang, Z. Xue, MicroRNA-216b-3p inhibits lung adenocarcinoma cell growth via regulating PDZ binding kinase/T-LAK-cell-originated protein kinase. *Exp. Ther. Med.* **15**, 4822–4828 (2018).
180. F. Chen, R. Li, C. Wang, L. Cao, Y. Wang, L. Yu, T-LAK cell-originated protein kinase is essential for the proliferation of hepatocellular carcinoma SMMC-7721 cells. *Cell Biochem. Funct.* **31**, 736–742 (2013).
181. J.-H. Chen, Y.-X. Liang, H.-C. He, J.-Y. Chen, J.-M. Lu, G. Chen, Z.-Y. Lin, X. Fu, X.-H. Ling, Z.-D. Han, F.-N. Jiang, W.-D. Zhong, Overexpression of PDZ-binding kinase confers malignant phenotype in prostate cancer via the regulation of E2F1. *Int. J. Biol. Macromol.* **81**, 615–623 (2015).
182. X. Dou, J. Wei, A. Sun, G. Shao, C. Childress, W. Yang, Q. Lin, PBK/TOPK mediates geranylgeranylation signaling for breast cancer cell proliferation. *Cancer Cell Int.* **15**, 27 (2015).
183. G. Gao, T. Zhang, Q. Wang, K. Reddy, H. Chen, K. Yao, K. Wang, E. Roh, T. Zyкова, W. Ma, J. Ryu, C. Curiel-Lewandrowski, D. Alberts, S. E. Dickinson, A. M. Bode, Y. Xing, Z. Dong, ADA-07 suppresses solar ultraviolet-induced skin carcinogenesis by directly inhibiting TOPK. *Mol. Cancer Ther.* **16**, 1843–1854 (2017).
184. T. Gao, Q. Hu, X. Hu, Q. Lei, Z. Feng, X. Yu, C. Peng, X. Song, H. He, Y. Xu, W. Zuo, J. Zeng, Z. Liu, L. Yu, Novel selective TOPK inhibitor SKLB-C05 inhibits colorectal carcinoma growth and metastasis. *Cancer Lett.* **445**, 11–23 (2019).
185. D. Herrero-Martín, D. Osuna, J. L. Ordóñez, V. Sevillano, A. S. Martins, C. Mackintosh, M. Campos, J. Madoz-Gúrpide, A. P. Otero-Motta, G. Caballero, A. T. Amaral, D. H. Wai, Y. Braun, M. Eisenacher, K.-L. Schaefer, C. Poremba, E. de Alava, Stable interference of EWS-FLI1 in an Ewing sarcoma cell line impairs IGF-1/IGF-1R signalling and reveals TOPK as a new target. *Br. J. Cancer* **101**, 80–90 (2009).
186. F. Hu, R. B. Gartenhaus, D. Eichberg, Z. Liu, H.-B. Fang, A. P. Rapoport, PBK/TOPK interacts with the DBD domain of tumor suppressor p53 and modulates expression of transcriptional targets including p21. *Oncogene* **29**, 5464–5474 (2010).
187. F. Hu, R. B. Gartenhaus, X. F. Zhao, H.-B. Fang, S. Minkove, D. E. Poss, A. P. Rapoport, c-Myc and E2F1 drive PBK/TOPK expression in high-grade malignant lymphomas. *Leuk. Res.* **37**, 447–454 (2013).
188. Y. Ikeda, J.-H. Park, T. Miyamoto, N. Takamatsu, T. Kato, A. Iwasa, S. Okabe, Y. Imai, K. Fujiwara, Y. Nakamura, K. Hasegawa, T-LAK cell-originated protein kinase (TOPK) as a prognostic factor and a potential therapeutic target in ovarian cancer. *Clin. Cancer Res.* **22**, 6110–6117 (2016).
189. M. Joel, A. A. Mughal, Z. Grieg, W. Murrell, S. Palmero, B. Mikkelsen, H. B. Fjerdingstad, C. J. Sandberg, J. Behnan, J. C. Glover, I. A. Langmoen, B. Stangeland, Targeting PBK/TOPK decreases growth and survival of glioma initiating cells in vitro and attenuates tumor growth in vivo. *Mol. Cancer* **14**, 121 (2015).
190. T. Kato, H. Inoue, S. Imoto, Y. Tamada, T. Miyamoto, Y. Matsuo, Y. Nakamura, J.-H. Park, Oncogenic roles of TOPK and MELK, and effective growth suppression by small molecular inhibitors in kidney cancer cells. *Oncotarget* **7**, 17652–17664 (2016).
191. D. J. Kim, Y. Li, K. Reddy, M.-H. Lee, M. O. Kim, Y.-Y. Cho, S.-Y. Lee, J.-E. Kim, A. M. Bode, Z. Dong, Novel TOPK inhibitor HI-TOPK-032 effectively suppresses colon cancer growth. *Cancer Res.* **72**, 3060–3068 (2012).
192. B. Lei, W. Qi, Y. Zhao, Y. Li, S. Liu, X. Xu, C. Zhi, L. Wan, H. Shen, PBK/TOPK expression correlates with mutant p53 and affects patients' prognosis and cell proliferation and viability in lung adenocarcinoma. *Hum. Pathol.* **46**, 217–224 (2015).
193. Y. Liu, H. Liu, H. Cao, B. Song, W. Zhang, W. Zhang, PBK/TOPK mediates promyelocyte proliferation via Nrf2-regulated cell cycle progression and apoptosis. *Oncol. Rep.* **34**, 3288–3296 (2015).
194. T. Ohashi, S. Komatsu, D. Ichikawa, M. Miyamae, W. Okajima, T. Imamura, J. Kiuchi, K. Nishibeppu, T. Kosuga, H. Konishi, A. Shiozaki, H. Fujiwara, K. Okamoto, H. Tsuda, E. Otsuji, Overexpression of PBK/TOPK contributes to tumor development and poor outcome of esophageal squamous cell carcinoma. *Anticancer Res.* **36**, 6457–6466 (2016).
195. T. Ohashi, S. Komatsu, D. Ichikawa, M. Miyamae, W. Okajima, T. Imamura, J. Kiuchi, T. Kosuga, H. Konishi, A. Shiozaki, H. Fujiwara, K. Okamoto, H. Tsuda, E. Otsuji, Overexpression of PBK/TOPK relates to tumour malignant potential and poor outcome of gastric carcinoma. *Br. J. Cancer* **116**, 218–226 (2017).
196. J.-H. Park, H. Inoue, T. Kato, M. Zewde, T. Miyamoto, Y. Matsuo, R. Salgia, Y. Nakamura, TOPK (T-LAK cell-originated protein kinase) inhibitor exhibits growth suppressive effect on small cell lung cancer. *Cancer Sci.* **108**, 488–496 (2017).
197. X. Song, S. Yin, E. Zhang, L. Fan, M. Ye, Y. Zhang, H. Hu, Glycycoumarin exerts anti-liver cancer activity by directly targeting T-LAK cell-originated protein kinase. *Oncotarget* **7**, 65732–65743 (2016).
198. S. Stauffer, Y. Zeng, J. Zhou, X. Chen, Y. Chen, J. Dong, CDK1-mediated mitotic phosphorylation of PBK is involved in cytokinesis and inhibits its oncogenic activity. *Cell. Signal.* **39**, 74–83 (2017).
199. M. Sugimori, Y. Hayakawa, M. Koh, T. Hayashi, R. Tamura, S. Kuroda, Targeting the T-Lak cell originated protein kinase by OTS964 shrinks the size of power-law coded heterogeneous glioma stem cell populations. *Oncotarget* **9**, 3043–3059 (2018).
200. E. Uchida, S. Suwa, R. Yoshimoto, K. Watanabe, T. Kasama, O. Miura, T. Fukuda, TOPK is regulated by PP2A and BCR/ABL in leukemia and enhances cell proliferation. *Int. J. Oncol.* **54**, 1785–1796 (2019).
201. O. S. Vishchuk, H. Sun, Z. Wang, S. P. Ermakova, J. Xiao, T. Lu, P. Xue, T. N. Zvyagintseva, H. Xiong, C. Shao, W. Yan, Q. Duan, F. Zhu, PDZ-binding kinase/T-LAK cell-originated protein kinase is a target of the fucoidan from brown alga *Fucus evanescens* in the prevention of EGF-induced neoplastic cell transformation and colon cancer growth. *Oncotarget* **7**, 18763–18773 (2016).
202. M.-Y. Wang, Z.-R. Lin, Y. Cao, L.-S. Zheng, L.-X. Peng, R. Sun, D.-F. Meng, P. Xie, J.-P. Yang, L. Cao, L. Xu, B.-J. Huang, C.-N. Qian, PDZ binding kinase (PBK) is a theranostic target for nasopharyngeal carcinoma: Driving tumor growth via ROS signaling and correlating with patient survival. *Oncotarget* **7**, 26604–26616 (2016).
203. J. Xiao, Q. Duan, Z. Wang, W. Yan, H. Sun, P. Xue, X. Fan, X. Zeng, J. Chen, C. Shao, F. Zhu, Phosphorylation of TOPK at Y74, Y272 by Src increases the stability of TOPK and promotes tumorigenesis of colon. *Oncotarget* **7**, 24483–24494 (2016).
204. J. Yang, D. Yuan, T. Xing, H. Su, S. Zhang, J. Wen, Q. Bai, D. Dang, Ginsenoside Rh2 inhibiting HCT116 colon cancer cell proliferation through blocking PDZ-binding kinase/T-LAK cell-originated protein kinase. *J. Ginseng Res.* **40**, 400–408 (2016).
205. M. Zheng, S. Luan, S. Gao, L. Cheng, B. Hao, J. Li, Y. Chen, X. Hou, L. Chen, H. Li, Proton pump inhibitor ilaprazole suppresses cancer growth by targeting T-cell-originated protein kinase. *Oncotarget* **8**, 39143–39153 (2017).
206. F. Zhu, T. A. Zyкова, B. S. Kang, Z. Wang, M. C. Ebeling, Y. Abe, W.-Y. Ma, A. M. Bode, Z. Dong, Bidirectional signals transduced by TOPK-ERK interaction increase tumorigenesis of HCT116 colorectal cancer cells. *Gastroenterology* **133**, 219–231 (2007).
207. M. Bellon, L. Lu, C. Nicot, Constitutive activation of Pim1 kinase is a therapeutic target for adult T-cell leukemia. *Blood* **127**, 2439–2450 (2016).
208. C. Blanco-Aparicio, A. M. G. Collazo, J. Oyarzabal, J. F. Leal, M. I. Albarán, F. R. Lima, B. Pequeño, N. Ajenjo, M. Becerra, P. Alfonso, M. I. Reymundo, I. Palacios, G. Mateos, H. Quiñones, A. Corrión, A. Carnero, P. Pevarello, A. R. Lopez, J. Fominaya, J. Pastor, J. R. Bischoff, Pim 1 kinase inhibitor ETP-45299 suppresses cellular proliferation and synergizes with PI3K inhibition. *Cancer Lett.* **300**, 145–153 (2011).
209. J. Chen, M. Kobayashi, S. Darmanin, Y. Qiao, C. Gully, R. Zhao, S. Kondo, H. Wang, H. Wang, S.-C. J. Yeung, M.-H. Lee, Hypoxia-mediated up-regulation of Pim-1 contributes to solid tumor formation. *Am. J. Pathol.* **175**, 400–411 (2009).
210. D. Deng, L. Wang, Y. Chen, B. Li, L. Xue, N. Shao, Q. Wang, X. Xia, Y. Yang, F. Zhi, MicroRNA-124-3p regulates cell proliferation, invasion, apoptosis, and bioenergetics by targeting PIM1 in astrocytoma. *Cancer Sci.* **107**, 899–907 (2016).
211. R.-F. Fan, Y. Lu, Z.-G. Fang, X.-Y. Guo, Y.-X. Chen, Y.-C. Xu, Y.-M. Lei, K.-F. Liu, D.-J. Lin, L.-L. Liu, X.-F. Liu, PIM-1 kinase inhibitor SMI-4a exerts antitumor effects in chronic myeloid leukemia cells by enhancing the activity of glycogen synthase kinase 3 β . *Mol. Med. Rep.* **16**, 4603–4612 (2017).

212. S. Herzog, M. A. Fink, K. Weitmann, C. Friedel, S. Hadlich, S. Langner, K. Kindermann, T. Holm, A. Böhm, E. Eskilsson, H. Miletic, M. Hildner, M. Fritsch, S. Vogelgesang, C. Havemann, C. A. Ritter, H. E. Meyer zu Schwabedissen, B. Rauch, W. Hoffmann, H. K. Kroemer, H. Schroeder, S. Bien-Möller, Pim1 kinase is upregulated in glioblastoma multiforme and mediates tumor cell survival. *Neuro Oncol.* **17**, 223–242 (2015).
213. X. Hou, Y. Yu, J. Feng, J. Wang, C. Zheng, Z. Ling, M. Ge, X. Zhu, Biochemical changes of salivary gland adenoid cystic carcinoma cells induced by SGI-1776. *Exp. Cell Res.* **352**, 403–411 (2017).
214. W. Jie, Q.-Y. He, B.-T. Luo, S.-J. Zheng, Y.-Q. Kong, H.-G. Jiang, R.-J. Li, J.-L. Guo, Z.-H. Shen, Inhibition of Pim-1 attenuates the proliferation and migration in nasopharyngeal carcinoma cells. *Asian Pac. J. Trop. Med.* **5**, 645–650 (2012).
215. O. F. Karatas, Antiproliferative potential of miR-33a in laryngeal cancer Hep-2 cells via targeting PIM1. *Head Neck* **40**, 2455–2461 (2018).
216. J.-E. Kim, J. E. Son, H. Jeong, D. Joon Kim, S. K. Seo, E. Lee, T. G. Lim, J. R. Kim, H. Chen, A. M. Bode, K. W. Lee, Z. Dong, A novel cinnamon-related natural product with Pim-1 inhibitory activity inhibits leukemia and skin cancer. *Cancer Res.* **75**, 2716–2728 (2015).
217. A. N. Kirschner, J. Wang, R. van der Meer, P. D. Anderson, O. E. Franco-Coronel, M. H. Kushner, J. H. Everett, O. Hameed, E. K. Keeton, M. Ahdesmaki, S. E. Grosskurth, D. Huszar, S. A. Abdulkadir, PIM kinase inhibitor AZD1208 for treatment of MYC-driven prostate cancer. *J. Natl. Cancer Inst.* **107**, dju407 (2015).
218. C. O. Leung, C. C. Wong, D. N. Fan, A. K. Kai, E. K. Tung, I. M. Xu, I. O. Ng, R. C. Lo, PIM1 regulates glycolysis and promotes tumor progression in hepatocellular carcinoma. *Oncotarget* **6**, 10880–10892 (2015).
219. J.-Q. Li, X. Yang, X.-M. Zhou, PIM1 gene silencing inhibits proliferation and promotes apoptosis of human esophageal cancer cell line Eca-109. *Cancer Biomark. Sect. Dis. Markers* **18**, 149–154 (2017).
220. J. Li, X. F. Hu, B. E. Loveland, P. X. Xing, Pim-1 expression and monoclonal antibody targeting in human leukemia cell lines. *Exp. Hematol.* **37**, 1284–1294 (2009).
221. K. Li, Y. Li, D. Zhou, Y. Fan, H. Guo, T. Ma, J. Wen, D. Liu, L. Zhao, Synthesis and biological evaluation of quinoline derivatives as potential anti-prostate cancer agents and Pim-1 kinase inhibitors. *Bioorg. Med. Chem.* **24**, 1889–1897 (2016).
222. Y. Liao, Y. Feng, J. Shen, Y. Gao, G. Cote, E. Choy, D. Harmon, H. Mankin, F. Hornicek, Z. Duan, Clinical and biological significance of PIM1 kinase in osteosarcoma. *J. Orthop. Res. Off. Publ. Orthop. Res. Soc.* **34**, 1185–1194 (2016).
223. K. Liu, H. Gao, Q. Wang, L. Wang, B. Zhang, Z. Han, X. Chen, M. Han, M. Gao, Hispidulin suppresses cell growth and metastasis by targeting PIM1 through JAK2/STAT3 signaling in colorectal cancer. *Cancer Sci.* **109**, 1369–1381 (2018).
224. A. S. Mawas, V. J. Amaya, R. Suzuki, K. Kushitani, M. M. Mohi El-Din, Y. Takeshima, PIM1 knockdown inhibits cell proliferation and invasion of mesothelioma cells. *Int. J. Oncol.* **50**, 1029–1034 (2017).
225. D. Morishita, M. Takami, S. Yoshikawa, R. Katayama, S. Sato, M. Kukimoto-Niino, T. Umehara, M. Shirouzu, K. Sekimizu, S. Yokoyama, N. Fujita, Cell-permeable carboxyl-terminal p27(Kip1) peptide exhibits anti-tumor activity by inhibiting Pim1 kinase. *J. Biol. Chem.* **286**, 2681–2688 (2011).
226. S. Mou, G. Wang, D. Ding, D. Yu, Y. Pei, S. Teng, Q. Fu, Expression and function of PIM kinases in osteosarcoma. *Int. J. Oncol.* **49**, 2116–2126 (2016).
227. H. Nakano, N. Saito, L. Parker, Y. Tada, M. Abe, K. Tsuganezawa, S. Yokoyama, A. Tanaka, H. Kojima, T. Okabe, T. Nagano, Rational evolution of a novel type of potent and selective proviral integration site in Moloney murine leukemia virus kinase 1 (PIM1) inhibitor from a screening-hit compound. *J. Med. Chem.* **55**, 5151–5164 (2012).
228. R. L. Schroeder, N. Goyal, M. Bratton, I. Townley, N. A. Pham, P. Tram, T. Stone, J. Geathers, K. Nguyen, J. Sridhar, Identification of quinones as novel PIM1 kinase inhibitors. *Bioorg. Med. Chem. Lett.* **26**, 3187–3191 (2016).
229. B. Shannan, A. Watters, Q. Chen, S. Mollin, M. Dörr, E. Meggers, X. Xu, P. A. Gimotty, M. Perego, L. Li, J. Bencic, C. Krepler, P. Brafford, J. Zhang, Z. Wei, G. Zhang, Q. Liu, X. Yin, K. L. Nathanson, M. Herlyn, A. Vulter, PIM kinases as therapeutic targets against advanced melanoma. *Oncotarget* **7**, 54897–54912 (2016).
230. R. D. Smedt, S. Peirs, J. Morscio, F. Matthijssens, J. Roels, L. Reunes, B. Lintermans, S. Goossens, T. Lammens, N. V. Roy, A. Touzart, S. Jenni, Y.-C. Tsai, F. Lovisa, L. Mussolin, V. Serafin, F. V. Nieuwerburgh, D. Deforce, A. Uttebroeck, T. Tousseyen, B. Burkhardt, W. Klapper, B. D. Moerloose, Y. Benoit, E. Macintyre, J.-P. Bourquin, G. Basson, B. Accordi, B. Bornhauser, J. Meijerink, P. Vandenberghe, P. Van Vlierberghe, Pre-clinical evaluation of second generation PIM inhibitors for the treatment of T-cell acute lymphoblastic leukemia and lymphoma. *Haematologica* **104**, e17–e20 (2018).
231. M. Thomas, K. Lange-Grünweller, U. Weirauch, D. Gutsch, A. Aigner, A. Grünweller, R. K. Hartmann, The proto-oncogene Pim-1 is a target of miR-33a. *Oncogene* **31**, 918–928 (2012).
232. J. Wang, P. D. Anderson, W. Luo, D. Gius, M. Roh, S. A. Abdulkadir, Pim1 kinase is required to maintain tumorigenicity in MYC-expressing prostate cancer cells. *Oncogene* **31**, 1794–1803 (2012).
233. Q. Wang, Y. Jiang, R. Guo, R. Lv, T. Liu, H. Wei, H. Ming, X. Tian, Physcion 8-O-β-glucopyranoside suppresses tumor growth of hepatocellular carcinoma by downregulating PIM1. *Biomed. Pharmacother. Biomedecine Pharmacother.* **92**, 451–458 (2017).
234. U. Weirauch, N. Beckmann, M. Thomas, A. Grünweller, K. Huber, F. Bracher, R. K. Hartmann, A. Aigner, Functional role and therapeutic potential of the Pim-1 kinase in colon carcinoma. *Neoplasia* **15**, 783–794 (2013).
235. Y. Wu, Y. Deng, J. Zhu, Y. Duan, W. Weng, X. Wu, Pim1 promotes cell proliferation and regulates glycolysis via interaction with MYC in ovarian cancer. *Oncotargets Ther.* **11**, 6647–6656 (2018).
236. J. Xie, J. Bai, SGI-1776, an imidazo pyridazine compound, inhibits the proliferation of ovarian cancer cells by inactivating Pim-1. *Zhong Nan Da Xue Xue Bao Yi Xue Ban* **39**, 649–657 (2014).
237. D. Xu, S. A. Allsop, S. M. Witherspoon, J. L. Snider, J. J. Yeh, J. J. Fiordalisi, C. D. White, D. Williams, A. D. Cox, A. T. Baines, The oncogenic kinase Pim-1 is modulated by K-Ras signaling and mediates transformed growth and radioresistance in human pancreatic ductal adenocarcinoma cells. *Carcinogenesis* **32**, 488–495 (2011).
238. B. Yan, E. X. Yau, S. Samanta, C. W. Ong, K. J. Yong, L. K. Ng, B. Bhattacharya, K. H. Lim, R. Soong, K. G. Yeoh, N. Deng, P. Tan, Y. Lam, M. Salto-Tellez; Singapore Gastric Cancer Consortium, Clinical and therapeutic relevance of PIM1 kinase in gastric cancer. *Gastric Cancer* **15**, 188–197 (2012).
239. C. Ye, C. Zhang, H. Huang, B. Yang, G. Xiao, D. Kong, Q. Tian, Q. Song, Y. Song, H. Tan, Y. Wang, T. Zhou, X. Zi, Y. Sun, The natural compound Myricetin effectively represses the malignant progression of prostate cancer by inhibiting PIM1 and disrupting the PIM1/CXCR4 interaction. *Cell. Physiol. Biochem.* **48**, 1230–1244 (2018).
240. C. Zhang, Y. Qie, T. Yang, L. Wang, E. Du, Y. Liu, Y. Xu, B. Qiao, Z. Zhang, Kinase PIM1 promotes prostate cancer cell growth via c-Myc-RPS7-driven ribosomal stress. *Carcinogenesis* **40**, 52–60 (2019).
241. G. Zhang, Z. Liu, G. Cui, X. Wang, Z. Yang, MicroRNA-486-5p targeting PIM-1 suppresses cell proliferation in breast cancer cells. *Tumour Biol.* **35**, 11137–11145 (2014).
242. M. Zhang, T. Liu, H. Sun, W. Weng, Q. Zhang, C. Liu, Y. Han, W. Sheng, Pim1 supports human colorectal cancer growth during glucose deprivation by enhancing the Warburg effect. *Cancer Sci.* **109**, 1468–1479 (2018).
243. B. Zhao, L. Liu, J. Mao, Z. Zhang, Q. Wang, Q. Li, PIM1 mediates epithelial-mesenchymal transition by targeting Smads and c-Myc in the nucleus and potentiates clear-cell renal-cell carcinoma oncogenesis. *Cell Death Dis.* **9**, 307 (2018).
244. X. Zhu, J. Xu, S. Hu, J. Feng, L. Jiang, X. Hou, J. Cao, J. Han, Z. Ling, M. Ge, Pim-1 acts as an oncogene in human salivary gland adenoid cystic carcinoma. *J. Exp. Clin. Cancer Res.* **33**, 114 (2014).
245. R. C. Botham, T. M. Fan, I. Im, L. B. Borst, L. Dirikolu, P. J. Hergenrother, Dual small-molecule targeting of procaspase-3 dramatically enhances zymogen activation and anticancer activity. *J. Am. Chem. Soc.* **136**, 1312–1319 (2014).
246. A. D. Joshi, R. C. Botham, L. J. Schlein, H. S. Roth, A. Mangraviti, A. Borodovsky, B. Tyler, S. Joslyn, J. S. Looper, M. Podell, T. M. Fan, P. J. Hergenrother, G. J. Riggins, Synergistic and targeted therapy with a procaspase-3 activator and temozolomide extends survival in glioma rodent models and is feasible for the treatment of canine malignant glioma patients. *Oncotarget* **8**, 80124–80138 (2017).
247. P. W. Lucas, J. M. Schmit, Q. P. Peterson, D. C. West, D. C. Hsu, C. J. Novotny, L. Dirikolu, M. I. Churchwell, D. R. Doerge, L. D. Garrett, P. J. Hergenrother, T. M. Fan, Pharmacokinetics and derivation of an anticancer dosing regimen for PAC-1, a preferential small molecule activator of procaspase-3, in healthy dogs. *Invest. New Drugs* **29**, 901–911 (2011).
248. J. Ma, D. Chen, K. Lu, L. Wang, X. Han, Y. Zhao, P. Gong, Design, synthesis, and structure-activity relationships of novel benzothiazole derivatives bearing the *ortho*-hydroxy N-carbamoylhydrazone moiety as potent antitumor agents. *Eur. J. Med. Chem.* **86**, 257–269 (2014).
249. V. Patel, K. Balakrishnan, M. J. Keating, W. G. Wierda, V. Gandhi, Expression of executioner proapoptotic caspases and their activation by a procaspase-activating compound in chronic lymphocytic leukemia cells. *Blood* **125**, 1126–1136 (2015).
250. J. Peh, T. M. Fan, K. L. Wycislo, H. S. Roth, P. J. Hergenrother, The combination of vemurafenib and procaspase-3 activation is synergistic in mutant BRAF melanomas. *Mol. Cancer Ther.* **15**, 1859–1869 (2016).
251. Q. P. Peterson, D. C. Hsu, C. J. Novotny, D. C. West, D. Kim, J. M. Schmit, L. Dirikolu, P. J. Hergenrother, T. M. Fan, Discovery and canine preclinical assessment of a nontoxic procaspase-3-activating compound. *Cancer Res.* **70**, 7232–7241 (2010).
252. H. S. Roth, P. J. Hergenrother, Derivatives of procaspase-activating compound 1 (PAC-1) and their anticancer activities. *Curr. Med. Chem.* **23**, 201–241 (2016).
253. F. Wang, Y. Liu, L. Wang, J. Yang, Y. Zhao, N. Wang, Q. Cao, P. Gong, C. Wu, Targeting procaspase-3 with WF-208, a novel PAC-1 derivative, causes selective cancer cell apoptosis. *J. Cell. Mol. Med.* **19**, 1916–1928 (2015).
254. F. Wang, L. Wang, Y. Li, N. Wang, Y. Wang, Q. Cao, P. Gong, J. Yang, C. Wu, PAC-1 and its derivative WF-210 inhibit angiogenesis by inhibiting VEGF/VEGFR pathway. *Eur. J. Pharmacol.* **821**, 29–38 (2018).
255. D. C. West, Y. Qin, Q. P. Peterson, D. L. Thomas, R. Palchaudhuri, K. C. Morrison, P. W. Lucas, A. E. Palmer, T. M. Fan, P. J. Hergenrother, Differential effects of procaspase-3 activating compounds in the induction of cancer cell death. *Mol. Pharm.* **9**, 1425–1434 (2012).

256. S. Zaman, R. Wang, V. Gandhi, Targeting executioner procaspase-3 with the procaspase-activating compound B-PAC-1 induces apoptosis in multiple myeloma cells. *Exp. Hematol.* **43**, 951–962.e3 (2015).
257. X. Zhai, Q. Huang, N. Jiang, D. Wu, H. Zhou, P. Gong, Discovery of hybrid dual *N*-acylhydrazone and diaryl urea derivatives as potent antitumor agents: Design, synthesis and cytotoxicity evaluation. *Molecules* **18**, 2904–2923 (2013).

Acknowledgments: We thank the following individuals for sharing plasmids and cell lines used in this work: C. Vakoc (CSHL), C. dos Santos (CSHL), K. Chang (CSHL), L. Trotman (CSHL), M. Jost and J. Weissman (UCSF), J. van den Berg and R. Medema (Netherlands Cancer Institute), H. Goodarzi (UCSF), D. Solomon (UCSF), D. Livingston (Harvard), J. Lum (University of Victoria), H. Tsao and K. Flaherty (MGH), S. Karuppaiah (Ohio State University), and S. Murphy (Duke University). **Funding:** Research in the Sheltzer Lab is supported by an NIH Early Independence Award (1DP5OD021385), a Breast Cancer Alliance Young Investigator Award, a Damon Runyon-Rachleff Innovation Award, a Gates Foundation Innovative Technology Solutions grant, and a CSHL-Northwell Translational Cancer Research grant. This work was performed with assistance from the CSHL Flow Cytometry Shared Resource, which is supported by the

CSHL Cancer Center Support grant 5P30CA045508. A.L. and C.J.G. are supported by NSF Graduate Research Fellowships. **Author contributions:** A.L., C.J.G., and J.M.S. designed the experiments, performed the experiments, interpreted the results, and wrote the paper. A.P., K.M.J., C.A., M.L.Y., E.I.S., D.A.L., L.L., A.R.C., Z.C.G., and C.T. performed the experiments and interpreted the results. **Competing interests:** The authors declare that they have no competing interests. **Data and materials availability:** All data associated with this study are present in the paper or the Supplementary Materials.

Submitted 29 January 2019
Resubmitted 19 June 2019
Accepted 1 August 2019
Published 11 September 2019
10.1126/scitranslmed.aaw8412

Citation: A. Lin, C. J. Giuliano, A. Palladino, K. M. John, C. Abramowicz, M. L. Yuan, E. L. Sausville, D. A. Lukow, L. Liu, A. R. Chait, Z. C. Galluzzo, C. Tucker, J. M. Sheltzer, Off-target toxicity is a common mechanism of action of cancer drugs undergoing clinical trials. *Sci. Transl. Med.* **11**, eaaw8412 (2019).



Science Webinars

AAAS

Science Webinars help you keep pace with emerging scientific fields!

Stay informed about scientific breakthroughs and discoveries.

Gain insights into current research from top scientists.

Take the opportunity to ask questions during live broadcasts.



Get alerts about upcoming free webinars.

Sign up at: webinar.sciencemag.org/stayinformed

CANCER

An innate-like V δ 1 $^+$ $\gamma\delta$ T cell compartment in the human breast is associated with remission in triple-negative breast cancer

Yin Wu^{1,2,3,4*}, Fernanda Kyle-Cezar^{1,2*}, Richard T. Woolf^{1,5}, Cristina Naceur-Lombardelli⁶, Julie Owen⁶, Dhruba Biswas^{4,7}, Anna Lorenc¹, Pierre Vantourout^{1,2}, Patrycja Gazinska^{3,8}, Anita Grigoriadis³, Andrew Tutt^{3,8}, Adrian Hayday^{1,2†}

Innate-like tissue-resident $\gamma\delta$ T cell compartments capable of protecting against carcinogenesis are well established in mice. Conversely, the degree to which they exist in humans, their potential properties, and their contributions to host benefit are mostly unresolved. Here, we demonstrate that healthy human breast harbors a distinct $\gamma\delta$ T cell compartment, primarily expressing T cell receptor (TCR) V δ 1 chains, by comparison to V δ 2 chains that predominate in peripheral blood. Breast-resident V δ 1 $^+$ cells were functionally skewed toward cytotoxicity and IFN- γ production, but not IL-17, which has been linked with inflammatory pathologies. Breast-resident V δ 1 $^+$ cells could be activated innately via the NKG2D receptor, whereas neighboring CD8 $^+$ $\alpha\beta$ T cells required TCR signaling. A comparable population of V δ 1 $^+$ cells was found in human breast tumors, and when paired tumor and non-malignant samples from 11 patients with triple-negative breast cancer were analyzed, progression-free and overall survival correlated with V δ 1 $^+$ cell representation, but not with either total $\gamma\delta$ T cells or V δ 2 $^+$ T cells. As expected, progression-free survival also correlated with $\alpha\beta$ TCRs. However, whereas in most cases TCR $\alpha\beta$ repertoires focused, typical of antigen-specific responses, this was not observed for V δ 1 $^+$ cells, consistent with their innate-like responsiveness. Thus, maximal patient benefit may accrue from the collaboration of innate-like responses mounted by tissue-resident V δ 1 $^+$ compartments and adaptive responses mounted by $\alpha\beta$ T cells.

INTRODUCTION

$\gamma\delta$ T cells comprise a highly conserved third lineage of lymphocytes that uses somatic gene rearrangement to encode the defining antigen receptor (1, 2). Although this is a hallmark of adaptive immunity, subsets of murine $\gamma\delta$ T cells also display innate-like activity, manifest in rapid responses to self-encoded “stress antigens” such as ligands for the NKG2D receptor (3–6). This is known as lymphoid stress surveillance (7).

Given that NKG2D ligands are up-regulated by overactivity of epidermal growth factor receptor (EGFR) signaling and DNA damage (8, 9), it is natural that lymphoid stress surveillance might contribute to cancer immunosurveillance (10). $\gamma\delta$ T cell-deficient mice show greatly increased susceptibility to cancer in several systems (4, 11–13), and many attempts are ongoing to exploit their activities clinically (14). Such approaches may enhance the efficacy of current immuno-therapies such as checkpoint blockade and, in particular, chimeric antigen receptor (CAR) T cells, which have shown limited success in treating solid tumors. Moreover, the capacity of some $\gamma\delta$ T cell subsets to secrete chemokines and cytokines and/or to present anti-

gen argues strongly for their potential to promote the therapeutic potentials of other cell types (12, 15–17).

In mice, signature $\gamma\delta$ T cell compartments are associated with discrete tissues such as epidermis, dermis, lung, uterus, and intestinal epithelium (18–25), seemingly offering optimal capacity to detect and respond to malignant transformation of neighboring cells. Accordingly, $\gamma\delta$ T cell-deficient mice have increased susceptibility to skin carcinogens owing to the lack of dendritic epidermal $\gamma\delta$ T cells (5). Whether local $\gamma\delta$ T cell compartments populate all tissues is unresolved. Nonetheless, the prospect of a mouse breast-associated compartment was supported by the fact that the representation, albeit variable, of $\gamma\delta$ T cells in lactating mammary glands was at least four-fold higher than in draining lymph nodes. Moreover, those cells used a variety of $\gamma\delta$ T cell receptors (TCR $\gamma\delta$ s), distinguishing them from skin- and gut-resident $\gamma\delta$ T cell compartments (26).

There has been long-standing interest in the degree to which tissue-associated $\gamma\delta$ T cell compartments might be conserved in humans and whether or not they contribute to cancer immunosurveillance. On the one hand, humans harbor no obvious counterparts of dendritic epidermal $\gamma\delta$ T cells; on the other hand, jawless vertebrates have skin-resident and gut intraepithelial cells with many parallels to $\gamma\delta$ T cells, suggesting that such compartments have been conserved for over half a billion years (27). We therefore hypothesized that sub-optimal methods for the detection and/or extraction of T cells from human tissues might have confounded attempts to identify and characterize conserved extralymphoid $\gamma\delta$ T cell compartments. This hypothesis is consistent with inefficiencies and biases reported both for extracting TCR $\alpha\beta$ $^+$ tissue-resident memory T (T_{RM}) cells (28) and for visualizing tumor-infiltrating lymphocytes (TILs) *in situ* (29) and derives support from our recent characterization of a large intraepithelial $\gamma\delta$ T cell compartment in the human gut (30).

¹Peter Gorer Department of Immunobiology, School of Immunology & Microbial Sciences, King's College London, London SE1 9RT, UK. ²Immunosurveillance Laboratory, Francis Crick Institute, 1 Midland Road, London NW1 1AT, UK. ³Breast Cancer Now Research Unit, Innovation Hub, Cancer Centre at Guy's Hospital, Faculty of Life Sciences and Medicine, King's College London, London SE1 9RT, UK. ⁴Cancer Research UK Lung Cancer Centre of Excellence, University College London Cancer Institute, University College London, London WC1E 6DD, UK. ⁵St John's Institute of Dermatology, King's College London, London SE1 9RT, UK. ⁶KHP Cancer Biobank, Innovation Hub, Cancer Centre at Guy's Hospital, Faculty of Life Sciences and Medicine, King's College London, London SE1 9RT, UK. ⁷Bill Lyons Informatics Centre, University College London Cancer Institute, University College London, London WC1E 6DD, UK. ⁸Breast Cancer Now Research Centre, Institute of Cancer Research, London SW3 6JB, UK.

*These authors contributed equally to this work.

†Corresponding author. Email: adrian.hayday@kcl.ac.uk

Copyright © 2019
The Authors, some
rights reserved;
exclusive licensee
American Association
for the Advancement
of Science. No claim
to original U.S.
Government Works

In this regard, the care of women in a large breast cancer risk surveillance and treatment practice offered a rare opportunity to analyze the status of $\gamma\delta$ T cells in healthy tissue obtained from: reduction mammoplasty or risk-reducing mastectomy; malignant tissue from wide local resection; and paired malignant and nonmalignant tissues from therapeutic mastectomies. Additionally, the importance of investigating the possible existence of local $\gamma\delta$ T cells was underlined by evidence that TIL densities were positive prognostic indicators in some types of breast cancer (31, 32). Despite this, the potential of immunotherapy in breast cancer remains unclear with disappointing response rates to current immunotherapies, such as checkpoint blockade (33, 34).

RESULTS

$V\delta 1$ T cells compose a major human breast-resident $\gamma\delta$ subset and are skewed toward cytotoxicity

Our initial goal was to assess the status of T cells resident within healthy human breast. However, the obtainment and characterization of lymphocytes from healthy human tissues has commonly been confounded by poor and irreproducible yields and low cell viability. To redress this problem, Clark and colleagues (35–38) developed a “grid” explant culture system that permitted the recovery and characterization of large numbers of healthy skin-resident and lung-resident T cells without substantively changing their phenotype.

We therefore applied grids to disaggregated breast tissue from 29 healthy subjects undergoing reduction mammoplasties or risk-reducing mastectomies. Compared to the limited and variable recovery and poor viability of lymphocytes examined directly ex vivo, grids facilitated the recovery and maintenance of CD3⁺ natural killer (NK) cells/innate lymphoid cells (ILCs), $\gamma\delta$ T cells, and CD4⁺ and CD8⁺ $\alpha\beta$ T cells in every case, albeit there was some enrichment of NK/ILC and $\gamma\delta$ T cells (table S1 and Fig. 1A).

As is common for peripheral blood (PB) $\gamma\delta$ T cells (39), $\gamma\delta$ T cell representation in breast showed considerable interindividual variation (Fig. 1B). However, breast-extractable cells were clearly distinct from PB $\gamma\delta$ T cells by TCRV δ chain usage. Whereas most PB cells express V δ 2 paired to V γ 9, most donors’ breast $\gamma\delta$ T cells were predominantly V δ 1⁺ (median, 60.5% of $\gamma\delta$ T cells), as are most human skin-resident and gut-resident $\gamma\delta$ T cells (Fig. 1B) (40). In all cases, there was some representation of V δ 2⁺ T cells (median, 13.6% of $\gamma\delta$ T cells) and of cells expressing neither V δ 1 nor V δ 2 (median, 20.45% of $\gamma\delta$ T cells), which, in some cases, were almost exclusively V δ 3⁺ (fig. S1A).

The phenotypic consistency of $\gamma\delta$ T cells in grid cultures and counterpart cells examined directly ex vivo was apparent from the expression patterns of several biologically important surface markers, albeit CD69 was expressed by more cells in grid culture (fig. S1, B and C, top two rows). By multiparameter analysis of a subset of donors, we could deduce a consensus V δ 1⁺ T cell phenotype that resembled that of extralymphoid $\gamma\delta$ T cell subsets in other tissues of mice and humans (4, 41–44), namely, uniform positivity for the activating NK cell receptor NKG2D, and for CD69, and largely lacking the lymphoid T cell costimulator, CD28 (Fig. 1C and fig. S1C, bottom row). On average, ~20% of breast V δ 1⁺ T cells expressed PD-1, whereas slightly more expressed the epithelial interaction integrin, CD103 ($\alpha_E\beta_7$), albeit with high interindividual variation (Fig. 1C and fig. S1C, bottom row).

To assess the cells’ functional potential, they were incubated with phorbol 12-myristate 13-acetate (PMA) and ionomycin, which jointly

mimic TCR signaling, and analyzed for intracellular cytokine production and for surface expression of CD107a, a marker of degranulation and exocytosis of cytolytic mediators such as granzymes and perforin. Breast-associated V δ 1⁺ T cells combined CD107a expression with tumor necrosis factor (TNF) and interferon- γ (IFN- γ) production (Fig. 1D), a T-cytolytic type 1 (T_{c1}) phenotype that among CD8⁺ TCR $\alpha\beta$ ⁺ TILs is considered highly patient beneficial (45–48). Cells from some donors expressed interleukin-13 (IL-13) (median, 5.2% of $\gamma\delta$ T cells), which was recently linked to T cell tumor surveillance (49), but there was no production of IL-17A, an effector cytokine commonly produced by mouse $\gamma\delta$ T cells, in which species it has been associated with tumor promotion (50–52).

Because IL-17 production by human $\gamma\delta$ T cells is reportedly difficult to observe (53), we tested whether breast-resident $\gamma\delta$ T cells would respond in culture to IL-17-skewing conditions, namely, IL-1 β , IL-6, IL-23, IL-2 ± transforming growth factor- β (TGF- β) (54). However, whereas breast-resident CD4⁺ $\alpha\beta$ T cells extracted and maintained together with V δ 1⁺ T cells in the identical breast explant cultures (table S1) produced IL-17A [median, 16.5% (using IL-2) and 12.6% (using IL-2 + IL-15) of CD4⁺ T cells] and markedly increased production in IL-17-skewing conditions (medians, 41.5 and 35.5%, respectively) (Fig. 1E), breast V δ 1⁺ T cells produced negligible IL-17A under all circumstances (Fig. 1E).

To place the phenotypes of breast V δ 1⁺ T cells into context, similar analyses were performed on coextracted V δ 2⁺ and V δ 1⁻V δ 2⁻ $\gamma\delta$ T cells, on CD4⁺ and CD8⁺ $\alpha\beta$ T cells, and on CD3⁻ lymphocytes that will include NK and ILC. The greatest similarities to V δ 1⁺ T cells were shown by V δ 2⁺ and V δ 1⁻V δ 2⁻ $\gamma\delta$ cells and by CD8⁺ $\alpha\beta$ T cells, although some such cells expressed CD28, and CD8⁺ $\alpha\beta$ T cells were more uniformly CD103⁺ (fig. S1D). NK and ILC were also similar to V δ 1⁺ T cells except that they uniformly lacked PD-1. Last, and as anticipated, CD4⁺ $\alpha\beta$ T cells lacked NKG2D expression and were mostly CD28⁺ and CD103⁻ (fig. S1D), consistent with a recently described tissue-resident CD4⁺ phenotype (55).

Upon activation, breast-associated CD8⁺ $\alpha\beta$ T cells were functionally most similar to V δ 1⁺ T cells in their T_{c1} phenotype, showing an even greater frequency of IFN- γ -producing cells (fig. S1E). Likewise, breast-explanted CD4⁺ $\alpha\beta$ T cells included more IL-13 producers than did V δ 1⁺ T cells. In sum, the healthy breast harbored a complex lymphoid ecosystem of multiple cell types with related but distinct phenotypes.

Human breast V δ 1⁺ T cells are innate-like

Murine skin-resident $\gamma\delta$ T cells can respond in vivo to NKG2D ligand up-regulation without overt TCR stimulation (5). In relation to cancer, this is potentially important because NKG2D ligands are up-regulated by DNA damage (8) and EGFR overactivity (9). We therefore investigated whether breast-explanted V δ 1⁺ T cells would respond to plate-bound recombinant MICA protein, an NKG2D ligand commonly expressed by tumors. MICA provoked a subset of V δ 1⁺ T cells to produce TNF and IFN- γ and to up-regulate CD107a in a response inhibited by anti-NKG2D (Fig. 2A). Conversely, CD8⁺ $\alpha\beta$ T cells within the identical grid cultures did not make significant responses to MICA relative to controls (Fig. 2A and fig. S2A), whereas both cell types showed increased responses when MICA was provided as a costimulator to anti-CD3 (Fig. 2B) (56, 57). The innate-like responsiveness of other breast $\gamma\delta$ T cells was challenging to examine because even in cases where they composed a greater proportion of tissue $\gamma\delta$ T cells, non-V δ 1⁺ cells were usually too few to assay reliably (fig. S2B). Despite this, we observed some NKG2D-dependent,

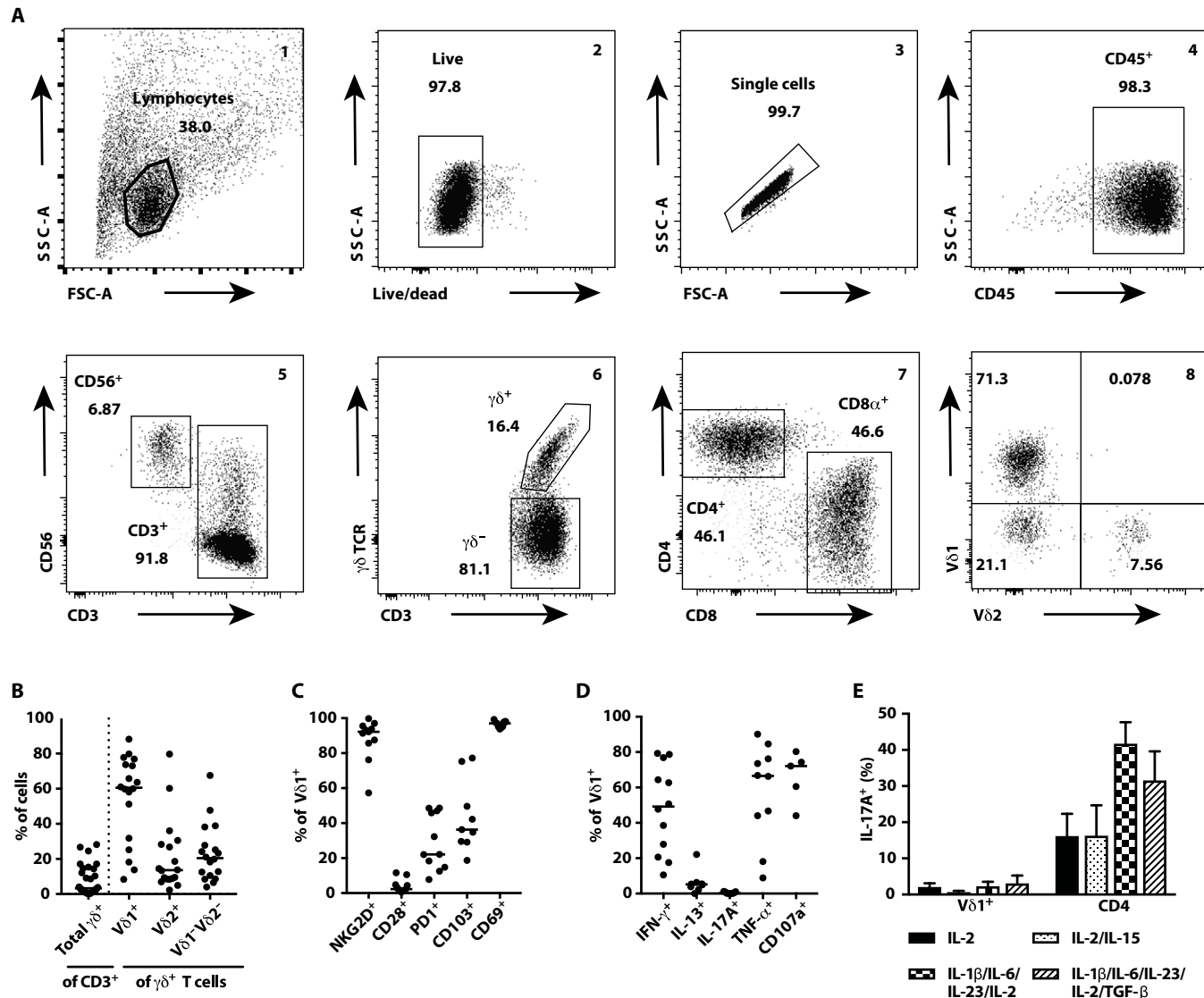


Fig. 1. Healthy human breast tissue harbors tissue-resident Vδ1⁺, Tc1-skewed γδ T cells. (A) Representative flow cytometry plots showing the gating strategy to identify lymphocytes including γδ T cell subsets isolated from human breast tissue and following grid culture. Lymphocytes were gated on size and scatter (1), followed by live-dead exclusion (2), a singlet gate (3), and CD45 (4) before subsetting (5 to 8). (B) Summary dot plots showing TCRγδ⁺ cells isolated from healthy human breast tissue, expressed as a percentage of recovered CD3⁺ cells (n = 29) (median indicated). In a subset of these, Vδ chain usage was quantified and expressed as percentage of pan-TCRγδ⁺ (n = 18) (medians indicated). (C) Expression of cell surface markers NKG2D, CD28, PD-1, CD103, and CD69 on Vδ1⁺ T cells (n = 9 to 11) (medians indicated). (D) Functional phenotype of tissue-resident Vδ1⁺ T cells. Dot plots showing intracellular cytokine staining for IFN-γ (n = 12), IL-13 (n = 8), IL-17A (n = 9), TNF (n = 10), and cell surface CD107a (n = 5) expression, after in vitro stimulation of bulk CD3⁺ cultures with PMA and ionomycin (4 hours) (medians indicated). (E) Summary data showing the percentages of breast-resident Vδ1⁺ or CD4 αβ T cells stained intracellularly for IL-17A. Cells were isolated by explant culture and then grown in two forms of IL-17-skewing media, followed by in vitro activation with PMA and ionomycin (4 hours) (n = 3, except for Vδ1⁺ cells grown in TGF-β-containing medium, where n = 2) (mean with SEM indicated).

innate-like responses among Vδ1⁻ Vδ2⁻ T cells but not among breast Vδ2⁺ T cells (fig. S2B).

It was also reported that innate-like γδ T cells make strong, TCR-independent responses to combinations of a STAT (signal transducer and activator of transcription)-signaling cytokine and an IL-1 family member (58). Breast-explanted Vδ1⁺ T cells produced IFN-γ in response to IL-12 + IL-18 but not to either alone, whereas CD4⁺ and CD8⁺ αβ T cells responded significantly less well to IL-12 + IL-18 (fig. S2C). In sum, the healthy breast harbored a mixture of innate-like Vδ1⁺ T cells and primarily adaptive αβ T cells.

Innate-like γδ T cells in human breast cancers

The identification of innate-like γδ T cells in healthy human breast formed a backdrop to examining the tissue-associated lymphoid compartment in breast cancer subjects. Although breast cancers vary in lymphoid infiltrates (32, 59), γδ T cells were invariably recovered and were largely comparable to those from healthy tissue in terms of TCR usage: Vδ1 was predominant, although the tumor samples included some examples where either Vδ2⁺ cells or Vδ1⁻Vδ2⁻ cells predominated (fig. S3A). As with γδ T cells from healthy breast, cells isolated from tumors using grids were phenotypically comparable

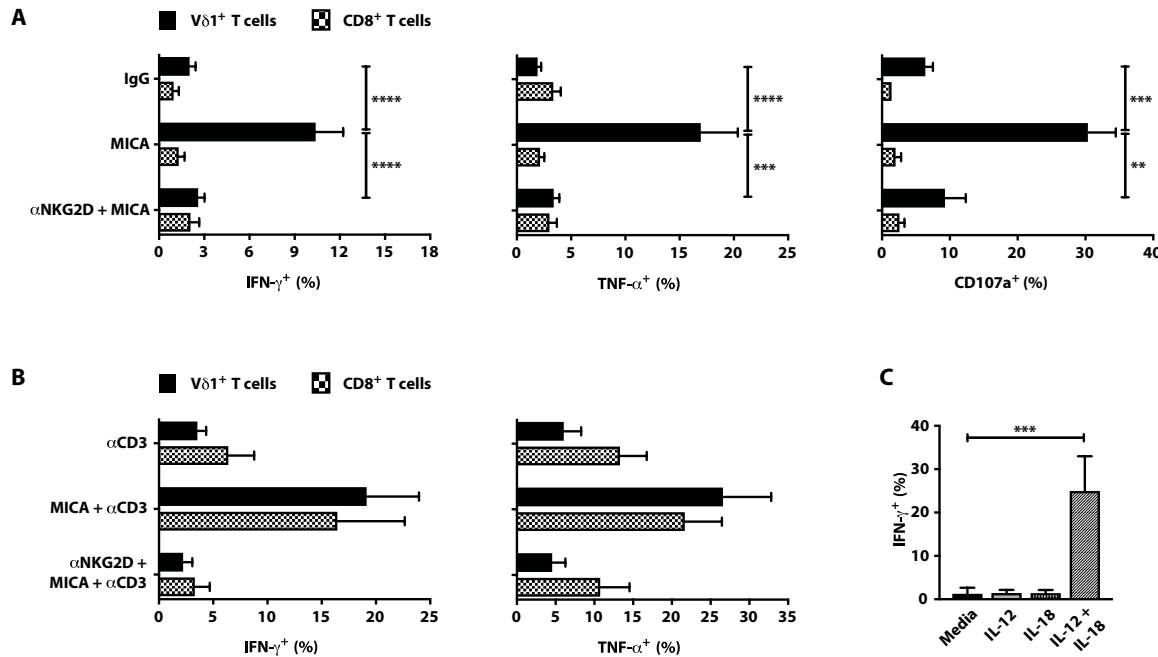


Fig. 2. Breast tissue–resident V δ 1 $^+$ T cells are innate-like. (A) Summary data showing intracellular staining for IFN- γ ($n = 19$ for V δ 1 $^+$ and $n = 15$ for CD8 $^+$), TNF ($n = 17$ for V δ 1 $^+$ and $n = 13$ for CD8 $^+$), and cell surface CD107a ($n = 10$ for V δ 1 $^+$ and $n = 5$ for CD8 $^+$) expression, after in vitro activation of breast-resident V δ 1 $^+$ cells or of V δ 1 $^+$ and CD8 $^+$ $\alpha\beta$ T cells from within the same cultures, exposed to plate-bound recombinant MICA (10 μ g/ml) in the presence of brefeldin A (BFA). Plotted as percentage of parent V δ 1 $^+$ or CD8 $^+$ gate. (B) Summary data showing intracellular staining for IFN- γ ($n = 6$ for V δ 1 $^+$ and $n = 6$ for CD8 $^+$) and TNF ($n = 5$ for V δ 1 $^+$ and $n = 5$ for CD8 $^+$) after in vitro activation of breast tissue–resident V δ 1 $^+$ and CD8 $^+$ $\alpha\beta$ T cells with low-dose plate-bound anti-CD3 antibody (50 ng/ml) with or without plate-bound recombinant MICA (10 μ g/ml) in the presence of BFA. Where indicated, MICA-stimulated cells were pretreated with anti-human NKG2D antibody (plotted as percentage of parent V δ 1 $^+$ or CD8 $^+$ gate). (C) Summary data for breast-resident V δ 1 $^+$ T cells, showing intracellular IFN- γ production after in vitro activation with IL-12 ($n = 3$) or IL-18 ($n = 3$) or IL-12 + IL-18 ($n = 9$) and with medium alone ($n = 9$). For all panels, mean with SEM is indicated. ** $P \leq 0.01$, *** $P \leq 0.001$, and **** $P \leq 0.0001$, Kruskal-Wallis with post hoc Dunn's test corrected for multiple testing.

with those examined directly ex vivo, albeit grid cells again showed higher expression of CD69 and, to some extent, NKG2D (fig. S3B). The similarities of TCR usage and surface marker expression for $\gamma\delta$ T cells from tumor and nonmalignant tissue were particularly apparent in paired samples from 26 subjects (Fig. 3A and fig. S3C). Moreover, this comparability extended to other lymphocyte subsets simultaneously harvested from the paired samples (fig. S3D).

Likewise, the functional potential of V δ 1 $^+$ TILs was comparable to those of nonmalignant breast V δ 1 $^+$ T cells, in being T_{c1} skewed and IL-17 deficient (Fig. 3B). V δ 1 $^+$ TILs were again responsive to NKG2D ligands and IL-12 + IL-18 in the absence of overt $\gamma\delta$ TCR signaling, whereas co-isolated CD8 $^+$ $\alpha\beta$ TILs did not show significant responses to MICA relative to controls, although they did respond better to IL-12 + IL-18 than did counterparts from healthy breast (Fig. 3C).

Given their strong cytolytic responsiveness, we tested the capacity of breast-derived $\gamma\delta$ T cells to kill two breast tumor cell lines, MCF7 and HCC1954, for which tumor cell lysis was distinguished from lymphocyte death by quantitating cytokeratin 18 release (60). Note that because $\gamma\delta$ T cells are not MHC (major histocompatibility complex)-restricted, it was possible to assess their functional responses to nonautologous tumor lines. $\gamma\delta$ T cells from healthy breast donors ($n = 4$) reproducibly killed MCF7 cells at an effector:target (E:T) ratio of 5:1 (fig. S3E), and using this ratio, we found that cells from healthy breast and from tumor samples ($n = 4$) showed comparable capacity to kill MCF7 and HCC1954 (Fig. 3D). However, whereas NKG2D receptor blockade reduced killing by $\gamma\delta$ T cells from healthy

breast, killing by TCR $\gamma\delta$ $^+$ TILs was less affected (Fig. 3D). We also observed primary tumor cell killing by autologous TCR $\gamma\delta$ $^+$ TILs for the one patient from whom primary tumor cells could be grown and stably maintained (fig. S3F). In sum, primary $\gamma\delta$ T cells obtained from breast cancers were functionally competent, could respond innately via NKG2D engagement, and could lyse breast tumor cells, albeit this was not overtly NKG2D dependent.

V δ 1 $^+$ TILs and durable remission

Given the functional T_{c1} skew of $\gamma\delta$ TILs, we wished to examine their status in relation to clinical outcome in an aggressive subset of breast cancer where time to events is relatively short. To this end, we sought patients with triple-negative breast cancer (TNBC) from whom we could access sufficient paired tumor and nonmalignant tissues and for whom accurate clinical follow-up data were available. Those criteria were met by 11 patients treated at Guy's and St Thomas' Hospitals, London (BTBC study REC no.: 13/LO/1248), for whom there were biobanked, formalin-fixed paraffin-embedded (FFPE) samples. Patients were otherwise unselected. All patients had localized or locoregional TNBC [American Joint Committee on Cancer (AJCC) stage I to III] and had surgery with curative intent. Five of 11 remained in complete remission at last follow-up (range, 48 to 63 months; table S2; demarcated in blue in the figures that follow), whereas six had relapsed with distant metastatic disease within 18 months (range, 6 to 18 months; table S2; demarcated in red in the figures that follow).

FFPE blocks were needle-dissected to delineate tumor and nonmalignant tissue for genomic DNA extraction. Given the difficulty

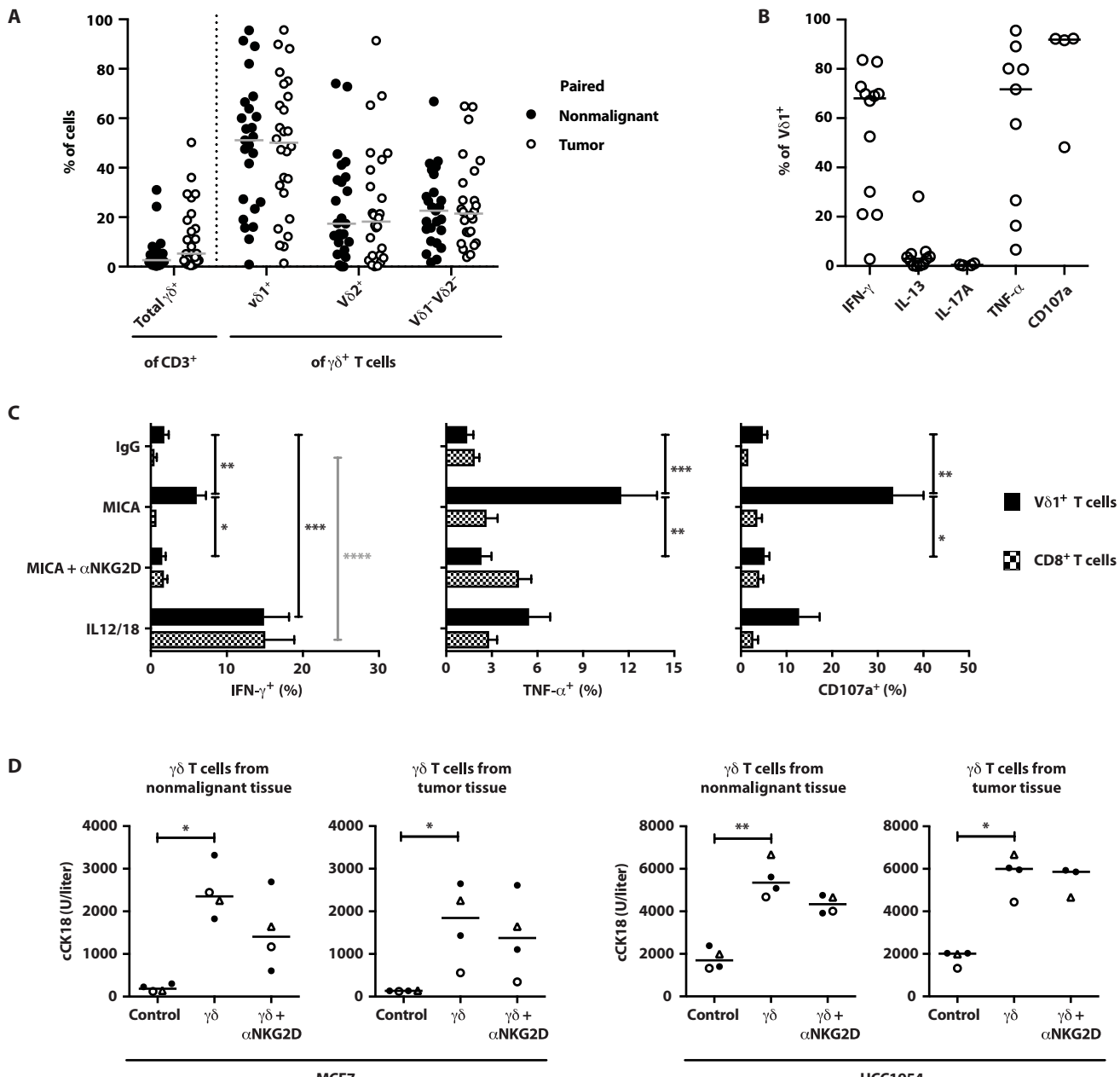


Fig. 3. Innate-like $\nu\delta 1^+$ Tc1 cells are a major subset of breast TILs. (A) $\gamma\delta$ T cells were consistently isolated from human breast tumor samples obtained from mastectomies after grid culture. Dot plots showing numbers of TCR $\gamma\delta^+$ cells isolated from paired nonmalignant breast tissue (●) or tumor (○) expressed as a percentage of CD3⁺ T cells. $\gamma\delta$ T cells were further phenotyped for $\nu\delta 1^+$, $\nu\delta 2^+$, and $\nu\delta 1\nu\delta 2^-$ TCR usage expressed as a percentage of TCR $\gamma\delta^+$ T cells ($n = 25$) (medians indicated). (B) Breast tumor-infiltrating $\nu\delta 1^+$ T cells are functionally skewed. Dot plots showing intracellular cytokine staining for IFN- γ ($n = 12$), IL-13 ($n = 11$), IL-17A ($n = 4$), TNF ($n = 9$), and cell surface CD107a expression ($n = 4$), after in vitro activation with PMA (10 ng/ml) and ionomycin (1 μ g/ml) in the presence of BFA (medians indicated). (C) Summary data showing intracellular staining for IFN- γ ($n = 9$ to 12, depending on activating condition), TNF ($n = 7$), and cell surface CD107a ($n = 4$ to 7, depending on activating condition) expression after in vitro activation of $\nu\delta 1^+$ and CD8⁺ $\alpha\beta$ T cells with plate-bound recombinant MICA (10 μ g/ml) in the presence of BFA or in vitro activation with IL-12 (100 ng/ml) and IL-18 (100 ng/ml). Where indicated, MICA-stimulated cells were pretreated with blocking anti-human NKG2D antibody (mean with SEM indicated). (D) Tumor cell lines, MCF7 and HCC1954, were incubated with negatively sorted $\gamma\delta$ T cells ($\gamma\delta$) derived from nonmalignant breast tissue or breast tumor at E:T of 5:1, in the presence ($\gamma\delta + \alpha$ NKG2D) or absence ($\gamma\delta$) of a blocking anti-NKG2D antibody for 48 hours. Cell lines without effector $\gamma\delta$ T cells were used as negative controls (Control). Dot plots show concentrations of caspase-cleaved cytokeratin 18 (cCK18). Each data point represents the mean of two technical replicates; the median values for those data points are indicated by a horizontal line (note that there were only three donors for the killing assay of HCC1954 cells by tumor-derived $\gamma\delta$ T cells in the presence of anti-NKG2D). ▲ and ○ are two donors for which there were paired nonmalignant breast tissue and breast tumor. * $P < 0.05$, ** $P \leq 0.01$, *** $P \leq 0.001$, and **** $P \leq 0.0001$, Kruskal-Wallis with post hoc Dunn's test corrected for multiple testing.

of immunohistochemical approaches in detecting $\gamma\delta$ T cells in FFPE (61), we used quantitative genomic DNA sequencing of rearranged TCR α and TCR δ chain genes to infer absolute counts of $\alpha\beta$ and $\gamma\delta$ T cells. This approach has been shown to be more sensitive than immunohistochemistry for detecting TILs (29) and is used clinically, for example, to assess minimal residual disease.

We found that both $\alpha\beta$ and $\gamma\delta$ T cells were significantly more abundant per microgram of DNA extracted from tumor tissue versus paired nonmalignant tissue (Fig. 4A and fig. S4A). However, it was notable that in cases of remission, the numbers of TCR α , TCR $\gamma\delta$, TCRV $\delta 1$, and TCRV $\delta 2$ DNAs were invariably enriched in paired malignant versus nonmalignant tissue, whereas the pattern in relapsed cases was essentially random (fig. S4A). Moreover, in addition to enrichment relative to healthy tissue, there were conspicuously more TCR α^+ and V $\delta 1^+$ TCRs per microgram of total tumor DNA in remission cases versus relapse (Fig. 4B). Thus, in indicating positive clinical outcome, the dynamics of small numbers of V $\delta 1^+$ T cells were as potent as the much larger-scale dynamics of $\alpha\beta$ T cells, defined subsets of which have been shown to predict survival in TNBC (62). Conversely, this was not so for either total TCR $\gamma\delta$ or V $\delta 2$ TCRs (Fig. 4B), the latter possibly reflective of cells infiltrating from the PB.

Notable manifestations of the correlations were evident from Kaplan-Meier plots of progression-free survival (PFS), where limited representation (less than median values) of intratumoral TCR α and V $\delta 1$ TCRs was predictive of poor PFS, whereas neither total TCR $\gamma\delta$ nor V $\delta 2^+$ TCRs predicted outcome (Fig. 4C). Furthermore, there was a positive and significant correlation of intratumor TCR α with V $\delta 1$ TCRs (Spearman $r = 0.75$, $P \leq 0.01$) (fig. S4B), whereas neither total TCR $\gamma\delta$ nor V $\delta 2$ TCRs correlated with TCR α . Moreover, no TCR α -TCR δ correlation existed in nonmalignant tissue (fig. S4B). In addition, V $\delta 1$ TCRs predicted overall survival (OS), although TCR α did not (Fig. 4D).

In situ evidence of innate-like V $\delta 1^+$ TILs

Having established significant positive correlates of TCR $\alpha\beta^+$ T cells with PFS and of V $\delta 1^+$ T cells with PFS and OS, we assessed their TCR repertoires. When represented as circular tree plots, the V $\delta 1^+$ repertoires in tumors compared to paired nonmalignant tissue showed no clear overall focusing (examples shown in Fig. 5A), as quantitated by D50 (the smallest number of clones accounting for 50% of the total number of sequences observed) from paired nonmalignant and tumor tissues (table S3). Focusing would have suggested an adaptive TCR-driven response, as we observed for the TCR α repertoires of most tumors versus paired normal tissue (examples shown in Fig. 5B), consistent with previous reports (62, 63).

To further analyze the data, we also calculated the Gini coefficient (a statistical measure of distribution where 0 is fully polyclonal and 1 is monoclonal) for V $\delta 1$ TCRs from paired nonmalignant and tumor tissues (table S3). Note that the tumor TCRs were down-sampled so that equivalent numbers of TCRs were compared within each patient. The same treatment was then applied to TCR α , although we considered only the most abundant 10% of TCR α TCRs, given recent evidence that the most relevant antigen-reactive $\alpha\beta$ T cells commonly sit within this fraction (64). For each patient, we then calculated the delta of the Gini coefficient of paired tumor tissues and nonmalignant tissues for both V $\delta 1$ and TCR α : Note that tumor focusing would be reflected by positive Δ Gini coefficient (Fig. 5C). We then likewise calculated the delta of the D50 values for paired tumor and nonmalignant tissues for both V $\delta 1$ and TCR $\alpha\beta$: Note that tumor focusing

would be reflected by negative Δ D50 (Fig. 5C). These analyses confirmed quantitatively that TCR α repertoire focusing occurred in all but two tumor samples (KCL-059 and KCL-202), whereas V $\delta 1$ repertoires showed no bias either toward focusing or toward diversification (Fig. 5C).

As a complementary approach, we also applied repertoire metrics to non-down-sampled (raw) TCR reads, using normalized measures of clonality (normalized Shannon entropy, Gini coefficient, and D50), as previously used by others (29, 63). These methods also suggested tumor repertoire focusing for TCR α (significance was reached for D50), whereas there was no such finding for V $\delta 1$ (fig. S5 and table S4). Collectively, these data strongly suggest that the V $\delta 1^+$ cell responses were not driven by clonotypic antigens.

Given that, among TCR gene rearrangements, TCR δ harbors the highest potential for junctional diversity (65), it was not surprising that no public V $\delta 1$ sequences were observed across different donors' tumors (Fig. 6A). However, there was some V $\delta 1$ sequence overlap between tumors and tissue from the same donor (fig. S6). Although the sample size was small, the lack of public sequences would also be consistent with TCR-agnostic, innate-like regulation of tissue-resident V $\delta 1^+$ T cells. By contrast, assessment of a comparably sized sample showed that some V $\delta 2$ TCRs were shared across multiple donors (Fig. 6B). Most shared sequences reflected TCRs reactive to phospho-antigens that can be up-regulated in tumors (66), with a conserved hydrophobic residue in position 97 (table S5) specifically associated with phospho-antigen-mediated selection of the V $\delta 2^+$ repertoire (67, 68).

DISCUSSION

The past decade has witnessed a sea change in cancer immunology, with the realization that tumors are often antigenic and that tumor-reactive T cells can provide patient-beneficial responses, particularly if derepressed by checkpoint blockade (69, 70). Hence, there is considerable interest in the immune ecology of tumors. Over the same period, it became clear that several extralymphoid tissues in which tumors commonly form ordinarily harbor large myeloid and lymphocyte compartments, including $\gamma\delta$ T cells that become tissue resident during the cells' development and systemic $\alpha\beta$ T cells that become T_{RM} cells after priming in secondary lymphoid organs (71, 72).

Although positive clinical outcomes in TNBC have been associated with CD8 $^+$ TCR $\alpha\beta^+$ T_{RM} cells (62), there has been little investigation of whether a human breast-resident $\gamma\delta$ T cell compartment exists that might influence breast cancer outcomes (73). This study addresses this point by first establishing a tissue-resident $\gamma\delta$ T cell compartment in healthy human mammary tissue. This may be evolutionarily conserved because TCR $\gamma\delta^+$ lymphocytes were reported in alveolar mammary epithelia of lactating cows (74) and were associated with lactating mammary glands in mice (26). To characterize human breast-resident $\gamma\delta$ T cells in sufficient numbers, we used grid cultures previously used to elucidate key features of human skin and lung T cells (35–38). Although this is a limitation, there was strong phenotypic consistency with breast $\gamma\delta$ T cells examined directly ex vivo. This permitted our description of the compartment as mostly V $\delta 1^+$, NKG2D $^+$, CD69 $^+$, partly CD103 $^+$, and with a T_{c1} phenotype lacking IL-17 production. This is very distinct from PB $\gamma\delta$ T cells but shares features with human intestinal epithelial $\gamma\delta$ T cells (40).

In addition, human breast $\gamma\delta$ T cells were innately responsive to NKG2D activators, whereas collocated $\alpha\beta$ T cells required coincident TCR stimulation. Thus, healthy human breast V $\delta 1^+$ cells have an

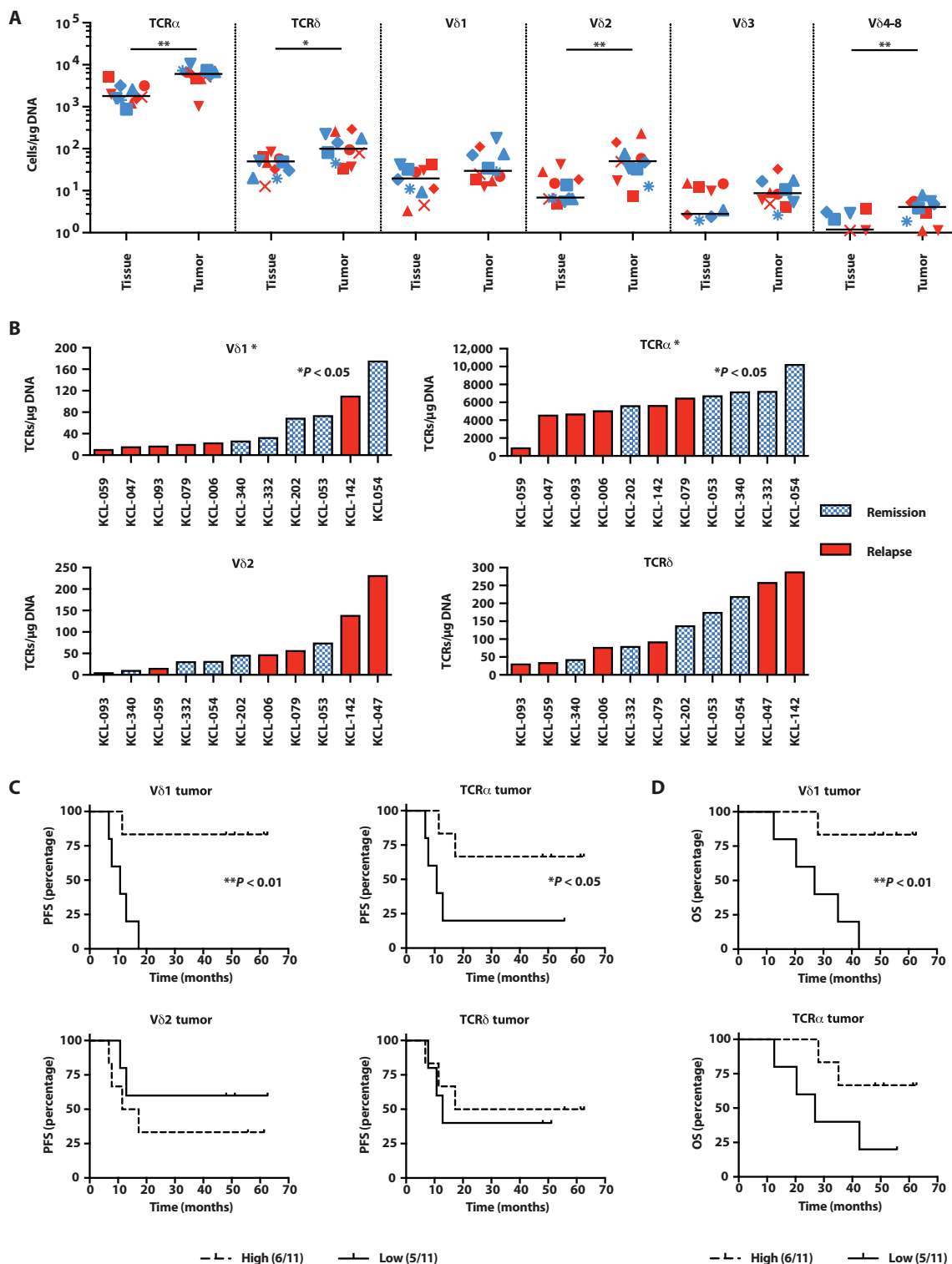


Fig. 4. V δ 1 $^+$ T cells in TNBC are predictive of disease-free survival and OS. **(A)** Overall landscape of T cell subsets in nonmalignant breast tissue (“Tissue”) and matched tumor tissue (“Tumor”), determined by quantitative sequencing of rearranged TCR genes from patients undergoing mastectomy for TNBC. Absolute TCR copies (a surrogate for T cell numbers) are plotted per microgram of input DNA. Individual patients plotted: red, patients with relapsed disease; blue, patients in remission (median bar plotted). *P < 0.05 and **P ≤ 0.01, Wilcoxon matched pairs signed rank test. **(B)** Intratumoral presence of $\alpha\beta$ T cells and $\gamma\delta$ T cells in patients with subsequent relapsed disease versus those who remained in remission. *P < 0.05, Kolmogorov-Smirnov test. **(C)** PFS (months from surgery) split on median T cell subsets found in 11 TNBC tumors. *P < 0.05 and **P ≤ 0.01, Gehan-Breslow-Wilcoxon test. **(D)** OS (months from surgery) split on median T cell subsets found in 11 TNBC tumors. *P < 0.05 and **P ≤ 0.01, Gehan-Breslow-Wilcoxon test.

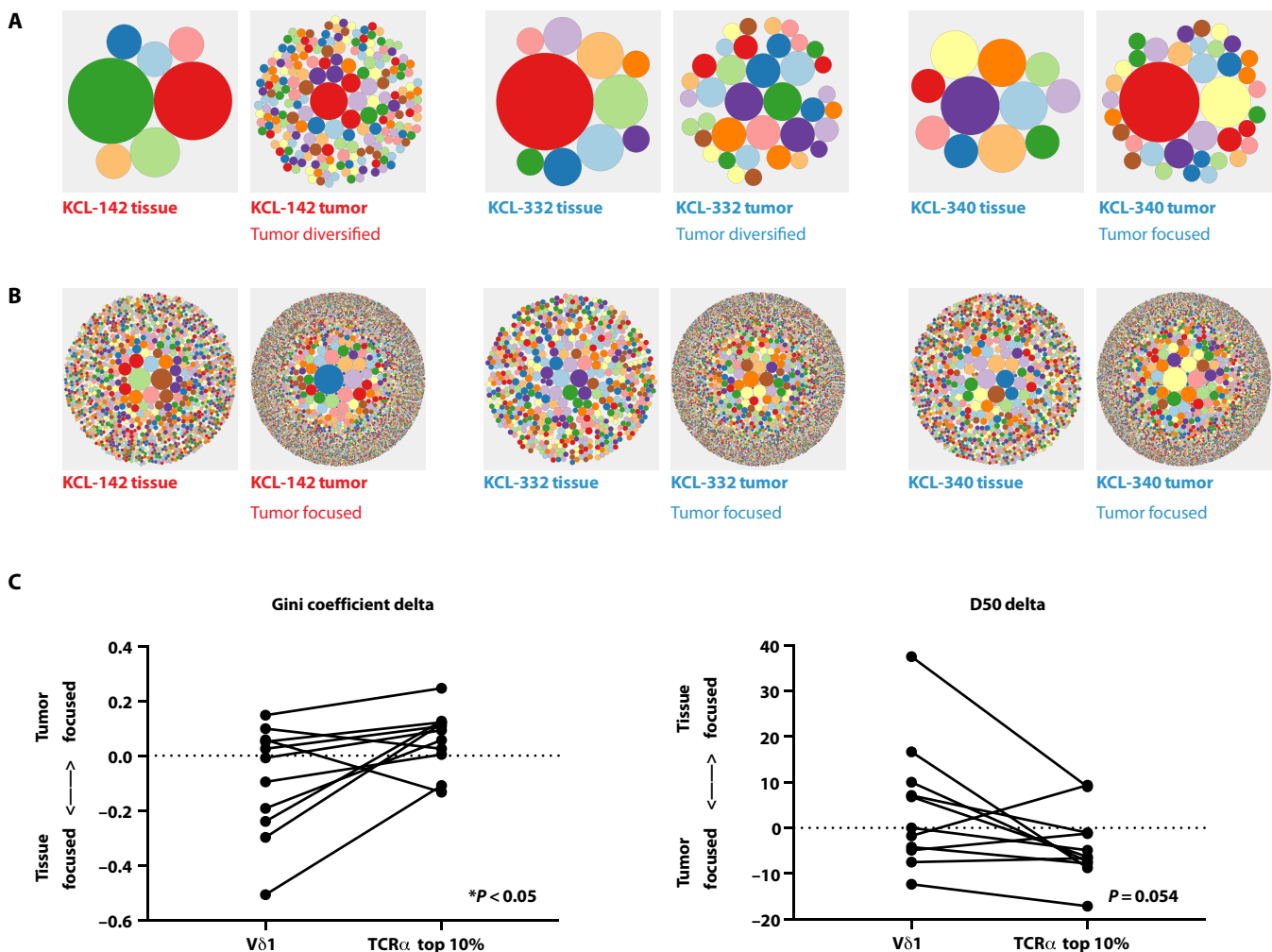


Fig. 5. Lack of tumor V δ 1 $^+$ TCR focusing relative to focusing of TCR α sequences. (A) Examples of circular tree plots of the V δ 1 $^+$ repertoire in paired nonmalignant tissue (“tissue”) and tumor tissue (“tumor”), where each circle represents a unique TCR clonotype and the size of the circle is proportional to the representation of the specified clone. Plots were generated from total V δ 1 $^+$ TCRs. (B) Examples of circular tree plots of the TCR α repertoire in paired nonmalignant tissue (“tissue”) and tumor tissue (“tumor”). Plots were generated from total TCR α $^+$ TCRs. (C) V δ 1 $^+$ and TCR α $^+$ sequences in nonmalignant and tumor tissue were down-sampled (within each patient) to equivalent numbers to calculate diversity metrics. The degree of repertoire focusing was assessed by the delta of the Gini coefficient and the delta D50 of sequences of V δ 1 chains and the top 10% in abundance of TCR α sequences in tumor versus paired nonmalignant repertoires. To test whether the degree of repertoire focusing was different between V δ 1 $^+$ and TCR α $^+$ compartments in individual patients, the Wilcoxon matched pairs signed-rank test was used to compare Δ Gini and Δ D50. All sequences were analyzed on the basis of amino acid sequence. $n = 11$.

inherent potential to detect and respond rapidly to local cells en route to malignancy. Some of these signature properties may be shared with local V δ 1 $^-$ V δ 2 $^+$ T cells, which are often V δ 3 $^+$, although these cells were most often present in very small numbers.

Within breast tumors, V δ 1 $^+$ T cells and $\alpha\beta$ T cells were frequently more abundant than in paired healthy tissue, particularly in patients in remission. This likely reflects an inflection point at which an activating immune response to the tumors occurred. Furthermore, when extracted from breast tumors, the comparatively expanded V δ 1 $^+$ and $\alpha\beta$ T cell populations were functionally competent, retaining the innate responsiveness and T_c1 potential of cells from healthy breast. These observations evoked evidence that PD-1 $^+$ breast cancer TILs responded functionally to restimulation (75) and that their presence could be associated with favorable outcome (62). Although only few patients were available for in-depth analysis in this study, they were sufficient to show significant positive correlations of tumor-derived

V δ 1 $^+$ and $\alpha\beta$ T cells with clinical outcome, with V δ 1 TCRs correlating with both PFS and OS. It is therefore attractive to hypothesize that maximum patient benefit accrues from a collaboration of the innate responsiveness of local V δ 1 $^+$ cells with the antigen-specific modus operandi of $\alpha\beta$ T cells, particularly CD8 $^+$ TCR $\alpha\beta$ $^+$ T_{RM} cells (62).

At least two patient-beneficial facets of collaboration between V δ 1 $^+$ and TCR $\alpha\beta$ $^+$ T cells may be envisioned. First, by recognizing tumors via innate stimuli, V δ 1 $^+$ T cell responses may not be limited either by the number of neoantigen-generating somatic mutations or by immune-evasive suppression of peptide antigen presentation (47, 76–79). The innate stimuli may include ligands for several NK receptors (43), including but not limited to NKG2D.

Second, the cytolytic, T_c1 phenotype of V δ 1 $^+$ cells may be augmented by the cells’ capacity to promote tissue immunogenicity via chemokine secretion and possibly via direct antigen presentation (16, 17, 80). A critical role of tissue-resident V δ 1 $^+$ cells may be to orchestrate

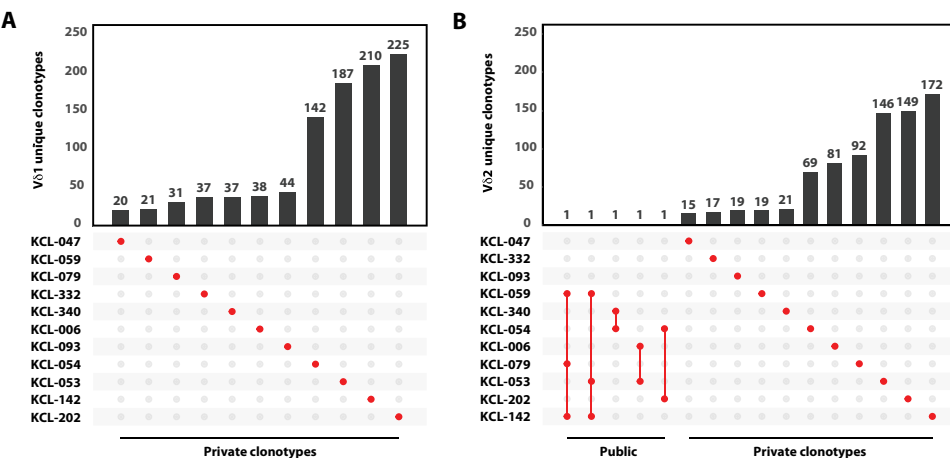
Fig. 6. No detectable public intratumoral V δ 1 $^+$ clonotypes. (A) Intersections of V δ 1 $^+$ clonotypes between 11 patient tumor samples. Vertical bars represent the number of unique TCRs and the dot matrix represents sharing of TCRs across patients. A shared or public clonotype would be represented by at least two red dots (sharing between two patients) joined by a vertical red line. Private sequences are presented by an unconnected single red dot. (B) Intersections of V δ 2 $^+$ clonotypes between 11 patient tumor samples. All sequences were analyzed on the basis of amino acid sequence.

multicomponent local immune responses to defined challenges while remaining tolerant to others. In this context, tissue/tumor immunogenicity might be effectively enhanced in the clinic by agents promoting the activities of local V δ 1 $^+$ T cells, or by the cells' adoptive transfer, in concert with the activation/derepression of adaptive T cells. Because $\gamma\delta$ T cells are not MHC-restricted, they might be adoptively transferred from heterologous donors, and because they are naturally tissue resident, local V δ 1 $^+$ cells may cope with hypoxic environments that prove hostile to systemic lymphocytes (81, 82).

Such considerations may pertain to other human tissues harboring local $\gamma\delta$ T cell compartments, such as the gut, and may underpin reportedly strong correlations of $\gamma\delta$ T cells with favorable clinical outcomes across a broad spectrum of human tumors (83). Nonetheless, in this study, neither total $\gamma\delta$ TCRs nor V δ 2 $^+$ TCRs correlated with clinical outcome. This emphasizes the fact that $\gamma\delta$ T cells comprise biologically distinct subsets, as is the case for $\alpha\beta$ T cells or ILCs. Even among intratumoral CD8 $^+$ T cells, which are traditionally associated with patient benefit, most benefit in TNBC was attributable to a discrete subset of local CD8 $^+$ T_{RM} cells (62). In mice, functionally different $\gamma\delta$ T cell subsets have been reported to either mediate or repress tumor immunosurveillance (84, 85). Most often, IL-17 has been implicated in tumor promotion by $\gamma\delta$ T cells (50–52), whereas IL-17-producing cells are seemingly rare in humans, wherein the predominant phenotype is cytolytic and TNF/IFN- γ producing (86), as described here.

In mice, the innate responsiveness of $\gamma\delta$ T cells and their suppression of IL-17 production were induced developmentally by subset-specific, tissue-specific selecting elements of the butyrophilin-like (Btlnl/BTNL) family, members of which can also regulate human $\gamma\delta$ T cells (30, 40, 58, 87). It is therefore possible that such elements act locally to select and regulate human breast-resident V δ 1 $^+$ T cells, in which regard the mammary gland is one of reportedly few tissues expressing BTNL9 (88).

Our study did not focus on interactions of breast V δ 1 $^+$ T cells with other breast-resident immune cells including B cells (32). Likewise, spatial relationships between breast $\gamma\delta$ T cells and tumor-associated tertiary lymphoid structures were not determined (31, 32). In practical terms, clinical studies have suggested that human breast cancer, including TNBC, can be vulnerable to immune attack (33, 34), yet the efficacy of immunotherapies in this indication has been relatively poor. We strongly believe that this may be redressed by shifting therapies away from their unique focus on conventional, adaptive T cell responses and by learning from the natural ecology of the local breast T cell compartment. In particular, we believe that this may



promote the immunogenicity of tumor tissues that drives and sustains patient-beneficial adaptive responses.

MATERIALS AND METHODS

Study design

The aim of this study was to ascertain whether the human breast might contain a tissue-resident $\gamma\delta$ T cell compartment and to determine whether this might be protective in breast cancers. This study was undertaken first by demonstrating the reproducible presence of $\gamma\delta$ T cells in healthy breast tissue with a particular focus on V δ chain usage. Then, we determined their functional potential and whether they might be consistent with protective tumor immunosurveillance. These approaches were subsequently applied to $\gamma\delta$ T cells in breast tumors. Colocated $\alpha\beta$ T cells isolated using the same protocol and maintained in the same culture conditions were used as controls. Having established the presence of $\gamma\delta$ T cells in human breast tissue and tumors and their innate-like immunosurveillance capacity in vitro, we examined the presence of these cells in situ (via their DNA rearrangements) and correlated this to prognosis in clinical samples. We also sought in situ evidence, particularly TCR repertoire clonality, for cells functioning in an innate-like immunosurveillance capacity, as was established ex vivo. Detailed study design, sample sizes, replicates, and inclusion/exclusion criteria are provided in the figure legends or in Materials and Methods. The sample sizes and experimental repetitions were sufficient to permit rigorous statistical analysis as described in the figure legends and Materials and Methods. All antibodies and key reagents are listed in table S6. Primary data are reported in data file S1.

Clinical material

Human breast samples were obtained from adult female patients undergoing breast reduction or risk-reducing mastectomy (29 patients) or breast tumor resection (90 patients) after informed consent as part of a noninterventional clinical trial (BTBC study REC no.: 13/LO/1248, IRAS ID 131133; principal investigator: A.T; study title: "Analysis of functional immune cell stroma and malignant cell interactions in breast cancer in order to discover and develop diagnostics and therapies in breast cancer subtypes"). This study had local research ethics committee approval and was conducted adhering to the principles of the Declaration of Helsinki. Specimens were collected from surgery into sterile saline and transported immediately to cut up.

A histopathologist or pathology-trained technician identified and collected tumor material and ipsilateral nonadjacent normal breast tissue from surgical specimens from which lymphocytes were subsequently isolated as described below. Demographics of the patients are detailed in table S2. In addition to the patients above, for TCR sequencing experiments, tumor and paired nonmalignant tissue DNA was extracted from bio-banked FFPE blocks from 11 patients with AJCC stage I to III TNBC who had mastectomies for which we could access sufficient material and accurate clinical follow-up data. No other criteria were applied. The 11 cases were also part of the BTBC clinical trial described above.

Primary lymphocyte extraction and culture

For direct ex vivo isolation, fresh breast tumor or tissue was coarsely minced with scalpels and then dissociated using the MACS human tumor dissociation kit on a gentleMACS dissociator as per the manufacturer's instructions (Miltenyi Biotec). Samples were washed twice with sterile RPMI 1640 and used immediately for downstream assays. Lymphocytes were also harvested using a grid explant system adapted from a protocol first described by Clark and colleagues (35). Briefly, fresh breast tumor or tissue was minced using scalpels and placed onto rat tail collagen (100 µg/ml; BD Biosciences)-coated Cellfoam grids (Cytomatix Pty Ltd.). Each grid was placed into a separate well of a 24-well tissue culture plate and cultured in complete medium [Iscove's modified Dulbecco's medium (Life Technologies), 10% heat-inactivated fetal bovine serum (FBS; Life Technologies), L-glutamine (292 µg/ml; Life Technologies), penicillin (100 U/ml; Life Technologies), streptomycin (100 µg/ml; Life Technologies), and 2-mercaptoethanol (3.5 µl/liter; Life Technologies)] supplemented with recombinant human IL-2 (rhIL-2) (100 IU/ml; Proleukin; Novartis Pharmaceuticals UK Ltd.) and rhIL-15 (10 ng/ml; BioLegend). The grids were maintained for 3 weeks in culture at 37°C/5% CO₂, and the lymphocytes were harvested by washing the wells/grids with 0.01 mM Hepes/Hanks' balanced salt solution.

Flow cytometry and fluorescence-activated cell sorting

Cells were washed in sterile phosphate-buffered saline (PBS) to remove traces of serum and stained for 20 min at room temperature with LIVE/DEAD Fixable Aqua (Thermo Fisher Scientific) in PBS. Subsequent surface staining was carried out in fluorescence-activated cell sorting (FACS) buffer (PBS, 2% fetal calf serum, and 1 mM EDTA) for 20 min at 4°C (see table S6) before washing twice with FACS buffer and fixing with CellFIX (BD) for 10 min at room temperature. For intracellular cytokine staining, fixed cells were washed twice with Intracellular Staining Permeabilization Wash Buffer (BioLegend) and stained for 20 min at room temperature before two further washes with Intracellular Staining Permeabilization Wash Buffer. Samples were acquired on a BD FACSCanto II or BD LSRFortessa and were analyzed using FlowJo software (FlowJo LLC). For FACS, cells were not fixed and sorted on a BD FACSAria II as detailed below. Antibodies are listed in table S6 and were used at 1:50 dilution unless otherwise specified.

In vitro lymphocyte activation assays

Directly isolated and grid explant-isolated lymphocytes were stimulated with PMA (10 ng/ml; Sigma) and ionomycin (1 µg/ml; Sigma) in the presence of brefeldin A (BFA; 20 µg/ml; Sigma) for 4 hours at 37°C/5% CO₂ before surface marker and intracellular cytokine staining and acquisition on a BD FACSCanto or Fortessa. For plate-bound

NKG2D ligand assays, lymphocytes were harvested from explant cultures 24 hours before activation and rested in complete media without cytokine supplementation. After resting, lymphocytes were transferred to 96-well flat-bottom cell culture plates (Corning) coated with rhMICA (10 µg/ml; R&D Systems), anti-CD3 (50 ng/ml; BioLegend), anti-CD3 (50 ng/ml; BioLegend) and rhMICA (10 µg/ml; R&D Systems), or mouse immunoglobulin G2a (IgG2a) (50 ng/ml; BioLegend) at 100,000 cells per well in 100 µl of complete medium. Plates were incubated for 6 hours at 37°C/5% CO₂ in the presence of IL-15 (10 ng/ml; BioLegend) and BFA (20 µg/ml; Sigma). Where CD107a was used as a functional readout, anti-human CD107a antibody (1:400 final concentration; BioLegend) was also added at the start of the assay along with monensin at 1× (BioLegend). For NKG2D-blocking conditions, anti-NKG2D antibody (10 µg/ml; clone 1D11; BioLegend) was added to lymphocytes just before plating.

For cytokine activation assays, lymphocytes were incubated with IL-12 (100 ng/ml; PeproTech) and/or IL-18 (100 ng/ml; Medical and Biological Laboratories) for a total of 24 hours at 37°C/5% CO₂ with BFA (20 µg/ml; Sigma) added for the last 4 hours before surface and intracellular cytokine staining for flow cytometry. For IL-17-skewing assays, breast tissue explants were cultured in complete medium and in conditions as described above with the addition of rhIL-2 ± rhIL-15, rhIL-1β, rhIL-6, rhIL-23, and rhTGF-β for 3 days. These cells were then activated with PMA and ionomycin in the presence of BFA (20 µg/ml) for 4 hours at 37°C/5% CO₂ before surface and intracellular cytokine staining for flow cytometry.

Cytotoxicity assays

Grid explant-derived γδ T cells from breast tissues and tumors were isolated by FACS via depletion of TCRαβ⁺ and NKp46⁺ cells. Target cells, MCF7 and HCC1954 [Cancer Research UK (CRUK)/Francis Crick Institute Cell Service], were seeded at 10,000 cells per well in 96-well flat-bottom plates (Corning) 24 hours prior. Fifty thousand negatively sorted γδ T cells were added to target cells in the presence or absence of blocking NKG2D antibody (10 µg/ml; BioLegend). Cells were incubated at 37°C for 48 hours, after which supernatants were collected and stored at -20°C until further analysis. Target cell apoptosis was measured using enzyme-linked immunosorbent assay (ELISA) for the epithelial cell-specific caspase-cleaved cytokeratin 18 (Diapharma), according to the manufacturer's instructions.

Cell lines and culture conditions

Target MCF7 and HCC1954 cell lines were sourced from CRUK Cell Services (Clare Hall, London) and maintained in Dulbecco's modified Eagle's medium (Life Technologies), supplemented with 10% heat-inactivated FBS (Life Technologies), penicillin (100 U/ml; Life Technologies), and streptomycin (100 µg/ml; Life Technologies) at 37°C/5% CO₂. HCC1954 cells were maintained in RPMI 1640 (Gibco) supplemented with 10% heat-inactivated FBS (Life Technologies), penicillin (100 U/ml; Life Technologies), and streptomycin (100 µg/ml; Life Technologies) at 37°C/5% CO₂.

DNA extraction

DNA was extracted from FFPE paired tumor tissue and normal tissue blocks of 11 patients with TNBC treated with mastectomy as part of the BTBC study. Tumor tissue was needle microdissected after sectioning. The QIAamp DNA FFPE Tissue kit (Qiagen) was used per the manufacturer's instructions to extract DNA. DNA was quantified

using a Qubit fluorometer, and material from patients with $>1\ \mu\text{g}$ of DNA from both tumor and normal tissue was sent for quantitative TCR α/δ locus sequencing by Adaptive Biotechnologies.

TCR sequencing

TCR sequencing was performed by Adaptive Biotechnologies. The Adaptive Biotechnologies platform uses genomic DNA and can quantitate T cell numbers. Reads were aligned and annotated by Adaptive Biotechnologies, and data were output as .csv files (available from <https://osf.io/d4eu6/>) for downstream analysis from the immunoSEQ Analyzer (<https://clients.adaptivebiotech.com/login>). Output was filtered on in-frame CDR3s as well as TCR α to TCR α V-J family joins for TCR $\alpha\beta$ and TCRD to TCRD V-J family joins for TCR $\gamma\delta$ T cells. We normalized the absolute counts of TCRs to $1\ \mu\text{g}$ of input DNA for each sample to enable normalized comparison of infiltrating T cell numbers across all samples. All analyses were carried out using CDR3 amino acid sequences as opposed to nucleotide sequences.

Clonal repertoire analysis

To compare clonality metrics within each patient between paired tumor and nonmalignant tissue, we down-sampled TCRs from each pair of samples. For V δ 1, TCRs from tumor and nonmalignant tissue were down-sampled to the number of clones in the smaller sample with probability of drawing a clonotype equal to its frequency in the full sample. Down-sampling with replacement was performed 200 times. For TCR $\alpha\beta$, clonotypes were ordered in decreasing frequency, and the top 10% of total TCRs in each pair of tumor and nonmalignant tissue were used for down-sampling as described above. Clonality metrics were then applied to the down-sampled data, and the median values were plotted. As an alternative, we also applied normalized measures of clonality (normalized Shannon entropy, Gini coefficient, and D50) to the raw data. TreeMaps were generated using the Macro-focus TreeMap program (www.treemap.com). We visualized shared clonotype patients using the UpSet R package (<https://ieeexplore.ieee.org/abstract/document/6876017> and <https://vcg.github.io/upset>).

Statistical analysis

Statistical significance was determined by Kolmogorov-Smirnov test, log-rank test, Wilcoxon matched pairs signed-rank test, or Mann-Whitney test, as indicated in the figure legends using Prism 7 software (GraphPad). All findings were considered significant at a *P* value threshold of <0.05 . Where results of statistical test are shown, **P* < 0.05, ***P* ≤ 0.01, ****P* ≤ 0.001, and *****P* ≤ 0.0001 unless otherwise indicated.

SUPPLEMENTARY MATERIALS

stm.sciencemag.org/cgi/content/full/11/513/eaax9364/DC1

Fig. S1. Explant culture permitted the isolation of substantial numbers of human tissue-resident lymphocytes.

Fig. S2. V δ 1 $^+$ T cells display innate-like responsiveness.

Fig. S3. $\alpha\beta$ and $\gamma\delta$ T cells could be isolated from breast tumors and phenotypically resemble those from healthy tissue.

Fig. S4. Both $\alpha\beta$ and $\gamma\delta$ T cells are enriched in tumors compared with paired nonmalignant tissue.

Fig. S5. V δ 1 $^+$ T cells show no evidence of tumoral clonal focusing in contrast to $\alpha\beta$ T cells.

Fig. S6. There is limited V δ 1 repertoire overlap between tumor and paired nonmalignant tissue within patients.

Table S1. Lymphocyte subtypes observed ex vivo after enzymatic digestion and in grid explant cultures.

Table S2. Clinical features of KCL TNBC cohort.

Table S3. Clonality metrics of down-sampled TCRs.

Table S4. Clonality metrics of raw TCRs.

Table S5. Public intratumoral phospho-antigen reactive V δ 2 CDR3 sequences and samples in which they were shared.

Table S6. Antibodies and key reagents table.

Data file S1. Primary data.

[View/request a protocol for this paper from Bio-protocol](#).

REFERENCES AND NOTES

- A. C. Hayday, H. Saito, S. D. Gillies, D. M. Kranz, G. Tanigawa, H. N. Eisen, S. Tonegawa, Structure, organization, and somatic rearrangement of T cell gamma genes. *Cell* **40**, 259–269 (1985).
- M. B. Brenner, J. McLean, D. P. Dialynas, J. L. Strominger, J. A. Smith, F. L. Owen, J. G. Seidman, S. Ip, F. Rosen, M. S. Krangel, Identification of a putative second T-cell receptor. *Nature* **322**, 145–149 (1986).
- V. Groh, A. Steinle, S. Bauer, T. Spies, Recognition of stress-induced MHC molecules by intestinal epithelial $\gamma\delta$ T cells. *Science* **279**, 1737–1740 (1998).
- M. Girardi, D. E. Oppenheim, C. R. Steele, J. M. Lewis, E. Glusac, R. Filler, P. Hobby, B. Sutton, R. E. Tigelaar, A. C. Hayday, Regulation of cutaneous malignancy by $\gamma\delta$ T cells. *Science* **294**, 605–609 (2001).
- J. Strid, S. J. Roberts, R. B. Filler, J. M. Lewis, B. Y. Kwong, W. Schpfer, D. H. Kaplan, A. C. Hayday, M. Girardi, Acute upregulation of an NKG2D ligand promotes rapid reorganization of a local immune compartment with pleiotropic effects on carcinogenesis. *Nat. Immunol.* **9**, 146–154 (2008).
- D. H. Raulet, S. Gasser, B. G. Gowen, W. Deng, H. Jung, Regulation of ligands for the NKG2D activating receptor. *Annu. Rev. Immunol.* **31**, 413–441 (2013).
- A. C. Hayday, $\gamma\delta$ T cells and the lymphoid stress-surveillance response. *Immunity* **31**, 184–196 (2009).
- S. Gasser, S. Orsulic, E. J. Brown, D. H. Raulet, The DNA damage pathway regulates innate immune system ligands of the NKG2D receptor. *Nature* **436**, 1186–1190 (2005).
- P. Vantourout, C. Willcox, A. Turner, C. M. Swanson, Y. Haque, O. Sobolev, A. Grigoriadis, A. Tutt, A. Hayday, Immunological visibility: Posttranscriptional regulation of human NKG2D ligands by the EGF receptor pathway. *Sci. Transl. Med.* **6**, 231ra49 (2014).
- V. Groh, R. Rhinehart, H. Sechrist, S. Bauer, K. H. Grabstein, T. Spies, Broad tumor-associated expression and recognition by tumor-derived $\gamma\delta$ T cells of MIC α and MIC β . *Proc. Natl. Acad. Sci. U.S.A.* **96**, 6879–6884 (1999).
- M. Girardi, E. Glusac, R. B. Filler, S. J. Roberts, I. Propperova, J. Lewis, R. E. Tigelaar, A. C. Hayday, The distinct contributions of murine T cell receptor (TCR) $\gamma\delta$ + TCR $\alpha\beta$ + T cells to different stages of chemically induced skin cancer. *J. Exp. Med.* **198**, 747–755 (2003).
- Y. Gao, W. Yang, M. Pan, E. Scully, M. Girardi, L. H. Augenlicht, J. Craft, Z. Yin, $\gamma\delta$ T cells provide an early source of interferon γ in tumor immunity. *J. Exp. Med.* **198**, 433–442 (2003).
- Z. Liu, I.-E. A. Eltoum, B. Guo, B. H. Beck, G. A. Cloud, R. D. Lopez, Protective immunosurveillance and therapeutic antitumor activity of $\gamma\delta$ T cells demonstrated in a mouse model of prostate cancer. *J. Immunol.* **180**, 6044–6053 (2008).
- J. P. Fisher, J. Heijerijns, M. Yan, K. Gustafsson, J. Anderson, $\gamma\delta$ T cells for cancer immunotherapy: A systematic review of clinical trials. *Oncimmunology* **3**, e27572 (2014).
- M. Girardi, J. Lewis, E. Glusac, R. B. Filler, L. Geng, A. C. Hayday, R. E. Tigelaar, Resident skin-specific $\gamma\delta$ T cells provide local, nonredundant regulation of cutaneous inflammation. *J. Exp. Med.* **195**, 855–867 (2002).
- M. Brandes, K. Willimann, B. Moser, Professional antigen-presentation function by human $\gamma\delta$ T cells. *Science* **309**, 264–268 (2005).
- Y. Wu, W. Wu, W. M. Wong, E. Ward, A. J. Thrasher, D. Goldblatt, M. Osman, P. Digard, D. H. Canaday, K. Gustafsson, Human $\gamma\delta$ T cells: A lymphoid lineage cell capable of professional phagocytosis. *J. Immunol.* **183**, 5622–5629 (2009).
- G. Stingl, K. C. Gunter, E. Tschachler, H. Yamada, R. I. Lechner, W. M. Yokoyama, G. Steiner, R. N. Germain, E. M. Shevach, Thy-1+ dendritic epidermal cells belong to the T-cell lineage. *Proc. Natl. Acad. Sci. U.S.A.* **84**, 2430–2434 (1987).
- D. M. Asarnow, W. A. Kuziel, M. Bonyhadi, R. E. Tigelaar, P. W. Tucker, J. P. Allison, Limited diversity of $\gamma\delta$ antigen receptor genes of Thy-1+ dendritic epidermal cells. *Cell* **55**, 837–847 (1988).
- T. Goodman, L. Lefrancois, Expression of the $\gamma\delta$ T-cell receptor on intestinal CD8+ intraepithelial lymphocytes. *Nature* **333**, 855–858 (1988).
- S. Kyes, E. Carew, S. R. Carding, C. A. Janeway Jr., A. Hayday, Diversity in T-cell receptor gene usage in intestinal epithelium. *Proc. Natl. Acad. Sci. U.S.A.* **86**, 5527–5531 (1989).
- S. Itohara, A. G. Farr, J. J. Lafaille, M. Bonneville, Y. Takagaki, W. Haas, S. Tonegawa, Homing of a $\gamma\delta$ thymocyte subset with homogeneous T-cell receptors to mucosal epithelia. *Nature* **343**, 754–757 (1990).
- N. Sumaria, B. Roediger, L. G. Ng, J. Qin, R. Pinto, L. L. Cavanagh, E. Shklovskaya, B. Fazekas de St Groth, J. A. Triccas, W. Weninger, Cutaneous immunosurveillance by self-renewing dermal $\gamma\delta$ T cells. *J. Exp. Med.* **208**, 505–518 (2011).

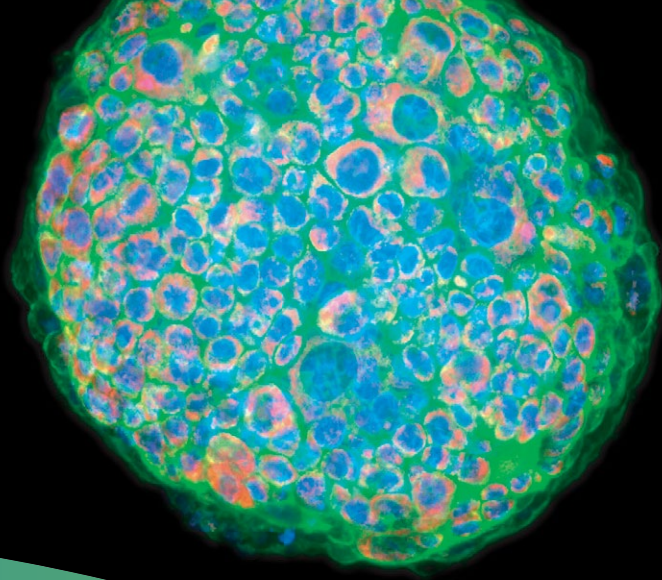
24. D. Guy-Grand, P. Vassalli, G. Eberl, P. Pereira, O. Burlen-Defranoux, F. Lemaître, J. P. Di Santo, A. A. Freitas, A. Cumano, A. Bandeira, Origin, trafficking, and intraepithelial fate of gut-tropic T cells. *J. Exp. Med.* **210**, 1839–1854 (2013).
25. P. Vantourout, A. Hayday, Six-of-the-best: Unique contributions of $\gamma\delta$ T cells to immunology. *Nat. Rev. Immunol.* **13**, 88–100 (2013).
26. C. Reardon, L. Lefrancois, A. Farr, R. Kubo, R. O'Brien, W. Born, Expression of $\gamma\delta$ T cell receptors on lymphocytes from the lactating mammary gland. *J. Exp. Med.* **172**, 1263–1266 (1990).
27. M. Hirano, P. Guo, N. McCurley, M. Schorpp, S. Das, T. Boehm, M. D. Cooper, Evolutionary implications of a third lymphocyte lineage in lampreys. *Nature* **501**, 435–438 (2013).
28. E. M. Steinert, J. M. Schenkel, K. A. Fraser, L. K. Beura, L. S. Manlove, B. Z. Iggyártó, P. J. Southern, D. Masopust, Quantifying memory CD8 T cells reveals regionalization of immunosurveillance. *Cell* **161**, 737–749 (2015).
29. D. B. Page, J. Yuan, D. Redmond, Y. H. Wen, J. C. Durack, R. Emerson, S. Solomon, Z. Dong, P. Wong, C. Comstock, A. Diab, J. Sung, M. Maybody, E. Morris, E. Brogi, M. Morrow, V. Sacchini, O. Elemento, H. Robins, S. Patil, J. P. Allison, J. D. Wolchok, C. Hudis, L. Norton, H. L. McArthur, Deep sequencing of T-cell receptor DNA as a biomarker of clonally expanded TILs in breast cancer after immunotherapy. *Cancer Immunol. Res.* **4**, 835–844 (2016).
30. D. Melandri, I. Zlatareva, R. A. G. Chaleil, R. J. Dart, A. Chancellor, O. Nussbaumer, O. Polyakova, N. A. Roberts, D. Wesch, D. Kabelitz, P. M. Irving, S. John, S. Mansour, P. A. Bates, P. Vantourout, A. C. Hayday, The $\gamma\delta$ TCR combines innate immunity with adaptive immunity by utilizing spatially distinct regions for agonist selection and antigen responsiveness. *Nat. Immunol.* **19**, 1352–1365 (2018).
31. R. Salgado, C. Denkert, S. Demaria, N. Sirtaine, F. Klauschen, G. Pruner, S. Wienert, G. Van den Eynden, F. L. Baehner, F. Penault-Llorca, E. A. Perez, E. A. Thompson, W. F. Symmans, A. L. Richardson, J. Brock, C. Criscitiello, H. Bailey, M. Ignatiadis, G. Floris, J. Sparano, Z. Kos, T. Nielsen, D. L. Rimm, K. H. Allison, J. S. Reis-Filho, S. Loibl, C. Sotiriou, G. Viale, S. Badve, S. Adams, K. Willard-Gallo, S. Loi, The evaluation of tumor-infiltrating lymphocytes (TILs) in breast cancer: Recommendations by an International TILs Working Group 2014. *Ann. Oncol.* **26**, 259–271 (2015).
32. L. Buisseret, S. Garaud, A. de Wind, G. Van den Eynden, A. Boisson, C. Solinas, C. Gu-Trantien, C. Naveaux, J.-N. Lodewyckx, H. Duvillier, L. Craciun, I. Veys, D. Larsimont, M. Piccart-Gebhart, J. Stagg, C. Sotiriou, K. Willard-Gallo, Tumor-infiltrating lymphocyte composition, organization and PD-1/PD-L1 expression are linked in breast cancer. *Oncimmunology* **6**, e1257452 (2016).
33. R. Nanda, L. Q. M. Chow, E. C. Dees, R. Berger, S. Gupta, R. Geva, L. Pusztai, K. Pathiraja, G. Aktan, J. D. Cheng, V. Karantzal, L. Buisseret, Pembrolizumab in patients with advanced triple-negative breast cancer: Phase Ib KEYNOTE-012 Study. *J. Clin. Oncol.* **34**, 2460–2467 (2016).
34. P. Schmid, S. Adams, H. S. Rugo, A. Schneeweiss, C. H. Barrios, H. Iwata, V. Diéras, R. Hegg, S.-A. Im, G. Shaw Wright, V. Henschel, L. Molinero, S. Y. Chui, R. Funke, A. Husain, E. P. Winer, S. Loi, L. A. Emens, Atezolizumab and nab-paclitaxel in advanced triple-negative breast cancer. *N. Engl. J. Med.* **379**, 2108–2121 (2018).
35. R. A. Clark, B. F. Chong, N. Mirchandani, K.-I. Yamanaka, G. F. Murphy, R. K. Dowgert, T. S. Kupper, A novel method for the isolation of skin resident T cells from normal and diseased human skin. *J. Invest. Dermatol.* **126**, 1059–1070 (2006).
36. R. A. Clark, B. Chong, N. Mirchandani, N. K. Brinster, K.-I. Yamanaka, R. K. Dowgert, T. S. Kupper, The vast majority of CLA+T cells are resident in normal skin. *J. Immunol.* **176**, 4431–4439 (2006).
37. R. Purwar, J. Campbell, G. Murphy, W. G. Richards, R. A. Clark, T. S. Kupper, Resident memory T cells (TRM) are abundant in human lung: Diversity, function, and antigen specificity. *PLOS ONE* **6**, e16245 (2011).
38. R. A. Clark, R. Watanabe, J. E. Teague, C. Schlapbach, M. C. Tawa, N. Adams, A. A. Dorosario, K. S. Chaney, C. S. Cutler, N. R. LeBoeuf, J. B. Carter, D. C. Fisher, T. S. Kupper, Skin effector memory T cells do not recirculate and provide immune protection in alemtuzumab-treated CTCL patients. *Sci. Transl. Med.* **4**, 117ra7 (2012).
39. S. Esin, M. Shigematsu, S. Nagai, A. Eklund, H. Wigzell, J. Grunewald, Different percentages of peripheral blood $\gamma\delta$ T cells in healthy individuals from different areas of the world. *Scand. J. Immunol.* **43**, 593–596 (1996).
40. R. Di Marco Barros, N. A. Roberts, R. J. Dart, P. Vantourout, A. Jandke, O. Nussbaumer, L. Deban, S. Cipolat, R. Hart, M. L. Iannitto, A. Laing, B. Spencer-Dene, P. East, D. Gibbons, P. M. Irving, P. Pereira, U. Steinhoff, A. Hayday, Epithelia use butyrophilin-like molecules to shape organ-specific $\gamma\delta$ T cell compartments. *Cell* **167**, 203–218.e17 (2016).
41. J. C. Ribot, A. deBarros, B. Silva-Santos, Searching for “signal 2”: Costimulation requirements of $\gamma\delta$ T cells. *Cell. Mol. Life Sci.* **68**, 2345–2355 (2011).
42. G. Chodaczek, V. Papanna, M. A. Zal, T. Zal, Body-barrier surveillance by epidermal $\gamma\delta$ TCRs. *Nat. Immunol.* **13**, 272–282 (2012).
43. A. R. Almeida, D. V. Correia, A. Fernandes-Platzgummer, C. L. da Silva, M. G. da Silva, D. R. Anjos, B. Silva-Santos, Delta one T cells for immunotherapy of chronic lymphocytic leukemia: Clinical-grade expansion/differentiation and preclinical proof of concept. *Clin. Cancer Res.* **22**, 5795–5804 (2016).
44. S. Hunter, C. R. Willcox, M. S. Davey, S. A. Kasatskaya, H. C. Jeffery, D. M. Chudakov, Y. H. Oo, B. E. Willcox, Human liver infiltrating $\gamma\delta$ T cells are composed of clonally expanded circulating and tissue-resident populations. *J. Hepatol.* **69**, 654–665 (2018).
45. V. Shankaran, H. Ikeda, A. T. Bruce, J. M. White, P. E. Swanson, L. J. Old, R. D. Schreiber, IFN γ and lymphocytes prevent primary tumour development and shape tumour immunogenicity. *Nature* **410**, 1107–1111 (2001).
46. J. Gao, L. Z. Shi, H. Zhao, J. Chen, L. Xiong, Q. He, T. Chen, J. Roszik, C. Bernatchez, S. E. Woodman, P.-L. Chen, P. Hwu, J. P. Allison, A. Futreal, J. A. Wargo, P. Sharma, Loss of IFN- γ pathway genes in tumor cells as a mechanism of resistance to anti-CTLA-4 therapy. *Cell* **167**, 397–404.e9 (2016).
47. J. M. Zaretsky, A. Garcia-Diaz, D. S. Shin, H. Escuin-Ordinatas, W. Hugo, S. Hu-Lieskovian, D. Y. Torrejon, G. Abril-Rodriguez, S. Sandoval, L. Barthly, J. Saco, B. Homett Moreno, R. Mezzadra, B. Chmielowski, K. Ruchalski, I. P. Shintaku, P. J. Sanchez, C. Puig-Saus, G. Cherry, E. Seja, X. Kong, J. Pang, B. Berent-Maoz, B. Comin-Anduix, T. G. Graeber, P. C. Tume, T. N. M. Schumacher, R. S. Lo, A. Ribas, Mutations associated with acquired resistance to PD-1 blockade in melanoma. *N. Engl. J. Med.* **375**, 819–829 (2016).
48. M. Ayers, J. Lunceford, M. Nebozhyn, E. Murphy, A. Loboda, D. R. Kaufman, A. Albright, J. D. Cheng, S. P. Kang, V. Shankaran, S. A. Piha-Paul, J. Yearley, T. Y. Seiwert, A. Ribas, T. K. McClanahan, IFN- γ -related mRNA profile predicts clinical response to PD-1 blockade. *J. Clin. Invest.* **127**, 2930–2940 (2017).
49. G. Crawford, M. D. Hayes, R. C. Seoane, S. Ward, T. Dalessandro, C. Lai, E. Healy, D. Kipling, C. Proby, C. Moyes, K. Green, K. Best, M. Haniffa, M. Botto, D. Dunn-Walters, J. Strid, Epithelial damage and tissue $\gamma\delta$ T cells promote a unique tumor-protective IgE response. *Nat. Immunol.* **19**, 859–870 (2018).
50. P. Wu, D. Wu, C. Ni, J. Ye, W. Chen, G. Hu, Z. Wang, C. Wang, Z. Zhang, W. Xia, Z. Chen, K. Wang, T. Zhang, J. Xu, Y. Han, T. Zhang, X. Wu, J. Wang, W. Gong, S. Zheng, F. Qiu, J. Yan, J. Huang, $\gamma\delta$ T17 cells promote the accumulation and expansion of myeloid-derived suppressor cells in human colorectal cancer. *Immunity* **40**, 785–800 (2014).
51. S. B. Coffelt, K. Kersten, C. W. Doornbehal, J. Weiden, K. Vrijland, C.-S. Hau, N. J. M. Verstegen, M. Ciampicotti, L. J. A. C. Hawinkels, J. Jonkers, K. E. de Visser, IL-17-producing $\gamma\delta$ T cells and neutrophils conspire to promote breast cancer metastasis. *Nature* **522**, 345–348 (2015).
52. C. Jin, G. K. Lagoudas, C. Zhao, S. Bullman, A. Bhutkar, B. Hu, S. Arme, D. Sandel, X. S. Liang, S. Mazzilli, M. T. Whary, M. Meyerson, R. Germain, P. C. Blainey, J. G. Fox, T. Jacks, Commensal microbiota promote lung cancer development via $\gamma\delta$ T cells. *Cell* **176**, 998–1013.e16 (2019).
53. N. Caccamo, C. La Mendola, V. Orlando, S. Meraviglia, M. Todaro, G. Stassi, G. Sireci, J. J. Fournié, F. Dieli, Differentiation, phenotype, and function of interleukin-17-producing human V9V62 T cells. *Blood* **118**, 129–138 (2011).
54. P. Muranski, N. P. Restifo, Essentials of Th17 cell commitment and plasticity. *Blood* **121**, 2402–2414 (2013).
55. L. K. Beura, N. J. Fares-Frederickson, E. M. Steinert, M. C. Scott, E. A. Thompson, K. A. Fraser, J. M. Schenkel, V. Vezy, D. Masopust, CD4 $^{+}$ resident memory T cells dominate immunosurveillance and orchestrate local recall responses. *J. Exp. Med.* **216**, 1214–1229 (2019).
56. V. Groh, R. Rhinehart, J. Randolph-Habecker, M. S. Topp, S. R. Riddell, T. Spies, Costimulation of CD8 $\alpha\beta$ T cells by NKG2D via engagement by MIC induced on virus-infected cells. *Nat. Immunol.* **2**, 255–260 (2001).
57. A. M. Jamieson, A. Diefenbach, C. W. McMahon, N. Xiong, J. R. Carlyle, D. H. Raulet, The role of the NKG2D immunoreceptor in immune cell activation and natural killing. *Immunity* **17**, 19–29 (2002).
58. M. Wencker, G. Turchinovich, R. Di Marco Barros, L. Deban, A. Jandke, A. Cope, A. C. Hayday, Innate-like T cells straddle innate and adaptive immunity by altering antigen-receptor responsiveness. *Nat. Immunol.* **15**, 80–87 (2013).
59. C. Solinas, D. Marcoux, S. Garaud, J. R. Vitória, G. Van den Eynden, A. de Wind, P. De Silva, A. Boisson, L. Craciun, D. Larsimont, M. Piccart-Gebhart, V. Detours, D. T. de Roodenbeke, K. Willard-Gallo, BRCA gene mutations do not shape the extent and organization of tumor infiltrating lymphocytes in triple negative breast cancer. *Cancer Lett.* **450**, 88–97 (2019).
60. K. F. Goliwas, J. R. Richter, H. C. Pruitt, L. M. Araysi, N. R. Anderson, R. S. Samant, S. M. Lobo-Ruppert, J. L. Berry, A. R. Frost, Methods to evaluate cell growth, viability, and response to treatment in a tissue engineered breast cancer model. *Sci. Rep.* **7**, 14167 (2017).
61. A. A. Jungbluth, D. Frosina, M. Fayad, M. P. Pulitzer, A. Dogan, K. J. Busam, N. Imai, S. Gnjatic, Immunohistochemical detection of $\gamma\delta$ T lymphocytes in formalin-fixed paraffin-embedded tissues. *Appl. Immunohistochem. Mol. Morphol.* **27**, 581–583 (2018).
62. P. Savas, B. Virassamy, C. Ye, A. Salim, C. P. Mintoff, F. Caramia, R. Salgado, D. J. Byrne, Z. L. Teo, S. Dushyanthen, A. Byrne, L. Wein, S. J. Luen, C. Poliness, S. S. Nightingale, A. S. Skandarajah, D. E. Gyorki, C. M. Thornton, P. A. Beavis, S. B. Fox, Single-cell profiling of breast cancer T cells reveals a tissue-resident memory subset associated with improved prognosis. *Nat. Med.* **24**, 986–993 (2018).

63. A. M. Sherwood, R. O. Emerson, D. Scherer, N. Habermann, K. Buck, J. Staffa, C. Desmarais, N. Halama, D. Jaeger, P. Schirmacher, E. Herpel, M. Kloos, A. Ulrich, M. Schneider, C. M. Ulrich, H. Robins, Tumor-infiltrating lymphocytes in colorectal tumors display a diversity of T cell receptor sequences that differ from the T cells in adjacent mucosal tissue. *Cancer Immunol. Immunother.* **62**, 1453–1461 (2013).
64. W. Schepers, S. Kelderman, L. F. Fanchi, C. Linnemann, G. Bendle, M. A. J. de Rooij, C. Hirt, R. Mezzadra, M. Slagter, K. Dijkstra, R. J. C. Kluij, P. Snaebjornsson, K. Milne, B. H. Nelson, H. Zijlmans, G. Kenter, E. E. Voest, J. B. A. G. Haanen, T. N. Schumacher, Low and variable tumor reactivity of the intratumoral TCR repertoire in human cancers. *Nat. Med.* **25**, 89–94 (2019).
65. E. P. Rock, P. R. Sibbald, M. M. Davis, Y. H. Chien, CDR3 length in antigen-specific immune receptors. *J. Exp. Med.* **179**, 323–328 (1994).
66. H.-J. Gober, M. Kistowska, L. Angman, P. Jenö, L. Mori, G. De Libero, T. Human, Human T cell receptor $\gamma\delta$ cells recognize endogenous mevalonate metabolites in tumor cells. *J. Exp. Med.* **197**, 163–168 (2003).
67. F. Davodeau, M. A. Peyrat, M. M. Hallet, I. Houde, H. Vié, M. Bonneville, Peripheral selection of antigen receptor junctional features in a major human $\gamma\delta$ subset. *Eur. J. Immunol.* **23**, 804–808 (1993).
68. S. Yamashita, Recognition mechanism of non-peptide antigens by human T cells. *Int. Immunol.* **15**, 1301–1307 (2003).
69. F. S. Hodin, S. J. O'Day, D. F. McDermott, R. W. Weber, J. A. Sosman, J. B. Haanen, R. Gonzalez, C. Robert, D. Schadendorf, J. C. Hassel, W. Akerley, A. J. M. van den Eertwegh, J. Lutzky, P. Lorigan, J. M. Vaubel, G. P. Linette, D. Hogg, C. H. Ottensmeier, C. Lebbé, C. Peschel, I. Quirt, J. I. Clark, J. D. Wolchok, J. S. Weber, J. Tian, M. J. Yellin, G. M. Nichol, A. Hoos, W. J. Urba, Improved survival with ipilimumab in patients with metastatic melanoma. *N. Engl. J. Med.* **363**, 711–723 (2010).
70. S. L. Topalian, F. S. Hodin, J. R. Brahmer, S. N. Gettinger, D. C. Smith, D. F. McDermott, J. D. Powderly, R. D. Carvajal, J. A. Sosman, M. B. Atkins, P. D. Leming, D. R. Spigel, S. J. Antonia, L. Horn, C. G. Drake, D. M. Pardoll, L. Chen, W. H. Sharfman, R. A. Anders, J. M. Taube, T. L. McMiller, H. Xu, A. J. Korman, M. Jure-Kunkel, S. Agrawal, D. McDonald, G. D. Kollia, A. Gupta, J. M. Wigginton, M. Sznoł, Safety, activity, and immune correlates of anti-PD-1 antibody in cancer. *N. Engl. J. Med.* **366**, 2443–2454 (2012).
71. E. G. Perdiguer, K. Klaproth, C. Schulz, K. Busch, E. Azzoni, L. Crozet, H. Garner, C. Trouillet, M. F. de Brujin, F. Geissmann, H.-R. Rodewald, Tissue-resident macrophages originate from yolk-sac-derived erythro-myeloid progenitors. *Nature* **518**, 547–551 (2015).
72. D. Masopust, A. G. Soeren, Tissue-resident T cells and other resident leukocytes. *Annu. Rev. Immunol.* **37**, 521–546 (2019).
73. N. A. Zumwalde, J. D. Haag, D. Sharma, J. A. Mirrilees, L. G. Wilke, M. N. Gould, J. E. Gumperz, Analysis of immune cells from human mammary ductal epithelial organoids reveals V62+ T cells that efficiently target breast carcinoma cells in the presence of bisphosphonate. *Cancer Prev. Res. (Phila.)* **9**, 305–316 (2016).
74. T. Yamaguchi, M. Hiratsuka, K. Asai, K. Kai, K. Kumagai, Differential distribution of T lymphocyte subpopulations in the bovine mammary gland during lactation. *J. Dairy Sci.* **82**, 1459–1464 (1999).
75. C. A. Egelston, C. Avalos, T. Y. Tu, D. L. Simons, G. Jimenez, J. Y. Jung, L. Melstrom, K. Margolin, J. H. Yim, L. Kruper, J. Mortimer, P. P. Lee, Human breast tumor-infiltrating CD8⁺ T cells retain polyfunctionality despite PD-1 expression. *Nat. Commun.* **9**, 4297 (2018).
76. N. A. Rizvi, M. D. Hellmann, A. Snyder, P. Kvistborg, V. Makarov, J. J. Havel, W. Lee, J. Yuan, P. Wong, T. S. Ho, M. L. Miller, N. Rekhtman, A. L. Moreira, F. Ibrahim, C. Bruggeman, B. Gasmi, R. Zappasodi, Y. Maeda, C. Sander, E. B. Garon, T. Merghoub, J. D. Wolchok, T. N. Schumacher, T. A. Chan, Mutational landscape determines sensitivity to PD-1 blockade in non-small cell lung cancer. *Science* **348**, 124–128 (2015).
77. N. McGranahan, A. J. S. Furness, R. Rosenthal, S. Ramskov, R. Lyngaa, S. K. Saini, M. Jamal-Hanjani, G. A. Wilson, N. J. Birkbak, C. T. Hiley, T. B. K. Watkins, S. Shafii, N. Muruganesu, R. Mitter, A. U. Akcar, J. Linares, T. Marafioti, J. Y. Henry, E. M. Van Allen, D. Miao, B. Schilling, D. Schadendorf, L. A. Garraway, V. Makarov, N. A. Rizvi, A. Snyder, M. D. Hellmann, T. Merghoub, J. D. Wolchok, S. A. Shukla, C. J. Wu, K. S. Peggs, T. A. Chan, S. R. Hadrup, S. A. Quezada, C. Swanton, Clonal neoantigens elicit T cell immunoreactivity and sensitivity to immune checkpoint blockade. *Science* **351**, 1463–1469 (2016).
78. N. McGranahan, R. Rosenthal, C. T. Hiley, A. J. Rowan, T. B. K. Watkins, G. A. Wilson, N. J. Birkbak, S. Veeriah, P. Van Loo, J. Herrero, C. Swanton; TRACERx Consortium, Allele-specific HLA loss and immune escape in lung cancer evolution. *Cell* **171**, 1259–1271.e11 (2017).
79. R. Rosenthal, E. L. Cadieux, R. Salgado, M. A. Bakir, D. A. Moore, C. T. Hiley, T. Lund, M. Tanić, J. L. Reading, K. Joshi, J. Y. Henry, E. Ghorani, G. A. Wilson, N. J. Birkbak, M. Jamal-Hanjani, S. Veeriah, Z. Szallasi, S. Loi, M. D. Hellmann, A. Feber, B. Chain, J. Herrero, S. A. Quezada, J. Demeulemeester, P. Van Loo, S. Beck, N. McGranahan, C. Swanton, Neoantigen-directed immune escape in lung cancer evolution. *Nature* **567**, 479–485 (2019).
80. M. Brandes, K. Willimann, G. Bioley, N. Lévy, M. Eberl, M. Luo, R. Tampe, F. Lévy, P. Romero, B. Moser, Cross-presenting human $\gamma\delta$ T cells induce robust CD8⁺ $\alpha\beta$ T cell responses. *Proc. Natl. Acad. Sci. U.S.A.* **106**, 2307–2312 (2009).
81. A. Facciabene, X. Peng, I. S. Hagemann, K. Balint, A. Barchetti, L.-P. Wang, P. A. Gimotty, C. B. Gilks, P. Lal, L. Zhang, G. Coukos, Tumour hypoxia promotes tolerance and angiogenesis via CCL28 and T_{reg} cells. *Nature* **475**, 226–230 (2011).
82. T. R. Cox, R. M. H. Rumney, E. M. Schoof, L. Perryman, A. M. Høye, A. Agrawal, D. Bird, N. A. Latif, H. Forrest, H. R. Evans, I. D. Huggins, G. Lang, R. Linding, A. Gartland, J. T. Erler, The hypoxic cancer secretome induces pre-metastatic bone lesions through lysyl oxidase. *Nature* **522**, 106–110 (2015).
83. A. J. Gentles, A. M. Newman, C. L. Liu, S. V. Bratman, W. Feng, D. Kim, V. S. Nair, Y. Xu, A. Khuong, C. D. Hoang, M. Diehn, R. B. West, S. K. Plevritis, A. A. Alizadeh, The prognostic landscape of genes and infiltrating immune cells across human cancers. *Nat. Med.* **21**, 938–945 (2015).
84. W. He, J. Hao, S. Dong, Y. Gao, J. Tao, H. Chi, R. Flavell, R. L. O'Brien, W. K. Born, J. Craft, J. Han, P. Wang, L. Zhao, J. Wu, Z. Yin, Naturally activated V γ 4 γ 8 T cells play a protective role in tumor immunity through expression of eomesodermin. *J. Immunol.* **185**, 126–133 (2010).
85. J. Hao, S. Dong, S. Xia, W. He, H. Jia, S. Zhang, J. Wei, R. L. O'Brien, W. K. Born, Z. Wu, P. Wang, J. Han, Z. Hong, L. Zhao, Z. Yin, Regulatory role of V γ 1 γ 8 T cells in tumor immunity through IL-4 production. *J. Immunol.* **187**, 4979–4986 (2011).
86. A. C. Hayday, $\gamma\delta$ T cell update: Adaptate orchestrators of immune surveillance. *J. Immunol.* **203**, 311–320 (2019).
87. C. Harly, Y. Guillaume, S. Nedellec, C.-M. Peigné, H. Mönkkönen, J. Mönkkönen, J. Li, J. Kuball, E. J. Adams, S. Netzer, J. Déchanet-Merville, A. Léger, T. Herrmann, R. Breathnach, D. Olive, M. Bonneville, E. Scotet, Key implication of CD277/butyrophilin-3 (BTN3A) in cellular stress sensing by a major human $\gamma\delta$ T-cell subset. *Blood* **120**, 2269–2279 (2012).
88. Oncomine, 2019; www.oncomine.org/.

Acknowledgments: We thank A. Clifford, S. Irshad, and T. Alaguthurai for consenting and recruiting patients and current and former colleagues for helpful advice and discussions. We thank the flow cytometry service units of the Peter Gorer Department of Immunobiology and the Guy's and St Thomas' Hospital Trust Biomedical Research Centre (BRC) for outstanding support. **Funding:** The work was supported by a Wellcome Trust (WT) Investigator Award (106292/Z/14/Z) to A.H. and by the Francis Crick Institute, which receives its core funding from CRUK (FC001093), the UK Medical Research Council (FC001093), and the WT (FC001093). F.K.-C. was funded by a BRC fellowship. Y.W. was funded by a National Institute for Health Research fellowship. R.T.W. was funded by a Medical Research Council (UK) fellowship and a National Institute for Health Research lectureship. A.G. and A.T. were funded by Breast Cancer Now funding at King's College London. The work was conducted as part of the CRUK Cancer Immune Therapy Accelerator (CITA) and the CRUK City of London Major Centre. **Author contributions:** F.K.-C., Y.W., R.T.W., and A.H. conceived the study and designed experiments. F.K.-C. and Y.W. performed and analyzed experiments. C.N.-L., J.O., and P.G. processed patient samples and provided technical assistance. A.G., A.L., D.B., and P.V. assisted with data analysis. A.T. recruited patients. F.K.-C., Y.W., and A.H. wrote the manuscript. A.T. and A.H. supervised the study. **Competing interests:** A.H. is a cofounder and equity holder in GammaDelta Therapeutics PLC. **Data and materials availability:** All data associated with this study are present in the paper or Supplementary Materials. TCR sequences are deposited at <https://osf.io/d4eu6/>.

Submitted 12 May 2019
Accepted 19 September 2019
Published 9 October 2019
10.1126/scitranslmed.aax9364

Citation: Y. Wu, F. Kyle-Cezar, R. T. Woolf, C. Naceur-Lombardelli, J. Owen, D. Biswas, A. Lorenc, P. Vantourout, P. Gazinska, A. Grigoriadis, A. Tutt, A. Hayday, An innate-like V δ 1 γ 8 T cell compartment in the human breast is associated with remission in triple-negative breast cancer. *Sci. Transl. Med.* **11**, eaax9364 (2019).



CAPTURE the micro moments that matter

NEW Water Immersion Objectives

Gain the sensitivity to capture more phenotypic data at greater depths. Our high-content imagers and team are here to help your lab simplify imaging and analysis of complex, 3D assay workflows and fast-track discoveries.



Learn more at
moleculardevices.com/water

For Research Use Only. Not for use in diagnostic procedures.
© 2020 Molecular Devices, LLC. All Rights Reserved. The trademarks mentioned herein are the property of Molecular Devices, LLC or their respective owners.

1:41 PM JUL 05, 2023

THE MOMENT YOUR
RESEARCH MOVES FROM
BENCH TO BEDSIDE



THE DIFFERENCE OF **BREAKTHROUGH RESEARCH** **TO ENABLE MORE CURES**

WITH BD AS YOUR PARTNER IN IMMUNO-ONCOLOGY FROM BENCH TO BEDSIDE. BD is your partner in immuno-oncology from discovery research to clinical applications, with a range of high-performance solutions designed to give you high-quality, reliable research data for even the most complex experiments. More solutions. More answers. More data you can trust. Discover more with BD at your side. **Discover the new BD.**

Learn more at bd.com/Immuno-oncology

For Research Use Only. Not for use in diagnostic or therapeutic procedures.
BD, San Jose, CA, 95131, U.S.

BD and the BD Logo are trademarks of Becton, Dickinson and Company or its affiliates. © 2019 BD. All rights reserved. (0619)



Advancing the
world of health



be INSPIRED
drive DISCOVERY
stay GENUINE

Flexible Precision.

NEBNext Direct® Custom Ready Panels for NGS target enrichment

Employing the unique NEBNext Direct hybridization-based enrichment method, NEBNext Direct Custom Ready Panels allow rapid customization of targeted gene panels for Illumina® sequencing. Select from a list of genes for which baits have been carefully designed and optimized to give complete coverage of the full coding regions. High quality panels can be designed by you and rapidly delivered, from any combination of genes. NEBNext Direct Custom Ready Panels provide the content you want with the performance you need.

- Choose from a single gene to hundreds of genes
- Experience unmatched specificity and coverage uniformity
- Eliminate synthesis and optimization steps for faster turnaround
- Improve sensitivity with our Unique Molecule Index (UMI)
- Generate results in one day with our automation-friendly workflow

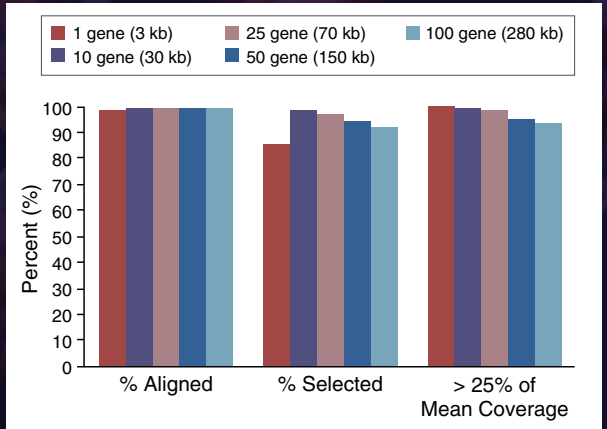
For more information visit

NEBNextDirect.com

For research use only; not intended for diagnostic use.
One or more of these products are covered by patents, trademarks and/or copyrights owned or controlled by New England Biolabs, Inc.
For more information, please email us at gbd@neb.com.
The use of these products may require you to obtain additional third party intellectual property rights for certain applications.
ILLUMINA® is a registered trademark of Illumina, Inc.
© Copyright 2018, New England Biolabs, Inc.; all rights reserved.



NEBNext Direct Custom Ready Panels demonstrate optimum performance across a wide range of panel sizes



Key target enrichment metrics demonstrate consistent performance across a range of panel sizes. 100 ng of DNA was tested against panels of 1, 10, 25, 50 and 100 genes, and sequenced using Illumina® paired-end 150 bp sequencing. Larger panels included all genes present in smaller panels.

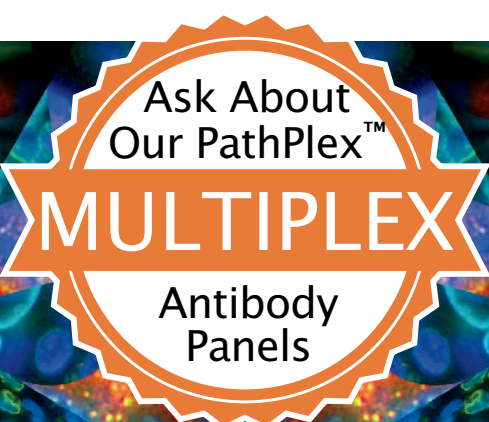


Brilliant visualization

See the difference to make big breakthroughs
in your tumor microenvironment research

In the world of next generation immuno-oncology research, having confidence in your immunoassay results is vital. Unfortunately, 75% of antibodies in today's market are non-specific or simply do not work at all.* That's why at Bethyl, we manufacture and validate every antibody on-site to ensure target specificity and sensitivity. More than 10,000 independent citations over the past 15 years have proven that our antibodies will function as designed in your assay — and we offer a 100% guarantee. Work with Bethyl to bring your discovery into full focus.

See our data at bethyl.com/immuno-oncology



Ask About
Our PathPlex™

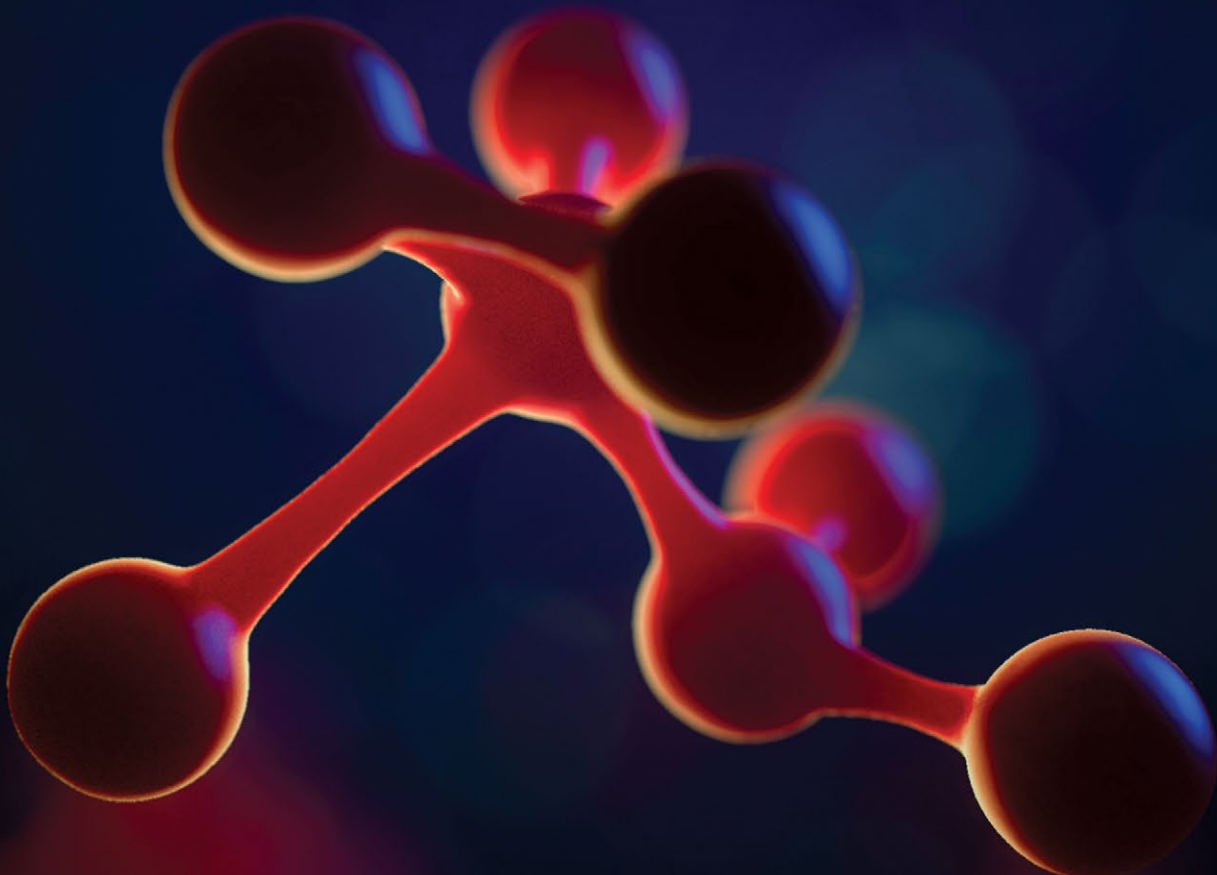
MULTIPLEX

Antibody
Panels

*Weller, MG, Analytical Chemistry Insights:11, 21-27 (2016).
Antibodies shown: PD-L1 (A700-016) & Lamin A/C (A303-430A)
©2019 Bethyl Laboratories, Inc. All rights reserved.



BETHYL
LABORATORIES, INC.
Really Good Antibodies



Publish your research in the *Science* family of journals

The *Science* family of journals (*Science*, *Science Advances*, *Science Immunology*, *Science Robotics*, *Science Signaling*, and *Science Translational Medicine*) are among the most highly-regarded journals in the world for quality and selectivity. Our peer-reviewed journals are committed to publishing cutting-edge research, incisive scientific commentary, and insights on what's important to the scientific world at the highest standards.

Submit your research today!

Learn more at ScienceMag.org/journals

Science
JOURNALS AAAS